Computational fluid dynamics of gassed-stirred fermenters

Gunyol, Ozgur

DOI
10.4233/uuid:9b1d76da-8da9-4bb0-b8df-957652831e90

Publication date
2017

Document Version
Final published version

Citation (APA)
Gunyol, O. (2017). *Computational fluid dynamics of gassed-stirred fermenters*. [Dissertation (TU Delft), Delft University of Technology]. https://doi.org/10.4233/uuid:9b1d76da-8da9-4bb0-b8df-957652831e90

Important note
To cite this publication, please use the final published version (if applicable).
Please check the document version above.

Computational fluid dynamics of gassed-stirred fermenters

Computational fluid dynamics of gassed-stirred fermenters

Proefschrift

ter verkrijging van de graad van doctor
aan de Technische Universtiteit Delft,
op gezag van de Rector Magnificus prof.ir. K.C.A.M. Luyben,
voorzitter van het College van Promoties,
in het openbaar te verdedigen op
dinsdag 26 september 2017 om 15:00 uur

door

Özgür GÜNYOL

Master of Science in Process Engineering
Hamburg University of Technology, Germany
geboren te Ankara, Turkije

This dissertation has been approved by the
promotor: Prof.dr. R.F. Mudde

Composition of the doctoral committee:

Rector Magnificus	chairperson
Prof.dr. R.F. Mudde	Delft University of Technology, promotor
Independent members:	
Prof.dr.ir. J.J. Derksen	University of Aberdeen
Prof.dr.ir. H.E.A. van den Akker	University of Limerick, Delft University of Technology
Prof.dr.ir. N.G. Deen	Eindhoven University of Technology
Prof.dr. D.J.E.M. Roekaerts	Delft University of Technology
Prof.dr.ir. M.K. de Kreuk	Delft University of Technology
Other members:	
Prof.dr.ir. H.J. Noorman	DSM N.V., Delft University of Technology
Reserve member:	
Prof.dr. C.R. Kleijn	Delft University of Technology

This research was funded by Koninklijke DSM N.V.

Cover design: Özlem Günyol & Mustafa Kunt

Printed by GVO drukkers & vormgevers B.V. in the Netherlands

ISBN 978-94-6332-236-2

Summary

The current understanding of the transport phenomena involved in the operation of industrial fermenters is not sufficient. This is reflected by the limitations seen in their design and operation. A better insight in the local processes taking place (hydrodynamics, gas dispersion, mixing, microbial kinetics) is required to be able to make a step change in the design of those reactors. At the scale of industrially relevant fermenters, experimental methods become quickly limited when detailed information is needed. It was the aim of this research to provide a framework where such information could be gained by means of Computational Fluid Dynamics (CFD) simulations with a manageable computational burden so that it could readily be used by the industrial practitioners.

The main focus of this thesis is on the hydrodynamics of bubbly flows in stirred reactors, although, scalar mixing and substrate uptake kinetics studies were also conducted. Because the literature on the standard configured lab/pilot scale single-impeller reactors is vast and the experimental data is abundant, we chose to start with such a system first and, with the learnings gained, move ultimately to realistic industrial scale multi-impeller fermenters. We also limited ourselves to Rushton type radial pumping disk turbine systems, again on the basis of available data for validation, and also due to time limitations.

Single-phase

A single-phase flow study was conducted initially that formed the first level of validation of the modelling approach developed. Both SM (sliding mesh) and MRF (multiple reference frame) techniques were adopted, which are the standard impeller modelling approaches in the majority of recent literature. Multiple turbulence modelling approaches were also adopted at this stage, namely the conventional $k-\varepsilon$ model and the realisable and RNG variations of it, as well as the more rigorous RSM (Reynolds stress model). Results showed that good predictions of the turbulent flow characteristics could be obtained by a simplified modelling approach where computational costs were greatly reduced by assuming flow periodicity thus limiting the domain to only a 60° sector of the reactor, employing a steady-state MRF model and using the conventional $k-\varepsilon$ model. Additional levels of complexity in the modelling approach did not result in a significant improvement generally for the predicted quantities reported. One major finding in this respect was that, good predictions of the turbulent energy dissipation ε, the dissipation-based power draw N_{P_ε} and the turbulent kinetic energy

k were possible, provided that the grid had a sufficient resolution. In previous studies that employ $k-\varepsilon$ model, substantial underpredictions (up to 50%) of those quantities were commonly reported and this was widely regarded as a well-known limitation of the turbulence model in literature. Using a grid of 140k (for a 60° sector), the underprediction of N_{P_ε} was only 5%. Predictions of the impeller flow number were also in good agreement with the experimental values, both for the tank and the fermenter. Those findings suggested a good basis for an efficient and affordable multiphase simulation framework for gassed-stirred systems where computational costs could be about an order of magnitude higher than that for single-phase simulations.

Two-phase

The two-phase simulations were mainly based on the conventional Euler–Euler (two-fluid) framework because gassing rates could be significant in standard operation of fermenters. There has been (and still is) considerable debate about the proper formulation of the two-fluid model equations, particularly about the closure relations. Therefore, we provided a substantial review of the theoretical framework in this thesis. We hope that this would serve the young researchers in the area well.

The two-phase flow study was started initially with the modelling of the single-impeller tank. It became quickly clear that the prediction of the overall gas holdup and the gas distribution in the tank was a real challenge (which seemed specific to stirred systems as bubble column simulations were found not to be suffering from this). The drag formulation was the prominant modelling factor although all the drag laws implemented (including those for deforming bubbles) still substantially underpredicted the holdup unless a turbulence modulation was used. The Brucato model used for this purpose was found not to be universally valid at varying stirring and gassing rates and for large-scale multi-impeller systems. In this respect, it does not come as a surprise that many studies in literature typically use constant slip velocities from experiments or fitted parameters in their drag models which are tuned to a specific operating condition. Although we do not have yet an universally valid drag formulation for turbulent gassed-stirred systems (which is an active research area), the flow regime transition from loading to flooding in the fermenter was predicted well with the modelling approach adopted. Furthermore, for the high gas loading case in the fermenter, the Ishii & Zuber multiparticle drag law accounting for the bubble swarm effect resulted in a good prediction of holdup without employing a fitted parameter or a turbulent modulation. At those relatively high gas loadings ($\sim$ 20%), we recommend the degassing outlet boundary condition over the pressure outlet, especially if the top impeller is close to the free surface.

Bubble size predictions made with the discrete population balance model (with standard breakage and coalescence kernels of Luo) were generally good. Spatial distribution of Sauter diameter throughout the tank was predicted reasonably well, except near the impeller where d_{32} was overpredicted at several locations. For the fermenter studied, there was no local bubble size measurement data available to compare, possibly due to experimental difficulties at such a scale. The overall mean Sauter diameters predicted were much larger than that for the lab-scale standard stirred tank, and were in accordance with the bubble size range commonly observed in industrial fermenters, namely $6-10$ mm.

Scalar mixing

The tracer response study conducted in the fermenter (single-phase) showed that the turbulent Schmidt number was the key parameter for predicting the mixing time in a system with multiple radial turbines that is prone to compartmentalisation. In the simple turbulence modelling approach adopted (steady RANS), Sc_t compensates for the lack of convective exchange of tracer by the mean flow across the impeller zones. The value of the turbulent Schmidt number depends on the local flow characteristics and a wide range of values ($0.1 \leq Sc_t \leq 1.3$) have been used in literature depending on the particular application. Using the value of $Sc_t = 0.2$, we obtained good predictions of mixing and lag times as well as the full tracer response curves for both 70 and 115 rpm operation. Tracer injection and detection locations also influence the shape of response curves and the computed mixing time. Shortest mixing times were detected near the axial center of the fermenter, in agreement with the experiments. The injection method has also an influence if injection points are not localised in a single impeller compartment. The shortest mixing time was achieved when the tracer was introduced individually at each impeller region. Again, results showed that a good prediction of scalar macro– and mesomixing, in terms of mixing times and tracer response curves, could be obtained by the rather simple and computationally cheap modelling approach.

Case study: 30 m^3 fermenter

In the final part of the thesis, we applied the approach developed throughout this study to an industrially relevant case, namely, the substrate uptake kinetics in the gassed-stirred fermenter. Monod kinetics was used to model the glucose limited growth of Saccharomyces cerevisiae. General trends of substrate gradients were well captured with the adopted simulation method. This is despite our finding that species mass conservation was not satisfied due to a limitation in the Fluent code when the Eulerian multiphase model with species transport was coupled with periodic boundary conditions. The predicted glucose substrate concentrations in the tank (using again the value of $Sc_t = 0.2$ from the earlier mixing study) were also fairly good with respect to the measurements reported in literature, giving a mean error of 30.1%.

Overall, results outlined above suggest that the established modelling framework could be used as a computationally managable tool that supports bioreactor design, optimisation and troubleshooting. There are clear limitations, both due to our current understanding of turbulent bubbly flows and their modelling, and due to the simplified modelling approach undertaken. For a more detailed analysis including the transient effects (e.g. start-up, feed rate changes, macroinstabilities developed in the reactor, complex biokinetics with history effects, etc.) one has to resort to a different computational strategy such as an Euler–Langrange framework (to track actual local kinetics of microbial clusters along their trajectories) coupled with the sliding mesh technique (to include impeller–baffle interactions) in a full 360° sector domain (to capture macroinstabilities and asymmetric gas cavity regimes). Furthermore, a smaller time step will have to be taken if one is interested to model detailed metabolics, as we found out that the time evolution of concentrations were more sensitive to the time step than the steady-state values reached. However, the RANS approach for turbulence would continue to be the workhorse as DNS and LES seem still out of reach for practical

use in the modelling of industrial scale fermenters. The computational cost of such a transient approach would be dramatically higher. A two-stage process could then be employed where initial steady characteristics are resolved for a large number of situations by the modelling approach presented in this thesis and a detailed transient analysis is performed in the second stage for a limited number of cases.

Samenvatting

De huidige kennis over transport verschijnselen in industriële vergisters is niet volledig. Dit uit zich in beperkingen in het ontwerp en gebruik van deze vergisters. Een beter inzicht in de lokale processen in de reactor (hydrodynamica, de verspreiding van gassen, mengen en microbiële kinetica) is noodzakelijk om de volgende stap te maken in het ontwerp van de reactor. Echter, op een industriële schaal zijn de experimentele methoden al snel beperkt wanneer gedetailleerde informatie vereist is. Het doel van dit onderzoek is om een methode te bepalen waarmee deze informatie verkregen kan worden via computational fluid dynamics (CFD) simulaties met een berekeningslast die geschikt zijn voor de industriële gebruiker.

De focus van dit onderzoek ligt op de hydrodynamica van stromingen met bellen in reactoren met een roerwerk. Daarnaast zijn ook scalaire mengprocessen en substraat opname studies uitgevoerd. Aangezien er veel literatuur en experimentele data beschikbaar is over de standaard geconfigureerde lab/pilot schaal reactoren met een enkelvoudige impeller, is er besloten om te starten met dit systeem. De daarbij opgedane kennis is gebruikt als start voor een studie over realistische multi-impeller reactoren op een industriële schaal. Verder is er op basis van de hoeveelheid beschikbare data en tijd gekozen om te focusseren op Rushton type disk turbine systemen.

Eenfase

Als eerste is een eenfase stromingsstudie uitgevoerd. Deze studie vormt de eerste validatie van de ontwikkelde modelleringsaanpak. Zowel SM (sliding mesh) als MRF (multiple reference frame) technieken zijn gebruikt. Deze technieken worden standaard toegepast in de meerderheid van de recente literatuur. Ook zijn verschillende technieken voor het modelleren van turbulentie al in deze fase van het onderzoek gebruikt, namelijk het algemeen gebruikte $k - \varepsilon$ model en de realiseerbare en RNG variabelen daarvan, alsmede het meer rigoreuze RSM (Reynolds stress model). De resultaten lieten zien dat het mogelijk is om goede voorspellingen te doen van de turbulente stromingskarakteristieken op basis van een gesimplificeerd model waar de berekeningskosten sterk verkleind werden door aan te nemen dat de stroming een rotatiesymmetrie bezit. Daarmee wordt het domein verkleind tot een 60° sector van de reactor, waarbij een MRF model in stationaire toestand en het conventionele $k - \varepsilon$ model gebruikt worden. Het toevoegen van extra lagen van complexiteit leidde niet tot een significante verbetering in de voorspellende waarden van het model. Een belangrijke bevinding was dat goede voorspellingen van de dissipatie van turbulentie energie ε, de

op dissipatie gebaseerde impeller krachtconsumptie N_{P_ε} en de turbulente kinetische energie k mogelijk waren wanneer het grid voldoende resolutie bevatte. In eerdere studies die gebruik maken van het $k-\varepsilon$ model werden substantiële onderschattingen (tot 50%) van deze hoeveelheden gerapporteerd en dit wordt algemeen gezien als een bekende beperking van het turbulentie model in de literatuur. Echter, bij het gebruik van een grid van 140k (voor een 60° sector) was de voorspelde waarde voor N_{P_ε} slechts 5% te laag. De voorspellingen van het impeller stromingsgetal lagen in lijn met de experimentele waardes, zowel voor de tank als voor de vergister. Deze bevindingen laten een goede basis zien voor een efficiënt en betaalbaar meerfasen simulatie framework voor roerwerk aangedreven systemen met gastoevoer, waarbij de berekeningskosten een orde van grootte hoger zijn dan voor eenfase simulaties.

Twee fasen

De twee fasen simulaties zijn voornamelijk gebaseerd op het conventionele Euler–Euler (two-fluid model) framework, omdat de gastoevoersnelheid significant kan zijn in de standaard operatie van vergisters. Er was (en is) veel debat over de juiste formulering van de vergelijkingen in het two-fluid model, specifiek over de sluitingsrelaties. Om die reden hebben we besloten om een uitgebreid overzicht van de theorie op te nemen in deze thesis. We hopen dat dat de jonge onderzoekers in dit vakgebied zal helpen.

De twee fasen stromingsstudie startte in eerste instantie met het modelleren van de enkelvoudige impeller tank. Al snel werd het duidelijk dat de voorspellingen over de totale hoeveelheid vastgehouden gas en de verdeling van het gas in de tank een uitdaging vormden (specifiek voor systemen waarin geroerd werd, dit gold niet voor bubbel kolom simulaties). De wrijvingskracht formulering was de prominente modelleringsfactor, hoewel de gebruikte wetten van de wrijvingskracht (inclusief die voor vervormde bubbels) de hoeveelheid vastgehouden gas nog steeds substantieel onderschatte, behalve wanneer een aanpassing voor turbulentie werd toegepast. Het Brucato model dat voor dit doel wordt gebruikt, bleek niet in alle gevallen valide resultaten te geven bij wisselende roer- en gas toevoersnelheden en voor grote multi-impeller systemen. Vandaar dat het niet als een verrassing komt dat veel literatuurstudies een constante – bij experimenten gemeten – slipsnelheid gebruikten, of de parameters aanpassen in hun wrijvingskracht modellen, zodat ze passen in een specifieke operatie conditie. Hoewel er geen universele wrijvingskracht formulering voor turbulente, roerder aangedreven systemen met gastoevoer (wat een actieve onderzoekstak is) bestaat, was het gekozen framework in staat om de overgang van looding tot floading in de vergister goed te voorspellen. Daarnaast, in de casus van de hoog gas geladen vergister, resulteert de Ishii & Zuber multiparticle wrijvingskracht wet – die het bubble swarm effect meeneemt – in een goede voorspellings voor de hoeveelheid vastgehouden gas, zonder dat daarbij een aangepaste parameter of een turbulentie aanpassing moest worden gebruikt. Voor deze relatief hoog gas belading ($\sim$ 20%) raden we de ontgassingsoutlet grens conditie aan in plaats van de druk outlet, met name wanneer de top impeller dicht bij het vrije oppervlak zit.

De voorspellingen van belgrootte door middel van het discrete population balance model (met standaard opbreek- en samenvoegkernen van Luo) waren over het algemeen goed. De ruimtelijke distributie van de Sauter diameter door de tank werd redelijk goed voorspeld, behalve in de buurt van de impeller waar de d_{32} op verschillende plekken

werd overschat. Voor de vergister in de studie was er geen experimentele data over de lokale belgrootte aanwezig om die te kunnen vergelijken. Dit komt waarschijnlijk door de moeilijkheid om op zo'n grootte te experimenteren. Het gemiddelde van Sauter diameters die het model voorspelde waren veel groter dan voor de lab schaal standaard roertank en lagen in lijn met de verschillende belgroottes die normaal geobserveerd worden in industriële vergisters, namelijk $6 - 10$ mm.

Scalaire menging

De tracer response studie uitgevoerd in de vergister (eenfase) wees uit dat het turbulentie Schmidt nummer de belangrijkste parameter is voor het voorspellen van de mengtijd in een systeem met meerdere radiale turbines dat snel compartimenten vormt. In de gebruikte eenvoudige turbulentie modelleer aanpak (steady RANS), compenseert Sc_t voor het gebrek aan convectieve uitwisseling van de tracer door de mean flow langs de impeller zones. De waarde van het turbulentie Schmidt nummer hangt af van de lokale stromingskarakteristieken en een grote reikwijdte van waardes ($0.1 \leq Sc_t \leq 1.3$) wordt gebruikt in de literatuur afhankelijk van het specifieke gebruik. Bij het gebruik van de waarde $Sc_t = 0.2$, werden goede voorspellingen van de meng- en vertragingstijd verkregen, net als de volledige tracer response curve voor zowel 70 en 115 rpm in operatie. De keuze van injectie en detectie locaties voor de tracer hebben ook een invloed op de vorm van de response curves en de berekende mengtijd. De kortste berekende mengtijden werden waargenomen rond het midden van de verticale as van de vergister. Dat komt overeen met de experimentele resultaten. De injectiemethode heeft ook een invloed als de injectiepunten zich niet in een enkelvoudig impeller compartiment bevinden. De kortste mengtijd werd bereikt wanneer de tracer in elke impeller regio individueel werd toegevoegd. Ook hier lieten de resultaten een goede voorspellende waarde zien van de scalaire macro- en mesomengen. De mengtijden en tracer response curves konden worden verkregen middels een simpele en berekeningstechnisch goedkope modelleringsaanpak.

Case study: 30 m^3 vergister

In de laatste delen van de thesis is de aanpak die tijdens de studie is ontwikkeld toegepast op een industrie relevante casus, namelijk de substraat opname kinetiek in een roerder aangedreven vergister met gastoevoer. Monod kinetiek is gebruikt om de glucose gelimiteerde groei van Saccharomyces cerevisiae te modelleren. De algemene trends van substraat gradient werden goed weergegeven in de gekozen simulatie methode. Dit is ondanks de bevinding dat massabehoud niet voldoende is door een beperking in de Fluent code als het Eulerian multifase model met soorten transport werd gekoppeld aan periodieke grens condities. De voorspelde glucose substraat concentraties in de tank (waarbij weer de waardes $Sc_t = 0.2$ vanuit de eerdere mengstudies zijn gebruikt) waren redelijk goed wanneer vergeleken met de metingen die in de literatuur gerapporteerd worden, waarbij de gemiddelde afwijking 30.1% is.

Alles samen genomen laten de bovengenoemde resultaten zien dat de vastgestelde modelleringsaanpak gebruikt kan worden als een bruikbare berekeningsmethode die het ontwerp, optimalisatie en probleemoplossend vermogen van de bioreactor ondersteunt.

Er zijn duidelijke beperkingen, zowel door onze huidige kennis van turbulente stromingen met bubbels en hun modellering, als door de versimpelde modelleringsaanpak die is gekozen. Voor een gedetailleerdere analyse inclusief de tijdsbepaalde effecten (opstarten, veranderingen in voedingssnelheid, macroinstabiliteiten die zich ontwikkelde in de reactor, complexe biokinetiek die rekening houdt met de impact van de historie van de bacteriën op het huidige proces, etc.) moet men een andere berekeningsstrategie kiezen zoals het Euler–Langrange framework (om daadwerkelijke lokale kinetiek van microbiale clusters in hun trajecten te volgen) gekoppeld met de sliding mesh techniek (om impeller–baffle interacties vast te leggen) in een volledig 360° sector domein (om macroinstabiliteit en asymetrische gas holte regimes vast te leggen). Verder zal een kleinere tijdsstap nodig zijn wanneer men een gedetailleerd metabolisme wil modelleren, aangezien er aangetoond is dat de tijdevolutie van concentraties gevoeliger is voor de gekozen tijdsstap dan de waardes die bereikt werden in stabiele toestand. Echter, de RANS aanpak voor turbulentie zou nog steeds het werkpaard zijn aangezien DNS en LES nog steeds niet geschikt zijn voor gebruik in het modelleren van vergisters op een industriële schaal. De berekeningskosten voor zulke tijdsbepaalde methoden zullen dramatisch hoger zijn. Een twee-fase proces zou kunnen worden toegepast wanneer de initiële stabiele karakteristieken voor een groot aantal situaties duidelijk zijn geworden via de modelleringsmethode voorgesteld in deze thesis en een gedetailleerde analyse is uitgevoerd in de tweede fase voor een gelimiteerd aantal casussen.

Contents

Nomenclature

Roman Symbols

$\mathbf{a}$	unit vector parallel to rotation axis	–
a	aggregation kernel	$\mathrm{m^3\ s^{-1}}$
a, b	unknown exponent	
A	area	$\mathrm{m^2}$
$\mathbf{A}$	area vector	$\mathrm{m^2}$
A_b	projected area of a bubble in the direction of its motion	$\mathrm{m^2}$
a_i, a	interfacial area per unit volume	$\mathrm{m^{-1}}$
$\mathcal{A}_\mathrm{spa}$	surface area available for the gas outflow at the sparger	$\mathrm{m^2}$
a_x	local interfacial area per unit volume	$\mathrm{m^{-1}}$
B	impeller blade width	m
$B_\mathrm{br}, B_\mathrm{ag}$	particle birth rate (due to breakup or aggregation)	$\mathrm{s^{-1}}$
C	impeller-to-tank base clearance	m
c	constant	
c	molar concentration	$\mathrm{mol\ m^{-3}}$
C_A	added mass coefficient	–
C_β	crossing trajectories model constant	–
C_D	drag coefficient	–
C_e	ethanol concentration	$\mathrm{kg\ m^{-3}}$
c_k	mass fraction of phase k	–
C_k	molecular and turbulent transfer term	$\mathrm{m^3\ s^{-3}}$

C_L	lift coefficient	–
$C_{\mathrm{L}\Omega}$	rotational lift coefficient	–
$C_\mu, C_{\varepsilon 1}, C_{\varepsilon 2}, C_{\varepsilon 3}$	turbulence model constants	–
C	mean mass concentration	kg m^{-3}
C	mean molar concentration	mol m^{-3}
C_s	glucose concentration	kg m^{-3}
C_sf	glucose feed concentration	kg m^{-3}
C_TD	turbulent dispersion model constant	–
C_x	biomass concentration	kg m^{-3}
D	impeller diameter	m
$D_\mathrm{br}, D_\mathrm{ag}$	particle death rate (due to breakup or aggregation)	s^{-1}
d_b	bubble diameter	m
d_e	volume equivalent bubble diameter	m
D_m	laminar (molecular) diffusion coefficient in the mixture	m^2 s^{-1}
D_t	turbulent diffusivity	m^2 s^{-1}
D^t	effective turbulent dispersion coefficient	m^2 s^{-1}
$\underline{\underline{\mathbf{D}}}^\mathrm{t}_{12}$	fluid-particle dispersion tensor	m^2 s^{-1}
$\mathbf{e}$	unit vector	–
e	energy	J
E	pumping efficiency	–
E	engulfment rate constant	s^{-1}
$\mathbf{f}, \mathbf{F}$	force on a single bubble	N
f_B	binary breakage volume fraction	–
F_D	averaged drag function	s^{-1}
F_D	drag force	N
$\mathbf{F}_\mathrm{e}$	external body force per unit volume	N m^{-3}
F_g	gravitational force	N
$f_i, f_{\mathrm{bin},i}$	volume fraction of bin i	–
F_p	pressure force	N
$\mathbf{g}$, g	gravitational acceleration	m s^{-2}

g	breakage frequency	s^{-1}
G_k	turbulent kinetic energy generation term	$\mathrm{m}^2\ \mathrm{s}^{-3}$
G_l	particle diameter (or length) growth rate	$\mathrm{m}\ \mathrm{s}^{-1}$
G_v	particle volume growth rate	$\mathrm{m}^3\ \mathrm{s}^{-1}$
H	liquid height	m
$\underline{\underline{\mathbf{I}}}$	identity tensor	–
I_r	relative turbulence intensity	–
$\mathbf{J}$	mass diffusion flux	$\mathrm{kg}\ \mathrm{m}^{-2}\ \mathrm{s}^{-1}$
k	constant	
k	first order rate constant	s^{-1}
k	turbulent kinetic energy per unit mass	$\mathrm{m}^2\ \mathrm{s}^{-2}$
k_{12}	fluid-particle velocity covariance	$\mathrm{m}^2\ \mathrm{s}^{-2}$
K_a	particle shape factor based on surface area	–
k_L	liquid side mass transfer coefficient	$\mathrm{m}\ \mathrm{s}^{-1}$
k_P	turbulent kinetic energy at the wall-adjacent cell centroid	$\mathrm{m}^2\ \mathrm{s}^{-2}$
K_s	saturation constant	$\mathrm{kg}\ \mathrm{m}^{-3}$
K_v	particle shape factor based on volume	–
l	intermediate length scales of turbulence	m
L_C	integral scale of concentration fluctuations	m
I_s	intesity of segregation	–
L_D	characteristics length scale of turbulent dispersive mesomixing	m
L^t, L	integral length scale of turbulence	m
$\dot{m}$	mass transfer per unit area of interface per unit time	$\mathrm{kg}\ \mathrm{m}^{-2}\ \mathrm{s}^{-1}$
$\mathbf{M}$	mean interfacial momentum transfer term	$\mathrm{N}\ \mathrm{m}^{-3}$
$\dot{m}_\mathrm{g}$	mass flow rate of gas	$\mathrm{kg}\ \mathrm{s}^{-1}$
$\mathbf{n}$	unit vector normal to surface	–
$\mathcal{N}$	number of bins in the discrete model	–
N	impeller rotational frequency	s^{-1}
N	local average number density function in physical space	m^{-3}
n	average number density function in particle space	m^{-6}

n	number of impellers	–
n	number of phases	–
$\dot{n}_0$	nucleation rate	$\mathrm{m^{-3}\ s^{-1}}$
n_b	local bubble number density	$\mathrm{m^{-3}}$
$\dot{n}$	molar flow rate	$\mathrm{mol\ s^{-1}}$
N_m	total number of measurement locations	–
$\mathcal{O}$	order of magnitude	–
P	mean pressure	$\mathrm{N\ m^{-2}}$
P	power	W
p	pressure	$\mathrm{N\ m^{-2}}$
P_B	binary particle breakage probability	–
P_C	binary particle collision probability	–
P_c	sublayer resistance function for the species law-of-the-wall	–
P_g	power input under gassed conditions	W
P_gas	power input due to gas flow	W
Q	impeller liquid discharge rate	$\mathrm{m^3\ s^{-1}}$
Q_b	inward flow rate of liquid volume in the bubble wake	$\mathrm{m^3\ s^{-1}}$
Q_F	volumetric flow rate of the feed	$\mathrm{m^3\ s^{-1}}$
Q_G	impeller liquid discharge rate under gassed conditions	$\mathrm{m^3\ s^{-1}}$
Q_g	gas inflow rate	$\mathrm{m^3\ s^{-1}}$
Q_R	flow rate of the recirculated gas	$\mathrm{m^3\ s^{-1}}$
$q_\mathrm{s,max}$	maximum specific substrate consumption rate	$\mathrm{s^{-1}}$
$\mathbf{r}$	position vector from the origin of a rotating frame	m
r	radius	m
r_s	substrate consumption rate	$\mathrm{kg\ m^{-3}\ s^{-1}}$
$\mathbf{S}$	momentum source term	$\mathrm{N\ m^{-3}}$
S	substrate	–
$\underline{\underline{\mathbf{S}}}$	mean strain-rate tensor	$\mathrm{s^{-1}}$
$\underline{\underline{\mathbf{s}}}$	instantaneous strain-rate tensor	$\mathrm{s^{-1}}$
S	mass source term	$\mathrm{kg\ m^{-3}\ s^{-1}}$

S	surface	m^2
s_η	characteristic rate of strain of Kolmogorov eddies	s^{-1}
S_w	surface of walls	m^2
Sr	trapping parameter	–
T	tank diameter	m
t_m	mixing time	s
$\tilde{\mathbf{u}}$	undisturbed liquid velocity	$\mathrm{m\ s}^{-1}$
$\mathbf{U}$	mean velocity	$\mathrm{m\ s}^{-1}$
$\mathbf{u}$	instantaneous velocity	$\mathrm{m\ s}^{-1}$
U	uniformity index	–
$U_\parallel$	wall-parallel mean velocity	$\mathrm{m\ s}^{-1}$
$U_\parallel^*$	dimensionless wall-parallel mean velocity (in Fluent)	–
$U_\parallel^+$	dimensionless wall-parallel mean velocity	–
$\mathbf{u}_\mathrm{b}$	bubble velocity	$\mathrm{m\ s}^{-1}$
u_η	characteristic velocity of Kolmogorov eddies	$\mathrm{m\ s}^{-1}$
U_g	mean velocity of sparging gas	$\mathrm{m\ s}^{-1}$
$U_\mathrm{g,s}$	superficial gas velocity	$\mathrm{m\ s}^{-1}$
u_L	characteristic velocity of integral scale of turbulent motion	$\mathrm{m\ s}^{-1}$
U_P	mean velocity at the wall-adjacent cell centroid	$\mathrm{m\ s}^{-1}$
$\mathbf{U}_\mathrm{r}$	mean relative velocity	$\mathrm{m\ s}^{-1}$
$\mathbf{u}_\mathrm{r}, \mathbf{v}_\mathrm{r}$	relative velocity	$\mathrm{m\ s}^{-1}$
$\mathbf{U}_\mathrm{R}$	velocity relative to a rotating frame	$\mathrm{m\ s}^{-1}$
U_T	mean terminal velocity	$\mathrm{m\ s}^{-1}$
u_τ	friction velocity	$\mathrm{m\ s}^{-1}$
$\mathbf{v}$	bubble velocity	$\mathrm{m\ s}^{-1}$
V	volume	m^3
v	fluid particle volume	m^3
$\mathcal{V}_\mathrm{b}$	bubble volume	m^3
$\mathcal{V}_{\mathrm{D_f}}$	drift volume	m^3

$\mathcal{V}_\mathrm{l}$	liquid volume in tank	m^3
$\mathcal{V}_\mathrm{spa}$	sparger volume	m^3
$\mathcal{V}_\mathrm{t}$	tank volume	m^3
vvm	gas volume per minute per volume of liquid in the vessel	min^{-1}
$\dot{\mathbf{X}}$	deformation velocity due to change in external particle coordinate space	$\mathrm{m\ s}^{-1}$
$\mathbf{x}$	position vector	m
X	biomass	–
X	general variable	
$\mathbf{x}_\mathrm{b}$	position vector to bubble centre	m
Y	mean mass fraction	–
y	axial axis	
y	instantaneous mass fraction	–
y	wall-normal distance	m
y^*	dimensionless wall distance	–
y^+	wall coordinate, dimensionless wall distance	–
y^+_vis	dimensionless thickness of the viscous sublayer	–
y_P	distance from the wall-adjacent cell centroid to the wall	m

Greek Symbols

α	volume fraction	–
β	the ratio of turbulent intensity to bubble rise velocity	–
β	probability density function (PDF) of particle breakage	–
ε_BL	energy dissipation rate in the boundary layer	$\mathrm{W\ kg}^{-1}$, $\mathrm{m}^2\ \mathrm{s}^{-3}$
χ	phase indicator function	–
χ_c	critical dimensionless energy for breakup	–
η, λ_K	Kolmogorov's microscale	m
δ	boundary layer thickness	m
δ	Dirac delta function	–
η_r	characteristic time ratio	–
ε	turbulent specific kinetic energy dissipation rate	$\mathrm{W\ kg}^{-1}$, $\mathrm{m}^2\ \mathrm{s}^{-3}$

η	daughter particle size distribution	–
Γ	torque	N m
$\dot{\gamma}$	boundary layer shear rate	s^{-1}
κ	von Kármán constant, 0.4187	–
λ	bulk viscosity	N m^{-2} s
λ	eddy length scale	m
λ_B	Batchelor length scale	m
λ_{RT}	Rayleigh–Taylor instability length	m
μ	dynamic viscosity	N m^{-2} s
ν	kinematic viscosity	m^2 s^{-1}
$\boldsymbol{\Omega}$	angular velocity	s^{-1}
Ω	domain boundary	
$\dot{\omega}_B$	arrival frequency of eddies on particles	m^{-4} s^{-1}
Ω_B	particle breakage rate	m^{-3} s^{-1}
$\dot{\omega}_C$	particle collision frequency	m^3 s^{-1}
Ω_C	particle coalescence rate	m^3 s^{-1}
Π	dimensionless group of inertial-to-buoyancy forces	–
Π_ε	source term in turbulent dissipation rate equation	kg m^{-1} s^{-4}
Π_k	source term in turbulent kinetic energy equation	kg m^{-1} s^{-3}
$\dot{\boldsymbol{\Phi}}$	deformation velocity due to change in internal particle coordinate space	
ϕ	gas holdup	–
ϕ	internal particle coordinate	
ϕ_x	local gas holdup	–
ρ	density	kg m^{-3}
σ	standard deviation	
σ	surface tension coefficient	kg s^{-2}
$\underline{\underline{\boldsymbol{\sigma}}}$	stress tensor	N m^{-2}
$\underline{\underline{\boldsymbol{\Sigma}}}$	average stress tensor	N m^{-2}
σ_ε	turbulence constant	–
σ_k	turbulence constant	–

σ^{t}	single-phase turbulent Schmidt number	–
σ_{21}^{t}	dispersion Prandtl number	–
$\underline{\underline{\boldsymbol{\tau}}}$	viscous stress tensor	N m^{-2}
$\underline{\underline{\mathbf{T}}}$	average viscous stress tensor	N m^{-2}
τ_{B}	Batchelor time scale	s
τ_{C}	Corrsin micromixing time scale	s
τ_{D}	characteristics time scale of turbulent dispersive mesomixing	s
τ_E	time scale of micromixing by engulfment	s
τ_η	characteristics time scale of Kolmogorov eddies	s
τ_{I}	characteristics time scale of turbulent inertial-convective mesomixing	s
τ_L	characteristics time scale of integral scale of turbulence	s
$\tau_{\mathrm{m},\eta}$	molecular diffusion time at the Kolmogorov scale	s
τ_{p}	particle relaxation time	s
τ_{r}	reaction time constant	s
τ^{t}	characteristics time scale of the energetic turbulent eddies	s
τ_{12}^{t}	eddy–particle interaction time	s
τ_{w}	wall shear stress	N m^{-2}
θ	rotational angle	rad
ξ	dimensionless eddy size, λ/d	–
ξ	dynamic pressure coefficient	–
ξ_{r}	ratio of mean relative velocity to vertical turbulent velocity	–

Dimensionless Numbers

Da	Damköhler number	$\frac{\text{mixing time}}{\text{reaction time}} = \frac{\text{reaction rate}}{\text{scalar dissipation rate}}$
Eo	Eötvös number	$\frac{g\lvert\Delta\rho\rvert d_{\mathrm{e}}^2}{\sigma}$
Fl	aeration (gas flow) number	$\frac{Q_{\mathrm{g}}}{ND^3}$
Fr	Froude number	$\frac{N^2 D}{g}$

Mo	Morton number	$\frac{g\|\Delta\rho\|\mu_1^4}{\rho_1^2\sigma^3}$
N_P	power number	$\frac{P}{\rho N^3 D^5}$
N_Q	impeller flow number	$\frac{Q}{ND^3}$
Re	mean Reynolds number	$\frac{\rho_1\|\mathbf{U}_2-\mathbf{U}_1\|d_2}{\mu_1}$
Re	impeller Reynolds number	$\frac{\rho N D^2}{\mu}$
Re_b	bubble Reynolds number	$\frac{d_\mathrm{e}\|\mathbf{v}-\tilde{\mathbf{u}}_{\mathbf{x}_\mathrm{b}}\|}{\nu_1}$
Sc	molecular Schmidt number	$\frac{\mu}{\rho D_\mathrm{m}}$
Sc_t	turbulent Schmidt number	$\frac{\mu_\mathrm{t}}{\rho D_\mathrm{t}}$
We	Weber number	$\frac{\rho_1\|\mathbf{v}-\tilde{\mathbf{u}}_{\mathbf{x}_\mathrm{b}}\|^2 d_\mathrm{b}}{\sigma}$

Abbreviations

ASMM	algebraic slip mixture model
BC	boundary condition
bit	bubble induced turbulence
BL	boundary layer
const	constant
CoV	coefficient of variance, concentration variance
degas	degassing boundary condition
DM	discrete method for population balances
MRF	multiple reference frame model
MW	molecular weight
PBM	population balance model
PDF	probability density function
PO	pressure outlet boundary condition
PSD	particle size distribution

QMOM	quadrature method of moments
rms	root-mean-square
rpm	stirrer rotations per minute
SM	sliding mesh model
spa	sparger
sti	stirrer
TD	turbulent dispersion force
Upw	Upwind discretisation scheme
VM	virtual mass force
VOF	phase volume fraction equation

Subscripts and Superscripts

$\bar{}$	mean value
$'$	fluctuation with respect to the mean value
$\parallel$	vertical or parallel direction
1	continuous phase
2	dispersed phase
a	axial direction
B	buoyancy
b	bubble
CD	complete dispersion
d	drift
e	external
exp	expansion
F	flooding
g	gas, gassed condition
hp	hydrostatic pressure
I	inertial
i	interface
k	phase index

l	liquid
lm	log mean
m	mixture
pg	pressure gradient
p	particle (bubble, drop or solid particle)
rms	root-mean-square
R	recirculation
r	radial direction
r	reference value
r	relative
spa	sparger
td	turbulent dispersion
t	turbulent
u	ungassed condition

Chapter 1

General introduction

1.1 Motivation

Fermentation and fermenters

Fermentation involves conversion of carbohydrates into alcohols and acids and is a crucial component of many applications in bio-industry (e.g. production of yeast, vitamin C, citric acid, penicillin, etc.). In fermentation processes large scale gassed–stirred tanks are used frequently. Due to this scale, these reactors are equipped with multiple impellers.

Current limitations

A number of limitations are encountered in the design and operation of those fermenters, which hamper a further improvement in the performance of the fermenters:

- yield losses when scaling-up pilot scale results,
- limited process intensity (i.e. the rate of carbon feed supply and related productivity) due to limitations in air supply, carbon dioxide or heat removal, or liquid mixing,
- performance differences of same processes in apparently similar vessels,
- vital concentrations cannot be controlled within desired ranges (e.g. dissolved O_2, precursor molecules, ammonia, phosphate, etc.).

The current understanding of the transport phenomena involved in the operation of fermenters is insufficient to deal in a satisfactory way with the limitations listed above. A better insight in the local hydrodynamics and mass transfer is required to make a step change.

Computational fluid dynamics (CFD)

Starting from early 90's, significant progress has been made in the area of computational fluid dynamics (CFD) for modeling and understanding the flow and transport phenomena in process equipment. One of the obvious advantages of CFD is the degree of detail that can be obtained. By its nature CFD is based on local processes, just like the real processes, in contrast to many engineering approaches that in many cases can only deal with a limited number of compartments with idealized behavior to describe the process.

1.2 Objective of the thesis

It is the goal of this thesis to contribute to further improvement of the performance of fermenters by utilisation of computational fluid dynamics (CFD) methods that could provide a better insight in the local hydrodynamics and mass transfer.

It should be stressed here that CFD is a valuable tool that can be used by the engineer, but it does not produce the final answers. It rather assists in understanding the transport phenomena at a much more detailed level that can not be obtained by other means. It's an emerging tool to quantify local flow and concentration fields in large scale fermenters, using fundamental knowledge on transport phenomena and reaction kinetics. Hence, it could be a key instrument to determine the best locations for feed inlets, gas ejectors, etc. Furthermore, CFD could provide a clear picture on how differences in fermenter geometry and operating conditions will influence the performance of processes. An example is to identify zones where oxygen or sugar is depleted, as observed in some fermentations, and apply design or process condition changes to overcome those. In addition, the cell-damaging effect of local shear forces could be clarified and prevented.

1.3 Scope of the thesis

Despite the constantly increasing computational power for decades, we are still far away from completely solving the flow and transport phenomena in every possible detail at the scale of industrial fermenters. Simulations of gassed-stirred systems can be based on two general approaches: the Euler–Lagrange and the Euler–Euler approach. The former tracks the individual bubbles through the liquid and has thus the largest potential but it requires computational power that is beyond current abilities. The latter treats the gas bubbles as a kind of continuum, just like the liquid phase.

For the simulation of turbulent flows in aerated stirred tanks at not too low gas fractions, the Euler–Euler (two-fluid) model is computationally the most feasible approach, and is the model of choice in this study. In the Euler–Euler model, all the phases are treated mathematically as interpenetrating continua. Therefore, the volume fraction field is a continuous function of space and time. Momentum and continuity equations are solved for each phase, and coupling is achieved through the pressure and the interfacial forces (e.g. drag, virtual mass, turbulent dispersion, lift). The conservation

equations are derived by ensemble averaging the local instantaneous balance equations for each phase.

This thesis concentrates on the hydrodynamics of gassed-stirred fermenters. Population balances that keep track of the bubble size distribution are used to deal with the different bubble sizes present that influence the mass transfer directly.

1.4 Setup of the thesis

Organisation of the remainder of this thesis is outlined below. We also include below a reading guideline for the "reader with the little time".

- Chapter 2 is based mainly on our publication (Günyol and Mudde, 2009), where single-phase flow results on the fully turbulent flow in a laboratory-scale standard stirred tank and a large-scale multi-impeller fermenter are presented. A comparison with the experimental data was also made.
- In Chapter 3, the general characteristics (flow regimes, power uptake, etc.) of bubbly flow in stirred tanks with Rushton impellers is given for both single- and multi-impeller systems.
- Chapter 4–8 are the theory chapters where we introduce and discuss the Euler–Euler model, turbulence closure modelling for bubbly flows, the modelling of interphase forces, the modelling of impellers and the population balance modelling, respectively.
- Chapter 9 and 10 describe the application of the two-phase modelling approach to gas dispersion in a standard stirred tank and a production scale (30 m^3) fermenter. Results are presented and compared with the experimental data.
- In Chapter 11, the theory of turbulent mixing is provided and a scalar mixing study in the 30 m^3 fermenter is given.
- Chapter 12 is the final chapter of results, where we report on the sugar (glucose) uptake kinetics in the 30 m^3 fermenter. It builds on the gas dispersion and mixing studies reported in Chapter 10 and 11, and applies the simulation methodology developed earlier on to a real industrial fermentation case with the addition of kinetics modelling.
- Chapter 13 concludes the thesis by summarising the results of the research and by providing recommendations for future work.

1.4.1 Reading guideline

The reader who is familiar with the theoretical concepts dealt with in this thesis (i.e. Euler-Euler modelling of turbulent stirred tanks, population balance modelling, turbulent mixing) could directly visit the chapters where we present the findings. Those are Chapter 2, 9, 10, 11 and 12. Before doing so, one may still consider a brief introduction to the subject of gas dispersion in single- and multi-impeller systems provided by

Chapter 3. Finally, Chapter 13 outlines the overall conclusions and recommendations and is therefore recommended.

Chapter 2

Single-phase flow in a standard stirred tank and a multi-impeller fermenter

This chapter is based mainly on our publication (Günyol and Mudde, 2009). We present single-phase simulations of the fully turbulent flow in a standard stirred tank reactor and a large-scale multi-impeller fermenter, both stirred by Rushton turbines. The mean flow characteristics and the turbulence predictions were obtained by solving the Reynolds-averaged Navier–Stokes (RANS) equations using the commercial computational fluid dynamics (CFD) code, Fluent 6.3. The standard, realisable and RNG $k-\varepsilon$ models, and the Reynolds stress model (RSM) were employed for modelling of the turbulence. The moving reference frame (MRF) model was used for the modelling of the moving parts. Results showed that using the standard $k-\varepsilon$ model, good predictions of the impeller power number can be calculated from the integrated turbulence kinetic energy dissipation rate as long as the grid resolution is sufficient. The underprediction in the power number was only 5% unlike the earlier studies, where values up to 50% were reported. The impeller flow number calculated was also in good agreement with the experimental values reported in the literature. The predictions of the turbulence kinetic energy and the turbulence energy dissipation profiles at the impeller discharge stream revealed that, despite its simple form, the standard $k-\varepsilon$ model gave the best predictions, except in the close vicinity of the blade tip, where the RSM model matched better with the experimental data.

2.1 Introduction

Stirred tank reactors, operating in single or multiphase mode, are commonly used in chemical and bioprocess industries. They provide good mixing characteristics, enhance gas–liquid/gas–liquid–solid contact, and thereby enhance the mass transfer and chemical/biochemical reaction rates in the vessel, due to the mechanical energy input by the

impeller. Because these processes depend highly on the local conditions in the tank, information of the local hydrodynamics is crucial for modelling and design of these reactors. Providing the required data by means of experimental techniques is limited, if not impossible, especially if the scale of the system is large. Therefore, a computational approach can prove to be useful for effectively acquiring the information needed.

Over the last decade, significant progress has been made in the area of computational fluid dynamics (CFD) for modelling and understanding the flow and transport phenomena in process equipment. One of the obvious advantages of CFD is the degree of detail that can be obtained. By its nature, CFD is based on local processes, just like the real processes, in contrast to many engineering approaches. With the continuous increase of computational power, CFD became a powerful tool, from which the information gained can be applied to optimise and/or intensify the stirred tank reactors. However, solving the flow and transport phenomena in every possible detail at the scale of industrial process equipments is still practically not possible.

A particular feature of CFD modelling of stirred systems is that a proper model to account for the impeller rotation is needed. There are several methods proposed in literature, which were reviewed in detail by Brucato et al. (1998a). One of the simplest approach is to use a fixed coordinate system, and to model the impeller implicitly by imposing boundary conditions in the impeller swept region. The main disadvantage of this method is that the imposed boundary conditions are based on experimental data or on an empirical model. As in the case of multiphase flows, this data might not be available (Deen, 2001). This is not an issue in the so-called snapshot method, because the impeller is modelled by introducing source terms into the momentum equations. Steady-state simulations are performed for several impeller positions to describe the flow, and ensemble averaging is employed over the simulated impeller positions. Ranade (1997) and Ranade et al. (2002a) used this method for a stirred tank with a Rushton turbine together with a $k-\varepsilon$ model for the turbulence, and found good agreement with the experimental data. Derksen and van den Akker (1999) also used source terms to describe the impeller rotation. By performing transient large eddy simulations (LES) to account for turbulence, they found very good results.

The majority of the recent literature, however, is based on two other models, where the impeller is modelled explicitly in a rotating coordinate system. These are the sliding mesh (SM) model and the multiple reference frames (MRF) model. In the SM model, a moving zone consisting of the impeller and a stationary zone consisting of the rest of the tank is defined. Two zones share a common grid interface, and they slide relative to each other along this interface in discrete time steps. The method is inherently transient, which makes it computationally expensive. The MRF, however, is an alternative steady-state model, which is gaining considerable popularity recently. A reasonable agreement between SM and MRF computations was reported in earlier studies (Luo et al., 1994; Lane, 2005a), whereas the computational time was about an order of magnitude less with the MRF method. As impeller–baffle interactions are expected to be negligible in this study, and the transient dynamic flow features and start–up characteristics of the tank are not of interest, we used the MRF method. Details of the model are given in the next section.

A "standard" reference geometry is established of a stirred tank with a Rushton turbine operating in the turbulent regime and is usually employed in literature in order to keep

the geometrical similarity between different systems investigated. It consists of a tank filled upto a liquid height H equal to the tank diameter T. The impeller diameter D is $T/3$, and the off-bottom clearance C is usually $T/3$ or $T/4$. Impeller has usually six blades, having a blade height of $D/5$ and a blade length of $D/4$, which are placed uniformly on a disc of diameter $3D/4$. Four vertical baffles having a width of $T/10$ are separated by 90° and attached to the wall.

Accurate prediction of turbulence quantities is very important for the modelling of the processes that are often carried out in stirred tank reactors. For instance, the bubble size, when gas is sparged into the reactor, is related to the turbulence dissipation rate, due to bubble break-up. When the bubble size changes, the mass transport across the phases also changes to a great extent, effecting substantially the ongoing processes. Dissipation is also very important for species mixing, chemical/biochemical and crystallisation processes carried out in the reactor.

Most of the published literature of stirred tanks utilises the conventional standard $k-\varepsilon$ turbulence model, which has some shortcomings related to the typical flow structure in the tank. The characteristic flow generated by a Rushton turbine is mainly in the radial and tangential directions, with strong swirling near the impeller, due to the trailing vortex pair formed at the blade. The impeller produces a strong radial jet, which impinges at the tank wall, and consequently splits into two axial streams in the direction below and above the impeller plane. Afterwards, they change direction and return back to the impeller, forming the well-known double recirculation loop structure. These characteristic flow features present a challenge for the $k-\varepsilon$ turbulence model, which is known to be less successfull for highly swirling flows with strong streamline curvature and rotation. It is reported in many previous studies that the turbulence kinetic energy and its dissipation rate are underpredicted with this model. It is reported in many previous studies that the turbulence kinetic energy and its dissipation rate are underpredicted with this model (Murthy and Joshi, 2008; Lane, 2005a; Yeoh et al., 2004; Ng and Yianneskis, 2000). However, Deglon and Meyer (2006) reported that, poor predictions often noted in literature may be due to numerical errors rather than inadequacies in the turbulence model.

Some other studies also investigated the performance of more rigorous turbulence models, namely the Reynolds stress model (RSM) and LES. The RSM, although being a RANS type of model where all turbulence scales are modelled, does not suffer from the isotropy assumption underlying the $k-\varepsilon$ model, and therefore is able to resolve anisotropic flow features typical for Rushton turbines near the impeller. However, computational costs are an order of magnitude higher than $k-\varepsilon$ (Murthy and Joshi, 2008). The LES model is arguably the most comprehensive in the limit of affordability of computational costs. The filtering process carried out in its formulation enables the large turbulence scales, which are known to be anisotropic, to be directly solved without modelling. Smaller scales, which are isotropic in nature and carry less of the total turbulence energy, are modelled by an appropriate subgrid scale model. By construction, it can resolve the complex transient dynamics (such as unstable precessional vortices) in the stirred tank. Derksen and van den Akker (1999) reported promising results with LES, which was implemented within the Lattice–Boltzmann framework.

Bartels et al. (2002) performed one of the first reported direct numerical simulation (DNS) study of a stirred tank, where all the turbulence scales are resolved without

simplifying assumptions. Simulations were performed in the transitional turbulence regime ($Re = 7300$) of a standard tank ($H = T = 0.152$ m, $C = T/3$). The computational mesh of about 2 million cells was employed for a 180° sector of the tank assuming flow symmetry. They compared the results with their $k-\varepsilon$ simulations and found that $k-\varepsilon$ gave in general good predictions of the flow. However, DNS results were in better agreement with the experimental data especially for the turbulent kinetic energy, k, near the blade, where $k-\varepsilon$ constantly underpredicted the maximum value. They also found that DNS results predicted higher k in the lower part of the tank, in contrast to the experimental data. They commented that their grid resolution may not have been sufficiently fine at those locations. No results were reported for the turbulence dissipation predictions.

Ng and Yianneskis (2000), based on the simulations with the SM model on a standard configured stirred tank ($H = T = 0.100$ m, $C = T/3$, $Re = 40,000$), reported that the total dissipation was underestimated by 50% with the $k-\varepsilon$ model. Turbulent kinetic energy was found to be well predicted away from the blades, whereas underpredicted by 40% near the blade at the impeller discharge stream. They employed a grid of 239k cells, and simulated only half of the tank (180° sector) due to symmetry. They also calculated the volume-averaged dissipation for the impeller swept volume, impeller discharge volume, and the remainder of the tank, and found that, in contrast to some other studies, only a small portion of the total dissipation, 12% was in the impeller swept region. Highest dissipation was in the bulk of the tank, 57%, and at the discharge stream, it was 31%. Note that, in the vicinity of the impeller, the local values of dissipation are far higher than that in the bulk, but because the volume of this region is small, then the total dissipation is less. They also pointed out the discrepancy of the measured ϵ data in literature, attributing this difference to the experimental estimates of the macro length scales of turbulence.

Zhou and Kresta (1996) pointed out the difficulties of measuring local dissipation values, because all three instantaneous velocities need to be measured simultaneously. They reviewed various simplified approaches in literature. They also provided, from their laser Doppler anemometry (LDA) measurements, a zonal distribution of dissipation rates in the selected volumes in a tank of $D = T/2$. 43.5% of the total energy dissipated was found to be in the impeller swept and impeller discharge region, which provides confidence to the simulation results of Ng and Yianneskis (2000).

Yeoh et al. (2004) made a comparative study to that of Ng and Yianneskis (2000) and employed both LES and $k-\epsilon$ ($Re = 40,000$, 250k cells for 180° sector) and used the SM model. They found that the power number calculated from the integrated dissipation in the tank, N_{P_ε}, was underpredicted by 45% with $k-\varepsilon$, whereas overpredicted by 15% with LES. They also found from the LES data that, the turbulence isotropy hypothesis is applicable in most parts of the tank except for the impeller discharge stream.

Recently, Murthy and Joshi (2008) compared the performance of standard $k-\varepsilon$, RSM and LES models against their LDA measurements for various impellers including a Rushton turbine. They used a standard tank ($H = T = 0.30$ m, $C = T/3$, $Re = 45,000$), and for the RANS simulations, they employed a mesh of 575k for the full 360° sector of tank without any symmetry assumption. The impeller was modelled using the SM approach. They found that although the axial velocity profiles were well predicted by all three turbulence models, for radial and tangential profiles, LES and

RSM were superior to $k-\varepsilon$ especially near the impeller. For k, LES was superior and both RSM and $k-\varepsilon$ consistently underpredicted k, particularly near the impeller. They did not report on local profiles of ε in the tank. Instead, they compared the measured power number (N_P) with the predicted ones from integrated dissipation (N_{P_ε}) and torque (N_{P_Γ}). They found that all the models underpredicted N_{P_ε}, LES by 8%, RSM by 20% and $k-\varepsilon$ by 23%. Predictions of N_{P_Γ} were much better, and the maximum underprediction was only 4%, obtained from the simulation with $k-\varepsilon$. They also did a grid independency test and concluded that the turbulent kinetic energy and the power number were already practically grid independent for a mesh of 475k.

Another recent study comparing the RANS and LES predictions is that of Delafosse et al. (2008). They used the standard $k-\epsilon$ model together with the SM method for a standard tank ($H = T = 0.45$ m, $C = T/3$, $Re = 56,250$). The computational mesh consisted of approximately 1 million cells for the full 360° of tank. Second order schemes were used both for temporal and spatial discretization. Results showed that, both RANS and LES gave good predictions of the mean velocity field. Although the total kinetic energy was predicted good with RANS, the respective amounts of turbulent and periodic kinetic energy due to passage of the impeller blades were not correct. For the turbulent dissipation rate, a correct order of magnitude was obtained with RANS, but the distribution in the vicinity of the impeller stream was not represented well. LES simulations were in better agreement with the trend of experimental data.

In contrast to the widely accepted view that the poor predictions of turbulence quantities are due to the inadequacies in the $k-\epsilon$ model, Deglon and Meyer (2006) found that accurate predictions could be obtained provided very fine grids coupled with higher–order discretization schemes are used. They performed simulations of the same tank modelled by Bartels et al. (2002) and used several grid resolutions, finest one having about 2 million grid cells for a 180° sector of tank. Impeller was modelled using the MRF method. Their results showed that both a high grid resolution and a higher–order discretization scheme (e.g. QUICK) were necessary for accurate predictions of the power number calculated from the torque. However, such an influence was not found for the predictions of the mean fluid velocity provided the grid was not too coarse. They found that there was a dramatic improvement in the predicted turbulent kinetic energy profiles near the impeller and in the impeller discharge stream as the grid resolution increased. However, even using the finest grid, there was still an underprediction in the impeller discharge stream, as the simulation had been performed by using the first–order upwind scheme. When they finally used higher–order central and QUICK schemes on the finest grid, predictions were substantially improved, and the results were comparable with the experimental data. They concluded that the poor predictions of turbulence quantities often noted in literature may be due to numerical errors rather than inadequacies in the turbulence model. They did not report on the predictions of turbulence energy dissipation.

In this study, we used four different RANS models. Three of them are in the class of $(k-\varepsilon)$-type models, namely the standard, realisable and renormalisation group theory (RNG) $k-\varepsilon$ models. The fourth one is the RSM. Our main objective is, in view of the comparative study of different modelling approaches, to present a computationally efficient route to investigate the hydrodynamics and the turbulence features of the single-phase flow in a standard stirred tank reactor and a large-scale multi-impeller fermenter. We compared our results to both experimental and numerical data available

in the literature. The findings presented may provide a basis for efficient and affordable multi-phase simulations of stirred systems.

2.2 Modelling

2.2.1 Governing equations

The fundamental equations governing the fluid flow are the mass conservation (continuity) and the momentum conservation (Navier–Stokes) equations. Analytical solution to these equations is possible only under very limited cases, and therefore, a numerical approach is necessary.

Fluid flow in equipment at an industrially relevant scale is mostly fully turbulent. Resolving such a flow at every possible scale is computationally not feasible. A common practice for practical engineering applications is to model all turbulence scales present in the flow and to solve for the average (mean) flow quantities, which is called the Reynolds-averaged Navier–Stokes (RANS) approach. In the RANS approach, the instantaneous value of any flow variable is decomposed into a mean and a fluctuating part; that is, for the instantaneous fluid velocity vector, $\mathbf{u} = \mathbf{U} + \mathbf{u}'$, where $\mathbf{U}$ is the mean velocity vector and $\mathbf{u}'$ is the turbulent fluctuating velocity component[1]. After employing time (or ensemble) averaging, the continuity and the momentum equation for an incompressible fluid, written in terms of mean quantities, are obtained respectively as

$$\nabla \cdot \mathbf{U} = 0, \tag{2.1}$$

$$\frac{\partial}{\partial t}(\rho \mathbf{U}) + \nabla \cdot (\rho \mathbf{U}\mathbf{U}) = -\nabla P + \nabla \cdot (\underline{\underline{\mathbf{T}}} + \underline{\underline{\mathbf{T}}}^t) + \rho \mathbf{g} + \mathbf{F}, \tag{2.2}$$

where P is the mean static pressure, and $\rho\mathbf{g}$ and $\mathbf{F}$ are the gravitational body force and external body forces (e.g. centrifugal and Coriolis force in a rotating reference frame), respectively. $\underline{\underline{\mathbf{T}}}$ is the mean viscous stress tensor, given for a Newtonian incompressible fluid as

$$\underline{\underline{\mathbf{T}}} = \mu \left(\nabla \mathbf{U} + \nabla (\mathbf{U})^T \right). \tag{2.3}$$

The mean turbulent stress tensor, $\underline{\underline{\mathbf{T}}}^t = -\rho \overline{\mathbf{u}'\mathbf{u}'}$, arises from the nonlinear convective term of the Navier–Stokes equation (second term of Eq. 2.2), and expresses the loss of information as a result of the averaging process. It represents the apparent stresses, the so-called Reynolds (or turbulent) stresses, due to turbulent motions. In order to close Eq. 2.2, the unknown Reynolds stresses, $-\rho \overline{\mathbf{u}'\mathbf{u}'}$, need to be modelled by a turbulence model.

In this study, we used mainly the standard $k-\varepsilon$ turbulence model. The Boussinesq hypothesis was employed to relate the Reynolds stresses with the mean velocity gradients with a proportionality constant, the so-called eddy viscosity (or turbulent viscosity), μ_t, based on an analogy to the molecular viscosity. Turbulent eddies are considered as molecules, colliding and exchanging momentum and obeying laws similar to the kinetic

[1] Throughout this thesis, we mainly denote averaged quantities with capital letters (F), scalars with lightface italic (f), vectors with boldface ($\mathbf{f}$) and tensors with double underlined boldface ($\underline{\underline{\mathbf{f}}}$)

theory of gasses (Ranade, 2002), allowing the description of the Reynolds stresses as

$$-\rho\overline{\mathbf{u}'\mathbf{u}'} = \mu_t(\nabla\mathbf{U} + \nabla\mathbf{U}^T) - \frac{2}{3}(\rho k + \mu_t\nabla\cdot\mathbf{U})\underline{\underline{\mathbf{I}}}, \tag{2.4}$$

where k is the turbulent kinetic energy, defined by normal turbulent stresses as $k = \frac{1}{2}\overline{u_i'u_i'}$. The turbulent viscosity, which is not a material property (in contrast to its molecular counterpart) but a local flow property, is assumed to be a scalar quantity (isotropic turbulence assumption), and modelled as

$$\mu_t = \rho C_\mu \frac{k^2}{\varepsilon}, \tag{2.5}$$

where C_μ is an empirical coefficient of value 0.09 and ε is the dissipation rate of the turbulent kinetic energy. Transport equations for k and ε are provided in order to close the set of equations:

$$\frac{\partial(\rho k)}{\partial t} + \frac{\partial(\rho U_i k)}{\partial x_i} = \frac{\partial}{\partial x_j}\left[\left(\mu + \frac{\mu_t}{\sigma_k}\right)\frac{\partial k}{\partial x_j}\right] + G - \rho\varepsilon, \tag{2.6}$$

$$\frac{\partial(\rho\varepsilon)}{\partial t} + \frac{\partial(\rho U_i \varepsilon)}{\partial x_i} = \frac{\partial}{\partial x_j}\left[\left(\mu + \frac{\mu_t}{\sigma_\varepsilon}\right)\frac{\partial \varepsilon}{\partial x_j}\right] + \frac{\varepsilon}{k}(C_1 G - C_2\rho\varepsilon), \tag{2.7}$$

with the model constants $C_1 = 1.44$, $C_2 = 1.92$, $\sigma_k = 1.0$ and $\sigma_\varepsilon = 1.3$. G represents the generation of turbulence kinetic energy due to mean velocity gradients:

$$G = \frac{1}{2}\mu_t\left[\nabla\mathbf{U} + (\nabla\mathbf{U})^T\right]^2. \tag{2.8}$$

There are two variations to standard $k-\epsilon$ model that were used in this study, namely, the realisable and RNG $k-\epsilon$ models. Both of these models were reported to have shown substantial improvements over the standard $k-\varepsilon$ model where the flow features include strong streamline curvature, vortices, and rotation (Fluent, 2006). Both of these models have similar forms of transport equations for k and ε. The differences arise in the method of calculating the turbulent viscosity, the turbulent Prandtl numbers governing the turbulent diffusion of k and ε, and the generation and destruction terms in the ε equation.

Because all these $(k-\varepsilon)$-type, two-equation models assume a scalar isotropic turbulent (eddy) viscosity, their performance may be questionable, especially near a Rushton type of impeller where the flow is not unidirectional, and exhibits strong radial and tangential components. Consequently, the Reynolds Stress Model (RSM) was applied. In RSM, instead of employing the Boussinesq hypothesis, transport equations are solved for each of the terms in the Reynolds stress tensor, and an additional scale-determining equation is solved for ε. Computational expense is much higher, because seven equations are solved (in 3D), instead of two. One of the important terms in transport equations of Reynolds stresses, which is often responsible for the accuracy of RSM, is the pressure-strain term. We modelled this term by the quadratic pressure–strain model (Speziale et al., 1991), which is known to perform better for flows with streamline curvature. Note that, because the additional transport equations employed in RSM make use of additional closure assumptions and modelling constants, the performance of the model may not necessarily be any better than a two-equation model (Lane, 2005a; Fluent, 2006). Further details and the equations being solved by the RSM, as well as the realisable and RNG $k-\varepsilon$ models can be found elsewhere (Fluent, 2006).

2.2.2 Modelling of the impeller

In the absence of baffles, flow in the stirred tank would be at steady-state (from the point of view of RANS approach) with respect to a rotating reference frame with the rotational speed of the impeller. Then, it would be sufficient to solve the Navier–Stokes equations in a rotating reference frame, where the body force term $\mathbf{F}$ in Eq. 2.2 consists of the centrifugal and the Coriolis forces:

$$\frac{\partial}{\partial t}(\rho\mathbf{U}_\mathrm{R})+\nabla\cdot(\rho\mathbf{U}_\mathrm{R}\mathbf{U}_\mathrm{R}) = -\nabla P+\nabla\cdot(\underline{\underline{\mathbf{T}}}_\mathrm{R}+\underline{\underline{\mathbf{T}}}^\mathrm{t}_\mathrm{R})+\rho\mathbf{g}-\rho(2\boldsymbol{\Omega}\times\mathbf{U}_\mathrm{R}+\boldsymbol{\Omega}\times\boldsymbol{\Omega}\times\mathbf{r}), \quad (2.9)$$

where $\mathbf{U}_\mathrm{R}$ is the velocity in the rotating frame and can be written in terms of the angular velocity $\boldsymbol{\Omega}$ and the position vector $\mathbf{r}$ as $\mathbf{U}_\mathrm{R} = \mathbf{U} - \boldsymbol{\Omega}\times\mathbf{r}$. The stress tensors are also of the same form as given before but written in terms of relative velocity derivatives.

Multiple reference frames (MRF) method

When there are baffles located in the stirred tank, a special consideration is needed, as the flow is transient both at a stationary and a rotating reference frame. There are different approaches for the modelling of baffled-stirred tanks, as mentioned before. Among those, we used the MRF model introduced by Luo et al. (1994), which is widely used in the recent literature.

In the MRF approach, the computational domain is divided into two zones. For the inner zone with the impeller, a rotational reference frame is defined in which the impeller is at rest, and the corresponding momentum equation is solved (Eq. 2.9). For the outer zone consisting of the tank wall and baffle, a fixed inertial reference frame is defined in which the tank walls and baffles are at rest, and the standard momentum equation is solved (Eq. 2.2). At the interface between the two zones, the flow is assumed to be steady, and coupling of the two solutions is achieved by matching velocities locally via velocity transformations from one frame to the other. It is a steady-state method (because the tank components are stationary at the corresponding frame of reference) and therefore avoids the large computational demands associated with the SM method.

The MRF model is an approximation, since it solves the flow for a fixed position of the impeller with respect to the baffles. However, it can provide a reasonable model of the time-averaged flow for mixing tanks with small impeller to tank diameter ratio, such as $D/T = 1/3$, as the impeller–baffle interactions are then relatively weak.

2.2.3 Characteristic integrated quantities

Power number

In stirred systems, energy transmitted per unit time by the impeller to the fluid is a basic parameter for the performance of the process (e.g. phase contact, mixing, gas dispersion), and is called the power draw, P. For geometrically similar tanks, it can be found, by an analysis of drag on the impeller blades under turbulent flow, that

$P \propto \rho N^3 D^5$ (Tatterson, 1991). Forming an equality, the so-called "power number N_P" is introduced, which is analogous to a drag coefficient:

$$N_P = \frac{P}{\rho N^3 D^5}. \tag{2.10}$$

For baffled tanks in the fully turbulent regime, N_P approaches to a constant value, independent of Reynolds number, when $Re > 20,000$ (Nienow, 1998).

Bujalski et al. (1987) did an extensive study on the power measurements of standard configured tanks of different scales, which were geometrically similar to the one we investigated in this work ($H = T$, $D = T/3$, $C = T/4$, etc.). All the experiments were performed in the fully turbulent regime. They used a strain gauge/telemetry system to measure the torque, and the power draw was then calculated using the relation

$$P_\Gamma = 2\pi N \Gamma. \tag{2.11}$$

The error in their torque measurements were as low as 2%. They found that the calculated N_P values were varying in the range of $4.60 - 5.96$. Surprisingly, the scale of the tank had an influence on N_P. Their measurements also showed that, the power number was a weak function of the geometrical parameters of the impeller, such as the material thickness x for the blade and the disk. N_P increases as x decreases. From a regression analysis on all their data, they proposed a relation valid for (0.22 m $\leq T \leq$ 1.83 m) and ($0.01 \leq x/D \leq 0.05$):

$$N_P = 2.5 \left(\frac{x}{D}\right)^{-0.2} \left(\frac{T}{T_0}\right)^{0.065}, \tag{2.12}$$

with a maximum deviation of $\pm 3\%$. T_0 is a reference tank diameter equal to 1 m. Using this relation, they also obtained a very good fit for other data reported in literature. Note that we did not take into account the finite thickness of the tank components in this study. Therefore, the power number values calculated from our simulations are expected to be slightly overpredicted.

In CFD simulations, power draw can be obtained from the torque Γ on the rotating parts about the axis of rotation:

$$\Gamma = \left(\int_S \mathbf{r} \times (\Sigma \cdot \mathbf{n})\, dS \right) \cdot \mathbf{a} \tag{2.13}$$

Integration is carried out over the surface S consisting of the rotating parts. $\mathbf{r}$ is the position vector, Σ is the mean total stress tensor, $\mathbf{n}$ is the unit vector normal to the surface and $\mathbf{a}$ is the unit vector parallel to the axis of rotation. Eq. 2.11 is used to calculate the power draw.

When the flow is fully turbulent, turbulence dissipation should dominate over the viscous dissipation due to mean velocity gradients, hence, the total turbulence energy dissipation in the tank liquid volume; that is

$$P_\varepsilon = \int_{\mathcal{V}_l} \rho\, \varepsilon\, dV \tag{2.14}$$

should account for most of the energy dissipation. Therefore, due to energy conservation, it is expected that $P_\varepsilon = P_\Gamma$. Hence, the power number can also be calculated

from Eq. 2.14. However, in literature, mostly the values calculated from torque are reported due to widely observed tendency of $k-\varepsilon$ turbulence model to underpredict the turbulent dissipation in stirred tank flows.

Flow number

Another important characteristic quantity for stirred systems is the impeller primary discharge flow rate, Q. It is a measure of the pumping capacity of an impeller, which directly effects the convective flow, and the circulation and mixing times in the tank. Q is defined as the volumetric discharge flow rate through the surface swept by the blade tip:

$$Q = \int_{S_{\text{swept}}} U_r \, dS, \tag{2.15}$$

where S_{swept} stands for the area swept by the blade tip and U_r for the radial velocity.

Impeller pumping capacity is usually reported in nondimensional form called the impeller flow number or pumping number, N_Q:

$$N_Q = \frac{Q}{ND^3}. \tag{2.16}$$

As for the power number, the flow number also converges to a constant value when the flow becomes fully turbulent, that is $Re > 20,000$ (Nienow, 1998). Experimental values reported in the literature for Rushton turbines show a large variation. Revill (1982) attributed this to the differences in the calculation of Q or the accuracy of different experimental techniques to measure the radial velocity profile near the impeller, and after reviewing literature, he recommended $N_Q = 0.75 \pm 0.15$ for $1/5 < D/T < 1/2$ and $3/10 < C/T < 1/2$. Among others, Nienow (1998) reported values varying in the range of $0.72 - 0.78$ and Costes and Couderc (1988) reported a value of 0.73.

Substantial increases in N_Q were reported over relatively short distances from the impeller, indicating that not only the directly pumped flow by impeller, but also the entrained flow contributed to the measurement of pumping capacities in such cases (Tatterson, 1991).

Multiple impellers

Power draw in tanks with multiple Rushton turbines depends on impeller spacing C_I. When the impellers are not closely spaced, parallel independent flow patterns form with the same double-loop recirculation structure as in single-impeller tanks. Such a condition is met when $C_I/D \gtrapprox 1.5$ and then the total power draw scales with the number of impellers, hence $(N_P)_n = n(N_P)_{n=1}$, n being the number of impellers (Nienow, 1998). As flow fields near the impellers hardly interact with each other at such a condition, the same relation is expected to hold also for the impeller discharge flow, hence, for the flow number, N_Q.

2.3 Implementation

The modelling equations given in the previous section were solved by using the commercial finite-volume-based CFD solver Fluent 6.3 (Fluent Inc.). Two different stirred reactors were considered: a standard stirred tank (Fig. 2.1) and a large-scale multi-impeller fermenter (Fig. 2.2). Both systems are equipped with four full length baffles and stirred by a six-blade Rushton turbine (Fig. 2.1(b)) mounted on a central shaft. The bottom walls were assumed be flat. The working fluid was water with density $\rho = 1000$ kg/m^3 and viscosity $\mu = 0.001$ Ns/m^2.

2.3.1 Boundary conditions and numerical set-up

All solid parts were modelled as zero-thickness surfaces with no-slip condition. The liquid surface was treated as a flat, zero-stress surface. The boundary layer at walls was modelled by applying standard wall functions, which avoids the need for a very fine grid in near-wall regions to resolve the boundary layer. The impeller shaft was assumed to extend from the free surface down to the bottom wall in order to ensure high mesh quality. The fermenter was modelled as a flat-bottomed cylindrical tank. The geometry and mesh were built by the commercial software Gambit from Fluent Inc. In order to reduce the computational time, only 60° sector (i.e. 1/6) of the full domain was modelled, including a single impeller blade and a baffle, employing rotational periodic condition at the vertical cross-sectional planes. Note that, this would, in reality, correspond to a simulation of a tank with six baffles due to symmetry. However, this additional baffling is expected to alter the flow field only locally near the baffles, because the swirling flow has already been stopped by four baffles and the baffles have little effect on the flow in the radial and axial directions (Lane, 2005a). The grid interface between the moving and the stationary zone was set at a region extending axially from the impeller centreline in the range of $(-D/4, D/4)$ for the tank and $(-D/2, D/2)$ for the fermenter, and located radially at midway between the impeller tip and the baffle.

We used the higher order QUICK (quadratic upstream interpolation for convective kinetics) scheme for discretisation of the convective terms in the modelling equations. Our test simulations showed that the first-order upwind scheme resulted in high numerical diffusion and inaccurate results, whereas the values predicted by the second-order upwind and QUICK schemes were very similar. The simulation was set up as a two-phase problem with zero gas fraction. In this way, the simulation results could be used as an initial solution for two-phase simulations later. Pressure–velocity coupling was achieved by the SIMPLE (phase-coupled semi-implicit method for pressure-linked equations) algorithm (Vásquez and Ivanov, 2000). Simulations were considered converged when the sum of the residuals (imbalance in the algebraic equation summed over all computational cells and scaled by a factor representative of the flow rate of the variable) was lower than 1×10^{-5}. At this level of convergence, the monitored quantities (e.g. impeller torque, impeller discharge flow rate, integrated turbulent dissipation) had already reached a steady value.

2.3.2 Solution domain and computational mesh

Standard stirred tank reactor

A laboratory-scale standard stirred tank with a single impeller was investigated first, with the dimensions $H = T = 1$ m and $C = T/4$. Four different finite volume meshes were generated for this tank (Fig. 2.3). The coarsest one that was used to test different models had 47k ($65 \times 36 \times 20$) structured elements, where the impeller blade surface was resolved by 56 grid cells. The medium mesh consisted of 140k ($97 \times 60 \times 24$) structured elements (192 cells/blade). The highest grid resolution was achieved by increasing the grid nodes of the coarse mesh two times in each dimension, so that the final size was $8 \times 47\text{k} = 374\text{k}$ (224 cells/blade). Finally, in order to check the effect of rotational periodicity assumption, the coarse mesh was extended to a full 360° of the tank. The final mesh size in this case is $6 \times 47\text{k} = 281\text{k}$. Under all operating conditions (see Table 2.1), the flow is fully turbulent, that is, the impeller Reynolds number $Re = \rho N D^2/\mu > 20 \times 10^3$, N being the impeller rotational speed $[s^{-1}]$.

Multi-impeller fermenter

In fermentation processes, large-scale stirred tanks are used. Because of this scale, these reactors are equipped with multiple impellers. In the present work, we also did simulations of the flow in such a reactor. It had a total volume of 30 m^3 (liquid volume of 22 m^3) and was stirred by 4 Rushton impellers on a single shaft. It was filled upto a liquid level of $H = 6.55$ m and had a diameter of $T = 2.09$ m. Bottom and mutual impeller clearances were $C = 0.54T$ and $C_I = 0.70T$ respectively, and the baffle width was $0.08T$. The remaining parts were scaled with T and D in the same manner as given for the standard stirred tank geometry.

The grid consisted of 324k ($260 \times 52 \times 24$) structured elements (120 cells/blade). For each impeller, a corresponding "moving zone" was defined as shown in Fig. 2.3(e). The reactor was operating in the fully turbulent regime. More details are given in Table 2.2.

2.4 Results and Discussion

2.4.1 Integral quantities

Flow number

The predictions of power and flow numbers from simulations with the $k - \varepsilon$ model are given in Table 2.3 and Table 2.4. For the standard tank, we report only the values from 180 rpm simulations. Variation in the results for higher stirring rates (i.e. higher Re) were $< 0.2\%$. The same Reynolds number independency was also observed in fermenter simulations. Note that these results confirm the experimental evidence that N_P and N_Q are independent of Re at fully turbulent flow.

Predicted flow numbers for both reactors are found to be within the range of experimental results published in the literature, and relatively insensitive to the grid density.

Lane (2005a) did CFD simulations of the same standard tank configuration. Using a mesh of 44k elements and the MRF model, he obtained $N_Q = 0.75$. However, he calculated the discharge flow rate Q across a cylindrical surface not exactly at the blade tip diameter D, but at $1.02D$. This introduces the possibility that the calculated discharge flow rate includes also some entrained flow as discussed before. Our simulations showed that the flow number increased from the original value of 0.70 to 0.74, when such an extended surface was used.

Simulations with the multi-impeller fermenter revealed that flow numbers for all impellers are almost the same, confirming that parallel independent flow patterns are formed. This is expected because the impeller spacing was large enough ($C_I/D \approx 2$). Vrábel et al. (2000) did mixing experiments and compartmental type of modelling of the same fermenter being studied in this work. He did not measure the flow number, probably due to experimental difficulties at such a scale. Instead, he used $N_Q = 0.75$ as recommended by Revill (1982) in his model.

Power number

Simulations showed that the power number calculated from turbulent dissipation, N_{P_ε}, is the most grid sensitive parameter, whereas the one calculated from torque, N_{P_Γ}, is hardly changing with the grid resolution and therefore can be considered as the grid independent value. N_{P_ε}, as predicted from the simulation with the coarse grid, is 15% lower than N_{P_Γ}. This points to an underprediction of N_{P_ε} with the $k-\varepsilon$ model. When we go from coarse (47k) to medium grid (140k), there is 11% relative increase in N_{P_ε}. Going further to the fine grid (374k) results only in an additional 0.2% increase in N_{P_ε}, and the corresponding mismatch with respect to N_{P_Γ} arrives to a plateau of 5%. Therefore, we can conclude that the medium grid has a sufficient resolution, at least, as far as the integral turbulence quantities are concerned. Moreover, the underprediction in the integrated dissipation is much less (i.e. 5%) than the substantial underpredictions reported in literature (e.g. 50% by Lane (2005a)). Recently, simulations of Murthy and Joshi (2008) resulted in a relative mismatch between N_{P_ε} and N_{P_Γ} of values 20% for $k-\varepsilon$, 18% for RSM and 10% for LES.

From the comparison of results for 60° and 360° domains, which have the same grid resolution, it can be seen that the 60° periodicity assumption does not have a significant effect on the integral quantities. There is only a slight increase (maximum 4%) in power draw, which can be attributed to the additional velocity gradients (hence dissipation) created by the extra baffles, as a result of the underlying symmetry assumption.

Experimental power data is available only under gassed condition for this tank (Barigou and Greaves, 1992). However, Bujalski et al. (1987) made detailed measurements of geometrically similar tanks. For the tanks of comparable size to our case, they obtained the values $N_P = 5.59$ (for $T = 0.61$ m) and $N_P = 5.96$ (for $T = 1.83$ m), which correspond well with the CFD predictions given in Table 2.3.

Lane (2005a) found a somewhat lower value, $N_{P_\Gamma} = 5.0$, in his CFD study of the same tank, using a computational mesh of size 44k (60° sector, 8×7 cells/blade). He also did simulations of a smaller standard configured tank ($H = T = 0.294$ m, $C = T/3$), where he employed three different grids: 109k (180° sector, 6×10 cells/blade), 56k (60° sector, 8×9 cells/blade) and 440k (60° sector, 18×20 cells/blade). He reported that,

using the 109k grid, which has a smaller grid density than the coarse grid used in this study, the predicted N_{P_Γ} was only 4% lower than the experimental value, whereas the underprediction was 46% for N_{P_ϵ}. The predictions of the mean velocity components were similar with both 109k and 56k grids, which have a similar grid density but different extent of the tank domain. When the fine grid (440k) was used, the velocities were in better agreement with the experimental data and the k and ϵ values were substantially increased, although they were still underpredicted by as much as 35% and 25% respectively.

The power numbers calculated for the fermenter were also found to be insensitive to the stirring speed (hence to Re) as expected, because the flow is fully turbulent. The torque on each impeller was found to be almost identical and so is the power draw. The mismatch between N_{P_ε} and N_{P_Γ} is maximum 7.6%. The predicted N_{P_Γ} is ~ 5.75 for all impellers, and is in very good agreement with the experimental value of 5.8 reported by Noorman et al. (1993) and Vrábel et al. (2000).

Effect of grid resolution

From the results mentioned above, it can be concluded that a high-density grid is necessary, for accurate prediction of turbulent quantities (in particular integrated dissipation), an issue that was also pointed out among others by Deglon and Meyer (2006) and Khopkar and Ranade (2006). Grid resolution in the vicinity of the impeller is important because trailing vortices and high local dissipation values are encountered here. However, the findings of Ng and Yianneskis (2000) that only 12% of the total dissipation is at impeller swept volume, whereas 31% in the impeller stream and 57% in the bulk, suggest that the grid resolution at these regions may also be important in order to accurately predict the total dissipation.

We note that, even if we use a coarse mesh, our underprediction of the dissipation was much less than what was obtained with a finer mesh in some earlier studies (e.g. Yeoh et al. (2004)). Therefore, we cannot conclude that the large underprediction in the earlier studies are fully caused by the insufficient grid resolution. Actually, there are large deviations in the results between different studies even with the comparable grid resolution (e.g. 45% underprediction by Yeoh et al. (2004) versus 23% by Murthy and Joshi (2008)) showing that there should be other reasons why some studies had such high underpredictions. Without having a complete information on the mesh, the solver and the numerical settings of the simulations of these studies, it is difficult to identify the causes precisely.

2.4.2 Turbulence predictions

The predictions of k and ε at the impeller discharge stream (at impeller centreline) are given in Fig. 2.4 for the tank and the fermenter. Because the normalised profiles were not changing with the impeller speed, only the profiles for 180 and 115 rpm cases are shown for the tank and the fermenter, respectively. Predictions for the fermenter are given only for the bottom impeller, because the other impellers had practically the same profile. Comparison is made to the LDA data from Wu and Patterson (1989) for a standard tank ($T = 0.27$ m, $C = T/3$ at $Re = 29,000$). They estimated the

error in the calculation of dissipation to be $\sim$ 15%. Note that their tank was not completely geometrically similar to ours, due to a larger impeller clearance. However, at the impeller discharge stream, where the highest levels of turbulence energy and its dissipation are encountered in the tank, it is expected that the effect of the clearance would be less pronounced.

Predictions show that, near the impeller blade, both k and ϵ are overpredicted, the latter to a larger extent. This might be due to the fact that, at the impeller surfaces, boundary layers might not be completely developed, and therefore, use of wall functions in this region might not be justified (Yeoh et al., 2004). In the remaining part, agreement is better with the experimental data. However, it should be borne in mind that some overprediction of the turbulence quantities is expected because the thickness of the impeller disk and blades were not taken into account in the modelling. Moreover, the comparison is made against experimental measurements in a tank that has different impeller clearance and size. Because of the scale effect mentioned before, the turbulence predictions are expected to be higher than what would be for a smaller tank. Fig. 2.4(a) shows that the grid independency is achieved at the medium mesh (140k). However, all the meshes resulted in qualitatively similar profiles of k and ϵ except near the blade and the baffle, where wall functions are in effect. Profiles of ϵ show a sudden jump near the baffle due to velocity gradients formed here.

Simulations with different turbulence models revealed that, the standard $k-\varepsilon$ model gives surprisingly the best predictions, except near the blade tip (Fig. 2.4(b)). Note that we used the standard model constants for all turbulence models. The realisable $k-\varepsilon$ model predictions are somewhat closer to that of the standard model, in general, whereas the profile from the RNG model is both qualitatively and quantitatively in disagreement. The RSM was the only model that was able to predict the trend of the experimental data near the blade tip. Although it predicted the shape of the measurement profile closely, there is a discrepancy especially for the dissipation. The difference is larger in the fermenter simulations (Fig. 2.4(c)). It should be noted that the RNG and RSM simulations were more difficult to converge, and the residual sums were not as low as 1×10^{-5}, unlike the other simulations.

2.4.3 Velocity fields

The characteristic mean flow field for the stirred tank and the fermenter can be seen in Fig. 2.5. The jet from the impeller, which is inclined slightly upward, impinges on the tank wall and splits into upward and downward streams that form the two recirculation loops. The velocity field for the fine grid (Fig. 2.5(a)) is somewhat weaker in comparison to that for the coarse grid (Fig. 2.5(b) and (c)) because the energy dissipation was higher for the fine grid, as discussed before. The velocity field obtained from the simulation with the full tank domain (Fig. 2.5(c)) is slightly different from those obtained with the 60° domain. Note that because there are four baffles in the full domain, the velocity field plane has a different angular location with respect to the baffles than that for the 60° domain.

The mean flow field for the fermenter (Fig. 2.5(d)) shows the independent double-loop structure at each impeller, in agreement with the findings that the power and the flow numbers were practically the same for each impeller. Because of flow symmetry, the

flow fields at axially midway between the impellers resemble as if there were frictionless planes that separate the tank into four independent single-impeller compartments. Measurements of Roušar and van den Akker (1994) in a 3-impeller system also confirm this. They found that the impeller zones were separated by a horizontal plane located just at the midway between them where the mean axial velocities were all zero. Hence, the mass exchange between impeller zones is only by means of the turbulent diffusion.

The trailing vortex pair formed at the upper and lower part of the impeller blades are shown in Fig. 2.6(c). The flow circulation can be seen at the cross-sectional regions where the vortices cut through the impeller swept surface. These vortices rotate at high speed in opposite directions, with maximum shear rates up to $\sim 100N$ [s^{-1}]. They originate from a combined effect of the vortex motion in the stagnation zone at the rear of the vertical inside edge of the blade and the wrapping of the vortex sheets behind both horizontal edges as illustrated in Fig. 2.6(a) and 2.6(b) (van't Riet and Smith, 1975). Another stagnation zone is located at the front side of the blade near the middle point. Fig. 2.6(d) shows that both stagnation points were captured in the simulations.

In Fig. 2.7, radial profiles of circumferentially averaged mean velocities at the impeller centerline level are plotted for the standard tank (180 rpm, $k-\varepsilon$ model case). A comparison was also made with respect to the LDA date of Wu and Patterson (1989) mentioned earlier and the simulation data (MRF and SM) that Lane (2005a) reported for radial velocities. Radial and tangential velocity predictions agree well with the experimental data, whereas the axial velocities near the impeller blade show a decreasing trend and were underpredicted for the cases with the domain symmetry assumption. In the bulk region, agreement is still good. Radial velocity profiles show the similar trend to that of Lane (2005a), though are in better correspondence with the measurements especially near the blade. Variation in velocity profiles with respect to the grid resolution and the domain symmetry is generally rather small. This indicates that simulations with the 46k mesh and the six fold domain reduction are able to capture the general features of the flow field well at the impeller centerline plane.

A similar comparison was made for the fermenter (115 rpm, $k-\varepsilon$ model case) in Fig. 2.8. Note that we compare here the predictions for the multi-impeller fermenter with the experimental data from a standard single-impeller tank due to lack of data. Thus we expect some differences as flow characteristics are not exactly the same. Despite this, tangential velocity profiles are predicted remarkably close to the experimental data. Variation among the different impellers is also very small for tangential velocity profiles. Radial velocity profiles have also small variation among the different impellers and agreement with the measurements is rather good, though in the bulk region velocities are consistently higher. That is, the impeller discharge flow dissipates radially slower in the large fermenter relative to that in the small standard tank. The axial velocity predictions show the largest deviation from the experimental profile, which was also observed in the standard tank predictions. Here, however, the underprediction near the impeller blade is much higher and is extended further away from the blade. Variation among the different impellers is also very large. The top impeller profile is the closest to the experimental profile, as the flow characteristics is closest to a single impeller system due to geometric similarity. Middle impellers that have confined recirculation loops have rather flat axial velocity profiles. The bottom impeller profile shows even an opposite trend with respect to the others, that is, the flow is axially downwards

near the impeller and upwards near the baffle and the wall. Because the impeller is further away from the bottom wall relative to a standard-configured single-impeller system (impeller–bottom wall clearances are $C = 0.54T$ and $C = 0.25T$, respectively), the recirculation stream under the impeller plane returns back to the impeller weaker relative to the upper recirculation stream above the impeller plane. Due to this imbalance, the impeller discharge stream is directed slightly downwards, which could also be seen in the velocity field given in Fig. 2.5(d). This imbalance is in the opposite way for the single-impeller tank as the impeller is much closer to the bottom wall and further away from the free surface, leading to an upwards directed impeller discharge stream (see Fig. 2.5(a)–(c)).

2.5 Conclusions

A computationally cheap and efficient approach for CFD simulations of the fully turbulent flow in a laboratory-scale standard stirred tank and a large-scale multi-impeller fermenter is presented. Computational costs were greatly reduced by first, reducing the domain to only a 60° sector (1/6) of the full tank by assuming flow periodicity; second, employing a steady-state MRF model; and third, using the conventional $k-\varepsilon$ model. Effects of the underlying assumptions of the modelling simplifications on the results were tested by performing simulations using a mesh for full tank without any symmetry assumption and by implementing the realisable and RNG $k-\varepsilon$ models as well as the RSM model. Results showed that above-mentioned simplified approach did not result in any significant change for the predicted quantities presented in this work.

Despite the substantial underpredictions (up to 50%) of ε, N_{P_ε}, and k reported in many previous studies in the literature that employ $k-\varepsilon$ model, we found good predictions of these quantities. Using a grid of 140k, the underprediction of N_{P_ε} was only 5%. Moreover, $k-\varepsilon$ model was able to give good predictions of k and ε profiles at the impeller discharge stream, except in the close vicinity of the impeller blade, where ε was overpredicted. At this region, the RSM was the only model that was able to predict the experimental trend. Our results, in general, agree with that of Deglon and Meyer (2006) regarding that good predictions of turbulence quantities can be obtained by using computationally cheap MRF method and the standard $k-\epsilon$ model, provided the grid resolution is fine enough and higher–order discretization schemes are used. However, it is likely that there are other factors contributing to the differece in results obtained with the $k-\epsilon$ model in some other previous studies. This is an issue that needs further investigation. Predictions of the impeller flow number were also found to be in good agreement with the experimental values, both for the tank and the fermenter.

It is important to note the following aspect, which is evident from our results. Although k and ϵ profiles (except near the blade and the baffle), the power number based on torque (N_{P_Γ}), and the flow number seem to be almost grid independent already with the coarse mesh (47k), the power number based on integrated dissipation (N_{P_ϵ}) does change significantly by mesh refinement. Therefore, a grid independence study that does not consider N_{P_ϵ} may result in false conclusions.

The findings presented in this study may provide a basis for efficient and affordable multi-phase simulations of stirred systems.

Tables

Table 2.1: Simulation cases for the standard stirred tank

	Case 1	Case 2	Case 3
Stirring speed [rpm]	180	250	285
Impeller tip speed [m/s]	3.1	4.4	5.0
Impeller Reynolds number	330,000	460,000	530,000

Table 2.2: Simulation cases for the fermenter

	Case 1	Case 2	Case 3
Stirring speed [rpm]	70	115	133
Impeller tip speed [m/s]	2.6	4.2	4.9
Impeller Reynolds number	570,000	940,000	1,090,000

Table 2.3: Predicted power and flow numbers for the standard stirred tank (180 rpm, $k-\varepsilon$ model)

	47k mesh (60° domain)	140k mesh (60° domain)	374k mesh (60° domain)	281k mesh (360° domain)
N_Q	0.70	0.71	0.72	0.72
N_{P_ε}	4.84	5.37	5.38	4.74
N_{P_Γ}	5.69	5.67	5.68	5.48

Table 2.4: Predicted power and flow numbers (divided by impeller number) for the fermenter ($k-\varepsilon$ model)

	Experimental	70 rpm	115 rpm	133 rpm
$N_Q/4$	0.75[a]	0.74	0.74	0.74
$N_{P_\varepsilon}/4$	5.8[b]	5.32	5.32	5.31
$N_{P_\Gamma}/4$	5.8[c]	5.76	5.75	5.74

[a] Value used by Vrábel et al. (2000) based on the recommendation by Revill (1982)
[b] Based on thermal measurements of the dissipated heat (Noorman et al., 1993)
[c] Based on power measurements (Vrábel et al., 2000)

Figures

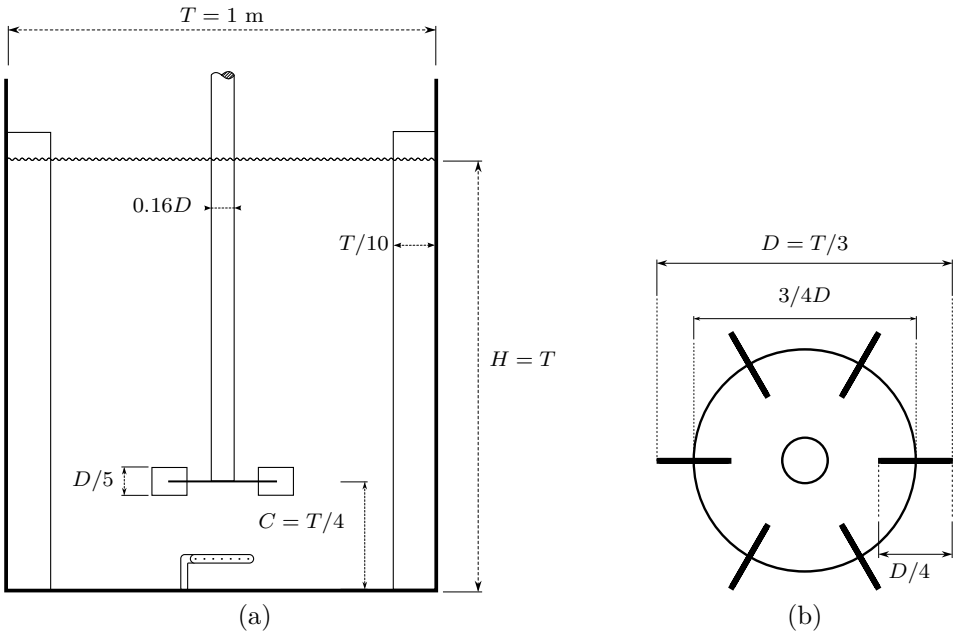

Figure 2.1: Configuration of the standard stirred tank (a). The impeller is a Rushton turbine (b).

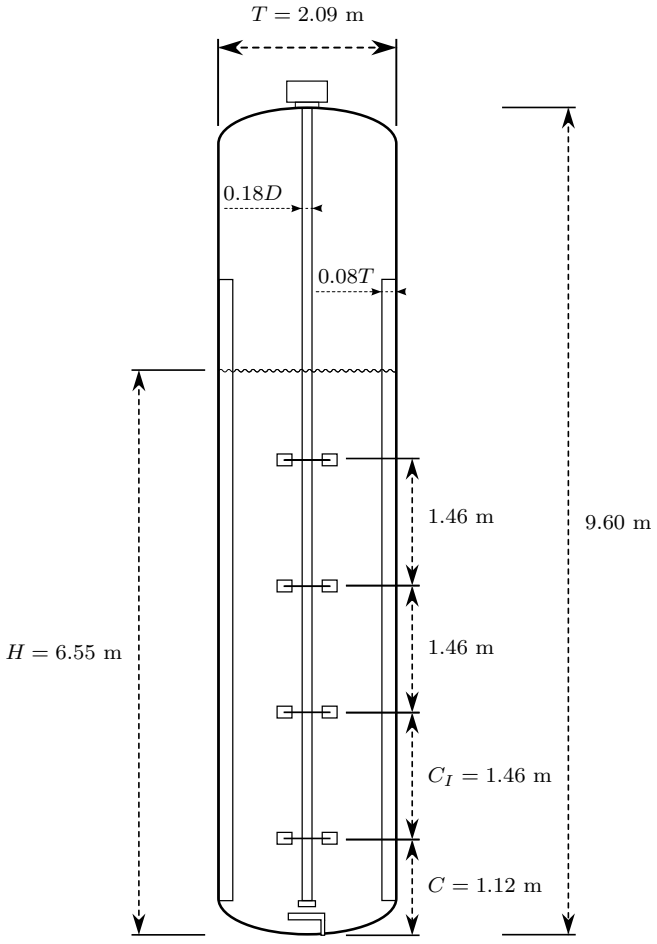

Figure 2.2: Configuration of the 30 m^3 fermenter. The impeller is a Rushton turbine as given in Fig. 2.1(b).

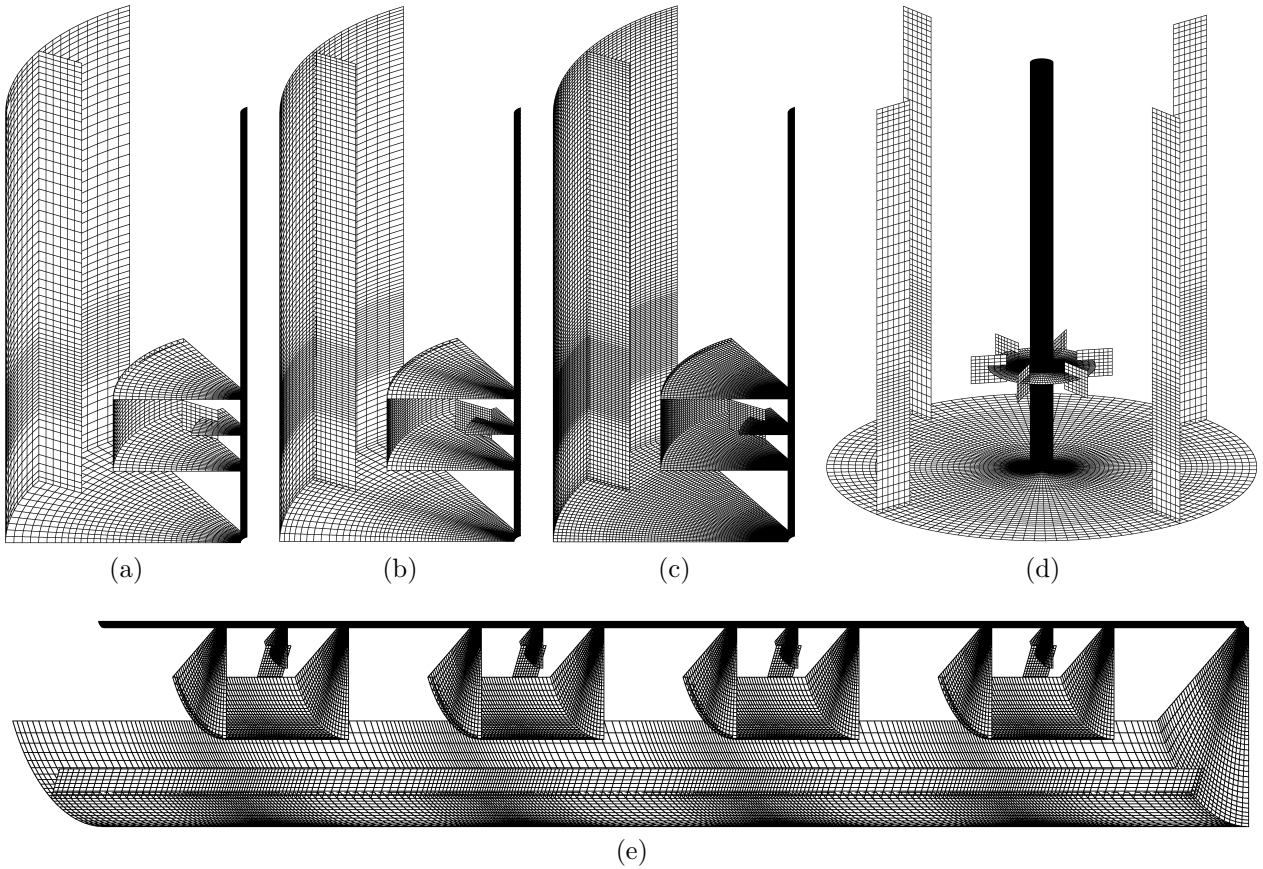

Figure 2.3: Surface plots of computational grids used in simulations (MRF grid interface is also shown). (a) Coarse mesh: 47k ($65 \times 36 \times 20$), (b) Medium mesh: 140k ($97 \times 60 \times 24$), (c) Fine mesh: 374k ($130 \times 72 \times 40$), (d) Mesh for full 360° tank ($6 \times 47\text{k} = 281\text{k}$), and (e) Fermenter: 324k ($260 \times 52 \times 24$).

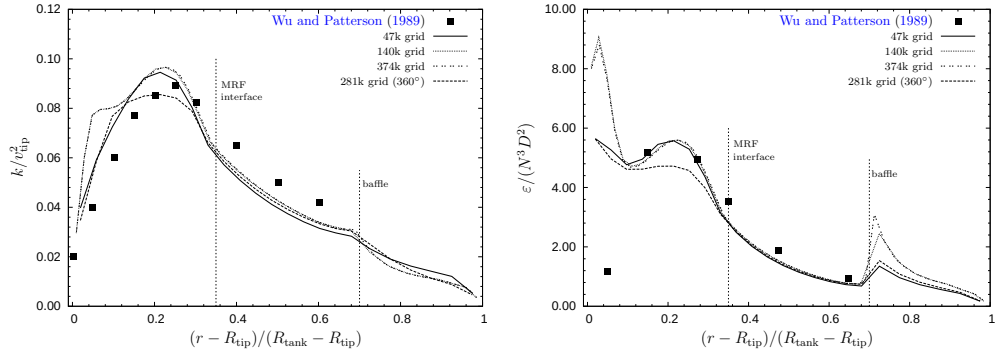

(a) Tank (180 rpm, $k - \varepsilon$)

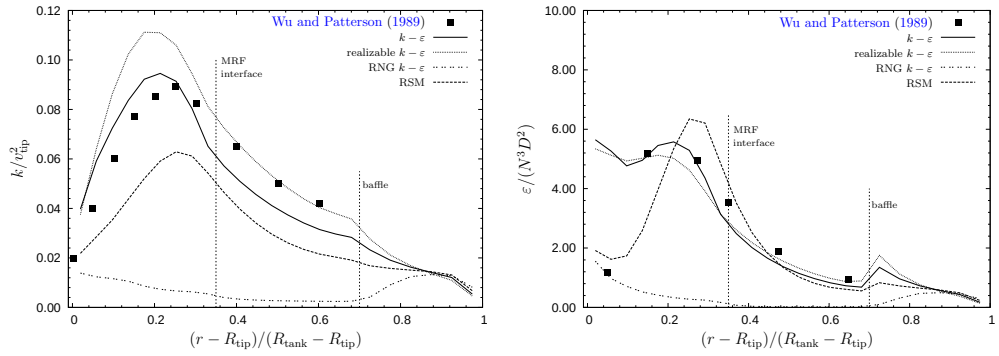

(b) Tank (180 rpm, 47k grid)

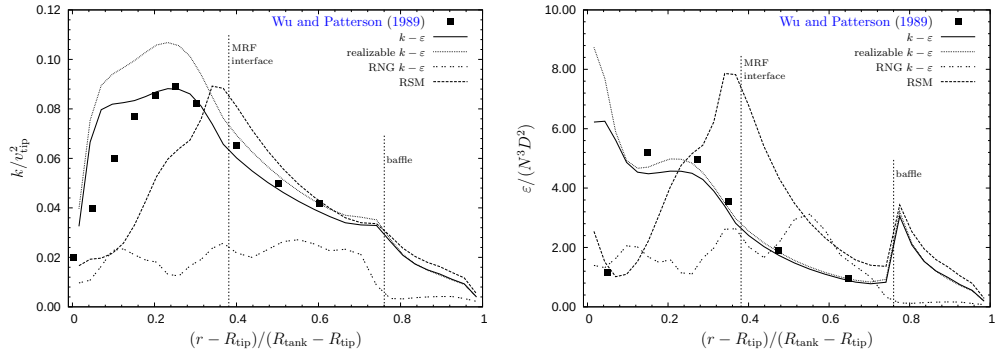

(c) Fermenter (115 rpm, bottom impeller)

Figure 2.4: Normalised turbulence kinetic energy and its dissipation rate at impeller discharge stream (at impeller centreline) plotted for different turbulence models and grids. Profiles extend from blade tip to tank wall.

Figure 2.5: Mean velocity fields at the plane midway between baffles and blades ($k-\varepsilon$ model). (a) 180 rpm, 140k grid (tank), (b) 180 rpm, 47k grid (tank), (c) 180 rpm, full 360° tank (mid-blade plane at 30° to the baffle downstream, and −60° to the baffle upstream), (d) 115 rpm, fermenter (plane rotated 90° counterclockwise).

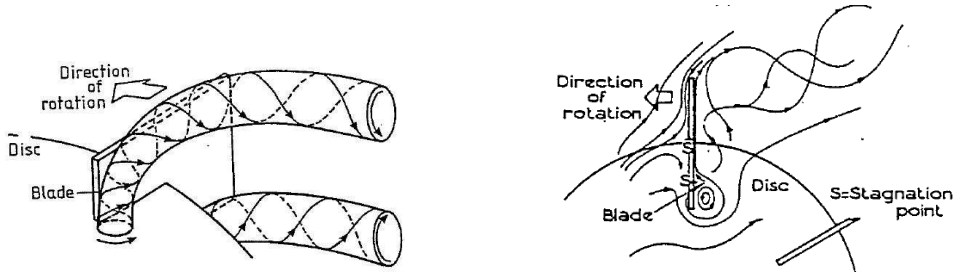

(a) (b)

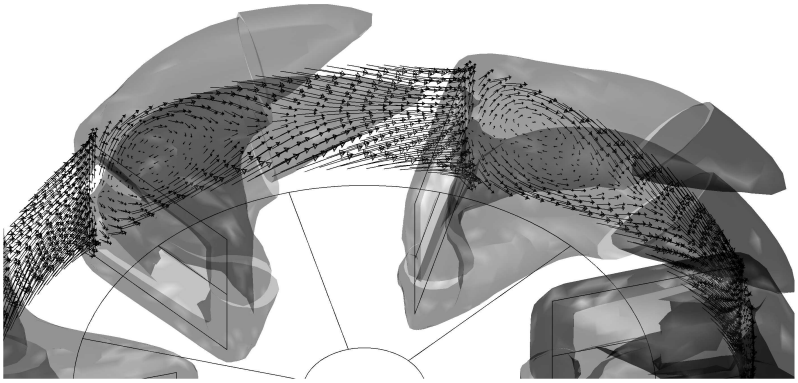

(c)

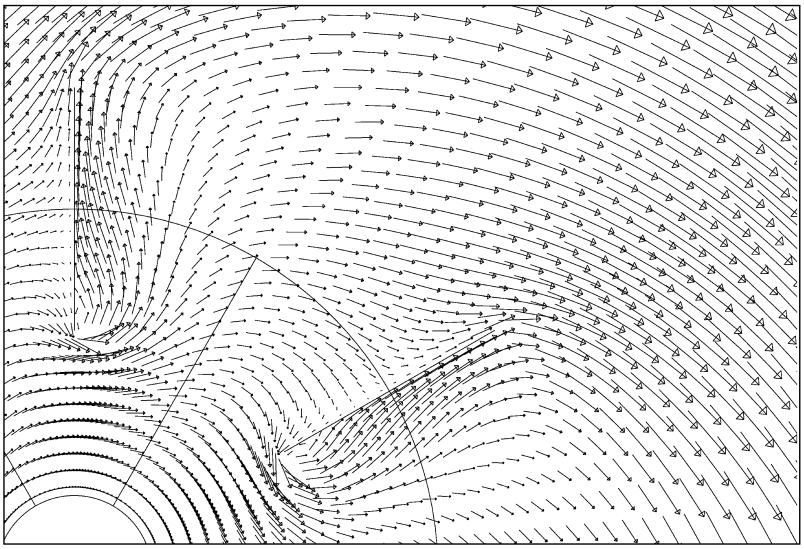

(d)

Figure 2.6: (a, b): Schematic representation of the trailing vortex pair and the flow field near the impeller blade showing the stagnation points, S (from van't Riet and Smith (1975)). (c, d): Velocity field (periodically repeated) with respect to the rotating reference frame (180 rpm counterclockwise, 140k grid, standard tank, $k-\varepsilon$ model), (c) at the plane swept by the impeller blades (iso-surface of vorticity magnitude of 100 s^{-1} is also shown), and (d) just above the impeller centreline plane (axial location at 0.27 m).

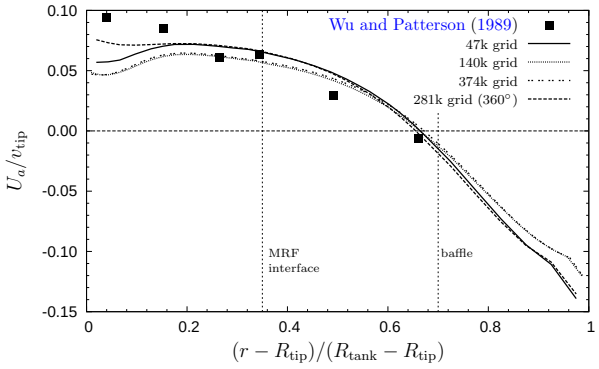

(a) Axial velocity

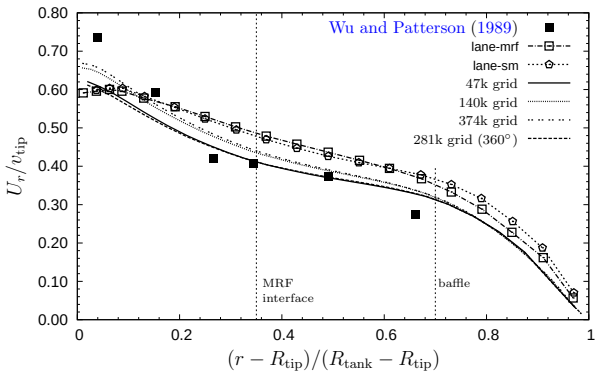

(b) Radial velocity

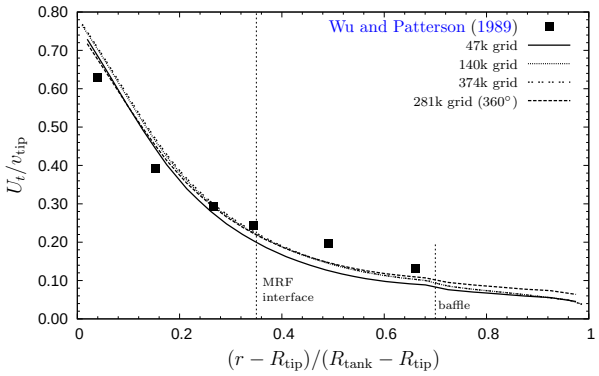

(c) Tangential velocity

Figure 2.7: Radial profiles of circumferentially averaged mean velocity (normalised with the impeller tip speed) at the impeller disk level, plotted for different grids for the standard tank (180 rpm, $k - \varepsilon$ model).

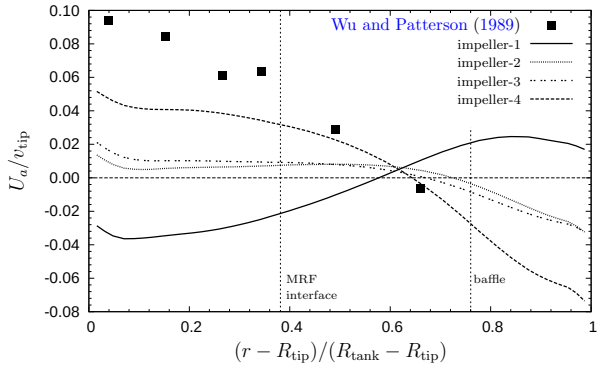

(a) Axial velocity

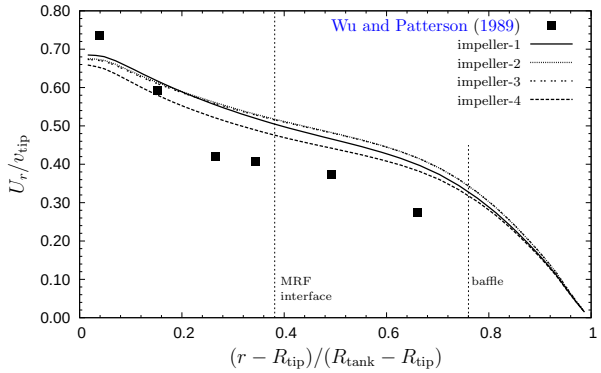

(b) Radial velocity

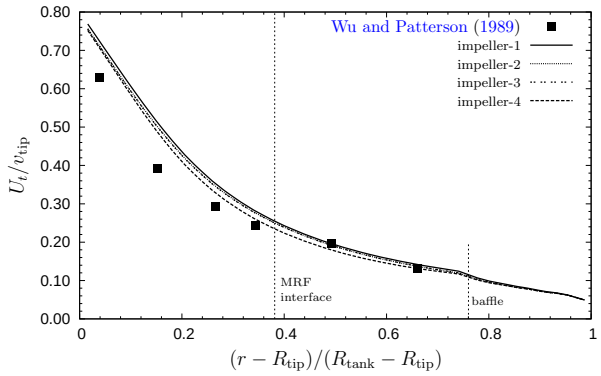

(c) Tangential velocity

Figure 2.8: Radial profiles of circumferentially averaged mean velocity (normalised with the impeller tip speed) at the impeller disk levels in the fermenter (115 rpm, $k-\varepsilon$ model); impellers numbered from the bottom (1) to the top (4). Experimental data of Wu and Patterson (1989) is from a standard single-impeller tank.

Chapter 3

Gas dispersion in stirred tanks

In this chapter, the characteristic features of the gas–liquid flow in stirred tanks with Rushton impellers will be given. Firstly, we will discuss the standard stirred tank geometry with single impeller. Later, the gas dispersion into stirred systems with multiple impellers will follow.

3.1 Flow characteristics of a standard stirred tank

3.1.1 Characteristic integrated quantities

Power and flow number

In the absence of gas dispersion, two important parameters characterising the performance of stirred tanks are the power consumption, P, and the impeller primary discharge flow rate, Q. These parameters are usually expressed in terms of dimensionless numbers, namely the power number N_P and the impeller flow number N_Q:

$$N_P = \frac{P}{\rho_l N^3 D^5}, \tag{3.1}$$

$$N_Q = \frac{Q}{N D^3}, \tag{3.2}$$

where ρ_l is the liquid density, N is the stirring frequency and D is the impeller diameter. For baffled tanks in the fully turbulent regime, that is when the impeller Reynolds number $Re = \rho_l N D^2/\mu_l > 20,000$, μ_l being the liquid viscosity, both N_P and N_Q approach to a constant value independent of Re, provided that no surface vortex is present (Tatterson, 1991; Nienow, 1998).

In single-phase operation, impeller power consumption can be calculated from a drag analysis on the impeller blades under turbulent flow (see e.g. Tatterson (1991)). An alternative calculation following van't Riet and Tramper (1991) is as follows. In turbulent flow, most of the power transmitted to the liquid is converted into kinetic energy

of the impeller volumetric discharge flow, Q (see Eq. 2.15):

$$P = \frac{1}{2}\rho_{\mathrm{l}} Q \overline{u_{\mathrm{r}}^2}, \tag{3.3}$$

where u_{r} is the radial discharge velocity of a radially pumping impeller. The discharge flow can be approximated by the flow through the area swept by the impeller blade tips:

$$Q = (\pi D H_{\mathrm{blade}})\overline{u_{\mathrm{r}}} \tag{3.4}$$

For standard geometry tanks, $H_{\mathrm{blade}} = \mathrm{const}.D$, that is the blade height scales with the impeller diameter. Assuming further that $\overline{u_{\mathrm{r}}} = \pi N D$ and $\overline{u_{\mathrm{r}}}^2 = \overline{u_{\mathrm{r}}^2}$, we have

$$Q = \mathrm{const} \cdot N D^3, \tag{3.5}$$

$$P = N_P \rho_{\mathrm{l}} N^3 D^5, \tag{3.6}$$

the dimensionless proportionality constant being the power number, N_P. When the flow is not fully turbulent, N_P is not constant, but a function of Re only. Note that the above proportionality holds for all stirrer types, that is $P \propto \rho_{\mathrm{l}} N^3 D^5$.

Gas flow number and Froude number

For gas-sparged systems operating in the turbulent regime, two other dimensionless numbers mainly characterise the gassed flow pattern, namely the gas flow number and the Froude number. The gas flow number (or aeration number), is proportional to the ratio of the gas flow rate to the pumping capacity of the impeller:

$$Fl = \frac{Q_{\mathrm{g}}}{N D^3}, \tag{3.7}$$

Q_{g} being the gas flow rate from the sparger. The Froude number,

$$Fr = \frac{N^2 D}{g}, \tag{3.8}$$

is the ratio of inertial forces to gravitational forces (i.e. $Fr = F_{\mathrm{I}}/F_g \propto U^2/gL$, see Table 3.1), g being the gravitational acceleration. Note that the total gas entering the impeller region consists, in general, of not only freshly sparged gas Q_{g} but also recirculated gas that has been dispersed by the impeller Q_{R}, which is not included in the definition of gas flow number. Q_{R} cannot be obtained with high accuracy from a any general correlation, as it depends on the bubble size and therefore the coalescence characteristics of the system (Middleton, 1992). Furthermore, the gas flow number might be misleading sometimes especially when comparing different cases with varying impeller speed and varying gassing rate. A high gas flow number, for instance, may result from high gas flow rate or low stirring speed, which are different states. Power draw and the Q_{R} could also be quite different for the same Fl (Tatterson, 1991).

In gas–liquid mixing systems, the gas flow number and the Froude number are frequently used to describe the process condition in the reactor. Several such relations have been proposed in literature that describe the gassed power draw, two-phase flow regime in the vessel and type of the cavities formed at the impeller blades. In the coming sections, we present some of those correlations.

3.1.2 Gassed power uptake and impeller discharge flow correlations

When gas is dispersed into the tank and gas cavities start to form at the impeller blades, the liquid–impeller contact area decreases to an extent that depends on the gas–liquid flow regime. As a result, the power transmitted by the impeller to the liquid decreases. Similarly, impeller liquid discharge flow rate (i.e. impeller pumping) also decreases as part of the flow is now occupied by the gas. Bakker and Van den Akker (1994) assumed that the decrease in pumping capacity is proportional to the decrease in power consumption:

$$N_{Q_G} = N_Q \frac{N_{P_g}}{N_P}, \tag{3.9}$$

where N_{Q_G} is the impeller flow number under gassed conditions. They further assumed that the ungassed and gassed velocities are kinematically similar at any point in the tank. Thus, they scaled the single-phase flow velocities calculated by CFD with the gassed to ungassed power ratio determined experimentally, and predicted the liquid velocities under gassed conditions as

$$\mathbf{u}_{1,g} = \mathbf{u}_1 \left(\frac{P_g}{P}\right)^n, \tag{3.10}$$

where the scaling exponent was proposed as $n = 1$ in the whole flow field.

Measurements of Roušar and van den Akker (1994) also support Eq. 3.9 that the decrease in pumping capacity is proportional to the decrease in power consumption. They found that the flow field at the impeller depends mainly on the power consumption of the impeller for both ungassed and gassed conditions. Hence, P_g/P fully determines the boundary conditions at the impeller tip. They also found that the assumption $n = 1$ for the scaling exponent in Eq. 3.10 holds true around the impeller, however in the far regions the bubble swarm changes the liquid flow field significantly.

P_g/P is a function of gas flow number at constant Froude number and the shape of such power curves depends on Fr (Bakker et al., 1994). Various correlations have been proposed in literature for predicting P_g/P as a function of geometric parameters. The power ratio is expected to depend also on physical properties of the system such as the surface tension, because those may affect the gas cavity formed at the impeller. However, the effect of those properties was found to be not significant (Joshi et al., 1982).

In their review paper, Joshi et al. (1982) recommend the correlation proposed by Hughmark (1980) for flat-blade turbines, which covers a wide range of variables and has a dimensionless character:

$$\frac{P_g}{P} = 0.10 \left(\frac{Q_g}{N\mathcal{V}_l}\right)^{-1/4} \left(\frac{N^2 D^4}{gB\mathcal{V}_l^{2/3}}\right)^{-1/5}. \tag{3.11}$$

Note that the above relation consists of modified gas flow number and Froude number groups. The liquid volume ($\mathcal{V}_l$) has been used in the gas flow number rather than the impeller diameter cube. The impeller discharge stream diameter is defined as the blade width, B (for standard configured tanks, $B = D/5$, see Fig. 2.1). With those

modifications, the average absolute deviation from the experimental values was reduced to 11.7 % for a wide range of conditions (tank diameters from 0.165 to 1 m, gas flow rates from 0.2 to 1.8 vvm) represented by 391 data sets.

Bakker et al. (1994) recommended a correlation in terms of gas flow number and Froude number, which is valid for radial turbines mounted directly above a gas sparger:

$$P_\mathrm{g}/P = \left[1 - (b - a\,\mu_\mathrm{l})\,Fr^d\,\tanh(c\,Fl)\right]. \tag{3.12}$$

The constants for a flat blade type were given as $a = 0.72$, $b = 0.72$, $c = 24$ and $d = 0.25$. The form of the relation implies that the constant a carries the unit of reciprocal of the dynamic viscosity μ_l [Pa.s].

In Section 9.3.1 and 9.3.2, we explain the calculation of gassed power number (including pneumatic power input due to gas flow) and flow number within a CFD framework.

3.1.3 Gas holdup, bubble size and interfacial area correlations

In addition to the gassed power consumption, the interfacial area generated in gas-sparged tanks is also a crucial design parameter as it characterises the gas–liquid mass transfer. Again, various correlations are available, either directly predicting the interfacial area, or predicting the gas holdup and the mean bubble size in terms of separate correlations which can then be combined to describe the interfacial area.

Prediction of gas holdup itself is also important, because high holdups may cause liquid levels to go beyond acceptable limits as well as limit the amount of liquid a tank can hold. Gas holdup, ϕ, is the dimensionless volume fraction of the gas phase in the dispersion. A volume or area balance on a tank cross section, summed over all bubbles gives an estimate of ϕ (Tatterson, 1991):

$$U_\mathrm{T} \sum(\pi d_\mathrm{b}^2) = U_\mathrm{g,s}(\pi T^2), \tag{3.13}$$

where U_T is the bubble terminal rise velocity and $U_\mathrm{g,s}$ is the superficial gas velocity:

$$U_\mathrm{g,s} = \frac{Q_\mathrm{g}}{(\pi/4)T^2}. \tag{3.14}$$

Holdup, which is also the dimensionless area fraction of bubbles (i.e. the ratio $\sum(\pi d_\mathrm{b}^2)/T^2$), is then:

$$\phi = \frac{\sum d_\mathrm{b}^2}{T^2} = \frac{U_\mathrm{g,s}}{U_\mathrm{T}}. \tag{3.15}$$

Gas holdup is a function of the physical properties of the liquid, the geometric parameters, the power input and the gas flow rate. At constant superficial gas velocity and power per unit mass, gas holdup remains constant (Bakker et al., 1994). Correlations proposed in literature are usually in the form:

$$\phi = c_\phi \left(\frac{P_\mathrm{g}}{\mathcal{V}_\mathrm{l}}\right)^a U_\mathrm{g,s}^b, \tag{3.16}$$

in which the gas flow rate is expressed in terms of the superficial gas velocity. Bakker et al. (1994) recommended, for air–water systems agitated with a single impeller, the

constants $c_\phi = 0.16 \pm 0.04$, $a = 0.33$ and $b = 0.67$ (SI units have to be used as the correlation was not made dimensionless). Those constants depend on the reactor geometry, the impeller type and the physical properties of the fluid. Concave-blade turbines generally give a larger holdup than flat-blade turbines, however the differences were found to be within the accuracy margin of measurements of the constants.

Given the success of representing gassed power ratio in terms of modified gas flow and Froude numbers by Eq. 3.11, Hughmark (1980) used a similar form to predict gas holdup. A Weber number based on the fluctuating velocity was used in place of the Froude number. Analysis of 208 data sets (gas holdups from 0.02 to 0.17, tank diameters up to 0.457 m) and assuming a constant bubble size of 2.5 mm for the entire data set (which was within the bubble size range of the experimental data used), the following correlation was proposed:

$$\phi = 0.74 \left(\frac{Q_\mathrm{g}}{N\mathcal{V}_\mathrm{l}}\right)^{1/2} \left(\frac{N^2D^4}{gB\mathcal{V}_\mathrm{l}^{2/3}}\right)^{1/2} \left(\frac{d_\mathrm{b}N^2D^4}{\sigma\mathcal{V}_\mathrm{l}^{2/3}}\right)^{1/4}, \tag{3.17}$$

which showed very good agreement between the correlation and the data with an average absolute deviation of 11.5 %. They did not include the liquid viscosity as a variable in their analysis, because there was no consistent experimental evidence showing a dependence.

Hughmark (1980) also made an analysis of the bubble size data. Eötvös number provided a dimensionless respresentation of bubble diameter which could then be correlated with gas holdup, power ratio and any of the dimensionless groups from Eq. 3.17. The following equation was proposed:

$$\frac{d_\mathrm{b}^2 g\rho_\mathrm{l}}{\sigma} = 5.5 \frac{\phi^{1/2}}{\left(\dfrac{N^2D^3}{gB\mathcal{V}_\mathrm{l}^{2/3}(P_\mathrm{g}/P)^{2/3}}\right)^{1/2}}. \tag{3.18}$$

Average absolute deviation between calculated and experimental values for the 39 data sets (incluing water–air and water, ethanol and ethyl acetate systems) was 10.6 %.

Equations 3.11, 3.17 and 3.18 can be combined to provide a correlation for interfacial area:

$$a = 1.38 \left(\frac{g\rho_\mathrm{l}}{\sigma}\right)^{1/2} \left(\frac{Q_\mathrm{g}}{N\mathcal{V}_\mathrm{l}}\right)^{1/3} \left(\frac{N^2D^4}{gB\mathcal{V}_\mathrm{l}^{2/3}}\right)^{0.592} \left(\frac{d_\mathrm{b}N^2D^4}{\sigma\mathcal{V}_\mathrm{l}^{2/3}}\right)^{0.187}. \tag{3.19}$$

Here, the bubble size in the Weber number is still assumed as 2.5 mm. Above equation appeared to apply over a vessel size range of 10 to 15,000 L and for gas superficial velocities to 5.3 cm/s. For scaling up with geometric similarity and with constant volume of gas to volume of liquid, interfacial area is a function of $N^{1.22}D^{0.906}$.

Experimental data of Calderbank (1958) suggests that the mass transfer coefficients (k_L) are a function of liquid phase diffusivity but not of power input or gas flow rate in stirred vessels. Thus, mass transfer coefficients can be calculated from $k_\mathrm{L}a$ data with Eq. 3.19.

Correlations have been proposed also to predict $k_{\mathrm{L}}a$ directly, which are in the same form as in Eq. 3.16:

$$k_{\mathrm{L}}a = c_{kla}\left(\frac{P_{\mathrm{g}}}{\mathcal{V}_{\mathrm{l}}}\right)^{a} U_{\mathrm{g,s}}^{b}. \tag{3.20}$$

For air–water systems agitated with a single impeller, Bakker et al. (1994) recommended $c_{kla} = 0.015 \pm 0.005$, $a = 0.6$ and $b = 0.6$ (SI units have to be used as the correlation was not made dimensionless). Those constants are strongly influenced by liquid properties and presence of contaminants. Although they also depend on impeller type, variation in $k_{\mathrm{L}}a$ for different impeller types were found to be usually within 30% around the average.

If a spherical bubble shape is assumed, the following relation holds between holdup, interfacial area and bubble diameter:

$$a = \frac{6\phi}{d_{\mathrm{b}}}. \tag{3.21}$$

Note, however, that local values of holdup and bubble size show large variations throughout the tank and not necessarily follow the relation above. For the standard gassed–stirred tank configuration we studied in the present work, Barigou and Greaves (1996) proposed two correlations for the mean interfacial area as given in Eq. 9.1 and 9.2. They are based on an integration carried over the local gas–liquid interfacial area (a_x) distributions, which were calculated from the measured local holdup (ϕ_x) and Sauter mean diameter values according to

$$a_x = \frac{6\phi_x}{d_{32}}. \tag{3.22}$$

It is apparent from the relation above that d_{32} is a very usuful parameter as it is directly related to the local interfacial area and holdup. Note, however, that for a complete description of the internal structure of the dispersion (in particular for mass transfer rate calculations), one still needs the bubble size distribution information in addition to the mean bubble parameters.

3.1.4 Mixing time

Another crucial parameter for the heat and mass transfer performance of gassed–stirred reactors is the mixing time. Empirical correlations have been proposed for the dimensionless mixing time, Nt_{mix}. Those are discussed in Section 11.2.1.

3.1.5 Flow regimes and cavity types

Gas–liquid flow in stirred tanks is a complex phenomenon. The two-phase flow regime occurring can be studied in two parts. Near the impeller blades, there is the formation of gas-filled cavity structures. In the bulk of the tank, phenomena such as two-phase flow patterns, gas recirculation, gas inflow via sparger and/or surface entrainment and impeller flooding occur (Nienow et al., 1977). The two-phase flow regime as a whole influences the amount of power that can be transmitted by the impeller to the process

liquid. This makes the prediction of the power draw a difficult task. However, it is also a very important one, as processes commonly carried out in these reactors (e.g. mass transfer) are affected by this parameter (Nienow et al., 1977).

Gas is dispersed into the tank mainly from the cavity structure developed at the impeller. A roll vortex pair formed behind the horizontal edges of the blades leave the outer edge as trailing vortices out into the tank bulk volume. van't Riet and Smith (1974) found that the high speed rotation of these vortices produced a very strong centrifugal field. There was a sharp increase in the centrifugal acceleration at large Re in the region close to the vortex core. The maximum value was found for $Re > 15000$, which was 18 times larger than that produced by the rigid rotation of the impeller tip. For a tip speed of 4 m/s, which is typical for mixing operations, and an impeller diameter of 17.6 cm, this produced a centrifugal field as large as $300\,g$. Hence, due to resulting adverse pressure gradients, bubbles in the vicinity of the vortex region are drawn violently into the core within milliseconds and form the ventilated cavities.

The type of cavities formed at the vortices described above depends on the gas inflow rate Q_g and also on the stirring rate N, as it affects both the intensity of the vortices and the amount of gas recirculating back to the impeller (Q_R). At very high speeds, entrained gas from the free surface may also contribute to Q_R.

Flooding vs looding regime

At low stirring rates, pressure gradient force due to gravitational acceleration (buoyancy) dominates over that due to centripetal acceleration, hence bubbles pass through the impeller region without being captured. There is hardly any dispersion. This is the so-called "flooding" regime, where no stable cavity may develop. Impeller blades are still in contact with the liquid, hence the gassed power consumption, P_g, is not substantially lower than the ungassed value P (Middleton, 1992).

If the stirring rate is increased beyond the value N_F, bubbles start to be drawn into the trailing vortices and the impeller is called to be "loaded". Gas dispersion begins as bubbles break off from the cavities developed, but is mainly limited to the upper part of the tank above the impeller level, which is operating now similar to a bubble column.

Vortex, clinging, large, $3-3$, ragged cavities

Bruijn et al. (1974) found that at low gassing rates ($Fl < 0.01$), the trailing vortex structure retained and the "vortex cavities" formed. They had little effect on the power consumption of the impeller, since the change in the drag of the blade was not significant.

When the gas flowrate was increased ($Fl \approx 0.01$ and tip speed higher than 1.5 m/s), they observed that the vortex cavity expanded by increasing gas inflow and began to attach to the horizontal edge of the blade, forming what they called the "clinging cavity". The reduction in power draw was more pronounced in this case, since the drag of the blade was reduced as the vortex core was filled with more gas and some hydrodynamic smoothing of the blade took place.

As the gas flow rate was increased further ($Fl \approx 0.03$, exact value depending on tank size due to recirculation effects), the vortex structure started to diminish, and the clinging cavities transformed one by one into the "large cavities" with characteristic clear smooth surfaces that totally blanketed the blade surface. This resulted in both decreasing of the radial liquid outflow from the stirrer due to blockage by the cavity and also streamlining of the blade. As a consequence of the streamlining effect, the downpressure behind the blade rose almost up to the static pressure level near the blade. Hence, the bubble capture weakened and the drag decreased to about half of its original value, leading to a lower P_g.

Bruijn et al. (1974) found that at a given impeller diameter, there was a minimum stirrer speed at which a large cavity could be formed, which was marked by a Froude number of 0.1. At $Fr < 0.1$, only clinging and vortex cavities were observed. They also reported that when 3 large cavities were formed, the arrangement was almost always three-symmetric, that is large cavities form preferentially behind alternate blades, giving the "$3-3$" (3 large, 3 clinging) structure. Smith and Warmoeskerken (1985) found that at intermediate gas flow rates the large cavities cannot be formed when $Fr < 0.045$, which is less conservative than the value given by Bruijn et al. (1974). They also pointed out the remarkable stability of the $3-3$ structure. Even at high gas rates that 6 large cavities were developed, these occurred in two different sizes still in the $3-3$ configuration.

Nienow et al. (1985) found that at extreme gas flow rates, the impeller became overloaded and the $3-3$ structure was transformed into 6 large unstable "ragged cavities" that oscillate violently. Experiments of Smith and Warmoeskerken (1985) showed that ragged cavities occurred at the same time as the transition to flooding, hence relations for predicting flooding–loading transition (see Eq. 3.23) can be used to mark this change in the cavity structure.

Gassed power studies are usually carried out in two ways; either the stirring rate or the gas inflow rate is kept constant, while the other one is varied. If N is held constant and Q_g is increased (i.e. Fl increased), a monotonic decrease in the gassed power draw P_g is observed until the flooding is complete (Bruijn et al., 1974; Nienow et al., 1977). Several cavity types develop in sequence as described before: 6 vortex cavities, 6 clinging cavities and the stable $3-3$ arrangement of alternate large and clinging cavities (Smith and Warmoeskerken, 1985; Nienow et al., 1985). If Q_g is held constant and N is increased (i.e. Fl decreased), P_g increases approximately according to Eq. 3.1 (i.e. $P_g \propto N^3$).

Complete dispersion N_{CD} vs gross recirculation N_R

The change of P_g with Fl is more complex (Nienow et al., 1977). A minimum in the power curve is observed at a stirring rate N_{CD} that corresponds to the complete dispersion condition, where gas dispersion into the region below the impeller level starts. As small gas recirculation patterns begin to appear, P_g starts increasing again until a maximum value is reached at N_R where the transition to "gross gas recirculation" takes place and much of the gas is now recirculated back to the impeller (Middleton, 1992). Beyond N_R, the gassed power decreases dramatically as large amount of recirculating gas, up to $Q_R = 4\,Q_g$ (Nienow et al., 1977), is contributing to the total gas entering

the impeller region.

Correlations for flow regimes and cavity structures

Several empirical correlations have been proposed in literature for the transition between the different bulk flow regimes as well as different cavity structures in standard tanks stirred by a 6-blade Rushton turbine. Nienow et al. (1985) suggested the following empirical correlation for the flooding–loading transition, which fitted well both to their experimental data in Birmingham and to that of Warmoeskerken and Smith (1985) in Delft:

$$Fl_{\mathrm{F}} = 30 \left(\frac{D}{T}\right)^{3.5} Fr_{\mathrm{F}}. \tag{3.23}$$

Eq. 3.23 is valid for both coalescing and non-coalescing systems with $0.29\ \mathrm{m} < H = T < 1.2$, $0.25 < C/H < 0.4$ and $0.22 < D/T < 0.5$. The correlation is in agreement with the semi-theoretical analysis of Warmoeskerken and Smith (1984) showing that the relationship should be linear of the form $Fl = \mathrm{const} \cdot Fr$. Their calculation is based on the idea that at flooding condition, the radial liquid velocity induced by the impeller pumping and the axial liquid velocity induced by the rising bubbles should be in balance. The complete dispersion condition is also given by Nienow et al. (1985) as

$$Fl_{\mathrm{CD}} = 0.2 \left(\frac{D}{T}\right)^{0.5} Fr_{\mathrm{CD}}^{0.5}, \tag{3.24}$$

which is valid for non-coalescing systems with $0.3\ \mathrm{m} < H = T < 1.8\ \mathrm{m}$ and $C/H = 1/4$. They reported that N_{CD} was dependent on the impeller clearance and $C/H = 1/4$ was found to be an optimum value. At lower clearances, the upper part of the tank was operating similar to a bubble column, whereas at higher clearances, the speed and power required to disperse the gas below the impeller level rapidly increased.

The transition from loading to complete gas recirculation regime is given by Nienow et al. (1977), which, after rearranging, leads to

$$Fl_{\mathrm{R}} = 13 \left(\frac{D}{T}\right)^{5} Fr_{\mathrm{R}}^{2}. \tag{3.25}$$

Smith and Warmoeskerken (1985) found that the transition from clinging to $3-3$ structure can be given by

$$Fl = 3.8 \times 10^{-3} \left(\frac{Re^2}{Fr}\right)^{0.067} \left(\frac{D}{T}\right)^{-0.5}, \tag{3.26}$$

which fitted well to their experiments of air dispersion in tap-water in tanks of $0.3\ \mathrm{m} < H = T < 1.2\ \mathrm{m}$ and $0.25 < D/T < 0.59$ (C/H was not specified).

3.2 Flow characteristics of stirred tanks with multiple impellers

3.2.1 Gassed power uptake and impeller discharge flow

Roušar and van den Akker (1994) measured the power uptake and the velocity profiles in one, two and three Rushton turbines on the same shaft. Cui et al. (1996a) made an attempt to correlate a large amount of data (739 data points) in literature, both from single- and multi-impeller tanks with water–air systems close to standard conditions. Most of the data was from single impeller systems, whereas one data set was for a two-impeller system and another one was for a three-impeller system. We describe the findings below.

Single-impeller or bottom impeller

In multi-impeller systems, the reduction in power uptake is largest for the bottom impeller (cf. single-phase case where all impellers draw the same power beyond certain impeller–impeller clearance). This is because most of the gas from the sparger will flow through the bottom impeller region while only part of this gas flow can pass through the other impellers.

Measurements of Roušar and van den Akker (1994) showed that the performance of the bottom impeller was independent of the upper impellers. Addition of second and third impellers did not influence the liquid flow around the bottom impeller and hence the power drawn from it. The rest of the power was equally distributed between the second and third impeller because they had exactly the same outlet liquid velocity at the impeller tip.

Interaction of the gas flow from the sparger with a single-impeller in a stirred tank and with the bottom impeller of a multi-impeller tank at different scales are expected to be similar (Cui et al., 1996a). An exception, of course, is the local static pressure difference. Cui et al. (1996a) found that the experimental data for gassed power reduction both for single-impeller tanks and for bottom impellers in multi-impeller configurations correlated as $(1 - P_g/P) = f(Q_g N^{0.25} D^{-2})$, where there were two distinct regimes:

- for $Q_g N^{0.25}/D^2 \leq 0.055$:

$$1 - \frac{P_g}{P} = 9.9 \left(\frac{Q_g N^{0.25}}{D^2} \right), \tag{3.27}$$

- for $Q_g N^{0.25}/D^2 > 0.055$:

$$1 - \frac{P_g}{P} = 0.52 + 0.62 \left(\frac{Q_g N^{0.25}}{D^2} \right). \tag{3.28}$$

Above correlations are valid for SI units (as they were not made dimensionless) and were obtained from data measured at a wide range of conditions ($T : 0.23 - 1.83$ m, $N : 0.9 - 10$ s^{-1}, $Fl : 0 - 0.23$, $T/D : 2 - 3$). They did not find a strong dependence

on the tank diameter ratio, T/D, thus T does not appear in the relations. The relative errors were below 6 % for both. From the fact that all the data from a wide range of experimental conditions (i.e. geometries, stirring speeds and gas flow numbers) fall approximately into one line, they concluded that the above corelation gave rather good prediction despite of very diverse conditions and that bottom impellers behaved similar to single impellers.

Top and middle impellers

Roušar and van den Akker (1994) found that the liquid circulation through the second and third impeller was higher than the bottom one. This was also suggested by the higher power draw of the upper impeller.

From the large data set that Cui et al. (1996a) analysed, it was clear that the top and middle impellers behaved differently from the bottom impeller. The reduction of power draw at the top and middle impellers was identical (thus could be treated together), and was much lower than that at the bottom impellers under the same operating conditions. This suggested that larger gas cavities were generated at the bottom impeller. This is plausable, since the bottom impeller is subjected to the direct gas flow from the sparger, while the other impellers experience a gas flow regime determined more by the local gas distribution in the tank. Their regression analysis also revealed that relative power uptake for the top and middle impellers scales differently than that for the bottom impellers, that is, $(1 - P_g/P) = f(Q_g N)$. The data again fell into two distinct regimes:

- for $Q_g N \leq 0.013$:
$$1 - \frac{P_g}{P} = K_1 Q_g N, \tag{3.29}$$
- for $Q_g N > 0.013$:
$$1 - \frac{P_g}{P} = K_2 + K_3 Q_g N, \tag{3.30}$$

where K_1, K_2 and K_3 depend on the tank geometry and equal respectively to 37.6, 0.375 and 8 for the case they studied ($T = 0.604$ m, $D = 0.256$ m, $H = 2.2$ m). The maximum relative error in above relations were 2.3 %. Note that Eq 3.29 and 3.30 are valid for SI units (as they were not made dimensionless) and do not contain geometry parameters, because they were obtained from the measurements of only one stirred tank due to lack of available data. Hence, they can not be used as a generic correlation.

One peculiar observation was that the transition for the gassed power draw for all impellers (i.e. transition both from Eq 3.27 to 3.28 and from Eq 3.29 to 3.30) occured always at $P_g/P \approx 0.5$, independent of the location of the impeller. This regime transition occured at a much higher aeration rate for the top and middle impellers than a single or bottom impeller under the same condition.

Effect of gassing on turbulent kinetic energy

Roušar and van den Akker (1994) found that the turbulent kinetic energy profile was not significantly influenced by the gas flowrate. The decrease of mean flow due to reduced impeller power uptake under gassing is apparently compensated by the increase of energy transfer from the gas phase. They suggested that data from single-phase measurements could be used also for gassed operation.

3.2.2 Mixing time

Mixing time correlations for multi-impeller systems are discussed in Section 11.2.1.

3.2.3 Flow regimes and cavity types

General flow regime characterisation of multi-impeller systems is complicated due to possiblity of very large number of geometric variations (e.g. different combinations of impeller designs, spacings, sparger location including sparging directly into individual impellers, baffling arrangements, etc.). Employing a combination of radial and axial turbines, for instance, could be beneficial for good overall mixing throughout the whole reactor because using multiple Rushton turbine systems may give rise to flow compartmentalisation even in gas–liquid systems (Middleton and Smith, 2004).

Here, we will restrict ourselves to typical designs with radial pumping disk turbine systems such as the fermenter studied in this thesis. In this respect, the study of Smith et al. (1987) is a commonly cited work regarding flow and cavity regime transition for such a multi-impeller system (Tatterson, 1991; Middleton and Smith, 2004). They developed a flow regime map for a sytem with 3 disk turbines ($H/T = 3$, $T/D = 2.5$ and impeller spacing of $2.5D$). Main findings were:

- Under gas sparging, the bottom impeller behaved as a single impeller. In Section 10.1.3, we discuss this further and develop also a flow regime map for the bottom impeller based on this observation. The upper impellers behaved differently because they received gas only via recirculation and had a larger share of this recirculated gas relative to the bottom impeller.

- For the bottom impeller, the cavity regime transition from vortex-clinging to $3-3$ structure occured at about the same operating conditions as that for a single impeller system. The same transition occured at much higher gassing rates for the upper impellers which received only recirculated gas. When the bottom impeller transitioned to $3-3$ structure, the power draw from the upper impellers was higher than that from the bottom impeller. At higher gassing rates, this power difference diminished as the upper impellers also developed the $3-3$ structure which occured for all higher impellers when

$$Fr \cdot Fl = 1.85 \left(\frac{T}{D}\right)^{-5}. \tag{3.31}$$

- The bottom impeller flooded much earlier than the upper impellers. The latter happened at a gas flow number about twice as much as that for the flooding transition of the bottom impeller.
- The two upper impellers behaved similarly over the whole range of the gas flow number and draw more power than the bottom impeller.

Impeller power uptake discussion given earlier provides also a basis for the flow and cavity regime changes in a multi-impeller system. In Section 10.3, we discuss further about the flow characteristics of the fermenter studied in this thesis together with the simulation results.

Tables

Table 3.1: Fundamental forces relevant to multiphase systems (Wörner, 2003). Forces act on a volume element ($\mathcal{V} \propto L^3$), a surface (area) element ($\mathcal{A} \propto L^2$) or a line (curve) element ($\mathcal{C} \propto L$), L being a linear dimension.

	type	force	force per unit volume
Inertial force F_I	volume force	$\propto \mathcal{V}\rho U^2 L^{-1}$	$\propto \rho U^2 L^{-1}$
Viscous force F_μ	surface force	$\propto \mathcal{A}\mu U L^{-1}$	$\propto \mu U L^{-2}$
Pressure force F_p	surface force	$\propto \mathcal{A}\Delta p$	$\propto \Delta p L^{-1}$
Buoyancy force F_B	volume force	$\propto \mathcal{V} g \Delta\rho$	$\propto g\Delta\rho$
Gravitational force F_g	volume force	$\propto \mathcal{V}\rho g$	$\propto \rho g$
Surface tension force F_σ	line force	$\propto \mathcal{C}\sigma$	$\propto \sigma L^{-2}$

Chapter 4

Two-fluid model

In the modelling of gas-sparged stirred tanks by CFD methodologies there are several levels of complexities. First of all, a proper model to account for the impeller rotation is needed. Another complexity for the CFD model comes from the fact that the multiphase flows are much more complex in nature than the single-phase flows. There are a number of different flow regimes that the multiphase flows can manifest. Even for a particular flow regime, with the change of an operating parameter (e.g. gas flow rate, bubble size), the dominating physical phenomena may change, which should be accounted for in the numerical model. For the simulation of turbulent flows in aerated stirred tanks at not too low gas fractions, the so-called Euler–Euler (two-fluid) model is computationally the most feasible approach. In this study the Euler–Euler model was used, which is explained in the following sections.

4.1 Local instantaneous flow equations

The fundamental description of the exact flow of a two-phase mixture is given by local instantaneous mass (continuity) and momentum (Navier–Stokes) equations for each phase, valid in the interior of corresponding phase, along with the corresponding interphase jump conditions relating quantities at each side of the interface to one another. These read

$$\frac{\partial}{\partial t}(\rho_k) + \nabla \cdot (\rho_k \mathbf{u}_k) = 0, \tag{4.1}$$

$$\sum_{k=1}^{2} \rho_k (\mathbf{u}_k - \mathbf{u}_i) \cdot \mathbf{n}_k = \sum_{k=1}^{2} \dot{m}_k = 0, \tag{4.2}$$

for mass conservation, and

$$\frac{\partial}{\partial t}(\rho_k \mathbf{u}_k) + \nabla \cdot (\rho_k \mathbf{u}_k \mathbf{u}_k) = \nabla \cdot \underline{\underline{\boldsymbol{\sigma}}}_k + \rho_k \mathbf{g}, \tag{4.3}$$

$$\sum_{k=1}^{2} \left[\rho_k \mathbf{u}_k (\mathbf{u}_k - \mathbf{u}_i) - \underline{\underline{\boldsymbol{\sigma}}}_k \right] \cdot \mathbf{n}_k = \sum_{k=1}^{2} (\dot{m}_k \mathbf{u}_k - \underline{\underline{\boldsymbol{\sigma}}}_k \cdot \mathbf{n}_k) = 0. \tag{4.4}$$

for linear momentum conservation (Lathouwers, 1999). Here, $\mathbf{u}_k$ is the instantaneous velocity vector for phase k ($k = 1$ for the continuous phase, $k = 2$ for the dispersed phase), $\mathbf{n}_k$ the outward pointing normal at an interface with respect to phase k, $\mathbf{u}_i$ the velocity of the interface and $\underline{\underline{\boldsymbol{\sigma}}}_k$ the stress tensor. In the above given jump conditions the effect of surface tension has been neglected. When there is no phase change, $\dot{m}_k$ (interfacial mass efflux from phase k) terms vanish. In addition to the set of equations given above, a thermodynamic relation between pressure and density is also needed to close the system.

The stress tensor is expressed for Newtonian fluids by the constitutive relation

$$\underline{\underline{\boldsymbol{\sigma}}}_k = -p_k \underline{\underline{\mathbf{I}}} + \mu_k \left[\nabla \mathbf{u}_k + (\nabla \mathbf{u}_k)^T\right] + \left[-\frac{2}{3}\mu_k + \lambda_k\right](\nabla \cdot \mathbf{u}_k)\underline{\underline{\mathbf{I}}} \tag{4.5}$$

where the bulk viscosity λ_k is identically zero for low density monatomic gases and not expected to be significant for dense gasses and liquids (Bird et al., 1960), hence usually taken as zero. The strain-rate tensor $\underline{\underline{\mathbf{S}}}_k$ is defined by

$$\underline{\underline{\mathbf{S}}}_k \equiv \frac{1}{2}\left[\nabla \mathbf{u}_k + (\nabla \mathbf{u}_k)^{\mathrm{T}}\right], \tag{4.6}$$

hence, for incompressible flow, the viscous part of the stress tensor is described by

$$\underline{\underline{\boldsymbol{\tau}}}_k = 2\mu_k \underline{\underline{\mathbf{S}}}_k. \tag{4.7}$$

Above given microscopic description of the two-phase mixture is extremely difficult and expensive to solve for the simulation of bubbly flows on a scale and gas loading relevant for industrial applications. Fundamental difficulties are three fold (Ishii and Hibiki, 2006): (i) the problem is a multi-boundary problem, involving multiple deformable moving interfaces, where their positions and motions are unknown (hence, special interface tracking algorithms are needed such as the Volume-of-fluid (VOF) method), (ii) due to the motion of the interfaces and presence of turbulence, the variables fluctuate, (iii) there are large discontinuities of properties at the interfaces that cause large local jumps in variables in space and time.

4.2 Ensemble averaging

A practical approach used routinely for large-scale simulations is the two-fluid (also denoted as "Euler–Euler") method, in which both continuous and dispersed phases are treated mathematically as interpenetrating and interacting continua in a fixed coordinate system (Eulerian approach). This is achieved by multiplying the local instantaneous equations given above by the so-called phase indicator function $\chi_k(\mathbf{x}, t)$ ($\chi_k = 1$ if the position vector $\mathbf{x}$ is in phase k at time t, otherwise $\chi_k = 0$) in order to filter out phase k and then employing averaging. The fine flow details are lost after the averaging process and a macroscopic description of the system is obtained (averaging is not essential though, macroscopic equations can also be postulated without reference to microscopic equations (Drew, 1983)). Averaging can be based on, for instance, time or volume, provided that there is a clear separation of small and large temporal and spatial scales in the system, and the averaging is performed on the mesoscale so that

the results are insensitive to the choice of averaging time or volume. The most general approach, however, which does not possess such constraints, is the ensemble averaging defined for an exact microscopic field $f(\mathbf{x}, t)$ as

$$\langle f \rangle(\mathbf{x}, t) = \int_{\Omega} f(\mathbf{x}, t; \omega)\ d\mu(\omega), \tag{4.8}$$

where $\langle f \rangle(\mathbf{x}, t)$ is the corresponding averaged field, $d\mu(\omega)$ is the probability of observing realisation ω, and Ω is the set of all possible realisations (Drew, 1983). It can be interpretted as the statistical mean of a quantity of interest (a scalar, vector or tensor) at a given position and time over a large number of experiments with the same initial and boundary conditions. Both the time and space averages can be viewed as approximations to ensemble averaging, and in the case of statistically stationary homogenous flow, all three should lead to identical results according to the ergodicity hypothesis (Enwald et al., 1996).

In the derivation of the averaged equations (for a full derivation, see e.g. Drew (1983) for ensemble averaging approach and Ishii and Hibiki (2006) for time averaging approach), it was assumed that the averaging operation has the following properties (Drew, 1983; Enwald et al., 1996):

$$\langle f + g \rangle = \langle f \rangle + \langle g \rangle \tag{4.9}$$

$$\langle \langle f \rangle g \rangle = \langle f \rangle \langle g \rangle \tag{4.10}$$

$$\langle \text{constant} \rangle = \text{constant} \tag{4.11}$$

$$\left\langle \frac{\partial f}{\partial t} \right\rangle = \frac{\partial}{\partial t} \langle f \rangle \tag{4.12}$$

$$\langle \nabla f \rangle = \nabla \langle f \rangle \tag{4.13}$$

$$\langle \nabla \cdot f \rangle = \nabla \cdot \langle f \rangle. \tag{4.14}$$

The first three relations above are called Reynolds' rules, the fourth is called Leibniz' rule, and the last two are called Gauß' rule. Furthermore, the definition of χ_k and its fundamental property that it is advected by the local velocity $\mathbf{u}_k$, that is $\partial/\partial t(\chi_k) + \mathbf{u}_k \cdot \nabla \chi_k = 0$ (Drew, 1983), are used. The general form of the averaged balance equations obtained are (Lathouwers, 1999)

$$\frac{\partial}{\partial t} \langle \chi_k \rho_k \rangle + \nabla \cdot \langle \chi_k \rho_k \mathbf{u}_k \rangle = 0, \tag{4.15}$$

$$\frac{\partial}{\partial t} \langle \chi_k \rho_k \mathbf{u}_k \rangle + \nabla \cdot \langle \chi_k \rho_k \mathbf{u}_k \mathbf{u}_k \rangle = \nabla \cdot \langle \chi_k \underline{\underline{\boldsymbol{\sigma}}}_k \rangle + \langle \chi_k \rho_k \mathbf{g} \rangle - \langle \underline{\underline{\boldsymbol{\sigma}}}_k \cdot \nabla \chi_k \rangle. \tag{4.16}$$

The last term in the momentum equation, $\mathbf{M}_k = -\langle \underline{\underline{\boldsymbol{\sigma}}}_k \cdot \nabla \chi_k \rangle$, stands for the averaged interfacial momentum transfer. It represents the averaged effect of the viscous stresses and pressure at the interface. The gradient of χ_k is non-zero at the interface only, acting as a delta function picking out the interface and can be expressed as $\nabla \chi_k = \mathbf{n}_k (\partial \chi / \partial n)$. Multiplying the instantaneous jump condition Eq. 4.4 by $\partial \chi / \partial n$ (and knowing that $\mathbf{n}_1 = -\mathbf{n}_2$) and averaging gives the average momentum jump condition constraint

$$\sum_{k=1}^{2} \mathbf{M}_k = \sum_{k=1}^{2} \langle -\underline{\underline{\boldsymbol{\sigma}}}_k \cdot \nabla \chi_k \rangle = 0, \tag{4.17}$$

where we assumed that there is no interfacial mass transfer. The mass jump condition vanishes completely in such a case. The effect of surface tension was also neglected, as mentioned earlier.

4.3 Decomposition of variables and weighted averaged equations

In bubbly flows, the actual velocities deviate from their mean value, which in turn result in fluctuations in other variables (e.g. pressure, stress). Velocity fluctuations are not only due to turbulent eddies as in the single-phase turbulent flow, but also due to the motion in the phases induced by the motion of the interfaces (Drew and Passman, 1999), which also contribute to the momentum transport. These velocity fluctuations are not resolved by the two-fluid model; their effect on the variables, regardless of their source, is taken in to account by decomposing the variables into their mean and fluctuating part (i.e. $f_k = \overline{f}_k + f'_k$).

The averaged equations given earlier contain averages of products of the dependent variables. They should be transformed into a form containing the products of the average variables themselves so that the system can be solved (Enwald et al., 1996). This is achieved by using the definition of the phasic (χ_k-weighted) average $\overline{f}_k^{\chi_k}$ and mass-weighted (Favré) average $\overline{f}_k^{\chi_k\rho_k}$:

$$\overline{f}_k^{\chi_k} \equiv \frac{\langle \chi_k f \rangle}{\langle \chi_k \rangle} = \frac{\langle \chi_k f \rangle}{\alpha_k}, \tag{4.18}$$

$$\overline{f}_k^{\chi_k\rho_k} \equiv \frac{\langle \chi_k \rho_k f \rangle}{\langle \chi_k \rho_k \rangle} = \frac{\langle \chi_k \rho_k f \rangle}{\alpha_k \overline{\rho}_k^{\chi_k}}. \tag{4.19}$$

Here, the phase fraction $\alpha_k(\mathbf{x}, t)$, although frequently called as "volume fraction" —a concept closely connected to the volume averaging—, is the average fraction of the occurrences of component k at point $\mathbf{x}$ at time t (i.e. $\alpha_k = \langle \chi_k \rangle$) as pointed out by Drew and Passman (1999). Due to the axiom of continuity, it is subject to the condition that $\sum_{k=1}^{2} \alpha_k = 1$. In this study, the density of both phases are assumed to be constant, hence $\overline{f}_k^{\chi_k} = \overline{f}_k^{\chi_k\rho_k}$. Note that, in the following, we denote averaged quantities with capital letters (i.e. $\underline{\underline{\mathbf{\Sigma}}}_k = \underline{\underline{\boldsymbol{\sigma}}}_k^{\chi_k}$, $\mathbf{U}_k = \overline{\mathbf{u}}_k^{\chi_k}$, $P_k = \overline{p}_k^{\chi_k}$, etc.). With these, the decomposed weighted and averaged balance equations can be written as

$$\frac{\partial}{\partial t}(\alpha_k \rho_k) + \nabla \cdot (\alpha_k \rho_k \mathbf{U}_k) = S_k, \tag{4.20}$$

$$\frac{\partial}{\partial t}(\alpha_k \rho_k \mathbf{U}_k) + \nabla \cdot (\alpha_k \rho_k \mathbf{U}_k \mathbf{U}_k) = \nabla \cdot \alpha_k (\underline{\underline{\mathbf{\Sigma}}}_k + \underline{\underline{\mathbf{\Sigma}}}_k^{\mathrm{Re}}) + \alpha_k \rho_k \mathbf{g} + \mathbf{M}_k + \mathbf{S}_k. \tag{4.21}$$

The averaged stress tensor term in Eq. 4.21 can be split into pressure and viscous stress components

$$\nabla \cdot \alpha_k \underline{\underline{\mathbf{\Sigma}}}_k = \nabla \cdot \alpha_k (-P_k \underline{\underline{\mathbf{I}}} + \underline{\underline{\mathbf{T}}}_k) = -\alpha_k \nabla P_k - P_k \nabla \alpha_k + \nabla \cdot (\alpha_k \underline{\underline{\mathbf{T}}}_k), \tag{4.22}$$

where the averaged viscous stress tensor $\underline{\underline{\mathbf{T}}}_k = \overline{\underline{\underline{\boldsymbol{\tau}}}}_k^{\chi_k}$ is often assumed to obey the Newtonian strain–stress relation similar to its microscopic counterpart $\underline{\underline{\boldsymbol{\tau}}}_k$, hence

$$\begin{aligned}\underline{\underline{\mathbf{T}}}_k &= 2\mu_k \left[\underline{\underline{\mathbf{S}}}_k - \frac{1}{3}(\nabla \cdot \mathbf{U}_k)\underline{\underline{\mathbf{I}}}\right] + \lambda_k(\nabla \cdot \mathbf{U}_k)\underline{\underline{\mathbf{I}}} \\ &= \mu_k \left[\nabla \mathbf{U}_k + (\nabla \mathbf{U}_k)^{\mathrm{T}}\right] + \left[-\frac{2}{3}\mu_k + \lambda_k\right](\nabla \cdot \mathbf{U}_k)\underline{\underline{\mathbf{I}}},\end{aligned} \tag{4.23}$$

where the bulk viscosity λ_k is usually neglected as noted earlier and the mean strain-rate tensor $\underline{\underline{\mathbf{S}}}_k$ is defined by

$$\underline{\underline{\mathbf{S}}}_k \equiv \frac{1}{2}\left[\nabla \mathbf{U}_k + (\nabla \mathbf{U}_k)^{\mathrm{T}}\right]. \tag{4.24}$$

Drew (1983) discusses that, unlike in single-phase turbulent flow, inviscid equations are ill-posed in two-phase flows, implying that inviscid model is nowhere valid for two-phase flows, i.e. viscous or eddy stresses are important everywhere. Note that the last term in Eq. 4.23 does not vanish unlike in the case of single-phase incompressible flow, since the continuity equation includes the phase fraction, which is a function of space and time.

The so-called Reynolds (fluctuation) stress tensor $\underline{\underline{\boldsymbol{\Sigma}}}_k^{\mathrm{Re}}$ in Eq. 4.21 arises after velocity decomposition and averaging due to the non-linear convection term in the underlying Navier–Stokes equation

$$\begin{aligned}\langle \chi_k \rho_k \mathbf{u}_k \mathbf{u}_k \rangle &= \langle \chi_k \rho_k (\overline{\mathbf{u}}_k^{\chi_k \rho_k} + \mathbf{u}_k')(\overline{\mathbf{u}}_k^{\chi_k \rho_k} + \mathbf{u}_k') \rangle \\ &= \langle \chi_k \rho_k \rangle \overline{\mathbf{u}}_k^{\chi_k \rho_k} \overline{\mathbf{u}}_k^{\chi_k \rho_k} + \langle \chi_k \rho_k \mathbf{u}_k' \mathbf{u}_k' \rangle \\ &= \alpha_k \rho_k \mathbf{U}_k \mathbf{U}_k - \alpha_k \underline{\underline{\boldsymbol{\Sigma}}}_k^{\mathrm{Re}},\end{aligned} \tag{4.25}$$

where we have, by definition,

$$\underline{\underline{\boldsymbol{\Sigma}}}_k^{\mathrm{Re}} \equiv -\frac{\langle \chi_k \rho_k \mathbf{u}_k' \mathbf{u}_k' \rangle}{\alpha_k} \tag{4.26}$$

$$= -\rho_k \overline{\mathbf{u}_k' \mathbf{u}_k'}^{\chi_k \rho_k}. \tag{4.27}$$

The Reynolds stresses represent the effect of fluctuations on the mean flow. It is similar to the turbulent stress tensor in turbulence modelling of single-phase flow. However, as mentioned before, in two-phase bubbly flow, the fluctuations resulting in this stress term are not necessarily of turbulence origin. Bubbles with non-zero slip velocity also induce fluctuations in the mean flow, hence a corresponding stress arises. As for its molecular counterpart $\underline{\underline{\boldsymbol{\Sigma}}}_k$, a closure relation is needed also for $\underline{\underline{\boldsymbol{\Sigma}}}_k^{\mathrm{Re}}$, because the information at the microscopic scale is lost due to averaging. The closure of this term is the topic of the turbulence modelling and is presented in the next chapter. Note that, the stresses in the gas phase momentum equation (both $\underline{\underline{\boldsymbol{\Sigma}}}_2$ and $\underline{\underline{\boldsymbol{\Sigma}}}_2^{\mathrm{Re}}$) can be neglected in turbulent bubbly flows, because the dominant terms are the interfacial momentum transfer and the presure gradient (Lathouwers, 1999).

The remaining terms in Eq. 4.20 and Eq. 4.21 are S_k and $\mathbf{S}_k$, which represent the mass and momentum source terms respectively (e.g. gas inflow from the sparger). An additional body force term will arise, when the momentum equation is written with respect to a rotating reference frame. This will be discussed in Chapter 7.

4.3.1 Decomposition of interfacial transfer $\mathbf{M}_k$

The averaged momentum flux at the interfaces, $\mathbf{M}_k = -\langle \underline{\underline{\boldsymbol{\sigma}}}_k \cdot \nabla\chi_k \rangle$, can also be decomposed into a form involving the interfacially averaged pressure and viscous stress contributions. For this purpose, the definition of an interface weighted ($\nabla\chi_k$-weighted) average $\overline{f}_{k,\mathrm{i}}^{\nabla\chi_k}$ is used:

$$\overline{f}_{k,\mathrm{i}}^{\nabla\chi_k} \equiv \frac{\langle f_k \mathbf{n}_k \cdot \nabla\chi_k \rangle}{\langle \mathbf{n}_k \cdot \nabla\chi_k \rangle} = \frac{\langle f_k \mathbf{n}_k \cdot \nabla\chi_k \rangle}{a_\mathrm{i}}, \tag{4.28}$$

where $a_\mathrm{i} = \langle \mathbf{n}_k \cdot \nabla\chi_k \rangle$ denotes the average interfacial area per unit volume. The definition above is used to introduce the interfacial-area averaged pressure $P_{k,\mathrm{i}} = \overline{p}_k^{\nabla\chi_k}$ and viscous stress $\underline{\underline{\mathbf{T}}}_{k,\mathrm{i}} = \overline{\underline{\underline{\boldsymbol{\tau}}}}_k^{\nabla\chi_k}$, in order to separate the mean field effects from local effects in $\mathbf{M}_k$. Furthermore, the pressure and stress can be splitted into an interfacial mean and a fluctuating part, hence $p'_{k,\mathrm{i}} = p_k - P_{k,\mathrm{i}}$ and $\underline{\underline{\boldsymbol{\tau}}}'_{k,\mathrm{i}} = \underline{\underline{\boldsymbol{\tau}}}_k - \underline{\underline{\mathbf{T}}}_{k,\mathrm{i}}$ (Drew and Passman, 1999). The phase interaction term can then be written as

$$\begin{aligned}
\mathbf{M}_k &= -\langle \underline{\underline{\boldsymbol{\sigma}}}_k \cdot \nabla\chi_k \rangle \\
&= -\langle [-p_k \underline{\underline{\mathbf{I}}} + \underline{\underline{\boldsymbol{\tau}}}_k] \cdot \nabla\chi_k \rangle \\
&= \langle p_k \nabla\chi_k \rangle - \langle \underline{\underline{\boldsymbol{\tau}}}_k \cdot \nabla\chi_k \rangle \\
&= P_{k,\mathrm{i}} \langle \nabla\chi_k \rangle - \underline{\underline{\mathbf{T}}}_{k,\mathrm{i}} \cdot \langle \nabla\chi_k \rangle - \langle \underline{\underline{\boldsymbol{\sigma}}}'_{k,\mathrm{i}} \cdot \nabla\chi_k \rangle \\
&= P_{k,\mathrm{i}} \nabla\alpha_k - \underline{\underline{\mathbf{T}}}_{k,\mathrm{i}} \cdot \nabla\alpha_k + \mathbf{M}'_k,
\end{aligned} \tag{4.29}$$

where

$$\underline{\underline{\boldsymbol{\sigma}}}'_{k,\mathrm{i}} = -p'_{k,\mathrm{i}} \underline{\underline{\mathbf{I}}} + \underline{\underline{\boldsymbol{\tau}}}'_{k,\mathrm{i}} = -(p_k - P_{k,\mathrm{i}}) \underline{\underline{\mathbf{I}}} + (\underline{\underline{\boldsymbol{\tau}}}_k - \underline{\underline{\mathbf{T}}}_{k,\mathrm{i}}), \tag{4.30}$$

$$\mathbf{M}'_k = -\langle \underline{\underline{\boldsymbol{\sigma}}}'_{k,\mathrm{i}} \cdot \nabla\chi_k \rangle = \langle [p_k - P_{k,\mathrm{i}}] \nabla\chi_k \rangle - \langle [\underline{\underline{\boldsymbol{\tau}}}_k - \underline{\underline{\mathbf{T}}}_{k,\mathrm{i}}] \cdot \nabla\chi_k \rangle. \tag{4.31}$$

Here, the term $\mathbf{M}'_k = -\langle \underline{\underline{\boldsymbol{\sigma}}}'_{k,\mathrm{i}} \cdot \nabla\chi_k \rangle$, usually called the generalised drag force, is associated with the sum of the forces acting on the interface at phase k, because the other terms, i.e. $P_{k,\mathrm{i}} \nabla\alpha_k$ and $\underline{\underline{\mathbf{T}}}_{k,\mathrm{i}} \cdot \nabla\alpha_k$, vanish in homogenous mixtures. It is non-zero only in the presence of relative velocity between the phases, hence represents the hydrodynamic contributions. First term on the r.h.s. of Eq. 4.31 gives rise to forces such as the form drag, virtual mass and lift due to the imbalance of pressure at the interface. The second term is responsible for the viscous effects such as the skin drag and the history force arising from wake and boundary-layer formation due to the imbalance of viscous forces. $\mathbf{M}'_k$ is to be closed by empirical relations, which will be discussed in Chapter 6.

Using the above relations and Eq. 4.22, the r.h.s of the momentum equation (Eq. 4.21) can now be written in the following form

$$\begin{aligned}
-\alpha_k \nabla P_k + (P_{k,\mathrm{i}} - P_k) \nabla\alpha_k - \underline{\underline{\mathbf{T}}}_{k,\mathrm{i}} \cdot \nabla\alpha_k + \mathbf{M}'_k + \nabla \cdot \alpha_k (\underline{\underline{\mathbf{T}}}_k + \underline{\underline{\boldsymbol{\Sigma}}}_k^{\mathrm{Re}}) \\
+ \alpha_k \rho_k \mathbf{g} + \mathbf{S}_k.
\end{aligned} \tag{4.32}$$

4.4 Closure approximations

In order to have a closed set of macroscopic balance equations, approximations have to be made for the unclosed terms. Several postulated principles provide guidelines in the

derivation of physically and mathematically sensible constitutive laws for the closure. These are mainly

- *well-posedness*, i.e. the set of differential equations describing the motion has a solution, which depends continuously on the initial and boundary conditions,
- *frame indifference*, i.e. closure relations should not depend on the reference frame,
- *entropy inequality*, i.e. second law of thermodynamics should be satisfied,
- *separation of components*, i.e. a variable expressing a self-interaction of phase k, such as $\underline{\underline{\mathbf{\Sigma}}}_k$, should depend only on the variables associated with phase k.

Further details and implications of these principles are given in Drew and Passman (1999) and Ishii and Hibiki (2006).

Pressure term

We first consider the bulk and interface pressures in Eq. 4.32. As we assumed that the surface tension effects are negligible in this work, the averaged momentum jump condition at the interface can be assumed to take the form $P_{1,\mathrm{i}} = P_{2,\mathrm{i}}$ (Drew, 1983).

Owing to the low density of the gas phase and to the assumption that the gas phase is finely dispersed in the liquid phase, we can further assume that $P_{2,\mathrm{i}} \approx P_2$ (Antal et al., 1991; Drew and Passman, 1999; Lathouwers, 1999). However, in the liquid phase, the flow attains locally higher speed relative to the far-field due to the flow deflection around the bubble. Therefore, a difference in pressure is also expected. Stuhmiller (1977) obtained a general expression starting from the analysis of inviscid flow around a single sphere, which is assumed to be unaffected by the neighbour spheres (i.e. the suspension is dilute):

$$P_{1,\mathrm{i}} = P_1 - \xi\rho_1|\mathbf{U}_1 - \mathbf{U}_2|^2. \tag{4.33}$$

This relation, which is the manifestation of the Bernoulli theorem for the variation of pressure in inviscid flow, has been proposed even if the continuous phase is viscous (Drew and Passman, 1999). For dilute flows with spherical particles, the dynamic pressure coefficient is $\xi = 1/4$, when the boundary layer is attached to the particle. Despite this approximate relation, it is usually assumed (also in Fluent) that the pressure difference in the liquid phase is also negligible like in the gas phase, i.e. $P_{1,\mathrm{i}} = P_1$ (Ishii and Hibiki, 2006; Drew, 1983; Enwald et al., 1996). This implies that the mean pressure field is shared by both phases, i.e. $P_1 = P_2 = P$. Therefore, the mean pressure serves as an extra coupling term between the phases in addition to the jump condition $\sum_{k=1}^{2} \mathbf{M}'_k = 0$ (see Eq. 4.35). Note, however, that this simple and traditional way of treating the pressures, i.e. assuming that they are all equal, $P_1 = P_2$ and $P_k = P_{k,\mathrm{i}}$, results in an ill-posed two-fluid model according to Lathouwers (1999).

Stress term

We consider next the term $-\underline{\underline{\mathbf{T}}}_{k,\mathrm{i}} \cdot \nabla\alpha_k$ in Eq. 4.32. This term represents the combined effect of the interfacial viscous stress and the void gradient. It is particularly important

for separated flows, where it dominates over $\mathbf{M}'_k$, however, for bubbly flows, the effect of this term has generally been neglected (Ishii and Hibiki, 2006). This is also the case for the two-fluid implementation in Fluent, and to keep the current model relatively simple, we did no attempt to include it. Note, however, that according to Ishii and Hibiki (2006), it is important for proper modelling of the interfacial momentum coupling.

4.4.1 Final momentum equation

Finally, with the above given approximations, the momentum equation can now be simplified to its final form

$$\frac{\partial}{\partial t}(\alpha_k \rho_k \mathbf{U}_k) + \nabla \cdot (\alpha_k \rho_k \mathbf{U}_k \mathbf{U}_k) = -\alpha_k \nabla P + \nabla \cdot \alpha_k (\underline{\underline{\mathbf{T}}}_k + \underline{\underline{\boldsymbol{\Sigma}}}_k^{\mathrm{Re}}) + \mathbf{M}'_k + \alpha_k \rho_k \mathbf{g} + \mathbf{S}_k. \tag{4.34}$$

It can be shown by differentiating the relation $\sum_{k=1}^{2} \alpha_k = 1$ that the momentum jump condition given in Eq. 4.17 reduces to

$$\begin{aligned} \sum_{k=1}^{2} \mathbf{M}_k &= \sum_{k=1}^{2} P_{k,\mathrm{i}} \nabla \alpha_k - \sum_{k=1}^{2} \underline{\underline{\mathbf{T}}}_{k,\mathrm{i}} \cdot \nabla \alpha_k + \sum_{k=1}^{2} \mathbf{M}'_k = 0 \\ &= P \sum_{k=1}^{2} \nabla \alpha_k + \sum_{k=1}^{2} \mathbf{M}'_k = 0 \\ &= \sum_{k=1}^{2} \mathbf{M}'_k = 0. \end{aligned} \tag{4.35}$$

We still need closure models for $\underline{\underline{\boldsymbol{\Sigma}}}_k^{\mathrm{Re}}$ and $\mathbf{M}'_k$, which will be dealt with separately in Chapter 5 and 6, respectively. Excluding those, we have now for n phases, $4n + 1$ conservation equations (Eqs. 4.20, 4.34 and the condition that $\sum_{k=1}^{2} \alpha_k = 1$) and $4n+1$ unknowns ($\mathbf{U}_k$, α_k, P), hence the system is closed.

Chapter 5

Turbulence closure modelling

Even in single-phase turbulent flow, exact solution of local instantaneous fluctuations is not available and an approximate solution by direct numerical simulation (DNS) is too expensive. Although exact transport equations for the Reynolds stress tensor can be derived from the Navier–Stokes equations (see e.g. Lathouwers (1999)), the set of equations is not closed due to the averaging process. Therefore, the Reynolds stresses are modelled.

There is no general agreement on a model, which can be used for all type of flows. Simple two-equation models such as the $k-\varepsilon$ and variants have been used widely for the simulation of flows relevant to industrial applications with a reasonable success. For turbulent multiphase flows, extensions of these models have been used, however results are found to be sensitive to model parameters (Drew and Passman, 1999). Difficulties emerge due to complex interaction of the phases and the various physical mechanisms involved depending on the type of multiphase system (gas–liquid, gas–solid, gas–liquid–solid, etc.) and the flow regime (dispersed, stratified, etc.). This gives rise to additional terms in the equations, which need to be modelled. However, the physical basis of these models is not as well established and understood as in the case of single-phase turbulent flow.

Here, we limit our discussion to bubbly flows only and to the $k-\varepsilon$ model in particular, which we primarily used in this work. The range of flow parameters considered in our study is such that the average force by bubbles on the continuous phase cannot be neglected, hence the use of two-fluid model incorporating the two-way coupling is justified. Furthermore, the bubble diameter is of the order $1-10$ mm, which is larger than the Kolmogorov scale, therefore the turbulence in the continuous phase may be influenced by the presence of bubbles. This influence can be in either way, that is, it may enhance or suppress the turbulence depending on the operating conditions (Lathouwers, 1999). Gas holdups of interest in this study are relatively low, about $15-20\,\%$ at most. We therefore assume that the dispersion can be considered dilute in the majority of the flow domain and the dispersed phase fluctuating properties depend mainly on the continuous phase turbulence rather than the hydrodynamic interactions between bubbles. This allows to write gas-side turbulence quantities in terms of the mean characteristics of the liquid phase and the ratio of the particle relaxation time

and eddy–particle interaction time [1].

5.1 Turbulence in the liquid phase

Velocity fluctuations in the liquid phase are caused by both liquid phase turbulence in the usual sense and by the random velocity field induced by the bubbles. The first contribution is due to the time-dependent vortical structures as in single-phase turbulence. These vortices span a wide range of temporal and spatial scales and cascade the energy taken from the mean velocity gradients down to the Kolmogorov scale. On top of this, there is the contribution due to presence of bubbles. Experimental evidence shows that the interfaces can alter the different mechanisms of turbulence in the liquid phase (e.g. production, redistribution and dissipation) by modifying the characteristic scales of the turbulence (Chahed et al., 2003). This second bubble-induced contribution is the combination of three effects (Lance and Bataille, 1991; Lathouwers, 1999): (i) perturbations generated by the relative velocity of bubbles, (ii) wakes behind the bubbles inducing small-scale fluctuations, (iii) deformation of interfaces. In order to distinguish between these two different mechanisms, the first contribution due to "true turbulence" is usually called "shear-induced" turbulence, while the latter is called "pseudo-turbulence" or "bubble-induced" turbulence. It would have been useful to separate these two random processes precisely, both for the interpretation of experimental results and for the modelling of $\underline{\underline{\Sigma}}_k^{\mathrm{Re}}$, however, according to Lance and Bataille (1991), this is difficult as these mechanisms are coupled together.

In stirred bubbly flows, a significant part of the turbulence is generated via the action of the impeller. Therefore, it is usually assumed that the turbulence is dominated by the impeller-induced flow and the influence of the bubbles is minimal. According to Lane (2005a), an attempt to take into account the bubble-induced turbulence by introducing an additional Reynolds stress term resulted in only a very small correction.

5.1.1 Modified $k-\varepsilon$ model

Turbulence in the liquid phase is modelled similarly to standard $k-\varepsilon$ modelling for single-phase flow (Launder and Spalding, 1974), but with a modified set of equations with extra terms that include interphase turbulent momentum transfer. Closure assumptions are obtained by considering only turbulent motions at large scales with respect to the mean particle size (Viollet and Simonin, 1994). The Boussinesq hypothesis is employed to relate the local mean Reynolds stress linearly to the local mean strain rate with a proportionality constant, the so-called eddy viscosity (or turbulent viscosity), μ^{t}, based on an analogy to the molecular viscosity. Turbulent eddies are considered as molecules, colliding and exchanging momentum and obeying laws similar to the kinetic theory of gasses (Ranade, 2002), allowing the description of the Reynolds

[1] "Particle" is used as a general term in this text, which may denote both a solid particle and a fluid particle, such as a drop or a bubble

stresses for the liquid phase ($k = 1$), $\underline{\underline{\boldsymbol{\Sigma}}}_1^{\mathrm{Re}} = -\rho_1 \overline{\mathbf{u}_1' \mathbf{u}_1'}^{\chi_1 \rho_1}$, as

$$\underline{\underline{\boldsymbol{\Sigma}}}_1^{\mathrm{Re}} = -\frac{2}{3}\rho_1 k_1 \underline{\underline{\mathbf{I}}} + 2\mu_1^{\mathrm{t}} \left[\underline{\underline{\mathbf{S}}}_1 - \frac{1}{3}(\nabla \cdot \mathbf{U}_1)\underline{\underline{\mathbf{I}}} \right] \tag{5.1}$$

$$= -\frac{2}{3}\left[\rho_1 k_1 + \mu_1^{\mathrm{t}}(\nabla \cdot \mathbf{U}_1)\right]\underline{\underline{\mathbf{I}}} + \mu_1^{\mathrm{t}}\left[\nabla \mathbf{U}_1 + (\nabla \mathbf{U}_1)^{\mathrm{T}}\right]. \tag{5.2}$$

This concept, however, is faulty. Turbulent eddies are distributed entities interacting continuously and the large, energy containing eddies are often of a comparable size to the characteristic scale of the mean flow. Molecules, on the other hand, are discrete and collide only intermittently, and their mean free-path is small with respect to the macroscopic dimensions of the flow (Davidson, 2004). For bubbly flows, the Boussinesq relation is expected to prevail when the system is dilute and the main mechanism of turbulence production is mean velocity gradients (Lathouwers, 1999). Note that, μ_1^{t} is not a material property (in contrast to its molecular counterpart) but a local flow property. In the standard $k-\varepsilon$ model, μ_1^{t} is modelled as a scalar quantity and estimated from a typical turbulent velocity scale ($k^{1/2}$) and a turbulent length scale ($k^{3/2}/\varepsilon$), hence

$$\mu_1^{\mathrm{t}} = \rho_1 C_\mu \frac{k_1^2}{\varepsilon_1}. \tag{5.3}$$

The empirical coefficient C_μ has a value of 0.09. The turbulent kinetic energy of liquid phase, k_1, represents the kinetic energy of the fluctuating motion, defined as half the sum of the normal turbulent stresses. With the assumption of isotropic turbulence, i.e. $\overline{(u_{x,1}')^2} = \overline{(u_{y,1}')^2} = \overline{(u_{z,1}')^2}$, it reduces to

$$k_1 \equiv \frac{1}{2}\overline{u_{i,1}' u_{i,1}'} = \frac{3}{2}\overline{(u_1')^2} = \frac{3}{2}u_{\mathrm{rms},1}^2, \tag{5.4}$$

where the root-mean-square (r.m.s.) velocity is denoted by $u_{\mathrm{rms},1} = \left[\overline{(u_1')^2}\right]^{1/2}$. The dissipation rate of the turbulent kinetic energy by viscous action is represented by ε_1. In analogy to the viscous dissipation rate of the mean flow kinetic energy, that is,

$$\left(\underline{\underline{\mathbf{T}}}_1/\rho_1\right) : \underline{\underline{\mathbf{S}}}_1 = 2\nu_1 \underline{\underline{\mathbf{S}}}_1 : \underline{\underline{\mathbf{S}}}_1, \tag{5.5}$$

it is defined as

$$\begin{aligned} \varepsilon_1 &= \overline{(\underline{\underline{\boldsymbol{\tau}}}_1'/\rho_1) : \underline{\underline{\mathbf{s}}}_1'} \\ &= 2\nu_1 \overline{\underline{\underline{\mathbf{s}}}_1' : \underline{\underline{\mathbf{s}}}_1'}, \end{aligned} \tag{5.6}$$

where $\underline{\underline{\mathbf{s}}}_1'$ is the instantaneous strain-rate tensor for the velocity fluctuations and $\nu_1 = \mu_1/\rho_1$ is the kinematic viscosity.

A characteristics time scale of the energetic turbulent eddies could be written as

$$\tau_1^{\mathrm{t}} = \frac{3}{2} C_\mu \frac{k_1}{\varepsilon_1} \tag{5.7}$$

(Viollet and Simonin, 1994) and the length scale associated with the turbulent eddies can be calculated from τ_1^{t} and the r.m.s. velocity:

$$L_1^{\mathrm{t}} = \tau_1^{\mathrm{t}} u_{\mathrm{rms},1} = \tau_1^{\mathrm{t}} \sqrt{\frac{2}{3}k_1} = \sqrt{\frac{3}{2}} C_\mu \frac{k_1^{3/2}}{\varepsilon_1}. \tag{5.8}$$

Transport equations for k_1 and ε_1 are needed in order to close the system and solve for $\underline{\underline{\boldsymbol{\Sigma}}}_1^{\mathrm{Re}}$. An exact equation for k_1 can be obtained by subtracting the averaged momentum equation from the instantaneous one (which gives the equation for the fluctuating velocity) and then multiplying it with the fluctuating velocity itself and time-averaging the result (Venneker, 1999), or by contracting the exact transport equation for the Reynolds stress (Lathouwers, 1999):

$$\frac{\partial}{\partial t}(\alpha_1\rho_1 k_1) + \nabla\cdot(\alpha_1\rho_1\mathbf{U}_1 k_1) = -\alpha_1\rho_1 \underbrace{\left(\underline{\underline{\boldsymbol{\Sigma}}}_1^{\mathrm{Re}}/\rho_1\right) : (\nabla\mathbf{U}_1)}_{G_{k,1}} + \\ + \nabla\cdot\alpha_1 \underbrace{\left[-\frac{1}{2}\rho_1\mathbf{u}_1'(\mathbf{u}_1'\cdot\mathbf{u}_1') + \mathbf{u}_1'\cdot\underline{\underline{\boldsymbol{\sigma}}}_1'\right]}_{\rho_1 C_{k,1}} - \alpha_1\rho_1 \underbrace{\overline{(\underline{\underline{\boldsymbol{\tau}}}_1'/\rho_1) : (\nabla\mathbf{u}_1')}}_{\varepsilon_1} - \underbrace{\langle\underline{\underline{\boldsymbol{\sigma}}}_1' : (\mathbf{u}_1'\nabla\chi_1)\rangle}_{\Pi_{k,1}}. \tag{5.9}$$

The underbraced terms need closure by constitutive equations. A transport equation for ε_1 is also written, however it has a less firm basis than the exact equation for k_1 given above. The final "modelled" transport equations solved in the $k-\varepsilon$ model are

$$\frac{\partial}{\partial t}(\alpha_1\rho_1 k_1) + \nabla\cdot(\alpha_1\rho_1\mathbf{U}_1 k_1) = \nabla\cdot\alpha_1 \underbrace{\left[\left(\frac{\mu_1^{\mathrm{t}}}{\sigma_k}+\mu_1\right)\nabla k_1\right]}_{\rho_1 C_{k,1}} + \alpha_1\rho_1 G_{k,1} - \alpha_1\rho_1\varepsilon_1 + \Pi_{k_1}, \tag{5.10}$$

$$\frac{\partial}{\partial t}(\alpha_1\rho_1\varepsilon_1) + \nabla\cdot(\alpha_1\rho_1\mathbf{U}_1\varepsilon_1) = \nabla\cdot\alpha_1\left[\left(\frac{\mu_1^{\mathrm{t}}}{\sigma_\varepsilon}+\mu_1\right)\nabla\varepsilon_1\right] + \alpha_1\rho_1\frac{\varepsilon_1}{k_1}(C_{1\varepsilon}G_{k,1} - C_{2\varepsilon}\varepsilon_1) + \Pi_{\varepsilon_1}. \tag{5.11}$$

Standard model constants are used in this study (i.e. $\sigma_k = 1.0$, $\sigma_\varepsilon = 1.3$, $C_{1\varepsilon} = 1.44$, $C_{2\varepsilon} = 1.92$), which have been determined from extensive single-phase flow experiments with free turbulent shear flows (Launder and Spalding, 1974). In the equations above, $C_{k,1}$ is the turbulent and molecular transport term (molecular part, μ_1, is usually neglected at high Re) modelled by the eddy-viscosity based gradient diffusion hypothesis. $G_{k,1}$ is the generation rate of turbulent kinetic energy due to the mean velocity gradients (rate of work of the Reynolds stress). In Fluent, it is modelled, in line with the Boussinesq hypothesis, as

$$G_{k,1} = 2\nu_1^{\mathrm{t}}\underline{\underline{\mathbf{S}}}_1 : \underline{\underline{\mathbf{S}}}_1, \tag{5.12}$$

where $\nu_1^{\mathrm{t}} = \mu_1^{\mathrm{t}}/\rho_1$ is the turbulent kinematic viscosity. Π_{k_1} is the additional source term that does not appear in the single-phase equations and represents the influence of the dispersed phase fluctuating motion on the continuous phase. It acts at the interfaces and can be interpreted as production or dissipation due to interfacial work performed by the interfacial forces such as drag, virtual mass, etc. (Lathouwers, 1999).

5.1.2 Modelling of Π_{k_1}

A relation for the fluid–particle turbulent interaction term Π_{k_1} is given in the turbulence model developed by Bel F'dhila and Simonin (1992) for bubbly flows. They made special attempts in the averaging process to account for the nonlinear dependence of the averaged interfacial momentum transfer on the turbulent velocities, because large

fluctuations and/or highly nonlinear interactions may have a strong effect on $\mathbf{M}'_k$. As a result, their correlations include the separate contributions due to fluctuations in drag and added mass forces (both of which are important for bubbly flows) and also in free-stream fluid pressure gradient experienced by the bubble. They assumed that bubbles interact only slightly and derived the turbulence model and the Eulerian closure assumptions for $\mathbf{M}'_k$ by averaging from the statistical characteristics of a single rigid spherical particle placed in an homogenous turbulent flow in a Lagrangian frame. The closure of $\mathbf{M}'_k$ is given in Section 6.6.4. Here, we explain only the turbulence model.

In the derivation of the continuous phase turbulence equations, Bel F'dhila and Simonin considered only the larger eddies with respect to the mean bubble diameter. Thus, the spatial average of the disturbance flows induced by the particles was neglected and equations are related to the locally undisturbed continuous phase turbulence written in terms of locally undisturbed continuous phase instantaneous velocity. In accordance with Lance et al. (1991), the interfacial force contribution due to the wakes behind the particles was assumed to be in equilibrium with the corresponding viscous dissipation rate in the wakes. They indicated that these assumptions were crucial for the derivation and can be very crude in turbulent bubbly flows when the particle size is comparable to the integral scale of the turbulence. They derived a relation for Π_{k_1} directly from the instantaneous momentum equation for locally undisturbed flow that reads

$$\Pi_{k_1} = -\alpha_2 \langle \mathbf{f}_2 \cdot \mathbf{u}'_1 \rangle_2 \tag{5.13}$$

$$= \left(\frac{\rho_2}{\rho_2 + \rho_1 C_\mathrm{A}} \right) \alpha_2 \rho_1 F_\mathrm{D} (\langle \mathbf{u}'_1 \cdot \mathbf{u}'_\mathrm{r} \rangle_2 + \mathbf{U}_\mathrm{d} \cdot \mathbf{U}_\mathrm{r}) \tag{5.14}$$

$$= \left(\frac{\rho_2}{\rho_2 + \rho_1 C_\mathrm{A}} \right) \alpha_2 \rho_1 F_\mathrm{D} (k_{12} - 2k_1 + \mathbf{U}_\mathrm{d} \cdot \mathbf{U}_\mathrm{r}). \tag{5.15}$$

Here, $\mathbf{U}_\mathrm{r}$ is the mean relative velocity and defined in Eq. 5.22. $\mathbf{f}_2$ is the force per volume induced by the surrounding flow on a single particle (bubble) following the expression proposed by Tchen (1947), but neglecting the lift and history force terms (see Section 6.6.4). The ensemble averaging operator associated to the phase k is denoted by $\langle . \rangle_k$ (e.g. by definition, the drift velocity is $\mathbf{U}_\mathrm{d} \equiv \langle \mathbf{u}'_1 \rangle_2 = \overline{\mathbf{u}'_1}^{\chi_2}$). The added mass coefficient, C_A, is usually taken as 0.5, i.e. the value for spherical particles in dilute systems. For heavy particles with respect to the continuous phase density (i.e. $\rho_2 \gg \rho_1$), the factor in Eq. 5.15 converges to unity, $\rho_2/(\rho_2 + \rho_1 C_\mathrm{A}) \approx 1$, and the added mass effects are negligible. For bubbly flows, this is not the case and the added mass effects may have a significant effect on Π_{k_1}. However, in the Fluent implementation, this factor is not taken into account and there is an extra factor of α_1, presumably to ensure the limiting behaviour when the continuous phase is not present (i.e. as $\alpha_1 \to 0$, $\Pi_{k_1} \to 0$). The equation being solved in Fluent reads

$$\Pi_{k_1} = \alpha_1 \alpha_2 \rho_1 F_\mathrm{D} (k_{12} - 2k_1 + \mathbf{U}_\mathrm{d} \cdot \mathbf{U}_\mathrm{r}). \tag{5.16}$$

The fluid-particle velocity covariance k_{12}, representing the correlation between continuous and dispersed phase velocity fluctuations averaged upon the dispersed phase, is given by

$$k_{12} = \langle \mathbf{u}'_1 \cdot \mathbf{u}'_2 \rangle_2, \tag{5.17}$$

which is calculated from Eq. 5.35 given in Section 5.2. In Fluent, the averaged drag function, F_D, is calculated according to Eq. 6.36. Bel F'dhila and Simonin defined F_D

in a form to account approximately for high bubble concentrations and the non-linear dependence on the relative velocity fluctuations:

$$F_{\mathrm{D}} = \frac{3}{4}\frac{\langle C_{\mathrm{D}}\rangle}{\overline{d}_{\mathrm{b}}}\langle|\mathbf{u}_{\mathrm{r}}|\rangle_2, \tag{5.18}$$

where the averaged drag coefficient $\langle C_{\mathrm{D}}\rangle$ comes from the drag law being chosen. They used the following approximated form by modifying the drag law from Schiller and Naumann (1933):

$$\langle C_{\mathrm{D}}(Re_{\mathrm{b}})\rangle \approx C_{\mathrm{D}}(\langle Re_{\mathrm{b}}\rangle) = \frac{24}{\langle Re_{\mathrm{b}}\rangle}\left(1 + 0.15\langle Re_{\mathrm{b}}\rangle^{0.687}\right)\alpha_1^{-1.7}, \tag{5.19}$$

$$\langle Re_{\mathrm{b}}\rangle = \frac{\alpha_1\rho_1\langle|\mathbf{u}_{\mathrm{r}}|\rangle_2\overline{d}_{\mathrm{b}}}{\mu_1}, \tag{5.20}$$

$$\langle|\mathbf{u}_{\mathrm{r}}|\rangle_2 \approx \sqrt{\mathbf{U}_{\mathrm{r}}\cdot\mathbf{U}_{\mathrm{r}} + \langle\mathbf{u}'_{\mathrm{r}}\cdot\mathbf{u}'_{\mathrm{r}}\rangle_2}. \tag{5.21}$$

Here, the local instantaneous relative velocity is given by $\mathbf{u}_{\mathrm{r}} = \mathbf{u}_2 - \tilde{\mathbf{u}}_1$, where $\tilde{\mathbf{u}}_1$ denotes the locally undisturbed continuous phase instantaneous velocity, i.e. the velocity if the bubbles were not present.

5.1.3 Drift velocity $\mathbf{U}_{\mathrm{d}}$

It is important to notice that the mean relative velocity $\mathbf{U}_{\mathrm{r}}$ in the equations given above is not simply the difference between the averaged phase velocities, but the difference and an extra contribution term, the drift velocity $\mathbf{U}_{\mathrm{d}}$, which arises due to the correlation between the instantaneous distribution of bubbles and the turbulent fluid motion at large characteristic length scales with respect to the bubble diameter:

$$\begin{aligned}\mathbf{U}_{\mathrm{r}} = \langle\mathbf{u}_{\mathrm{r}}\rangle_2 &= \langle\mathbf{u}_2\rangle_2 - \langle\tilde{\mathbf{u}}_1\rangle_2\\ &= \mathbf{U}_2 - \langle[\langle\tilde{\mathbf{u}}_1\rangle_1 + \mathbf{u}'_1]\rangle_2\\ &= \mathbf{U}_2 - [\langle\mathbf{U}_1\rangle_2 + \langle\mathbf{u}'_1\rangle_2]\\ &= \mathbf{U}_2 - [\mathbf{U}_1 + \mathbf{U}_{\mathrm{d}}],\end{aligned} \tag{5.22}$$

and the drift velocity is defined accordingly as

$$\mathbf{U}_{\mathrm{d}} = \langle\tilde{\mathbf{u}}_1\rangle_2 - \mathbf{U}_1 = \langle\mathbf{u}'_1\rangle_2, \tag{5.23}$$

that is, the turbulent fluctuations in the liquid phase averaged at the positions of the bubbles, $\langle\mathbf{u}'_1\rangle_2$. Although $\langle\mathbf{u}'_1\rangle_1$ and $\langle\mathbf{u}'_2\rangle_2$ are zero by definition, $\langle\mathbf{u}'_1\rangle_2$ is not, due to the above mentioned correlation between the turbulent fluctuations and the bubble distribution. The net effect of these fluctuations is in such a way that it causes bubbles to drift from the regions of high bubble concentration to the lower ones, thereby diminishing the void fraction gradients; an effect similar to molecular diffusion by thermal motion of molecules. As the concentration becomes gradually uniform, $\mathbf{U}_{\mathrm{d}}$ vanishes (i.e. $\langle\mathbf{u}'_1\rangle_2 \to \langle\mathbf{u}'_1\rangle_1 = 0$ as $\nabla\alpha_2 \to 0$). In line with these observations, the drift velocity is usually modelled as a gradient diffusion, such as in the model proposed by Viollet and Simonin (1994), which reads

$$\mathbf{U}_{\mathrm{d}} = -\underline{\underline{\mathbf{D}}}^{\mathrm{t}}_{12}\cdot\left(\frac{1}{\alpha_2}\nabla\alpha_2 - \frac{1}{\alpha_1}\nabla\alpha_1\right), \tag{5.24}$$

where $\underline{\underline{\mathbf{D}}}^{\mathrm{t}}_{12}$ is the fluid-particle dispersion tensor. This formulation was derived from the transport equation for the dispersed phase mass fraction in a way that is consistent with the expected limiting behaviour as the particle size approaches to zero. That is, the particles having sufficiently small inertia become fluid followers (tracers), hence $\mathbf{U}_{\mathrm{r}}$, being connected to the average interfacial momentum exchange term $\mathbf{M}'_k$ (see Chapter 6), has to approach to zero. Then, $\mathbf{U}_{\mathrm{d}}$ represents the dispersion of the bubbles due to the transport by continuous phase turbulence. This is an important effect, because the averaging method being employed do not permit a diffusive term in the mass balance equations that would account for the dispersion of bubbles (Lahey et al., 1993; Mudde and Simonin, 1999).

In Fluent, a so-called dispersion Prandtl number, $\sigma^{\mathrm{t}}_{21} = 0.75$, is introduced in the calculation of $\mathbf{U}_{\mathrm{d}}$, hence

$$\mathbf{U}_{\mathrm{d}} = -\frac{\underline{\underline{\mathbf{D}}}^{\mathrm{t}}_{12}}{\sigma^{\mathrm{t}}_{21}} \cdot \left(\frac{1}{\alpha_2} \nabla \alpha_2 - \frac{1}{\alpha_1} \nabla \alpha_1 \right). \tag{5.25}$$

The fluid-particle dispersion tensor $\underline{\underline{\mathbf{D}}}^{\mathrm{t}}_{12}$, based on a semi-empirical analysis, is expressed in terms of the fluid-particle velocity covariance tensor $\langle \mathbf{u}'_1 \mathbf{u}'_2 \rangle_2$ and the eddy–particle interaction time (characteristic time of the fluid turbulence viewed by the particles or Lagrangian integral time scale) τ^{t}_{12}:

$$\underline{\underline{\mathbf{D}}}^{\mathrm{t}}_{12} = \tau^{\mathrm{t}}_{12} \langle \mathbf{u}'_1 \mathbf{u}'_2 \rangle_2, \tag{5.26}$$

which is, for practical calculations, limited to its diagonal part (Thai Van et al., 1994):

$$\underline{\underline{\mathbf{D}}}^{\mathrm{t}}_{12} = \tau^{\mathrm{t}}_{12} \frac{k_{12}}{3} \underline{\underline{\mathbf{I}}}. \tag{5.27}$$

The eddy–particle interaction time τ^{t}_{12} can be calculated theoretically in terms of the fluid Langrangian correlation function computed along particle trajectories. This interaction time is influenced by what is called "effect of crossing trajectories", a concept first proposed by Yudine in 1959 (Csanady, 1963). Particles with non-zero mean relative velocity change their fluid-particle neighbourhood continuously; in other words, they cut through eddies that would otherwise disperse them over a wide region. Therefore, they lose their velocity correlation more rapidly than diffusing fluid particles of continuous phase, which change their turbulent velocity only due to the eddy-decay process. Consequently, when the terminal velocity is large, the fluctuation frequency of the particles is $U_{\mathrm{T}}/L^{\mathrm{t}}_{\parallel}$, i.e. the ratio of the mean terminal velocity to the typical eddy diameter in the vertical direction (direction parallel to $\mathbf{U}_{\mathrm{T}}$). When the terminal velocity is small, the velocity fluctuations are mainly due to the eddy-decay with a typical frequency of (roughly) $u'_{\parallel}/L^{\mathrm{t}}_{\parallel}$, where $u'_{\parallel}$ denotes the vertical turbulent root-mean-square (r.m.s.) velocity. For the case of heavy solid particles, the analysis of Csanady (1963) showed a decrease of dispersion in vertical and perpendicular directions by a factor of the order $\xi_{\mathrm{r}} = U_{\mathrm{T}}/u'_{\parallel}$. There is an additional decrease by a factor of 2 in the perpendicular direction, because of the so-called "continuity effect", i.e. particles falling out of an eddy fall into its back-flow. Interpolation formulas were derived for vertical and perpendicular directions in a way to give the correct limit behaviour as $U_{\mathrm{T}} \to 0$ and $U_{\mathrm{T}} \to \infty$. Following the formula for only the case of vertical direction, the

effective particle turbulent dispersion coefficient (for long diffusion times) is written as

$$D_2^{\mathrm{t}} = D_1^{\mathrm{t}} \left(\frac{1}{\sqrt{1 + C_\beta \xi_{\mathrm{r}}^2}} \right) \tag{5.28}$$

(Simonin, 1990), and the eddy–particle interaction time as

$$\tau_{12}^{\mathrm{t}} = \frac{\tau_1^{\mathrm{t}}}{\sigma_1^{\mathrm{t}}} \left(\frac{1}{\sqrt{1 + C_\beta \xi_{\mathrm{r}}^2}} \right), \tag{5.29}$$

with single-phase turbulent Schmidt number of the continuous phase taken as $\sigma_1^{\mathrm{t}} = 1.0$ (Bel F'dhila and Simonin, 1992). The empirical parameter C_β is related to the Langrangian over Eulerian characteristic length scales ratio, and comparison with the experiments of Wells and Stock resulted in values of $C_\beta = 0.45$ in the direction parallel to the mean relative velocity, and $C_\beta = 1.8$ in the orthogonal directions (Simonin, 1990). In Fluent, it is calculated by the relation $C_\beta = 1.8 - 1.35\cos^2\theta$ (the angle between the mean particle velocity and the mean relative velocity being θ), which is consistent with the limiting empirical values. In accordance with the turbulence isotropy assumption, Bel F'dhila and Simonin used

$$\xi_{\mathrm{r}} = \frac{|\mathbf{U}_{\mathrm{r}}|}{L_1^{\mathrm{t}}/\tau_1^{\mathrm{t}}} = \frac{|\mathbf{U}_{\mathrm{r}}|}{\sqrt{\frac{2}{3}k_1}}. \tag{5.30}$$

Note that, when the mean relative velocity is zero, then $\xi_{\mathrm{r}} = 0$, and the dispersion coefficient for the dispersed phase is reduced to the continuous phase one, i.e. $D_2^{\mathrm{t}} = D_1^{\mathrm{t}}$. In bubbly flows, contrary to particle-laden flows, inertial effects result in $D_{12}^{\mathrm{t}} \geq D_1^{\mathrm{t}}$ (Simonin, 1990).

From the equations given above, the interfacial source term Π_{k_1} in the continuous phase turbulence kinetic energy equation can be calculated. They will also prove useful when formulating the dispersed phase turbulent quantities, which is the topic of the Section 5.2.

5.1.4 Modelling of Π_{ε_1}

The last term left to be closed is the corresponding source term in the dissipation equation, Π_{ε_1}. Bel F'dhila and Simonin (1992) modelled this term according to Elghobashi and Abou-Arab (1983) with respect to the turbulent dissipation time scale:

$$\Pi_{\varepsilon_1} = C_{3\varepsilon} \frac{\varepsilon_1}{k_1} \Pi_{k_1}, \tag{5.31}$$

where the model constant $C_{3\varepsilon} = 1.2$ is determined from turbulent gas–particle jet flows and as stated by Elghobashi and Abou-Arab (1983), it requires no modification when predicting jets laden with particles smaller than 200 microns. In deriving the equations, it was assumed that the system is dilute so that no collisions occur. The same model is used in Fluent.

Owing to the equilibrium between the interphase production and wake dissipation, the interfacial source terms Π_{k_1} and Π_{ε_1} have been neglected in some studies of turbulent bubbly flows, e.g. in Lathouwers (1999).

5.2 Turbulence in the gas phase

Turbulence predictions in the dispersed phase also follow from the work of Simonin and coworkers. Relations are derived by extending the Tchen's theory (Tchen, 1947) on dispersion of discrete particles suspended in a homogenous and steady continuous phase turbulence (see Hinze (1975), p. 460, for a discussion of the theory and its assumptions). Some of these were already given in the previous section. The dispersed phase turbulent kinetic energy and the fluid–particle velocity covariance are expressed as algebraic functions of the continuous phase turbulent kinetic energy. Thus, unlike in the continuous phase case, no separate transport equations are solved. Inherent assumption again is that the dispersed phase concentration is dilute, hence the inter-particle collisions are negligible and the dispersed phase fluctuations are mainly caused by the continuous phase turbulence. Two relevant time scales are used in the equations that characterise the interaction between the fluctuating motions, namely the eddy–particle interaction time τ_{12}^{t} and the mean particle relaxation time (characteristic time of the particle response to the surrounding fluid motion) associated with the inertial effects acting on the particle, τ_{p}, which is written as

$$\tau_{\mathrm{p}} = \frac{1}{F_{\mathrm{D}}}\left(\frac{\rho_2}{\rho_1} + C_{\mathrm{A}}\right) = \frac{4}{3}\frac{d_{\mathrm{b}}}{C_{\mathrm{D}}\langle|\mathbf{u}_{\mathrm{r}}|\rangle}\left(\frac{\rho_2}{\rho_1} + C_{\mathrm{A}}\right). \tag{5.32}$$

In Fluent, there is an extra factor of α_1 similar to the treatment of Π_{k_1} (Eq. 5.16), hence τ_{p} is calculated from

$$\tau_{\mathrm{p}} = \frac{1}{\alpha_1 F_{\mathrm{D}}}\left(\frac{\rho_2}{\rho_1} + C_{\mathrm{A}}\right) = \frac{4}{3}\frac{d_{\mathrm{b}}}{\alpha_1 C_{\mathrm{D}}\langle|\mathbf{u}_{\mathrm{r}}|\rangle}\left(\frac{\rho_2}{\rho_1} + C_{\mathrm{A}}\right). \tag{5.33}$$

Considering the simplest case that the fluid turbulence Langrangian function computed along particle trajectories takes an exponential form, the dispersed phase turbulent kinetic energy k_2 and the covariance between the velocity fluctuations of each phase, k_{12}, are given by (Simonin, 1990; Bel F'dhila and Simonin, 1992)

$$k_2 = \frac{1}{2}\overline{u'_{i,2}u'_{i,2}} = \langle k_1\rangle_2\left(\frac{b^2+\eta_{\mathrm{r}}}{1+\eta_{\mathrm{r}}}\right), \tag{5.34}$$

$$k_{12} = \langle \mathbf{u}'_1 \cdot \mathbf{u}'_2\rangle_2 = 2\langle k_1\rangle_2\left(\frac{b+\eta_{\mathrm{r}}}{1+\eta_{\mathrm{r}}}\right), \tag{5.35}$$

with

$$b = \frac{1+C_{\mathrm{A}}}{\dfrac{\rho_2}{\rho_1}+C_{\mathrm{A}}}, \qquad \eta_{\mathrm{r}} = \tau_{12}^{\mathrm{t}}/\tau_{\mathrm{p}}, \qquad \langle k_1\rangle_2 \cong k_1. \tag{5.36}$$

In the fluid–fluid and fluid–particle correlations given above, the characteristic time ratio η_{r} accounts simultaneously for particle inertia and crossing trajectories effects. Note also that the dispersed phase statistical quantities are related to $\langle k_1\rangle_2$, the continuous phase turbulent kinetic energy viewed by the particles (i.e. Langrangian), which cannot be directly associated with k_1, the predicted one within the Eulerian framework. Nevertheless, it was assumed that $2\langle k_1\rangle_2 = \langle[u_{1,i} - \langle u_{1,i}\rangle_2][u_{1,i} - \langle u_{1,i}\rangle_2]\rangle_2 \cong 2k_1$. This arises from Tchen's assumption that during the motion of the particle, the neighbourhood will be formed by the same fluid, and was identified as the most questionable

assumption of the theory (Hinze, 1975; Simonin, 1990). Deutsch and Simonin (1991) reported that LES simulations of light particles ($\rho_2/\rho_1 = 0.001$) suspended in homogenous steady turbulence showed a large statistical bias due to the correlation between the instantaneous distribution of the particles and k_1. It was found that $\langle k_1 \rangle_2$ was considerably lower (up to 50 %), indicating an instantaneous accumulation of bubbles at the regions of low turbulent velocity. The agreement was reasonable for the case of heavy particles ($\rho_2 > \rho_1$). The effect of this bias was proposed to be neglected until further developments (Bel F'dhila and Simonin, 1992).

Finally, according to Bel F'dhila and Simonin, various components of the gas phase Reynolds stress tensor $\underline{\underline{\boldsymbol{\Sigma}}}_2^{\mathrm{Re}}$ and the fluid–particle covariance tensor $\langle \mathbf{u}_1' \mathbf{u}_2' \rangle_2$, which are needed to close the gas phase momentum equations and the interfacial momentum transfer, can be predicted by assuming that the Boussinesq approximation (Eq. 5.2) holds for the dispersed phase. This requires a turbulent viscosity for the gas phase, ν_2^{t}, to be specified. For bubbly flows, expression for ν_2^{t} should include the contribution of added mass and liquid pressure forces. Bel F'dhila and Simonin found that although the form of such a relation was strongly dependent on the closure model used for the undisturbed liquid pressure contribution, numerical predictions in the gas phase were virtually independent of the closure model used for the deviatoric components of $\underline{\underline{\boldsymbol{\Sigma}}}_2^{\mathrm{Re}}$ and $\langle \mathbf{u}_1' \mathbf{u}_2' \rangle_2$, and practically, they could be neglected in the gas phase momentum equation. Similarly, as mentioned earlier, Lathouwers (1999) found that both viscous and turbulent stresses in the gas phase momentum equation could be safely neglected altogether, i.e. $\underline{\underline{\boldsymbol{\Sigma}}}_2 = 0$ and $\underline{\underline{\boldsymbol{\Sigma}}}_2^{\mathrm{Re}} = 0$. In view of these findings, no attempt was made towards modelling of $\underline{\underline{\boldsymbol{\Sigma}}}_2^{\mathrm{Re}}$ in this study.

5.3 Near-wall treatment

In wall-bounded turbulent flows, presence of no-slip boundaries have an important effect on the fluid flow and accordingly on the transported quantities. It is also those regions which are responsible for the damping as well as for the generation of turbulence (due to production of turbulent kinetic energy by large gradients in the mean velocity). Those interactions may lead to non-trivial turbulent effects.

5.3.1 Boundary layer

The boundary layer at near-wall regions consists of three distinct parts that are taken into account in the turbulence model implementation in Fluent.

Viscous (laminar) sublayer ($y^+ < 5$)

Adjacent to the wall, the flow is nearly laminar and the molecular viscosity plays a dominant role in the transport of momentum and scalars. The thickness of the viscous sublayer is given by the wall coordinate, y^+:

$$y^+ \equiv \frac{u_\tau}{\nu} y, \tag{5.37}$$

which is the wall-normal distance (y) made dimensionless with the kinematic viscosity and the wall shear velocity (also called the friction velocity), u_τ:

$$u_\tau = \sqrt{\tau_w/\rho}, \tag{5.38}$$

with τ_w denoting the wall shear stress (also called the skin friction).

In the viscous sublayer, described as $y^+ < 5$ (i.e. below 5 wall units), there is a simple linear relationship between the wall coordinate y^+ and the normalised wall-parallel mean velocity, $U_\parallel^+$:

$$U_\parallel^+ = y^+, \tag{5.39}$$

in which $U_\parallel^+$ is defined as

$$U_\parallel^+ \equiv \frac{U_\parallel}{u_\tau}. \tag{5.40}$$

Eq. 5.39 is basically the laminar stress–strain relationship and the wall-parallel mean velocity as a function of distance from the wall, $U_\parallel(y)$, could be retrieved from above relations:

$$U_\parallel(y) = \frac{u_\tau^2}{\nu} y = \frac{\tau_w}{\mu} y, \tag{5.41}$$

showing that it varies linearly in the laminar sublayer.

Log-law layer ($y^+ > 60$)

At the other end of the boundary layer, the effect of viscosity is less pronounced and the transport mechanism is mainly the turbulence. In this region, the variation of $U_\parallel^+$ follows a log-law:

$$U_\parallel^+ = \frac{1}{\kappa} \ln y^+ + c, \tag{5.42}$$

with the von Kármán constant $\kappa = 0.4187$ and the empirical roughness parameter $c = 5.45$.

The upper limit of the turbulent logarithmic layer depends on the Reynolds number, after which starts the turbulent outer layer where the flow velocity reaches essentially the freestream velocity and remains constant due to strong mixing.

Intermediate buffer layer ($5 < y^+ < 60$)

In the intermediate region between the viscous sublayer and the log-law layer, both viscosity and turbulence play an important role. In this buffer layer, neither Eq. 5.39 nor 5.42 holds. Largest deviation from either law occurs when two equations intercept at about $y^+ = 11$.

5.3.2 Wall function approach

Throughout this thesis, we used the standard wall function approach in Fluent (2009) in order to take into account the boundary layers effects. In the wall function approach,

viscosity effected first two regions (viscous sublayer and buffer) of the boundary layer are not resolved. Instead, semi-empirical formulas (wall functions) are used to link the solution variables at the near-wall cells to the corresponding quantities on the wall. The standard wall functions consists of the law-of-the-wall for the mean velocity and scalars, and formulae for the near-wall turbulent quantities.

Law-of-the-wall for velocity

In Fluent, the law-of-the-wall for mean velocity is expressed in terms of the mean dimensionless velocity $U_{\parallel}^{*}$ (in analogy to U^{+}) and implemented in the following form:

$$U_{\parallel}^{*} \equiv \frac{U_P C_\mu^{1/4} k_P^{1/2}}{\tau_{\mathrm{w}}/\rho} = \begin{cases} y^{*} & y^{*} < 11.225 \\ \dfrac{1}{\kappa}\ln(y^{*}) + 5.45 & y^{*} > 11.225 \end{cases} \tag{5.43}$$

The distance from the wall y^{*} (in analogy to y^{+}) is defined as

$$y^{*} \equiv \frac{\rho C_\mu^{1/4} k_P^{1/2} y_P}{\mu}, \tag{5.44}$$

where the mean velocity, turbulent kinetic energy and distance to the wall at the wall-adjacent cell centroid P are denoted as U_P, k_P and y_P, respectively. Note that, in Fluent, law-of-the-wall for mean velocity is based on y^{*} rather than y^{+}. They are approximately equal in equilibrium turbulent boundary layers.

In the range $30 < y^{*} < 300$, the logarithmic law for the mean velocity is a fairly good approximation, though the upper limit can extend from about 100 for low Re flows up to few thousands for high Re flows. In Fluent, if the wall-adjacent cells are located such that $y^{*} > 11.225$, then the log-law is employed. If $y^{*} < 11.225$, then the laminar stress–strain relationship is used.

Law-of-the-wall for species

Based on the Reynolds' analogy between momentum and energy transport (relating the heat flux to the wall to the momentum flux to the wall), a similar logarithmic law can be written for the mean temperature. Assuming further that species transport behaves analogously to heat transport, the law-of-the-wall for species can be defined. In Fluent, it is expressed in terms of the dimensionless mass fraction Y^{*} and for constant property flow with no viscous dissipation reads as

$$Y^{*} \equiv \frac{(Y_{i,w} - Y_i) C_\mu^{1/4} k_P^{1/2}}{J_{i,w}/\rho} = \begin{cases} Sc \cdot y^{*} & y^{*} < y_c^{*} \\ Sc_{\mathrm{t}} \left[\dfrac{1}{\kappa}\ln(y^{*}) + 5.45 + P_c \right] & y^{*} > y_c^{*} \end{cases}, \tag{5.45}$$

where Y_i is the local mean mass fraction for species i and $J_{i,w}$ is its diffusion flux at the wall. Above form of the log-law for species is essentially equivalent to $Y^{*} = Sc_{\mathrm{t}}[U_{\parallel}^{*} + P_c]$. The parameter P_c, derived from the heat transfer analogy (by replacing the Prandtl

numbers by the corresponding Schmidt numbers) accounts for the resistance to transfer across the viscous sublayer. For smooth walls, it takes the form

$$P_c = 9.24 \left[\left(\frac{Sc}{Sc_\mathrm{t}} \right)^{3/4} - 1 \right] \left[1 + 0.28\, \mathrm{e}^{-0.007(Sc/Sc_\mathrm{t})} \right], \tag{5.46}$$

with the molecular and turbulent Schmidt numbers, $Sc = \nu/D_\mathrm{m}$ and $Sc_\mathrm{t} = \nu_t/D_\mathrm{t}$, respectively. The law-of-the-wall for species, in analogy with that for the mean velocity, comprises also two different laws:

- linear law for the concentration sublayer where molecular diffusivity dominates
- logarithmic law for the turbulent region where turbulent effects are important

The dimensionless concentration sublayer thickness y_c^* is computed from the following procedure. Knowing $Sc = \nu/D_\mathrm{m}$ from the physical properties of the fluid, y_c^* is specified as the y^* value at which the linear law and the logarithmic law profiles intersect.

Turbulence quantities at wall

In the $k-\epsilon$ model implementation in Fluent, the transport equation for k (Eq. 5.10) is solved also at the wall-adjacent cells. At the wall, zero diffusive flux condition with respect to the local wall-normal coordinate n is employed:

$$\frac{\partial k}{\partial n} = 0. \tag{5.47}$$

The source terms in the k equation, namely the production of kinetic energy G_k due to mean velocity gradients and its dissipation rate ε are assumed to be equal at the wall-adjacent cells according to the local equilibrium hypothesis. The production of k is then computed as follows based on the logarithmic law:

$$G_k \approx \tau_\mathrm{w} \frac{\partial U}{\partial y} = \tau_\mathrm{w} \frac{\tau_\mathrm{w}/\rho}{\kappa\, C_\mu^{1/4} k_P^{1/2} y_P}, \tag{5.48}$$

whereas the dissipation term at the wall-adjacent cells is computed from

$$\varepsilon_P = \frac{C_\mu^{3/4} k_P^{3/2}}{\kappa\, y_P}, \tag{5.49}$$

instead of solving the transport equation for ε given in Eq. 5.11.

Grid requirements

Excessive grid refinement in the wall-normal direction should be avoided near the wall because wall functions are used for the viscosity effected layers and wall-adjacent cell centroid is assumed to be outside this region. When $y^+ < 15$, the wall functions will gradually result in unbounded errors in wall shear stress. In our simulations, this was the case only in few cases listed below, for limited number of wall-adjacent cells located on the impeller blades:

- Case 3 and 4 for the standard tank with the 140k mesh (see Chapter 9)
- Case 5 for the fermenter (see Chapter 10 and 12)

High grid resolution at those locations were needed in order to resolve the gradients sufficiently. Maximum y^+ values encountered in simulations were in the range $1000 - 2500$. It should be, however, noted that, in achieving accurate results, overall resolution of the boundary layer is actually more important than achieving certain values of y^+ (Fluent, 2009).

Overall, the standard wall functions work reasonably well for wall-bounded flows. In situations where there are large deviations from the ideal conditions assumed in their derivation, especially the constant-shear and local equilibrium assumptions (e.g. in near-wall flows with large pressure gradients), more sophisticated near-wall modelling approaches are recommended by Fluent (2009).

Chapter 6

Interfacial momentum transfer

The two-fluid model, by definition, incorporates two-way coupling via the momentum jump condition $\mathbf{M}_1' + \mathbf{M}_2' = 0$ (Eq. 4.35) for the interfacial transfer term $\mathbf{M}_k' = -\langle \underline{\underline{\boldsymbol{\sigma}}}_{k,\mathrm{i}}' \cdot \nabla \chi_k \rangle$ in Eq. 4.34. A closure model is also needed for this term (either for $\mathbf{M}_1'$ or $\mathbf{M}_2'$, the remaining one being calculated from the jump condition). The closure relations are usually derived by extending results from simplified systems such as forces exerted on a single isolated spherical particle moving in an infinite fluid.

6.1 Rise of an isolated bubble

Bubbles are closely approximated by spheres, when the interfacial tension and/or viscous forces are dominant over the inertia forces (Clift et al., 1978). This is the case for bubbles with volume equivalent diameter $d_\mathrm{e} \equiv (6\mathcal{V}_\mathrm{b}/\pi)^{1/3}$ of the order of 1 mm rising steadily in water, and the rise velocity is about 25 cm/s (Spelt and Biesheuvel, 1997). This corresponds to a characteristic Reynolds number for bubble motion $Re_\mathrm{b} = \mathcal{O}(10^2)$, where Re_b is defined, as usual, as the ratio of inertial forces F_I to viscous forces F_μ (see Table 3.1):

$$Re_\mathrm{b} \equiv \frac{F_\mathrm{I}}{F_\mu} = \frac{\rho_1 d_\mathrm{e} |\mathbf{v} - \tilde{\mathbf{u}}_{\mathbf{x}_\mathrm{b}}|}{\mu_1} \tag{6.1}$$

Here, $\mathbf{v}(t)$ is the bubble velocity and $\tilde{\mathbf{u}}_{\mathbf{x}_\mathrm{b}} = \tilde{\mathbf{u}}\{\mathbf{x}_\mathrm{b}(t), t\}$ is the undisturbed liquid velocity at the position of the bubble centre $\mathbf{x}_\mathrm{b}(t)$. Such small bubbles rise along a rectilinear path in otherwise motionless fluid. Very large bubbles also rise rectilinear, however they take a spherical cap shape (Wörner, 2003). Both in the spherical and spherical cap regimes, the rise velocity increases with diameter rather independent of the purity of the system (see Fig. 6.1(b)).

In the present study, we are interested in bubbles of diameter about $1 - 10$ mm, where bubbles generally take an ellipsoidal form and $Re_\mathrm{b} = \mathcal{O}(10^2 - 10^3)$. As apparent from Fig. 6.1(b), the motion of bubbles in this intermediate regime is complex and the dependence on the purity of the system is significant. When the system is contaminated, there is a monotonic increase of the terminal velocity with diameter and the motion is rectilinear. When the system is pure, the terminal velocity initially increases with

diameter until reaching a local maximum, then decreases until a local minimum, and finally increases again. For diameters smaller than the value at the local maximum, the bubble has a stable ellipsoidal shape moving rectilinear. For larger diameters, the bubble shape is still stable, but wake instabilities inducing oscillations in the bubble path result in a zigzag or helical path. This, in turn, causes a decrease in the vertical component of the bubble velocity. At even larger diameters, oscillations start both in bubble shape (i.e. wobbling) and the path (Wörner, 2003).

For freely rising bubbles (or freely falling drops) in infinite media, the bubble shape regimes can generally be correlated graphically, such as the well-known one given by Clift et al. (1978). In addition to the Reynolds number, two more dimensionless numbers are used to construct such correlations, namely the Eötvös number Eo,

$$Eo \equiv \frac{F_\mathrm{B}}{F_\sigma} = \frac{g|\Delta\rho|d_\mathrm{e}^2}{\sigma}, \tag{6.2}$$

where $|\Delta\rho| = |\rho_2 - \rho_1|$. It is the ratio of buoyancy forces F_B to surface tension forces F_σ (see Table 3.1). The other one is the Morton number Mo,

$$Mo \equiv \frac{F_\mathrm{B} F_\mu^4}{F_\mathrm{I}^2 F_\sigma^3} = \frac{g|\Delta\rho|\mu_1^4}{\rho_1^2\sigma^3}, \tag{6.3}$$

which depends only on the material properties, hence has a constant value for a given isothermal incompressible two-phase system. For air bubbles in water, $Mo = 2.5 \times 10^{-11}$.

The graphical correlation of Clift et al. (1978) reveals that bubbles and drops in the intermediate size range, $d_\mathrm{e} = 1 - 15$ mm, are in most practical systems ellipsoidal (except the ones in systems of high Morton number, which are never ellipsoidal). At larger diameters, about $d_\mathrm{e} > 18$ mm, other regimes such as spherical-cap or ellipsoidal-cap are encountered, provided that $Eo > 40$ and $Re > 1.2$.

6.2 Equation of motion for an isolated bubble

Generally, several effects play a role in the motion of a bubble in a continuous fluid, namely the viscous effects, the flow homogeneity and the flow steadiness. Writing the force $\mathbf{f}_\mathrm{b}$ exerted on a single isolated bubble of volume $\mathcal{V}_\mathrm{b}$, moving at velocity $\mathbf{v}(t)$ in a fluid with unsteady nonuniform velocity field $\tilde{\mathbf{u}}(\mathbf{x}, t)$, and applying Newton's second law gives the equation of motion of the bubble:

$$(\rho_2 \mathcal{V}_\mathrm{b}) \frac{d\mathbf{v}}{dt} = \mathbf{f}_\mathrm{b}. \tag{6.4}$$

The total force on the bubble can be written as the sum of the surface and body forces acting on it:

$$\mathbf{f}_\mathrm{b} = \mathbf{f}_{\mathcal{A}_\mathrm{b}} + \mathbf{f}_{\mathcal{V}_\mathrm{b}}. \tag{6.5}$$

Relevant body forces, such as the gravitational force $\mathbf{f}_\mathrm{g} = \rho_2 \mathcal{V}_\mathrm{b} \mathbf{g}$, can be included in $\mathbf{f}_{\mathcal{V}_\mathrm{b}}$. In principle, $\mathbf{f}_{\mathcal{A}_\mathrm{b}}$ is given by the surface integral of the stress tensor over the bubble surface $\mathcal{A}_\mathrm{b}$, i.e. for incompressible Newtonian fluids

$$\mathbf{f}_{\mathcal{A}_\mathrm{b}} = \oint_{\mathcal{A}_\mathrm{b}} \underline{\underline{\boldsymbol{\sigma}}}_1 \cdot \mathbf{n}_2 \, dS = \oint_{\mathcal{A}_\mathrm{b}} (-p_1 \underline{\underline{\mathbf{I}}} + 2\mu_1 \underline{\underline{\mathbf{s}}}_1) \cdot \mathbf{n}_2 \, dS. \tag{6.6}$$

Following Wörner (2003), the pressure p_1 can further be decomposed into its static and dynamic components to give three contributions:

$$p_1 = \rho_1 \mathbf{g} \cdot \mathbf{x} + P_{\mathrm{pg,e}} \mathbf{e}_{\mathrm{pg,e}} \cdot \mathbf{x} + p_{1,\mathrm{dyn}}, \tag{6.7}$$

corresponding to the hydrostatic pressure, external constant pressure gradient ($\mathbf{e}_{\mathrm{pg,e}}$ being the unit vector in the direction of this gradient) and dynamic pressure, respectively. Hence, the total surface force is distributed in the form $\mathbf{f}_{\mathcal{A}_\mathrm{b}} = \mathbf{f}_\mathrm{hp} + \mathbf{f}_{\mathrm{pg,e}} + \mathbf{f}_{\mathcal{A}_\mathrm{b},\mathrm{dyn}}$. Substituting Eq. 6.7 into Eq. 6.6, the relation for the total surface force can be obtained. The Gauß divergence theorem is employed for the part $\mathbf{f}_\mathrm{hp} + \mathbf{f}_{\mathrm{pg,e}}$:

$$\begin{aligned}
&- \oint_{\mathcal{A}_\mathrm{b}} (\rho_1 \mathbf{g} \cdot \mathbf{x} + P_{\mathrm{pg,e}} \mathbf{e}_{\mathrm{pg,e}} \cdot \mathbf{x}) \cdot \mathbf{n}_2 dS = - \int_{\mathcal{V}_\mathrm{b}} \nabla (\rho_1 \mathbf{g} \cdot \mathbf{x} + P_{\mathrm{pg,e}} \mathbf{e}_{\mathrm{pg,e}} \cdot \mathbf{x})\, dV, \\
&= - \int_{\mathcal{V}_\mathrm{b}} \left[\underbrace{\nabla (\rho_1 \mathbf{g} + P_{\mathrm{pg,e}} \mathbf{e}_{\mathrm{pg,e}})}_{=0 \cdot \underline{\underline{\mathbf{I}}}} \cdot \mathbf{x} + \underbrace{\nabla \mathbf{x}}_{=\underline{\underline{\mathbf{I}}}} \cdot (\rho_1 \mathbf{g} + P_{\mathrm{pg,e}} \mathbf{e}_{\mathrm{pg,e}}) \right] dV, \\
&= -\mathcal{V}_\mathrm{b} (\rho_1 \mathbf{g} + P_{\mathrm{pg,e}} \mathbf{e}_{\mathrm{pg,e}}).
\end{aligned} \tag{6.8}$$

If we include also the gravitational body force, we obtain the following expression for the resultant surface and body forces acting on the bubble:

$$\mathbf{f}_\mathrm{b} = -(\rho_1 - \rho_2) \mathcal{V}_\mathrm{b} \mathbf{g} - \mathcal{V}_\mathrm{b} P_{\mathrm{pg,e}} \mathbf{e}_{\mathrm{pg,e}} + \underbrace{\oint_{\mathcal{A}_\mathrm{b}} (-p_{1,\mathrm{dyn}} \underline{\underline{\mathbf{I}}} + 2\mu_1 \underline{\underline{\mathbf{s}}}_1) \cdot \mathbf{n}_2 \, dS}_{\mathbf{f}_{\mathcal{A}_\mathrm{b},\mathrm{dyn}}}. \tag{6.9}$$

The integral above involving the dynamic pressure and viscous terms represents the hydrodynamic force $\mathbf{f}_{\mathcal{A}_\mathrm{b},\mathrm{dyn}}$, which can have components parallel and perpendicular to the relative velocity vector of the bubble such as drag, added mass, lift and history forces. It can be solved analytically only for special cases such as for a rigid sphere moving with constant velocity at very low Reynolds number (creeping flow) in an otherwise stagnant viscous fluid. Stokes (1871) proposed first a solution for this simplified case, which was later extended by Basset to transient flow (see e.g. Wörner (2003)).

Generally, $\mathbf{f}_{\mathcal{A}_\mathrm{b},\mathrm{dyn}} = f\{\mathbf{v}(t), \tilde{\mathbf{u}}_{\mathbf{x}_\mathrm{b}}\}$, that is, it is a nonlinear function of liquid and bubble velocities. When the bubble size is of the order 1 mm or larger, Stokes' law is not valid and no general expression exists for $\mathbf{f}_{\mathcal{A}_\mathrm{b},\mathrm{dyn}}$ (Spelt and Biesheuvel, 1997; Magnaudet and Legendre, 1997; Chahed et al., 2003). There are several proposals in literature, resulting from theoretical or numerical calculations under restricted idealised flow conditions.

6.2.1 Inviscid flow

One idealised flow condition is that the carrier fluid is sufficiently clean (i.e. the bubble surface has approximately the zero-shear condition) and the ratio of inertial forces to viscous forces, $F_\mathrm{I}/F_\mu = Re$, is large enough. In such cases, the boundary layer vorticity is smaller on a bubble and confined to a thin wake region, compared to a solid particle moving at the same Reynolds number (Magnaudet and Eames, 2000). Therefore, the inviscid flow theory can provide a useful basis for describing the flow

outside the boundary layer. In such a case, the resulting surface force on a body arises only from the pressure distribution over the surface, hence Eq. 6.6 reduces to

$$\mathbf{f}_{\mathcal{A}_\mathrm{b}} = \oint_{\mathcal{A}_\mathrm{b}} -p_1 \underline{\underline{\mathbf{I}}} \cdot \mathbf{n}_2 \, dS. \tag{6.10}$$

Auton et al. (1988) derived an approximate relation for the forces exerted on a single rigid sphere rising in an unsteady, inviscid, uniform straining flow, which is rotational and three-dimensional. It was assumed that (i) the change of the velocity over the sphere radius is small compared to the relative velocity (weak strain), i.e. $r_\mathrm{b}\|\nabla\tilde{\mathbf{u}}\| \ll |\mathbf{v}-\tilde{\mathbf{u}}_{\mathbf{x}_\mathrm{b}}|$; (ii) the length scale of changes in the fluid velocity gradient is large compared to the sphere radius (locally homogenous strain), i.e. $\|\nabla\tilde{\mathbf{u}}\| \gg r_\mathrm{b}\|\nabla(\nabla\tilde{\mathbf{u}})\|$; and (iii) the time scale of the change in the relative velocity is large compared with the time it takes for a fluid element to pass around the sphere volume, i.e. $|\partial(\mathbf{v}-\tilde{\mathbf{u}}_{\mathbf{x}_\mathrm{b}})/\partial t| \ll |\mathbf{v}-\tilde{\mathbf{u}}_{\mathbf{x}_\mathrm{b}}|^2/r_\mathrm{b}$ (Auton et al., 1988; Lathouwers, 1999). The expression derived for the $\mathbf{f}_\mathrm{b}$ reads

$$\mathbf{f}_\mathrm{b} = \rho_1 \mathcal{V}_\mathrm{b}\left[\frac{\mathcal{D}_1\tilde{\mathbf{u}}_{\mathbf{x}_\mathrm{b}}}{\mathcal{D}t} - C_\mathrm{A}\left(\frac{d\mathbf{v}}{dt} - \frac{\mathcal{D}_1\tilde{\mathbf{u}}_{\mathbf{x}_\mathrm{b}}}{\mathcal{D}t}\right) - C_\mathrm{L}(\mathbf{v}-\tilde{\mathbf{u}}_{\mathbf{x}_\mathrm{b}})\times\boldsymbol{\omega}\right] - (\rho_1-\rho_2)\mathcal{V}_\mathrm{b}\mathbf{g}, \tag{6.11}$$

where $\mathcal{D}_k/\mathcal{D}t$ denotes the derivative following an element of phase k:

$$\begin{aligned}\frac{\mathcal{D}_k}{\mathcal{D}t} &\equiv \frac{\partial}{\partial t} + u_{k,x}\frac{\partial}{\partial x} + u_{k,y}\frac{\partial}{\partial y} + u_{k,z}\frac{\partial}{\partial z} \\ &= \frac{\partial}{\partial t} + \mathbf{u}_k \cdot \nabla.\end{aligned} \tag{6.12}$$

Hence, $\mathcal{D}_1\tilde{\mathbf{u}}_{\mathbf{x}_\mathrm{b}}/\mathcal{D}t$ is the change of liquid velocity at the bubble position, as seen by a liquid element in the absence of the bubble (i.e. liquid acceleration at the location of the bubble's centre):

$$\frac{\mathcal{D}_1\tilde{\mathbf{u}}_{\mathbf{x}_\mathrm{b}}}{\mathcal{D}t} = \left.\frac{\mathcal{D}_1\tilde{\mathbf{u}}}{\mathcal{D}t}\right|_{\mathbf{x}=\mathbf{x}_\mathrm{b}} = \left[\frac{\partial\tilde{\mathbf{u}}}{\partial t} + (\tilde{\mathbf{u}}\cdot\nabla)\tilde{\mathbf{u}}\{\mathbf{x},t\}\right]_{\mathbf{x}=\mathbf{x}_\mathrm{b}}. \tag{6.13}$$

As discussed by Maxey and Riley (1983) and Auton et al. (1988), there had been errors and controversy in the definition of the correct acceleration for the liquid, which allows for the spatial variations in $\tilde{\mathbf{u}}$ and the particle motion. In Eq. 6.11, the vorticity of the liquid is given by $\boldsymbol{\omega} = \nabla\times\tilde{\mathbf{u}}_{\mathbf{x}_\mathrm{b}}$.

Pressure gradient force $\mathbf{f}_\mathrm{pg}$

The first term on the r.h.s. in Eq. 6.11 represents the inertial force experienced by a liquid of volume $\mathcal{V}_\mathrm{b}$ due to its acceleration:

$$\mathbf{f}_\mathrm{pg} = \rho_1\mathcal{V}_\mathrm{b}\left(\frac{\mathcal{D}_1\tilde{\mathbf{u}}_{\mathbf{x}_\mathrm{b}}}{\mathcal{D}t}\right), \tag{6.14}$$

and is independent of the presence of the bubble. Batchelor (1967) gives an explanation to this contribution as follows. Suppose that the liquid surrounding the bubble has an uniform acceleration of $\mathbf{a}_1$ relative to an inertial reference frame. One can then choose

moving axes such that the far-field liquid velocity (or, equivalently, the liquid velocity in the absence of the bubble) is zero and remains so. Consequently, the equation of motion relative to such accelerating axes should include a fictitious uniform body force $-\mathbf{a}_1$ per unit mass. Therefore, an additional contribution arises both to the pressure, i.e. $-\rho_1 \mathbf{a}_1 \cdot \mathbf{x}$, and to the total force experienced by the bubble, i.e. $\rho_1 \mathcal{V}_\mathrm{b} \mathbf{a}_1$. The latter one is an effective "buoyancy" force, analogous to the force due to the action of gravity on the liquid.

Note that, $\tilde{\mathbf{u}}\{\mathbf{x}(t), t\}$ satisfies the Euler equation for an inviscid fluid, hence the ambient fluid acceleration can be written as

$$\frac{\mathcal{D}_1 \tilde{\mathbf{u}}_{\mathbf{x}_\mathrm{b}}}{\mathcal{D}t} = -\left(\frac{1}{\rho_1}\right) \nabla p_{1,\mathrm{dyn}}. \tag{6.15}$$

Here, gravity does not appear in the equation, because the dynamic pressure $p_{1,\mathrm{dyn}}$ arises fully from the effect of the liquid motion unlike the static pressure component giving rise to the buoyancy term in Eq. 6.8. Now, Eq. 6.14 can also be expressed as the force on the bubble because of the ambient dynamic pressure gradient:

$$\mathbf{f}_\mathrm{pg} = -\mathcal{V}_\mathrm{b} \nabla p_{1,\mathrm{dyn}}. \tag{6.16}$$

This force acts in the opposite direction to the pressure gradient and tends to move the bubble toward the regions of low pressure, such as the centre of vortices.

Substituting the definition of the liquid material derivative $\mathcal{D}_1 \tilde{\mathbf{u}}_{\mathbf{x}_\mathrm{b}}/\mathcal{D}t$ in Eq. 6.13 into Eq. 6.14 shows that this inertial force has a steady and an unsteady component, corresponding to spatial and temporal accelerations, respectively. At uniform but time-dependent flows,

$$\mathbf{f}_\mathrm{pg} = \rho_1 \mathcal{V}_\mathrm{b} \left(\frac{\partial \tilde{\mathbf{u}}_{\mathbf{x}_\mathrm{b}}}{\partial t}\right). \tag{6.17}$$

When the flow is steady but nonuniform,

$$\mathbf{f}_\mathrm{pg} = \rho_1 \mathcal{V}_\mathrm{b} [(\tilde{\mathbf{u}}_{\mathbf{x}_\mathrm{b}} \cdot \nabla) \tilde{\mathbf{u}}_{\mathbf{x}_\mathrm{b}}]. \tag{6.18}$$

Added mass force $\mathbf{f}_\mathrm{A}$

The second term, the added mass (or virtual mass[1]) force, originates from the fact that the bubble, when in relative acceleration with respect to the liquid, feels the inertia of the liquid it accelerates by its motion:

$$\mathbf{f}_\mathrm{A} = -\rho_1 \mathcal{V}_\mathrm{b} C_\mathrm{A} \left(\frac{d\mathbf{v}}{dt} - \frac{\mathcal{D}_1 \tilde{\mathbf{u}}_{\mathbf{x}_\mathrm{b}}}{\mathcal{D}t}\right). \tag{6.19}$$

Darwin (1953) proposed that this volume of liquid being accelerated, which is associated with the added mass, is essentially equal to the "drift volume", i.e. the volume of liquid displaced forward by the motion of the bubble. He made an inviscid analyses of a solid body moving uniformly in an infinite irrotational fluid and passing through an infinite

[1] Note the difference between the virtual and added mass of a body, as pointed out by Geurst (1985). The virtual mass, being the sum of the added mass and the actual mass of the body, is practically equal to the added mass for the case of air bubbles in water.

plane of marked fluid perpendicular to the motion. The body is initially infinitely far upstream of the marked plane and is finally infinitely far downstream. He found an unexpected result that after the passage of the body, the marked fluid particles are actually drifted forward, rather than backward, with respect to their initial position, the volume enclosed between the initial and final positions being defined as the drift volume. This volume transported forward (drift volume) amounts to $\mathcal{V}_{\mathrm{D_f}} = C_{\mathrm{A}}\mathcal{V}_{\mathrm{b}}$, where the added mass coefficient C_{A} can be seen geometrically as a measure of the bluffness of the body, assuming a higher value as the bubble becomes more oblate, hence displaces forward a larger volume of fluid. In bounded flows, in addition to $\mathcal{V}_{\mathrm{D_f}}$, there is also a negative displacement (or reflux) required by continuity, which spreads uniformly across the bounded flow (Magnaudet and Eames, 2000).

For a sphere, $C_{\mathrm{A}} = 1/2$. Lamb (1932) derived approximately $C_{\mathrm{A}} = 2$ for ellipsoidal bubbles moving along helical paths (Lathouwers, 1999). For bubbles of effective diameter 2.5–5.5 mm, $\mathcal{V}_{\mathrm{D_f}}$ was observed to increase from $0.5\mathcal{V}_{\mathrm{b}}$ (the value for irrotational flow past sphere) to $3.0\mathcal{V}_{\mathrm{b}}$, as the Reynolds number increased from 500 to 1300 (Magnaudet and Eames, 2000).

For air bubbles in water, the added mass force has an important effect on the bubble dynamics, as its magnitude is $\mathcal{O}(\rho_1/\rho_2) \approx 10^3$ times larger than the rate of change of the bubble momentum. Note that, even in the absence of a relative acceleration, a bubble may experience an added mass force due to sudden expansion or compression, i.e. due to change in the bubble size. A similar effect arises if C_{A} varies with time or if the continuous fluid is compressible. In such cases, the fluid impulse, $\rho_1\mathcal{V}_{\mathrm{b}}C_{\mathrm{A}}(\mathbf{v}-\tilde{\mathbf{u}}_{\mathbf{x}_{\mathrm{b}}})$, should be contained within the time derivative.

By substituting the definition of $\mathcal{D}_1\tilde{\mathbf{u}}_{\mathbf{x}_{\mathrm{b}}}/\mathcal{D}t$, the added mass force can also be decomposed into a time-dependent and a steady part similar to the inertial pressure gradient force given above. That is, for uniform but time-dependent flows, temporal accelerations give rise to

$$\mathbf{f}_{\mathrm{A}} = -\rho_1\mathcal{V}_{\mathrm{b}}C_{\mathrm{A}}\left(\frac{d\mathbf{v}}{dt} - \frac{\partial\tilde{\mathbf{u}}_{\mathbf{x}_{\mathrm{b}}}}{\partial t}\right). \tag{6.20}$$

When the flow is steady but nonuniform undergoing spatial acceleration,

$$\mathbf{f}_{\mathrm{A}} = \rho_1\mathcal{V}_{\mathrm{b}}C_{\mathrm{A}}[(\tilde{\mathbf{u}}_{\mathbf{x}_{\mathrm{b}}}\cdot\nabla)\tilde{\mathbf{u}}_{\mathbf{x}_{\mathrm{b}}}]. \tag{6.21}$$

Finally, an interesting effect of the added mass force on bubbles (i.e. for the case of $\rho_2 \ll \rho_1$) can be obtained from Eq. 6.11. Consider a spherical bubble of negligible mass, which moves from rest under the action of gravity through a liquid (which is set in irrotational motion and is at rest at infinity). The initial acceleration of such a bubble is $-2\mathbf{g}$. For a clean bubble, this initial acceleration remains until either the bubble starts to be deformed or the velocity becomes comparable with the terminal velocity.

Lift force $\mathbf{f}_{\mathrm{L}}$

The third term in Eq. 6.11 arises from the rotational part of the flow due to the interaction between the vorticity and the relative velocity, and is called as the lift force. When a rigid body moves through a sheared flow, vorticity is generated parallel

to the direction of motion. This appears as an attached horseshoe vortex that induces a downtrust on the surrounding fluid, hence a corresponding lift force acts on the body (Magnaudet and Eames, 2000), which is given as

$$\mathbf{f}_{\mathrm{L}} = -\rho_1 \mathcal{V}_{\mathrm{b}} C_{\mathrm{L}} (\mathbf{v} - \tilde{\mathbf{u}}_{\mathbf{x}_{\mathrm{b}}}) \times \nabla \times \tilde{\mathbf{u}}_{\mathbf{x}_{\mathrm{b}}}. \tag{6.22}$$

The lift coefficient is given in terms of combined effects of inertially and rotationally induced forces, i.e. $C_{\mathrm{L}} = \frac{1}{2}(1 + C_{\mathrm{A}}) + C_{\mathrm{L}\Omega}$, where $C_{\mathrm{L}\Omega}$ is the rotational lift coefficient. For a sphere, $C_{\mathrm{L}\Omega} = -1/4$ and $C_{\mathrm{L}} = 1/2$ (Auton, 1987; Auton et al., 1988). For bodies axisymmetric about the relative velocity vector, $C_{\mathrm{L}} = C_{\mathrm{A}}$, provided that the vorticity is weak and the flow is steady (Magnaudet and Eames, 2000).

Hydrostatic pressure force $\mathbf{f}_{\mathrm{hp}}$ and gravitational force $\mathbf{f}_{\mathrm{g}}$

Finally, the hydrostatic pressure (buoyancy) and gravitational force contribution, i.e. the net buoyancy force, is given by the last term:

$$\mathbf{f}_{\mathrm{hp}} + \mathbf{f}_{\mathrm{g}} = -(\rho_1 - \rho_2)\mathcal{V}_{\mathrm{b}}\mathbf{g}. \tag{6.23}$$

Validity of inviscid solution

In practice, the inviscid assumption is questionable even when the Reynolds number is high, because small amounts of impurities can immobilise the bubble surface, hence the viscous effects become important. This is arguably because the contaminants tend to accumulate at the interface and are swept to the rear as the bubble rises. This results in a surface tension gradient (low at the rear, high at the front), which in turn causes a tangential stress acting against the surface motion. This so-called Marangoni effect is more pronounced for small bubbles (Batchelor, 1967; Clift et al., 1978).

However, experimental evidence and numerical simulations show that the above given inviscid results can still be generalised to real flows with finite Reynolds number, at least for the case of added mass force (Magnaudet and Eames, 2000). These results show that the added mass coefficient is not effected by viscous effects and still attain the inviscid value, $C_{\mathrm{A}} = 0.5$ for the case of sphere, which can be extended to nonspherical bodies. It is independent of Reynolds number, strength of acceleration, and also of the boundary condition (no-slip or zero-shear) imposed on the sphere surface.

6.2.2 Viscous effects

Stationary drag force $\mathbf{f}_{\mathrm{D}}$

The most important contribution to the hydrodynamic force $\mathbf{f}_{\mathcal{A}_{\mathrm{b}},\mathrm{dyn}}$ is the steady-state drag force. It is a resisting force experienced by a particle moving steadily through the surrounding fluid and acts in the opposite direction to the particle relative velocity.

From general momentum arguments, this resisting force can be related to the inward flow rate of liquid volume in the wake of a bubble (Batchelor, 1967). Here, the term

"wake" refers to the region of non-zero vorticity downstream to a bubble in an otherwise uniform stream of fluid. For a solid particle, vorticity is generated as a result of a non-zero jump in velocity (due to no-slip condition) at the boundary of a region of irrotational flow, and it is initially infinite. For a bubble, vorticity is generated as a result of a non-zero jump in velocity derivatives (due to zero tangential stress condition) and it is finite. This vorticity generated on the bubble surface is convected downstream and diffused by viscosity (apart from being changed due to local distortion and rotation of the liquid). Far downstream to the bubble, direct effect of the presence of bubble disappears and the departure from the free-stream velocity, U, is small due to the action of frictional forces to make the velocity uniform. At this asymptotic region, Batchelor (1967) analysed the steady wake of a body on which only the drag force acts. The deficit of velocity, $U - u$, in the wake region is equivalent to the superposition of 'inflow' towards the bubble on the uniform fluid stream. Integrating this deficit over the wake cross-section gives the volumetric flow rate of this inflow, Q_b. This is related to the steady drag force through the relation that holds for any non-lifting body at any Reynolds number, provided that it moves steadily with a wake whose width increases less rapidly than its length (Batchelor, 1967; Magnaudet and Eames, 2000):

$$\mathbf{f}_\mathrm{D} = -\rho_1 Q_\mathrm{b}(\mathbf{v} - \tilde{\mathbf{u}}_{\mathbf{x}_\mathrm{b}}). \tag{6.24}$$

Due to conservation of mass, this inflow in the wake must be compensated by the same amount of flow away from the bubble in the irrotational flow region outside the wake, which acts as a source-like contribution of strength Q_b.

Eq. 6.9 shows that both the pressure field and the viscous stresses contribute to the resisting force on a bubble. For a bubble moving steadily through liquid, the tangential stress integrated over the bubble surface gives rise to the so-called viscous (friction) drag. The normal stress at the bubble surface induces several forces (such as lift and lift induced drag). The force due to the component of the net pressure force parallel and in opposite direction to the relative velocity of the bubble is called as the pressure (form) drag. In the limit of infinite Reynolds number for a streamlined or slender body (where no boundary layer separation occurs) in irrotational flow, the boundary layer and the bubble wake have zero thickness, hence the pressure drag is zero, corresponding to the value for fully irrotational flow (Batchelor, 1967). For bluff bodies such as spheres at not too small Re_b , the boundary layer is no longer attached to the whole surface, because there is a large fall in the stream speed over the rear part of the body. This avoids the development of a steady state boundary layer. At this rear region enclosed by the separated boundary layer, the presure is low with respect to the high pressure zone at the front stagnation point. Therefore, although the viscous drag is about the same per unit surface as that for a slender body, the pressure drag is greater by a large factor. The order of magnitude of this pressure drag is expected to be $\frac{1}{2}\rho_1|\mathbf{v} - \tilde{\mathbf{u}}_{\mathbf{x}_\mathrm{b}}|^2$ (which is the overpressure at the front stagnation point with respect to that in the absence of the body) times the frontal area of the body, because the pressure variations around the body surface can be related to the velocity variations via Bernouilli's theorem, at least over the front part, where the streamlines do not separate (Batchelor, 1967). Following the same argument, the drag coefficient is usually defined in terms of this pressure force (see Eq.6.26).

No general theory is available for determining the drag force, except for two idealised cases (Magnaudet and Eames, 2000): (i) at very low Reynolds numbers ($Re_\mathrm{b} < 1$), i.e.

in the creeping flow limit; (ii) at high Re_b for the case of steadily moving spherical bubbles with uncontaminated surfaces, where the bubble surface can be described by a zero-shear-stress boundary condition. The drag force can then be determined from a balance between the rate of work done by the drag force, $\mathbf{f}_\mathrm{D} \cdot (\mathbf{v} - \tilde{\mathbf{u}}_{\mathbf{x}_\mathrm{b}})$, and the rate of total viscous dissipation in the liquid. For most practical cases, however, these conditions are not met. Therefore, an empirical expression is usually employed and the definition of the drag coefficient C_D, i.e. the ratio of drag force to dynamic pressure force (or inertial force), is used to correlate experimental results:

$$\mathbf{f}_\mathrm{D} = -\frac{1}{2}\rho_1 \mathcal{A}_{\mathrm{b},\perp} C_\mathrm{D} |\mathbf{v} - \tilde{\mathbf{u}}_{\mathbf{x}_\mathrm{b}}| (\mathbf{v} - \tilde{\mathbf{u}}_{\mathbf{x}_\mathrm{b}}), \tag{6.25}$$

with

$$C_\mathrm{D} \equiv \frac{|\mathbf{f}_\mathrm{D}|}{\frac{1}{2}\rho_1 \mathcal{A}_{\mathrm{b},\perp} |\mathbf{v} - \tilde{\mathbf{u}}_{\mathbf{x}_\mathrm{b}}|^2}, \tag{6.26}$$

where $\mathcal{A}_{\mathrm{b},\perp}$ is the projected area of the bubble on to a plane normal to the relative velocity, $\mathbf{v}_\mathrm{r} = \mathbf{v} - \tilde{\mathbf{u}}_{\mathbf{x}_\mathrm{b}}$. When translating single-bubble results to the averaged interfacial momentum transfer term $\mathbf{M}'_k$, the concept of volume equivalent diameter d_e (i.e. the diameter of a sphere of the same volume as the bubble),

$$d_\mathrm{e} \equiv \left(\frac{6\mathcal{V}_\mathrm{b}}{\pi}\right)^{1/3}, \tag{6.27}$$

is usually used assuming that the gas phase is fully dispersed in the entire domain and is monodisperse (either locally or globally). The projected area is commonly based on d_e (which is usually what is measured experimentally), i.e. $\mathcal{A}_{\mathrm{b},\perp} = \pi d_\mathrm{e}^2/4$, which is not strictly equal to the actual projected area. Note that C_D should then be defined in terms of d_e. In Section 6.7, various models for the calculation of C_D are given in detail.

History force $\mathbf{f}_\mathrm{H}$

For unsteady motions, there is an additional viscous effect, the so-called history (or Basset) force. It represents the effect of acceleration on the viscous drag and the boundary layer and wake development, which depends on the entire acceleration history. For a sphere, it is written as

$$\mathbf{f}_\mathrm{H} = \frac{3}{2} d_\mathrm{b}^2 \sqrt{\pi \mu_1 \rho_1} \int_{-\infty}^{t} \left[\frac{d(\tilde{\mathbf{u}}_{\mathbf{x}_\mathrm{b}} - \mathbf{v})}{dt}\right]_{t=\tau} \frac{d\tau}{\sqrt{t-\tau}}. \tag{6.28}$$

Here, the history integral includes the past acceleration weighted as $(t-\tau)^{-1/2}$, where $(t-\tau)$ is the time elapsed since the past acceleration. The form of the history integral arises from diffusion of vorticity from the particle (Clift et al., 1978). Due to its complicated time-integral form, this force is usually not taken into account in practical analyses. According to Merle et al. (2005), memory of the flow is much shorter for a clean bubble than a for a solid sphere due to slip at the bubble surface and the history force can be neglected relative to the quasi-steady drag, as long as the relative acceleration $|\partial(\mathbf{v} - \tilde{\mathbf{u}}_{\mathbf{x}_\mathrm{b}})/\partial t|$ is not large compared to $|\mathbf{v} - \tilde{\mathbf{u}}_{\mathbf{x}_\mathrm{b}}|^2/d_\mathrm{b}$. This force is also neglected in the two-fluid model implementation of Fluent.

Viscous effects on lift

In the limit of inviscid flow, the lift force as calculated by Auton is given in Eq. 6.22. In the creeping flow limit, there is no sideway force acting on a single rigid sphere, whatever the velocity profile is, provided that the flow is unidirectional (Saffman, 1965). However, in the intermediate regions, the situation is rather complicated and less known. Numerical investigations of a clean spherical bubble for intermediate Reynolds numbers show that, for $Re_\mathrm{b} \leq 5$, the lift coefficient is governed by the inertial effects due to vorticity generation at the bubble surface inducing disturbance in the far-field, rather than the vorticity of the undisturbed flow. C_L depends strongly on the shear and decreases sharply with increasing Re_b (Magnaudet and Eames, 2000). For the same range, Saffman (1965) calculated the lift force for the case of a solid sphere moving relative to a very viscous fluid with uniform simple shear.

For $Re_\mathrm{b} \geq 5$, C_L was found to be a weakly increasing function of Re_b and independent of the flow shear for weak–to–moderate shears. For $Re_\mathrm{b} > 50$, the lift force is mainly due to pressure variation at the surface and the inviscid value $C_\mathrm{L} = 0.5$ is almost fully reached already at $Re_\mathrm{b} = 500$. In this range, the vorticity of undisturbed flow and the stretching/tilting of it due to velocity gradients induced by the presence of the bubble are the dominant mechanisms producing the lift. This is substantially different from solid spheres in the same range, where the lift is due to asymmetries of the boundary layer and of the separated wake (Magnaudet and Eames, 2000). Moreover, solid particles rotate in sheared flow due to the torque applied on them. This is not possible for clean spherical bubbles.

Experimental evidence shows that surface contamination has a very significant effect on the lift. About an order of magnitude increase in C_L was found with respect to the inviscid value suggesting that the mechanisms involved are very different than that for clean bubbles (Magnaudet and Eames, 2000).

Experiments including also deformed bubbles reveal that small spherical bubbles tend to move towards the pipe wall, which is well expressed by the shear-induced lift expression given in Eq. 6.22. However, large deformed bubbles move towards the centre due to the slanted wake behind a bubble (Tomiyama, 1998; Ishii and Hibiki, 2006). This shows the complex interaction between a bubble wake and a shear field. Tomiyama et al. (2002), by measuring the trajectories of single air bubbles in simple shear flows, proposed an empirical correlation for the net lift coefficient accounting both for the shear and wake induced effects.

6.3 A general equation of motion

For the general case of a bubble in transient motion in a nonuniform flow field, $\mathbf{f}_\mathrm{b}$ cannot be calculated analytically. Hence, for practical purposes, the common approach is to use empirical expressions for the relevant forces and combine them linearly. The

resultant force is written in the form $\mathbf{f}_\mathrm{b} = \mathbf{f}_\mathrm{D} + \mathbf{f}_\mathrm{A} + \mathbf{f}_\mathrm{L} + \mathbf{f}_\mathrm{pg} + \mathbf{f}_\mathrm{hp} + \mathbf{f}_\mathrm{g}$:

$$\begin{aligned}\mathbf{f}_\mathrm{b} = &-\frac{1}{2}\rho_1 \mathcal{A}_{\mathrm{b},\perp} C_\mathrm{D} |\mathbf{v} - \tilde{\mathbf{u}}_{\mathbf{x}_\mathrm{b}}| (\mathbf{v} - \tilde{\mathbf{u}}_{\mathbf{x}_\mathrm{b}}) - \rho_1 \mathcal{V}_\mathrm{b} C_\mathrm{A} \left(\frac{d\mathbf{v}}{dt} - \frac{\mathcal{D}_1 \tilde{\mathbf{u}}_{\mathbf{x}_\mathrm{b}}}{\mathcal{D}t} \right) \\ &- \rho_1 \mathcal{V}_\mathrm{b} C_\mathrm{L} (\mathbf{v} - \tilde{\mathbf{u}}_{\mathbf{x}_\mathrm{b}}) \times \boldsymbol{\omega} - \mathcal{V}_\mathrm{b} \nabla p_{1,\mathrm{dyn}} - (\rho_1 - \rho_2) \mathcal{V}_\mathrm{b} \mathbf{g}. \end{aligned} \tag{6.29}$$

This linearty is probably justified for slightly non-homogenous flows (Lathouwers, 1999). Moreover, at high finite Reynolds numbers, the distinction between the viscous history effects and the purely inertial added mass effects become rather vague, because of the coupling between various mechanisms. This is not the case in the Stokes regime, where due to linearity of the equation of motion, quasi-steady drag, added mass and history forces can be clearly identified (Magnaudet and Eames, 2000).

Note that for an air–water system, the bubble inertia can be neglected against the liquid inertia (i.e. $\rho_2 \ll \rho_1,\ \rho_2 \approx 0$), hence $\mathbf{f}_\mathrm{g}$ in the last term of Eq. 6.29 and the l.h.s. of Eq. 6.4 vanish, resulting in $\mathbf{f}_\mathrm{b} = 0$ in the above equation.

6.4 Rise of a bubble in a swarm

So far, we considered only the simple case that the bubble is isolated and its motion is not influenced by the presence of other bubbles. In practice, this can be taken as an approximation to the motion of a bubble in dilute dispersed flows. Most industrial applications, however, involves considerable amount of volumetric concentration of the dispersed phase, hence the flow is much more complex.

The motion of a bubble in a swarm is influenced by the surrounding flow field disturbed by the relative motion of other bubbles. When the concentration of bubbles increase, bubble–bubble interactions become larger and the terminal rise velocity of the bubble is changed. For a suspension of monodisperse rigid spheres, Richardson and Zaki (1954) proposed the following empirical relation for the effect of particle concentration:

$$\frac{U_{\mathrm{T},\alpha}}{U_\mathrm{T}} = (1 - \alpha_2)^{n-1}, \tag{6.30}$$

where U_T denotes the terminal velocity of an isolated particle and $U_{\mathrm{T},\alpha}$ is that of a particle in a suspension of phase fraction α_2. The exponent n in the above equation depends on whether the bubble rising in a swarm is in the so-called "hindered rise" or "cooperative (unhindered) rise" regime (Wörner, 2003).

The hindered regime takes place when the bubbles are nearly spherical. The motion of a bubble is hindered by the presence of others, because the free area available for the flow of the displaced liquid decreases with the bubble concentration within the swarm. This results in steeper velocity gradients in the liquid and therefore larger shearing stresses (Richardson and Zaki, 1954). The rise velocity in the swarm decreases as the bubble concentration increases. In such a case, $n > 1$.

The cooperative rise regime is typical for large distorted bubbles, where there is a significant entrainment of bubbles in each others wake. This leads to what is called "channelling" or "streaming", and the rise velocity increases with the gas fraction. Thus, $n < 1$.

In Section 6.7.7, we discuss the modification of single-bubble drag laws to take into account this swarm effect.

6.5 Bubble entrainment in vortical flows

Vortical structures in the flow have a profound effect on the bubble distribution and residence time in the flow. Bubbles can be captured and transported by the vortices due to the relative effect of the inertial force directed towards low-pressure regions such as the vortex core. This is because of the acceleration field inducing a buoyancy like force, which is discussed in Section 6.2.1. The corresponding force responsible for the bubble migration can be represented in terms of an inertial force due to liquid acceleration (Eq. 6.14) or, equivalently, in terms of a pressure gradient force (Eq. 6.16).

The entrapment of bubbles rising perpendicular to a vortex axis is outlined by Magnaudet and Eames (2000). They considered a Rankine vortex of radius r_v characterised by a uniform vorticity $\omega = 2\Omega_\mathrm{v}$, where Ω_v is the angular velocity of the vortex. The exterior flow is irrotational. The flow is described by a forced vortex at the central core surrounded by a free (irrotational) vortex. Therefore, the tangential velocity increases linearly with distance from the vortex axis, r, according to $u_\theta = \Omega_\mathrm{v} r$ for $r < r_\mathrm{v}$ and decreases as $u_\theta = \Omega_\mathrm{v} r_\mathrm{v}^2/r$ for $r > r_\mathrm{v}$. Note that the flow pattern in a liquid stirred in a large closed cylindrical tank can be approximated by this model with the impeller radius $r_\mathrm{imp} = r_\mathrm{v}$ and the stirring rate $\Omega_\mathrm{imp} = \Omega_\mathrm{v}$.

The entrapment of bubbles in such a flow depends on two dimensionless groups: (i) $\Pi = \Omega_\mathrm{v}^2 r_\mathrm{v}/g$, the relative strength of the inertial force attracting bubbles into the vortex centre and the buoyancy force; and (ii) the trapping parameter $Sr = \Omega_\mathrm{v} r_\mathrm{v}/u_\mathrm{t}$, where u_t is the terminal rise velocity of the bubble in a stagnant liquid. Results show that when the vortex strength is fixed ($Sr = 1$), the bubbles are captured only when the strength of the inertia force increased from $\Pi = 1$ to 10. When the vortex strength is increased ($Sr = 2$), entrapment is possible also at $\Pi = 1$. The equilibrium position of the bubble is determined by the balance of forces acting on it and given by the condition $\mathbf{v} = 0$ in Eq. 6.29.

These studies are important for understanding bubble motion in turbulent flows. Moreover, interaction of bubbles with a vortical field may in turn influence the mixing characteristics of the system because of the reduced lateral gas dispersion and the change in the residence time.

6.6 Incorporation into two-fluid model

We mentioned in Section 4.3.1 that $\mathbf{M}_k'$ is associated with the sum of the hydrodynamic surface forces acting on the interface at phase k. Therefore, it should be related to $\mathbf{f}_{\mathcal{A}_\mathrm{b},\mathrm{dyn}}$, the dynamic part of $\mathbf{f}_{\mathcal{A}_\mathrm{b}}$, represented by the terms that involve the relative velocity between the phases such as drag, added mass and lift. Consequently, results obtained for an isolated bubble rising in an infinite liquid are extended to the case of gas dispersion in a liquid, assuming that the same linear superposition of forces also

applies to a bubble in a swarm:

$$\mathbf{M}'_k = -\langle \underline{\underline{\boldsymbol{\sigma}}}'_{k,\mathrm{i}} \cdot \nabla \chi_k \rangle \approx -n_\mathrm{b}(\mathbf{F}_{k,\mathrm{D}} + \mathbf{F}_{k,\mathrm{A}} + \mathbf{F}_{k,\mathrm{L}} + ...). \tag{6.31}$$

Here, the Langrangian description $\mathbf{f}_{\mathcal{A}_\mathrm{b},\mathrm{dyn}}$, written in terms of velocities $\mathbf{v}(t)$ and $\tilde{\mathbf{u}}_{\mathbf{x}_\mathrm{b}} = \tilde{\mathbf{u}}\{\mathbf{x}_\mathrm{b}(t), t\}$ that are defined only in the corresponding phase, is essentially translated into the Eulerian one, $\mathbf{F}_{\mathcal{A}_\mathrm{b},\mathrm{dyn}}$, written in terms of averaged field quantities $\mathbf{U}_1$ and $\mathbf{U}_2$ that are defined in the entire domain:

$$\begin{aligned} \mathbf{F} \equiv \overline{\mathbf{f}\{\mathbf{v}(t), \tilde{\mathbf{u}}_{\mathbf{x}_\mathrm{b}}\}} &\approx \mathbf{f}\{\overline{\mathbf{v}}(t), \overline{\tilde{\mathbf{u}}}_{\mathbf{x}_\mathrm{b}}\} \\ &\approx \mathbf{f}\{\mathbf{U}_2, \mathbf{U}_1\}. \end{aligned} \tag{6.32}$$

This is, in a way, a mean value approximation of the nonlinear interaction processes and, as a result, the effects of the turbulent fluctuations are ignored (Lathouwers, 1999). Section 6.6.4 discusses the inclusion of such effects in the interfacial transfer term.

In Eq. 6.31, it is assumed that the flow is locally monodisperse and n_b is the local number density (i.e. the number of bubbles per unit volume), which is unknown. The local number density can be connected to the local gas fraction (which is the only known parameter calculated from the gas phase continuity equation) by a further assumption of a volume equivalent diameter d_e,

$$n_\mathrm{b} = \frac{\alpha_2}{\mathcal{V}_\mathrm{b}} = \frac{6\alpha_2}{\pi d_\mathrm{e}^3}. \tag{6.33}$$

When the flow is assumed to be globally monodisperse, the volume equivalent diameter d_e is taken as constant in space and time in the entire computational domain. In Chapter 8, we discuss the modelling of bubble breakup and coalescence effects, where the flow is only locally monodisperse within the computational grid element (i.e. each particle within the grid cell experience the same force) and is globally polydisperse. The interfacial transfer term for the dispersed phase can now be given in the form

$$\mathbf{M}'_2 = -\mathbf{M}'_1 = (\mathbf{M}_{2,\mathrm{D}} + \mathbf{M}_{2,\mathrm{A}} + \mathbf{M}_{2,\mathrm{L}} + \mathbf{M}_{2,\mathrm{TD}} + ...). \tag{6.34}$$

Here, the turbulent dispersion force $\mathbf{M}_{2,\mathrm{TD}}$ is an additional contribution. It is not present in the single-bubble equation, since it arises due to the interaction of turbulence fluctuations and the instantaneous distribution of the dispersed phase.

Other contributions can be added to Eq. 6.34, such as the wall-lubrication (wall-lift) force, which represents the resisting force that bubbles feel when approaching immediately adjacent to a no-slip wall, due to slowed drainage of the liquid at the wall-side. In the following section, the force terms in Eq. 6.34 are explained further.

6.6.1 Mean drag force $\mathbf{M}_\mathrm{D}$

The mean drag force follows from the single-bubble formulation given in Eq. 6.25, which is now generalised to the case of gas dispersion:

$$\begin{aligned} \mathbf{M}_{2,\mathrm{D}} &= n_\mathrm{b}\mathbf{F}_{2,\mathrm{D}} \\ &= -\alpha_2\rho_1\frac{3}{4}\frac{C_\mathrm{D}}{d_\mathrm{e}}|\mathbf{U}_2 - \mathbf{U}_1|(\mathbf{U}_2 - \mathbf{U}_1) \\ &= -\alpha_2\rho_1 F_\mathrm{D}(\mathbf{U}_2 - \mathbf{U}_1), \end{aligned} \tag{6.35}$$

where the averaged drag function F_{D} is

$$F_{\mathrm{D}} = \frac{3}{4}\frac{C_{\mathrm{D}}}{d_{\mathrm{e}}}|\mathbf{U}_2 - \mathbf{U}_1|. \tag{6.36}$$

It is important to note that in the Fluent implementation, the drag expression is multiplied by α_1 in order to ensure the limiting behaviour when the continuous phase is not present (i.e. as $\alpha_1 \to 0$, $\mathbf{M}_{2,\mathrm{D}} \to 0$). Therefore, the mean drag force in Fluent is calculated according to

$$\begin{aligned}\mathbf{M}_{2,\mathrm{D}} = -\mathbf{M}_{1,\mathrm{D}} &= -\alpha_1\alpha_2\rho_1\frac{3}{4}\frac{C_{\mathrm{D}}}{d_{\mathrm{e}}}|\mathbf{U}_2 - \mathbf{U}_1|(\mathbf{U}_2 - \mathbf{U}_1) \\ &= -\alpha_1\alpha_2\rho_1 F_{\mathrm{D}}(\mathbf{U}_2 - \mathbf{U}_1).\end{aligned} \tag{6.37}$$

The drag coefficient C_{D} is a function of Reynolds number, turbulence, bubble concentration and shape, etc. We discuss the empirical models taking account such effects separately in Section 6.7.

6.6.2 Mean added mass force $\mathbf{M}_{\mathrm{A}}$

The averaged added mass force is also modelled after the single-bubble formulation given in Eq. 6.19:

$$\begin{aligned}\mathbf{M}_{2,\mathrm{A}} = -\mathbf{M}_{1,\mathrm{A}} &= n_{\mathrm{b}}\mathbf{F}_{2,\mathrm{A}} \\ &= -\alpha_2\rho_1 C_{\mathrm{A}}\left(\frac{D_2\mathbf{U}_2}{Dt} - \frac{D_1\mathbf{U}_1}{Dt}\right).\end{aligned} \tag{6.38}$$

Thus, bubbles feel a resisting inertial force in the direction opposite to their relative acceleration. Note that the material derivative is now defined with respect to the averaged phase velocity

$$\begin{aligned}\frac{\mathcal{D}_k}{\mathcal{D}t} &\equiv \frac{\partial}{\partial t} + \overline{\mathbf{u}}_k^{\chi_k\rho_k}\cdot\nabla \\ &= \frac{\partial}{\partial t} + \mathbf{U}_k\cdot\nabla.\end{aligned} \tag{6.39}$$

For dilute dispersions, the added mass coefficient is usually taken as the value for a single sphere in an infinite fluid, $C_{\mathrm{A}} = 0.5$. In general, it is not only a function of the bubble shape and orientation, but also the velocity and spatial distributions of the bubbles due to flow distortion by nearby bubbles. It is generally accepted that the special cases of uniformly forced and uniformly accelerated bubbles provide the two limits on C_{A} for uniformly dispersed equal-sized spherical bubbles. However, it was shown that the difference in C_{A} between these two limits is not significant even at high gas fractions, and the following simple expression proposed by Zuber can be used (Spelt and Sangani, 1998)

$$C_{\mathrm{A}} = 0.5\left(\frac{1+2\alpha_2}{1-\alpha_2}\right). \tag{6.40}$$

The expression above indicates that the added mass force (per bubble volume) increase significantly with increasing bubble concentration. Usually, the spatial distribution of

bubbles is not necessarily uniform. Dynamic simulations showed that bubble pairs aligned within an angle of about 55° with respect to the mean bubble velocity are repelled by each other due to a Bernoulli effect, whereas at larger angles, they are attracted towards each other. Thus, the probability of finding horizontally aligned bubbles is larger. The strength of turbulent fluctuations diminishes this behaviour, hence the steady-state distribution of bubbles is determined by the magnitude of the ratio of rise velocity of the bubbles to the root-mean-squared velocity of the bubbles. Bubbles form large clusters in horizontal planes when this ratio is large. For such clustered bubbly liquids, the added mass coefficient is much larger than that predicted by Eq. 6.40 (Spelt and Sangani, 1998).

In Fluent, a constant value of $C_\mathrm{A} = 0.5$ is taken in the implementation of the added mass force. In order to keep our model as simple as possible and considering the fact that the above mentioned correction is valid only for limited simplified configurations, we did no attempt to incorporate such effects in the present work and used the same constant value in simulations.

6.6.3 Mean lift force $\mathbf{M}_\mathrm{L}$

The averaged lift force acting on the bubbly phase is also generalised from the single-bubble formulation for inviscid flow given in Eq. 6.22:

$$\begin{aligned}\mathbf{M}_{2,\mathrm{L}} = -\mathbf{M}_{1,\mathrm{L}} &= n_\mathrm{b}\mathbf{F}_{2,\mathrm{L}} \\ &= -\alpha_2\rho_1 C_\mathrm{L}(\mathbf{U}_2 - \mathbf{U}_1)\times(\nabla\times\mathbf{U}_1),\end{aligned} \tag{6.41}$$

where $\overline{\boldsymbol{\omega}}_1 = \nabla\times\mathbf{U}_1$ is the mean liquid vorticity. We emphasise here the sign of the above equation as well as that of Eq. 6.38, which, in numerous papers and books, appears with an opposite sign.

For dilute systems with spheres, the lift coefficient is usually taken as the value derived for inviscid flow around a sphere, i.e. $C_\mathrm{L} = 0.5$. As mentioned in Section 6.2.1, viscous effects, surface contamination and bubble deformation all influence the lift force. Moreover, one can expect that C_L is also a function of the bubble concentration. Those effects arise from the phenomena that are not resolved by the two-fluid approach. Therefore, this may explain the inconsistency in various lift coefficients reported in the literature including even negative values, that is, to correct for the effects that are not accounted for in the modelling.

In the two-fluid implementation of Fluent, the mean lift force is modelled according to Eq. 6.41. Various other formulations intending to incorporate the above mentioned effects can be found in Ishii and Hibiki (2006). However, as also pointed out there, the lift force is still poorly understood and further investigation is needed for the applicability of single-bubble results to multiparticle bubbly flows. Therefore, we did not attempt to incorporate those effects in the present study.

Another concern regarding the standard lift force formulation given above is that it may lead to a wall-directed force acting on the gas phase even in the close proximity of the wall, thus resulting in a local maximum in gas fraction at the wall (Wörner, 2003). However, in reality, the distance between the centroid of a spherical bubble and the wall cannot be smaller than the bubble radius. As mentioned earlier, there is also

a resisting force due to slowed drainage of liquid adjacent to a no-slip wall. In order to circumvent those issues, a wall-lubrication force is sometimes introduced, which is non-zero only at the near-wall regions. Although there are some models proposed in the literature (see e.g. Antal et al. (1991)), according to Ishii and Hibiki (2006), more work has to be done to establish this force, hence it was not included in our model.

6.6.4 Turbulent dispersion force $\mathbf{M}_{\mathrm{TD}}$

The effect of turbulent fluctuations on $\mathbf{M}_k'$ has not been considered so far. However, due to turbulence interactions, fluctuations are also expected in the drag, added mass and lift forces as well as in the free-stream fluid pressure gradient experienced by the bubble.

In Section 5.1.2 and 5.1.3, the model proposed by Simonin and coworkers is presented partly, regarding to the concept of drift velocity and the calculation of the turbulence source terms representing the fluid–particle interactions. As mentioned there, as a result of the averaging process, the nonlinear dependence of the averaged interfacial momentum transfer on the turbulence velocities is accounted for in their model. We shall briefly describe that part here along with some simpler models for the turbulent dispersion force.

Model of Bel-F'dhila and Simonin

Bel F'dhila and Simonin (1992) consider a dilute suspension of small rigid spheres in translational motion of low Reynolds number. Since the motion is assumed to be purely translational without any rotational part, the lift force is not included in their analysis. Moreover, velocity shear does not produce a resultant force such as lift in the Stokes flow regime (Saffman, 1965; Maxey and Riley, 1983). The starting point of their derivation is the corrected and modified version of the particle equation of motion proposed originally by Tchen (1947) for low Reynolds number. Tchen's proposal was itself an extention of the equation for slow motion of a sphere to the case of a fluid moving with variable velocity, which was originally derived by Basset, Boussinesq, and Oseen for a fluid at rest (Hinze, 1975). Neglecting the history force, the Langrangian description of the volume force induced by the surrounding fluid flow on each point included in the dispersed phase is given by

$$\mathbf{f}_2 = \frac{\mathbf{f}_{\mathcal{A}_\mathrm{b}}}{\mathcal{V}_\mathrm{b}} = \underbrace{-\rho_1 \frac{3}{4}\frac{C_\mathrm{D}}{d_\mathrm{b}}|\mathbf{u}_\mathrm{r}|\,\mathbf{u}_\mathrm{r} - \rho_1 C_\mathrm{A}\left(\frac{d\mathbf{u}_2}{dt} - \frac{\mathcal{D}_1\tilde{\mathbf{u}}_1}{\mathcal{D}t}\right)}_{\frac{\mathbf{f}_{\mathcal{A}_\mathrm{b},\mathrm{dyn}}}{\mathcal{V}_\mathrm{b}}} + \underbrace{\rho_1\left[\frac{\mathcal{D}_1\tilde{\mathbf{u}}_1}{\mathcal{D}t} - \mathbf{g}\right]}_{\frac{\mathbf{f}_\mathrm{pg}}{\mathcal{V}_\mathrm{b}}}, \tag{6.42}$$

where $\mathbf{u}_\mathrm{r} = \mathbf{u}_2 - \tilde{\mathbf{u}}_1$ is the local instantaneous relative velocity, $\mathbf{u}_2$ is similar to $\mathbf{v}$, i.e. the translational velocity of the bubble containing the point, and $\tilde{\mathbf{u}}_1$ is also defined similar to $\tilde{\mathbf{u}}_{\mathbf{x}_\mathrm{b}}$, i.e. the liquid instantaneous velocity at the bubble position locally undisturbed by the presence of the bubble, but which remains turbulent. It can be theoretically obtained by spatial averaging at a scale large with respect to the bubble diameter, i.e. the spacial average of the disturbance flow due to presence of bubbles is

assumed to be negligible (Simonin, 1990). Although this assumption can be reasonable for small particles, for turbulent bubbly flows, when the bubble size is of the order of the integral scale of the turbulence, it can be very crude.

First two terms in Eq. 6.42 are the dynamic part of the surface force, i.e. the drag and added mass force, while the last term is due to stress applied on the bubble by the surrounding undisturbed flow field, which should occur if the bubble were withdrawn (i.e. free-stream pressure gradient force).

We note here that it is rather unclear in the treatment of Bel F'dhila and Simonin if the liquid velocity derivatives were taken following the bubble motion or that of a liquid element in the final formulation. We adopted here the latter one. According to Maxey and Riley (1983), some authors used incorrectly $\mathcal{D}_2\tilde{\mathbf{u}}_1/\mathcal{D}t$, which is the time derivative of the liquid velocity following the particle. However, $\mathcal{D}_1\tilde{\mathbf{u}}_1/\mathcal{D}t$, which is the liquid acceleration as observed at the instantaneous centre of the sphere, should have been used for a physically realistic representation. This is because, for a sphere that is small compared to the scale of spatial variations of the undisturbed flow, the effect of the undisturbed liquid stresses arising both from pressure and viscosity is to produce the same net force as would be exerted on a liquid sphere of the same size. Therefore, this force must be equal to the product of liquid mass and local liquid acceleration.

Furthermore, according to Hinze (1975), the most questionable assumption of Tchen is that the particle neighbourhood is formed by the same fluid during the motion of the particle. This requires that the particle displacement relative to that of the centroid of the liquid element should be smaller than the Kolmogorov's microscale $\eta_1 = (\nu_1^3/\varepsilon_1)^{1/4}$ during the available time determined by the characteristic deformation time of the liquid element $(\nu_1/\varepsilon_1)^{1/2}$. Therefore, the relative velocity must be smaller than the corresponding characteristic velocity $\eta_1/(\nu_1/\varepsilon_1)^{1/2} = (\varepsilon_1\nu_1)^{1/4}$. This means $|\mathbf{u}_2 - \tilde{\mathbf{u}}_1| \lesssim (\varepsilon_1\nu_1)^{1/4}$ and implies that $|\mathbf{u}_2 - \tilde{\mathbf{u}}_1| \ll |\tilde{\mathbf{u}}_1|$. Under such conditions, the difference between above mentioned two Langrangian derivatives becomes negligibly small to the degree of approximation considered in the analysis, i.e. $\mathcal{D}_2/\mathcal{D}t \approx \mathcal{D}_1/\mathcal{D}t$. Bel F'dhila and Simonin used, however, a modified version of Tchen's equation for large Reynolds number flows, where such an approximation is not justified.

By averaging the instantaneous particulate expression given above, the total mean interfacial force on the dispersed phase $\mathbf{M}_2'$ is derived, which must be related to the computed mean variables in an Eulerian frame. It is written as a summation of two parts: the part representing the disturbance by the bubbles induced by the relative velocity of the bubbles, i.e. due to $\mathbf{f}_\mathrm{r} = \mathbf{f}_{\mathcal{A}_\mathrm{b},\mathrm{dyn}}/\mathcal{V}_\mathrm{b}$, and an extra contribution due to turbulent part of the stress applied on the bubble by the undisturbed surrounding flow, i.e. due to fluctuating part of $\mathbf{f}_\mathrm{pg}/\mathcal{V}_\mathrm{b}$ (the contribution by the mean pressure gradient, $-\alpha_2\nabla P_1$, is already accounted for in the momentum equations):

$$\begin{aligned} -\alpha_2\nabla P_1 + \mathbf{M}_2' = \alpha_2\langle\mathbf{f}_2\rangle_2 &= \alpha_2\langle\mathbf{f}_\mathrm{r}\rangle_2 + \alpha_2\left\langle \rho_1\left[\frac{\mathcal{D}_1\tilde{\mathbf{u}}_1}{\mathcal{D}t} - \mathbf{g}\right]\right\rangle_2 \\ \mathbf{M}_2' &= \alpha_2\langle\mathbf{f}_\mathrm{r}\rangle_2 + \left\{\alpha_2\rho_1\left\langle\left[\frac{\mathcal{D}_1\tilde{\mathbf{u}}_1}{\mathcal{D}t} - \mathbf{g}\right]\right\rangle_2 + \alpha_2\nabla P_1\right\} \\ &= \alpha_2\langle\mathbf{f}_\mathrm{r}\rangle_2 + \alpha_2\langle\nabla\cdot\underline{\underline{\tilde{\boldsymbol{\sigma}}}}_1'\rangle_2, \end{aligned} \tag{6.43}$$

where the first term, representing the flow disturbance due to presence of bubbles, is

given as

$$\alpha_2\langle \mathbf{f}_\mathrm{r}\rangle_2 = -\alpha_2\rho_1 F_\mathrm{D}\mathbf{U}_\mathrm{r} - \alpha_2\rho_1 C_\mathrm{A}\frac{\mathcal{D}_2\mathbf{U}_\mathrm{r}}{\mathcal{D}t} - \nabla\cdot\alpha_2\rho_1 C_\mathrm{A}\langle \mathbf{u}_2'\mathbf{u}_\mathrm{r}'\rangle_2. \tag{6.44}$$

Here, the first two terms represent the mean value approximation to drag and added mass force, while the last term is the averaged fluctuating part of the added mass. The mean relative velocity $\mathbf{U}_\mathrm{r} = \langle \mathbf{u}_\mathrm{r}\rangle_2 = \mathbf{U}_2 - [\mathbf{U}_1 + \mathbf{U}_\mathrm{d}]$ (see Eq. 5.22) is a function of the drift velocity $\mathbf{U}_\mathrm{d}$ due to turbulent correlations. The calculation of $\mathbf{U}_\mathrm{d}$ and the averaged drag function F_D is given in Section 5.1.3 and 5.1.2, respectively. The second part arises due to non-homogeneous distribution of the undisturbed liquid pressure gradient on the interface after subtracting the mean pressure gradient contribution

$$\begin{aligned}
\alpha_2\langle\nabla\cdot\underline{\tilde{\boldsymbol{\sigma}}}_1'\rangle_2 &= \alpha_2\rho_1\left\langle\left[\frac{\mathcal{D}_1\tilde{\mathbf{u}}_1}{\mathcal{D}t} - \mathbf{g}\right]\right\rangle_2 - \{-\alpha_2\nabla P_1\}\\
&= \alpha_2\rho_1\left\langle -\left[\frac{\nabla\tilde{p}_1}{\rho_1}\right]\right\rangle_2 + \alpha_2\nabla P_1\\
&= -\alpha_2\nabla P_1 - \alpha_2\langle\nabla\tilde{p}_1'\rangle_2 + \alpha_2\nabla P_1\\
&= -\alpha_2\langle\nabla\tilde{p}_1'\rangle_2,
\end{aligned} \tag{6.45}$$

where $\tilde{p}_1 = P_1 + \tilde{p}_1'$ is the locally undisturbed (but turbulent) liquid pressure at the position of the bubble centre. An important point here, as mentioned by Hinze (1975), is that the local pressure gradient in the liquid surrounding the bubble is not only caused by the acceleration of the liquid, but also by viscous effects, if one is using Navier–Stokes equation rather than the inviscid Euler formulation. However, Tchen's theory assumes that $d_\mathrm{b} \ll \eta_1$ and that time intervals are smaller than the deformation time of a liquid element. Therefore, the liquid element containing the bubble can be considered to have a sufficiently uniform velocity such that the viscous effects within this element on $\nabla\tilde{p}_1$ can be neglected. These assumptions are obviously too crude for most applications of bubbly flows.

As a first approximation, the term $-\alpha_2\langle\nabla\tilde{p}_1'\rangle_2$ in Eq. 6.45 represents the correlation between the local instantaneous distribution of the bubbles and the liquid turbulent pressure gradient (the undisturbed liquid pressure gradient is assumed to be nearly constant on a single bubble surface). It accounts for the particle dispersion due to transport by liquid turbulent fluctuations and a "turbophoresis" mechanism introduced by the gradients of the fluid and fluid/particle turbulent stresses. It is approximated as

$$\begin{aligned}
-\alpha_2\langle\nabla\tilde{p}_1'\rangle_2 &\approx \nabla\cdot\alpha_2\rho_1\langle\mathbf{u}_1'\mathbf{u}_2'\rangle_2 - \frac{\alpha_2}{\alpha_1}\nabla\cdot\alpha_1\rho_1\langle\mathbf{u}_1'\mathbf{u}_1'\rangle_1\\
&\approx \rho_1\langle\mathbf{u}_1'\mathbf{u}_2'\rangle_2\cdot\nabla\alpha_2.
\end{aligned} \tag{6.46}$$

Here, in the last approximation, a dilute dispersion in homogenous turbulence is assumed, which results in a dispersive contribution term. For further details of the derivation, Bel F'dhila and Simonin (1992) can be referred. We give finally the resulting form of the total mean interfacial force on the dispersed phase:

$$\mathbf{M}_2' = -\alpha_2\rho_1 F_\mathrm{D}\mathbf{U}_\mathrm{r} - \alpha_2\rho_1 C_\mathrm{A}\frac{\mathcal{D}_2\mathbf{U}_\mathrm{r}}{\mathcal{D}t} - \nabla\cdot\alpha_2\rho_1 C_\mathrm{A}\langle\mathbf{u}_2'\mathbf{u}_\mathrm{r}'\rangle_2 + \rho_1\langle\mathbf{u}_1'\mathbf{u}_2'\rangle_2\cdot\nabla\alpha_2. \tag{6.47}$$

Note that in the Fluent implementation of the two-fluid model, the dispersion effect due to turbulent fluctuations is accounted only for the drag force via the drift velocity term in the definition of $\mathbf{U}_\mathrm{r}$. The dispersive effects on added mass and pressure terms are neglected. Moreover, F_D is calculated from Eq. 6.36 and, as mentioned in Section 6.6.1, the drag force is multiplied by α_1. By substituting the definition of $\mathbf{U}_\mathrm{r}$ in the drag term, we obtain the separate contributions by the mean drag and the turbulent dispersion force in the form solved by Fluent:

$$\mathbf{M}_{2,\mathrm{D}} + \mathbf{M}_{2,\mathrm{TD}} = -\alpha_1\alpha_2\rho_1 F_\mathrm{D}(\mathbf{U}_2 - \mathbf{U}_1 - \mathbf{U}_\mathrm{d}). \tag{6.48}$$

Thus, in Fluent, the turbulent dispersion force is modelled as

$$\mathbf{M}_{2,\mathrm{TD}} = -\mathbf{M}_{1,\mathrm{TD}} = \alpha_1\alpha_2\rho_1 F_\mathrm{D}\mathbf{U}_\mathrm{d}. \tag{6.49}$$

It is also expected that the lift force has a fluctuating component, which was not included in the model of Bel F'dhila and Simonin. However, according the Chahed et al. (2003), this turbulent contribution to the lift is expected to be negligible, owing to the relatively weak correlation between the fluctuating velocity and the fluctuating vorticity in the liquid. The reasoning behind their argument is that vorticity fluctuations are associated with high frequency of turbulence, hence have little interaction with the velocity fluctuations associated with the energy containing eddies. The correlation between them is inversely proportional to $\sqrt{Re}$.

Model of Lahey et al

The above given model of Simonin and coworkers seemed to be the most involved one accounting for the effects of fluctuations on drag, added mass and pressure gradient terms simultaneously. There are also simpler models proposed in literature. Some of them, by decomposing gas fraction as $\alpha_k = \bar{\alpha}_k + \alpha'_k$ and averaging the averaged continuity equation once more, obtained an additional diffusion term, $\nabla \cdot \overline{\alpha'_k \mathbf{u}'_k}$, in the continuity equation. According to Lahey et al. (1993), such a term cannot exist in the mass equation, because $\alpha_k \equiv \langle \chi_k \rangle$ being an average itself, α'_k does not exist. However, a dispersion force can occur in the momentum equation. Based on an analogy with the thermal diffusion of air molecules in the atmosphere, they proposed the following expression for the volumetric turbulent void dispersion force

$$\mathbf{M}_{2,\mathrm{TD}} = -\mathbf{M}_{1,\mathrm{TD}} = -C_\mathrm{TD}\rho_1 k_1 \nabla\alpha_2, \tag{6.50}$$

where C_TD is an empirical constant. Thus, the average effect of this force is to pull the bubbles in the direction of the negative gradient of the dispersed phase. As noted by Lathouwers (1999), this expression does not allow the anisotropy of dispersion and depends only on few parameters such as k_1. Moreover, the mechanistic coupling between the phases is not represented.

VOF diffusion model

Another simplified model which treats the turbulent dispersion as a diffusion term in the gas phase continuity equation (along the lines described in the previous section) is

that of Sokolichin et al. (2004). Here, the phase-averaged gas velocity is written as the sum of the bubble velocity plus a drift velocity representing the turbulent dispersion of bubbles. By inserting for the drift velocity an expression given by Simonin and coworkers, a turbulent diffusion term is obtained in the gas volume fraction equation (VOF). Note that authors neglected variations in the liquid phase volume fraction. For the general case, a similar diffusion term has to be added to the liquid phase continuity equation, hence the continuity equation for any phase k becomes

$$\frac{\partial}{\partial t}(\alpha_k \rho_k) + \nabla \cdot (\alpha_k \rho_k \mathbf{U}_k) = \nabla \left(\rho_k D_k^{\mathrm{t}} \nabla \alpha_k\right) + S_k, \tag{6.51}$$

S_k being a source term and D_k^{t} is the turbulent diffusion coefficient. The turbulent diffusion term, for the case of one primary and one secondary phase, satisfies the following mass conservation condition:

$$\nabla \left(\rho_1 D_1^{\mathrm{t}} \nabla \alpha_1\right) + \nabla \left(\rho_2 D_2^{\mathrm{t}} \nabla \alpha_2\right) = 0. \tag{6.52}$$

The diffusion coefficient for the gas phase is estimated from the gas phase turbulent viscosity:

$$D_2^{\mathrm{t}} = \frac{\mu_2^{\mathrm{t}}}{\rho_2 \, \sigma_2^{\mathrm{t}}}. \tag{6.53}$$

The turbulent diffusion term for the liquid phase continuity equation is then simply equal to that of the gas phase but with an opposite sign (from Eq. 6.52), i.e. $-\nabla \left(\rho_2 D_2^{\mathrm{t}} \nabla \alpha_2\right)$. In Fluent, the so-called dispersion Prandtl number is used as a model constant with the default value of $\sigma_2^{\mathrm{t}} = 0.75$. This, in essence, is a Schmidt number for the turbulent transport.

6.7 Drag laws for dispersed two-phase flows

Generally speaking, the drag coefficient of a single bubble in a bubble swarm depends on many parameters such as the particle Reynolds number, turbulence in the continuous fluid, bubble concentration in the neighbourhood, interface deformation and oscillation, bubble orientation, contamination, wall effects, etc.

In this section, we discuss briefly some commonly used drag models for bubbly flows, which provide constitutive relations for the drag coefficient. For an extensive review of the drag correlations available in literature, one can refer, among others, the book by Clift et al. (1978). Once C_{D} is known, then the mean drag force in the interfacial momentum transfer term can be calculated according to Eq. 6.37. Moreover, one can also calculate the terminal rise velocity of a bubble.

6.7.1 Spherical (undistorted) particles

Steady motion of a single spherical particle (solid or fluid) moving in an infinite fluid is a well studied case in literature, where three different regimes can be identified depending on the bubble Reynolds number Re_{b}:

Stokes' regime

In the creeping flow limit ($Re_\mathrm{b} \ll 1$), the steady-state drag on a rigid sphere depends linearly on the relative velocity. The drag coefficient is a function of Re_b and given by the Stokes' law:

$$C_\mathrm{D} = \frac{24}{Re_\mathrm{b}}. \tag{6.54}$$

Substituting into the definition of drag coefficient (Eq. 6.26), one can obtain the corresponding drag force,

$$\mathbf{f}_{\mathrm{D,Stokes}} = 3\pi\mu_1 d_\mathrm{b}(\mathbf{v} - \tilde{\mathbf{u}}_{\mathbf{x}_\mathrm{b}}). \tag{6.55}$$

This correlation is a reasonable approximation for most practical applications of low Re_b bubbly flows, because slight amounts of impurities are sufficient to immobilise the bubble surface.

Hadamard (1911) and Rybczynski (1911) extended independently the analysis of Stokes to spherical fluid particles free of any surface-active contaminants (thus the interfacial tension is constant) and obtained (Clift et al., 1978)

$$C_\mathrm{D} = \frac{24}{Re_\mathrm{b}}\left(\frac{2/3 + \mu_2/\mu_1}{1 + \mu_2/\mu_1}\right). \tag{6.56}$$

This relation gives the Stokes drag in the limit of a rigid sphere, i.e. when $\mu_2/\mu_1 \to \infty$. For a clean spherical bubble in a liquid, i.e. when $\mu_2/\mu_1 \to 0$, the drag force is reduced by a factor of 1/3:

$$C_\mathrm{D} = \frac{16}{Re_\mathrm{b}}. \tag{6.57}$$

For either case, $C_\mathrm{D}/3$ corresponds to the pressure drag and $2C_\mathrm{D}/3$ is the contribution by the viscous stress, either the deviatoric normal component (for clean bubbles) or the shear component (for rigid spheres), depending on the surface mobility (Clift et al., 1978). As first pointed out by Oseen, assumption that the inertia forces are negligible is inconsistent with the creeping flow solution itself at the regions far from the particle. However, no appreciable deviation from measurements is observed for $Re_\mathrm{b} < 1$ (Batchelor, 1967).

At small Re_b, it is normally expected that a bubble remains spherical when the surface tension is sufficiently strong against the deforming effect of viscous forces. That is, when σ/r_b (surface tension coefficient being σ) is large compared with the normal stress due to motion, of order $\mu_1|\mathbf{v} - \tilde{\mathbf{u}}_{\mathbf{x}_\mathrm{b}}|/r_\mathrm{b}$ (Batchelor, 1967). This can be characterised by the ratio F_μ/F_σ (see Table 3.1), which is defined as the Capillary number:

$$Ca \equiv \frac{F_\mu}{F_\sigma} = \frac{\mu_1|\mathbf{v} - \tilde{\mathbf{u}}_{\mathbf{x}_\mathrm{b}}|}{\sigma} \ll 1. \tag{6.58}$$

However, an interesting implication of the creeping flow assumption is that, across the interface, the normal stresses differ only by a constant amount $p_\mathrm{b} - p_1 = 2\sigma/r_\mathrm{b}$, therefore cannot cause any deformation. Thus, as long as the inertial forces are negligible (i.e. $Re_\mathrm{b} \ll 1$), bubbles and drops remain spherical no matter how small the surface tension forces (Batchelor, 1967; Clift et al., 1978).

Inertial (Newton's) regime

The other extreme, i.e. the high Re_b limit, is called the inertial (or Newton's) regime, where the pressure drag predominates. C_D is independent of Re_b for a rigid sphere and approaches approximately to a constant value of

$$C_\mathrm{D} = 0.445 \quad \text{for} \quad 750 - 1000 \leq Re_\mathrm{b} \leq 2 - 3.5 \times 10^5. \tag{6.59}$$

Beyond the critical value of about $Re_{\mathrm{b,c}} = 2 \times 10^5$, the boundary layer becomes turbulent soon after detachment and reattaches again to the surface as a result of increased rate of spreading by the turbulence. Due to enhanced momentum transfer in the turbulent boundary layer, it can resist the adverse pressure gradient more effectively without separation. Therefore, the separation point shifts downstream and the drag coefficient drops sharply to the value of 0.07 (Clift et al., 1978).

The boundary layer of a clean bubble is much thinner, and remains attached to the surface longer than that of a comparable rigid particle. Neglecting this thin boundary layer, one can approximate the drag force from the viscous dissipation rate in the external irrotational flow alone, which should balance the rate of work done by the drag force, $\mathbf{f}_\mathrm{D} \cdot (\mathbf{v} - \tilde{\mathbf{u}}_{\mathbf{x}_\mathrm{b}})$. In the asymptotic limit of high Re_b, such an approach leads to the conventional relation proposed by Levic for a clean spherical bubble (Magnaudet and Eames, 2000),

$$C_\mathrm{D} = \frac{48}{Re_\mathrm{b}}, \tag{6.60}$$

again $C_\mathrm{D}/3$ is due to pressure, $2C_\mathrm{D}/3$ is due to deviatoric normal viscous stress. From Eq. 6.26, one can obtain the corresponding drag force, which is twice the Stokes drag:

$$\mathbf{f}_{\mathrm{D,Levic}} = 6\pi\mu_1 d_\mathrm{b}(\mathbf{v} - \tilde{\mathbf{u}}_{\mathbf{x}_\mathrm{b}}). \tag{6.61}$$

Including the dissipation in the boundary layer and wake, Moore (1963) made an improved estimate,

$$C_\mathrm{D} = \frac{48}{Re_\mathrm{b}}\left[1 - \frac{2.21}{\sqrt{Re_\mathrm{b}}} + \mathcal{O}(Re_\mathrm{b}^{-5/6})\right]. \tag{6.62}$$

Under the assumption of a thin boundary layer and wake again, Moore (1965) extended his analysis to the case of ellipsoidal bubbles. However, as pointed out by Magnaudet and Eames (2000), such use of potential flow theory for highly deformed bubbles in the range of $Re_\mathrm{b} = 10^2 - 10^3$ (which is typical for ellipsoidal bubbles rising in water) has a limited practical applicability, because it fails to describe the flow in the wake region.

Viscous regime

In the region of intermediate Reynolds numbers, say $1 < Re_\mathrm{b} < 1000$, both viscous and inertial effects are important. The drag coefficient is a complex function of the Reynolds number and should be determined from empirical correlations. The drag force in this regime depends non-linearly on the relative velocity.

For solid spheres, the onset of boundary layer separation starts at about $Re_\mathrm{b} = 20$, marked by a change in the sign of vorticity. Until $Re_\mathrm{b} = 130$, the recirculating wake is stable. Beyond that point, wake instabilities start, because the vorticity generation is

no longer in balance with the vorticity convection and diffusion, and vortex shedding begins from the wake. For clean bubbles, the formation of an attached wake and the onset of wake shedding can be significantly delayed. For instance, wake shedding can occur as late as $Re_\mathrm{b} = 800$ (Clift et al., 1978).

Fluid particles at larger Re_b are characterised as the "distorted particles", where the vortex system developed behind the particle departs and creates a large wake region, which in turn distorts the particle itself and the following particles (Kolev, 2007).

6.7.2 Distorted bubbles

Bubbles and drops are nearly spherical at about $Re_\mathrm{b} = 500$ if the surface tension forces are sufficiently strong. However, beyond $Re_\mathrm{b} > 600$, significant shape deformations start to occur for bubbles and drops rising or falling freely in systems of practical importance (Clift et al., 1978). At large Re_b, a bubble is expected to remain spherical only when the pressure variation at the surface, of order $\rho_1|\mathbf{v} - \tilde{\mathbf{u}}_{\mathbf{x}_\mathrm{b}}|^2$, is much smaller than the pressure jump at the surface due to surface tension, $2\sigma/r_\mathrm{b}$, which can be expressed in terms of the Weber number:

$$We \equiv \frac{F_\mathrm{I}}{F_\sigma} = Ca \cdot Re_\mathrm{b} = \frac{\rho_1|\mathbf{v} - \tilde{\mathbf{u}}_{\mathbf{x}_\mathrm{b}}|^2 d_\mathrm{b}}{\sigma} \ll 1. \tag{6.63}$$

As mentioned earlier, small bubbles assume a spherical or slightly ellipsoidal shape and move in rectilinear paths. Larger bubbles are of a definite ellipsoidal shape and move along zigzag or helical paths. Such fluctuations in speed and direction associated with the secondary motion increases the mean drag, because the vertical terminal velocity of the bubble is smaller. Moreover, the motion of ellipsoidal bubbles can even be more complex due to superimposed shape oscillations that start with the onset of wake shedding. With further increase of size, bubbles become more distorted and the amplitude of the swerving motion decreases. Finally, the largest bubbles approach to a spherical cap shape, and their motion becomes practically rectilinear again (Harmathy, 1960).

In the present study, bubbles with $d_\mathrm{e} \leq 10$ mm are of interest, where $Re_\mathrm{b} = \mathcal{O}(10^2 - 10^3)$. Therefore, bubbles are mostly in the transitional or inertial regime and take a nearly spherical or ellipsoidal form. In the following sections, we explain briefly some commonly used drag correlations that are applicable to this range and that we used in this study. As these correlations are generally derived from experiments of a single particle moving steadily in an otherwise stagnant fluid of infinite extent, modifications are needed to take into account the effects induced by nearby particles and the turbulence in the surrounding liquid. Thus, those are also discussed briefly.

6.7.3 Effects of surfactants and deformation

In Fig. 6.1(a), the standard drag curve for rigid spheres is compared with the drag curves for air bubbles in pure and contaminated water, which are taken from the well-known experimental plot given by Clift et al. (1978). Note that, in contrast to drops,

bubbles are much more sensitive to surface contamination, because there is very little viscous resistance to internal circulation on the bubble side of the interface.

The figure clearly shows the deformation effects, i.e. at large Re_b, the drag coefficient increases above the value for a rigid sphere of the same volume, if C_D and Re_b are based on the volume-equivalent diameter d_e. This is because of the increased form drag by the oblate shape as compared to a sphere. When $20 < Re_\mathrm{b} < 700$, the deformation effects are less pronounced relative to the effects induced by the surface mobility and the internal circulation in the bubble. As a result, the drag for a pure system is smaller than that for a rigid sphere, whereas for a contaminated system, it is always larger.

At about $Re_\mathrm{b} = 450$, oscillations start and the drag curve for clean bubbles show a sharp increase. Both curves (pure and contaminated) coincide at the two extreme conditions, namely for very small and very large bubbles. For small (spherical) bubbles, this is because even the distilled water contains sufficient impurities to immobilise the bubble surface. Therefore, when $Re_\mathrm{b} < 20$, all three curves coincide. For large bubbles in the spherical cap regime ($Re_\mathrm{b} > 8000$), deformation effects dominate over the surface mobility effects, and both pure and contaminated bubbles approach to the same constant value, $C_\mathrm{D} = 8/3 = 2.67$.

Above observations imply that the surface contamination effects are most pronounced for bubbles in the ellipsoidal regime. Moreover, systems with high surface tension (e.g. air–water) are particularly sensitive to surfactants, because surface tension reductions are largest in those systems.

Effects of surface contamination and shape deformation can also be observed in Fig. 6.1(b), where we plotted the terminal velocities corresponding to the drag laws presented in Fig. 6.1(a) (see also Section 6.7.9) and the experimental curves for pure and contaminated water from Clift et al. (1978) again. A bubble of fixed d_e deforms significantly more in a purified system than in a contaminated one, because the surface mobility leads to a higher terminal velocity, hence a larger inertia force.

6.7.4 Schiller & Naumann drag law

One of the standard correlations that gives a reasonably good estimate of the drag coefficient of spherical particles is that proposed by Schiller and Naumann (1933). It is basically an extension to the Stokes drag to account for the inertial effects on drag force. Within the two-fluid framework of Fluent, it is implemented as

$$C_\mathrm{D} = \begin{cases} \dfrac{24}{Re_\mathrm{r}}(1 + 0.15\ Re_\mathrm{r}^{0.687}) & Re_\mathrm{r} \leq 1000 \\ 0.44 & Re_\mathrm{r} > 1000 \end{cases}, \tag{6.64}$$

where the relative Reynolds number is calculated from the mean flow as

$$Re_\mathrm{r} = \frac{\rho_1 d_\mathrm{e} |\mathbf{U}_2 - \mathbf{U}_1|}{\mu_1}. \tag{6.65}$$

At low Reynolds numbers, say $Re_\mathrm{b} < 1$, the correlation practically reduces to the Stokes drag, $C_\mathrm{D} = 24/Re_\mathrm{b}$. It has been found that the correction factor for inertial effects,

$(1 + 0.15\ Re_{\mathrm{r}}^{0.687})$, is appropriate not only for solid spheres, but also for spheroidal bubbles and drops at intermediate Reynolds numbers (Hayashi and Tomiyama, 2009).

Note that Schiller and Naumann (1933) originally proposed their correlation for solid spheres in the viscous regime with $Re_{\mathrm{b}} < 800$. However, we used here the usual implementation in commercial codes (e.g. Fluent, CFX), where it is extended to ensure the correct limiting behaviour in the inertial regime (i.e. $C_{\mathrm{D}} = 0.44$). This corresponds to $Re_{\mathrm{b}} \approx 1000$ in the above equation. The form of the correlation also indicates that, as Re_{b} increases, the drag coefficient becomes a weaker function of Re_{b}.

In Fig. 6.1(a), we plotted the Schiller–Naumann drag curve based on Eq. 6.64, which closely follows the standard drag curve. Because the correlation is based on a single solid sphere settling in an infinite medium, it is expected to be applicable to dilute and contaminated systems with bubbles that do not undergo significant deformation.

6.7.5 Ishii & Zuber drag law

Ishii and Zuber (1979) proposed a drag law, which takes into account the bubble deformation effects in the ellipsoidal and spherical-cap regimes. In the viscous regime, where the bubbles are approximately spherical, the drag coefficient is calculated as

$$C_{\mathrm{D,sphere}} = \begin{cases} \dfrac{24}{Re_{\mathrm{r}}}(1 + 0.1\ Re_{\mathrm{r}}^{0.75}) & Re_{\mathrm{r}} \leq 1000 \\ 0.44 & Re_{\mathrm{r}} > 1000 \end{cases} \tag{6.66}$$

In the so-called "distorted-bubble (or ellipsoidal) regime", the drag force is governed by shape distortions and irregular motions. Experimental data show that the terminal velocity is independent of the particle size. The drag coefficient depends only on the particle size and fluid properties, and not on the viscosity or velocity, and increases linearly with the particle size (Ishii and Zuber, 1979; Ishii and Hibiki, 2006). Therefore, a particle of fixed size has a constant C_{D}. Change in the bubble shape leads to an increase in the effective cross section, hence C_{D} can be scaled by the mean diameter rather than the Reynolds number. According to Harmathy (1960), in the distorted-bubble regime, the bubble shape in an infinite media is a function of Eötvös number ($Eo = g|\Delta\rho|d_{\mathrm{e}}^2/\sigma$) alone, and the Weber number does not impose any additional constraint for a given bubble shape and Eo. Therefore, for ellipsoidal bubbles, the proposed relation follows from these observations and the drag coefficient is expressed as independent of Re_{b}, but dependent on the bubble shape via Eo or the Rayleigh–Taylor instability length λ_{RT}:

$$\begin{aligned} C_{\mathrm{D,ellipse}} = \frac{2}{3} d_{\mathrm{e}} \sqrt{\frac{g|\Delta\rho|}{\sigma}} &= \frac{2}{3}\left(\frac{d_{\mathrm{e}}}{\lambda_{\mathrm{RT}}}\right) \\ &= \frac{2}{3}\sqrt{Eo}, \end{aligned} \tag{6.67}$$

where the Rayleigh–Taylor instability length is defined as

$$\lambda_{\mathrm{RT}} = \sqrt{\frac{\sigma}{g|\Delta\rho|}} = \frac{d_{\mathrm{e}}}{\sqrt{Eo}} \tag{6.68}$$

(Kolev, 2007). Here, the form of the drag correlation, being linear in particle size, suggests that the terminal velocity is independent of the particle size (i.e. substituting Eq. 6.67 into Eq. 6.94, d_e is eliminated).

At larger diameters, the bubble is further deformed into a spherical-cap and there is an upper limit on C_D due to hydrodynamic instability. The experimental data shows that the drag coefficient reaches a constant value of

$$C_{D,cap} = \frac{8}{3} = 2.67 \tag{6.69}$$

(Haberman and Morton (1953), see also Fig. 6.1(a)). Using Kelvin–Helmholtz stability analysis, the maximum stable cap bubble diameter is given approximately as

$$d_{cap,max} = 40\sqrt{\frac{\sigma}{g|\Delta\rho|}} = 40\lambda_{RT} \tag{6.70}$$

(Ishii and Hibiki, 2006), which corresponds to $Eo = 1600$ or $d_e = 11$ cm for air bubbles in water, and beyond this, large bubbles breakup due to instability.

Ellipsoidal to spherical cap transition occurs at about $Eo \geq 40$ or $d_e \geq 17$ mm (for air bubbles in water), but there is a long transitional region, $13 < Eo < 40$, in which the variation is very slow (Harmathy, 1960; Clift et al., 1978). However, the transition criteria used by Ishii and Hibiki (2006) is a somewhat lower value, $Eo \geq 16$, which corresponds to $d_e \geq 4\lambda_{RT}$ or $d_e \geq 11$ mm. In the present work, we adopted the procedure implemented in CFX, where the drag coefficient is calculated according to

$$\begin{aligned} C_{D,distorted} &= \min\{C_{D,ellipse}, C_{D,cap}\} \\ C_D &= \max\{C_{D,sphere}, C_{D,distorted}\}, \end{aligned} \tag{6.71}$$

and $C_{D,sphere}$ follows from the Schiller–Naumann drag law rather than Eq. 6.66. The selection criteria above is in agreement with the following conditions (Kolev, 2007):

- in the spherical (viscous) regime: $C_{D,sphere} > C_{D,ellipse}$,
- in the ellipsoidal (distorted) regime: $C_{D,sphere} \leq C_{D,ellipse} < C_{D,cap}$,
- in the spherical-cap regime: $C_{D,cap} \leq C_{D,ellipse}$.

Note that, the last criterium implies that the transition occurs at $Eo \geq 16$ (from Eq. 6.67 and 6.69), which is in agreement with that proposed by Ishii and Hibiki (2006).

When the present work was performed, Ishii–Zuber drag correlation was not available in Fluent. Therefore, we implemented it as an user defined subroutine written in C language.

6.7.6 Tomiyama drag law

Tomiyama and coworkers proposed drag correlations taking into account the varying degree of contamination in the system. The drag laws corresponding to pure, slightly-

contaminated and contaminated systems are given by

$$C_{\mathrm{D,pure}} = \max\left[\min\left\{\frac{16}{Re_{\mathrm{r}}}(1+0.15\ Re_{\mathrm{r}}^{0.687}), \frac{48}{Re_{\mathrm{r}}}\right\}, \frac{8}{3}\frac{Eo}{Eo+4}\right], \tag{6.72}$$

$$C_{\mathrm{D,slight-cont.}} = \max\left[\min\left\{\frac{24}{Re_{\mathrm{r}}}(1+0.15\ Re_{\mathrm{r}}^{0.687}), \frac{72}{Re_{\mathrm{r}}}\right\}, \frac{8}{3}\frac{Eo}{Eo+4}\right], \tag{6.73}$$

$$C_{\mathrm{D,cont.}} = \max\left[\frac{24}{Re_{\mathrm{r}}}(1+0.15\ Re_{\mathrm{r}}^{0.687}), \frac{8}{3}\frac{Eo}{Eo+4}\right], \tag{6.74}$$

respectively (Tomiyama, 1998). They pointed out that in case of an air–water system, the tap water may be regarded as contaminated or slightly-contaminated system, whereas water carefully distilled two or more times corresponds to a pure system. Good agreement with the experimental data was found in the range $10^{-2} < Eo < 10^{3}$, $10^{-14} < Mo < 10^{7}$ and $10^{-3} < Re_{\mathrm{r}} < 10^{5}$. The drag and terminal velocity curves for the Tomiyama drag law are plotted in Fig. 6.1(a) and 6.1(b), respectively.

Note that the Tomiyama law generalises the drag coefficient for ellipsoidal and spherical cup bubbles as $\frac{8}{3}\frac{Eo}{Eo+4}$, which is independent of the system contamination. However, examining the experimental curves from Clift et al. (1978) in Fig. 6.1(a), this seems, although valid in the spherical cap regime, not the case in the ellipsoidal regime.

We implemented the Tomiyama drag law as an user defined subroutine in Fluent.

6.7.7 High gas fraction effects

The effect of high bubble concentrations on the terminal rise velocities of individual bubbles (i.e. the swarm effect) has been discussed in Section 6.4. At high gas fractions, the motion of individual bubbles under the influence of neighboring bubbles is governed by the average interparticle distance. Assuming a simple cubic lattice of spheres, where the bubbles of diameter d_{b} are located at the corners of the cube of linear dimension l, a simple illustrative relation connecting the gas fraction to l (i.e. the shortest bubble–bubble distance) can be derived:

$$\alpha_2 = \frac{\mathcal{V}_{\mathrm{b}}}{\mathcal{V}_{\mathrm{cube}}} = \frac{\pi}{6}\left(\frac{d_{\mathrm{b}}}{l}\right)^3. \tag{6.75}$$

Above relation shows that α_2 drops rapidly with the ratio d_{b}/l. For instance, the maximum possible gas fraction corresponding to the maximum packing condition (i.e. $l = d_{\mathrm{b}}$) is 52.4 %. For gas fraction of 5 %, $l = 2.2d_{\mathrm{b}}$. Even for a dilute system, say of gas fraction 1 %, we have only $l = 3.7d_{\mathrm{b}}$, where wake effects might still be pronounced.

Consequently, the interphase forces derived originally for single particles moving through infinite media do not provide an accurate representation of the flow at high gas fractions anymore and new correlations for the multiparticle system are required, which take into account the bubble–bubble interactions. In order to keep our model sufficiently simple, and due to numerical instabilities, we considered only the modification of the drag in the present study, which is the dominant force. In principle, however, other interphase forces, such as added mass and lift forces, are expected to be influenced by the swarm effect as well.

We implemented the multiparticle drag law proposed by Ishii and Zuber (1979), which is explained briefly in the coming section. Other models are available, for instance that of Behzadi et al. (2004), which introduces empirical models for the modification of both drag and lift forces at high gas fractions. They point out that most models available in literature do not satisfy the limiting condition at zero gas fraction, i.e. the multiparticle formulation do not revert to the single-bubble one. And those that do, are not based on latest experimental data, hence may not be reliable.

The usual form of the modification models are such that the the single-particle formulation is multiplied by a correction factor, which is a function of the gas fraction. That is, for the drag force,

$$C_{\mathrm{D}}^{\alpha} = C_{\mathrm{D}} f(\alpha_2), \tag{6.76}$$

where C_{D}^{α} denotes the multiparticle drag coefficient. According to the above mentioned limiting criteria, it is expected that when $\alpha_2 \to 0$, then $f(\alpha_2) \to 1$, and therefore $C_{\mathrm{D}}^{\alpha} \to C_{\mathrm{D}}$.

Ishii & Zuber multiparticle drag law

Ishii and Zuber (1979) introduced the "mixture viscosity" concept and a simple drag similarity criterion between a single particle and a multiparticle system, in order to derive drag correlations for the dense particle regime. Comparing their correlations against a large set of experimental data, they found a satisfactory agreement at wide ranges of Reynolds number and particle concentration (from 50 to 95 %; such high concentrations were possible for deforming fluid particles in the absence of turbulent motions and particle coalescences, particularly for droplet suspension in liquids).

The mixture (or effective) viscosity concept is based on the following notion. A particle moving through a region restricted by other particles feels an extra resistance force as if the viscosity of the fluid is increased. This is due to the fact that the moving particle induces a motion to the surrounding fluid, and that, as a result of the deformation of fluid, induces translational and rotational motions to other particles in the neighbourhood. As these particles resist deformation more than the fluid, resulting effect is that a system of forces act on the fluid leading to extra stresses and hence the apparent increased viscosity.

The mixture viscosity is expected to be a function of the concentration of particles, the fluid viscosity, the particle viscosity (as it is a measure of the interface mobility) and the surface tension (due to its effect on particle collisions and coalescences). In Ishii-Zuber multiparticle drag law, it is calculated from the following relation, which is valid for both solid- and fluid-particle systems at all concentrations:

$$\frac{\mu_{\mathrm{m}}}{\mu_1} = \left(1 - \frac{\alpha_2}{\alpha_{\mathrm{dm}}}\right)^{-2.5\alpha_{\mathrm{dm}}\left(\frac{\mu_2+0.4\mu_1}{\mu_2+\mu_1}\right)}. \tag{6.77}$$

The maximum packing value for bubbly flow is taken as unity (since bubbles can deform and packed densely such as in foams), i.e. $\alpha_{\mathrm{dm}} = 1$. When $\mu_2 \ll \mu_1$, which is the case in our study, the above relation reduces to

$$\mu_{\mathrm{m}} = \frac{\mu_1}{1 - \alpha_2}. \tag{6.78}$$

The drag similarity hypothesis being introduced allows writing the multiparticle drag coefficient in the same functional form as for a single-particle system, but now the Reynolds number is given in terms of μ_m rather than μ_1. Then, following the single-particle relations given in Section 6.7.5, the multiparticle drag coefficient in the spherical particle regime is calculated according to:

$$C^\alpha_{\mathrm{D,sphere}} = \frac{24}{Re_{\mathrm{r,m}}}(1 + 0.1\ Re^{0.75}_{\mathrm{r,m}}). \tag{6.79}$$

where $Re_{\mathrm{r,m}}$ is

$$Re_{\mathrm{r,m}} = \frac{\rho_1 d_\mathrm{e}|\mathbf{U}_2 - \mathbf{U}_1|}{\mu_\mathrm{m}}. \tag{6.80}$$

In the distorted particle regime, the form of the Ishii-Zuber modification is simply a multiplication factor to the single-particle coefficient, and for ellipsoidal bubbles

$$\begin{aligned} C^\alpha_{\mathrm{D,ellipse}} &= f(\alpha_2) C_{\mathrm{D,ellipse}} \\ &= \left[\frac{1 + 17.67(f^*)^{6/7}}{18.67 f^*}\right]^2 \left(\frac{2}{3}\sqrt{Eo}\right) \\ f^* &= (1 - \alpha_2)^{1.5}. \end{aligned} \tag{6.81}$$

At large diameters such as spherical cap bubbles, the wake and the boundary layer can overlap as result of large wake regions. Hence, bubbles can be entrained in the wake of other bubbles. This regime is called the churn-turbulent flow regime, and if the continuous phase turbulence is sufficiently high, the transition from the distorted particle regime to the churn-turbulent flow regime takes place at about $\alpha_2 = 0.3$ (Ishii and Hibiki, 2006). The drag coefficient for this regime is given as

$$\begin{aligned} C^\alpha_{\mathrm{D,cap}} &= f(\alpha_2) C_{\mathrm{D,cap}} \\ &= (1 - \alpha_2)^2\ \frac{8}{3}. \end{aligned} \tag{6.82}$$

Note that the effect of particle concentration in the churn-turbulent flow regime is opposite to that in the other flow regimes, that is, C_D decreases with increasing α_2.

In the simulations, the proper flow regime is selected automatically similar to the criteria given in Eq. 6.71, that is, according to

$$\begin{aligned} C^\alpha_{\mathrm{D,distorted}} &= \min\{C^\alpha_{\mathrm{D,ellipse}}, C^\alpha_{\mathrm{D,cap}}\} \\ C^\alpha_\mathrm{D} &= \max\{C^\alpha_{\mathrm{D,sphere}}, C^\alpha_{\mathrm{D,distorted}}\}. \end{aligned} \tag{6.83}$$

Laakkonen (2006) performed test simulations of an agitated gas–liquid reactor using the Ishii-Zuber multiparticle drag law. He reported that no considerable difference was found compared to the single-bubble correlations, because the swarm effect becomes significant only at relatively high gas holdups (> 20 vol-%).

6.7.8 Turbulence effects

The motion of particles in free-stream turbulence is influenced by both the particle characteristics and that of the turbulent flow. Small particles tend to follow the fluid

motion, hence fluctuate due to turbulence, provided that the particle relaxation time, $\tau_\mathrm{p} = \frac{4}{3}\frac{d_\mathrm{b}}{C_\mathrm{D}\langle|\mathbf{u}_\mathrm{r}|\rangle}\left(\frac{\rho_2}{\rho_1} + C_\mathrm{A}\right)$, is small relative to the period of turbulent oscillations (Clift et al., 1978). When $Re_\mathrm{b} \ll 1$, i.e. the creeping flow regime, the terminal velocity of particle relative to fluid is unaffected by turbulence and is superimposed on the turbulent fluctuations.

Rigid particles of diameter much larger than the scale of turbulence show relatively little fluctuation. Instead, turbulence alters the flow field in the vicinity of a particle, hence the drag on the particle can be affected. Reynolds number for such particles can be well above the creeping flow regime, and the free-stream turbulence may increase or decrease the mean drag (Clift et al., 1978). The most pronounced effect is that the critical Reynolds number at which the transition to turbulent boundary layer occurs (and consequently C_D drops abruptly) is reduced by turbulence (at turbulence-free flows, $Re_\mathrm{b,c} \approx 3.65 \times 10^5$, see Eq. 6.59). Free-stream turbulence can be described by the relative turbulence intensity I_r (cf. Eq 5.30),

$$I_\mathrm{r} = \frac{\sqrt{\overline{(u_1')^2}}}{U_\mathrm{r}} = \frac{\sqrt{\frac{2}{3}k_1}}{U_\mathrm{r}} = \frac{u_\mathrm{rms,1}}{U_\mathrm{r}}, \tag{6.84}$$

where $\sqrt{\overline{(u_1')^2}} = u_\mathrm{rms,1}$ is the r.m.s. fluctuating velocity and U_r is the mean relative velocity. It was suggested that fluctuating pressure gradients trigger the boundary layer transition, and experiments with entrained spheres showed that $Re_\mathrm{b,c}$ decreased down to 400 for $I_\mathrm{r} = 0.4$ (Clift et al., 1978). At the supercritical range (i.e. $Re_\mathrm{b} > Re_\mathrm{b,c}$), it was found that C_D for entrained spheres, that had dropped suddenly due to boundary layer transition, started rising again until reaching a maximum which increased with I_r. Generally, for a rigid particle of a given size falling at its terminal velocity, the terminal velocity can be increased or decreased, depending on $\sqrt{\overline{(u_1')^2}}$.

Experimental and modelling studies for bubbles showed that turbulence in the continuous phase causes the decrease of bubble slip velocity. Spelt and Biesheuvel (1997) performed numerical simulations of the motion of small bubbles ($d_\mathrm{e} \approx 1$ mm) in isotropic low-intensity turbulence in the range $I_\mathrm{r} \ll 1$, where the relative turbulence intensity is now defined in terms of the bubble terminal rise velocity in a still fluid,

$$I_\mathrm{r} = \frac{u_\mathrm{rms,1}}{U_\mathrm{T}}. \tag{6.85}$$

They found that the bubble rise velocity was significantly reduced, down to 50% of the value in still fluid. Later on, the experiments of Poorte and Biesheuvel (2002) from the same group confirmed those results. They studied the motion of nearly spherical bubbles in isotropic turbulent flow generated by an active grid. They found that the average bubble rise velocity was significantly reduced, up to 35 % (depending on the structure of the turbulence), compared with the quiescent conditions. They pointed out that minor differences in the bubble size may lead to substantial difference in the reduction of their mean rise velocities or in their r.m.s. fluctuation velocities in grid-generated turbulence. Therefore, bubbles of different sizes may contribute in very different ways to the dynamics of the turbulent bubbly flows.

Theoretical analysis of Spelt and Biesheuvel (1997) indicates the following mechanism for the above mentioned reduction of bubble rise velocity: Fluctuations in one component of the lateral vorticity results in bubbles to move in the opposite lateral direction

under the influence of lift forces, and this motion is directed towards the regions of largest vertical velocity difference between the bubble and the liquid. As bubbles on average move upwards, they tend to move to regions of highest downwards liquid velocity and lowest upward liquid velocity. This lateral motion causes bubbles to slow down, because (*i*) under the action of viscosity, bubbles adapt their speed to liquid velocity fluctuations, which on average are directed downwards along the bubble path, and (*ii*) the lateral motion itself induces a downward lift force. They note that when the turbulence intensity is higher ($I_\mathrm{r} > 0.2$), above described mechanism loses its effect and another, but weaker, mechanism, which is related to inertia forces other than lift, causes a reduction in bubble rise velocity. This mechanism seem to be associated with the eddy zones; presumably not due to trapping in vortex cores, but rather due to being transported towards the downward flowing edges of the eddies, where the velocity reduction is predominantly caused by inertia forces rather than viscous forces.

In a further study, Spelt and Biesheuvel (1998) addressed also the case of high Reynolds number bubbles ($d_\mathrm{e} \approx 1$ mm) in isotropic turbulence of higher intensity, $I_\mathrm{r} = \mathcal{O}(1)$, and large turbulent length scales with respect to the typical length scale for velocity relaxation of the bubbles, i.e. $L_1^\mathrm{t}/(\tau_\mathrm{b} U_\mathrm{T}) \gg 1$, where $\tau_\mathrm{b} = (d_\mathrm{b}/2)^2/(18\nu_1) = U_\mathrm{T}/(2g)$ is the time constant defined for the bubble. They found a good agreement with the results of their previous work (Spelt and Biesheuvel, 1997) when the intensities were small ($I_\mathrm{r} < 0.8$), thus lift was the dominant inertial force. As I_r increased beyond 0.8, inertial forces resulted in ever increasing intensities of the velocity fluctuations (which became isotropic for $I_\mathrm{r} \approx 0.5$) and decreasing integral time-scales. They also compared their results for bubbles with that for the solid particles. The difference between the dispersion of small solid particles and the dispersion of bubbles lies in two aspects as they noted: the random forcing of the bubbles by lift forces and the reaction forces to local fluid accelerations. They showed that the diffusion coefficients hardly differed, but the above mentioned inertia forces did make the diffusion processes very different. The bubble velocity fluctuations were much larger, while the correlation of their velocities was significantly less.

Next, we briefly explain several drag modification models proposed in literature to take into account the turbulence effects. In the present work, the effect of turbulence on drag is assumed to be separate from that of the gas fraction (swarm effect). Therefore, the turbulence modification model operates either on the single-particle drag coefficient or on the multi-particle one, depending on the choice.

Model of Bakker and van den Akker

Bakker and Van den Akker (1994) proposed a simple model, in which the turbulence effects are accounted for by using a standard drag correlation together with a modified bubble Reynolds number based on a modified viscosity. Thus, their method resembles the drag correction model of Ishii and Zuber (1979) for swarm effects. Their proposal is given as

$$Re_\mathrm{b} = \frac{\rho_1 |\mathbf{U}_\mathrm{slip}|\, d_\mathrm{b}}{\mu_1^*}, \tag{6.86}$$

where $\mathbf{U}_\mathrm{slip} = \mathbf{U}_2 - \mathbf{U}_1$ and the modified viscosity is expressed as the liquid viscosity

increased by adding a term proportional to the turbulent viscosity:

$$\begin{aligned}\mu_1^* &= \mu_1 + C^* \rho_1 \frac{k_1^2}{\varepsilon_1} \\ &= \mu_1 + \left(\frac{C^*}{C_\mu}\right) \mu_1^{\mathrm{t}}. \end{aligned} \tag{6.87}$$

The extra term consisting of the model constant C^* accounts for the decrease in slip velocity due to enhanced momentum transport around the bubble by turbulence. It is expected to be dependent on the ratio of the bubble size to the turbulent lenght scale. That is, for bubbles smaller than the Kolmogorov length scale, C^* should be zero and should increase with the bubble size. Owing to the fact that not all turbulent eddies of all length scales can influence the momentum transport around the bubble, $C^* < C_\mu$. In order to avoid further complications in their model, Bakker and Van den Akker (1994) assumed a constant value of $C^* = 0.02$, which was found to give the best fit. Therefore, the recommended value of the modified viscosity is $\mu_1^* = \mu_1 + (2/9)\mu_1^{\mathrm{t}}$. As a result of this assumption, the model does not properly account for bubble size effects and turbulence.

Model of Brucato et al.

Brucato et al. (1998b) studied the settling velocities of a suspension of solid particles ($d_{\mathrm{p}} = 0.063{-}0.5$ mm) under the influence of free-stream turbulence in a Couette–Taylor apparatus ($Re_{\mathrm{p}} < 40$). The drag coefficients were found to be significantly increased, up to 40 times for the largest particles at the highest turbulence intensity. They used a novel experimental technique based on residence time measurements, which allows the direct measurement of average particle settling velocities in turbulent media and in turn, average particle drag coefficients (i.e. assuming gravity only as body force and zero average liquid velocity, C_{D} and the settling velocity is correlated via Eq. 6.96. Note that due to the quadratic relation, a 50 % decrease in the terminal settling velocity implies a four fold increase in C_{D}).

They emphasised that the reasons for the increase in drag due to free-stream turbulence were not fully understood yet. Among the various mechanisms being suggested, they found worth mentioning the two, for which there is experimental evidence:

- decrease in form drag due to wake modification
- a particle moving in a turbulent field is subjected to continuous accelerations due to the nonlinear relation between velocity and drag, and/or due to the added resistance of the “virtual mass” acceleration

Furthermore, they found that the model proposed previously by Magelli et al. (1990) describes their experimental data remarkably well. Magelli et al. measured axial solids concentration in multiple impeller tanks and derived average settling velocities by incorporating a simple one-dimensional sedimentation-dispersion model, where the axial turbulent dispersion coefficient for solids was assumed to be equal to that of the liquid, in line with their findings. They suggested that the ratio of the average settling velocity in the turbulent field to that in the still fluid, $U_{\mathrm{r,t}}/U_{\mathrm{r,still}}$, is uniquely correlated

with the ratio of the particle diameter to the Kolmogorov length scale of dissipative eddies, d_p/η_1, where

$$\eta_1 = \left(\frac{\nu_1^3}{\overline{\varepsilon}_1}\right)^{1/4}, \tag{6.88}$$

and $\overline{\varepsilon}_1$ is the mean energy dissipation rate per unit mass of liquid calculated from the overall mechanical power dissipation P (i.e. $\overline{\varepsilon}_1 = P/\rho_1 \mathcal{V}_1$, assuming that effect of solids concentration on power number is negligible). They found that, for small particles ($d_\mathrm{p} < 5 - 10\,\eta_1$), the settling velocity was not affected by turbulence, attributed to the negligible interaction between the particles and the energy dissipating eddies. For larger particles ($d_\mathrm{p} > 10\,\eta_1$), a significant decrease in settling velocity was observed (up to 60 %).

Brucato et al. calculated the values of η_1 based on the estimation of mechanical power dissipated by the shaft in their system, using a relationship for the torque on the shaft and the friction factor. From the overall power consumption, the corresponding average dissipation values were estimated assuming that the effect of the solids was negligible and the whole dissipation was concentrated in the liquid volume between the shaft and the outer cylinder. Plotting $U_{\mathrm{r,t}}/U_{\mathrm{r,still}}$ versus d_p/η_1 showed that the data points gather together well, therefore provides a confirmation to the proposition of Magelli et al.

An interesting observation was that the data points for irregular shaped particles and smooth spherical particles felt on to the same line, implying that particle shape does not have a significant effect on the drag increase phenomenon by turbulence. Moreover, the data of Magelli et al. was also in good agreement with their data points. As their system was entirely different (high aspect ratio tank with 4 Rushton turbines) and much larger, for which the macroscale turbulence characteristics was completely different, this was interpreted as the macroscale turbulence was not involved in the drag increase phenomenon. The same observation can be made according to Brucato et al., when the data obtained with radial pumping impellers and axial pumping impellers are plotted with respect to d_p/η_1, despite the substantially different macroscale characteristics of the turbulent fields generated. These findings imply that particle drags and terminal velocities are not expected to be affected by the gross recirculation zones characteristic to stirred tanks, provided that the particle size is sufficiently small.

Another point worth mentioning is that their experimental data indicates that the settling velocity of small particles, which are in the Stokes' regime when moving in a still fluid, is reduced by turbulence. This is contrary to the usually accepted view given in the beginning of this section, that is, in the creeping flow regime, the terminal velocity is unaffected by turbulence.

In an attempt to find a better correlation for the data obtained, Brucato et al. realised that a direct correlation was possible if the data was plotted in terms of normalised C_D reduction with respect to the ratio d_p/η_1 (in contrast to η_1/d_p as proposed by Magelli et al.). Resulting log–log plot showed that their data gather remarkably well on a straight line of slope 3 thus the following simple cubic law was proposed:

$$\frac{C_\mathrm{D}^\mathrm{t} - C_\mathrm{D}}{C_\mathrm{D}} = K\left(\frac{d_\mathrm{p}}{\eta_1}\right)^3, \tag{6.89}$$

where $K = 8.76 \times 10^{-4}$ is the correlation constant and C_D^t is the drag coefficient in a

turbulent fluid. Note that the drag coefficient, being related to the square of settling velocities (via Eq. 6.96), is susceptible to larger uncertainties than U_r, particularly for C_D^t values close to C_D. Given the uncertainties in accounting for the particle diameter, especially for the smallest particles for which the estimated error was not negligible, the authors indicated that the constant K might slightly depend on particle diameter.

In line with the above remark, Lane et al. (2000) proposed a value two orders of magnitude smaller, namely $K = 6.5 \times 10^{-6}$, based on his bubbly flow simulations of the stirred tank reactor that is also investigated here. Simulations were performed for only one case (for impeller speed of 180 rpm and gas flow rate of 0.00164 m^3/s, i.e. the Case 1 in this study; see Table 9.2). Therefore, no claims have been made on the generality of their method. The same K value was also used by other authors (Khopkar and Ranade, 2006; Zhang et al., 2008). We also used this recommended value for K in our implementation of the Brucato model.

Finally, it should be noted that, despite the highly non-uniform distribution of ε_1 in the Couette–Taylor apparatus, Kolmogorov microscale η_1 used in the original Brucato model is the global average value, since it is based on the global average energy dissipation rate, $\overline{\varepsilon}_1$, calculated from the overall power input. Therefore, the applicability of the model to other configurations is questionable.

Model of Lane et al.

In a later study, Lane (2005a) proposed another correlation based on data for both solid particles and gas bubbles taken from the studies of Brucato et al. (1998b), Spelt and Biesheuvel (1997) and Poorte and Biesheuvel (2002). Their model follows from the suggestion of Spelt and Biesheuvel (1997) that the motion of gas bubbles through a turbulent flow can be characterised by three dimensionless groups:

$$I_r = \frac{u_{rms,1}}{U_T}, \quad \mu^* = \frac{L_1^t}{\tau_p U_T}, \quad \frac{\tau_1^t}{\tau_p}, \tag{6.90}$$

where the integral length scale L_1^t (see Eq. 5.8), being a measure of the eddy size in the flow, characterises the spatial variation of the turbulence. The integral time scale τ_1^t (see Eq. 5.7) is a measure of the temporal variation of the turbulence. For relatively small bubble rise velocities, the measure of this being the ratio $I_r = u_{rms,1}/U_T$, the dimensionless group τ_1^t/τ_p (see Eq. 5.32), often called the Stokes number, shows how fast the bubble responds to the turbulent velocity fluctuations. Spelt and Biesheuvel originally used the vertical integral scale $L_{\parallel}^t$ rather than L_1^t. However, for isotropic turbulence, the integral length and time scales are related to each other as $L_1^t = \tau_1^t u_{rms,1}$. Therefore, the ratio of first two dimensionless groups results in the reciprocal of the last group, reducing the parameters to

$$\frac{I_r}{\mu^*} = \frac{\tau_p}{\tau_1^t}. \tag{6.91}$$

Hence, Lane used this ratio of characteristic time scales as the correlating parameter in his model. Plotting the data from various sources as the ratio of actual slip velocity in turbulent flow to terminal settling/rise velocity in stagnant conditions, U_{slip}/U_T, versus τ_p/τ_1^t, they found that all data fell on approximately the same line. There

was an apparent continuous decrease in slip velocity with increasing τ_p/τ_1^t. However, considering the fact that for very large values of this ratio, the bubble does not respond to turbulence, i.e. as $\tau_p/\tau_1^t \to \infty$, $U_{slip}/U_T \to 1$, they anticipated that the curve must have a minimum point beyond which it increases again to satisfy the above mentioned upper limit. Although the precise shape of the curve was unknown, they proposed the following correlation, which extrapolates consistently with this upper limit and led to good results in their CFD model:

$$\frac{U_{slip}}{U_T} = 1 - 1.4\left(\frac{\tau_p}{\tau_1^t}\right)^{0.7} \exp\left[-0.6\left(\frac{\tau_p}{\tau_1^t}\right)\right]. \tag{6.92}$$

This correlation was derived such that at low values of τ_p/τ_1^t, it follows preferentially the data for bubbles rather than that for solids. The corresponding relation for the ratio of the drag coefficients can be given by

$$\frac{C_D^t}{C_D} = \left(\frac{U_{slip}}{U_T}\right)^{-2} = \left\{1 - 1.4\left(\frac{\tau_p}{\tau_1^t}\right)^{0.7} \exp\left[-0.6\left(\frac{\tau_p}{\tau_1^t}\right)\right]\right\}^{-2}. \tag{6.93}$$

6.7.9 Terminal rise velocity

The steady terminal velocity, U_T, of a rigid bubble of arbitrary shape in free rise under the action of gravity can be calculated from a force balance. We first assume that the drag force is the only relevant interfacial force or the bubble moves in an otherwise stagnant infinite fluid (i.e. $\tilde{\mathbf{u}}_{\mathbf{x}_b} = 0$). Then, at steady-state, the hydrostatic pressure (buoyancy) and body forces acting should be balanced by the drag forces, i.e. $\mathbf{f}_{hp} + \mathbf{f}_g + \mathbf{f}_D = 0$. Thus, from relations $\mathbf{f}_{hp} + \mathbf{f}_g = -(\pi d_e^3/6)(\rho_1 - \rho_2)\mathbf{g}$ and $\mathbf{f}_D = -\frac{1}{2}\rho_1 \mathcal{A}_{b,\perp} C_D \mathbf{u}_r|\mathbf{u}_r|$, and assuming that $\mathcal{A}_{b,\perp} \approx \pi d_e^2/4$, we obtain

$$U_T = |\mathbf{u}_r| = \sqrt{\left|\frac{4}{3}\frac{\Delta\rho}{\rho_1}\mathbf{g}\frac{d_e}{C_D}\right|}, \tag{6.94}$$

where $\mathbf{u}_r = \mathbf{v} - \tilde{\mathbf{u}}_{\mathbf{x}_b}$. Inserting the Stokes' drag, $24/Re_b$, this relation gives

$$U_{T,Stokes} = \frac{g|\Delta\rho|d_e^2}{18\mu_1}. \tag{6.95}$$

For a clean spherical bubble in inertial regime, the terminal velocity is half the Stokes value, if one uses the approximation of Levic (i.e. $C_D = 48/Re_b$). Rearranging Eq. 6.94, one can obtain

$$C_D = \frac{4}{3}\frac{g d_e|\Delta\rho|}{\rho_1}\frac{1}{U_T^2} \tag{6.96}$$

$$= \frac{4}{3}\frac{MoRe_b^4}{We^3} = \frac{4}{3}\frac{Eo}{We}, \tag{6.97}$$

In Fig. 6.1(b), we plotted the terminal velocities for air bubbles in water according to the above relation using different drag correlations.

Figures

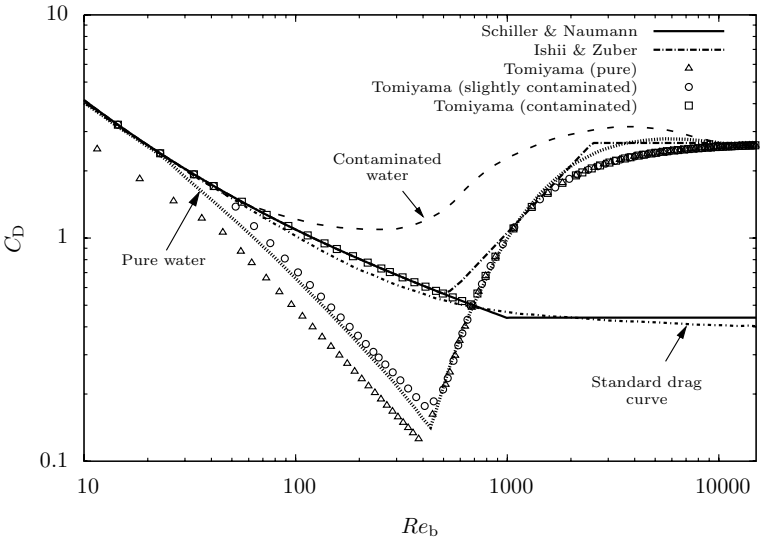

(a) Drag coefficients

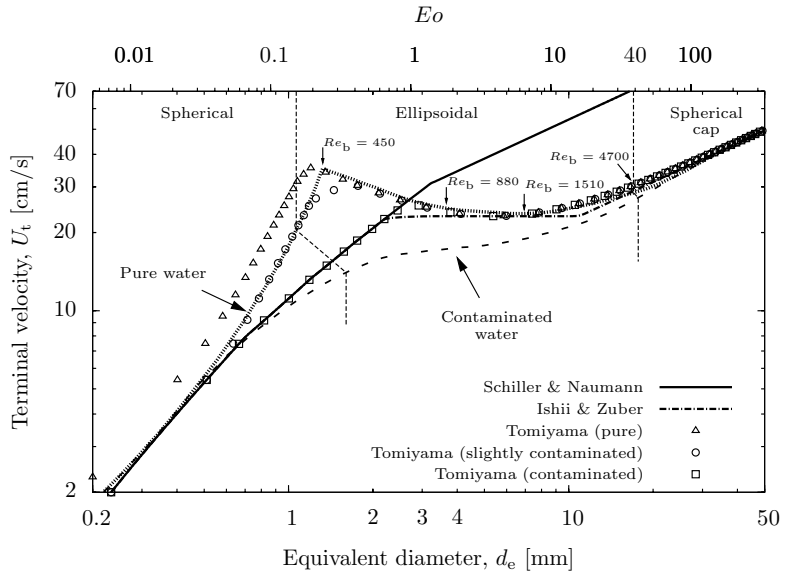

(b) Terminal velocities

Figure 6.1: Drag coefficients and corresponding terminal velocities for a single air bubble rising in infinite stagnant water, as calculated from various drag laws and Eq. 6.94. Experimental data for rigid spheres (i.e. the standard drag curve), for air bubbles in pure and contaminated water (at 20 °C), and bubble shape regimes are from Clift et al. (1978).

Chapter 7

Modelling of the impeller

The presence of solid parts moving in the tank requires consideration in the modelling. When the flow is induced solely by shear forces (e.g. the motion of the impeller disk or shaft inducing flow in the direction parallel to the wall), specifying simply a wall velocity boundary condition is sufficient to model the flow. However, when there is also a normal component of the motion where the flow is induced by normal forces as well (e.g. the motion of the impeller blades inducing flow in the direction normal to the wall), a special treatment is required to capture the effect of those normal forces. This can be accomplished by specifying a moving reference frame or moving/deforming mesh in the region containing the moving wall. The models that have been used in this study to serve this purpose are addressed in this chapter.

7.1 Equation of motion relative to steadily rotating axes

When there are no angular-dependent internals (e.g. baffles, inlet/outlet ports, etc.) in a cylindrical vessel stirred at constant angular velocity, it is possible to have a steady-state solution to the equations of fluid motion written with respect to a rotating frame attached to the impeller. This is, of course, justified only when the turbulence is modelled by the RANS approach (rather than being resolved), there are no circumferentially non-uniform variations in the flow and the gas–liquid flow regime does not exhibit strong transient characteristics in the mean flow. However, even when there are flow transients, the unsteady mass and momentum equations transformed to a rotating frame can be employed, because the unsteadiness is not originated from the interaction between stationary and rotating parts (i.e. impeller–baffle interaction). The mass and momentum equations then are in the same form with those written in an absolute (stationary) frame (i.e. Eq. 4.20 and 4.34) except an additional term $\mathbf{F}_{\mathrm{e},k,\mathrm{R}}$ in the momentum equation:

$$\frac{\partial}{\partial t}(\alpha_k \rho_k) + \nabla \cdot (\alpha_k \rho_k \mathbf{U}_{k,\mathrm{R}}) = S_k, \tag{7.1}$$

$$\frac{\partial}{\partial t}(\alpha_k \rho_k \mathbf{U}_{k,\mathrm{R}}) + \nabla \cdot (\alpha_k \rho_k \mathbf{U}_{k,\mathrm{R}} \mathbf{U}_{k,\mathrm{R}}) = -\alpha_k \nabla P + \nabla \cdot \alpha_k (\underline{\underline{\mathbf{T}}}_{k,\mathrm{R}} + \underline{\underline{\mathbf{\Sigma}}}^{\mathrm{Re}}_{k,\mathrm{R}}) + \mathbf{M}'_{k,\mathrm{R}} + \alpha_k \rho_k \mathbf{g} + \mathbf{S}_{k,\mathrm{R}} + \mathbf{F}_{\mathrm{e},k,\mathrm{R}}. \tag{7.2}$$

Above, all the terms with the subscript R are defined in terms of the relative velocity $\mathbf{U}_{k,\mathrm{R}}$ with respect to the rotating frame:

$$\mathbf{U}_{k,\mathrm{R}} = \mathbf{U}_k - \mathbf{\Omega} \times \mathbf{r}, \tag{7.3}$$

where $\mathbf{\Omega}$ is the angular velocity vector of the coordinate system relative to an inertial frame and $\mathbf{r}$ denotes the position vector from the origin of the rotating frame. Hence, $\mathbf{\Omega} \times \mathbf{r}$ is the "whirl" velocity (velocity due to the moving frame). The mean velocity in the inertial frame is denoted as $\mathbf{U}_k$ as usual.

Due to the frame rotation, the Coriolis and centrifugal accelerations arise and therefore the corresponding fictitious body forces are supposed to act on the fluid. Those are represented by the volumetric external force term $\mathbf{F}_{\mathrm{e},k,\mathrm{R}}$ in Eq. 7.2:

$$\mathbf{F}_{\mathrm{e},k,\mathrm{R}} = \mathbf{F}_{k,\mathrm{Coriolis}} + \mathbf{F}_{k,\mathrm{centrifugal}}, \tag{7.4}$$

where

$$\mathbf{F}_{k,\mathrm{Coriolis}} = -\alpha_k \rho_k \left[2\mathbf{\Omega} \times \mathbf{U}_{k,\mathrm{R}}\right] \tag{7.5}$$

$$\mathbf{F}_{k,\mathrm{centrifugal}} = -\alpha_k \rho_k \left[\mathbf{\Omega} \times (\mathbf{\Omega} \times \mathbf{r})\right] = -\alpha_k \rho_k \frac{1}{2} \nabla \left|\mathbf{\Omega} \times \mathbf{r}\right|^2. \tag{7.6}$$

Above given equations can be derived in the following way. Take any vector quantity, say $\mathbf{f} = f_1\mathbf{i} + f_2\mathbf{j} + f_3\mathbf{k}$, referred to a rotating frame with orthogonal unit vectors $\mathbf{i}, \mathbf{j}, \mathbf{k}$ and rotating about point O with angular velocity $\mathbf{\Omega}$. The change of $\mathbf{f}$ with respect to time as seen by an inertial observer at O, $[d\mathbf{f}/dt]_{\mathrm{I}}$, is then due to both change of the components f_1, f_2, f_3 in the moving frame and change of the unit vectors $\mathbf{i}, \mathbf{j}, \mathbf{k}$ due to frame rotation and given by

$$\left[\frac{d\mathbf{f}}{dt}\right]_{\mathrm{I}} = \sum_{\mathbf{i}} \left(\frac{df_1}{dt}\mathbf{i} + f_1 \frac{d\mathbf{i}}{dt}\right) = \sum_{\mathbf{i}} \left(\frac{df_1}{dt}\mathbf{i} + f_1 \mathbf{\Omega} \times \mathbf{i}\right)$$

$$\left[\frac{d\mathbf{f}}{dt}\right]_{\mathrm{I}} = \left[\frac{d\mathbf{f}}{dt}\right]_{\mathrm{R}} + \mathbf{\Omega} \times \mathbf{f}, \tag{7.7}$$

where $[d\mathbf{f}/dt]_{\mathrm{R}}$ denotes the rate of change of $\mathbf{f}$ as seen by an observer in the rotating frame. Applying this relation for the position vector $\mathbf{r}$ of a fluid element relative to O,

$$\left[\frac{d\mathbf{r}}{dt}\right]_{\mathrm{I}} = \left[\frac{d\mathbf{r}}{dt}\right]_{\mathrm{R}} + \mathbf{\Omega} \times \mathbf{r}$$

$$\mathbf{U}_{\mathrm{I}} = \mathbf{U}_{\mathrm{R}} + \mathbf{\Omega} \times \mathbf{r}, \tag{7.8}$$

gives the relation in Eq. 7.3 stating that the velocity of a fluid element seen in the absolute frame is equal to the velocity observed in the rotating frame augmented by the velocity imparted by the solid-body rotation $\mathbf{\Omega} \times \mathbf{r}$. Here we skip the phase index k for clarity. Repeating the same operation now for the inertial frame velocity $\mathbf{U}_{\mathrm{I}}$, one obtains the relation between the absolute and relative accelerations, where the Coriolis

and centrifugal acceleration terms arise (assuming no translational acceleration of the rotating frame and $\boldsymbol{\Omega}$ is constant):

$$\begin{aligned}\left[\frac{d^2\mathbf{r}}{dt^2}\right]_\mathrm{I} = \left[\frac{d\mathbf{U}_\mathrm{I}}{dt}\right]_\mathrm{I} &= \left[\frac{d\mathbf{U}_\mathrm{I}}{dt}\right]_\mathrm{R} + \boldsymbol{\Omega}\times\mathbf{U}_\mathrm{I} \\ &= \left[\frac{d(\mathbf{U}_\mathrm{R}+\boldsymbol{\Omega}\times\mathbf{r})}{dt}\right]_\mathrm{R} + \boldsymbol{\Omega}\times(\mathbf{U}_\mathrm{R}+\boldsymbol{\Omega}\times\mathbf{r}) \\ &= \left[\frac{d\mathbf{U}_\mathrm{R}}{dt}\right]_\mathrm{R} + \frac{d\boldsymbol{\Omega}}{dt}\times\mathbf{r} + \boldsymbol{\Omega}\times\left[\frac{d\mathbf{r}}{dt}\right]_\mathrm{R} + \boldsymbol{\Omega}\times(\mathbf{U}_\mathrm{R}+\boldsymbol{\Omega}\times\mathbf{r}) \\ \left[\frac{d\mathbf{U}_\mathrm{R}}{dt}\right]_\mathrm{R} &= \left[\frac{d\mathbf{U}_\mathrm{I}}{dt}\right]_\mathrm{I} - 2\boldsymbol{\Omega}\times\mathbf{U}_\mathrm{R} - \boldsymbol{\Omega}\times(\boldsymbol{\Omega}\times\mathbf{r}). \end{aligned} \tag{7.9}$$

Note that the time rate of change of $\boldsymbol{\Omega}$ is observed the same in both frames, since $\boldsymbol{\Omega}\times\boldsymbol{\Omega}$ identically vanishes when Eq. 7.7 is applied for $\boldsymbol{\Omega}$. Moreover, the spatial gradients, the gradients of the strain-rate tensor and the divergence of the velocity are invariant in the rotating frame. Thus the pressure gradient, viscous and velocity divergence terms are unchanged, and so the continuity equation.

The centrifugal force can be written as the gradient of a scalar, $-\alpha_k\rho_k\frac{1}{2}\nabla|\boldsymbol{\Omega}\times\mathbf{r}|^2$, and its effect is essentially equivalent to a contribution to the pressure (similar to gravity) provided that the fluid has an uniform density. Hence, it is sometimes implicitly included in the so-called "modified pressure" term together with the gravity. On the other hand, the Coriolis force has a different effect on the flow. It is a deflecting force acting on perpendicular direction to both the axis of rotation and the local velocity vector, thus does no work. It changes the direction of the component of $\mathbf{U}_{k,\mathrm{R}}$ perpendicular to $\boldsymbol{\Omega}$.

Furthermore, the centrifugal force applies to a fluid element even if it is motionless relative to the rotating frame. That is, inserting $\mathbf{U}_\mathrm{R}=0$ in Eq. 7.8 and 7.9, we obtain $\mathbf{U}_\mathrm{I}=\boldsymbol{\Omega}\times\mathbf{r}$ and $[d\mathbf{U}_\mathrm{I}/dt]_\mathrm{I}=\boldsymbol{\Omega}\times(\boldsymbol{\Omega}\times\mathbf{r})$. However, the Coriolis force applies only when the fluid element is in relative motion with respect to the rotating frame.

7.1.1 Lift and added mass forces in a rotating frame

Due to the frame rotation, additional terms arise in the lift and added mass forces. Performing the velocity transformation according to Eq. 7.3 on the inertial frame formulation of the mean lift force (i.e. Eq. 6.41), the following form is obtained:

$$\begin{aligned}\mathbf{M}_{2,\mathrm{L}} = -\mathbf{M}_{1,\mathrm{L}} &= -\alpha_2\rho_1 C_\mathrm{L}(\mathbf{U}_2-\mathbf{U}_1)\times(\nabla\times\mathbf{U}_1) \\ &= -\alpha_2\rho_1 C_\mathrm{L}(\mathbf{U}_{2,\mathrm{R}}+\boldsymbol{\Omega}\times\mathbf{r}-\mathbf{U}_{1,\mathrm{R}}-\boldsymbol{\Omega}\times\mathbf{r})\times(\nabla\times[\mathbf{U}_{1,\mathrm{R}}+\boldsymbol{\Omega}\times\mathbf{r}]) \\ &= -\alpha_2\rho_1 C_\mathrm{L}(\mathbf{U}_{2,\mathrm{R}}-\mathbf{U}_{1,\mathrm{R}})\times(\nabla\times\mathbf{U}_{1,\mathrm{R}}+2\boldsymbol{\Omega}). \end{aligned} \tag{7.10}$$

It has the same form as that of the inertial frame except an additional term $2\boldsymbol{\Omega}=\nabla\times\boldsymbol{\Omega}\times\mathbf{r}$ denoting the vorticity imparted to the fluid due to the frame rotation. Similar to the inertial formulation, the term $\overline{\boldsymbol{\omega}}_{1,\mathrm{R}}=\nabla\times\mathbf{U}_{1,\mathrm{R}}$ now represents the mean vorticity vector with respect to the rotating frame, i.e. the relative vorticity.

The mean added mass force in a rotating frame can be derived by substituting the relative accelerations for the liquid and gas phases (using Eq. 7.9) into the inertial

frame formulation given in Eq. 6.38:

$$\begin{aligned}\mathbf{M}_{2,\mathrm{A}} = -\mathbf{M}_{1,\mathrm{A}} &= -\alpha_2\rho_1 C_\mathrm{A}\left[\frac{D_2\mathbf{U}_2}{Dt} - \frac{D_1\mathbf{U}_1}{Dt}\right] \\ &= -\alpha_2\rho_1 C_\mathrm{A}\left[\frac{D_{2,\mathrm{R}}\mathbf{U}_{2,\mathrm{R}}}{Dt} + 2\boldsymbol{\Omega}\times\mathbf{U}_{2,\mathrm{R}} + \boldsymbol{\Omega}\times(\boldsymbol{\Omega}\times\mathbf{r})\right. \\ &\quad \left. - \frac{D_{1,\mathrm{R}}\mathbf{U}_{1,\mathrm{R}}}{Dt} - 2\boldsymbol{\Omega}\times\mathbf{U}_{1,\mathrm{R}} - \boldsymbol{\Omega}\times(\boldsymbol{\Omega}\times\mathbf{r})\right] \\ &= -\alpha_2\rho_1 C_\mathrm{A}\left[\frac{D_{2,\mathrm{R}}\mathbf{U}_{2,\mathrm{R}}}{Dt} - \frac{D_{1,\mathrm{R}}\mathbf{U}_{1,\mathrm{R}}}{Dt} + 2\boldsymbol{\Omega}\times(\mathbf{U}_{2,\mathrm{R}} - \mathbf{U}_{1,\mathrm{R}})\right].\end{aligned} \tag{7.11}$$

The rotating frame formulation given above has now an additional term accounting for the Coriolis effect, i.e. $2\boldsymbol{\Omega}\times(\mathbf{U}_{2,\mathrm{R}} - \mathbf{U}_{1,\mathrm{R}})$.

7.1.2 Relative and absolute velocity formulations

In Fluent, the momentum equation given in Eq. 7.2 is called the relative velocity formulation. An equivalent form can be derived from this, where the absolute velocity $\mathbf{U}_k$ is used as the dependent variable (Fluent, 2009). The resulting form, i.e. the absolute velocity formulation, is

$$\begin{aligned}\frac{\partial}{\partial t}(\alpha_k\rho_k\mathbf{U}_k) + \nabla\cdot(\alpha_k\rho_k\mathbf{U}_{k,\mathrm{R}}\mathbf{U}_k) = &-\alpha_k\nabla P + \nabla\cdot\alpha_k(\underline{\underline{\mathbf{T}}}_k + \underline{\underline{\boldsymbol{\Sigma}}}_k^{\mathrm{Re}}) + \mathbf{M}'_k \\ &+ \alpha_k\rho_k\mathbf{g} + \mathbf{S}_k - \alpha_k\rho_k\left(\boldsymbol{\Omega}\times\mathbf{U}_k\right),\end{aligned} \tag{7.12}$$

where the Coriolis and centrifugal forces are reduced to a single term according to $-\alpha_k\rho_k\left[\boldsymbol{\Omega}\times\mathbf{U}_{k,\mathrm{R}} + \boldsymbol{\Omega}\times(\boldsymbol{\Omega}\times\mathbf{r})\right] = -\alpha_k\rho_k\left(\boldsymbol{\Omega}\times\mathbf{U}_k\right)$.

In order to reduce the numerical diffusion in the solution, it is recommended to use a velocity formulation that leads to smallest velocities in the corresponding frame for the majority of the flow domain. Since the impeller size is relatively small in this study ($D = T/3$) and the solid body rotation is diminished by the baffles, it is expected that, in most of the domain, the fluid has a low swirl component. Therefore, we used the absolute velocity formulation as given in Eq. 7.12.

7.2 Modelling of the impeller in baffled tanks

In the presence of baffles in a stirred tank, the flow is transient with respect to both stationary and rotating reference frames. Therefore, special consideration is needed for the modelling of moving parts.

There are several methods proposed in literature to tackle this problem (for a review, see e.g. Brucato et al. (1998a) and Marshall and Bakker (2003)). One of the simplest method is to use a fixed coordinate system, and to model the impeller implicitly by imposing boundary conditions in the impeller swept region. The main disadvantage of this method is that the imposed boundary conditions are based on experimental data

or on an empirical model. As in the case of multiphase flows, this data might not be readily available (Deen, 2001).

Another approach is the so-called snapshot method. Since the impeller is modeled by introducing source terms into the momentum equations, availability of the experimental data is not an issue in this method. Steady-state simulations are performed for several impeller positions to describe the flow, and ensemble averaging is employed over the simulated impeller positions. Ranade (1997) and Ranade et al. (2002b) used this method for a stirred tank with a Rushton turbine together with $k - \varepsilon$ model for the turbulence and found good agreement with the experimental data. Derksen and van den Akker (1999) also used source terms to describe the impeller rotation. By performing transient Large Eddy Simulations (LES) to account for turbulence, they obtained very good results.

There are more advanced methods, where the impeller is modeled explicitly. These can be divided into two groups, namely the steady-state and transient methods, in the order of complexity. Multiple reference frames model is maybe the most widely used one among the steady-state group, where rotating and stationary reference frames are employed in the impeller region and in the tank bulk, respectively.

Among the transient models are the sliding and deforming mesh techniques. In the former one, the inner mesh surrounding the impeller slides past the outer mesh, hence the name sliding mesh model. Whereas in the latter one, the mesh is deformed or remeshed at every time step according to the new impeller position.

The multiple reference frames and the sliding mesh models were used with success in great majority of the recent literature. As they were also used in this study, we shall briefly explain them here.

7.2.1 Sliding mesh method

The relative motion between the impeller and baffles gives rise to transient interactions in the flow, such as the potential interactions due to pressure waves propagating both upstream and downstream and the wake interactions due to wakes from upstream blade convecting downstream. The extent of these interactions is expected to be high especially when the impeller diameter is large compared with the tank diameter. There are also low-frequency (i.e. lower than impeller frequency) flow instabilities observed in stirred tanks that involve slow asymmetric wobble of material or momentum across the tank (Marshall and Bakker, 2003). Moreover, one can be interested to resolve start-up transients or time-periodic flow details. Resolving those effects requires transient modelling of the impeller, such as in the sliding mesh (SM) technique, however with the downside of significantly higher computational costs.

In the SM technique, part of the computational domain moves relative to the stationary frame. That is, a selected mesh region encompassing the impeller is disconnected from the mesh of the tank bulk region and slides past the tank mesh. This motion is not continuous, but happens in discrete time steps. At each time step, the information exchange takes place between those separate domains at their common boundary, which is called the grid interface. This ensures the coupling of the rotating and stationary domains at all times.

For a rigid body rotation with constant speed, the time rate of change of any grid point in the moving (rotating) domain with the position vector $\mathbf{r}_{\text{grid}}$ is given by

$$\left[\frac{d\mathbf{r}_{\text{grid}}}{dt}\right]_{\text{I}} = \boldsymbol{\Omega} \times \mathbf{r}_{\text{grid}} = \mathbf{u}_{\text{grid}}, \tag{7.13}$$

which is known as the grid speed. The mass and momentum equations in the moving domain, written with respect to the stationary reference frame, are given in the following form similar to those written for the stationary domain, i.e. Eq. 4.20 and 4.34:

$$\frac{\mathcal{D}_{\text{grid}}}{\mathcal{D}t}(\alpha_k \rho_k) + \nabla \cdot [\alpha_k \rho_k (\mathbf{U}_k - \mathbf{u}_{\text{grid}})] = S_k, \tag{7.14}$$

$$\frac{\mathcal{D}_{\text{grid}}}{\mathcal{D}t}(\alpha_k \rho_k \mathbf{U}_k) + \nabla \cdot [\alpha_k \rho_k (\mathbf{U}_k - \mathbf{u}_{\text{grid}})\mathbf{U}_k] = -\alpha_k \nabla P + \nabla \cdot \alpha_k (\underline{\underline{\mathbf{T}}}_k + \underline{\underline{\boldsymbol{\Sigma}}}_k^{\text{Re}}) + \mathbf{M}'_k + \alpha_k \rho_k \mathbf{g} + \mathbf{S}_k + \mathbf{F}_{\text{e},k}. \tag{7.15}$$

Here, the following points should be emphasised:

- $\mathcal{D}_{\text{grid}}/\mathcal{D}t$ is the differentiation with respect to time following the moving domain,
- convecting velocity is the relative velocity, $\mathbf{U}_k - \mathbf{u}_{\text{grid}}$,
- all spatial derivatives are computed relative to the stationary frame as mentioned,
- solution of the equations given above involves surface and volume integral operations on the control volumes (grid cells), $\mathcal{V}_{\text{cell}}$, and at the boundary surface of control volumes, $\mathbf{S}_{\text{cell}}$. Since the mesh is not deforming, $\mathcal{V}_{\text{cell}}$ is constant. However, as the control volume moves, the orientation of area vectors change, hence $\mathbf{S}_{\text{cell}} = \mathbf{S}_{\text{cell}}(t)$.

Due to the relative discrete motion of the adjacent grids, the grid faces are not necessarily aligned on the grid interface. This necessitates the re-computation of the fluxes across the two non-conformal interface zones (i.e. the interface cell faces belonging to rotating and stationary grid domains) of the grid interface at every time step. To compute the interface flux, the intersection between the two interface zones is determined at each time step. Then the fluxes are interpolated from the resulting intersection faces, rather than from the original interface zone faces themselves (Fluent, 2009). For stirred tank flows, the convergence is achieved when the solution becomes time-periodic.

The SM is the most rigorous and accurate model available in Fluent. However, it is CPU intensive and may require many cycles (about 15-20 full revolutions of the grid) to reach steady-state.

7.2.2 Multiple reference frames method

An alternative steady-state approach, that circumvents the high computational demands associated with the SM is the multiple reference frames (MRF) method introduced by Luo et al. (1994). In the MRF approach, the computational domain is divided into two zones similar to SM methodology. At the inner zone surrounding the

impeller, the mass and momentum equations are solved in a rotating reference frame attached to the impeller. Thus, Eq. 7.1 and 7.2 (or 7.12 depending on the velocity formulation) are solved as given earlier. At the outer zone comprising the bulk of the tank with side walls and baffles, a stationary reference frame is specified. Therefore, no special treatment is required in this region and the governing equations being solved are the conventional ones (i.e. Eq. 4.20 and 4.34). Note that all the solid parts are at rest at their corresponding zone's frame, hence the flow is assumed to be steady in each zone (with the exception of the impeller shaft in the outer zone, which, however, is defined by the wall velocity condition and does not require transient modelling). Solving unsteady equations, however, is still possible as mentioned earlier, in order to resolve transients that are not originated from the interaction between stationary and rotating parts.

At the interface between the rotating and stationary zones, steady flow conditions are assumed. Hence, the velocity at the interface is the same (in inertial frame) for both zones. Full unsteady simulations of single-phase turbulent flow in a baffled tank stirred by a Rushton turbine showed that such a condition existed for a particular radial location of the interface (Luo et al., 1993, 1994). The location lies approximately at the midway between impeller blade tip and the baffle. We also used this midway location for the grid interface both for SM and MRF simulations.

In order to compute fluxes (mass, momentum, etc.) and facilitate implicit coupling between the zones, transformations of the velocity vector and velocity gradients are required across the interface (scalar quantities are frame-independent, hence transferred locally without any change). Fluent imposes the continuity of the inertial frame velocity $\mathbf{U}_k$ across the interface to ensure correct local values of velocity at the adjacent zones.

The MRF interface treatment in Fluent takes a different form depending on the choice of the velocity formulation. When the relative velocity formulation is chosen, velocities are calculated with respect to the corresponding zone's frame. At the interface, transformation of velocities from rotating frame to inertial frame is performed according to

$$\mathbf{U}_k = \mathbf{U}_{k,\mathrm{R}} + \boldsymbol{\Omega} \times \mathbf{r}, \tag{7.16}$$

which is the rearrangement of Eq. 7.3. Transformation of velocity gradients follows from the above relation and is given by

$$\nabla \mathbf{U}_k = \nabla \mathbf{U}_{k,\mathrm{R}} + \nabla(\boldsymbol{\Omega} \times \mathbf{r}). \tag{7.17}$$

When the absolute velocity formulation is chosen, all velocities are stored in the absolute (inertial) frame, although the governing equations are still written with respect to corresponding zone's frame. Therefore, no transformation is required at the interface.

The MRF model is an approximation, since it solves for a fixed position of the impeller with respect to the baffles (as the mesh is fixed). For this reason, it is also called the "frozen rotor" approach. However, it can provide a reasonable model of the time-averaged flow for mixing tanks with small impeller to tank diameter ratio, since the impeller–baffle interactions are then expected to be relatively weak (Fluent, 2009). MRF can also be used to obtain an initial solution for a transient SM calculation, thus reducing the computational time (number of cycles) to arrive at a periodic solution.

A comparison of the SM and MRF computations for a stirred tank is provided by Luo

et al. (1994) and Lane (2005a). They report that good agreement was found generally between the two models and between the MRF predictions and the experimental measurements, whereas the computational time is about ten times less with the MRF method. Our test simulations were also in agreement with the above observation, and therefore we mainly used the MRF methodology for most of our simulations.

Chapter 8

Population balance modelling

Bubbles traveling in highly turbulent flow in the vessel experience shearing forces induced by the impeller blades and by turbulent eddies on a scale comparable to the bubble size. Consequently, they may breakup and form smaller bubbles. If the dispersion is not very dilute, bubbles can also collide with each other and, depending on the collision conditions, they may coalesce to form bigger bubbles. Therefore, a model is needed in order to track the evolution of the bubble size.

In this study, we adopted the so-called discrete method (or classes method), in which scalar transport equations are solved for each pre-defined bubble class. Break-up and coalescence effects are taken into account by source and sink terms. In this chapter, we will provide an overview of the population balance model theory and the governing equations of the method adopted to compute bubble size distributions.

8.1 Population balance model theory

8.1.1 Particle state vector

In the general population balance formulation, the state of a particle (solid or fluid) is described by its so-called "internal" and "external" coordinates. While the external coordinates denote merely the location of the particle in physical space, the internal coordinates describe the particle with respect to characteristics internal to it such as its size, composition, temperature (or for age dependent bacterial growth, for instance, the age of the cells). One or more of either the internal and/or the external coordinates could be discrete while the others could be continuous (Ramkrishna, 2000; Fluent, 2009).

For most practical applications, the particle state could be characterised by a finite dimensional particle state vector written in terms of internal ($\boldsymbol{\phi}$) and external ($\mathbf{x}$) coordinates with respective domains, $\boldsymbol{\phi} \in \Omega_\phi$ and $\mathbf{x} \in \Omega_x$. It is postulated that there exists an average number density function defined on the particle state space, $n(\mathbf{x}, \boldsymbol{\phi}, t)$, which is the expectation or the average of the actual number density. It is assumed to

be sufficiently smooth to allow differentiation as many time as necessary. The average number of particles in an infinitesimal volume $dV_x\, dV_\phi$ (in particle state space) about the particle state $(\mathbf{x}, \boldsymbol{\phi})$ is then $n(\mathbf{x}, \boldsymbol{\phi}, t)\, dV_x\, dV_\phi$ and the total number of particles in the entire system is

$$\int_{\Omega_\phi} \int_{\Omega_x} n(\mathbf{x}, \boldsymbol{\phi}, t)\, dV_x\, dV_\phi. \tag{8.1}$$

The local average number density in physical space (i.e. the total number of particles per unit volume of physical space) is given by

$$N(\mathbf{x}, t) = \int_{\Omega_\phi} n(\mathbf{x}, \boldsymbol{\phi}, t)\, dV_\phi, \tag{8.2}$$

and the total volume fraction of all particles is

$$\alpha_2(\mathbf{x}, t) = \int_{\Omega_\phi} n(\mathbf{x}, \boldsymbol{\phi}, t)\, V(\phi)\, dV_\phi, \tag{8.3}$$

where $V(\phi)$ denotes the volume of a particle of internal state ϕ.

8.1.2 Continuous phase vector

The continuous phase variables, which have an influence on particles, could be described by a finite c-dimensional vector field that is a function only of the external coordinates and time: $\mathbf{Y}(\mathbf{x}, t) \equiv [Y_1(\mathbf{x}, t), Y_2(\mathbf{x}, t), ..., Y_c(\mathbf{x}, t)]$. Its spatial and temporal evolution is governed by transport laws and interaction with the particles (Ramkrishna, 2000).

8.1.3 Reynolds transport theorem

The Reynolds transport theorem is used in the derivation of the general population balance equation. Particles are assumed to be embedded in the so-called "particle space continuum" that extends to the space of internal and external coordinates. This continuum could be conceived as deforming in space and time according to the vector field $[\dot{\mathbf{X}}(\mathbf{x}, \boldsymbol{\phi}, \mathbf{Y}, t), \dot{\boldsymbol{\Phi}}(\mathbf{x}, \boldsymbol{\phi}, \mathbf{Y}, t)]$ relative to the fixed coordinates. Here, the deformation due to change in external coordinates represents motion through physical space with the velocity $\dot{\mathbf{X}}(\mathbf{x}, \boldsymbol{\phi}, \mathbf{Y}, t)$ and that in the internal coordinates refers to motion through an abstract property space with the "velocity" $\dot{\boldsymbol{\Phi}}(\mathbf{x}, \boldsymbol{\phi}, \mathbf{Y}, t)$. Particle number fluxes through physical and internal coordinate spaces could then be defined respectively as

$$n(\mathbf{x}, \boldsymbol{\phi}, t)\, \dot{\mathbf{X}}(\mathbf{x}, \boldsymbol{\phi}, \mathbf{Y}, t), \tag{8.4}$$

and

$$n(\mathbf{x}, \boldsymbol{\phi}, t)\, \dot{\boldsymbol{\Phi}}(\mathbf{x}, \boldsymbol{\phi}, \mathbf{Y}, t). \tag{8.5}$$

For any point in the aforementioned deforming continuum located initially at $(\mathbf{x}_0, \boldsymbol{\phi}_0)$, its location at a subsequent time t at coordinates $[\mathbf{X}(t; \mathbf{x}_0, \boldsymbol{\phi}_0), \boldsymbol{\Phi}(t; \mathbf{x}_0, \boldsymbol{\phi}_0)]$ should satisfy the following differential equations and initial conditions:

$$\frac{d\mathbf{X}}{dt} = \dot{\mathbf{X}}(\mathbf{x}, \boldsymbol{\phi}, \mathbf{Y}, t), \quad \frac{d\boldsymbol{\Phi}}{dt} = \dot{\boldsymbol{\Phi}}(\mathbf{x}, \boldsymbol{\phi}, \mathbf{Y}, t) \tag{8.6}$$

$$\mathbf{X}(0; \mathbf{x}_0, \boldsymbol{\phi}_0) = \mathbf{x}_0, \quad \boldsymbol{\Phi}(0; \mathbf{x}_0, \boldsymbol{\phi}_0) = \boldsymbol{\phi}_0. \tag{8.7}$$

We now apply the Reynolds transport theorem to the deforming particle state continuum on which the particles are assumed to be embedded at every point such that their distribution could be described by the continuous density function $n(\mathbf{x}, \boldsymbol{\phi}, t)$. The time evolution of an extensive property $\psi(\mathbf{x}, \boldsymbol{\phi})$ associated with a single particle located at $(\mathbf{x}, \boldsymbol{\phi})$ is related to the deformation in the particle space continuum. An arbitrarily selected domain Λ_0 in the particle space continuum at some arbitrary reference time $t = 0$ has a component Λ_{x_0} in the external coordinate space Ω_x and a component Λ_{ϕ_0} in the internal coordinate space Ω_ϕ. The domain deforms continuously thus at time t, we would have $\Lambda(t)$ with the components $\Lambda_x(t)$ and $\Lambda_\phi(t)$. The total amount of extensive property ψ associated with all the particles in the domain $\Lambda(t)$ is given by

$$\Psi(t) = \int_{\Lambda_\phi(t)} dV_\phi \int_{\Lambda_x(t)} dV_x \, \psi(\mathbf{x}, \boldsymbol{\phi}) \, n(\mathbf{x}, \boldsymbol{\phi}, t). \tag{8.8}$$

Generalisation of the Reynolds transport theorem in three-dimensional space to general vector spaces results in

$$\frac{d}{dt} \int_{\Lambda_\phi(t)} dV_\phi \int_{\Lambda_x(t)} dV_x \, \psi \, n = \int_{\Lambda_\phi(t)} dV_\phi \int_{\Lambda_x(t)} dV_x \left[\frac{\partial}{\partial t} \psi \, n + \nabla_\phi \cdot \dot{\boldsymbol{\Phi}} \psi n + \nabla_x \cdot \dot{\mathbf{X}} \psi n \right], \tag{8.9}$$

where the time differentiation is applied by keeping the domain Λ_0 fixed at all points (Ramkrishna, 2000). Spatial divergence (for fixed internal coordinates) is denoted by $\nabla_x \cdot$ and it operates without holding the environmental vector $\mathbf{Y}$ constant. The partial divergence $\nabla_\phi \cdot$ acting on any differentiable vector field $\mathbf{F}$ in the particle state space is defined as

$$\nabla_\phi \cdot \mathbf{F} \equiv \sum_{i=1}^{d} \left(\frac{\partial F_i}{\partial \phi_i} \right)_{\phi_k (k \neq i), \mathbf{x}, t} \tag{8.10}$$

for a Cartesian frame for the internal coordinates.

8.1.4 Population balance equation (PBE)

We now build on the previously described notion of continuously deforming domain $\Lambda(t)$ in particle state space into which the particles are embedded. The number of particles in $\Lambda(t)$ can only change by birth and death processes. Assigning $b(\mathbf{x}, \boldsymbol{\phi}, \mathbf{Y}, t)$ as the net birth rate per unit volume of particle state space (without going into details of birth and death mechanisms for the time being), a number conservation equation can be written as (Ramkrishna, 2000):

$$\frac{d}{dt} \int_{\Lambda_\phi(t)} dV_\phi \int_{\Lambda_x(t)} dV_x \, n = \int_{\Lambda_\phi(t)} dV_\phi \int_{\Lambda_x(t)} dV_x \, b(\mathbf{x}, \boldsymbol{\phi}, \mathbf{Y}, t), \tag{8.11}$$

which, by using the Reynolds transport theorem (Eq. 8.9) with $\psi \equiv 1$ for the left-hand side of the equation, results in

$$\int_{\Lambda_\phi(t)} dV_\phi \int_{\Lambda_x(t)} dV_x \left[\frac{\partial}{\partial t} n + \nabla_\phi \cdot \dot{\boldsymbol{\Phi}} \, n + \nabla_x \cdot \dot{\mathbf{X}} \, n - b \right] = 0. \tag{8.12}$$

Since the domain of integration is arbitrary and the integrand is continuous, the integrand must vanish everywhere in the particle state space, thus the general form of the

population balance equation is obtained:

$$\frac{\partial}{\partial t} n + \nabla_\phi \cdot \dot{\mathbf{\Phi}}\, n + \nabla_x \cdot \dot{\mathbf{X}}\, n = b. \tag{8.13}$$

We still need to specify initial and boundary conditions to solve the system.

Initial conditions

The initial condition should describe the distribution of particles in the particle state space and for the special case where all particles have the same internal state, say $\boldsymbol{\phi}_0$, could be given by

$$n(\mathbf{x}, \boldsymbol{\phi}, 0) = N_0\, g(\mathbf{x}) \delta(\boldsymbol{\phi} - \boldsymbol{\phi}_0), \tag{8.14}$$

where N_0 is the initial total population density, $g(\mathbf{x})$ is their spatial distribution and $\delta(\boldsymbol{\phi} - \boldsymbol{\phi}_0)$ is the Dirac delta function which has the properties

$$\delta(\boldsymbol{\phi} - \boldsymbol{\phi}_0) = 0 \quad (\boldsymbol{\phi} \neq \boldsymbol{\phi}_0), \tag{8.15}$$

$$\int_{\Omega_\phi} f(\boldsymbol{\phi}) \delta(\boldsymbol{\phi} - \boldsymbol{\phi}_0)\, dV_\phi = f(\boldsymbol{\phi}_0), \tag{8.16}$$

f being any function of $\boldsymbol{\phi}$.

Boundary conditions

The boundary condition should describe the component of the particle flux normal to the boundary or (equivalently) the number density at each point on relevant parts of the boundary. Integrating the general PBE (Eq. 8.13) over the entire particle state space with the domain boundaries $\partial\Omega_\phi$ and $\partial\Omega_x$ for internal and external coordinates, respectively, and using the divergence theorem, we obtain:

$$\frac{d}{dt} \int_{\Omega_\phi} dV_\phi \int_{\Omega_x} dV_x\, n = \int_{\Omega_\phi} dV_\phi \int_{\Omega_x} dV_x\, b - \oint_{\partial\Omega_\phi} \dot{\mathbf{\Phi}}\, n \cdot d\mathbf{A}_\phi - \oint_{\partial\Omega_x} \dot{\mathbf{X}}\, n \cdot d\mathbf{A}_x, \tag{8.17}$$

where $d\mathbf{A}_\phi$ and $d\mathbf{A}_x$ are local infinitesimal area vectors directed outwards at surfaces $\partial\Omega_\phi$ and $\partial\Omega_x$, respectively. The left-hand side of the equation represents the net rate of change of the total number of particles in the entire system, while the right-hand side describes the ways the total number can change. The first volume integral term on the right-hand side represents the total net birth rate for all particles in the entire space and the surface integral terms represent the rate at which particles are introduced or removed across the bounding surfaces of the particle state space. The first set of boundary condition could be specified by the notion that boundaries at infinity represent no sources or sinks so that the particle fluxes vanish there:

$$\dot{\mathbf{\Phi}}\, n \to 0, \quad ||\boldsymbol{\phi}|| \to \infty, \tag{8.18}$$

$$\dot{\mathbf{X}}\, n \to 0, \quad ||\boldsymbol{x}|| \to \infty, \tag{8.19}$$

which is the so-called regularity condition. If we consider the part of the boundary $\partial\Omega_\phi$ at which system characteristics originate (i.e. where the particles enter the system),

denoted by $\partial\Omega_\phi^0$, and $\mathbf{n}_\phi$ be the local outwards normal vector, the second boundary condition can be specified as

$$-\left(\dot{\mathbf{\Phi}}\cdot\mathbf{n}_\phi\right)n(\mathbf{x},\boldsymbol{\phi},t)=\dot{n}_0,\quad \boldsymbol{\phi}\in\partial\Omega_\phi^0, \tag{8.20}$$

where the nucleation rate $\dot{n}_0$ (particles m^{-3} s^{-1}) comes from physical models.

Open systems

Note that the previous treatment was for closed systems, implying that the particle flux vanished everywhere on the spatial domain boundary $\partial\Omega_x$. For open systems, parts of the domain boundary through which the particle flux enters and/or leaves the domain, i.e. $\partial\Omega_{x,\mathrm{in}}$ and $\partial\Omega_{x,\mathrm{out}}$, could be specified as permeable to the particle flux (no boundary condition needed on $\partial\Omega_{x,\mathrm{out}}$). In such a case, integrating the PBE (Eq. 8.13) over the spatial domain Ω_x and applying the divergence theorem results in

$$\frac{\partial}{\partial t}\int_{\Omega_x}dV_x\,n+\nabla_\phi\cdot\int_{\Omega_x}dV_x\,\dot{\mathbf{\Phi}}\,n+\int_{\Omega_{x,\mathrm{in}}}\dot{\mathbf{X}}\,n\cdot d\mathbf{A}_x+\int_{\Omega_{x,\mathrm{out}}}\dot{\mathbf{X}}\,n\cdot d\mathbf{A}_x=\int_{\Omega_x}dV_x\,b. \tag{8.21}$$

8.1.5 PBE formulation in Fluent

We can apply the general PBE (Eq. 8.13) for the case where the internal state is taken as the particle volume ($\phi=v$). The deformation velocity due to change in the internal coordinate is now the particle volume growth rate (i.e. $\dot{\mathbf{\Phi}}=G_v$), and that due to change in the external coordinate is simply the physical velocity (i.e. $\dot{\mathbf{X}}=\mathbf{u}$). The result is the transport equation solved in Fluent for the average volume-based number density function (also called volume number density), $n(v,t)$. For a discrete particle state (internal volume coordinate), this could be defined as the number of particles with volume between v and $v+\Delta v$ per unit volume of physical space (ΔN) and per particle class width Δv [particles m^{-3} m^{-3}]:

$$n(v,t)=\frac{\Delta N}{\Delta v}. \tag{8.22}$$

The transport equation is formulated below with the particle birth and death mechanisms elaborated rather than just the net birth rate as done earlier (Fluent, 2009):

$$\begin{aligned}&\frac{\partial}{\partial t}n(v,t)+\nabla\cdot\mathbf{u}\,n(v,t)+\underbrace{\nabla_v\cdot G_v\,n(v,t)}_{\text{growth}}=\\&\underbrace{\frac{1}{2}\int_0^v a(v-v',v')\,n(v-v',t)\,n(v',t)\,dv'}_{\text{birth due to aggregation}}-\underbrace{\int_0^\infty a(v,v')\,n(v,t)\,n(v',t)\,dv'}_{\text{death due to aggregation}}\\&+\underbrace{\int_{\Omega_v}p\,g(v')\,\beta(v:v')\,n(v',t)\,dv'}_{\text{birth due to breakage}}-\underbrace{g(v)\,n(v,t)}_{\text{death due to breakage}}.\end{aligned} \tag{8.23}$$

The boundary and initial conditions are:

$$n(v, t = 0) = n_v, \tag{8.24}$$
$$n(v = v_0, t)\, G_v = \dot{n}_0, \tag{8.25}$$

where v_0 is the volume of the newly formed particles. The terms in Eq. 8.23 are explained in the following sections.

Particle growth and dissolution

The growth rate may be defined based on particle volume [$m^3\ s^{-1}$] or particle diameter (length) [$m\ s^{-1}$], which are given, respectively, as

$$G_v = \frac{\partial v}{\partial t}, \tag{8.26}$$
$$G_l = \frac{\partial \mathcal{L}}{\partial t}. \tag{8.27}$$

The volume and surface area of a single particle is defined in terms of respective shape factors K_v and K_a:

$$v = K_v \mathcal{L}^3, \tag{8.28}$$
$$\mathcal{A} = K_a \mathcal{L}^2, \tag{8.29}$$

hence for a cube or a sphere, $K_a = 6K_v$. The volume based growth rate could now be related also to the linear growth rate:

$$\frac{\partial v}{\partial t} = \left(3K_v \mathcal{L}^2\right) \frac{\partial \mathcal{L}}{\partial t}, \tag{8.30}$$
$$G_v = \left(3K_v \mathcal{L}^2\right) G_l. \tag{8.31}$$

If particle dissolution is relevant, this could simply be modelled as negative growth.

Breakage

The breakage rate kernel in Fluent is described in the form

$$g(v')\, \beta(v : v'), \tag{8.32}$$

where $g(v')$ is the breakage frequency, i.e. the fraction of particles of volume v' breaking per unit time, and $\beta(v : v')$ is the probability density function (PDF) of particles that break from volume v' to a particle of volume v. It is also known as the particle fragmentation distribution function or daughter size distribution.

The birth rate of particles of volume v as a result of breakage is given by

$$B_{\text{br}} = \int_{\Omega_v} p\, g(v')\, \beta(v : v')\, n(v')\, dv', \tag{8.33}$$

which expresses that $g(v')\,n(v')\,dv'$ particles of volume v' break per unit time, giving rise to birth of $p\,g(v')\,n(v')\,dv'$ particles, and $\beta(v:v')\,dv'$ is the fraction of those with volume v. The number of daughter particles produced per parent (e.g. 2 for binary breakage) is denoted by p.

The death rate of particles of volume v as a result of breakage is given by

$$D_{\mathrm{br}} = g(v)\,n(v). \tag{8.34}$$

Various functional forms to the PDF $\beta(v:v')$ could be proposed, however they should satisfy the following physical constraints:

- the normalised number of breaking particles should sum to unity:

$$\int_0^{v'} \beta(v:v')\,dv = 1, \tag{8.35}$$

- the masses of the daughter particles should sum to the parent mass:

$$p\int_0^{v'} m(v)\beta(v:v')\,dv = m(v'), \tag{8.36}$$

- for binary breakage, β should be symmetric about $v/v' = 0.5$:

$$\beta(v'-v:v') = \beta(v:v'). \tag{8.37}$$

In this study, we used the model of Luo and Svendsen for the particle breakage frequency. This will be elaborated later in a separate section.

Aggregation

The aggregation kernel in Fluent is described in the form

$$a(v,v'), \tag{8.38}$$

which has the units m^3/s and could be expressed as a product of two quantities:

- the collision frequency between the particles of volume v and volume v',
- the so-called "efficiency of aggregation", i.e. the probability of particles of volume v coalescing with particles of volume v'.

The birth rate of particles of volume v as a result of aggregation is given by

$$B_{\mathrm{ag}} = \frac{1}{2}\int_0^{v} a(v-v',v')\,n(v-v')\,n(v')\,dv', \tag{8.39}$$

which expresses that particles of volume $v'-v$ aggregate with particles of volume v' to form particles of volume v per unit time. As each collision event involves two particles, there is a factor of $1/2$.

The death rate of particles of volume v as a result of aggregation is given by

$$D_{\mathrm{ag}} = \int_0^\infty a(v, v')\, n(v)\, n(v')\, dv'. \tag{8.40}$$

In this study, we used the coalescence model of Luo (1993) for the aggregation kernel. This will be elaborated later in a separate section.

8.1.6 Breakage rate model of Luo and Svendsen

A fluid particle (bubbles and drops) in a turbulent field is subjected to inertial and viscous forces which may lead to so-called turbulent and shear breakage mechanism, respectively. Turbulent breakage occurs due to the impact of fluctuating eddies (of scale similar or smaller than the particle as larger eddies would merely convect the particle) on the particle surface which induce surface oscillations (or deformations). Particles break when the increase in the surface energy due to deformations (caused by the kinetic energy of turbulent motion) is sufficiently large and this occurs usually as a binary breakage leading to two daughter particles (Luo and Svendsen, 1996). Shear breakage, on the contrary, occurs due to viscous shear and results in several daughter particles with varying volumes. In highly turbulent flow, viscous forces are usually negligible (and so is the shear breakage) as particles are much larger than the microscale of turbulence.

Luo and Svendsen (1996) proposed a breakage rate model for fluid particles based on the above given arguments and the theory of isotropic turbulence and probability, which is widely used in literature and also adopted in this study. It has the advantage over the earlier models that it consists of no unknown or adjustable parameters. We refer to the same paper for a brief discussion of the earlier work on breakage rates and daughter particle size distributions. Simplifying assumptions in the development of the model, which are usually justified for fully turbulent flows, are the following:

- isotropic turbulence,
- binary breakage,
- binary breakage volume fraction is a stochastic variable,
- occurance of breakage is determined by the kinetic energy of the arriving eddy,
- only eddies of scale equal or smaller than the particle diameter can induce oscillations.

The binary breakage volume fraction is defined as the ratio between daughter and parent particle volumes:

$$f_{\mathrm{B}} = \frac{v_I}{v} = \frac{d_I^3}{d^3} = \frac{d_I^3}{d_I^3 + d_{II}^3}, \tag{8.41}$$

where the subscript I and II identify either of the daughter particles. It can vary in the range $0 < f_{\mathrm{B}} < 1$ with $f_{\mathrm{B}} = 0$ or 1 represents no breakage and $f_{\mathrm{B}} = 0.5$ means equal binary breakage. No correlation was found experimentally between f_{B} and the

parent particle size and eddy size, thus supporting the choice of f_B as a stochastic variable in the model.

The general model for the fluid particle breakage rate in the turbulent flow regime takes the following form:

$$\Omega_B(v : vf_B) = \int_{\lambda_{min}}^{d} \dot{\omega}_{B,\lambda}(v)\, P_B(v : vf_B, \lambda)\, d\lambda. \tag{8.42}$$

Here, $\Omega_B(v : vf_B)$ is the breakage rate of particles of size v into a fraction between f_B and $f_B + df_B$ (i.e. one of the daughter particles has a volume between vf_B and $vf_B + v\, df_B$) for a continuous f_B, and into a fraction of f_B for a discrete f_B. The arrival or impact frequency of eddies of length scale between λ and $\lambda + d\lambda$ on to particles of size v is denoted by $\dot{\omega}_{B,\lambda}(v)$. Finally, $P_B(v : vf_B, \lambda)$ is the binary breakage probability of a particle of size v to give a daughter particle of size $v_I = vf_B$ when hit by an eddy of size λ.

Arrival frequency of eddies

The arrival frequency of eddies of length scale between λ and $\lambda + d\lambda$ on a fluid particle of size d is essentially the collision frequency between the two and is given for randomly moving eddies by

$$\dot{\omega}_{B,\lambda}(d) = \frac{\pi}{4}(d + \lambda)^2 \bar{u}_\lambda\, n_\lambda\, n, \tag{8.43}$$

where the number of fluid particles per unit dispersion volume is denoted by n. The number of eddies of size between λ and $\lambda + d\lambda$ per unit reactor volume is denoted by n_λ; it is calculated from the turbulent energy spectrum in the inertial subrange and decreases rapidly with increasing eddy size:

$$n_\lambda \approx 0.822 \frac{(1 - \alpha_2)}{\lambda^4}, \tag{8.44}$$

α_2 being the local fraction of dispersed phase. $\bar{u}_\lambda$ is the mean turbulent velocity of eddies of size λ and is also considered to be the relative velocity between particle and eddy. It is calculated on the basis of inertial subrange of isotropic turbulence:

$$\bar{u}_\lambda = \left(\frac{8\tilde{\beta}}{3\pi}\right)^{1/2} (\varepsilon_1 \lambda)^{1/3}, \tag{8.45}$$

where the measured value for the parameter $\tilde{\beta}$ was reported as 2.0 and, in Fluent, the theoretical value of $\tilde{\beta} = 2.41$ is used (Luo and Svendsen, 1996; Fluent, 2009). Note that the limitation of model parameters to the inertial subrange was not considered as a drawback by the authors since very small eddies would have very low energy contents and very short lifetimes. Without going into detailed derivation, the final relation for the arrival frequency of eddies is

$$\dot{\omega}_{B,\lambda}(d) = 0.923(1 - \alpha_2)\, n\, (\varepsilon_1 d)^{1/3} \frac{(1 + \xi)^2}{d^2 \xi^{11/3}}, \tag{8.46}$$

where $\xi = \lambda/d$ is the size ratio between an eddy and a particle.

Binary breakage probability (efficiency)

The probability of a fluid particle hit by an eddy to break up depends both on the energy content of the eddy and on the minimum energy required by the surface area increase due to breakup. The latter depends on the number and size of the daughter particles formed.

Luo and Svendsen calculated the energy contained in eddies of different size from an exponential energy-distribution density function, which was found to be equivalent to the common assumption that the velocity distribution of turbulent eddies is a normal density function. Since the condition for breakup is that the kinetic energy of hitting eddy exceeds the increase in surface energy required for breakage, the breakage probability is then equal to the probability of an arriving eddy to have this kinetic energy. The final relation for the conditional breakage probability is given as

$$P_{\mathrm{B}}(v : vf_{\mathrm{B}}, \lambda) = 1 - \int_0^{\chi_c} \exp(-\chi)\, d\chi = \exp(-\chi_c), \tag{8.47}$$

where $\chi = e(\lambda)/\bar{e}(\lambda)$ is the kinetic energy of an eddy of size λ normalised by its mean kinetic energy, and is based on the exponential energy density function, $P_e = \dfrac{1}{\bar{e}(\lambda)} \exp(-\chi)$. The critical dimensionless energy for breakup, χ_c, is expressed as

$$\chi_c = \frac{\bar{e}_i(d)}{\bar{e}(\lambda)} = \frac{12\left[f_{\mathrm{B}}^{2/3} + (1-f_{\mathrm{B}})^{2/3} - 1\right]\sigma}{\left(\dfrac{8\tilde{\beta}}{3\pi}\right)\rho_1\, \varepsilon_1^{2/3}\, d^{5/3}\, \xi^{11/3}}, \tag{8.48}$$

The increase in surface energy due to breakage of a particle of size d is denoted by $\bar{e}_i(d)$:

$$\bar{e}_i(d) = \left[f_{\mathrm{B}}^{2/3} + (1-f_{\mathrm{B}})^{2/3} - 1\right]\pi d^2\sigma, \tag{8.49}$$

and the term in brackets represents the increase in surface area due to breakage and is a symmetrical function about $f_{\mathrm{B}} = 0.5$.

Breakage rate expression

Substituting now Eq. 8.46 and 8.47 into Eq. 8.42, the final relation for the breakup rate of particles of size v or d into particle sizes of vf_{B} and $v(1-f_{\mathrm{B}})$ is obtained:

$$\frac{\Omega_{\mathrm{B}}(v : vf_{\mathrm{B}})}{(1-\alpha_2)n} =$$

$$0.923\left(\frac{\varepsilon_1}{d^2}\right)^{1/3} \int_{\xi_{\min}}^{1} \frac{(1+\xi)^2}{\xi^{11/3}} \exp\left\{ -\frac{12\left[f_{\mathrm{B}}^{2/3} + (1-f_{\mathrm{B}})^{2/3} - 1\right]\sigma}{\left(\dfrac{8\tilde{\beta}}{3\pi}\right)\rho_1\, \varepsilon_1^{2/3}\, d^{5/3}\, \xi^{11/3}} \right\} d\xi. \tag{8.50}$$

The limit of the integral given above, $\xi_{\min} = \lambda_{\min}/d$, is based on the minimum size of eddies in the inertial subrange of isotropic turbulence, $\lambda_{\min}$, rather than the microscale

of eddies, λ_{K}, as one would expect. This is because both the collision frequency $\dot{\omega}_{\mathrm{B},\lambda}(d)$ and the binary breakage probability $P_{\mathrm{B}}(v : vf_{\mathrm{B}}, \lambda)$ relations are valid only for this subrange. This, however, poses no limitation to the model since very small eddies would have very low energy contents and very short lifetimes thus have a negligible effect on the particle breakage as mentioned earlier. The minimum size of eddies in the inertial subrange was given as $\lambda_{\min}/\lambda_{\mathrm{K}} \approx 11.4 - 31.4$ (Luo and Svendsen, 1996).

Daughter particle size distribution

One advantage of the model of Luo and Svendsen over the earlier models is that it does not require a predefined daughter size distribution. The model directly calculates the "partial breakage rate" for particles of size v breaking into daughter particles with a given f_{B}.

As introduced earlier, for a continuous f_{B}, the $\Omega_{\mathrm{B}}(v : vf_{\mathrm{B}})$ describes the breakage rate of particles of size v into a size between v_I and $v_I + dv_I$ ($v_I = vf_{\mathrm{B}}$). Accordingly, for a continuous daughter particle size distribution $\eta(v : vf_{\mathrm{B}})$, the fraction of particles of size v that break into particles of size between v_I and $v_I + dv_I$ is represented by $\eta(v : vf_{\mathrm{B}})\, dv_I$. The daughter particle size distribution is then, by definition, given by

$$\eta(v : vf_{\mathrm{B}}) = \frac{2\displaystyle\int_{\xi_{\min}}^{1} (1+\xi)^2 \xi^{-11/3} e^{-\chi_c}\, d\xi}{v\displaystyle\int_0^1 \int_{\xi_{\min}}^{1} (1+\xi)^2 \xi^{-11/3} e^{-\chi_c}\, d\xi\, df_{\mathrm{B}}}. \tag{8.51}$$

General characteristics of the model

Some important characteristics of the model of Luo and Svendsen are:

- The model consists of no unknown or tuned parameters in contrast to the earlier models.
- Particle sizes as a result of breakage are functions of the initial particle size, the energy dissipation rate, and the physical properties of the system.
- Some earlier models acquired distribution functions that predict the highest probability for equal-sized breakage, which decreases as $v_I \to 0$ or v (i.e. inverse U-shape). Experimental results, however, showed the opposite. The dimensionless daughter particle size distribution, $\eta(v : vf_{\mathrm{B}})v$, predicted by this model is a U-shaped function with a non-zero minimum at $f_B = 0.5$, i.e. the lowest probability is found for equal-sized breakage. This is physically sound and agrees well with the experiments.
- The size distribution is also a function of the initial particle size. The model predicts that, as the particle size increases, the distribution becomes flatter and the effect of the energy dissipation rate becomes weaker. This is because larger bubbles are affected by a wider size range of eddies thus have a higher chance of equal-sized breakage.

- The distribution becomes flatter also with an increase in the energy dissipation rate, since the energy provided for breakage is higher.

- Breakage of small particle sizes from the initial larger particle occurs most frequently. This may happen in rapid succession thus resembling the breakage into more than two particles. Hence, in this way, the model may also cope with multiple breakages occurring almost simultaneously.

- With increasing particle size and dissipation rate, the specific breakage rate $\frac{\Omega_B(v:vf_B)}{(1-\alpha_2)n}$ increases, because larger particles are hit by wider range of eddies and the energy density is higher at larger dissipation rates.

- For very small particles, the specific breakage rate is close to zero as eddies hitting them have too little energy to break them. Higher energy levels thus dissipation rates are needed to break smaller drops.

8.1.7 Coalescence model of Luo

In this study, we used the binary coalescence model of Luo (1993) which is based on the common notion that coalescence of two fluid particles involves the following three stages:

- particles collide, trapping a small amount of liquid between them,

- trapped liquid drains out until a critical film thickness is reached,

- liquid film ruptures leading to coalescence.

A sufficiently large contact time is needed such that the liquid drainage and film rupture could eventually result in coalescence. This process could be analysed through the collision frequency and the efficiency (probability) of the collision (i.e. fraction of collisions leading to coalescence). Consequently, the coalescence rate between particle i (with size v_i or d_i) and particle j (with size v_j or d_j) could be expressed by

$$\Omega_C(v_i : v_j) = \dot{\omega}_C(v_i : v_j)\, P_C(v_i : v_j), \tag{8.52}$$

where Ω_C is the coalescence rate expressed as the rate of particle volume formation due to binary collisions [m^3/s], and $\dot{\omega}_C$ and P_C are the collision frequency [m^3/s] and the collision efficiency of the particles, respectively.

Following simplifying assumptions were made in the development of the model:

- isotropic turbulence,

- binary collisions (since the collision of more than two particles at the same time has a very small probability),

- particle sizes lie in the inertial subrange of isotropic turbulence.

Collision frequency

The binary particle collision frequency is a complex function of the particle number density, the size distribution and the continuous phase flow field. Isotropic turbulence assumption was made in order to determine the relative velocity between particles involved in turbulent collisions. Turbulence in many bubbly flows are known to be non-isotropic (e.g. bubble columns), however this was not seen as a drawback of the model as the fine-scale structure of most non-isotropic turbulent flows are locally nearly isotropic.

Another assumption is that particle sizes lie in the inertial subrange of isotropic turbulence. This is reasonable as particles are usually much larger than the turbulence microscale and much smaller than the characteristic length scale of the equipment of which the energy containing eddies have the same order. Assuming also that particles taking part in collisions take the same velocity of eddies of similar size and those particle velocities are statistically non-correlated in space (analogous to the motion of ideal gas molecules), the mean approach velocity of particles in turbulent collisions is calculated from the rms of the particle velocities:

$$\bar{u}_{ij} = \left(\bar{u}_i^2 + \bar{u}_j^2\right)^{1/2} = \bar{u}_i \left(1 + \xi_{ij}^{-2/3}\right)^{1/2}. \tag{8.53}$$

Here, $\xi_{ij} = d_i/d_j$ is the size ratio and $\bar{u}_{ij}$ is the characteristic collision velocity of particles with diameters d_i and d_j. The particle velocities $\bar{u}_i$ and $\bar{u}_j$ are calculated by Eq. 8.45 for the mean turbulent velocity of eddies of size λ in the inertial subrange of isotropic turbulence, by substituting d_i or d_j for λ.

With the approach velocity for turbulent collisions calculated as given above, the collision frequency is determined from an expression developed for binary drop collisions in turbulent air, analogous to that for collisions of gas molecules:

$$\dot{\omega}_{\mathrm{C}} = \frac{\pi}{4}(d_i + d_j)^2 \, \bar{u}_{ij} \, n_i \, n_j, \tag{8.54}$$

where n_i and n_j are the number densities of particle i and j, respectively. Note the similarity of this relation to that for the eddy arrival frequency in Eq. 8.43.

Collision efficiency (probability)

Collision efficiency is related to the forces acting on the colliding particles because the interaction time depends on those. The model of Luo is, in essence, based on the notions of the earlier coalescence theory. That is, collision of two fluid particles will result in coalescence if the interaction (contact) time, t_{I}, is sufficiently larger than the coalescence time, t_{C}, needed for drainage of the liquid film between particles to a critical rupture thickness. This is expressed in a simple functional form as

$$P_{\mathrm{C}} = \exp\left(-\frac{t_{\mathrm{C}}}{t_{\mathrm{I}}}\right). \tag{8.55}$$

Main difficulty lies in describing those two time scales which depend on the collision forces and the approach velocities. Furthermore, the surface properties of particles have

also a significant effect on the coalescence time. Despite the fact that many practical applications involve partially or fully immobile interfaces, lacking the fundamental knowledge on the coalescence time of those, Luo used an expression available for the coalescence time of fully mobile interfaces:

$$t_{\mathrm{C}} = 0.5\,\frac{\rho_1 \bar{u}_{ij} d_i^2}{(1-\xi_{ij})^2 \sigma}, \tag{8.56}$$

σ being the interfacial tension.

Luo (1993) developed a model for the interaction time of two equal- or unequal-sized fluid particles based on the parallel film concept. Here we give the final relation for the interaction time:

$$t_{\mathrm{I}} = 2\,t_{\max} = (1+\xi_{ij}) \left[\frac{(\rho_2/\rho_1 + C_{\mathrm{A}})}{3(1+\xi_{ij}^2)(1+\xi_{ij}^3)} \frac{\rho_1 d_i^3}{\sigma} \right]^{1/2}, \tag{8.57}$$

where $t_{\max}$ is the time between the first contact and when the film area between the two colliding particles reaches its maximum value. C_{A} is the virtual mass coefficient, which is taken as 0.5 in Fluent, i.e. the value for rigid spheres (see Section 6.2).

Substituting now Eq. 8.56 and 8.57 in Eq. 8.55, the final relation for the coalescence efficiency is obtained:

$$P_{\mathrm{C}} = \exp\left\{ -c_1 \frac{[0.75(1+\xi_{ij}^2)(1+\xi_{ij}^3)]^{1/2}}{(\rho_2/\rho_1 + C_{\mathrm{A}})^{1/2}(1+\xi_{ij}^3)} We_{ij}^{1/2} \right\}, \tag{8.58}$$

where c_1 is an adjustable constant of order unity. The Weber number is defined as

$$We_{ij} = \frac{\rho_1\, d_i\, \bar{u}_{ij}^2}{\sigma}. \tag{8.59}$$

Eq. 8.58 relates the coalescence probability to the Weber number, particle size ratio, the added mass coefficient and the physical properties of the system.

Coalescence rate can now be calculated from Eq. 8.52, 8.54 and 8.58 if the particle number densities are known.

8.2 Discrete method (DM) for the solution of PBE

We used the discrete method (also known as the classes or sectional method) to solve the PBE (Eq. 8.23) in Fluent, which is based on the work of Hounslow et al. (1988), Lister et al. (1995) and Ramkrishna (2000). In DM, the continuous particle size distribution (PSD) is represented by a number of discrete particle size classes, also called as bins. It has the advantage that the numerics is robust and it directly gives the PSD. Drawbacks are high computational costs when large number of bins are tracked and that the bins need to be specified a priori.

A moment-based method such as the quadrature method of moments (QMOM) could be an alternative to DM which has the advantage of lower computational costs (relatively small number of scalar equations are needed to track the first few moments of population), though reconstructing the PSD could be problematic.

Sanyal et al. (2005) compared the predictions obtained using the DM with 6, 12, 18 and 24 bins, and the QMOM with 6 moments (implying a quadrature approximation with 3 nodes) for a bubble column. They found that the DM solution was independent of the resolution of the internal coordinate only when the number of bins were greater than 12. On the other hand, results found using the QMOM with 6 moments and the DM with 12 and 18 bins were very similar. Despite those differences, they reported that the DM results obtained with 6 bins compared already very well with the experimental results. The computational effort (i.e. CPU time) per scalar solved was about the same for both methods, hence the costs for the DM with 6 bins and the QMOM with 6 moments would be similar in this respect.

Spatial distribution of the (Sauter) mean bubble sizes measured in the stirred tank studied in this work had a rather narrow span (see the measurements of Barigou and Greaves (1992) reported in Section 9.2.2) and, in Fluent, the PBM of the bubbly phase is coupled with the overall fluid dynamics via the Sauter mean diameter in momentum equations. We therefore decided to use the DM with relatively small number of bubble size classes (6 bins) in this study which also kept the computational demands in a managable level.

8.2.1 Numerical approach

The PBE in the Fluent DM formulation is written in terms of volume fraction of particle size i (Fluent, 2009):

$$\frac{\partial}{\partial t}(\rho_2\alpha_i)+\nabla\cdot(\rho_2 u_2\alpha_i)+\frac{\partial}{\partial v}\left(\frac{G_v\rho_2\alpha_i}{v}\right)=\rho_2 v_i(B_{\mathrm{ag},i}-D_{\mathrm{ag},i}+B_{\mathrm{br},i}-D_{\mathrm{br},i})+0^i\rho_2 v_0\dot{n}_0. \tag{8.60}$$

The volume fraction of particle size i is defined as

$$\alpha_i = v_i N_i \qquad i=0,1,...,\mathcal{N}-1, \tag{8.61}$$

where $\mathcal{N}$ is the number of size classes (bins), N_i is the average number density of particle size i in physical space, given by (see Eq. 8.2):

$$N_i(t)=\int_{v_i}^{v_{i+1}} n(v,t)\,dv, \tag{8.62}$$

and v_i is the volume of the particle size i. In Fluent, actual solution variable is the bin fraction f_i, that is, the fraction of the total gas volume contained in the bin i particles:

$$f_i=\frac{\alpha_i}{\alpha_2}=\frac{v_i N_i}{\alpha_2}. \tag{8.63}$$

The last term in Eq. 8.60 is due nucleation and the notation 0^i denotes that the term $\rho_2 v_0\dot{n}_0$ is calculated only for the discretised equation for the volume fraction of the smallest size v_0.

The growth rate term in Eq. 8.60 is discretised following Hounslow et al. (1988):

$$\frac{\partial}{\partial v}\left(\frac{G_v\rho_2\alpha_i}{v}\right)=\rho_2 v_i\left[\left(\frac{G_{v,i-1}\,N_{i-1}}{v_i-v_{i-1}}\right)-\left(\frac{G_{v,i}\,N_i}{v_{i+1}-v_i}\right)\right]. \tag{8.64}$$

The internal volume coordinate is discretised according to a geometric ratio:

$$\frac{v_{i+1}}{v_i} = \left(\frac{d_{i+1}}{d_i}\right)^3 = 2^q. \tag{8.65}$$

According to the Fluent User's Guide (Fluent, 2009), the ratio factor could be specified as $q = 1, 2, ...$, by the user. However, the Fluent technical support team confirmed us that q could take also a non-integer value. Furthermore, it is also possible to define arbitrary bin sizes via user input.

The discretisation for particle birth and death rates for breakage and aggregation (see Eq. 8.33, 8.34, 8.39 and 8.40) are described below. Note that, the birth processes due to breakage and aggregation produce particles that are between pre-defined size classes except in the case of uniform linear grid. Therefore, a special treatment is needed for birth terms to ensure number and mass preservation, which we also discuss below.

Breakage formulation

The breakage formulation in Fluent's implementation of DM follows from the method of Hagesæther et al. (2002) in which the breakage sources are distributed to the respective size bins while preserving volume (and mass, since all population classes have the same density) and number density. Hagesæther et al. (2002) used the factor two between each class ($q = 1$), because they claim that in their PBM formulation, factor lower than two ($q < 1$) complicates the allocation of particles into classes when coalescence or breakup occurs, and a factor higher than two ($q > 1$) decreases the accuracy of the simulations while decreasing computation time. In Fluent's implementation, no constraint is put on the choice of q as mentioned previously.

It should be emphasised that, in Fluent User's Guide (Fluent, 2009), method formulation is given in an inconsistent and incomplete manner with several errors. Here, we present it in a consistent form without fully reverting to the formulation of Hagesæther et al..

Assuming that there is no breakage in the smallest class, the general formulation for the birth and death rates due to breakage are

$$B_{\mathrm{br},i} = \sum_{j=i+1}^{\mathcal{N}} g(v_j)\, \beta(v_i : v_j)\, N_j, \tag{8.66}$$

$$D_{\mathrm{br},i} = g(v_i)\, N_i. \tag{8.67}$$

Note that, Fluent adopts here the notation of Hagesæther et al., where the smallest size bin index is $i = 1$ (rather than $i = 0$ as in the earlier definition adopted by Fluent).

In order to conserve number and volume, the actual birth rate source $B_{\mathrm{br},i}$ is adapted according to the method of Hagesæther et al., which assumes binary breakup, no breakage in the smallest class and that no daughter fragment may be smaller than the

smallest particle class. It's written as

$$B_{\mathrm{br},i} = \sum_{k=i+1,i\neq\mathcal{N}}^{\mathcal{N}} \Omega_{\mathrm{B}}(v_i : v_k) + \sum_{k=1,i\neq\mathcal{N}}^{i} x_{i+1,k}\,\Omega_{\mathrm{B}}(v_k : v_{i+1}) + \sum_{k=1,i\neq 1}^{i-1} (1 - x_{i,k})\,\Omega_{\mathrm{B}}(v_k : v_i), \qquad i = 1, ..., \mathcal{N} \tag{8.68}$$

with

$$\Omega_{\mathrm{B}}(v_i : v_k) = g(v_k)\,\beta(v_i : v_k)\,N_k. \tag{8.69}$$

In this formulation, the birth rate source for bin i does not only include the direct contribution due to breakage of particle of size v_k into daughter particle of size v_i (represented by $\Omega_{\mathrm{B}}(v_i : v_k)$). There are also partial contributions due to breakage of sizes v_{i+1} (i.e. $\Omega_{\mathrm{B}}(v_k : v_{i+1})$) and v_i (i.e. $\Omega_{\mathrm{B}}(v_k : v_i)$), producing daughter particles v_k (assumed to be identical to a size class lower than that of the parent) and complementary particles v_j that may fall between adjacent classes $v_i < v_j < v_{i+1}$ and $v_{i-1} < v_j < v_i$, respectively, thus have to be partly redistributed to the class i.

The redistribution process works in the following way. Let a particle of arbitrary size v breaking up into daughter particles of size v_j and v_k:

$$v \longrightarrow v_j + v_k, \tag{8.70}$$

where v_j is larger than or equal to the other daughter particle v_k, which is assumed have a size exactly matching one of the size classes lower than that of the parent. If the breakup volume fraction v_j falls between two adjacent classes, say $(i-1)$ and i, then it is redistributed to those two classes according to:

$$v_j = x_{i,k}\,v_{i-1} + (1 - x_{i,k})\,v_i, \tag{8.71}$$

thus, a (binary) breakup event results in the following:

$$v \longrightarrow v_k + x_{i,k}\,v_{i-1} + (1 - x_{i,k})\,v_i, \tag{8.72}$$

where $x_{i,k}$ is the fraction assigned to class $(i-1)$ and $(1-x_{i,k})$ is the fraction assigned to class i. The distribution fraction $x_{i,k}$ is simply the normalised volume difference:

$$x_{i,k} = \frac{v_i - v_j}{v_i - v_{i-1}}. \tag{8.73}$$

Both the volume and number balances are fulfilled in this formulation irrespective of how the bins are distributed (geometric, linear or arbitrary): one particle is divided into two classes, but the two classes sum up to one particle, and the volume balance is still satisfied.

For the case of geometric bin size distribution ($v_{i+1}/v_i = 2^q$), where

$$v_i = v_1 2^{(i-1)q} \qquad i = 1, ..., \mathcal{N}, \tag{8.74}$$

Hagesæther (2002) derived a relation for the case $q = 1$, by using Eq. 8.70, 8.71 and Eq 8.74:

$$x_{i,k} = 2^{1+k-i} \qquad k < i, \tag{8.75}$$

which satisfies the expected condition for equal-sized binary breakup that, for $v_k = v_{i-1}$, then $x_{i,k} = 1$ and v_j is reassigned entirely to v_{i-1}. Note that, for this special case of $q = 1$, a parent particle v_i would have a larger daughter particle v_j of size either exactly one class lower, v_{i-1} (i.e. equal-sized binary breakup), or between the class $(i-1)$ and i. For cases where the bin distribution around the parent particle is finer (such as geometric distributions with $q < 1$), v_j could fall between any of the lower adjacent classes.

For an arbitrary value of q, we derived a relation similar to that in Eq. 8.75:

$$x_{i,k} = \left(\frac{1}{2^q - 1}\right) 2^{(1+k-i)q} \qquad k < i. \tag{8.76}$$

Aggregation formulation

The aggregation source terms computed by Fluent are documented as follows, assuming that there is no coalescence in the largest class $v_{\mathcal{N}}$ (note the difference again that Fluent now assigns $i = 1$ as the smallest class index and $i = \mathcal{N}$ as the largest class index):

$$B_{\text{ag},i} = \sum_{k=1}^{\mathcal{N}} \sum_{j=1}^{\mathcal{N}} a(v_k, v_j) N_k \, N_j \, x_{k,j} \, \xi_{k,j}, \tag{8.77}$$

$$D_{\text{ag},i} = \sum_{j=1}^{\mathcal{N}} a(v_i, v_j) N_i \, N_j, \tag{8.78}$$

with

$$\xi_{k,j} = \begin{cases} 1 & \text{for} \quad v_i \le v_{\text{ag}} < v_{i+1}, \quad \text{where} \quad i \le \mathcal{N} - 1 \\ 0 & \text{otherwise} \end{cases} \tag{8.79}$$

Here, v_{ag} is the particle volume due to aggregation of particles k and j:

$$v_j + v_k \longrightarrow v_{\text{ag}}. \tag{8.80}$$

If v_{ag} falls between two adjacent size classes, then it is redistributed over those adjacent classes, say v_i and v_{i+1}, in a similar way to the breakup case given in Eq. 8.71:

$$v_{\text{ag}} = x_{k,j} v_i + (1 - x_{k,j}) v_{i+1}, \tag{8.81}$$

where

$$x_{k,j} = \frac{v_{i+1} - v_{\text{ag}}}{v_{i+1} - v_i}. \tag{8.82}$$

In this form, v_{ag} is reassigned entirely to v_i when $v_{\text{ag}} = v_i$ and none to v_i when $v_{\text{ag}} = v_{i+1}$. This redistribution function ensures again both number and volume conservation in an arbitrary choice of grid for the size coordinate, e.g. linear or geometric, fine or coarse (Ramkrishna, 2000, p. 153).

Boundary conditions

At the boundaries, bin fraction value (f_i) or the spatial particle volume flux (dv/dx_i) could be specified.

Source terms

Source terms for bin fractions could be specified at grid cells. In our simulations, the gas sparger was modelled by mass and momentum source terms. In this case, bin fraction sources to the PBE should sum to the total mass flow of the secondary phase [kg m^{-3} s^{-1}].

Coupling with the fluid dynamics

In Fluent, the PBM of the bubbly phase is coupled with the overall fluid dynamics via the Sauter mean diameter in momentum equations. The Sauter mean bubble diameter, d_{32}, is defined for the DM as:

$$d_{32} = \frac{\sum N_i \, L_i^3}{\sum N_i \, L_i^2}. \tag{8.83}$$

8.3 Mean bubble diameters from measurements

Various statistical parameters can be used to describe a "mean bubble size" in a polydisperse system. The decision as to which one to take relies on the type of application it is going to be used for.

In this study, we compare our simulation results for the standard gassed–stirred tank with the experimental measurements of Barigou and Greaves (1992) for the same tank. They developed a capillary probe technique to measure the local bubble-size distributions, where a suction probe withdraws a continuous stream of gas–liquid dispersion from the tank into a 0.39 mm glass capillary. The gas bubbles captured are in turn transformed into elongated slugs inside the capillary and detected by a pair of LED phototransistors.

They used the following definitions of the statistical parameters to represent the mean bubble sizes in their measurements:

- Sample mean bubble diameter, d_{10}:

$$d_{10} = \frac{\sum_{i=1}^{i=n_\mathrm{b}} d_i}{n_\mathrm{b}} \tag{8.84}$$

- Sauter mean bubble diameter, d_{32}:

$$d_{32} = \frac{\sum_{i=1}^{i=n_\mathrm{b}} d_i^3}{\sum_{i=1}^{i=n_b} d_i^2} \tag{8.85}$$

- Overall mean bubble diameter, D_{10}:

$$D_{10} = \frac{\sum_{i=1,j=1}^{i=nj,j=m} d_{ij}}{\sum_{j=1}^{j=m} n_j} \tag{8.86}$$

- Overall Sauter mean bubble diameter, D_{32}:

$$D_{32} = \frac{\sum_{i=1,j=1}^{i=nj,j=m} d_{ij}^3}{\sum_{i=1,j=1}^{i=nj,j=m} d_{ij}^2} \tag{8.87}$$

where n_b is the sample size, n is the sample size at a given position j, and m is the number of positions represented.

Chapter 9

Simulations of gas dispersion in a standard stirred tank

The aim of this study is to present a computationally efficient route to investigate the hydrodynamics of two-phase flow in an aerated stirred tank reactor. Several modelling approaches have been tested, and the results obtained were compared with both experimental and numerical data available in the literature.

The modelling equations given in the previous chapters were solved by using the commercial finite-volume-based CFD solver Fluent 6.3 and 12.0 (Ansys Inc.). The geometry and computational mesh were built by the commercial model builder and mesh generator Gambit (Ansys Inc.).

9.1 The gassed–stirred tank

9.1.1 Geometry

The same standard configured laboratory-scale stirred tank was adopted for this study, for which we presented the single-phase results in Chapter 2. It is a flat-bottomed cylindrical tank ($T = H = 1$ m) equipped with four full length baffles. A central shaft with a six-blade Rushton turbine ($D = T/3$) is located at an off-bottom clearance $C = T/4$. Further details are given in Fig. 2.1. The tank liquid volume is 0.783 m^3.

9.1.2 Working fluid and operating conditions

The working fluid was a water–air system, with the material properties given in Table 9.1. Considering the available experimental data, four different operating conditions were chosen for the numerical study, details of which are given in Table 9.2. Those conditions were also investigated numerically in an earlier study by Lane (2005a), hence provides a second set of reference data for the evaluation of the CFD model. The flow is fully turbulent in all cases.

9.1.3 Flow regime map

In Fig. 9.1 the operating conditions for the simulation cases are shown on the flow regime map constructed from Eq. 3.23–3.26.

9.2 Experimental results of Barigou and Greaves

Gas holdup and bubble size measurement data is available for this tank, which was obtained using air and softened water (via weak ion-exchange resin through a dual set of sediment filters), to represent a "pure" fast coalescing system (Barigou and Greaves, 1992, 1996). The impeller gas cavities directly influence the two-phase flow regime in the tank. The cavity structures observed at the impeller are reported by Barigou and Greaves (1996) and given in Table 9.2.

9.2.1 Local gas distributions

Gas holdup measurement data has been reported for this tank by Barigou and Greaves (1996), which are given in Fig. 9.4. Only a subset of their results are given in the figure, corresponding to the conditions which have been investigated in this study. The sparger was a single tube orifice. They reported that all the measurements were performed in the loaded impeller flow regime. This is in line with the flow regime map constructed in Fig. 9.1.

Experimental technique

Overall gas holdup values were obtained from the rise in the level of dispersion in the middle plane between two adjacent baffles (mid-baffle plane) detected by a capacitance sensing probe. To account for fluctuations in the dispersion level, a mean value was obtained by averaging values at different radial positions over a period of time.

Local holdup measurements were made by a conductivity (or resistivity) probe at 22 locations comprising the bulk, near-impeller and below-impeller regions in the tank. Values were obtained by time-averaging the processed signal from the probe. Sampling time used was sufficiently long to obtain statistically representative sample of bubbles in the range $500 - 1000$. The reproducibility of the measurements was reported to be better than 5% for the local holdup and 4% for the overall gas holdup.

Results

The main findings of Barigou and Greaves (1996) are outlined here.

Local bubble passage frequency:

1. Highest bubble passage frequency was always found at the impeller region. This is expected since bubbles are generated from the dispersion zones of the gas cavities

behind the impeller blades. Furthermore, the liquid in the vicinity of the impeller discharge stream is entrained (by momentum transfer and turbulence) vertically into this radial stream and brings more bubbles with it into this region.

2. The frequency decreases in the radial direction towards the wall. Three mechanisms lead to this behavior. Firstly, due to the coalescence as bubbles move towards the wall. Secondly, due to the disengagement of bubbles from the impeller discharge stream, both in upwards and downwards direction. Coalescence favors upwards shift due to increase in the bubble rise velocities. Thirdly, as a result of the reduced entrainment of bubbles from adjacent regions as the radial velocity of the discharge stream reduces with radial distance.

3. Below the impeller, bubble density rises with radial distance, since the flow is directed from the wall to the center of the tank with the highest downward liquid velocity near the wall. However at the central region, bubbles are present only at sufficiently high stirring rates.

4. With increasing N, the frequency increases everywhere in the tank accompanied by increased gas holdup. Largest increase takes place below the impeller level, where smaller bubbles with lower rise velocities are transported to this region due to downward liquid flow.

5. When the gas flow rate is increased at constant N, the impeller approaches the flooding condition becoming less effective in circulating the gas at lower regions.

6. When N is increased at constant gas load, the degree of dispersion (as measured by the coefficient of variation defined as the ratio of standard deviation to spatial mean bubble passage frequency) first rises with N, but then declines as agitation exceeds the speed of recirculation. Further increase in N is expected to result in more uniform bubble distributions (i.e. low degree of dispersion and lower coefficients of variation).

Local gas holdup:

1. Resistivity probe underestimated the local holdup values. This is revealed by comparing the mean integral holdup obtained for each matrix by two-dimensional integration with the corresponding overall holdup measured independently by the level detection method. The measurement error was about 18% for Case 1, 17% for Case 2, 14% for Case 3 and 12% for Case 4.

2. Three principle regions can be identified in the tank: i) circulation region below the impeller, ii) circulation region above the impeller, and iii) impeller discharge stream.

3. Below the impeller region, the holdup always increases towards the wall. In the central region below the impeller, however, significant gas dispersion is observed only at high N and high gas flow rate. Overall, the gas holdup below the impeller is much lower than that at the upper regions, the vicinity of the tank wall being the only exception. Hence, large impeller clearances are not preferable for a good gas dispersion in the tank.

4. In the impeller discharge stream, the holdup reduces towards the wall. The holdup level near the wall is dependent on the radial liquid velocity, which is directly related to N. Sufficiently high N is required for radial liquid momentum to overcome the buoyancy effects which drive the bubbles out of the discharge stream.

5. Above the impeller region, complete dispersion takes place provided that the tank is not at the flooding regime. Maximum radial holdup is observed around the center of the measurement plane. Significant values are observed also near the impeller shaft. Near the wall, the gas flows upwards at higher velocities together with the circulating liquid, whereas in the central region buoyancy acts in the opposite direction to the downwards flowing liquid resulting in a higher holdup here.

6. Close to the free surface, the gas distribution is fairly uniform.

7. With increasing N, holdup increases everywhere in the tank and the gas distribution becomes more uniform (i.e. lower coefficients of variation, defined as the ratio of standard deviation to spatial mean local gas holdup).

8. When the gas flow rate is increased at constant N, higher holdups are observed in the bulk region but the degree of spatial dispersion remains almost the same under the three gas flow rates investigated. In the central region below the impeller, however, the gas dispersion is reduced until at the highest gas flow rate, no bubbles are detected. Further increase in gas flow gives rise gradually to the flooding condition diminishing the pumping and circulating capacity of the impeller.

Note that the results for bubble passage frequency are in parallel with that for the local holdup as expected.

Interfacial area distributions:

They also calculated the local gas–liquid interfacial area (a_x) distributions by combining the local gas holdup (ϕ_x) data given in Fig. 9.4 with the bubble size distribution of Barigou and Greaves (1992) which were acquired on the same measurement grid, using the conventional relation $a_x = 6\phi_x/d_{32}$. Following results were reported:

1. Below the impeller plane, a_x decreases when moving away from the wall.

2. Near the impeller, a_x is significantly large due to high gas holdup and small bubble size here, and decreases sharply towards the wall.

3. Above the impeller, in the bulk region, the radial distribution of a_x shows a maximum between the center and the wall.

4. Near the surface, the radial distribution of a_x is very uniform.

5. They fitted their data into two correlations by using the mean integral interfacial area (a) obtained from two-dimensional integration of a_x:

$$a = 250N^{0.85}Q_g^{0.38}, \tag{9.1}$$

where the small exponent 0.38 indicates that increasing the aeration rate is advantageous only at low values of Q_g. The second correlation is a more common one, in a form similar to Eq. 3.20, involving the specific gassed power and the superficial gas velocity:

$$a = 186 \left(\frac{P_g}{\mathcal{V}_l} \right)^{0.30} U_{g,s}^{0.51}, \tag{9.2}$$

Both correlations showed a scatter within ± 15%.

6. The interfacial areas when an electrolyte system (air–0.15M NaCl) was used were significantly higher than that for the air–water system.

9.2.2 Bubble size distributions

In an earlier study, Barigou and Greaves (1992) reported the bubble size distributions in the same tank (see Fig. 9.5). They also reported the overall Sauter mean diameter, D_{32}, as calculated from Eq. 8.87, at the impeller and below impeller regions. Those are given in Table 9.4.

Experimental technique

The measurement technique was based on a 0.39 mm glass capillary tube, which was used to withdraw a continuous stream of gas–liquid dispersion from the vessel. The gas bubbles were transformed into elongated slugs in the capillary and then detected by a pair of LED phototransistors. Bubble sizes were determined on-line by a computer analysing the signals generated by the bubble slugs. The reproducibility error of the Sauter mean diameter was reported to be below 6% at all times.

Results

The main findings of Barigou and Greaves (1992) are given briefly here. Note that the measurement grid was located at the mid-baffle plane, so the results correspond to relative positions in this plane.

Variations of d_{32} (impeller region):

1. Smallest bubbles are located at the impeller region near the impeller tip where the turbulence level is high and so, in turn, is the rate of bubble breakage. Higher impeller speeds generated always smaller bubbles here. However, no systematic trend with respect to N was found at the impeller region away from the tip, which was argued to be a characteristics of a non-homogenous turbulence field here.

2. Bubble sizes are significantly higher at other locations indicating in turn higher coalescence rates at the impeller discharge stream.

3. At low gas flow rate, overall Sauter diameter fall steeply with the increase in N, whereas at higher Q_g the effect is reduced until, at the highest gas load used,

overall effect of N becomes negligible (see Table 9.4). This is an expected trend showing that although breakage is the dominating mechanism at low Q_g, at higher Q_g coalescence becomes increasingly important due to higher bubble density.

4. At constant N, increasing Q_g leads always to increasing bubble size. This is due to: (*i*) reduced turbulence levels with increased Q_g, as the mechanical power dissipation is reduced and the velocity fluctuations are dampened; (*ii*) increased bubble density resulting in higher bubble collision and coalescence rates.

5. At 180 rpm, when they increased the gas load from 1.64 l/s to 4.38 l/s, the impeller gas cavity regime changed from 6 vortex cavities to 6 large cavities, resulting in a 41% decrease in the total gassed power input and doubling of the overall gas holdup. This resulted in a considerable increase in bubble size. Increasing Q_g to the highest value of 6.87 l/s did not change the gas cavity structure (although their size was slightly increased), causing a 5% drop in total power dissipation, not significant enough to effect the bubble size.

Variations of d_{32} (region below impeller):

1. The circulation flow at the lower part of the tank leads to accumulation of bubbles in the central zone below the impeller. At higher N, circulation flow is stronger, hence more bubbles are trapped here. Bubble sizes are quite large relative to that in the impeller stream due to lower turbulence levels. As a result, bubble size here is mainly determined by the coalescence rate.

2. Bubble size increases radially towards the tank wall due to increasing gas holdup and bubble density leading to higher collision and coalescence rates. With increasing N, the bubble size is only slightly reduced. Increasing Q_g at constant N has a more significant increasing effect on d_{32} at lower gas flow rates.

Variations of d_{32} (bulk region):

1. Increasing N does not result in a significant effect on the overall Sauter diameter, D_{32}. It is argued that this is due to the dynamic equilibrium established here, where the effect of increased turbulence due to increased N is balanced by the increased coalescence due to rise in holdup.

2. In the central core of the bulk region, d_{32} does not show any significant spatial variation. In contrast, at regions near the tank wall and shaft, significant variations do exist. Values are particularly higher near the shaft and this effect is more pronounced at lower regions in the bulk. This is due to the downwards liquid flow near the shaft (hence higher holdups and coalescence rates) and upwards flow near the wall.

Effect of impurities:
Even a small quantities of impurities in the system can have a significant effect on the bubble size. This is mainly via retarding the coalescence processes, because the small changes in the physical properties such as the surface tension are not sufficient enough to influence the bubble disruption processes in turbulent flow. Hence, small

bubbles tend to keep their size once they are formed. Overall, bubble sizes are smaller in comparison to pure systems. Barigou and Greaves (1992) used a 0.15 M sodium chloride system to simulate a typical industrial system where the coalescence rate is suppressed, but not totally inhibited. They found the following:

1. Dispersions are finer and more uniform. Reduction in D_{32} is within the range of 22–34%.
2. Up to 70% increase in the total holdup was observed especially at high stirring rates.
3. As a result of the reduction in bubble size and increase in holdup, there is a large increase in interfacial area.
4. Near the impeller shearing edge, the difference between the Sauter diameter for the ionic and water system is small, because bubble breakage dominates here over the coalescence.
5. Circulation at the lower part of the tank starts at lower impeller speeds in the salt solution, because smaller bubbles with lower rising velocity are easily entrained.
6. Increasing N has a negligible effect on D_{32} in the upper part of the tank. In the impeller stream and the lower part of the tank, however, the reducing of D_{32} is significant.
7. Increasing Q_g at constant N significantly increases D_{32} (e.g. at 180 rpm, the increase is 33% below the impeller, 70% in the discharge stream and 26% in the bulk).
8. Overall, the mean bubble size in the electrolyte system is significantly lower. For Case 2, the difference in D_{32} was 35%, and in D_{10} was 54% (see Eq. 8.86 for the definition of D_{10}).

9.2.3 Power dissipation

Power dissipation data provided by Barigou and coworkers is very limited for both gassed and ungassed operation. Barigou and Greaves (1992) reported that the total specific power was 2.00 kW/m^3 for the Case 2. As mentioned before, they also found that, at constant stirring rate of 180 rpm, the power draw was reduced by 41% when the aeration rate was increased from 1.64 l/s (Case 1) to 4.38 l/s, due to cavity regime change from 6 vortex cavities to 6 large cavities. When it was increased further to 6.87 l/s (Case 3), the power draw was decreased by 5%. Hence, moving from Case 1 to Case 3 resulted in an overall 44% drop in power dissipation. Those values for relative change in power draw would also be valid for relative change in gassed/ungassed power ratio (P_g/P) at the same stirring rate.

We can make a comparison now with the estimates from the empirical correlations of Hughmark and Bakker et al. for P_g/P (see Section 3.1.2, Eq. 3.11 and 3.12). In Table 9.5, the correlation estimates are given for all four cases we studied. For the not studied case of $Q_g = 4.38$ l/s, Hughmark and Bakker correlations give $P_g/P = 0.66$ and

0.60, respectively. As a result, when going from 1.64 l/s to 4.38 l/s, correlations predict 22% and 26% decrease in power, respectively, compared to the measured decrease of 41%. Moving from this point to Case 3 results in further 11% and 14% reduction, respectively, despite the measured reduction of 5%. Overall, going from Case 1 to Case 3 amounts to 30% and 37% estimated decrease in power, respectively, while the experimental value was 44%.

Results above show that there is a clear discrepancy between the experimental values and the estimates of the two correlations. Trends are also different; correlations both under– and overpredict with respect to the experimental data. It is interesting to observe, however, that Bakker correlation agrees quite well with that of Hughmark (max 13% deviation).

9.2.4 Possible sources of experimental errors

Barigou and Greaves (1996) checked the accuracy of their local gas fraction measurements by comparing the integrated value with the total holdup measured. That is, the mean integral holdup value obtained from each matrix given in Fig. 9.4 through two-dimensional integration was compared with the corresponding overall mean value determined independently by the level detection method. They found that the integration underestimated the overall holdup by $10 - 20\%$, which shows that the resistivity probe underestimated the local gas holdup. However, the correspondence of those two values depends also on how well the two-dimensional matrix of local values represent the three-dimensional spatial variations in the reactor. Hence, the lack of sufficient resolution of the measurement grid especially at the critical locations such as sparger and impeller zone would also result in this discrepancy.

Lane (2005a) argues (as also discussed by Barigou and Greaves (1996)) that despite the good reproducibility of the experiments, there might be systematic errors involved. The capillary tube method employed would not detect bubbles smaller than the capillary size, i.e. $d_\mathrm{b} < 0.4$ mm. The bubble size distribution would be distorted due to this. However, the Sauter mean diameter estimates are expected to be less effected, because, despite their large surface area, small bubbles having small total volume would contribute less to d_{32}. The bubble withdrawal may be a source of error, since it was not performed under isokinetic conditions, hence the gas–liquid mixture changes its speed when entering the tube. The sampling may also be biased with respect to the bubble size due to the fact that small bubbles would tend to follow the liquid streamlines while the large bubbles would tend to deviate. Barigou and Greaves (1996) also observed that very small bubbles were deflected from the conductivity probe rather then being pierced. Furthermore, the probes themselves would disturb the flow locally, thus influence both the bubble size and local gas fraction measurements.

9.3 Characteristic integrated quantities

The calculation of the power number N_P and the impeller flow number N_Q within a CFD framework follows from the ungassed case described in Section 2.2.3. Here, we will provide relations for gas-sparged systems.

9.3.1 Power input and dissipation

Mechanical power input under gassed conditions, $P_{g,\Gamma}$

Mechanical power transmitted to the fluid by impellers is called "gassed power draw". This power mainly enters the liquid phase and its dissipation also takes place in the liquid phase since the volume fraction of the gas phase is relatively low (Tatterson, 1991). The dissipation of this energy by viscous action is called "gassed power consumption". Under steady-state conditions, power draw and power consumption should be equal.

Gassed power draw is typically used for the determination of gas holdup, gas–liquid interfacial area, mass transfer rates and operating costs. Due to this importance, many power draw correlations, expressed usually in terms of gassed/ungassed power ratio (P_g/P) have been proposed in literature for single– as well as multi–impeller systems (see e.g. Section 3.1.2 and 3.2.1 as well as Tatterson (1991); Middleton (1992); Cui et al. (1996a)). However, as mentioned in Section 3.1.5, its prediction is not a trivial task. Because, gassed power draw is influenced by the gas–liquid flow regime at the bulk of the tank and the gas cavity regime near the blades. Those are themselves dependent on the complex bubble dynamics, gassing rate, impeller rotational speed, system geometry and fluid properties and rheology.

Power draw is commonly expressed in terms of the power number. Under gassed conditions, the power number is calculated from the relation

$$N_{P_g} = \frac{P_g}{\rho_1 N^3 D^5}. \tag{9.3}$$

The gassed power draw can be calculated from torque acting on the rotating parts similar to Eq. 2.11:

$$\begin{aligned} P_{g,\Gamma} &= \Omega \Gamma_g \\ &= 2\pi N \Gamma_g. \end{aligned} \tag{9.4}$$

Here we denoted the power draw by $P_{g,\Gamma}$, that is, the mechanical power input by moving parts under gassed conditions as calculated via the torque. The impeller angular velocity Ω is

$$\Omega = \frac{u_{tip}}{r_{tip}} = \frac{(2\pi r_{tip})N}{r_{tip}} = 2\pi N, \tag{9.5}$$

r_{tip} being the radius at the impeller blade tip. The torque on the rotating parts about the axis of rotation under gassed conditions, Γ_g, can be calculated from the pressure and viscous forces acting upon (Harvey and Rogers, 1996; Campolo et al., 2003):

$$\Gamma_g = 6 \left[\mathbf{a} \cdot \int_A \alpha_1 \mathbf{r} \times \left(\underline{\underline{\boldsymbol{\Sigma}}}_1 \cdot d\mathbf{A} \right) \right], \tag{9.6}$$

where $\mathbf{a}$ is the unit vector parallel to the axis of rotation, $\mathbf{r}$ is the position vector and $d\mathbf{A}$ is the differential surface vector. The calculation of the liquid phase averaged stress tensor $\underline{\underline{\boldsymbol{\Sigma}}}_1$ is given in Eq. 4.22. The integration above is carried out over all the rotating surfaces A. Note however that, those surfaces consists of only 1/6 of the total surfaces in the tank, since we have assumed symmetry. Hence, the prefactor 6 in the equation.

Implementation of this relation showed that the influence of the shear forces on the impeller disc and shaft were negligible, which is in line with the fully turbulent flow condition in the vicinity of the impeller. Finally, one can also write the power draw in the following equivalent form:

$$P_{g,\Gamma} = 6\left[\mathbf{\Omega} \cdot \int_A \alpha_1 \mathbf{r} \times \left(\underline{\underline{\mathbf{\Sigma}}}_1 \cdot d\mathbf{A}\right)\right], \tag{9.7}$$

$\mathbf{\Omega}$ being the impeller angular velocity vector.

Pneumatical power input, P_{gas}

When gas is sparged into the reactor, there is also a pneumatical power input associated with the gas flow, P_{gas}. According to Groen (1994), P_{gas} can be of the order 1 kW/m^3 (depending on the scale and filling grade of the tank), whereas the typical value for the ungassed power input of Rushton turbines is $2-5$ kW/m^3.

The sparged gas interacts with the flow around the impeller and form gas-filled cavities behind impeller blades. This influences the liquid contact area, hence the hydrodynamic resistance of the blades. Therefore, while there is an additional power input due to gas flow, the power uptake of the impeller can drop to 40% of the ungassed value, to about $0.8-2$ kW/m^3. This means, the pneumatical power input is of the same order of magnitude as the mechanical power input. In such cases, the power input by the gas phase cannot be neglected. For effective dispersion and mixing in a tank, it has been recommended that $P_{g,\Gamma}/P_{gas} = 1-5$ (Groen, 1994).

The pneumatical power input can be divided into the following contributions:

- Gas expansion work and kinetic energy transfer during gas injection. Those are usually assumed to be small, about 6% of P_{gas}, and are neglected. An exception is when the tank operates under high pressure. At 10 atm, it was observed that the jetting power P_{jet} was significant, up to 50% of the mechanical power input by the impeller, due to increase in gas density by pressure (Tatterson, 1991).

  This jetting power due to the dissipation of the kinetic energy of gas jets from sparger holes with a velocity of u_g can be given by

  $$P_{jet} = \frac{1}{2} Q_g \rho_g u_g^2. \tag{9.8}$$

  In our CFD simulations, the momentum source term given in Eq. 9.29 takes into account the mean kinetic energy of gas injection in the gas phase. The turbulence energy due to gas injection is expected to be significant for high aeration rates and limited to a region near the sparger (Laakkonen et al., 2007). We assumed this contribution to be negligible and did not include any additional source term in turbulence equations to take into account gas injection.

- Rising bubbles contribute to power input, which can be modelled as pres-

sure/volume work per time (Tatterson, 1991; van't Riet and Tramper, 1991):

$$\begin{aligned} P_\mathrm{b} &= \dot{n}_\mathrm{g} R T_\mathrm{l} \ln\left(\frac{p_\mathrm{spa}}{p_0}\right) \\ &= Q_\mathrm{g}^\mathrm{lm}(p_\mathrm{spa} - p_0) \\ &= Q_\mathrm{g}^\mathrm{lm}\rho_\mathrm{l} g H, \end{aligned} \tag{9.9}$$

where R is the gas constant, T_l is the liquid temperature, H is the liquid height in the tank and p_spa and p_0 are the pressure at the sparger and liquid surface, respectively. The molar gas flow rate is given as

$$\dot{n}_\mathrm{g} = Q_\mathrm{g}^\mathrm{lm}\frac{p^\mathrm{lm}}{RT_\mathrm{l}}, \tag{9.10}$$

which is defined in terms of Q_g^lm, the gas flow rate at T_l and the log mean pressure p^lm:

$$p^\mathrm{lm} = \frac{p_\mathrm{spa} - p_0}{\ln(p_\mathrm{spa}/p_0)}. \tag{9.11}$$

Up to tank heights of 1 m, a rule of thumb is that each 0.01 m/s of gas superficial velocity $U_\mathrm{g,s}$ accounts for a dissipated power of 0.1 kW/m^3, and gradually decreases for larger tank heights (van't Riet and Tramper, 1991). The superficial gas velocity (at atmospheric conditions) in the tank is related to the tank diameter, $U_\mathrm{g,s} = Q_\mathrm{g}/(\pi T^2/4)$, and it ultimately determines the actual gas volume in the reactor. In order to account for hydrostatic pressure effects, the superficial velocity at a characteristic pressure of choice is usually used, $U_\mathrm{g,s}^\mathrm{c} = U_\mathrm{g,s}(p_0/p^\mathrm{c})$ (assuming ideal gas where $U_\mathrm{g,s}\ p$ = constant). For mass transfer calculations in stirred tanks (which takes place primarily in the stirrer region), van't Riet and Tramper (1991) recommend a characteristic pressure as the local pressure at the stirrer level, hence $U_\mathrm{g,s}^\mathrm{c} = U_\mathrm{g,s}(p_0/p_\mathrm{sti})$. For calculations of power input by gas flow, Groen (1994) and Vrábel et al. (2000) used the log mean pressure between the gas input location (i.e. the sparger level) and the liquid surface, as recommended by van der Lans (1985) and Heijnen et al. (1997):

$$U_\mathrm{g,s}^\mathrm{c} = U_\mathrm{g,s}\frac{p_0}{p^\mathrm{lm}}, \tag{9.12}$$

They calculated then the mean power input in their experiments due to the gas flow from the relation

$$P_\mathrm{b} = (m_\mathrm{l} g)U_\mathrm{g,s}^\mathrm{c}, \tag{9.13}$$

which, by using Eq. 3.14 and 9.12, can be rewritten as $P_\mathrm{b} = (Q_\mathrm{g}\rho_\mathrm{l} g H)\,\frac{p_0}{p^\mathrm{lm}}$, resulting in an equivalent form to Eq. 9.9.

In CFD calculations, the power transmitted to liquid by rising bubbles is inherently accounted for by the momentum equations. This power contribution from bubbles has a mean and a turbulent part. The turbulent energy associated with the bubbles is represented by the fluid–particle turbulent interaction term Π_{k_l} given in Eq. 5.16. The energy due to mean bubble motion is accounted for by the mean interfacial momentum transfer term $\mathbf{M}_\mathrm{l}'$ given in Eq. 6.34.

Energy dissipation under gassed conditions

Local energy dissipation is a crucial process parameter in gas-sparged reactors due to its effect on bubble size distribution, mixing in the tank and the mean drag force experienced by bubbles under turbulence interactions.

Under ungassed conditions in fully turbulent flow, the power input by impellers should be equal to the integrated turbulent energy dissipation in the tank under steady-state conditions (cf. Section 2.2.3). The total power transmitted to the liquid under gassed conditions was given in the previous section. This power can be dissipated by the following three mechanisms:

- Dissipation in the turbulent motion, $P_{\mathrm{g},\varepsilon}$:

  The power input by the impeller and the gas flow leads to formation of large eddies at the macro scale of the order of the main flow pattern. Based on estimation from the energy spectra, these large eddies consitute 20 % of the total energy, and have a direction, hence are not isotropic (Groen, 1994). They are not stable and they cascade their energy to smaller eddies with higher frequency by vortex stretching. These energy containing intermediate scale eddies cascade their energy to yet smaller eddies, which have no preferential direction, hence are isotropic. At the smallest scale, of the order of Kolmogorov length, all of the energy is dissipated into thermal energy by viscous action.

  The total turbulent dissipation can be calculated by the following integral:

  $$\begin{aligned} P_{\mathrm{g},\varepsilon} &= 6\left[\int_{\mathcal{V}_{\mathrm{tank}}} \alpha_1\rho_1\left(2\nu_1\overline{\underline{\underline{\mathbf{s}}}_1' : \underline{\underline{\mathbf{s}}}_1'}\right) dV\right] \\ &= 6\left[\int_{\mathcal{V}_{\mathrm{tank}}} \alpha_1\rho_1\varepsilon_1 dV\right], \end{aligned} \tag{9.14}$$

  ε_1 being the dissipation rate of the liquid turbulent kinetic energy by viscous action as defined in Eq. 5.6 and calculated from the turbulence model according to the transport equation given in Eq. 5.11. Due to the symmetry assumption again, the volume of the tank in the computational domain is 1/6 of the actual volume, hence the prefactor 6.

- Dissipation in the mean flow, $P_{\mathrm{g,vis}}$:

  Mean kinetic energy is dissipated at larger scales by viscous forces due to mean velocity gradients:

  $$P_{\mathrm{g,vis}} = 6\left[\int_{\mathcal{V}_{\mathrm{tank}}} \alpha_1\rho_1(2\nu_1\underline{\underline{\mathbf{S}}}_1 : \underline{\underline{\mathbf{S}}}_1) dV\right], \tag{9.15}$$

  which follows from the viscous dissipation rate of the mean flow kinetic energy as given in Eq. 5.5. The mean strain rate tensor $\underline{\underline{\mathbf{S}}}$ here should not be mistaken by the mean momentum source term $\mathbf{S}$.

- Dissipation in the boundary layers, $P_{\mathrm{g,BL}}$:

  Viscous energy dissipation takes place in the boundary layers at the walls (blade, disc, tank wall and baffle). Boundary layers are not resolved in our computational

model, but modelled by wall functions (see Section 5.3). Therefore, the viscous dissipation in the boundary layers at no-slip walls are not accounted for in the $P_{\mathrm{g,vis}}$ given above. Viscous energy dissipation in the boundary layers can be expressed as

$$P_{\mathrm{g,BL}} = 6\left[\int_{\mathcal{V}_{\mathrm{BL}}} \alpha_1 \rho_1 \varepsilon_{1,\mathrm{BL}}\, d\mathcal{V}_{\mathrm{BL}}\right] \tag{9.16}$$

$$= 6\left[\int_{S_{\mathrm{w}}} \int_{\delta} \alpha_1 \rho_1 \varepsilon_{\mathrm{BL},1}(S_{\mathrm{w}}, \delta)\, d\delta(S_{\mathrm{w}})\, dS_{\mathrm{w}}\right], \tag{9.17}$$

where $\mathcal{V}_{\mathrm{BL}}$ and δ are the volume and the thickness of the boundary layer, respectively, $\varepsilon_{\mathrm{BL},1}$ is the viscous dissipation in the boundary layer and S_{w} is the surface of the walls.

The boundary layer thickness can be written in terms of the dimensionless thickness of the boundary layers y^+, the wall shear velocity $u_{\tau,1}$ and the wall shear stress $\tau_{\mathrm{w},1}$ using Eq. 5.37 and 5.38:

$$\delta = \frac{\mu_1 y^+}{\rho_1 u_{\tau,1}} = \frac{\mu_1 y^+}{\sqrt{\rho_1 \tau_{\mathrm{w},1}}} \tag{9.18}$$

Viscous dissipation in the boundary layer can be expressed as:

$$\varepsilon_{1,\mathrm{BL}} = \frac{\tau_1}{\rho_1}\dot{\gamma}_1 = \frac{\mu_1}{\rho_1}\left(\dot{\gamma}_1\right)^2, \tag{9.19}$$

and the boundary layer shear rate, $\dot{\gamma}_1$, is not constant but depends on wall-normal distance y. It can be written in terms of y^+ and the normalised wall-parallel mean velocity $U_{\parallel,1}$ (using the definitions in Eq. 5.37, 5.38 and 5.40):

$$\dot{\gamma}_1 = \frac{\partial U_{\parallel,1}}{\partial y} = \left(\frac{\tau_{\mathrm{w},1}}{\mu_1}\right)\frac{\partial U^+_{\parallel,1}}{\partial y^+}, \tag{9.20}$$

hence using Eq. 5.39 and 5.42, we have

$$\dot{\gamma}_1 = \begin{cases} \dfrac{\tau_{\mathrm{w},1}}{\mu_1} & y^+ < y^+_{\mathrm{vis}} \\ \dfrac{\tau_{\mathrm{w},1}}{\mu_1}\left(\dfrac{1}{\kappa y^+}\right) & y^+ > y^+_{\mathrm{vis}} \end{cases} \tag{9.21}$$

where y^+_{vis} is the thickness of the viscous sublayer which is usually taken as the intercept of the Eq. 5.39 and 5.42, i.e. $y^+_{\mathrm{vis}} \approx 11.225$. Now, using Eq. 9.18, 9.19 and 9.21, and assuming that $y^+ >> y^+_{\mathrm{vis}}$, the inner integral in Eq. 9.17 becomes

$$\int_0^{\delta} \alpha_1 \rho_1 \varepsilon_{\mathrm{BL},1}(S_{\mathrm{w}}, \delta)\, d\delta(S_{\mathrm{w}})\, dS_{\mathrm{w}} = \alpha_1 \frac{\tau_{\mathrm{w},1}^{3/2}}{\sqrt{\rho_1}}\left[y^+_{\mathrm{vis}} + \frac{1}{\kappa^2 y^+_{\mathrm{vis}}}\right]. \tag{9.22}$$

With this, the total contribution of the viscous dissipation in the boundary layer could now be written as

$$P_{\mathrm{g,BL}} \approx 6\left(\frac{1}{\sqrt{\rho_1}}\sum_i \alpha_{1,i}\, \tau_{\mathrm{w},1,i}^{3/2}\left[y^+_{\mathrm{vis}} + \frac{1}{\kappa^2 y^+_{\mathrm{vis}}}\right] S_{\mathrm{w},i}\right). \tag{9.23}$$

Energy balance

Having all the energy input and dissipation terms identified above, we can now write an energy balance for the reactor which must hold under steady-state conditions:

$$P_{g,\Gamma} + P_{jet} + P_b = P_{g,\varepsilon} + P_{g,vis} + P_{g,BL}. \tag{9.24}$$

Since the tank operates in fully turbulent regime, the turbulent dissipation is expected to be the dominant mechanism over the viscous dissipation, thus

$$P_{g,\Gamma} + P_b \approx P_{g,\varepsilon}. \tag{9.25}$$

When the aeration rate is low and impeller motion is the major source of energy input, it could further simplified to $P_{g,\Gamma} \approx P_{g,\varepsilon}$.

Underestimation of turbulent dissipation in literature

As discussed in Chapter 2, it has been commonly reported that the turbulent energy dissipation is underestimated in CFD studies when the turbulence is modelled rather than resolved (Gentric et al., 2005; Lane et al., 2005b; Khopkar and Ranade, 2006; Laakkonen et al., 2007).

Gentric et al. (2005) reported that their single-phase sliding mesh simulations gave a better prediction of turbulence in comparison with the MRF method. They found that the local turbulent kinetic energy and dissipation rates were up to 3 times lower with the MRF approach. However, even with SM, the integrated dissipation rates were clearly underestimated. In their two-phase simulations, they calculated the power consumption estimated from the integrated dissipation minus the energy provided by the gas. It was still largely underestimated when compared to the measured value in the plant.

For the reasons mentioned above, in some studies (e.g. Laakkonen et al. (2007)), local dissipation rates calculated from CFD were scaled with the measured power consumption in the tank based on torque. Those modified values were used in the bubble size models being implemented. Other studies employed simply fitting coefficients for bubble break-up and coalescence source terms and/or for turbulent drag models (e.g. Lane et al. (2000, 2005b); Khopkar and Ranade (2006)).

9.3.2 Gassed flow number

As pointed out in Section 3.1.1, the pumping capacity of the impeller is reduced when gas is dispersed into the reactor. This is due to reduced contact of the impeller with the liquid phase and decrease of the available area for the impeller discharge flow. The discharge flow rate from the impeller under gassed conditions, Q_G, can be calculated from the following relation (Gentric et al., 2005; Khopkar and Ranade, 2006), which is in a form similar to Eq. 2.15:

$$Q_G = 6\left[\int_{-B/2}^{B/2}\int_{0}^{\pi/3} \alpha_1 U_r \left(\frac{D}{2}\right) d\theta\, dy\right] \tag{9.26}$$

The integration above is carried out at a periodic section of the radial impeller swept surface (i.e. $S_{\text{swept}}/6$), extending 60° in the circumferential direction and blade width of $B = D/5$ in the axial direction y. The impeller flow number under gassed conditions can now be calculated similar to Eq. 3.2:

$$N_{Q_G} = \frac{Q_G}{ND^3} \tag{9.27}$$

9.4 Numerical setup

9.4.1 Solution domain and computational mesh

In order to reduce the computational time, only a 60° sector (i.e. 1/6) of the full domain was modelled, including a single impeller blade and a baffle. Rotational periodic condition was employed at the vertical cross-sectional planes. Note that, due to symmetry, the simulation essentially represents a tank with six baffles. However, this additional baffling is expected to alter the flow field only locally near the baffles, because the swirling flow has already been stopped by four baffles and the baffles have little effect on the flow in the radial and axial directions (Lane, 2005a). We did, however, a test simulation modelling a full 360° sector in order to check the effect of rotational periodicity assumption.

Five different finite volume meshes were generated (Fig. 9.2).

- The coarse mesh: 47k ($65 \times 36 \times 20$) structured elements. Impeller blade surface was resolved by 56 grid cells.
- The medium mesh: 140k($97 \times 60 \times 24$) structured elements (192 cells/blade).
- The fine mesh: 374k×47k structured elements (224 cells/blade). This grid resolution was achieved by increasing the grid nodes of the coarse mesh two times in each dimension.

In order to test the influence of the boundary conditions used, two modifications to the coarse mesh were made:

- An extra water–gas disengagement region of $0.3H$ in height was added above the ungassed free surface level H resulting in a mesh of 58k ($80 \times 36 \times 20$).
- The 60° coarse mesh was extended to a full 360° sector of tank giving the 281k (6×47k) mesh.

Grid interface

The grid interface between the moving and stationary zones, as required by the MRF and SM models, was set at a region extending axially from the impeller centreline in the range of $(-D/4, D/4)$ and located radially at midway between the impeller tip and the baffle.

9.4.2 Boundary conditions

In order to see the effect of different modelling routes at boundaries, several options were tested.

Walls

All solid parts were modelled as zero-thickness surfaces with no-slip condition in this study. The boundary layer at walls was modelled by applying standard wall functions (see Section 5.3), which avoids the need for a very fine grid in near-wall regions to resolve the boundary layer. The impeller shaft was assumed to extend from the free surface down to the bottom wall in order to ensure high mesh quality.

Outlet

The free surface was modelled in three alternative ways:

- a flat "degassing" boundary, that imposes a symmetry condition for the liquid phase, while the gas phase is free to leave the domain;
- a flat "pressure outlet" boundary, where backflow is allowed only for the liquid phase;
- the free surface is represented explicitly by allowing for an additional (30% of liquid level) gas-filled "disengagement height" above the free surface and a pressure outlet boundary at the exit, where backflow is allowed only for the gas phase.

Inlet

The gas inflow from the sparger was also modelled in two different ways:

- implicitly, in which a separate ring-shaped fluid zone was defined, of about $D/2$ in diameter located about $0.6D$ below the impeller. Source terms for the gas phase mass, momentum and bubble bin-fraction equations were specified at this zone;
- explicitly, in which the above mentioned fluid zone was subtracted from the computational domain, resulting in a ring-shaped void bounded by solid surfaces. At the upper surface, a conventional "velocity inlet" boundary was defined. The remaining surfaces were no-slip wall boundaries.

The mass source term S_2 (see Eq. 4.20) is calculated from

$$S_2 = \frac{\dot{m}_\mathrm{g}}{\mathcal{V}_\mathrm{spa}} = \frac{\rho_\mathrm{g} Q_\mathrm{g}}{\mathcal{V}_\mathrm{spa}} = \frac{\rho_\mathrm{g} \mathcal{A}_\mathrm{spa} U_\mathrm{g}}{\mathcal{V}_\mathrm{spa}}, \tag{9.28}$$

where the mass and volume flow rate of sparging gas are given respectively by $\dot{m}_{\mathrm{g}}$ and Q_{g}, and U_{g} is the mean velocity of sparging gas. The sparger volume is denoted by $\mathcal{V}_{\mathrm{spa}}$ and the total surface area available for the gas outflow at the sparger is $\mathcal{A}_{\mathrm{spa}}$. The momentum source $\mathbf{S}_2$ (see Eq. 4.21) is related to the mass source as follows:

$$\begin{aligned} |\mathbf{S}_2| &= \frac{Q_{\mathrm{g}}}{\mathcal{A}_{\mathrm{spa}}} S_2 \\ &= \frac{\rho_{\mathrm{g}} \mathcal{A}_{\mathrm{spa}} U_{\mathrm{g}}^2}{\mathcal{V}_{\mathrm{spa}}}. \end{aligned} \tag{9.29}$$

From the relations above and using the geometric dimensions of the computational cells allocated for the modelling of the sparger (for which the source terms apply), one can calculate the source terms depending on the information of either the aeration rate Q_{g} or the gas injection velocity U_{g}. Note that, the gas sparging was assumed to be in perpendicular direction ($y-$axis), hence the source term was defined only for the $y-$momentum equation.

It should be noted that Barigou and Greaves (1992, 1996) used a single tube orifice (19 mm diameter) sparger in their experiments. They pointed out that using a more sophisticated arrangement, such as a ring sparger, seemed to give no advantage. Experiments of Nienow et al. (1985) and Warmoeskerken and Smith (1985) also showed that the geometry of the sparger and the impeller–sparger clearance did not have a significant effect on the flooding–loading transition and the power demand, provided the ring sparger was smaller in diameter than the impeller disk.

9.4.3 Population balance model (PBM)

In this study, we used the discrete method, in which scalar transport equations are solved for each pre-defined bubble class. Breakup and coalescence effects are taken into account by source and sink terms. These terms are calculated from breakage and aggregation kernels which follow from the Luo model. Details of the PBM model are given in Chapter 8. All PBM simulations were run in the transient mode in order to ease convergence.

Three sets of pre-defined bubble size classes (bins) were used in the simulations. These are given in Table 9.6.

Inlet source term for bin fraction

It was assumed that the initial size of sparged bubbles is 3 mm. Thus, at the sparger cells, a mass source term was defined for the appropriate bubble bin-fraction equation according to Eq. 9.28.

9.4.4 Discretisation schemes

We used both the QUICK and the second-order upwind scheme for discretisation of the convective terms in the momentum and turbulence equations. Details of those schemes

can be found in Fluent (2009). Single- and two-phase test simulations showed that the predictions by the second-order upwind and QUICK schemes were very similar. The volume fraction equation was always discretised by the QUICK scheme. A first-order upwind scheme was used for the scalar transport equations solved for the bubble size bins, since convergence with the higher-order schemes was not possible. Note that, for diffusive terms, Fluent always uses second-order accurate central-differenced scheme.

9.4.5 Pressure-velocity coupling

Pressure-velocity coupling was achieved by the phase-coupled semi-implicit method for pressure-linked equations (PC-SIMPLE) algorithm (Vásquez and Ivanov, 2000), in which the momentum equations of all phases and the pressure correction equation constructed from the total continuity are solved in a sequential fashion. In some simulations, the multiphase implicit coupled algorithm (Ghobadian and Vásquez, 2007) was used, in which the momentum equations and the shared pressure are solved simultaneously.

9.4.6 Convergence criteria

Simulations were considered converged when monitored relevant quantities (such as impeller torque, impeller discharge flow rate, integrated turbulent dissipation, volumetric gas outflow rate, bin fractions, Sauter diameter) had already reached a steady value or deviate within a narrow band around a steady value. At this level of convergence, the sum of the residuals (i.e. the imbalance in the algebraic equation summed over all computational cells and scaled by a factor representative of the flow rate of that variable) was within the range $10^{-3} - 10^{-5}$.

9.4.7 Solution initialisation

Simulations were first run in two-phase mode with zero gas flow rate. When a converged solution had been reached, then the gas flow was turned on starting from this initial solution. This was required in order to ease and speed-up convergence of two-phase simulations. In Fig. 9.6, typical single-phase velocity fields are given at variable locations in the tank for the standard case.

9.5 Results and discussion

CFD analysis results of the standard gassed–stirred tank are given in this section. Comparisons are made between the different modelling options used in this study, and between our results and that from Lane (2005a).

Numerical results are also compared with the experimental results from Barigou and Greaves (1992, 1996). It is important to notice that the measurements of local holdup and bubble size were made by the measurement grid placed at a mid-baffle plane. Hence, the effect of impeller rotation is reflected by those fixed-point measurements in

a time-averaged sense. Baffles are at a fixed position with respect to the measurement grid. CFD profiles plotted here, however, are circumferentially averaged profiles over the 60 degree section of the tank. Therefore, they represent spatially averaged values of the steady flow developed in the tank for a particular (fixed) impeller–baffle position (for MRF simulations).

9.5.1 Standard model

In order to provide a basis where we can compare the impact of different modelling options, we defined a "standard model" and use it as a reference data. The set of conditions chosen for the standard model are given in Table 9.3.

9.5.2 Earlier simulations

Some of the earlier simulation results where different modelling options had been investigated were reported previously (Günyol and Mudde, 2007a,b). The aim of those simulations was to investigate a computationally efficient and affordable route, which is able to capture sufficiently the physics involved. We also used the algebraic slip mixture model (ASMM) as an alternative to Euler–Euler multiphase modelling approach. The results reported here are from those simulations where we adopted:

- 47k mesh,
- fixed bubble size of 3 mm,
- degassing outlet condition.

Algebraic slip mixture model

The ASMM was of interest, since it was computationally cheaper. This is because only a single set of transport equations (mass, momentum and turbulence) are solved for the so-called mixture phase. An additional transport equation is solved for the volume fraction of the dispersed gas phase. The relative velocity between the phases is calculated from an algebraic empirical equation. Further details and the equations being solved are given in Appendix A.

The continuity and momentum equations for the mixture phase are obtained by summing up the respective equations for the liquid and gas phases. Hence, the interface momentum transfer term which has an opposite sign in liquid and gas phase equations drops after summation. Therefore, the interface interaction forces such as virtual mass and lift are not taken into account. The drag force is taken into account in the algebraic slip formulation.

ASMM is recommended for dilute bubbly flows where the gas volume fraction remains low and the phases moving at different velocities reach equilibrium over short spatial length scales (Fluent, 2006). In view of our goal to achieve a generic modelling approach, which applies also for industrial fermenters operating in dense bubbly flow regime, we decided to take the Euler–Euler approach in later simulations.

Convergence problems with lift and turbulent dispersion forces

Simulations did not converge when the lift force was included in the momentum equation. Lane (2005a) and Deen (2001) also report that their stirred tank simulations with the lift force did not converge. Convergence problems were also encountered in the Euler–Euler simulations when the turbulent dispersion effect in the momentum equation was taken into account, and therefore it was not included. Having these limitations, simulations have been performed for four different modelling options where MRF was used for the modelling of moving parts:

- Euler–Euler simulations with drag force,
- Euler–Euler simulations with drag and virtual mass force,
- ASMM simulations with drag force,
- ASMM simulations with drag and turbulent dispersion force (turbulent dispersion terms included in the momentum and turbulence equations).

The results are compared with the experimental data from Barigou and Greaves (1992, 1996) and the simulation results from Lane (2005a) where he reported Euler-Euler simulations results (with MRF model) for the same cases. The data taken for the comparison of the current simulations is from his model in which the drag relation from Ishii and Zuber (1979) was used, virtual mass and lift forces were neglected, and a simpler turbulent dispersion term was implemented in the form given in Eq. 6.51. Unless mentioned otherwise, a constant bubble size of 3 mm was assumed, which is also the case for the results reported here.

Convergence plots

Typical convergence profile of the overall gas holdup is shown in Fig. 9.7(a) and (b). The former one shows the effect of increasing gas flow rate at constant impeller speed of 180 rpm. By the increase of gas flow, overall gas holdup in the tank increases as expected. In the latter, a similar comparison is made by increasing the stirring rate at constant gas flow rate. As the stirring rate increases, the recirculation vortices in the tank become stronger, therefore more gas is entrained in the system.

Those results show that there is no substantial difference between the Euler-Euler and ASMM predictions of the total gas holdup at relatively low levels of stirring and gassing rates. The difference increases with the increase of stirring and gassing rates thus indicating that variation in the prediction of slip velocity is larger at higher turbulence levels and denser bubbly flow regimes. This seems to suggest that the underlying assumptions and the simple calculation method of slip velocity by ASMM may not be valid at more realistic process conditions.

Gas cavities

In Fig. 9.8, the top view of the gas velocity field (coloured in greyscale by gas volume fraction) with respect to the rotating reference frame is given for Case 4. Two recir-

culation zones form behind the impeller blade: at the front and rear end of the blade. These zones are responsible for the entrapment of the sparged gas and the formation of gas cavities. A higher density grid ($130 \times 72 \times 40$ cells) was used to capture the details of the gas cavity. The velocity field is plotted on a plane slightly above the impeller centerline ($y = 0.27$ H), where the core of the gas pocket is located. Considerable amount of gas accumulation (volume fractions $> 75\%$) is evident which is consistent with the large cavity regime observed by Barigou and Greaves for this case. This is also evident from the location of Case 4 operating point in the flow regime map in Fig. 9.1.

Comparison of different modelling options

In Fig. 9.9, a collection of contour plots (at the vertical mid-baffle plane) are given for different simulation cases and modelling options. Corresponding results are summarised in Table 9.7 in terms of overall holdup and ratios of gassed/ungassed power draw and impeller pumping rate.

For all simulation cases, predicted gas holdup values were considerably lower than the experimental values. This is mostly attributed to the assumption of constant bubble size of 3 mm in the computations and the relatively simple drag model which does not take into account the effects of bubble deformation, turbulence and high gas fractions. Furthermore, if bubble breakup effects are taken into account which are significant at highly turbulent regions (i.e. near the impeller), more bubbles are expected to disperse into both lower and bulk regions of the vessel due to less pronounced buoyancy effects. In later simulations, it was found that the increase in the drag force due to turbulence had a dramatic effect on the results. Those are reported in the coming sections.

The gas volume fraction contours in Fig. 9.9 show the expected tendencies according to the flow regime map given in Fig. 9.1. The lowest gas dispersion was obtained for the simulation Case 3, which stands closest to the flooding transition line and just at the limit of complete dispersion. In Euler–Euler simulations, bubbles are hardly dispersed; they rather rise up as a relatively thin plume like in a bubble column. No bubbles are captured in the lower part of the tank below the impeller level.

Approaching from Case 3 to Case 1 on the flow map, that is, decreasing the gas flow rate at constant impeller speed, the gas is entrained in a larger part of the upper bulk region of the tank. Euler–Euler simulation with the virtual mass force and the ASMM simulation (with and without the turbulent dispersion and the bubble induced turbulence terms) show some degrees of gas accumulation at the lower recirculation loop.

By increasing the impeller speed at constant gas flow rate, that is, going from Case 1 to Case 2, we are now on the gross gas recirculation boundary on the flow map. The gas bubbles start to appear also in the lower vortex region for the Euler–Euler simulation, and the gas dispersion in the bulk region is higher.

Finally, going from Case 2 to Case 4 by increasing both the impeller speed and the aeration rate, the gas entrainment in both upper and lower recirculation zones becomes more significant. The overall gas holdup value for the mixture model simulation is 6.8, being closest to the experimental value of 9.65. The same tendency of higher gas holdup

predictions with the mixture model holds for the simulation cases 2 and 4, where the stirring rate is higher.

The observations mentioned above are generally in agreement with the experimental observations of Barigou and Greaves (1996). They reported that the local gas holdup was highly non-uniform with most of the gas residing in the bulk region of the tank. They observed that the effect of the impeller speed was to increase the holdup at most positions and enhance uniformity in gas distribution. The effect of an increase in the gas flow rate was an almost uniform rise in the gas holdup in the bulk and a reduced gas circulation in the lower region of the vessel. They also indicated that in the lower part of the vessel, the holdup always increased towards the wall, with values near the center being in general low. Significant gas dispersion in the central area below the impeller was only achieved with the combination of highest impeller speed and gas flow rate.

Gas distribution

In order to compare above observations in a quantitative manner, the gas volume fraction profiles on the mid–baffle plane at different axial levels are given in Fig. 9.10 together with the experimental measurements from Barigou and Greaves (1996) and the simulation data from Lane (2005a). The axial levels correspond to locations z1, z2, z4 and z5, respectively, in Fig. 9.3. Lane adopted a fixed spatial bubble size distribution based on the experimental data.

Fig. 9.10(a) shows that observation of low gas volume fraction levels at the lower part of the tank is in agreement with the simulations. At the region close to the shaft, higher values were obtained in comparison to the results from Lane. This was probably due to differences in the modelling of the ring sparger close to this location. Lane modelled the ring sparger by defining mass and momentum source terms, same as in our simulations. However, the diameter and the axial position of the sparger were not clear. The experimental values for the local holdup, like the overall holdup values, were almost always higher than the simulation values. This is because the gas phase modelling was not sufficient.

Lane (2005a) did some modification to his default model, from which we took most of the data reported here. He proposed a new drag correlation accounting for the increase in drag coefficient on bubbles due to interaction between bubbles and turbulence (see Section 6.7.8). Bubble breakup and coalescence phenomena was also accounted for by introducing a bubble density equation. Furthermore, he modified his model at high gas fractions for better prediction of the gas cavities. With this revised model, Lane obtained significantly higher holdup values, close to the experimental measurements.

In Fig. 9.10(b), the volume fraction profile at the impeller stream (i.e. at axial height 0.25 H) is shown. The gas accumulated at the impeller disk gives rise to the initial high values close to the shaft. Going in the radially outward direction, gas fraction shows a sudden drop, as the trailing vortices drift away from the impeller blade. It increases again when we are arriving at the position with the two gas cavities which were emerged from the upper and lower part of the blades. By further going in the direction to the wall, there is hardly any gas encountered, since the impeller stream decelerates close to the wall, and the radial liquid momentum is not strong enough to

bring the bubbles near the wall before they rise up under the buoyancy effect.

At the upper bulk part of the tank, where most of the dispersion is taking place, the local holdup values from the experimental measurements and the simulations show a peak close to the center of the plane as shown in Fig. 9.10(c). This is because of the downwards flowing part of the liquid recirculation zone here, which acts in the opposite direction of the buoyancy of the bubbles. Coming close to the tank wall, we are now at the opposite side of the vortex eye, where the liquid coming from the impeller discharge stream is flowing upwards and therefore bubbles can easily escape, resulting in lower holdup values. The gas distribution for the Euler–Euler with the virtual mass force show at this location an unexpected profile in the close proximity of the impeller shaft. There is a steep increase in the gas fraction, which was not observed in other simulations. This is evident from the corresponding contour plot in Fig. 9.9, where there is a high amount of gas accumulation at this region. Somewhat higher levels of holdup are expected in such regions, where the liquid flow is principally downwards. However, such high values and steep gradients indicate an overprediction.

Finally, getting closer to the free surface, Fig. 9.10(d), a more homogenous distribution of the holdup is expected according to Barigou and Greaves (1996). However, the simulation profiles, although showing agreement in the first half of the plane, fail to agree in the second half close to the wall, falling rather steeply to zero level.

In general, the results show that, with the mixture model, gas dispersion in the tank seems slightly better (especially at the lower recirculation region below the impeller), and holdup values are relatively closer to the experimental measurements, when compared with the Euler–Euler results. This shows that the mixture model, which is computationally cheaper, can substitute the Euler–Euler model, at least for the operating conditions having been studied in this work.

Including the turbulent dispersion and the bubble induced turbulence in the mixture model simulations did not result in a considerable change in overall and local holdup values and in the power draw and impeller pumping rate. When the virtual mass force term was added in the Euler–Euler momentum equations, a slightly better gas dispersion both in the upper and the lower part of the tank was observed.

It is evident that neither the overall gas holdup nor the gas fraction distribution in the tank show a general agreement with the experimental data available. Assumption of monodisperse bubbles of 3 mm and employing a simple drag correlation developed for a single solid sphere moving in an infinite medium without the turbulence effects fail to represent the gas–liquid interactions. For a better prediction of the hydrodynamics of two-phase flow in the tank, it is anticipated that a model for tracking the bubble size distribution should be implemented. Furthermore, an appropriate treatment of the interface forces is needed for high gas fractions regions (e.g. gas cavities formed at the impeller blades) and for fully turbulent flow conditions.

Later simulations

In the coming sections we report on later simulations performed aiming at resolving the modelling issues pointed out here. Learnings from earlier results enabled us to further develop the physical modelling. We also investigate further the influence of alternative

boundary conditions applicable and different mesh densities.

9.5.3 Influence of boundary conditions

Inlet conditions

As mentioned earlier, Barigou and Greaves (1992, 1996) used a single tube orifice (19 mm diameter) sparger in their experiments and pointed out that using a ring sparger seemed to give no advantage. Their gas inlet velocity for Case 1 ($Q_g = 1.64\times10^{-3}$ m^3/s) was thus:

$$U_g = \frac{Q_g}{\frac{\pi}{4}\,0.019^2} = 5.78 \text{ m/s} \tag{9.30}$$

However, in our simulations where we assumed a ring sparger, the inlet velocity is:

$$U_g = \frac{Q_g}{\mathcal{A}_{spa}} = \frac{1.64 \times 10^{-3}/6}{7.875 \times 10^{-4}} = 0.347 \text{ m/s} \tag{9.31}$$

This is about 17 times lower than their value (division by 6 is due to domain symmetry).

In Fig. 9.11(c) and (d), we compare the simulation results for Case 1 with two different inlet BC's, as described in Section 9.4.2: (i) gas source terms, and (ii) velocity inlet condition. Both simulations were run with disengagement height above the free surface and a pressure outlet boundary at the outlet. There is practically no difference in gas distribution in the tank and in integral quantities such as holdup, power and gas flow numbers.

Outlet conditions

In Fig. 9.11(a), (b) and (c), we also show results with three alternative outlet conditions: (i) degassing condition, (ii) pressure outlet with only liquid backflow; and (iii) disengagement height above the free surface and a pressure outlet boundary at the outlet with only gas backflow. Those conditions are described in Section 9.4.2. Here again, there is no significant difference in gas distribution and in integral quantities with respect to different outlet conditions.

9.5.4 Mesh dependence

In Fig. 9.12, we investigate the effect of grid resolution on results. Single-phase simulation results with standard and refined grids are also given for a comparison. The clear effect of higher grid resolution is the reduced numerical diffusion, which is evident from the gas fraction contours. There are distinct high gas volume fraction regions which are well separated. At low grid resolution, those regions are not separated but rather smeared out. One can argue that, at low grid resolution, the gas dispersion is qualitatively more realistic due to added numerical diffusion. Gas distribution is expected to be more uniform (rather than a fine structure with sharp gradients) due to turbulence and other fluctuations. We will address the turbulent dispersion effects later.

Despite the significant difference in gas distribution, there is hardly any change in the overall gas holdup. The difference in power and flow numbers is relatively large in comparison with that for the ungassed case.

Overall, we did not see a significant benefit with increased grid resolution that would worth the extra computational effort. Therefore, we decided to use the standard grid resolution in later simulations.

9.5.5 Symmetry assumption

In order to evaluate the influence of rotational symmetry assumption, we run simulations with full domain consisting of 4 baffles and 6 impeller blades. In Fig. 9.13, the liquid velocity vectors for ungassed operation are compared with that from standard simulations with 6 fold symmetry (60° sector domain). There is no significant difference in velocity vectors. Gas flow numbers are also very similar. The power numbers (both dissipation and torque based calculations) are somewhat higher for the symmetry case. This is due to the inherent assumption of 6 baffles in the tank (instead of 4 as in the full domain simulations), when 6 fold symmetry is assumed.

Fig. 9.14 shows a similar comparison now for gassed operation (Case 1). Note that the contour plot for the "no symmetry" case is from a transient run with a time step of 0.001 s, where a periodic steady solution has been reached. Steady-state run and transient run with a larger time step, 0.005 s, resulted in asymmetric gas distribution between the right and left vertical planes. Results show that the holdup is slightly higher when symmetry is assumed, however there is no major effect of the symmetry assumption in gas distribution in the tank. Furthermore, convergence was more difficult when the full domain was simulated, which is reflected by the fluctuations in integral parameters.

Here again, results suggest that the extra computational effort, i.e. about 6 times longer computational time, is not worthed, as long as the integral characteristics are of interest. We used, therefore, the reduced 60° sector domain in later simulations.

9.5.6 Sliding mesh versus MRF model

In Fig. 9.15, a comparison of different impeller modelling approaches, namely sliding mesh (SM) versus multiple reference frame (MRF), is given. There is hardly any difference in overall gas holdup. The gas distribution in the mid-baffle plane is also quite similar, although gas is slightly less dispersed in the upper bulk region in SM simulations. The liquid velocity vectors also show slight difference, namely the upper and lower vortex centers are closer to the impeller level in SM simulations and the impeller discharge stream is inclined less in the upward direction. The power and flow numbers are also somewhat higher with SM. This seemed to be related to lower amount of gas in the impeller swept region below the impeller centerline.

The computational cost with the MRF is about an order of magnitude lower than that with the SM. Given the above results that no major difference has been observed, we decided to use MRF in the coming simulations.

9.5.7 Drag formulations

The drag correlation has a profound effect on the gas dispersion in the tank, as it accounts for most of the interfacial momentum exchange between the phases. Several drag correlations were employed in the simulations which are detailed in Section 6.7. As expected, the drag force was found to be the dominant force, together with the buoyancy force determining the global gas holdup in the reactor.

Schiller & Naumann versus Ishii & Zuber drag law

Previous simulations given above showed that the Schiller & Naumann drag law underestimates the gas holdup for the simulations with monodispersed 3 mm bubbles. This is due to inherent limitation of this drag law to dilute non-turbulent bubbly flows with spherical bubbles. In order to take into account the bubble deformation effects, we implemented the Ishii & Zuber drag law via an user subroutine written in C language. In Fig. 9.16, a comparison is made between Schiller & Naumann and Ishii & Zuber drag law. The mean axial slip velocity is lower with the Ishii & Zuber drag law, because it accounts for spherical cap and ellipsoidal bubble regimes as well. The resulting gas holdup, however, although slightly higher than that for the Schiller & Naumann drag law, is still significantly lower than the experimental value.

The gas distribution in the reactor changes considerably with the Ishii & Zuber drag formulation. Bubble entrainment now starts also in the recirculation region below the impeller due to lower slip velocities. The location of this gas region is slightly away from the vortex eye towards the region of downwards liquid flow (see liquid velocity vectors in Fig. 9.16(b)) where the liquid velocity is about the slip velocity. Same applies also to the upper recirculation region above the impeller. Now, with the lower slip velocity, there is larger amount of gas accumulation here with respect to the Schiller & Naumann case.

Turbulent drag modification: Brucato model

It is apparent from previous findings that the fully turbulent flow regime at which the tank operates has to be taken into account in the drag correlation. We implemented the Brucato model with the correlation constant adapted according to Lane (detailed in Section 6.7.8) for this purpose via an user subroutine.

In Fig. 9.17, the effect of turbulence on drag and, in turn, on gas distribution can be seen. There is a large decrease in the mean axial slip velocity, which causes a step increase in the gas holdup. The holdup is now quite close to the experimental value. The gas distribution in the tank also becomes much more uniform especially in the upper bulk region. At the lower recirculation loop, there is now a larger amount of gas accumulation. Note that, despite of the overall increase in gas holdup, the power number (hence the power drawn from impeller) is now significantly high. This is due to larger amount of gas being dispersed in the bulk and less amount of gas is present in the impeller region. In the Ishii & Zuber case, however, at the impeller centerline plane, all the incoming gas from the sparger is located around the impeller blades. This can be better seen from the corresponding gas fraction contours at the axial planes $y = 0.250$

m and $y = 0.233$ m (i.e. the impeller centerline plane and the plane just below it, respectively) given in Fig. 9.18 and Fig. 9.19. Nevertheless, such high level of gassed power draw (corresponding to a gassed/ungassed power ratio $P_g/P = 0.96$) seem to be too high. Unfortunately, there is no experimental data available. An estimation is possible from the Hughmark correlation (see Table 9.5), which, for this case, is 0.85.

In Fig. 9.19, the plane $y = 0.125$ m is situated axially at the core of the lower gas recirculation loop and shows the circumferential profile of this loop. The same plane for the Ishii & Zuber case (Fig. 9.18) shows hardly any gas, as the gas loop is located slightly above this plane. The incoming gas from the sparger just below this plane is also visible near the central shaft. As mentioned above, the gas cavities formed at impeller blades can be seen at the $y = 0.233$ and 0.250 m planes. The largest amount of gas is present at the plane $y = 0.435$ m for both cases, that coincides with the upper gas recirculation region. At the upper planes, the amount of gas progressively decreases.

A new method for Brucato correction: Kolmogorov microscale from energy balance

In an attempt to improve the predictions with the Brucato drag correction formulation, we devised a new approach. The Brucato correlation in Eq. 6.89 requires the calculation of the Kolmogorov length scale thus the turbulent energy dissipation ε_1, which, in some simulations, is highly fluctuating during iterations. Furthermore, accurate prediction of ε_1 in stirred vessels using the $k-\varepsilon$ method is also a well-known challenge as noted earlier. Computation of the torque on the rotating walls, on the other hand, is usually more robust and accurate, and converges also faster to a steady value.

We therefore make use of the energy balance given in Eq. 9.25 to retrieve the mean dissipation needed for the Brucato term from the total energy input to the system by stirring and gassing. Assuming that viscous dissipation is negligible (fully turbulent flow), the balance relation reads as

$$\int_{\mathcal{V}_{\text{tank}}} \alpha_1 \rho_1 \varepsilon_1 \, dV = \underbrace{2\pi N \Gamma_g}_{\text{mechanical}} + \underbrace{\left(\rho_1 g \int_{\mathcal{V}_{\text{tank}}} \alpha_1 \, dV \right) U^c_{g,s}}_{\text{pneumatic}}, \tag{9.32}$$

where the pneumatic power input due to gassing follows from Eq. 9.13. The characteristic superficial gas velocity (defined in Eq. 9.12) could be simplified by ignoring the hydrostatic pressure effects, i.e. taking the log mean pressure between the sparger and the free surface equal to the ambient pressure (if the liquid level above the sparger is assumed to be 1 m, then $p^{\text{lm}} \approx 1.05$ bar and $U^c_{g,s} \approx 0.95\, U_{g,s}$), which then reduces to the definition of superficial gas velocity:

$$U^c_{g,s} \approx U_{g,s} = \frac{Q_g}{\frac{\pi}{4} T^2}. \tag{9.33}$$

The mean turbulent energy dissipation could then be computed from

$$\bar{\varepsilon}_1 = \frac{\int_{\mathcal{V}_{\text{tank}}} \alpha_1 \rho_1 \varepsilon_1 \, dV}{\int_{\mathcal{V}_{\text{tank}}} \rho_1 \alpha_1 \, dV} = \frac{2\pi N \Gamma_{\text{g}}}{\rho_1 \int_{\mathcal{V}_{\text{tank}}} \alpha_1 \, dV} + g \left(\frac{Q_g}{\frac{\pi}{4} T^2} \right), \tag{9.34}$$

and this relation could be used to calculate the Kolmogorov length scale required for the Brucato drag correction term.

Simulations with this alternative approach were run for the Case 1. Results showed only little difference with respect to the original implementation of the Brucato correction thus are not presented here. The relative deviation in holdup and axial velocity were 3.0% and 6.2%, respectively. The gas distribution in the reactor was almost the same. We therefore kept the original implementation in the following simulations. Note, however, that the method could prove usefull in cases where fluctuations in the computation of turbulent dissipation causes numerical instabilities in simulations.

9.5.8 Turbulent dispersion force: VOF-diffusion vs Simonin model

In Section 6.6.4, two different dispersion force (TD) models have been introduced in detail, namely the Simonin and the Lahey models, both treating the turbulent dispersion as an interfacial momentum force in the phase momentum equations. We also mentioned that there are simpler models which, instead, introduce a turbulent diffusion term in the governing equations of phase volume fractions (VOF) and introduced the VOF diffusion model. Those models have been criticized as being based on invalid grounds. So far, we haven't yet taken into account the turbulent dispersion effect in our simulations, because convergence was not possible with the Simonin model.

Despite the questionable grounds of modelling this force as a diffusion term in the gas volume fraction equation, we run test simulations with the VOF diffusion model. Fig. 9.20 shows the influence of this term on the standard Schiller & Naumann case. Below the impeller level, there is now gas accumulation at the recirculation region, although the slip velocity (i.e. the drag formulation) is the same. Above the impeller level, the gas dispersion in the bulk is much more uniform. There is, however, no significant change in the integral quantities.

We did manage to achieve convergence with the more rigorous Simonin model in a test simulation where we have used the sliding mesh (SM) model for the impeller. In Fig. 9.21, a comparison is made between this simulation and the simulation with VOF diffusion model. Note that these specific simulations now are more comprehensive relative to that in Fig. 9.20, taking into account bubble deformation effects via Ishii & Zuber drag with turbulent drag modification (Brucato model). The virtual mass force (VM) is also included in the simulations. Furthermore, bubble breakup and coalescence dynamics are also taken into account via population balance modelling (PBM) using the discrete model (DM) and the pre-defined bubble size classes according to Set 3 in Table 9.6. We will discuss the influence of PBM later in a seperate section, so we restrict ourselves here to the differences due to the TD modelling.

Now with this comprehensive model we see that the gas dispersion progresses almost everywhere in the tank. Simonin model predicts larger amount of gas dispersion, which can be seen from the width of the sparged gas plume compared with that of the VOF diffusion model. Predicted gas holdup values, however, are now lower than that predicted by the monodisperse simulation with the same drag modulation, but without TD and VM (Fig. 9.17(b)).

Another peculiar observation is that, here again, the power numbers are too high, as we have seen in earlier simulations with the Brucato correction (see the discussion in Section 9.5.7). Here, including the TD, even higher values were obtained. This seems to be due to the following. If we compare the gas distribution with that for the Brucato case without TD (Fig. 9.17) as well as with that for TD (VOF diffusion) case with Schiller & Naumann drag (Fig. 9.20), we see that there is again high levels of gas dispersion, but now distributed unevenly, being mostly at bulk and near-wall regions and not at the region near the central shaft. This variation in gas dispersion level causes a variation in effective density at those regions which, in turn, further fuels the existing impeller driven gross liquid recirculation current. This, in turn, results in a larger liquid flow directed downwards at the center, which brings larger amounts of liquid back to the turbine. Hence, the liquid pumping duty of the impeller is higher, which is reflected by the large impeller flow number (0.93 for the TD (Simonin) case compared to 0.69 for the Brucato case without TD). This can also be seen from the mid-baffle plane liquid velocity vectors plotted in Fig. 9.21, where the upper recirculation loop extends axially much further upwards reaching almost the free surface level. This is not the case in other simulations where, near the wall, axially at about 3/4th of the liquid level, this liquid recirculation stream separates from the fluid near the free surface. Nevertheless, such high levels of power numbers (for the Simonin case even larger than that for the ungassed operation), still seem questionable.

9.5.9 Virtual mass force

A comparison of Fig. 9.22(b) and (c) shows that the inclusion of VM resulted in almost no change in the overall gas holdup. Gas distributions are quite similar, although one can see slight differences at locations where relative acceleration between the phases is large. One such location is the lower recirculation loop, where there is now larger amount of gas due to hinderence of gas bubbles here by VM (at the location where mean liquid flow is changing its direction to downwards). At the upper recirculation loop, the region of downwards liquid flow is larger extending up to the central shaft. Here, we see that the gas is dispersed to a wider area throughout this region, again presumably due to additional hinderence by VM.

There is somewhat larger difference in the power number predictions. Both dissipation and torque based power numbers are higher when VM is included meaning that power input is higher. Fig. 9.23 shows the gas distribution at the impeller centerline plane, which indicates the reason for this. Gas dispersion from the impeller is slightly higher with the VM case and less gas in entrapped behind the blades, hence hydrodynamic resistance is higher. This means a higher power input, and in turn, stronger vortices generated by the impeller blades which entrap higher levels of gas. As the total gas holdup is similar, it is this difference in gas distribution that gives different power

characteristics.

9.5.10 Lift force

Despite many attempts, it was not possible to achieve convergence when the lift force was included in the interface momentum exchange term. This issue seemed to be specific to stirred tank simulations (both MRF and SM), because our simulations of buoyancy driven gas–liquid flow in a bubble column (not reported here) run smoothly with the lift force.

Note that, Lane (2005a) and Deen (2001) also reported about this convergence problem with the lift force in their Eulerian stirred tank simulations.

9.5.11 Population balance model

Further comparison of models with the VOF diffusion with respect to polydispersity can be made from Fig. 9.22 and 9.23. This time the Schiller & Naumann drag model was used without any turbulence modification, hence all holdup predictions are lower relative to the previous case. Pre-defined bubble size bins are according to Set 1 in Table 9.6; hence are different from that used in the previous case given in Fig. 9.21. This set allows for larger size classes, i.e. 12 mm and 7.56 mm, instead of 4.50 mm maximum, in case such large bubbles can be present in the reactor (though experimental data suggests not).

There is a relative decrease in the predicted gas holdup with the inclusion of PBM. This is not surprising as the volume averaged Sauter mean diameter is about 3.5 mm, larger than the value assumed for monodisperse simulations, i.e. 3 mm. Hence, the slip velocity, as calculated from the Schiller & Naumann drag model, is slightly higher (i.e. 31 cm/s for 3.5 mm bubbles compared with 29 cm/s for 3mm bubbles; see Fig. 6.1(b)) and, in turn, the holdup is slightly lower.

In Fig. 9.24, the Sauter mean diameter distribution is given together with gas velocity vectors. Directly under the impeller disk, coalescence is dominating at the sparger stream where bubble sizes reach about 9 mm, an overall maximum in the reactor. Actually, the way we modelled the sparger, that is, via gas source terms at a ring shaped group of grid cells with no physical separation between the sparging bubbles (on contrary to real ring spargers) would inevitably cause higher collision frequencies especially near the point of entry thus stronger coalescence. Nevertheless, as noted earlier, Barigou et al. used a single tube orifice in their experiments and observed no major difference relative to a ring sparger. We also expect this modelling artifact to lessen once the sparged gas has been dispersed by the impeller.

In the gas cavity region behind the impeller blades and in the bulk region near the shaft, the bubble sizes are still large, about 5-6 mm. Smallest diameters are seen near the blade tips ($\approx$ 1.5 mm) and along the tank wall where the impeller discharge stream impinges and separates ($\approx$ 2 mm). Those regions are where highest shear levels are expected. Overall, predicted bubble sizes show the general trends in the measurements of Barigou et al. (see Fig. 9.5), though slightly larger values are predicted in the bulk region.

In Fig. 9.25 and 9.26, spatial distribution of bubble bin volume fraction, $\alpha_{2,\text{bin}-i}$, is given at mid-baffle and impeller centerline planes for all bins. This fraction is

$$\alpha_{2,\text{bin}-i} = \frac{\mathcal{V}_{2,\text{bin}-i}}{\mathcal{V}_{\text{total}}}, \tag{9.35}$$

which is the ratio of volume of bubbles in bin i to the total volume at a grid cell. The contour plots reaffirm the above conclusions from the Fig. 9.24. At the gas sparged region below the impeller, the largest volumetric contribution to the local gas content is due to large bubbles (i.e. 12.00 and 7.56 mm bubbles). Those bubbles are also present, though not as significant, at the upper bulk region far from the impeller. Initial bubble size of the sparged gas is 3 mm and those bubbles are quickly coalescing (also due to aforementioned sparger modelling approach) as this is a region of high bubble density thus high probability of collision. 3 mm bubbles are also entrapped behind the baffles at the impeller centerline plane. Smaller bubbles (1–2 mm) are carried along with the impeller discharge stream and trailing vortices from the blades.

Note that the local value of $\alpha_{2,\text{bin}-i}$ is itself a fraction of α_2, the local gas fraction (i.e. the summation of $\alpha_{2,\text{bin}-i}$ over all bins is α_2). Consequently, at low gas fraction regions, $\alpha_{2,\text{bin}-i}$ is also low, even though the share of a particular bin could be large. In order to indicate the volume of a particular bin with respect to the volume of all bins (i.e. total gas volume), the local bubble bin volume fraction is normalised by the local gas fraction, that is

$$\frac{\alpha_{2,\text{bin}-i}}{\alpha_2} = \frac{\mathcal{V}_{2,\text{bin}-i}}{\mathcal{V}_2} = f_{\text{bin}-i}, \tag{9.36}$$

which is the ratio of volume of bubbles in bin i to the total gas volume at a grid cell. This bubble bin fraction, $f_{\text{bin}-i}$, is also introduced as the solution variable in the discrete model implementation in Fluent.

In Fig. 9.27 and 9.28, spatial distribution of $f_{\text{bin}-i}$ is given at mid-baffle and impeller centerline planes for all bins. Here we can identify the regions where particular bubble size classes have a large share as a result of the local flow conditions. Large bubbles (12 mm) are present only at the central bulk region and sparger stream between the sparger and the impeller disk (including the low pressure zones behind the blades). Bubbles of about 8 mm are present at those locations as well, but they are also located at the lower recirculation region. Mid-range bubbles (3-2 mm) are more significantly present at the lower part of the tank and along the tank wall where the impeller discharge stream is divided into upper and lower axial streams. Smallest bubbles of about 1 mm prevail at those locations to a much lesser extent and they are located significantly at the immediate vicinity of the impeller blades (at the front, high pressure zones). In the majority of impeller centerline plane, 3 and 2 mm bubbles dominate. At the gas cavity zones behind the impeller blades however, almost solely larger bubbles are present (> 3 mm). We also clearly see that the sparged bubbles of initially 3 mm size do not breakup until they reach the impeller blades as smaller size classes are not present between the sparger and the impeller disk. This is not surprising as shear levels here are low and there is no transport of smaller bubbles from other regions to here. Similarly, those small bubbles are not present at the upper bulk region near the shaft either. In the contour plot of bin 3 (3 mm), we see unexpectedly very high levels of $f_{\text{bin}-3}$ below the sparger. This is because, at this location, the local gas fraction is very low and consists of solely bin 3 ($\alpha_2 \approx \alpha_{2,\text{bin}-3} = 5.577 \times 10^{-8}$), hence $\alpha_{2,\text{bin}-3}/\alpha_2 = f_{\text{bin}-3} \approx 1$.

9.5.12 Comparison of local gas fraction and d_{32} predictions with experiments

In Fig. 9.29, radial distributions of circumferentially averaged local gas fraction predicted by various drag models are compared with the experimental data from Barigou and Greaves (1996) and the simulation data from Lane (2005a) (from his revised final model). Predictions are for Case 1 and for a fixed bubble size of 3 mm. Overall, predictions with the Ishii & Zuber drag law and Brucato turbulence modification were rather close to the experimental data, except at axial levels just below and above the impeller plane (z1 and z3 planes). Those planes coincide with the lower and upper recirculation loops where large amount of gas entrapment was predicted when the Brucato correction was applied to the Ishii & Zuber drag coefficient (compare gas contour plots at z1 ($y = 0.125$ m) and z3 ($y = 0.435$ m) planes between Fig. 9.17(a) and Fig. 9.17(b), and between Fig. 9.18 and Fig. 9.19). Predictions with the Tomiyama drag law, also corrected for turbulence effects via the Brucato formulation, were very similar to that of Lane at upper planes (z3–z6), though not closer to the experimental data. Simulations with the Schiller & Naumann drag law has in almost all cases underpredicted the gas fractions as it does not take into account the extra drag due to bubble deformations and turbulence.

In Fig. 9.30, a similar comparison is made with respect to the models that take into account the turbulent dispersion force. Ishii & Zuber drag law with Brucato modification was used in all simulations, while PBM was used for bubble sizes in simulations with the TD. The "no TD" case with fixed bubble size (3 mm) provides the base for comparison which gave the best predictions in Fig. 9.29. We see now that with the inclusion of TD (both VOF and Simonin implementations), the above mentioned overprediction of gas fraction at lower and upper recirculation regions at z1 and z3 planes disappeared. This is simply due to the dispersive effect of TD at high gas fraction regions. In the remaining planes, however, local gas fractions are underestimated, while predictions were rather close to that of Lane. Overall gas holdup was also underpredicted by those TD cases (see Fig. 9.21). This suggests that turbulent dispersion effects were overestimated by both VOF and Simonin implementations. That is, gas bubbles diffuse out of the low pressure recirculation zones and leave the tank, thus causing in turn low local and overall holdup.

In Fig. 9.31, the TD model predictions are now compared in terms of local mean bubble size. In planes in the neighborhood of the impeller (z1–z3), predicted local Sauter mean diameter profiles are rather flat relative to experimental profiles. In z1 and z2 planes, near and just below the impeller tip, experimental d_{32} values are significantly smaller than predictions. In other planes (z4–z6), both simulations (VOF TD and Simonin TD) are similar and in good agreement with the measurements. Predictions of Lane, on the other hand, underestimates the Sauter diameters in almost all planes.

9.5.13 Final model

Based on the learnings from previous results, final simulations were performed on the following set of modelling options:

- Drag law: Ishii & Zuber drag
- Drag modification for turbulence: Brucato model (with the correlation constant recommended by Lane et al.)
- Non-drag interface forces: virtual mass force
- Mesh: 47k ($65 \times 36 \times 20$) structured elements (56 cells/blade), 140k ($97 \times 60 \times 24$) structured elements (192 cells/blade)
- Bubble size: monodisperse (3 mm, 4 mm), PBM (DM, 5 new bubble size classes were defined according to Set 2 in Table 9.6).

Summary of results obtained with the fine 140k mesh are given in Table 9.8. Detailed results are discussed below with respect to gas fraction contours and integral quantities (Fig. 9.32–9.35) and local gas fraction and d_{32} distributions (Fig. 9.36–9.43). Note that, the overall Sauter mean diameters reported were calculated by volume-weighted average over the whole computational domain. This volume averaged d_{32} was then compared with the value obtained by simple averaging of the experimental data from 22 measurement points in the mid-baffle plane (Fig. 9.3) This comparison is only indicative, as the CFD value takes into account the whole 60 degree section of the tank rather than distinct measurement locations of Barigou and Greaves.

Discussion of the experimental data regarding the distributions of local and overall gas fraction, local bubble frequency and size, and local interfacial area was already given in Section 9.2.

Case 1 (180 rpm$, Q_g = 1.64 \times 10^{-3}$ m^3/s)

Gas distribution: In Fig. 9.32, simulation results for Case 1 are reported for several modelling options. Results with both the standard and refined mesh as well as monodisperse and PBM setups are given. Note that, besides the standard bubble size of 3 mm used so far, we also did a test simulation with 4 mm size, as mean bubble sizes from PBM predictions were around this value.

In the flow regime constructed in Fig. 9.1, Case 1 is located above the complete dispersion but below the complete recirculation border. Gas volume fraction contours show gas accumulation at lower and upper recirculation zones (red indicates zones where local gas fraction $\geq 5.0\%$) and fairly uniform gas dispersion at bulk with gas fraction levels $2.5 - 3.0\%$.

Gas distribution in the DM + 140k case (d) seemed to be more uniform relative to the DM + 46k case (b), however, the gas holdup predictions are the same, i.e. $\approx$ 2.5% (mean holdup values are reported for both cases as gas holdup was fluctuating). Note that, gas fraction contours of those transient DM simulations are snapshots from arbitrary instants (rather than a time-average) when pseudo steady-state was reached, hence exact correspondence is not expected. Gas distribution with the 3 mm (a) and 4 mm (c) cases were similar, while the holdup was slightly higher due to lower slip velocity with 4 mm case. Overall, holdup predictions are now close to the experimental value of 2.97% reported by Barigou and Greaves.

In Fig. 9.36, radial distributions of circumferentially averaged local gas fraction are compared with the experimental data from Barigou and Greaves (1996) and the simulation data from Lane (2005a) (from his revised final model). At the lower and upper recirculation zones (z1 and z3 planes), most of the simulations overpredicted gas levels. The gas accumulation at recirculation zones would be lower if the turbulent dispersion force is taken into account. However, earlier simulations (see Fig. 9.30) showed that this would harm the predictions in other planes. The drag formulation seemed to be the reason for this excessive gas accumulation at those locations. In other planes, DM + 140k case generally predicted better than other modelling options as well as Lane predictions. Correspondence with the experimental gas fractions is good.

Here, we note again that, as mentioned in Section 9.2, resistivity probe technique used by Barigou and Greaves (1996) underestimated the local holdup values, as revealed by comparing the mean integral holdup with the corresponding overall holdup measured independently by level detection method. The measurement error was reported to be about 18% for Case 1, 17% for Case 2, 14% for Case 3 and 12% for Case 4.

Bubble size: Overall Sauter mean diameters (D_{32}, i.e. d_{32} averaged over the domain) predicted are around 4 mm relative to the experimental value of 3.5 mm (which we obtained by averaging experimental data points over the sampling locations). We also reported the ratio of overall Sauter mean diameter to mean Kolmogorov scale (based on mean turbulent dissipation), D_{32}/η_1, to indicate the extent of local interactions expected between bubble and energy dissipating eddies owing to the fact that not all turbulent eddies of all length scales can influence the momentum transport around the bubble. As described in Section 6.7.8, for small solid particles ($d_p < 5-10\eta_1$), the settling velocity was found not to be affected by turbulence, while, for larger particles ($d_p > 10\eta_1$), a significant decrease in settling velocity was observed (up to 60 %). Values from our simulations indicate significant turbulence effects on the bubble drag, justified also by the fact that holdups were always underestimated with drag models lacking turbulence modification.

In Fig. 9.40, radial distributions of circumferentially averaged local Sauter mean diameter are compared with the experimental data from Barigou and Greaves (1996) and the simulation data from Lane (2005a) (from his revised final model). In most planes, the course and refined mesh predictions are equally well. Agreement with the experimental data is in general good, except in the impeller plane (z2), where the predicted profile is rather flat and misses the small bubble size near the impeller tip (which we also observed in earlier predictions given in Fig. 9.31). Local d_{32} values (not circumferentially averaged) as low as 1.89 mm (i.e. the smallest bubble size class), however, are present around impeller swept regions at this plane. This shows that, at those locations, actual bubble size would possibly be smaller than the smallest bubble size class defined in simulations. Those locations however comprise only 0.56% of the total number of grid cells in the impeller plane (8 out of 1440). Note that, Barigou and Greaves measured a Sauter diameter smaller than 1.89 mm (0.79 mm) only at a single location in the measurement grid.

Power and gas pumping: Power and gas pumping characteristics are also compared in Fig. 9.32. Power densities (torque based) are about the same for all cases (≈0.77),

reflected also on torque based power numbers. Dissipation based power numbers were always lower than torque based ones.

As pointed out in Section 9.2.3, experimental power data is very limited. In the absence of experimental data, predictions via the Hughmark and Bakker et al. correlations are provided in Fig. 9.32. However, those correlations both under– and overpredict the experimental trends significantly as shown in Section 9.2.3. With this in mind, we see that simulation predictions of torque based gassed/ungassed power ratios (P_g/P) are higher with respect to the correlation estimates (12% higher for the DM + 140k case relative to the Hughmark estimate). We also see that, after mesh refinement, dissipation based power predictions improve and get closer to torque based predictions.

Gassed flow numbers are also similar for all cases (≈0.69). Gassed/ungassed liquid discharge ratios (Q_G/Q) are high (≈0.97), and are about the same as P_g/P values. This is expected and observed also by others (see Section 3.1.2 and Eq. 3.9). Furthermore, we also found that gas fraction levels at the area swept by the impeller tip (discharge area) were low, with values similar to the predicted gas holdup of around $2.5 - 3.1\%$.

Circumferentially averaged gas fraction profile in the impeller plane (Fig. 9.36(b)) shows gas levels of about 4.5% near the blade tip which increases up to 20% near the rear side of blade edge (not visible in the plot due to restricted vertical scale for clarity) for the DM + 140k case. Examination of 3D iso-surfaces of gas fraction revealed trailing vortex structures (in agreement with the cavity regime predicted in Fig. 9.1) of about 20% gas fraction located mostly at lower impeller tip and occupy limited blade area. Gas fraction further increases to about 50% near the lower rear blade edge, but restricted to a very small area. Note also that, Barigou and Greaves (1996) observed the regime of 6 vortex cavities for this case (see Table 9.2). Overall, the apparent overpredictions in gassed/ungassed power and liquid discharge ratios (with respect to correlation values) despite fairly well-predicted holdups seemed to indicate underprediction of gas levels at the gas cavity zones behind impeller blades. On the contrary, the gas fraction at lower and upper recirculation loops are overestimated with respect to the experimental data. This could be linked to insufficient representation of interface forces as well as lacking a bubble class below 1.89 mm in simulations as mentioned above. Small bubbles would more readily be entrained into the trailing vortices.

Another possibility is that the high gas fraction effects are not sufficiently taken into account. We did not use drag modification for high gas fraction (bubble swarm) effects for the standard tank simulations due to relatively low aeration rates. We did however implemented the Ishii & Zuber multiparticle drag law for the fermenter operating at high aeration (see Section 10.3.10), in line with the recommendation of Laakkonen (2006) that bubble swarm effect becomes important at holdups $> 20\%$. A simple estimate of bubble–bubble distance via Eq. 6.75 at relatively low gas fraction of 5% leads to $2.2\,d_b$, which is quite short. Therefore, locally, bubble swarm effects might still be significant.

Besides the swarm effect, another high gas fraction phenomenon is the formation of continuous gas pockets at impeller cavity zones. The Euler–Euler model adopted, however, treats the gas phase as discrete bubbly phase everywhere. The gas bubbles trapped behind impeller blades would coalesce at high gas fractions to form gas cavities where the local gas fraction would reach 100%. The interface momentum exchange would then approach to zero. Furthermore, depending on the cavity regime, the shape

of cavities might also have an influence on the flow around the impeller blades (e.g. streamlining shape to reduce drag) thus on the power transmitted to the liquid. This effect is not taken into account in the modelling approach adopted as gas–liquid interfaces are not resolved. However, the drag force formulation given in Eq. 6.37 ensures that the limiting behaviour is satisfied, i.e. when the gas fraction approaches 100%, the drag force vanishes.

Finally, the percent gas imbalance in the domain, $(\dot{m}_{\mathrm{g,in}} - \dot{m}_{\mathrm{g,out}})/\dot{m}_{\mathrm{g,in}} \times 100$, is also reported to provide an overview on the overall gas mass balance in simulations. Largest value was about 4.5% calculated for the refined DM case. The imbalance in other simulations was around 1% or less.

Case 2 $(250\ \mathrm{rpm}, Q_{\mathrm{g}} = 1.64 \times 10^{-3}\ \mathrm{m}^3/\mathrm{s})$

Gas distribution: Results for Case 2 are reported in Fig. 9.33. The stirring rate is now increased to 250 rpm at the same gassing rate as the Case 1. Flow regime changes from the complete dispersion to the complete recirculation (Fig. 9.1). Gas volume fraction contours show significantly higher gas levels at especially the lower recirculation zone (red indicates zones where local gas fraction $\geq 7.5\%$). Despite the flow regime map, gas dispersion in the bulk is less uniform than that for the Case 1.

Measured holdup is 3.65%, slightly higher than for Case 1. All simulations predicted higher values; the closest to the measured value is that obtained with the DM + 140k case. With the higher stirring rate thus higher turbulence level, all simulations predicted lower slip velocities and higher mean dissipation rates with respect to those predicted by Case 1 simulations. Decrease in slip velocities is due to increased D_{32}/η_1 values (via Brucato relation, Eq. 6.89) as a result of higher turbulence levels. The overprediction in holdup is probably due to Lane's correlation constant used in the Brucato model, which was established based on their simulation results of Case 1.

Radial distributions of gas fraction are given in Fig. 9.37. Again, gas accumulation at the lower and upper recirculation zones (z1 and z3 planes) is overpredicted significantly. In other planes, all simulations show similar predictions. Correspondence with the experimental gas fractions is reasonable, though a sharper decreases in gas levels is predicted at the z6 plane.

Bubble size: The overall Sauter diameter predicted is only slightly lower than that predicted for the Case 1 (4.0 versus 4.1 mm), a trend which we also observe in measured D_{32} values (3.36 versus 3.50 mm). It is important to notice again that the CFD value is the mean over the whole domain while the experimental value is the sample mean of limited measurement positions.

Radial distributions are given in Fig. 9.41. At the lower recirculation zone and near the impeller blade, the bubble size is overpredicted. In other planes, agreement with the experimental data is in general good. Note that, at two locations in the measurement grid (in the impeller discharge stream), Barigou and Greaves measured local Sauter diameters smaller than the largest bin size of 1.89 mm (0.49 and 1.01 mm).

Power and gas pumping: Power densities (torque based) predicted agree well with the experimental value reported, 2.00 kW/m^3. This was the only case for which the experimental power consumption data had been reported The Hughmark correlation predicted a slight decrease in P_g/P (from 85 to 82%), while the Bakker correlation showed an opposite trend (from 82 to 84%). Simulation values hardly change with respect to the Case 1 predictions and are significantly higher than the correlation values (in the range $84 - 92\%$ for dissipation based, and $95 - 97\%$ for torque based calculation).

Gassed/ungassed liquid discharge ratios predicted are also high, confirmative to high power ratios predicted, and are about the same as Case 1 values. This may indicate again the underprediction of gas levels at the gas cavity zones behind impeller blades. Examination of 3D iso-surfaces of the gas fraction showed trailing vortex structures (same as in Case 1) in agreement with the cavity regime predicted in Fig. 9.1 and the observations of Barigou and Greaves (see Table 9.2). From the upper rear blade corner, a vortex cavity of about 10% gas fraction emerges. Another one of about 20% gas emerges from the lower impeller disk surface just behind the blade and extends along the lower impeller blade area. Both are limited to a small blade area. Possible underprediction of gas levels near blades could again be due to lacking the bubble size class below 1.89 mm in the simulations.

Case 3 (180 rpm$, Q_g = 6.87 \times 10^{-3}$ m^3/s)

Gas distribution: With the increase of gassing rate relative to the Case 1 (rather than the stirring rate as in Case 2) there is a large increase in the experimental holdup value (7.72%) relative to Case 1 and 2 (Fig. 9.34). The flow regime is now just at the border of complete dispersion (see Fig. 9.1). Gas volume fraction contours for the DM + 140k case shows relatively higher gas levels at the upper recirculation zone relative to the lower one (red indicates zones where local gas fraction $\geq 15\%$), a trend opposite to Case 2. Gas dispersion in the bulk is the least uniform among all four cases. This is in line with the flow regime where Case 3 is located closest to the flooding transition line and just at the limit of complete dispersion.

Simulations failed to predict the measured increase in holdup, arriving at values similar to that for Case 2. Relative error in the holdup prediction is about 28% (for the DM + 140k case) with respect to the measured value. Mean turbulent dissipation is similar to Case 1 levels and much lower than that for the Case 2. With the increase of gassing rate, simulations were also less stable, which is reflected in high gas imbalance values.

Radial distributions of gas fraction are given in Fig. 9.38. Gas accumulation at the lower recirculation zones (z1) is overpredicted again, though not to the same extent as Case 2. Profiles for the upper recirculation zone (z3) show large deviations between different simulations. This is possibly due to the transient nature of the flow under those conditions. Time-averaged profiles are expected to average out those deviations. In higher planes, simulations underpredicted the gas fractions except for the monodispersed 3 mm case, which had the largest slip velocity due to smaller bubble size.

Bubble size: In line with the experimental data, the overall Satuer mean diameter predicted is larger than that for Case 1 and 2, owing to the reduced level of turbulence.

This is also reflected in lower values of $\overline{\varepsilon}$ and D_{32}/η_1.

Radial distributions are given in Fig. 9.42. At the z1 level near the impeller, Barigou and Greaves measured zero gas fraction hence a zero bubble size. Simulations however predicted gas dispersion into this region and a bubble size slightly lower than that at the recirculation loop. The same trend is seen also in the impeller plane and the agreement with the experimental data is good except near the blade tip. In other planes, profiles are flat and agree well with the measurement points. Note that, the smallest Sauter diameter measured by Barigou and Greaves for this case was 2.10 mm, located near the blade tip. Therefore, we expect the pre-defined bubble size bins in simulations to suffice.

Power and gas pumping: Power densities, power numbers, gassed/ungassed power and liquid discharge ratios are all lower than Case 1 and 2 levels. The correlation estimates for P_g/P are also significantly lower ($52-59\%$), while simulation predictions (torque based) are moderately lower than Case 1 and 2 levels, and are in the range $0.78-0.86\%$.

Barigou and Greaves (1992) reported that when moving from Case 1 to Case 3 by increasing the gas load, the impeller gas cavity regime changed from 6 vortex cavities to 6 large cavities, resulting in a 44% decrease in the total gassed power input (see Section 9.2.3). Simulation results and correlations show however $9-18\%$ and $30-37\%$ decrease, respectively.

The cavity regime is located between the clinging and $3-3$ mode (3 large, 3 clinging) according to Fig. 9.1. Barigou and Greaves (1992) observed 6 large cavities for this case. By examining 3D iso-surfaces of gas fraction, we observed a large pocket with gas fractions as high as 90%, covering all the lower blade area below the disc level and extending to the upper blade tip. We also observed a trailing vortex cavity of about $10-20\%$ gas fraction emerging from the upper horizontal blade edge. The large cavity structure limited to the lower half of the blade area allows larger power transport to liquid at the upper half.

Both the cavity and flow regimes of Case 3 seemed to be located at a transition state. This probaby caused the instabilities and fluctuations in simulations.

Case 4 (285 rpm$, Q_g = 6.87 \times 10^{-3}$ m^3/s)

Gas distribution: With the increase of stirring rate at the same gassing rate as in Case 3, the flow regime shifts now to the complete recirculation border (Fig. 9.1) and both measured and predicted holdups increase. Gas volume fraction contours (Fig. 9.35) show significant gas levels at the lower recirculation zone (red indicates zones where local gas fraction $\geq 20\%$). Gas dispersion in the bulk region is improved.

Turbulence levels are higher, as seen in dissipation and D_{32}/η_1 predictions, which are much higher than that of Case 1 and 3, and significantly higher than that of Case 2. As a result, slip velocities are lower and the holdup is higher. Yet, the predicted holdup is about 29% overestimated (for the DM + 140k case). This seems again to indicate that the Brucato model and the adopted correlation constant of Lane has a limited applicability under varying operating conditions.

Radial distributions of gas fraction are given in Fig. 9.39. Similar to Case 2, gas accumulation at the lower and upper recirculation zones is overpredicted; the former one being quite significantly. Predictions for the impeller plane is quite good. In other planes, simulations generally underpredicted the local holdup.

Bubble size: Experimental overall (sample-averaged) Sauter diameter is about the same value as for the Case 3, and so is the simulation value, while the prediction is about 12% higher than the experimental value. Note again that the experimental value is the average over limited number of sampling locations, while the simulation value is a full domain-average.

Radial distributions are given in Fig. 9.43. At the lower recirculation zone, the bubble size is overpredicted. In other planes, agreement with the experimental data is in general good, while being slightly higher than experimental values closer to the free surface. The smallest Sauter diameter reported by Barigou and Greaves for this case was 1.62 mm, located just near the blade tip. Therefore, we expect the pre-defined bubble size bins in simulations to suffice also for the Case 4.

Power and gas pumping: Hughmark and Bakker correlations predicted a small decrease in power ratio relative to Case 3 levels. Simulation with the fine mesh and PBM (DM + 140k) led to the lowest power ratio (torque based), namely 0.69, hence the largest reduction in power due to gassing. Reduction in the impeller liquid discharge flow for the same case however was about the Case 3 level.

The cavity regime for the Case 4 is located at the vortex/clinging border according to Fig. 9.1. Similar to Case 3, iso-surfaces of gas fraction for the DM + 140k case showed a trailing vortex cavity of about $10 - 20\%$ gas fraction emerging from the upper horizontal blade edge. Contrary to Case 3, at the lower blade area below the disc level, the maximum gas fraction was about 60% only and the cavity shape was still vortex/clinging type with average gas levels of about $30 - 40\%$. This cavity structure emerged from the lower impeller disk surface just behind the blade and extended along the lower impeller blade area, which we also observed in Case 2.

9.6 Conclusions

We presented a computationally efficient route to predict gas dispersion characteristics in a lab-scale standard designed stirred tank reactor with a Rushton turbine. Main conclusions of this chapter are:

- The grid resolution of 46k (for the computational domain of 60 degree sector of the reactor) was generally sufficient for the estimation of integral quantities such as gas holdup, though the turbulent energy dissipation prediction improved with further grid refinement.
- Standard Schiller & Naumann drag correlation for spheres significantly underestimated the gas holdups. Ishii & Zuber correlation improved predictions by taking bubble deformation effects into account. However, turbulence modification of

the drag force was required to bring holdup predictions close to the measured levels. The Brucato model (with the correlation constant of Lane) adopted for this purpose was found to have a limited applicability under varying operating conditions. Percent error in the holdup relative to the experimental data with the final model (with refined mesh and PBM) was -15.8, 42.5, -28.8 and 28.7%, for Case 1 to 4, respectively. The local gas fraction was overpredicted at several locations near the lower and upper recirculation loops.

- Simulations did not converge when the lift force was included in the interface momentum exchange term. Inclusion of the turbulent dispersion force (Simonin model) and the population balance model (discrete model) caused also stability issues with the steady state segregated solver. Convergence was achieved only using the transient solver with 1st order upwind discretisation for PBM bin fractions.

- Bubble size predictions with the discrete model for population balances (with standard breakage and coalescence kernels) were generally good. Overall Sauter diameters predicted (global volume average) were reasonably close to experimental data (sample-average of 22 measurement positions). Percent error in D_{32} relative to measurements with the final model (with refined mesh) was 17.1, 18.9, 13.4 and 11.6%, for Case 1 to 4, respectively. Local distribution of d_{32} at axial levels of the measurement grid were predicted also reasonably well, except at levels near the impeller where d_{32} was overpredicted at several locations.

- Direct experimental data on power consumption was available only for Case 2, for which a very good agreement was achieved with the final model. Due to scarcity of the experimental data on the power characteristics of the tank, comparisons were made with the correlation estimates (Hughmark and Bakker relations). Simulation values of gassed-to-ungassed power ratios were significantly higher than the correlation estimates. The relative reduction in power when moving from Case 1 to 3 was deduced from the experimental data of Barigou and Greaves, which was underpredicted by both the correlations and simulations, the latter being to a higher extent. For an accurate prediction of gassed power, the precise form of the impeller gas cavities is crucial. Although the gross characteristics of the impeller cavity regimes were captured by the simulations, the inherent limitation of the Euler–Euler framework adopted is that the gas phase is modelled as discrete bubbles and gas–liquid interfaces are not resolved. This does not allow to take a direct account of the shape of large and clinging cavities formed by coalescing bubbles behind the impeller blades, though some effects are partially modelled within the framework.

- The reduction in impeller liquid discharge flow (impeller pumping) due to gassing was generally similar to the reduction in impeller power draw due to gassing, which is supported also experimentally (as described in Section 3.1.2, Eq. 3.9).

Tables

Table 9.1: Material properties for the liquid and gas phases.

	Water	Air
Density, ρ [kg/m^3]	1000	1.225
Viscosity, μ [Ns/m^2]	1.000×10^{-3}	1.789×10^{-5}

Table 9.2: Two–phase simulation cases. Experimental data available from Barigou and Greaves is also gvien.

	Case 1	Case 2	Case 3	Case 4
Impeller speed [rpm]	180	250	180	285
Tip speed, $u_{\text{tip}} = \pi DN$ [m/s]	3.1	4.4	3.1	5.0
Gas flow rate, Q_g [l/s]	1.64	1.64	6.87	6.87
Gas flow rate [vvm], $60Q_g$[m^3/s]/$\mathcal{V}_{\text{tank}}$	0.13	0.13	0.53	0.53
Gas superficial vel., $U_{\text{g,s}}$ [cm/s]	0.21	0.21	0.88	0.88
Impeller Reynolds nr., $Re = \rho ND^2/\mu$	330,000	462,000	333,000	527,000
Gas flow number, $Fl = Q_{\text{g}}/ND^3$	0.015	0.011	0.062	0.039
Froude number, $Fr = N^2D/g$	0.306	0.589	0.306	0.766
Impeller cavity structures [a]	vortex	vortex	large	large
Ungassed power input [kW]	0.628	1.68	0.628	2.49
Specific ungassed power [kW/m^3]	0.802	2.15	0.802	3.18
Specific power[b] [kW/m^3]	–	2.00	–	–

[a]Barigou and Greaves (1996); [b]Barigou and Greaves (1992)

Table 9.3: Modelling conditions chosen for the standard model.

	Standard model
Interfacial forces	only drag force
Drag formulation	Schiller & Naumann law
Drag modification for turbulence	no
Drag modification for high gas fractions	no
Bubble size d_b	3 mm (monodisperse)
Outlet boundary condition	pressure outlet or degassing
Inlet boundary condition	mass and momentum source terms
Discretisation scheme	higher-order (QUICK or 2^{nd} order upw.)
Computational mesh	47k ($65 \times 36 \times 20$)
Rotational symmetry	60° sector (single blade & baffle)
Impeller model	MRF

Table 9.4: Effect of stirring and aeration rate on bubble size. Overall Sauter mean diameter, D_{32} [mm], values are given according to Barigou and Greaves (1992) as calculated from Eq. 8.87 in the mid–baffle plane measurement grid indicated in Fig. 9.3.

	Case 1 180 rpm 1.64 l/s	Case 2 250 rpm 1.64 l/s	Case 3 180 rpm 6.87 l/s	Case 4 285 rpm 6.87 l/s
Impeller region ($z2 = 0.250H$)	1.7	1.3	2.9	2.9
Below impeller region ($z1 = 0.125H$)	3.3	3.0	4.0	3.6

Table 9.5: Gassed power reduction, P_g/P [–], predictions according to the correlation of Hughmark (Eq. 3.11) and Bakker et al. (Eq. 3.12).

	Case 1	Case 2	Case 3	Case 4
Hughmark	0.85	0.81	0.59	0.55
Bakker	0.82	0.84	0.52	0.51

Table 9.6: Bubble size classes (bins) used in the PBM simulations. First two sets are defined according to a geometric ratio (with a constant volume ratio $v_{i+1}/v_i = d_{i+1}^3/d_i^3 = 2^q$, q being the ratio factor.)

	bin 0	bin 1	bin 2	bin 3	bin 4	bin 5
Set 1 ($q = 2$)	12.00 mm	7.56 mm	4.76 mm	3.00 mm	1.89 mm	1.19 mm
Set 2 ($q = 1$)	4.76 mm	3.78 mm	3.00 mm	2.38 mm	1.89 mm	–
Set 3	4.50 mm	3.75 mm	3.00 mm	2.00 mm	1.00 mm	0.50 mm

Table 9.7: Simulation results of the cases given in Fig. 9.9.

			Euler–Euler		ASMM	
	Exp./Cor.	Sim.[c]	Std.	VM	Std.	TD
Case 1						
Holdup [%]	2.97[a]	1.1	1.0	1.0	0.9	0.9
$P_{g,\Gamma}/P$	0.85[b]	0.96	0.78	0.74	0.84	0.88
Q_G/Q	–	0.97	0.82	0.83	0.98	0.98
Case 2						
Holdup [%]	3.65[a]	–	1.5	1.6	2.6	2.6
$P_{g,\Gamma}/P$	0.81[b]	–	0.86	0.71	0.86	0.88
Q_G/Q	–	–	0.82	0.85	0.98	0.98
Case 3						
Holdup [%]	7.76[a]	3.4	2.3	2.4	2.6	2.6
$P_{g,\Gamma}/P$	0.59[b]	0.83	0.88	0.88	0.84	0.86
Q_G/Q	–	0.83	0.79	0.79	0.97	0.98
Case 4						
Holdup [%]	9.65[a]	–	3.6	4.2	5.9	6.8
$P_{g,\Gamma}/P$	0.55[b]	–	0.85	0.67	0.80	0.82
Q_G/Q	–	–	0.74	0.76	0.94	0.94

[a]Experimental data from Barigou and Greaves (1996)
[b]Correlation of Hughmark (Eq. 3.11)
[c]Simulation data from Lane (2005a)

Table 9.8: Summary of results obtained with the final modelling options and the fine mesh (140k). The Ishii & Zuber drag law in conjunction with the Brucato turbulence correction was used. Virtual mass force was also taken into account. 5 new bubble size classes have been defined for the DM, which are denoted as Set 2 in Table 9.6.

	Case 1	Case 2	Case 3	Case 4
Holdup [%]	≈2.5	5.2	≈5.5	12.3
	2.97[a]	3.65[a]	7.52[a]	9.56[a]
Relative error in holdup (w.r.t. data[a]) [%]	-15.8	42.5	-28.8	28.7
Mean axial slip [cm/s]	≈7.8	6.4	7.3	5.6
Mean ε_1 [m^2/s^2]	0.71	1.98	0.65	2.60
Overall Sauter mean diameter, D_{32} [mm]	4.1	4.0	4.4	4.3
	3.50[a]	3.36[a]	3.88[a]	3.85[a]
Relative error in D_{32} (w.r.t. data[a]) [%]	17.1	18.9	13.4	11.6
D_{32}/η_1 [-]	119	150	125	174
Mean Re_b	315	255	335	256
Gassed power nr. ($P_{\mathrm{g},\varepsilon}/\rho_1 N^3 D^5$)	4.90	4.95	4.29	≈4.05
Gassed power nr. ($P_{\mathrm{g},\Gamma}/\rho_1 N^3 D^5$)	5.40	5.41	4.59	3.90
Power ratio ($P_{\mathrm{g},\Gamma}/P_\Gamma$)	0.95	0.95	0.81	0.84
Power ratio ($P_{\mathrm{g},\varepsilon}/P_\varepsilon$)	0.91	0.92	0.80	0.75
Specific power ($P_{\mathrm{g},\Gamma}/\mathcal{V}_\mathrm{l}$) [kW/m^3]	0.77	2.06	0.65	2.20
	–	2.00[a]	–	–
Gas flow nr. (Q_G/ND^3)	0.69	0.70	0.62	0.63
Impeller discharge ratio (Q_G/Q)	0.96	0.97	0.86	0.88

[a]Experimental data from Barigou and Greaves (1992)

Figures

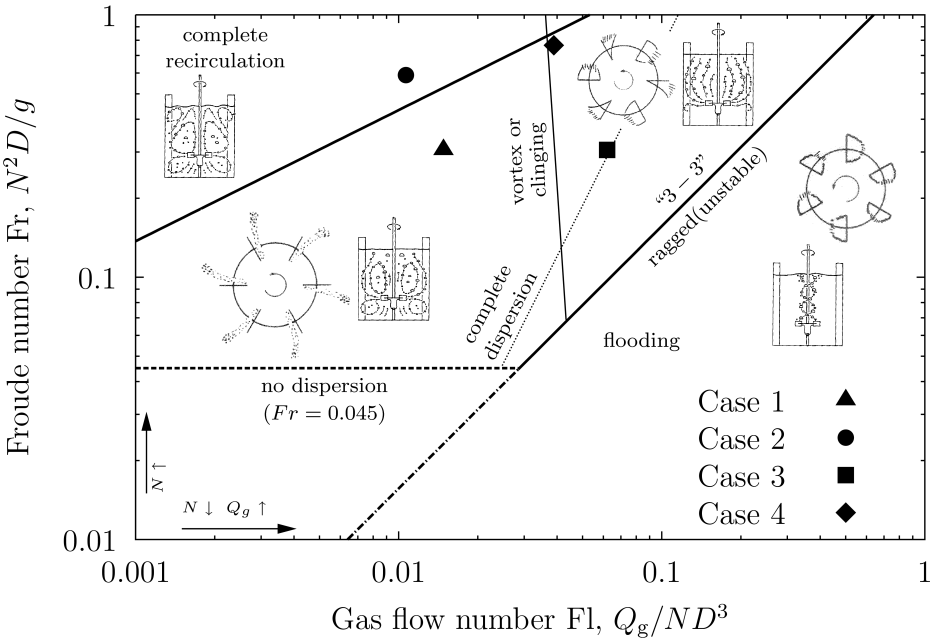

Figure 9.1: Flow regime map for the simulation cases. Schematic representation of the bulk flow patterns and the cavity types are from Nienow et al. (1977) and Smith and Warmoeskerken (1985), respectively.

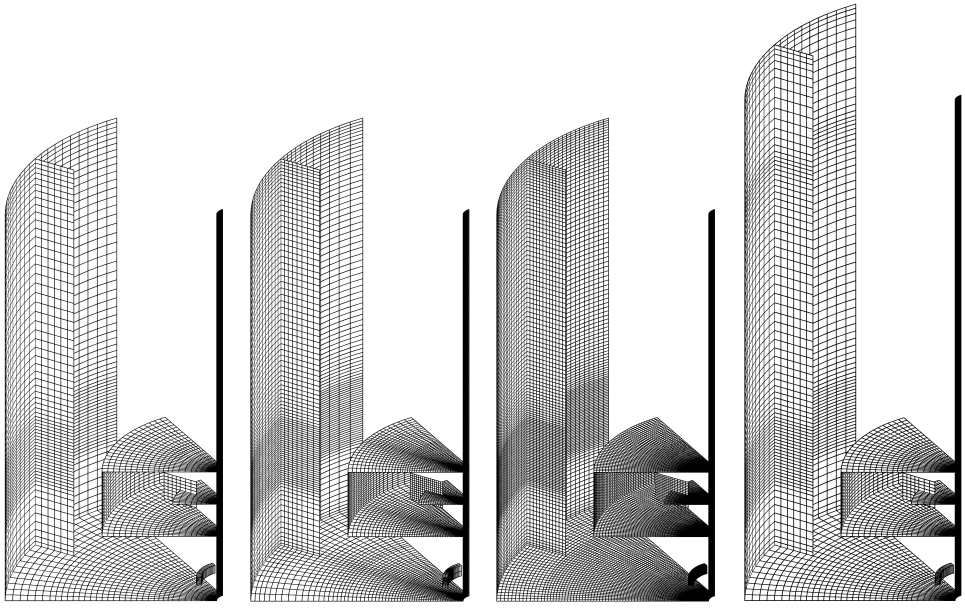

(a) (b) (c) (d)

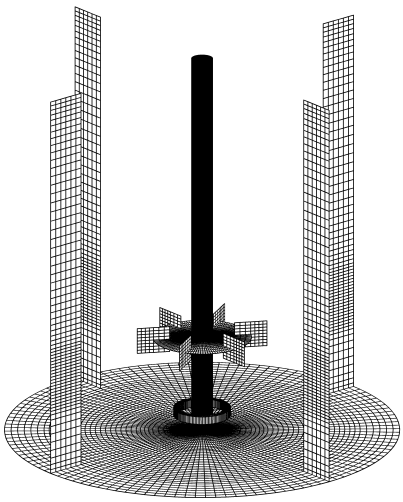

(e)

Figure 9.2: Surface plots of computational grids used in simulations. MRF (and SM) grid interface is also shown. (a) Coarse mesh: 47k ($65 \times 36 \times 20$), (b) Medium mesh: 140k ($97 \times 60 \times 24$), (c) Fine mesh: 374k ($130 \times 72 \times 40$), (d) Mesh with disengagement region: 58k ($80 \times 36 \times 20$), and (e) Mesh for full 360° sector: 281k (6×47k)

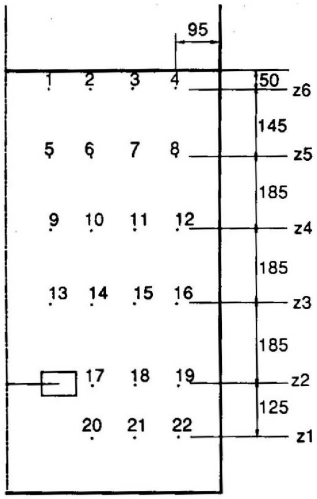

Figure 9.3: Measurement positions (in mm) in mid-plane between two adjacent baffles (mid-baffle plane) as given by Barigou and Greaves (1996).

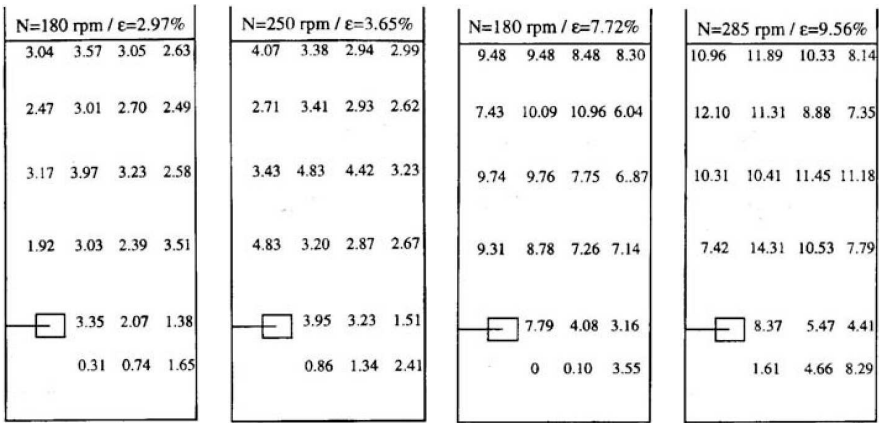

(a) Case 1 (b) Case 2 (c) Case 3 (d) Case 4

	Holdup [%]
Case 1 (180 rpm, $Q_g = 1.64 \times 10^{-3}$ m^3/s)	2.97
Case 2 (250 rpm, $Q_g = 1.64 \times 10^{-3}$ m^3/s)	3.65
Case 3 (180 rpm, $Q_g = 6.87 \times 10^{-3}$ m^3/s)	7.72
Case 4 (285 rpm, $Q_g = 6.87 \times 10^{-3}$ m^3/s)	9.56

Figure 9.4: Spatial distribution of gas holdup (%) measured by Barigou and Greaves (1996) in mid-plane between two adjacent baffles (mid-baffle plane). Overall gas holdup values in the tank are also given.

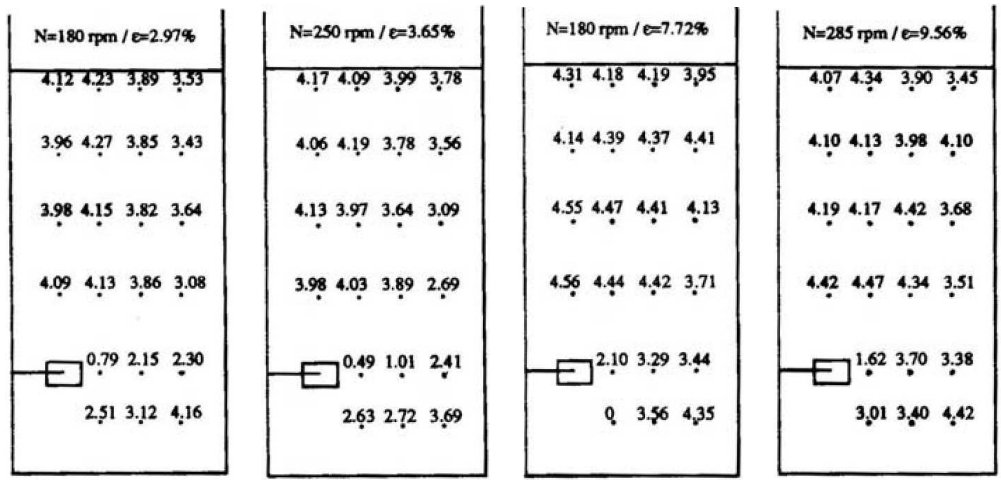

(a) Case 1 (b) Case 2 (c) Case 3 (d) Case 4

Figure 9.5: Spatial distribution of Sauter mean bubble diameter measured by Barigou and Greaves (1992) in mid-baffle plane.

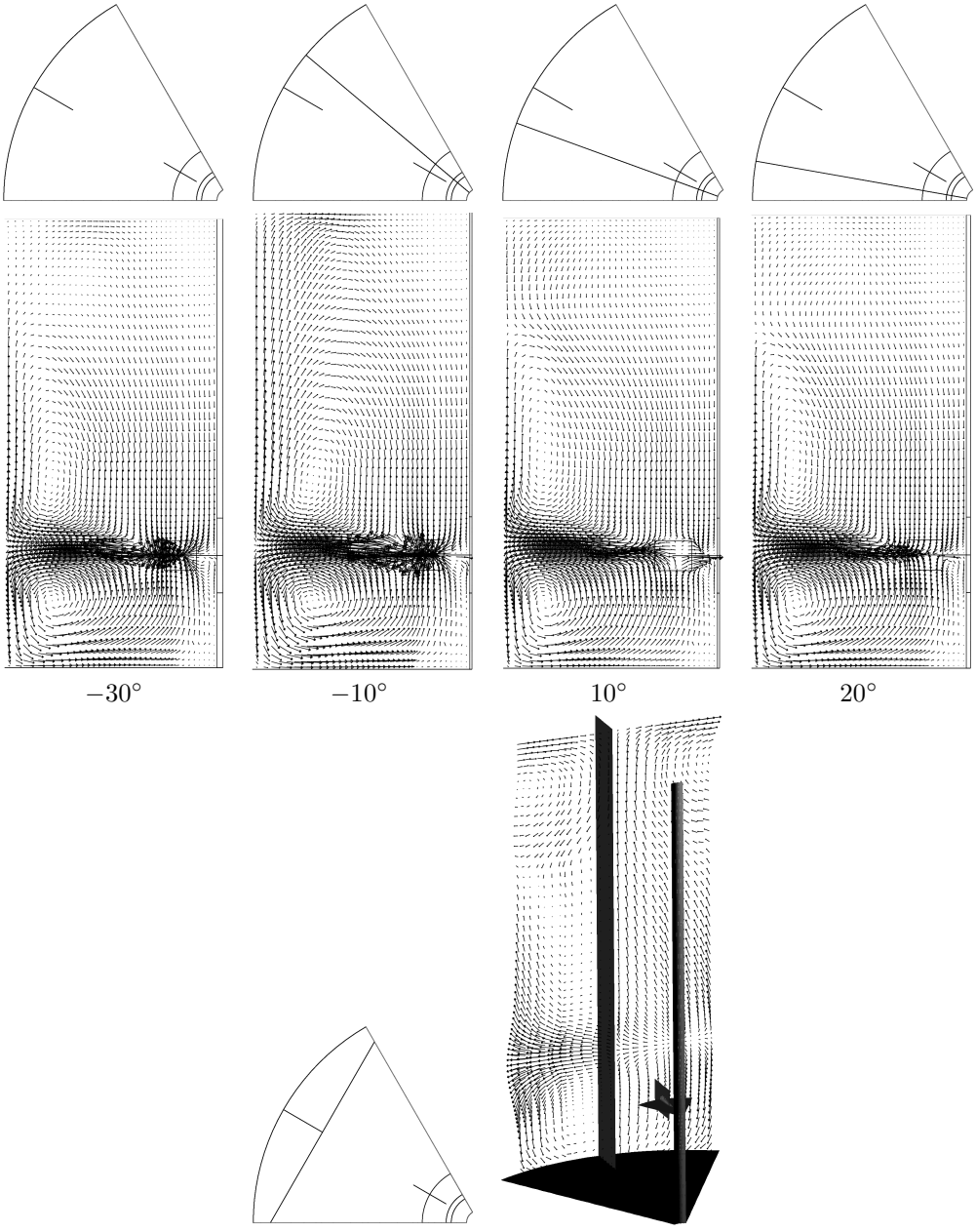

Case: 180 rpm, $Q_g = 0$

Figure 9.6: Single-phase velocity fields used as an initial solution for two-phase simulations. Planes are located at angular positions of −30 (mid-baffle plane), −10, 10, and 20 degrees w.r.t. the baffle ("−" sign referring to the direction opposite to impeller rotation), and at a position perpendicular to the baffle, showing the secondary vortex near the free surface. Top view of the plot planes are also shown. Impeller rotates counterclockwise.

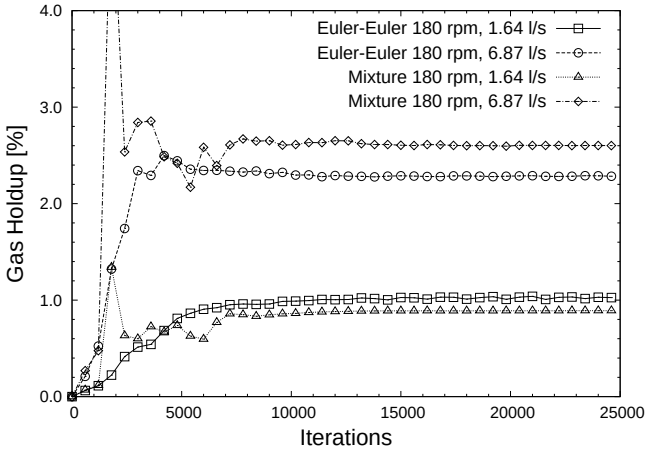

(a) Increase of gas flow rate

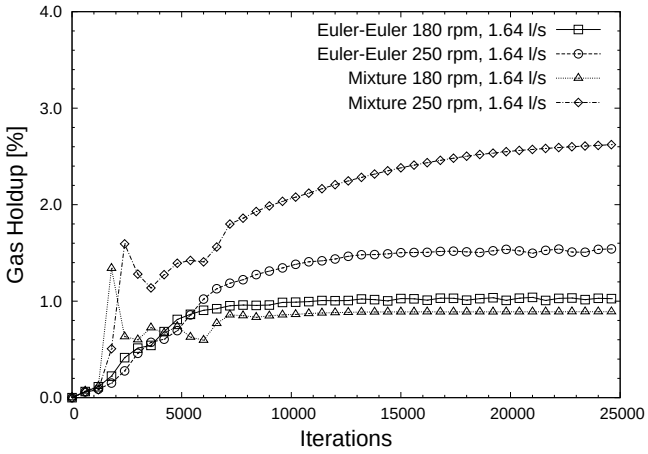

(b) Increase of stirring rate

Figure 9.7: Convergence profiles of the integrated gas holdup at the tank for Euler–Euler and algebraic slip mixture model simulations. (a) Cases 1 and 3 (see Table 9.2) are plotted to show the effect of increasing gas flow rate at constant stirring rate. (b) Case 1 and 2 are plotted to show the effect of increasing stirring rate at constant gas flow rate.

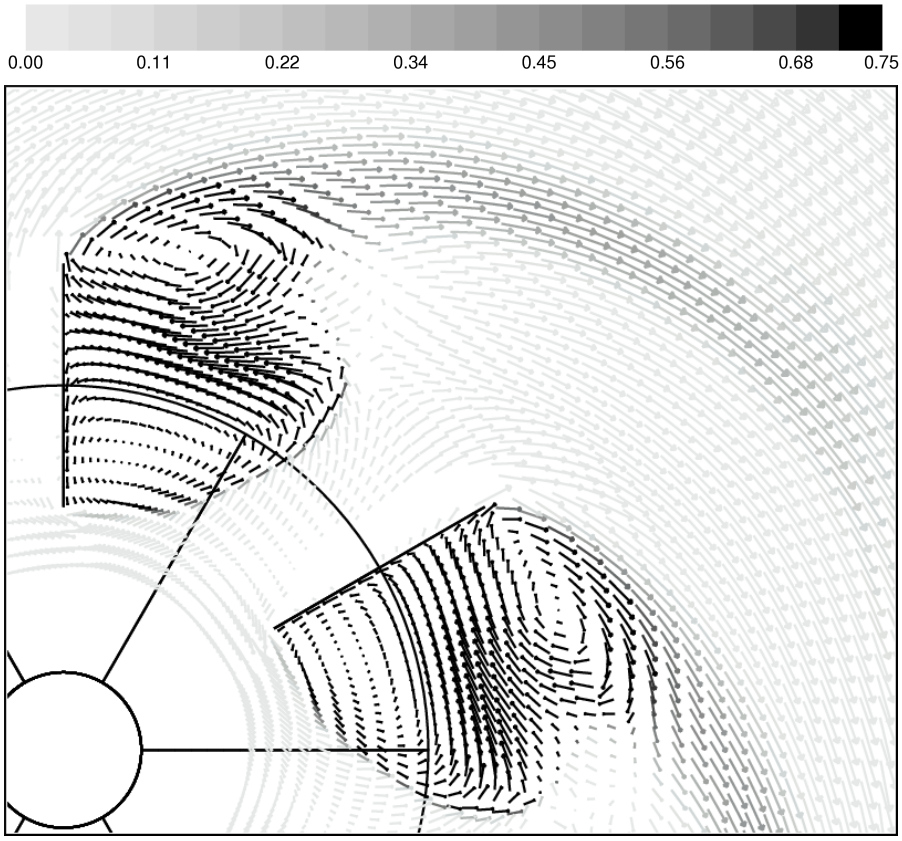

Figure 9.8: Gas velocity vectors (coloured in greyscale by gas volume fraction) w.r.t. the rotating reference frame for Case 4 (refined grid). Plotting plane is just above the impeller centerline ($y = 0.27H$).

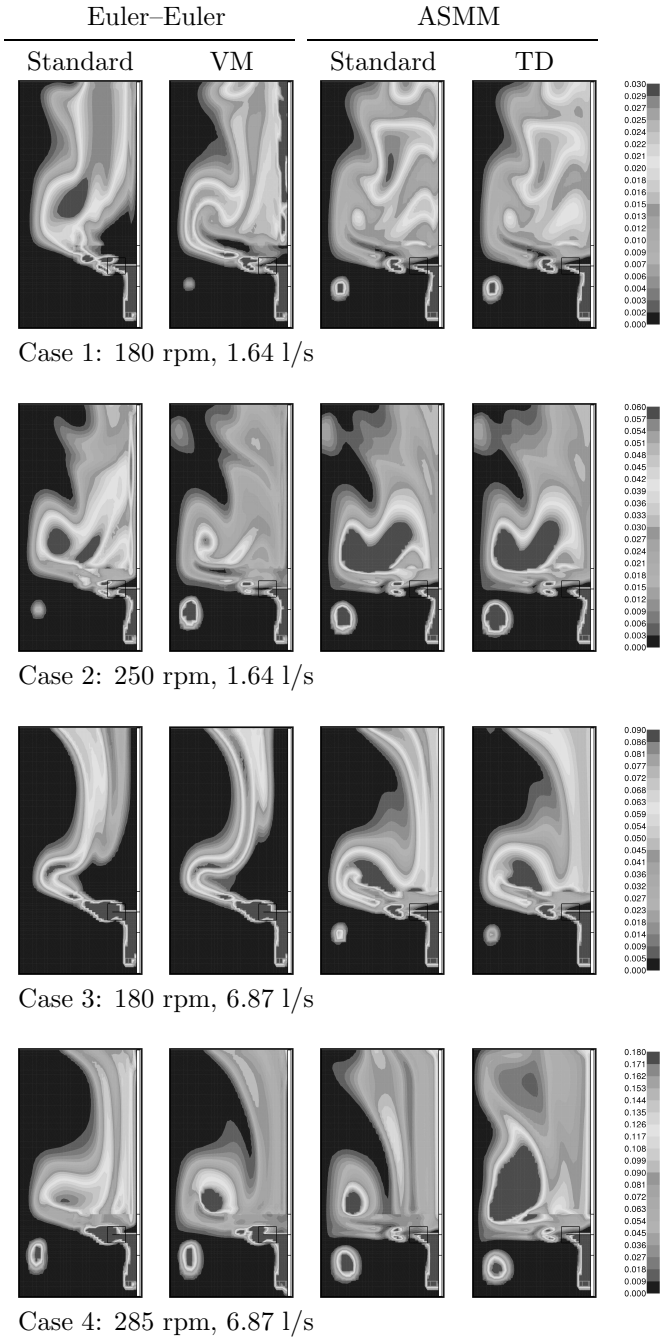

Figure 9.9: Results from earlier simulations as reported in (Günyol and Mudde, 2007a,b). Gas volume fraction contours are given at mid-baffle plane. Results for both Euler–Euler and algebraic slip mixture model (ASMM) are given. Standard (drag-only) case is compared with the cases in which the virtual mass (VM) force and turbulent dispersion (TD) force are also considered. See also Table 9.7.

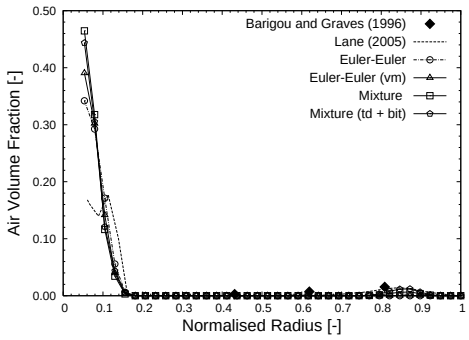

(a) Relative axial location z1=0.125H

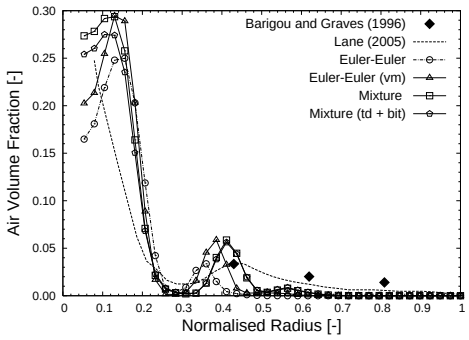

(b) Relative axial location z2=0.25H

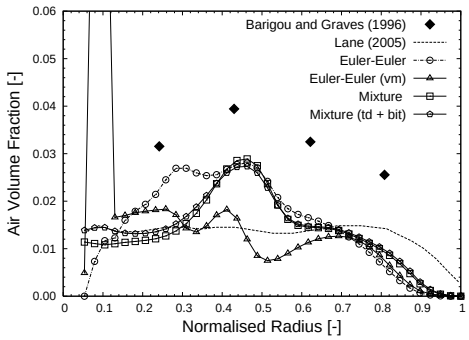

(c) Relative axial location z4=0.62H

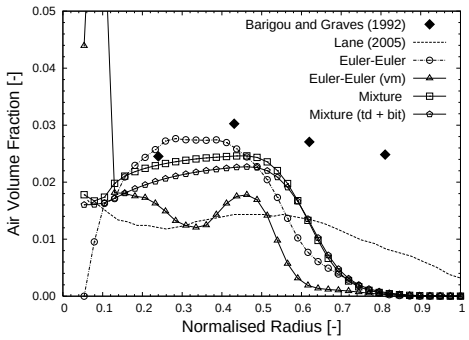

(d) Relative axial location z5=0.805H

Figure 9.10: Local gas volume fraction predictions for Case 1 plotted on the mid–baffle plane at different axial levels (indicated as z1, z2, z4 and z5, respectively, in Fig. 9.3). Bubble size is constant ($d_b = 3$ mm). A comparison is made with the experimental data from Barigou and Greaves (1996) and the simulation data from Lane (2005a).

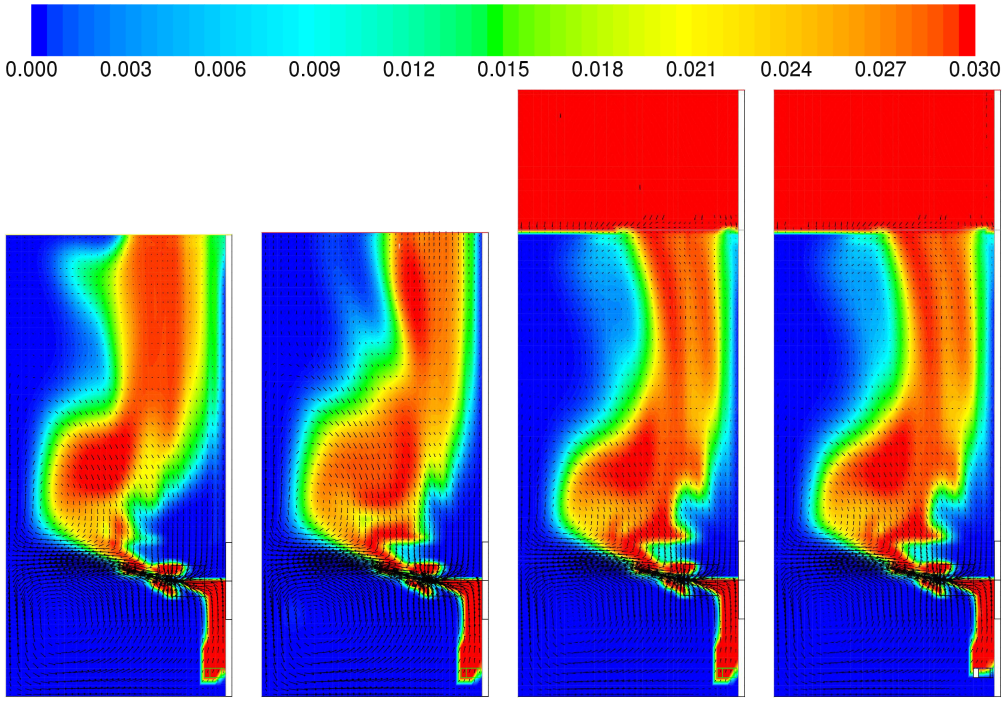

Case 1: 180 rpm, $Q_g = 1.64 \times 10^{-3}$ m^3/s
Model: $d_b = 3$ mm, Schiller & Naumann drag

	Holdup [%]	$\frac{P_{g,\varepsilon}}{\rho_1 N^3 D^5}$	$\frac{P_{g,\Gamma}}{\rho_1 N^3 D^5}$	$\frac{Q_G}{ND^3}$
(a) Degassing	1.05	≈ 3.81	3.12	0.64
(b) PO	1.04	≈ 3.72	3.15	0.63
(c) DH+PO	1.13	≈ 4.03	3.14	0.63
(d) DH+PO+VI	1.14	≈ 4.00	3.15	0.63
Exp.[a]	2.97	–	–	–

[a] Barigou and Greaves (1996)

Figure 9.11: Influence of inlet and outlet boundary conditions. Gas volume fraction contours and liquid velocity vectors are given at mid-baffle plane. Corresponding values for the gas holdup and power and flow numbers are given below ($\approx$ denotes the approximate mean value of a fluctuating quantity). Experimental values are also given. (a) Standard settings (degassing condition at outlet, mass and momentum sources for gas inflow), (b) pressure outlet (PO), mass and momentum sources for gas inflow, (c) disengagement height (DH) and pressure outlet, mass and momentum sources for gas inflow, (d) disengagement height and pressure outlet, velocity inlet boundary for gas inflow (VI) attached to sparger shaped void.

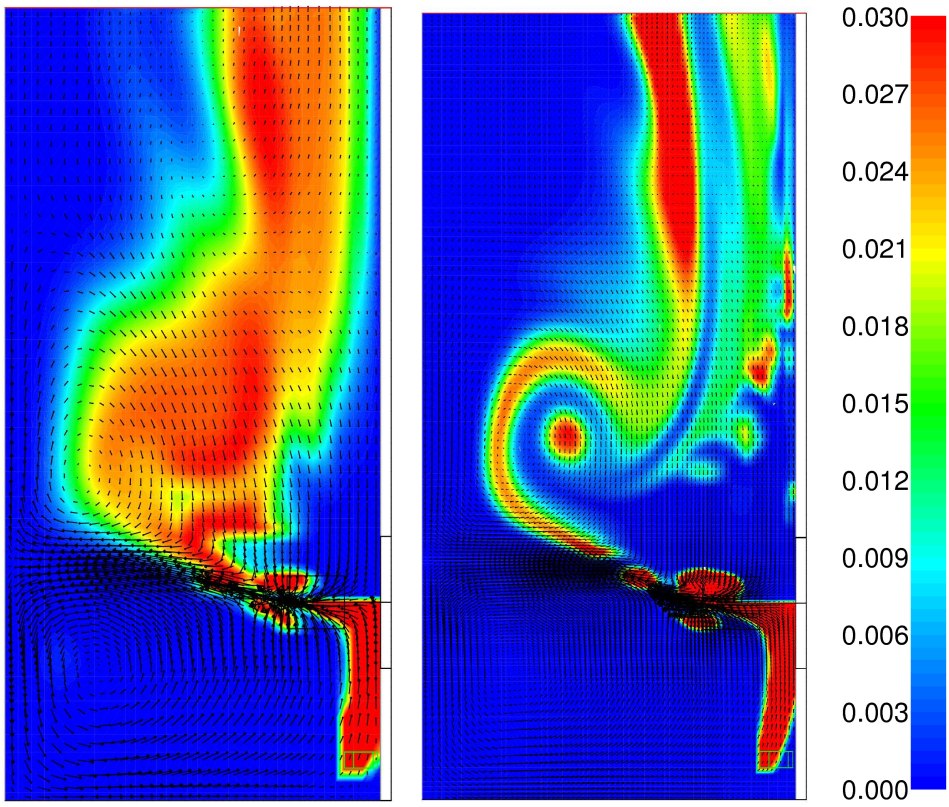

(a) (b)

Case 1: 180 rpm, $Q_g = 1.64 \times 10^{-3}$ m^3/s
Model: $d_b = 3$ mm, Schiller & Naumann drag, PO

	Holdup [%]	$\frac{P_{g,\varepsilon}}{\rho_1 N^3 D^5}$	$\frac{P_{g,\Gamma}}{\rho_1 N^3 D^5}$	$\frac{Q_G}{ND^3}$
(a) Standard grid	1.04	≈ 3.72	3.15	0.63
(b) Refined grid	1.00	(-)	2.88	0.56
Ungassed sim. (standard)	–	4.75	5.62	0.78
Ungassed sim. (refined)	–	5.38	5.68	0.80
Exp.[a]	2.97	–	–	–

[a] Barigou and Greaves (1996)

Figure 9.12: Influence of grid refinement. Gas volume fraction contours and liquid velocity vectors are given at mid-baffle plane. Corresponding values for the gas holdup and power and flow numbers are given below. (a) Standard grid: 47k ($65 \times 36 \times 20$), (b) Refined grid: 374k ($130 \times 72 \times 40$). Length of the velocity vectors are decreased for clarity for this case. (-) refers that a steady value was not achieved.

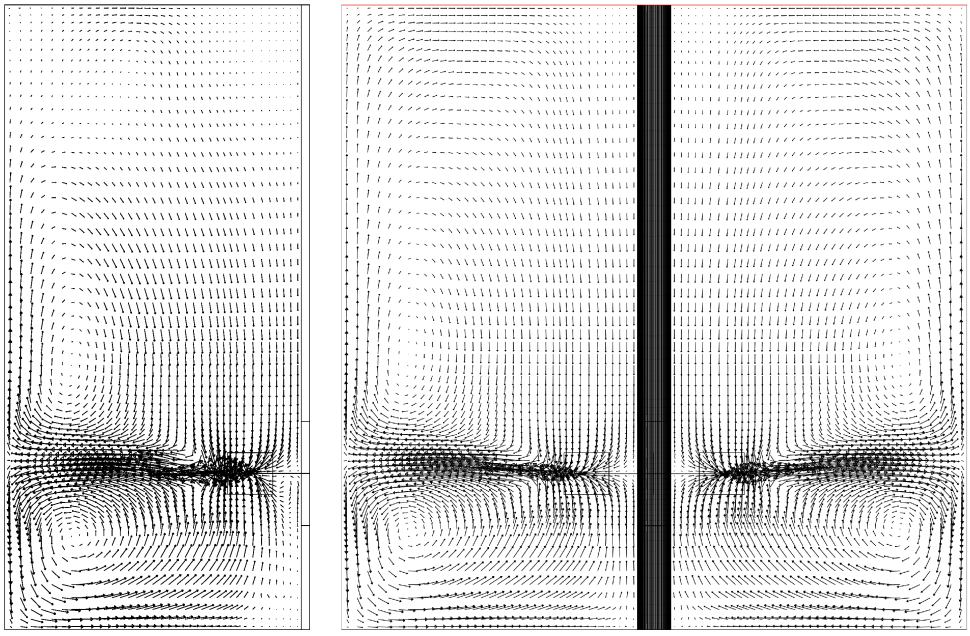

(a) (b)

Case: 180 rpm, $Q_g = 0$

	$\frac{P_\varepsilon}{\rho_1 N^3 D^5}$	$\frac{P_{g,\Gamma}}{\rho_1 N^3 D^5}$	$\frac{Q_G}{N D^3}$
(a) Symmetry (60° section)	4.75	5.62	0.78
(b) No symmetry (360° section)	4.61	5.39	0.80

Figure 9.13: Influence of rotational symmetry assumption. Velocity vectors in mid-baffle plane for unaerated operation. Corresponding values for the power and flow numbers are given below.

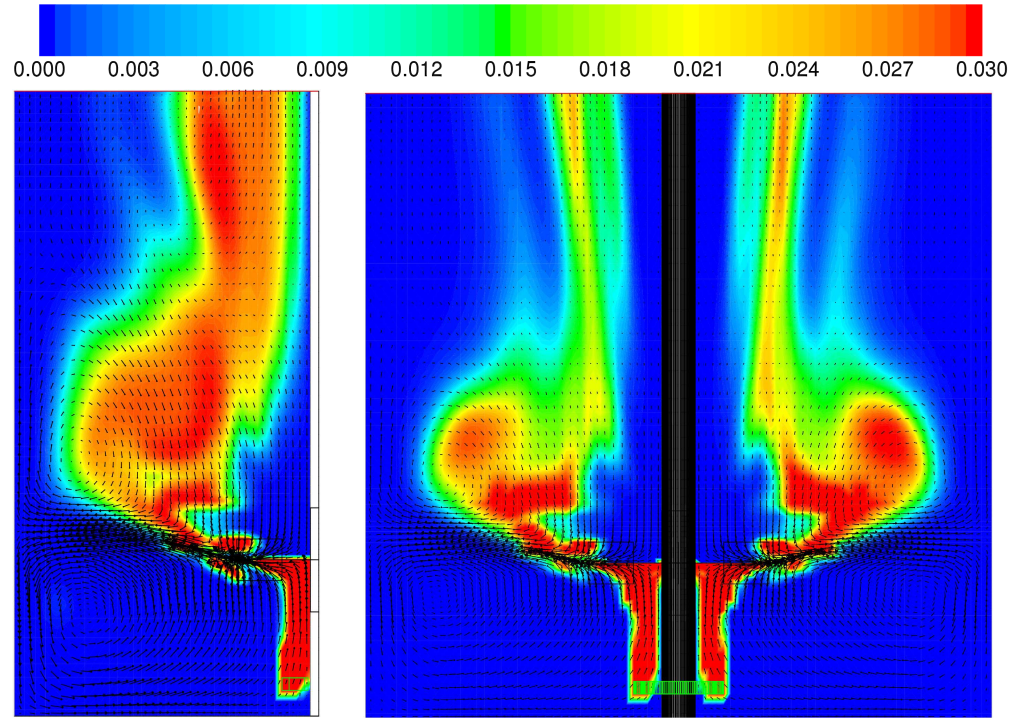

(a) (b)

Case 1: 180 rpm, $Q_g = 1.64 \times 10^{-3}$ m^3/s
Model: $d_b = 3$ mm, Schiller & Naumann drag, PO

	Holdup [%]	$\frac{P_{g,\varepsilon}}{\rho_1 N^3 D^5}$	$\frac{P_{g,\Gamma}}{\rho_1 N^3 D^5}$	$\frac{Q_G}{ND^3}$
(a) Symmetry	1.04	≈ 3.72	3.15	0.63
(b) No symmetry (transient)[a]	0.82	≈ 4.58	≈ 3.17	0.64
No symmetry (steady)	≈ 0.91	≈ 3.61	≈ 3.18	0.65
Exp.[b]	2.97	–	–	–

[a] $\Delta t = 0.001$ s; [b] Barigou and Greaves (1996)

Figure 9.14: Influence of rotational symmetry assumption. Gas volume fraction contours and liquid velocity vectors in mid-baffle plane for aerated operation. Contour plot for the "no symmetry" case corresponds to transient run with time step $\Delta t = 0.001$ s, where a periodic steady solution has been reached. Steady-state run and transient run with larger time step of $\Delta t = 0.005$ s resulted in asymmetric gas distribution between the right and left vertical planes (not shown here). Below the gas holdup and power and flow numbers are given.

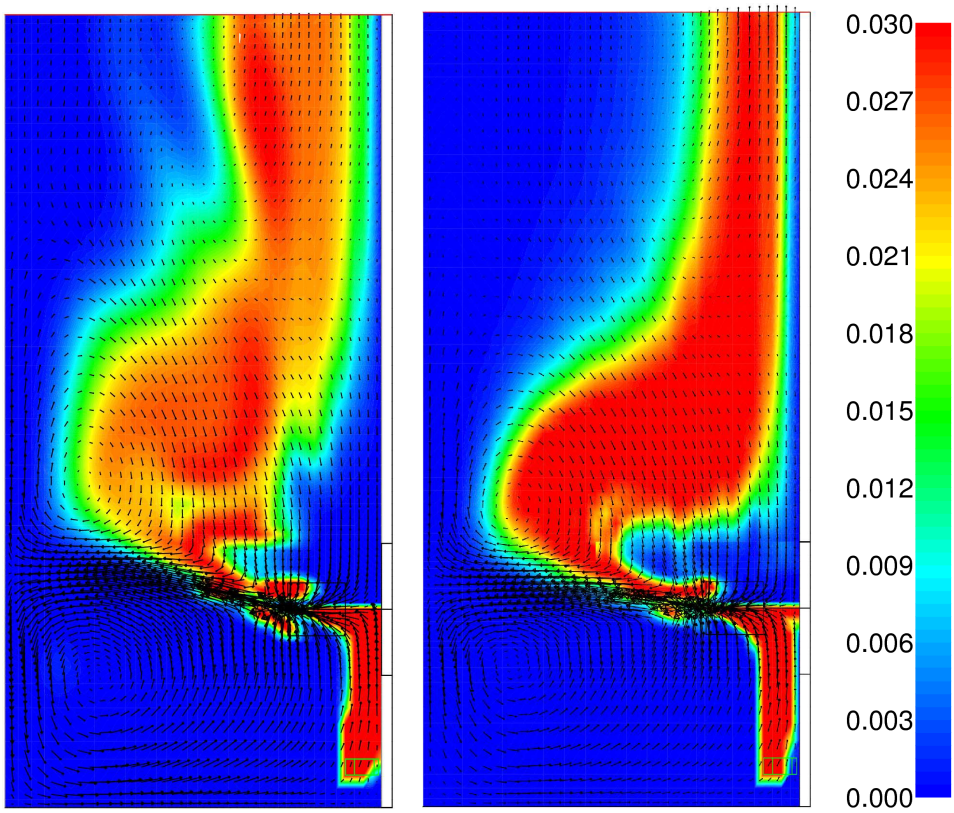

(a) (b)

Case 1: 180 rpm, $Q_g = 1.64 \times 10^{-3}$ m^3/s
Model: $d_b = 3$ mm, Schiller & Naumann drag, PO

	Holdup [%]	$\frac{P_{g,\varepsilon}}{\rho_1 N^3 D^5}$	$\frac{P_{g,\Gamma}}{\rho_1 N^3 D^5}$	$\frac{Q_G}{ND^3}$
(a) MRF	1.04	≈ 3.72	3.15	0.63
(b) SM (transient)[a]	0.99	≈ 4.42	3.74	0.72
Exp.[b]	2.97	–	–	–

[a] $\Delta t = 0.001$ s; [b] Barigou and Greaves (1996)

Figure 9.15: Comparison of different impeller modelling approaches: Multiple reference frame (MRF) versus Sliding mesh (SM). Gas volume fraction contours and liquid velocity vectors are given at mid-baffle plane. Corresponding values for the gas holdup and power and flow numbers are given below.

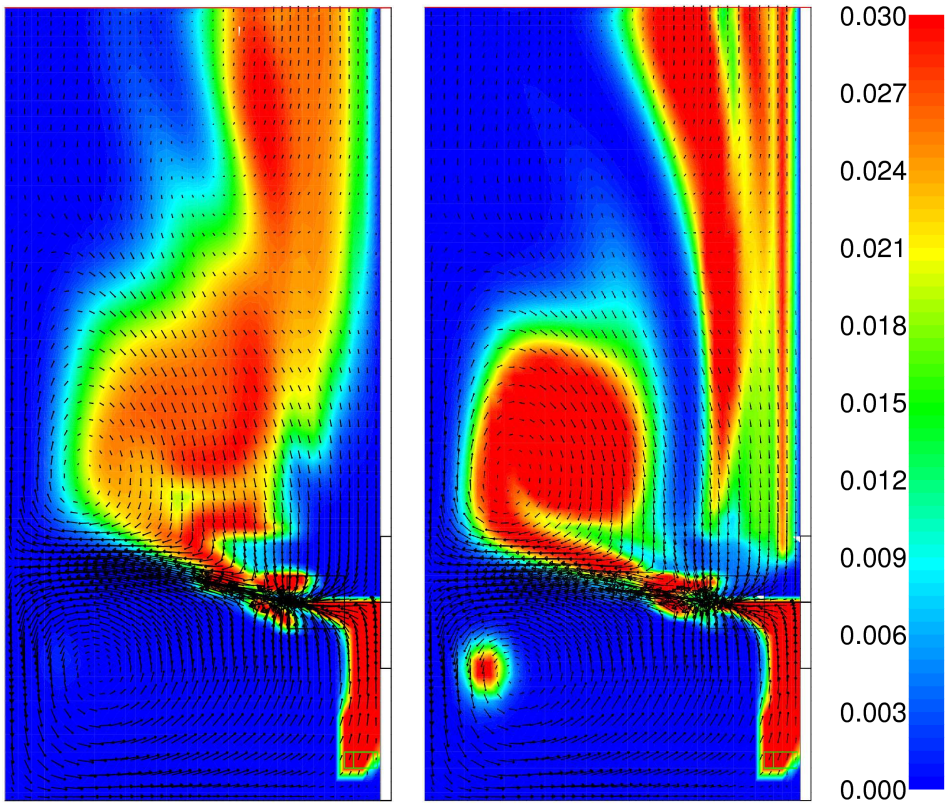

Case 1: 180 rpm, $Q_g = 1.64 \times 10^{-3}$ m^3/s
Model: $d_b = 3$ mm, PO

	(a)	(b)
Drag correlation	Schiller & Naumann	Ishii & Zuber
Holdup[a] [%]	1.04	1.12
Average axial slip velocity [cm/s]	28.3	23.7
$P_{g,\varepsilon}/\rho_1 N^3 D^5$	≈ 3.72	≈ 3.30
$P_{g,\Gamma}/\rho_1 N^3 D^5$	3.15	3.63
Q_G/ND^3	0.63	0.63

[a]Exp.: 2.97% (Barigou and Greaves, 1996)

Figure 9.16: Comparison of Ishii & Zuber and Schiller & Naumann drag laws. Gas volume fraction contours and liquid velocity vectors are given at mid-baffle plane.

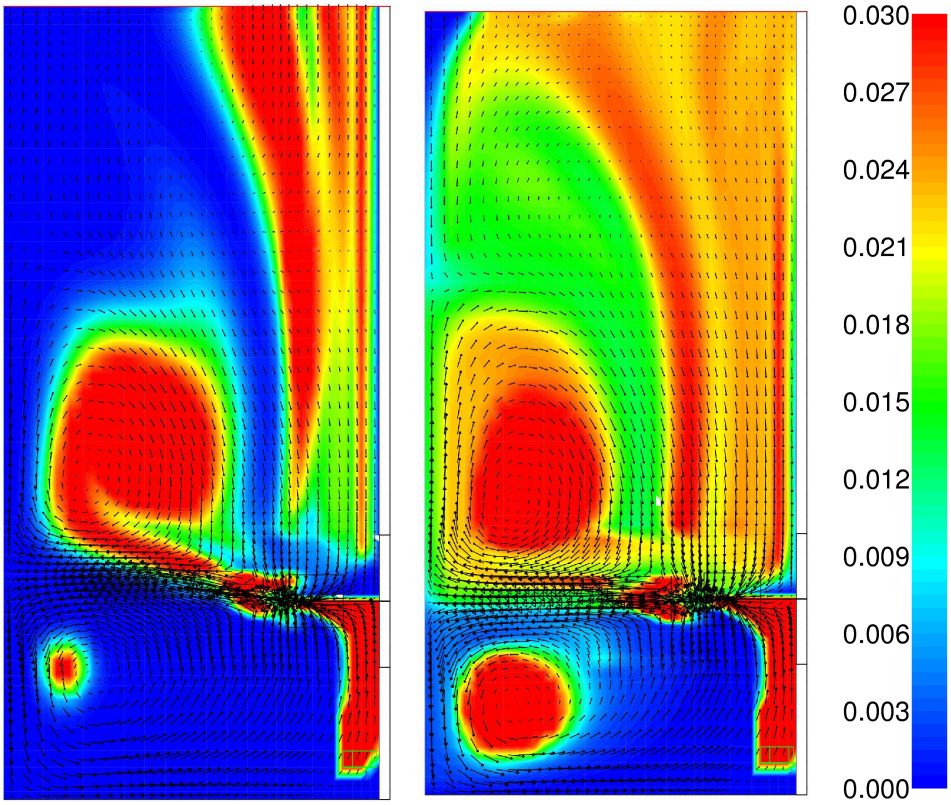

(a) (b)

Case 1: 180 rpm, $Q_g = 1.64 \times 10^{-3}$ m^3/s
Model: $d_b = 3$ mm, Ishii & Zuber drag, PO

	(a)	(b)
Turbulence drag modification	–	Brucato et al.
Holdup[a] [%]	1.12	2.77
Average axial slip velocity [cm/s]	23.7	10.3
$P_{g,\varepsilon}/\rho_1 N^3 D^5$	≈ 3.30	4.45
$P_{g,\Gamma}/\rho_1 N^3 D^5$	3.63	5.40
Q_G/ND^3	0.63	0.69

[a]Exp.: 2.97% (Barigou and Greaves, 1996)

Figure 9.17: Turbulence effects on drag force as modelled according to the correlation of Brucato et al. (1998b). Gas volume fraction contours and liquid velocity vectors are given at mid-baffle plane.

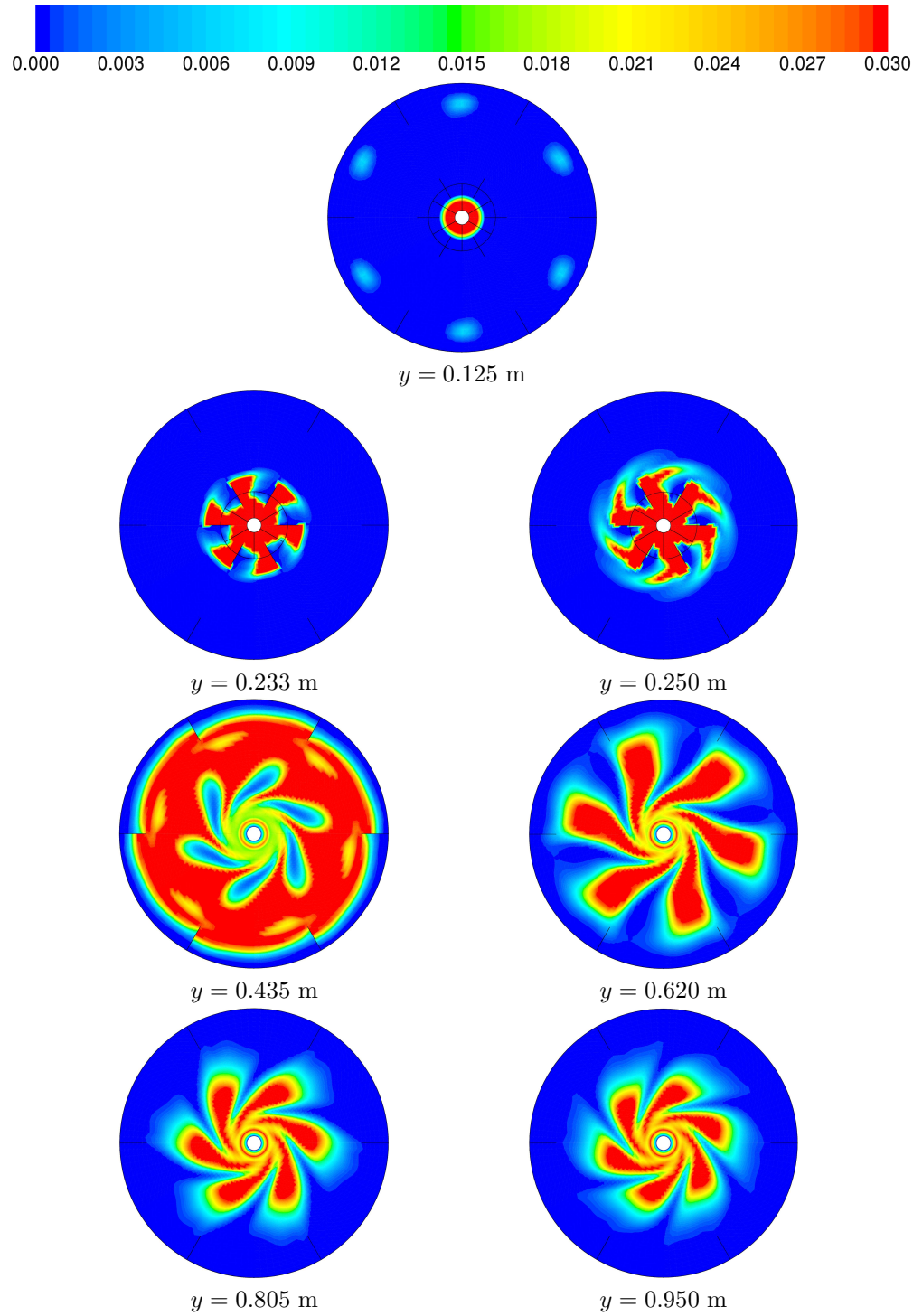

Figure 9.18: Gas volume fraction contours at axial planes for the Ishii & Zuber case in Fig. 9.17(a). Contour plots are given with (rotational) periodic repeat. Impeller rotates counterclockwise.

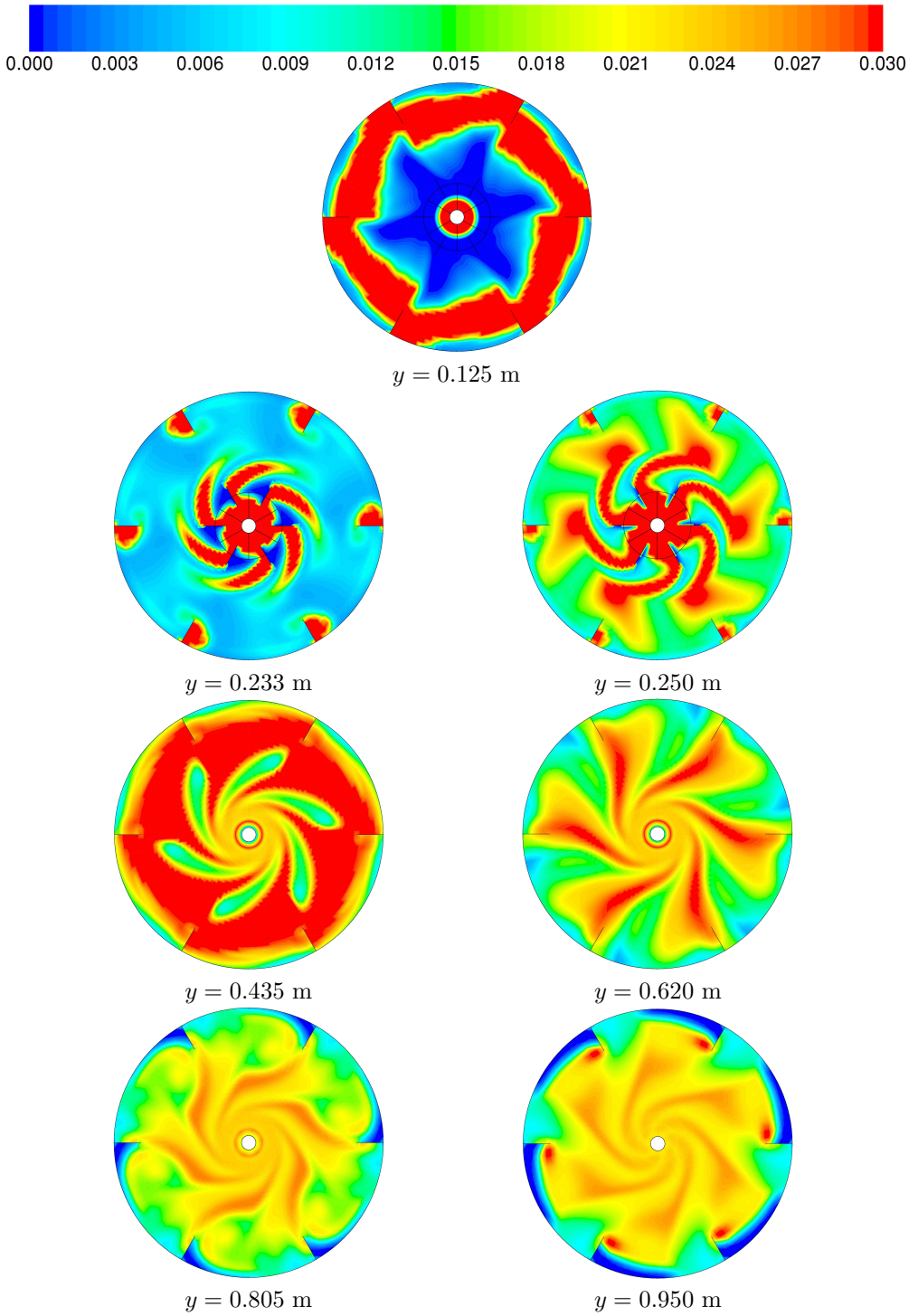

Figure 9.19: Gas volume fraction contours at axial planes for the Brucato case in Fig. 9.17(b). Contour plots are given with (rotational) periodic repeat. Impeller rotates counterclockwise.

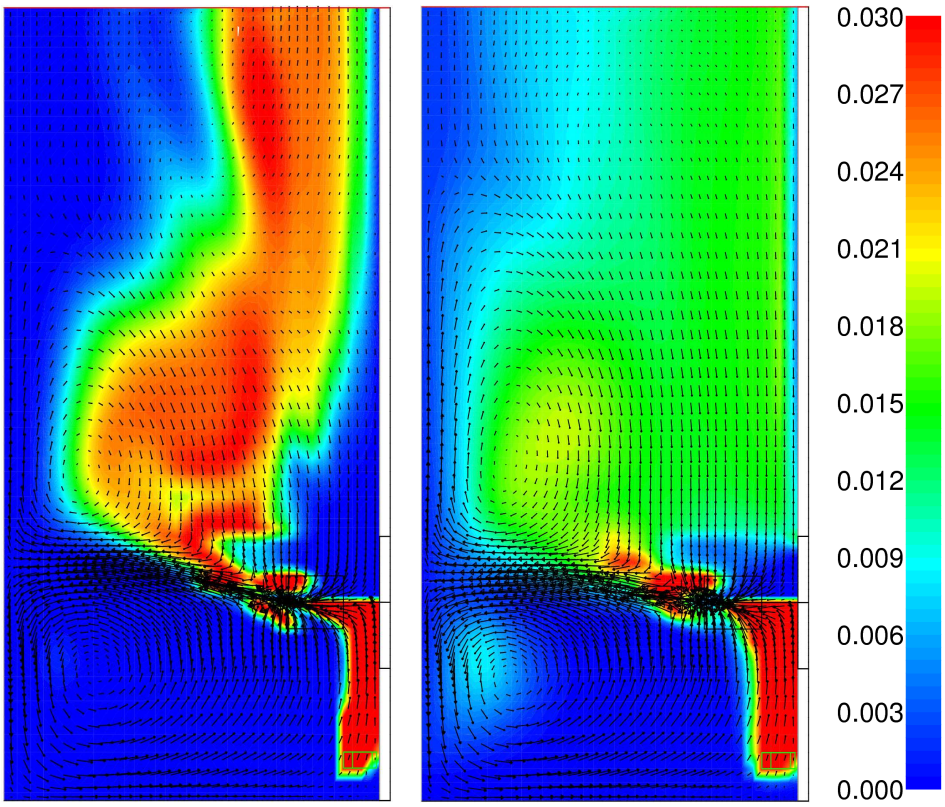

Case 1: 180 rpm, $Q_g = 1.64 \times 10^{-3}$ m^3/s
Model: $d_b = 3$ mm, Schiller & Naumann drag, PO

	Holdup [%]	$\frac{P_{g,\varepsilon}}{\rho_1 N^3 D^5}$	$\frac{P_{g,\Gamma}}{\rho_1 N^3 D^5}$	$\frac{Q_G}{ND^3}$
(a) No TD	1.04	≈ 3.72	3.15	0.63
(b) TD (VOF diffusion)	0.98	3.16	3.79	0.66
Exp.[a]	2.97	–	–	–

[a] Barigou and Greaves (1996)

Figure 9.20: Turbulent dispersion (TD) effects (as modelled by a diffusion term in volume fraction (VOF) equation). Gas volume fraction contours and liquid velocity vectors are given at mid-baffle plane.

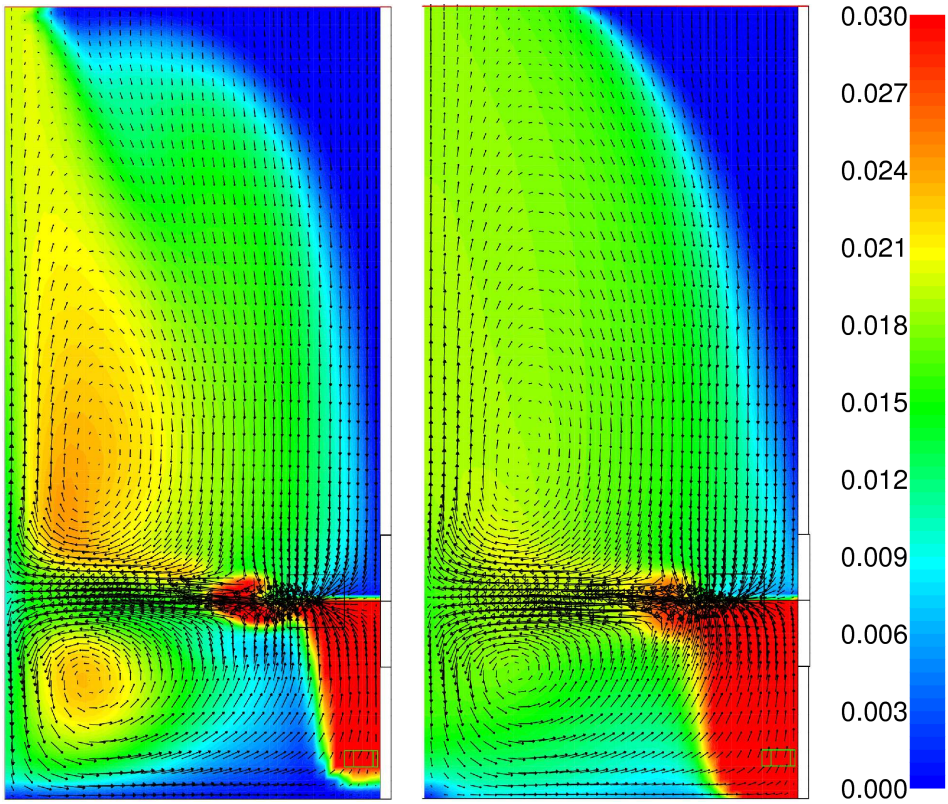

(a) (b)

Case 1: 180 rpm, $Q_g = 1.64 \times 10^{-3}$ m^3/s
Model: Ishii & Zuber drag, Brucato turbulence correction, VM, DM, PO, transient

	Holdup [%]	d_{32}	$\frac{P_{g,\varepsilon}}{\rho_1 N^3 D^5}$	$\frac{P_{g,\Gamma}}{\rho_1 N^3 D^5}$	$\frac{Q_G}{ND^3}$
(a) TD (VOF diffusion)	1.78	3.75	4.63	5.51	0.80
(b) TD (Simonin)[a]	1.65	3.63	5.23	6.44	0.93
Exp.[b]	2.97	–	–	–	–

[a]Sliding mesh simulation; [b]Barigou and Greaves (1996)

Figure 9.21: Simonin turbulent dispersion model compared with the turbulent dispersion modelled by a diffusion term in VOF equation. The discrete method (DM) was used to solve population balance equation. There are 6 bubble size classes (0.5 mm, 1.0 mm, 2.0 mm, 3.0 mm, 3.75 mm and 4.5 mm). Initial bubble size at the sparger is 3 mm. Convergence was achieved only when running in transient mode with 1st order upwind discretisation for PBM bin fractions. Gas volume fraction contours and liquid velocity vectors are given at mid-baffle plane.

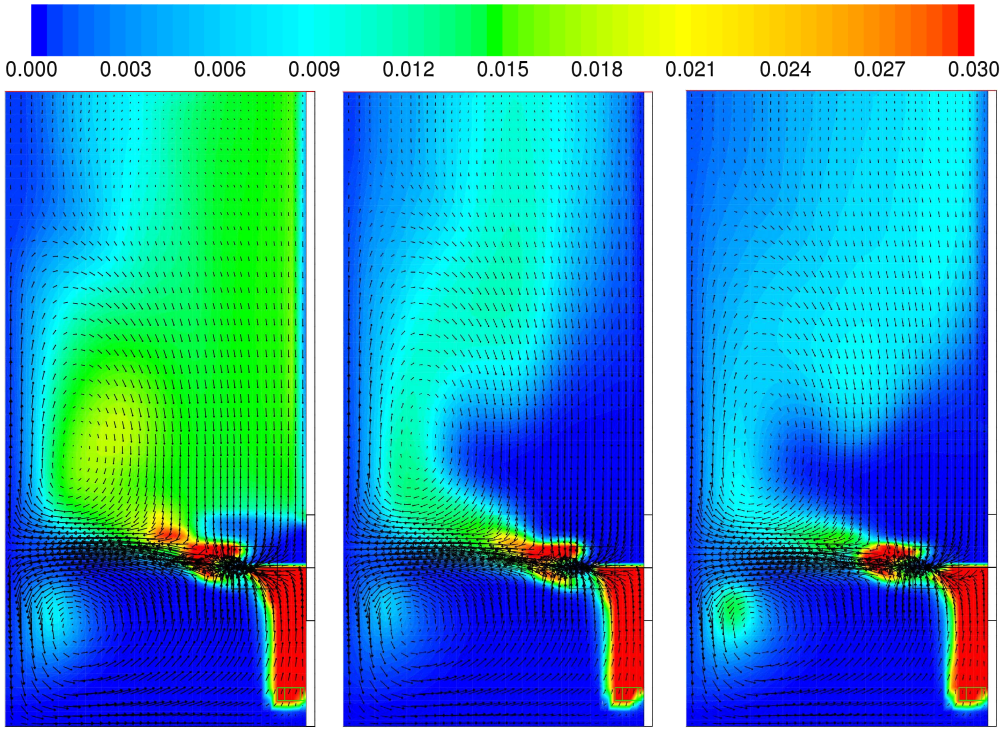

Case 1: 180 rpm, $Q_g = 1.64 \times 10^{-3}$ m^3/s
Model: Schiller & Naumann drag, PO, TD (VOF diffusion)

	Holdup [%]	$\frac{P_{g,\varepsilon}}{\rho_1 N^3 D^5}$	$\frac{P_{g,\Gamma}}{\rho_1 N^3 D^5}$	$\frac{Q_G}{ND^3}$
(a) $d_b = 3$ mm	0.98	3.16	3.79	0.66
(b) DM[a]	0.77	2.92	3.43	0.68
(c) DM + VM[a]	0.70	3.68	4.55	0.70
Exp.[b]	2.97	–	–	–

[a]Transient run; [b]Barigou and Greaves (1996)

Figure 9.22: Polydispersity and virtual mass force (VM) effects on simulations with turbulent dispersion (as modelled by a diffusion term in VOF equation). Population balance model used is the discrete model (DM) with 6 bubble size classes (1.2 mm, 1.9 mm, 3.0 mm, 4.8 mm, 7.6 mm and 12.0 mm). Initial bubble size at the sparger is 3 mm. Convergence was achieved only when running in transient mode with 1st order upwind discretisation for PBM bin fractions. Gas volume fraction contours and liquid velocity vectors are given at mid-baffle plane.

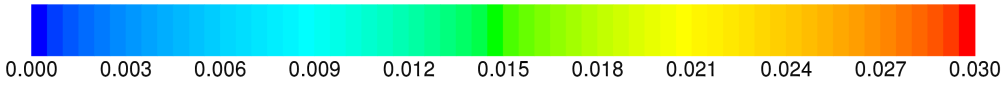

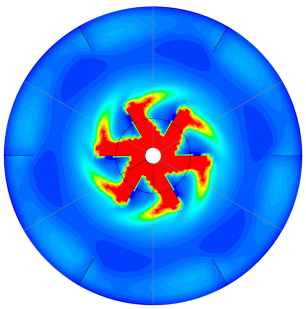

(a) $d_b = 3$ mm

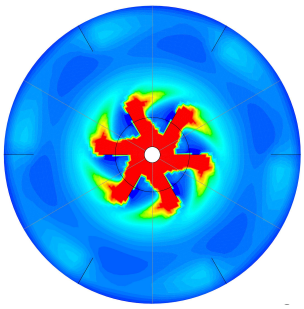

(b) DM

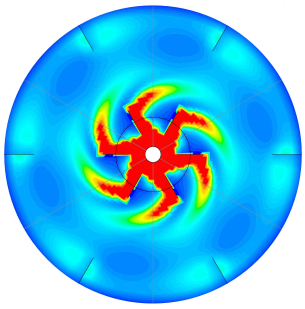

(c) DM + VM

Case 1: 180 rpm, $Q_g = 1.64 \times 10^{-3}$ m^3/s
Model: Schiller & Naumann drag, PO, TD (VOF diffusion)

Figure 9.23: Top view of gas volume fraction contours at the impeller centerline plane corresponding to simulation cases in Fig. 9.22.

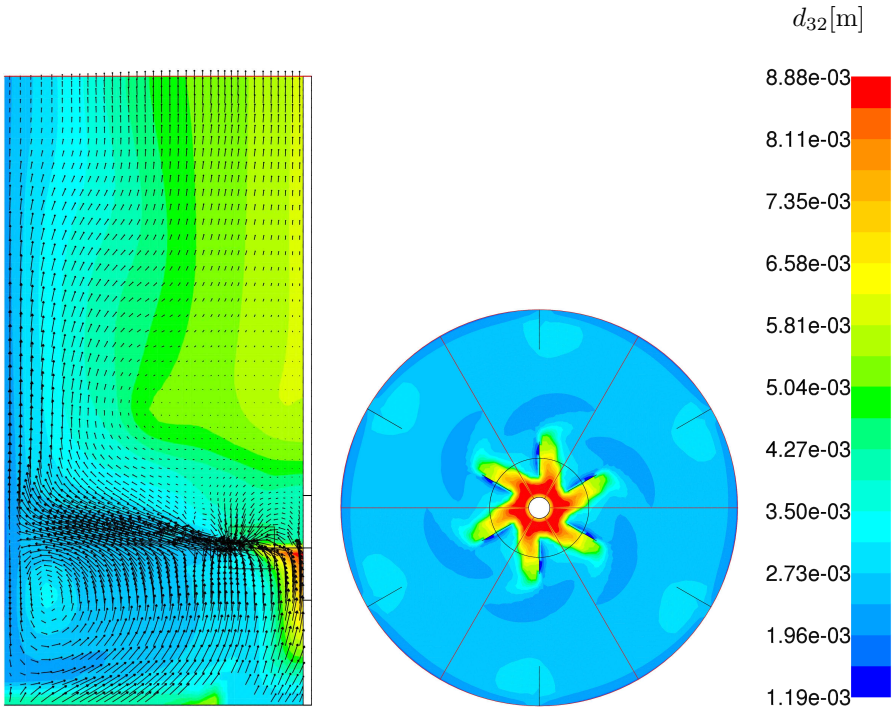

Case 1: 180 rpm, $Q_g = 1.64 \times 10^{-3}$ m^3/s
Model: Schiller & Naumann drag, PO, TD (VOF diffusion), DM

Figure 9.24: Sauter mean diameter distribution at mid-baffle (a) and impeller centerline (b) planes for the simulation case in Fig. 9.22(b) and Fig. 9.23(b). Gas velocity vectors are also plotted at the mid-baffle plane. Initial bubble size at the sparger is 3 mm. Overall (volume-averaged) Sauter mean diameter is $d_{32} = 3.5$ mm.

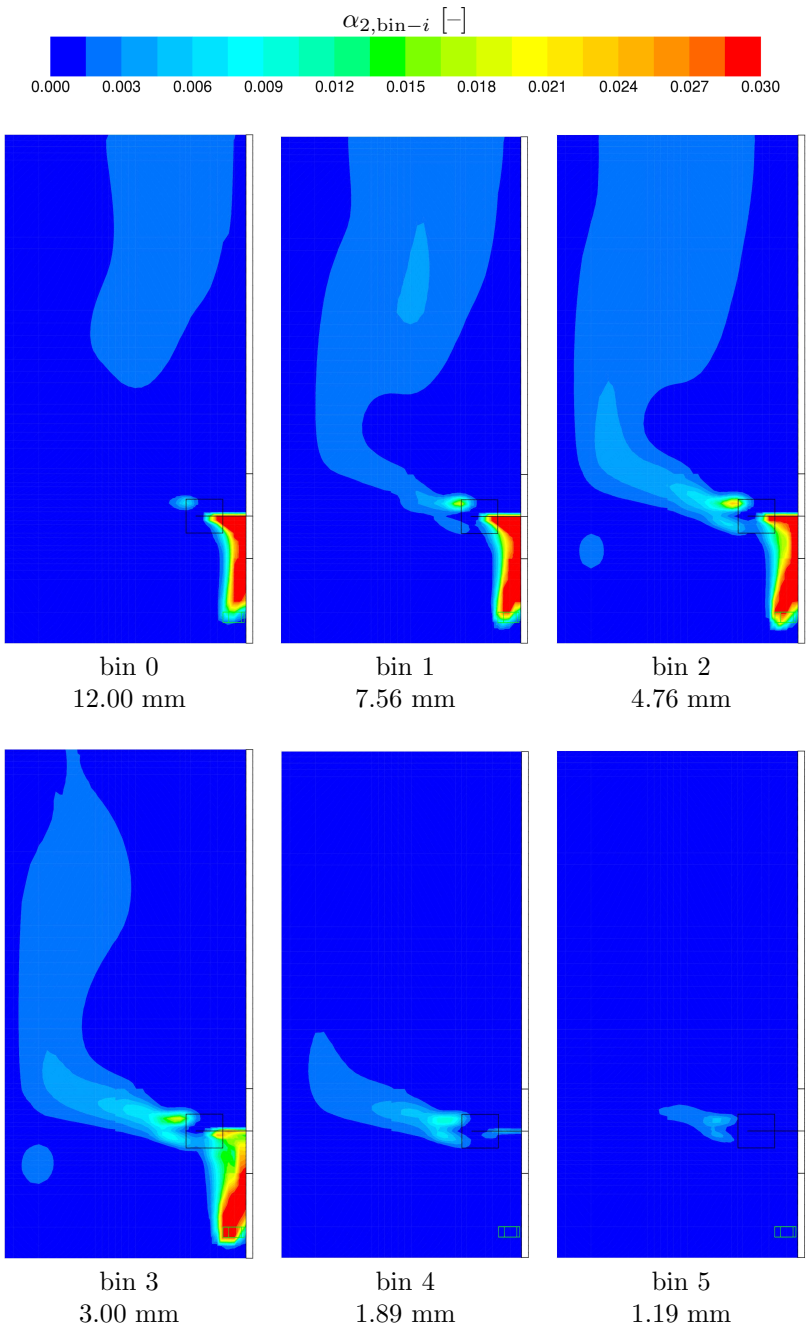

Case 1: 180 rpm, $Q_g = 1.64 \times 10^{-3}$ m^3/s
Model: Schiller & Naumann drag, PO, TD (VOF diffusion), DM

Figure 9.25: Spatial distribution of bubble bin volume fraction, $\alpha_{2,\mathrm{bin}-i}$, at mid-baffle plane (cont. Fig. 9.24). Initial bubble size at the sparger is 3 mm (bin 3).

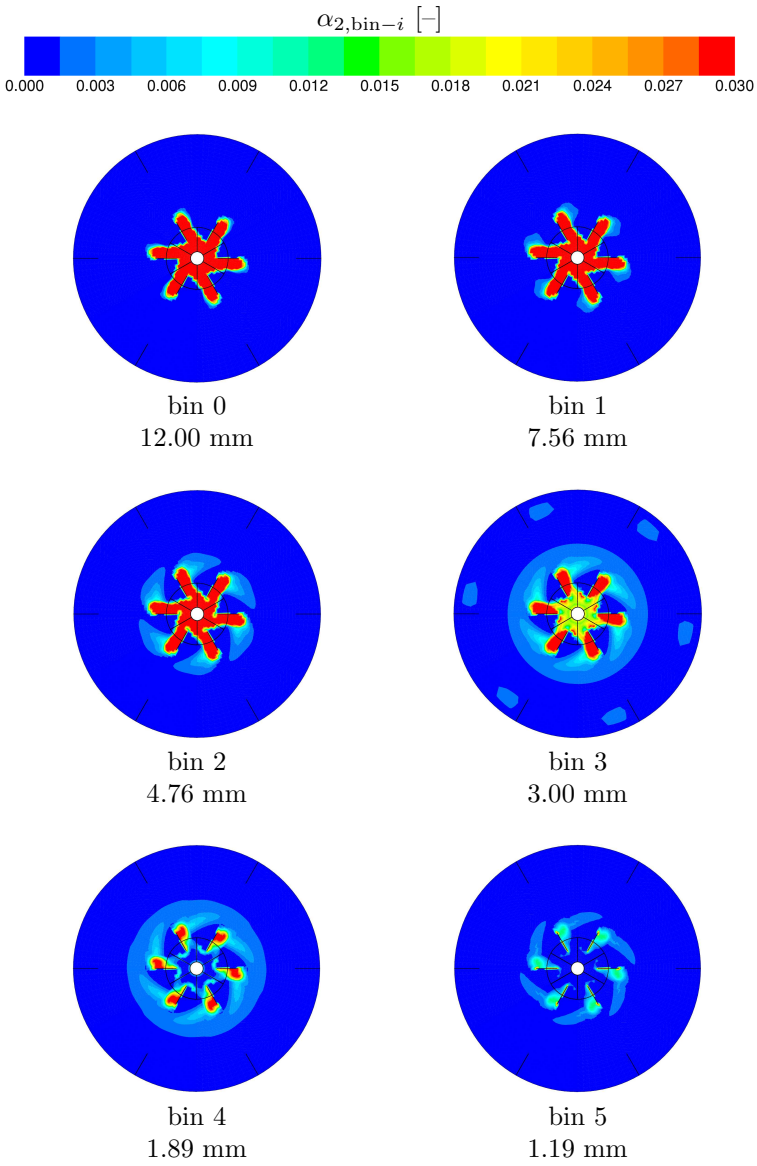

Case 1: 180 rpm, $Q_g = 1.64 \times 10^{-3}$ m^3/s
Model: Schiller & Naumann drag, PO, TD (VOF diffusion), DM

Figure 9.26: Spatial distribution of bubble bin volume fraction, $\alpha_{2,\mathrm{bin}-i}$, at impeller centerline plane (cont. Fig. 9.24). Initial bubble size at the sparger is 3 mm (bin 3).

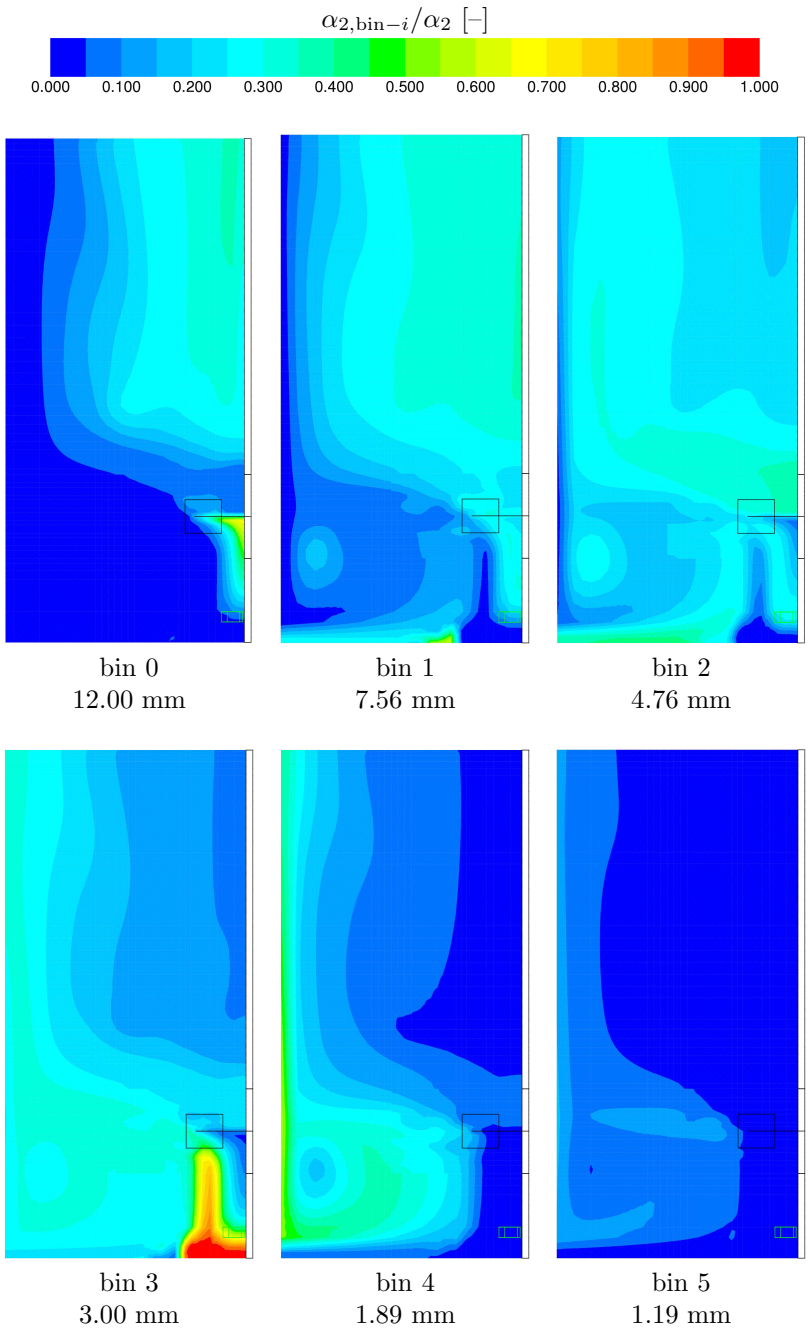

Case 1: 180 rpm, $Q_\mathrm{g} = 1.64 \times 10^{-3}$ m^3/s
Model: Schiller & Naumann drag, PO, TD (VOF diffusion), DM

Figure 9.27: Spatial distribution of bubble bin fraction, $f_{\mathrm{bin}-i} = \alpha_{2,\mathrm{bin}-i}/\alpha_2$, at mid-baffle plane (cont. Fig. 9.24). Initial bubble size at the sparger is 3 mm (bin 3).

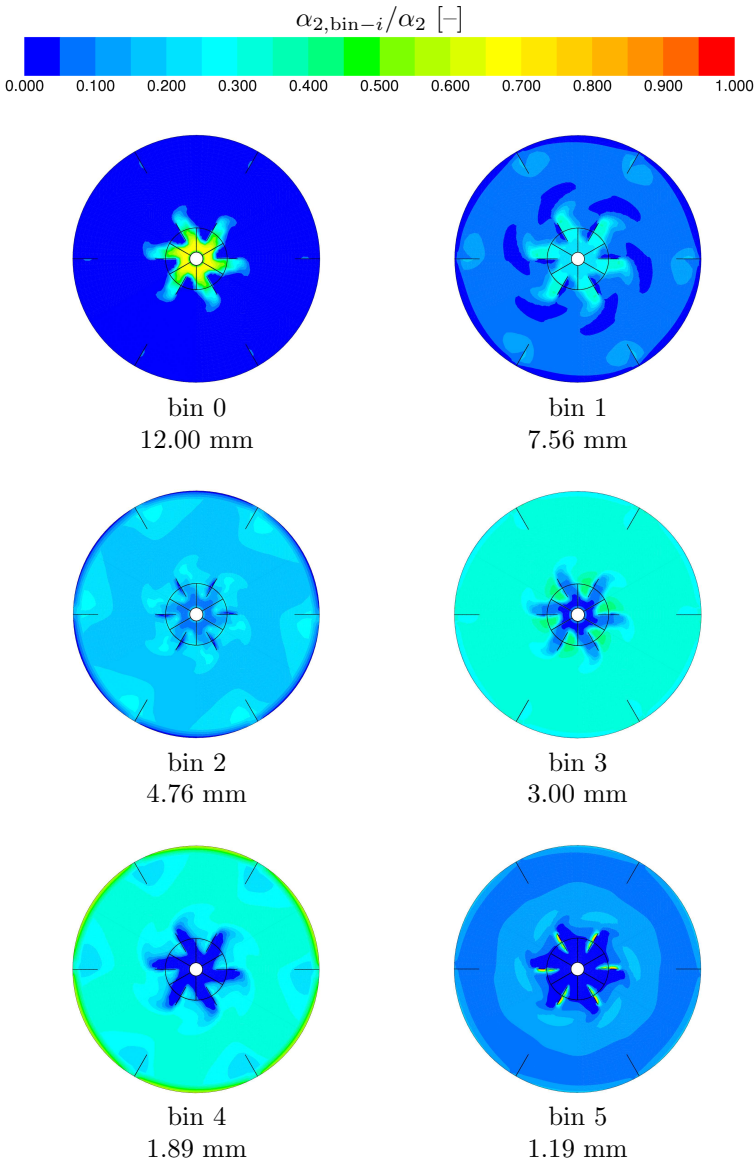

Case 1: 180 rpm, $Q_\mathrm{g} = 1.64 \times 10^{-3}$ m^3/s
Model: Schiller & Naumann drag, PO, TD (VOF diffusion), DM

Figure 9.28: Spatial distribution of bubble bin fraction, $f_{\mathrm{bin}-i} = \alpha_{2,\mathrm{bin}-i}/\alpha_2$, at impeller centerline plane (cont. Fig. 9.24). Initial bubble size at the sparger is 3 mm (bin 3).

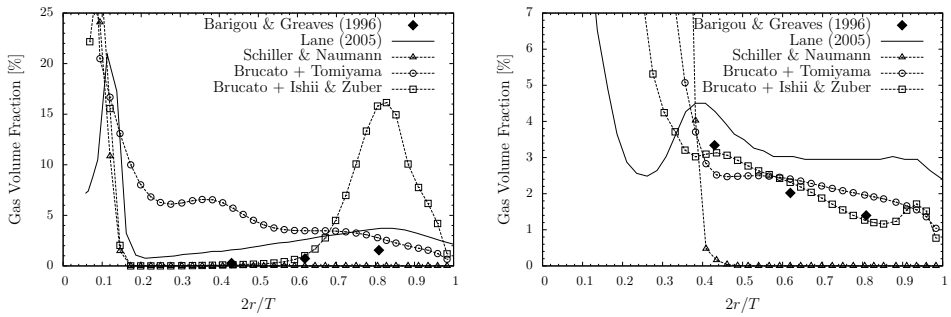

(a) Relative axial location z1=0.125H

(b) Relative axial location z2=0.250H

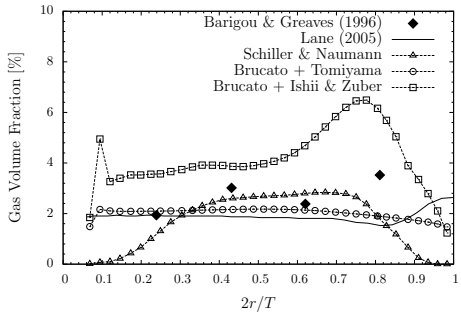

(c) Relative axial location z3=0.435H

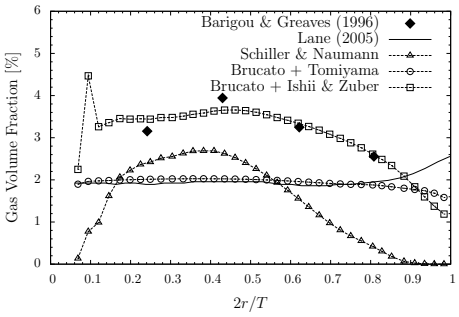

(d) Relative axial location z4=0.620H

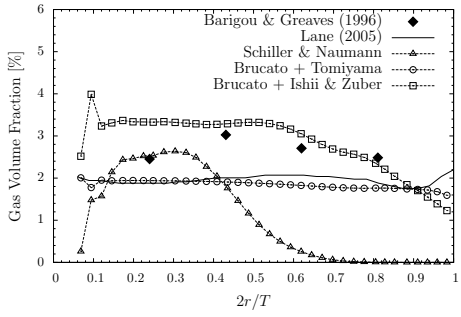

(e) Relative axial location z5=0.805H

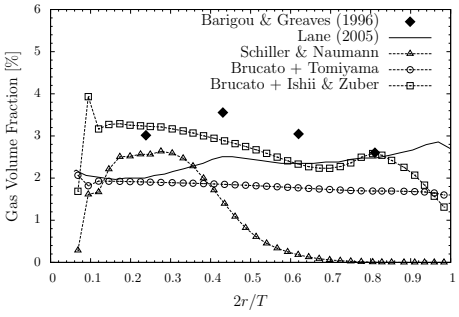

(f) Relative axial location z6=0.950H

Figure 9.29: Effect of different drag correlations (Schiller & Naumann, Ishii & Zuber, Tomiyama) and turbulent drag modification (Brucato) on the gas distribution for Case 1 ($d_b = 3$ mm). Circumferentially averaged gas volume fraction profiles at different axial levels (indicated as z1, z2, z4 and z5, respectively, in Fig. 9.3). Radial axis is normalized by the tank radius. A comparison is made with the experimental data from Barigou and Greaves (1996) and the simulation data from Lane (2005a) (from his revised final model).

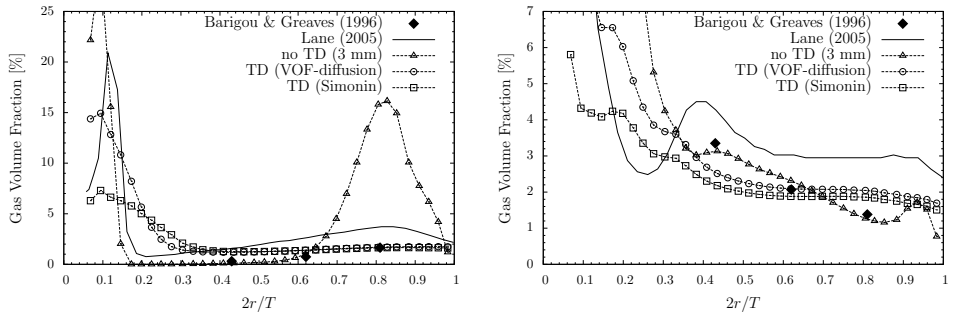

(a) Relative axial location z1=0.125H

(b) Relative axial location z2=0.250H

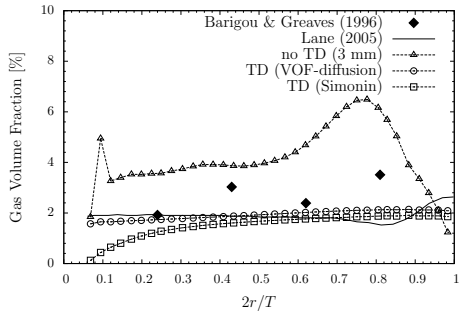

(c) Relative axial location z3=0.435H

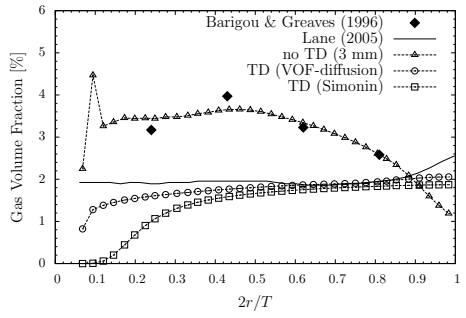

(d) Relative axial location z4=0.620H

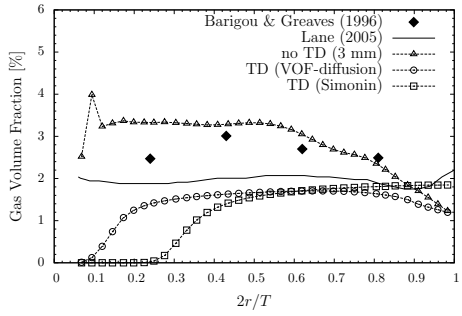

(e) Relative axial location z5=0.805H

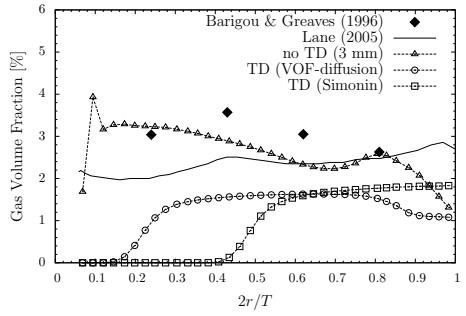

(f) Relative axial location z6=0.950H

Figure 9.30: Effect of turbulent dispersion models on the gas distribution for Case 1. Circumferentially averaged gas volume fraction profiles of the simulations given in Fig. 9.21 (Ishii & Zuber drag, Brucato turbulent drag modification). Radial axis is normalized by the tank radius. A comparison is made with the experimental data from Barigou and Greaves (1996) and the simulation data from Lane (2005a) (from his revised final model).

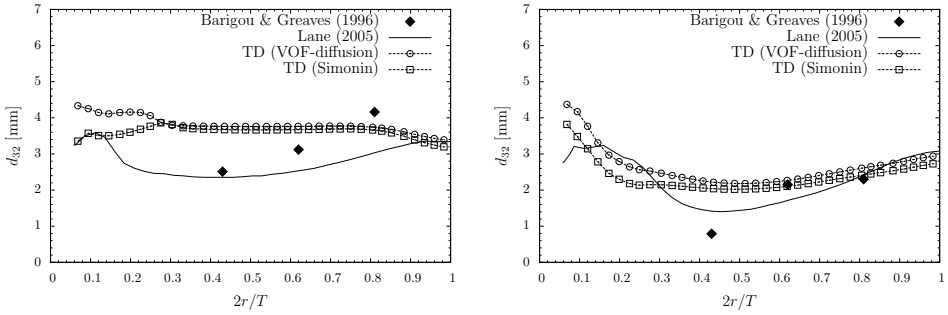

(a) Relative axial location z1=0.125H

(b) Relative axial location z2=0.250H

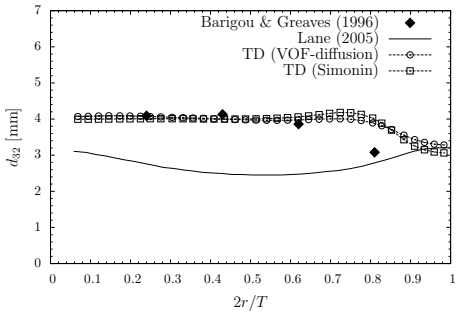

(c) Relative axial location z3=0.435H

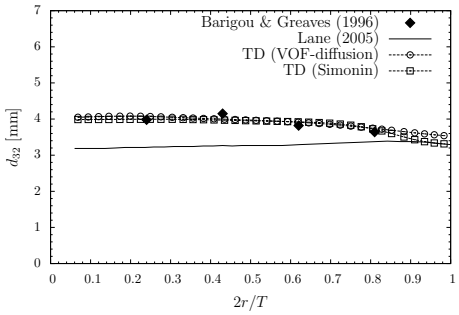

(d) Relative axial location z4=0.620H

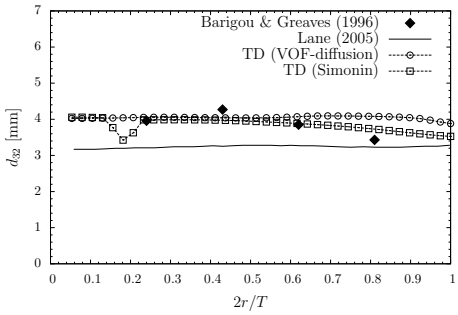

(e) Relative axial location z5=0.805H

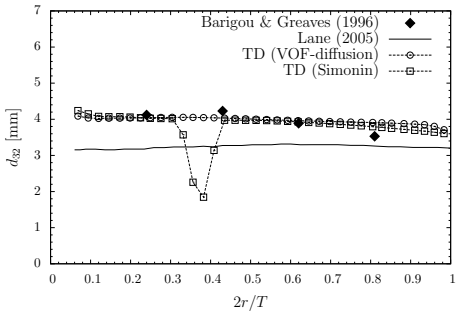

(f) Relative axial location z6=0.950H

Figure 9.31: Effect of turbulent dispersion (TD) models on the bubble size distribution for Case 1. Circumferentially averaged Sauter mean diameter profiles of the simulations given in Fig. 9.21 (Ishii & Zuber drag, Brucato turbulent drag modification). Radial axis is normalized by the tank radius. A comparison is made with the experimental data from Barigou and Greaves (1996) and the simulation data from Lane (2005a) (from his revised final model).

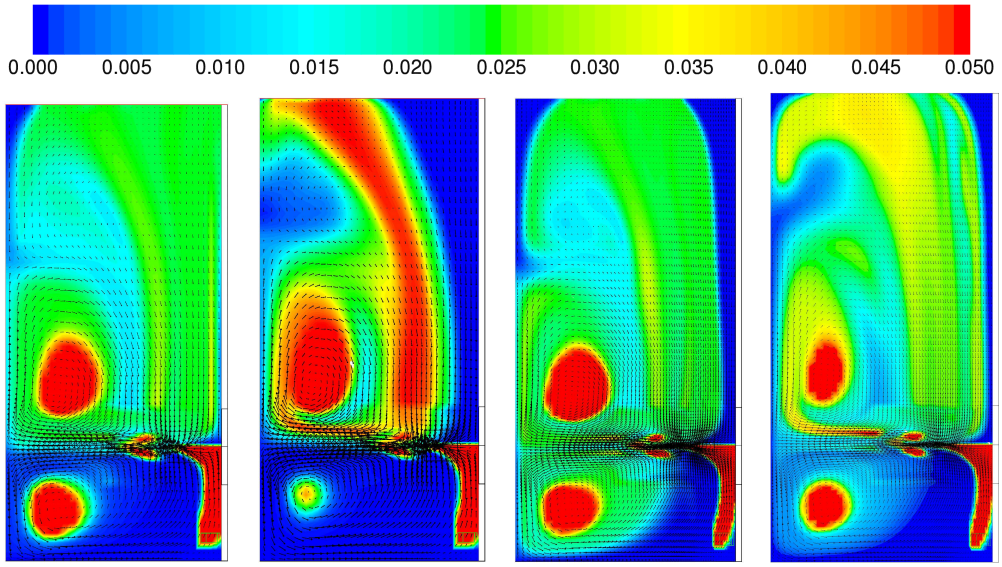

(a) 3mm, 46k (b) DM, 46k (c) 4mm, 140k (d) DM, 140k

Case 1: 180 rpm, $Q_g = 1.64 \times 10^{-3}$ m^3/s
Model: Ishii & Zuber drag, Brucato turbulence correction, VM

	Exp./Cor.	(a)	(b)	(c)	(d)
Holdup [%]	2.97[a]	2.8	≈2.5	3.1	≈2.5
Mean axial slip [cm/s]	–	10.3	≈7.8	7.1	≈7.8
Mean ε_1 [m^2/s^2]	–	0.65	0.64	0.73	0.71
D_{32} [mm]	3.50[a]	–	3.9	–	4.1
D_{32}/η_1 [-]	–	85	110	117	119
Mean Re_b	–	323	324	298	315
$P_{g,\Gamma}/\mathcal{V}_l$ [kW/m^3]	–	0.77	0.78	0.77	0.77
$P_{g,\varepsilon}/\rho_1 N^3 D^5$	–	4.45	≈4.40	4.99	4.90
$P_{g,\Gamma}/\rho_1 N^3 D^5$	–	5.40	≈5.50	5.41	5.40
$P_{g,\Gamma}/P_\Gamma$, $P_{g,\varepsilon}/P_\varepsilon$	0.85[b], 0.82[c]	0.95, 0.83	0.97, 0.82	0.95, 0.93	0.95, 0.91
Q_G/ND^3	–	0.69	≈0.72	0.70	0.69
Q_G/Q	–	0.96	≈1.00	0.97	0.96
Gas imbalance[d] [%]	–	1.2	≈0.8	-0.6	≈4.5

[a]Experimental data from Barigou and Greaves (1992)
[b]Correlation of Hughmark (Eq. 3.11)
[c]Correlation of Bakker et al. (Eq. 3.12)
[d]Gas mass imbalance, $(\dot{m}_{g,in} - \dot{m}_{g,out})/\dot{m}_{g,in} \times 100$

Figure 9.32: Comparison of simulations for Case 1 with the final modelling options (where 5 new bubble size classes were defined according to Set 2 in Table 9.6). Results with both 46k and 140k mesh are given. Gas volume fraction contours and liquid velocity vectors are given at mid-baffle plane.

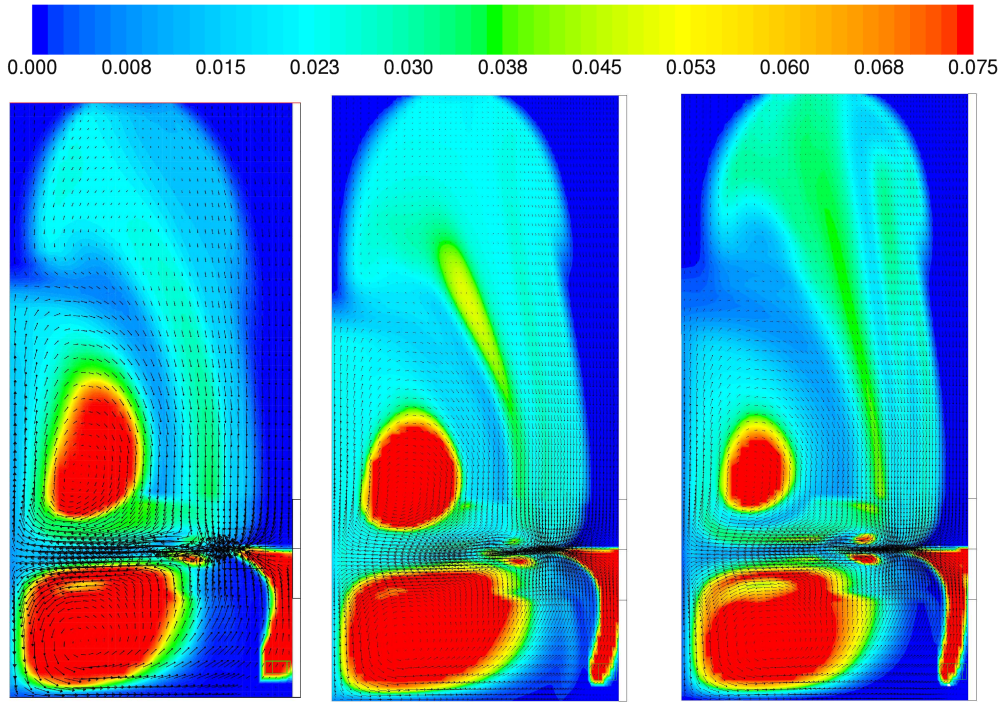

(a) 3mm, 46k (b) 4mm, 140k (c) DM, 140k

Case 2: 250 rpm, $Q_g = 1.64 \times 10^{-3}$ m^3/s
Model: Ishii & Zuber drag, Brucato turbulence correction, VM

	Exp./Cor.	(a)	(b)	(c)
Holdup [%]	3.65[a]	5.8	6.3	5.2
Mean axial slip [cm/s]	–	7.6	5.8	6.4
Mean ε_1 [m^2/s^2]	–	1.82	2.02	1.98
D_{32} [mm]	3.36[a]	–	–	4.0
D_{32}/η_1 [-]	–	110	151	150
Mean Re_b	–	247	252	255
$P_{g,\Gamma}/\mathcal{V}_l$ [kW/m^3]	2.00[a]	2.10	2.08	2.06
$P_{g,\varepsilon}/\rho_1 N^3 D^5$	–	4.50	4.97	4.95
$P_{g,\Gamma}/\rho_1 N^3 D^5$	–	5.52	5.48	5.41
$P_{g,\Gamma}/P_\Gamma$, $P_{g,\varepsilon}/P_\varepsilon$	0.81[b], 0.84[c]	0.97, 0.84	0.97, 0.92	0.95, 0.92
Q_G/ND^3	–	0.70	0.71	0.70
Q_G/Q	–	0.97	0.99	0.97
Gas imbalance[d] [%]	–	8.8	2.4	≈3.3

[a] Experimental data from Barigou and Greaves (1992)
[b] Correlation of Hughmark (Eq. 3.11)
[c] Correlation of Bakker et al. (Eq. 3.12)
[d] Gas mass imbalance, $(\dot{m}_{g,in} - \dot{m}_{g,out})/\dot{m}_{g,in} \times 100$

Figure 9.33: Comparison of simulations for Case 2 with the final modelling options (as detailed in Fig. 9.32).

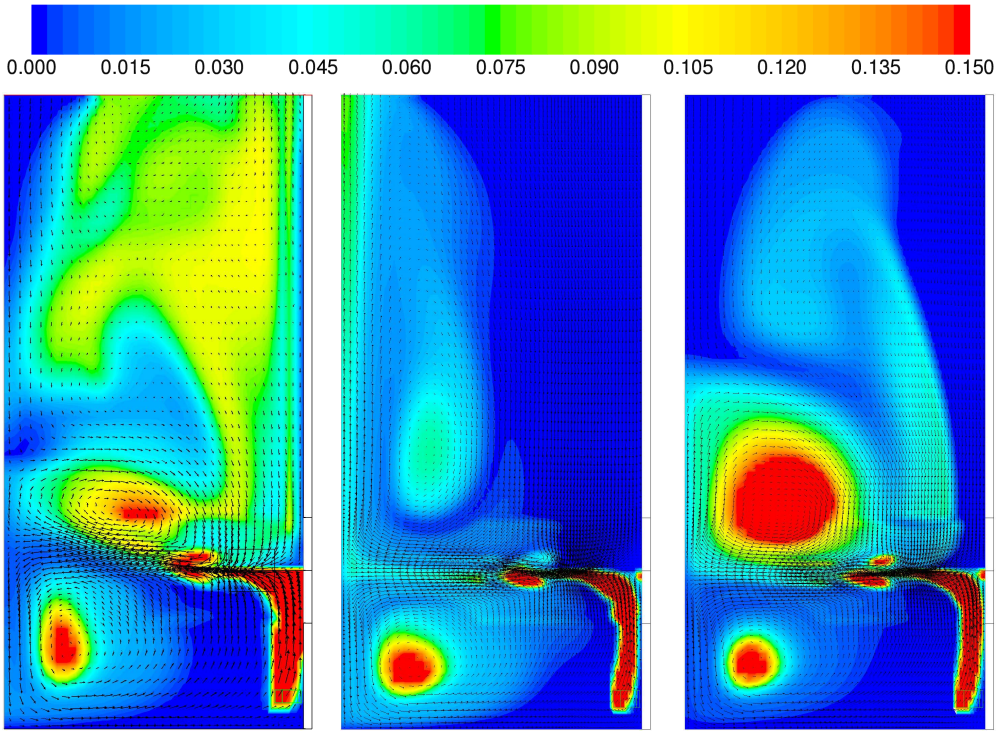

(a) 3mm, 46k (b) 4mm, 140k (c) DM, 140k

Case 3: 180 rpm, $Q_g = 6.87 \times 10^{-3}$ m^3/s
Model: Ishii & Zuber drag, Brucato turbulence correction, VM

	Exp./Cor.	(a)	(b)	(c)
Holdup [%]	7.72[a]	≈5.4	3.5	≈5.5
Mean axial slip [cm/s]	–	11.0	9.6	7.3
Mean ε_1 [m^2/s^2]	–	0.59	0.68	0.65
D_{32} [mm]	3.88[a]	–	–	4.4
D_{32}/η_1 [-]	–	83	115	125
Mean Re_b	–	356	404	335
$P_{g,\Gamma}/\mathcal{V}_l$ [kW/m^3]	–	0.63	0.70	0.65
$P_{g,\varepsilon}/\rho_1 N^3 D^5$	–	≈3.80	≈4.60	4.29
$P_{g,\Gamma}/\rho_1 N^3 D^5$	–	≈4.44	4.90	4.59
$P_{g,\Gamma}/P_\Gamma$, $P_{g,\varepsilon}/P_\varepsilon$	0.59[b], 0.52[c]	0.78, 0.71	0.86, 0.86	0.81, 0.80
Q_G/ND^3	–	≈0.61	≈0.66	0.62
Q_G/Q	–	≈0.85	≈0.92	0.86
Gas imbalance[d] [%]	–	≈-69	0.6	≈16

[a]Experimental data from Barigou and Greaves (1992)
[b]Correlation of Hughmark (Eq. 3.11)
[c]Correlation of Bakker et al. (Eq. 3.12)
[d]Gas mass imbalance, $(\dot{m}_{g,in} - \dot{m}_{g,out})/\dot{m}_{g,in} \times 100$

Figure 9.34: Comparison of simulations for Case 3 with the final modelling options (as detailed in Fig. 9.32).

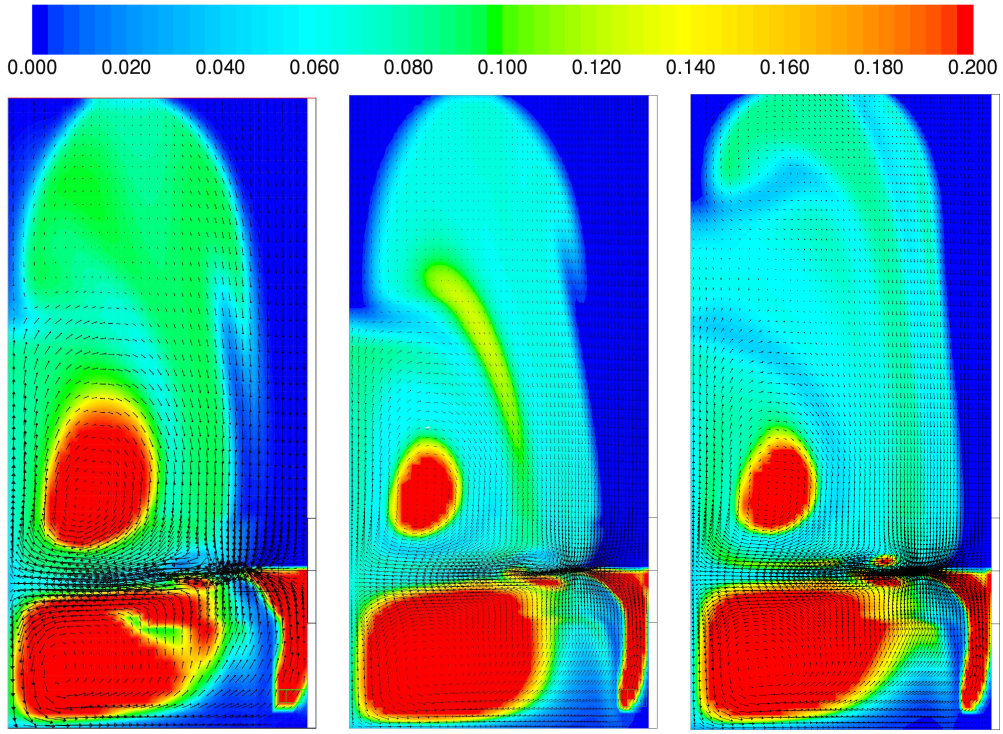

(a) 3mm, 46k (b) 4mm, 140k (c) DM, 140k

Case 4: 285 rpm, $Q_g = 6.87 \times 10^{-3}$ m^3/s
Model: Ishii & Zuber drag, Brucato turbulence correction, VM

	Exp./Cor.	(a)	(b)	(c)
Holdup [%]	9.56[a]	13.0	12.3	12.3
Mean axial slip [cm/s]	–	7.1	6.3	5.6
Mean ε_1 [m^2/s^2]	–	2.70	2.83	2.60
D_{32} [mm]	3.85[a]	–	–	4.3
D_{32}/η_1 [-]	–	122	164	174
Mean Re_b	–	234	277	256
$P_{g,\Gamma}/\mathcal{V}_l$ [kW/m^3]	–	2.91	2.91	2.20
$P_{g,\varepsilon}/\rho_1 N^3 D^5$	–	4.14	4.41	≈4.05
$P_{g,\Gamma}/\rho_1 N^3 D^5$	–	5.17	5.16	3.90
$P_{g,\Gamma}/P_\Gamma$, $P_{g,\varepsilon}/P_\varepsilon$	0.55[b], 0.51[c]	0.91, 0.77	0.91, 0.82	0.69, 0.75
Q_G/ND^3	–	0.69	0.68	0.63
Q_G/Q	–	0.96	0.94	0.88
Gas imbalance[d] [%]	–	≈-8.3	≈-11	≈2.1

[a]Experimental data from Barigou and Greaves (1992)
[b]Correlation of Hughmark (Eq. 3.11)
[c]Correlation of Bakker et al. (Eq. 3.12)
[d]Gas mass imbalance, $(\dot{m}_{g,in} - \dot{m}_{g,out})/\dot{m}_{g,in} \times 100$

Figure 9.35: Comparison of simulations for Case 4 with the final modelling options (as detailed in Fig. 9.32).

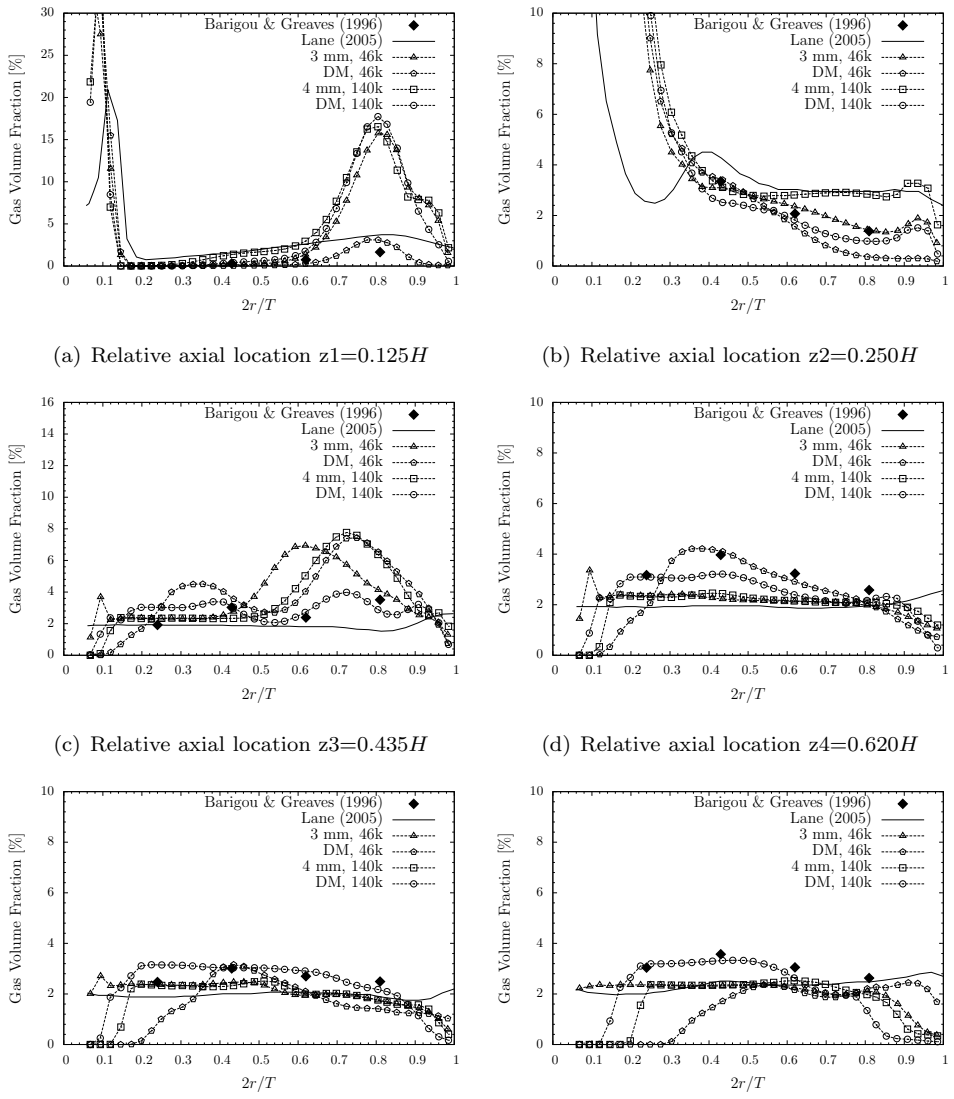

(a) Relative axial location z1=0.125H

(b) Relative axial location z2=0.250H

(c) Relative axial location z3=0.435H

(d) Relative axial location z4=0.620H

(e) Relative axial location z5=0.805H

(f) Relative axial location z6=0.950H

Figure 9.36: Circumferentially averaged gas volume fraction profiles of the simulations given in Fig. 9.32 (Case 1). Radial axis is normalized by the tank radius. A comparison is made with the experimental data from Barigou and Greaves (1996) and the simulation data from Lane (2005a) (from his revised final model).

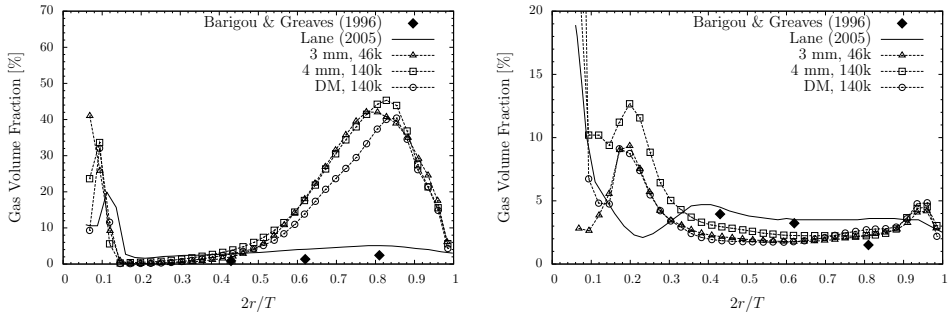

(a) Relative axial location z1=0.125H

(b) Relative axial location z2=0.250H

(c) Relative axial location z3=0.435H

(d) Relative axial location z4=0.620H

(e) Relative axial location z5=0.805H

(f) Relative axial location z6=0.950H

Figure 9.37: Circumferentially averaged gas volume fraction profiles of the simulations given in Fig. 9.33 (Case 2). Radial axis is normalized by the tank radius. A comparison is made with the experimental data from Barigou and Greaves (1996) and the simulation data from Lane (2005a) (from his revised final model).

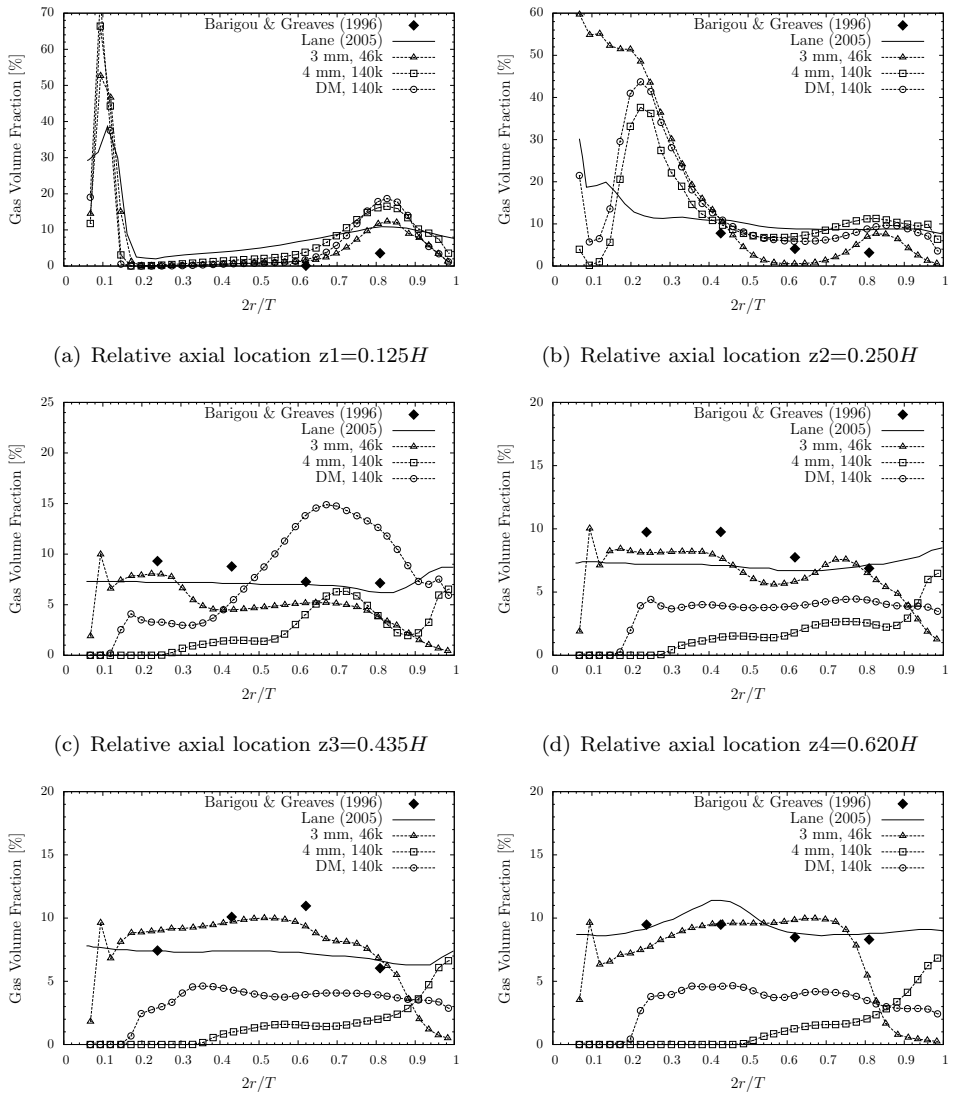

(a) Relative axial location z1=0.125H

(b) Relative axial location z2=0.250H

(c) Relative axial location z3=0.435H

(d) Relative axial location z4=0.620H

(e) Relative axial location z5=0.805H

(f) Relative axial location z6=0.950H

Figure 9.38: Circumferentially averaged gas volume fraction profiles of the simulations given in Fig. 9.34 (Case 3). Radial axis is normalized by the tank radius. A comparison is made with the experimental data from Barigou and Greaves (1996) and the simulation data from Lane (2005a) (from his revised final model).

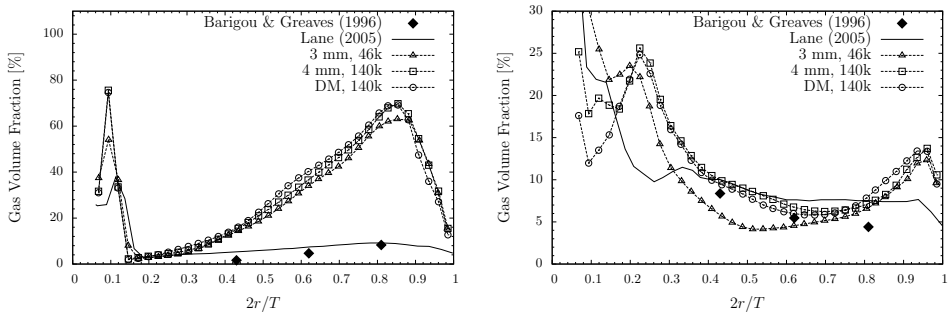

(a) Relative axial location z1=0.125H

(b) Relative axial location z2=0.250H

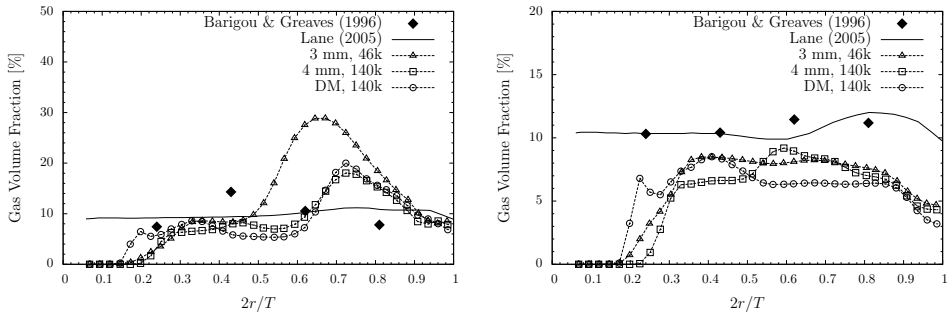

(c) Relative axial location z3=0.435H

(d) Relative axial location z4=0.620H

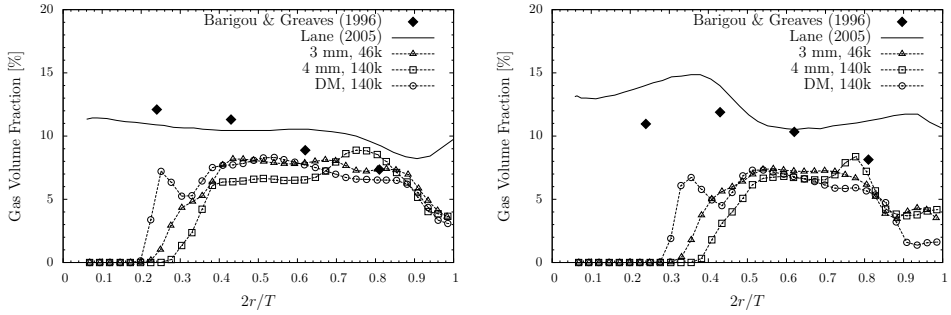

(e) Relative axial location z5=0.805H

(f) Relative axial location z6=0.950H

Figure 9.39: Circumferentially averaged gas volume fraction profiles of the simulations given in Fig. 9.35 (Case 4). Radial axis is normalized by the tank radius. A comparison is made with the experimental data from Barigou and Greaves (1996) and the simulation data from Lane (2005a) (from his revised final model).

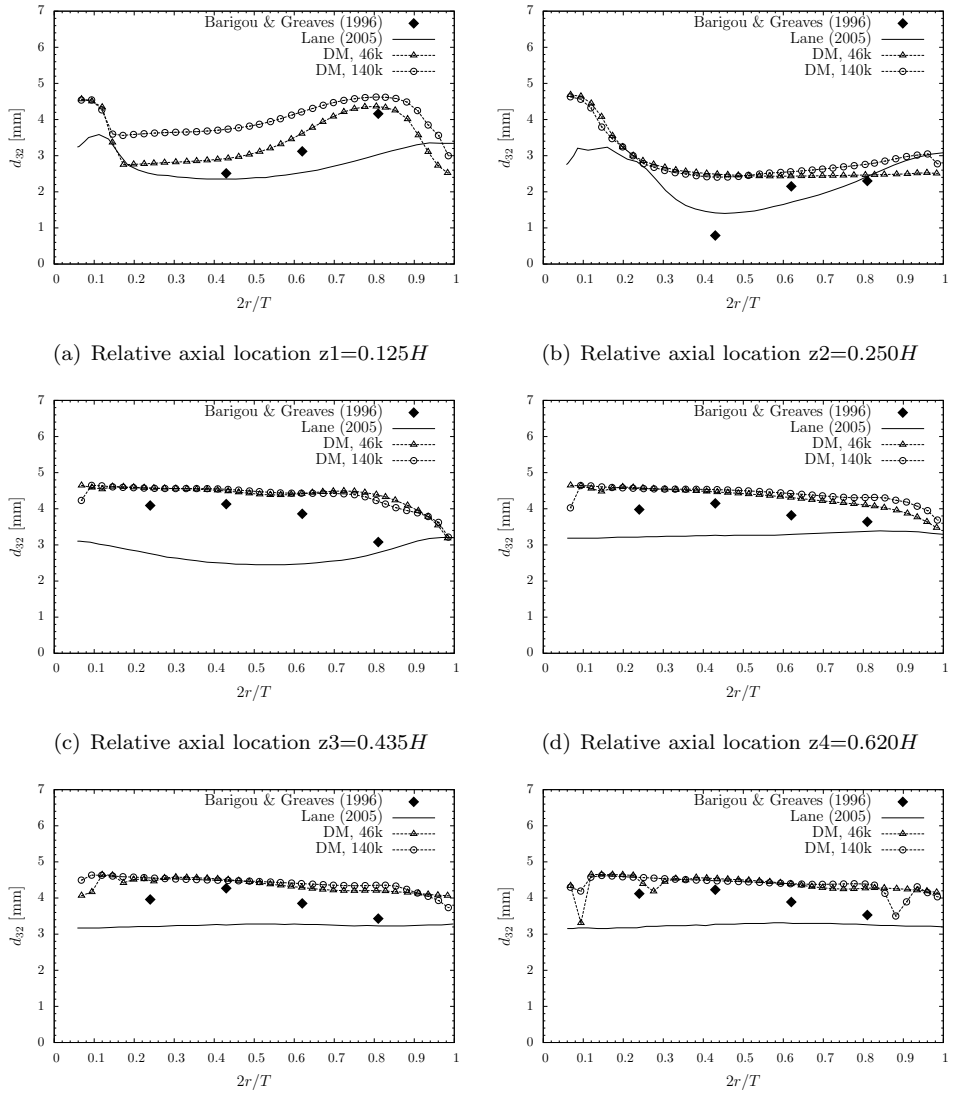

(a) Relative axial location z1=0.125H

(b) Relative axial location z2=0.250H

(c) Relative axial location z3=0.435H

(d) Relative axial location z4=0.620H

(e) Relative axial location z5=0.805H

(f) Relative axial location z6=0.950H

Figure 9.40: Circumferentially averaged Sauter mean diameter profiles of the simulations given in Fig. 9.32 (Case 1). Radial axis is normalized by the tank radius. A comparison is made with the experimental data from Barigou and Greaves (1992) and the simulation data from Lane (2005a) (from his revised final model).

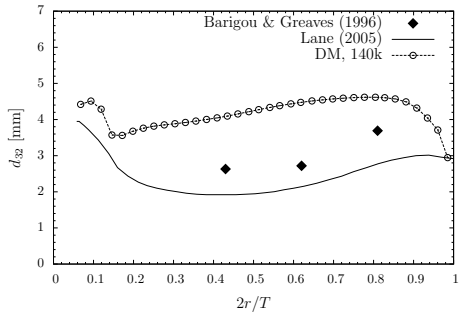

(a) Relative axial location z1=0.125H

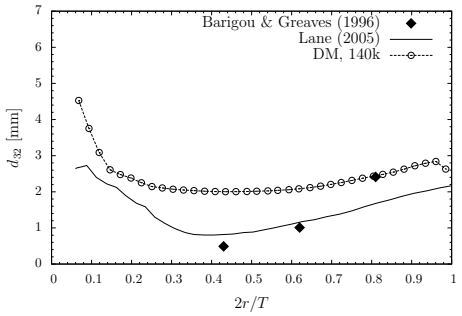

(b) Relative axial location z2=0.250H

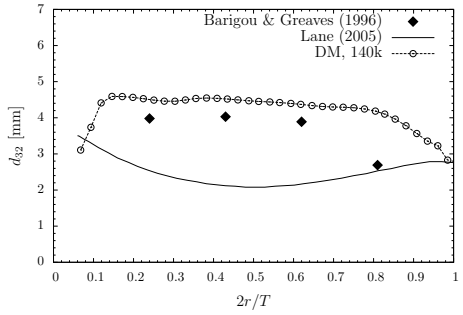

(c) Relative axial location z3=0.435H

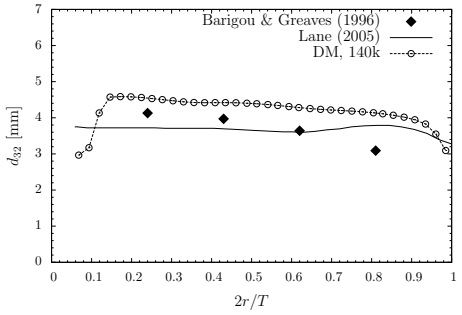

(d) Relative axial location z4=0.620H

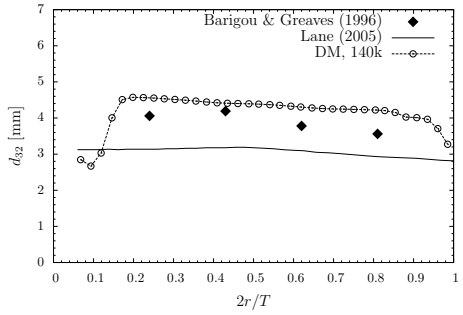

(e) Relative axial location z5=0.805H

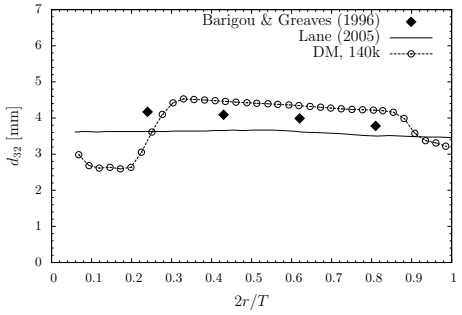

(f) Relative axial location z6=0.950H

Figure 9.41: Circumferentially averaged Sauter mean diameter profiles of the simulations given in Fig. 9.33 (Case 2). Radial axis is normalized by the tank radius. A comparison is made with the experimental data from Barigou and Greaves (1992) and the simulation data from Lane (2005a) (from his revised final model).

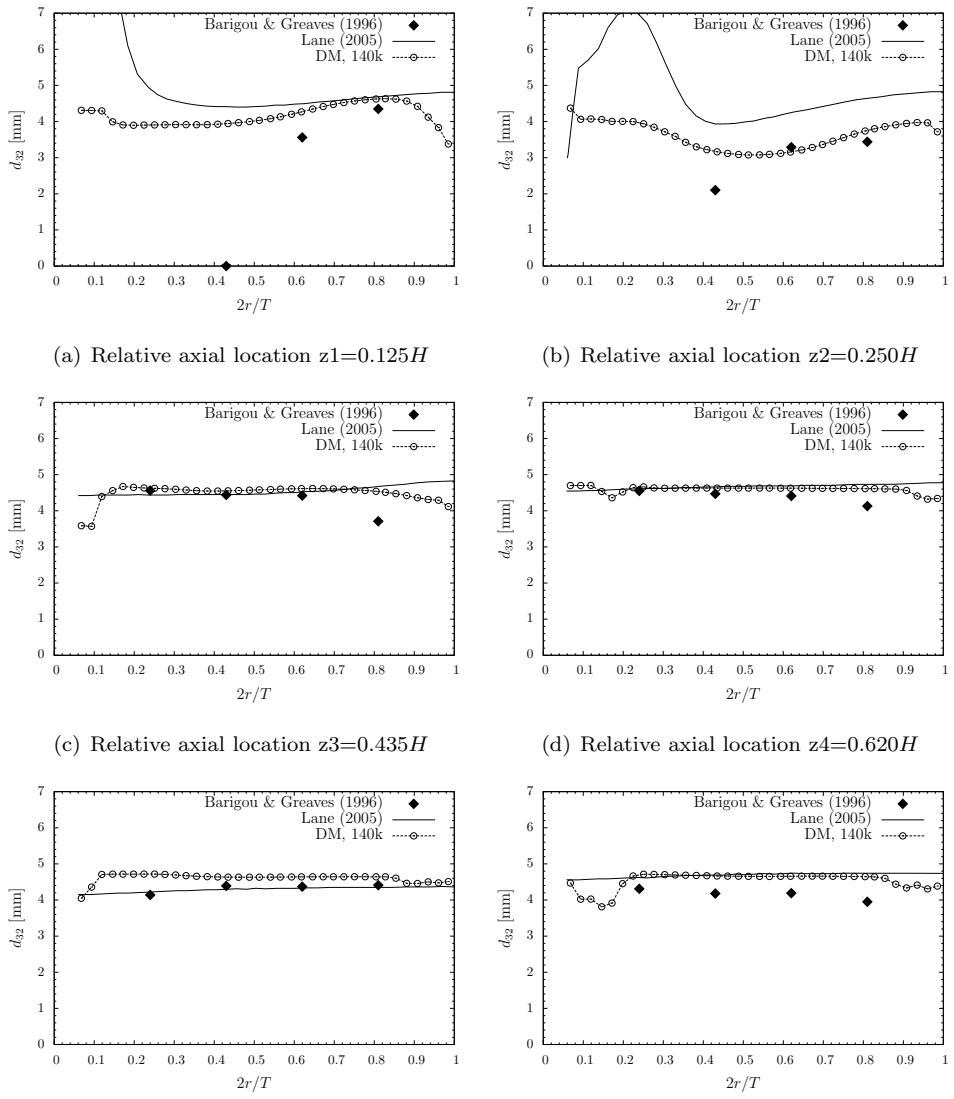

(a) Relative axial location z1=0.125H

(b) Relative axial location z2=0.250H

(c) Relative axial location z3=0.435H

(d) Relative axial location z4=0.620H

(e) Relative axial location z5=0.805H

(f) Relative axial location z6=0.950H

Figure 9.42: Circumferentially averaged Sauter mean diameter profiles of the simulations given in Fig. 9.34 (Case 3). Radial axis is normalized by the tank radius. A comparison is made with the experimental data from Barigou and Greaves (1992) and the simulation data from Lane (2005a) (from his revised final model).

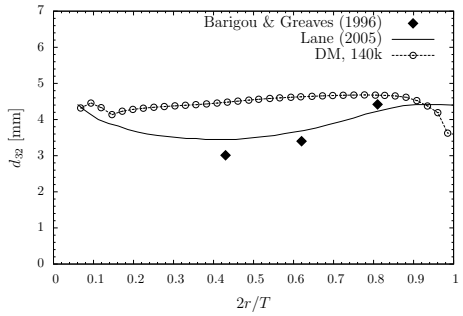

(a) Relative axial location z1=0.125H

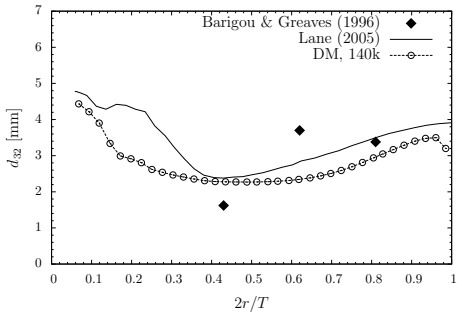

(b) Relative axial location z2=0.250H

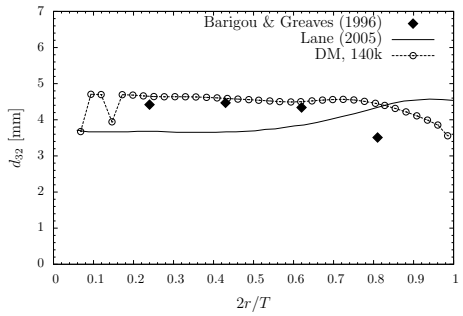

(c) Relative axial location z3=0.435H

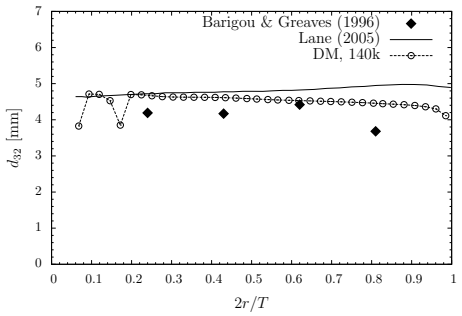

(d) Relative axial location z4=0.620H

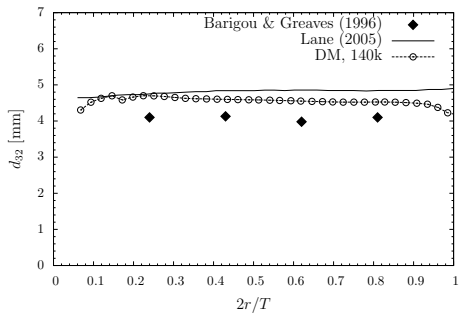

(e) Relative axial location z5=0.805H

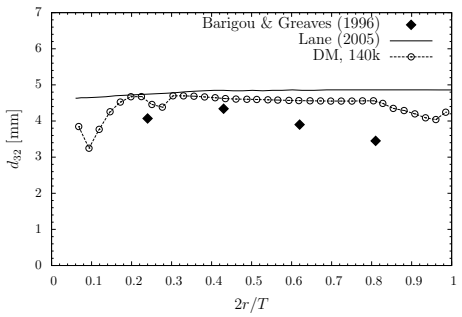

(f) Relative axial location z6=0.950H

Figure 9.43: Circumferentially averaged Sauter mean diameter profiles of the simulations given in Fig. 9.35 (Case 4). Radial axis is normalized by the tank radius. A comparison is made with the experimental data from Barigou and Greaves (1992) and the simulation data from Lane (2005a) (from his revised final model).

Chapter 10

Gas dispersion in a large-scale fermenter with multiple impellers

In fermentation processes large-scale gassed–stirred tanks are used. Due to this scale, these reactors are equipped with multiple impellers. In this chapter, we discuss simulations of the bubbly flow in such a reactor. The fermenter has a volume of 30 m^3 (liquid volume of 22 m^3) and is stirred by 4 Rushton impellers on a single shaft. It is aerated via a ring sparger located below the bottom impeller, and is equipped with 4 baffles. Note that it can be considered as a pilot-scale reactor given that much larger fermenters are available in industry.

The mean flow characteristics and the turbulence predictions were obtained by solving the Reynolds-averaged Navier-Stokes (RANS) equations combined with the standard $k-\varepsilon$ model by using the commercial CFD code Fluent 6.3 and 12.0 (Ansys Inc.). This is the most feasible approach, due to the large scale. For the modelling of moving parts, the moving reference frame (MRF) model was used.

Single-phase simulations predicted the relevant integral quantities well, namely the power and flow number. Those are reported in Chapter 2. The tracer mixing times were also in good agreement with the experimental values for a turbulent Schmidt number value of 0.2. Results of those are given in Chapter 11.

Two-phase flow modelling of the bubbly flow in the fermenter follows from the standard gassed-stirred tank case given Chapter 9. Euler-Euler approach was used to simulate gas dispersion into the tank. Population balance equations were solved to track the bubble sizes. Simulations showed that the drag force is the most important one among the other interfacial forces and should be corrected to account for the turbulence effects. Modification of the drag coefficient by the model of Brucato et al. (1998b) with the correlation coefficient from Lane et al. (2000) resulted in overprediction of holdups at high stirring rates. This shows that, it might not be directly applicable to multi-impeller large-scale systems. The simulations were able to predict the flow regime transition from loading to flooding, corresponding well with the experimental data.

10.1 The 30 m^3 fermenter

10.1.1 Geometry

The configuration of the fermenter is given in Fig. 2.2 and is the same as that for which we presented the single-phase results in Chapter 2. It is filled upto a liquid level of $H = 6.55$ m and has a diameter of $T = 2.09$ m. The liquid volume of the tank is 22 m^3. The impeller diameter is $D = T/3 = 0.70$ m, bottom and mutual impeller clearances are $C = 0.54T$ and $C_I = 0.70T$ respectively, and the baffle width is $0.08T$. The remaining parts are scaled with T and D in the same manner as given for the standard stirred tank geometry in Fig. 2.1.

10.1.2 Working fluid and operating conditions

The working fluid was a water–air system with the material properties same as those used in Chapter 9 and given in Table 9.1. Considering the available experimental data, five different operating conditions were chosen for the numerical study, details of which are given in Table 10.1. The flow is fully turbulent in all cases.

10.1.3 Flow regime map for the bottom impeller

We constructed a flow regime map for the lower impeller region of this reactor by using the standard stirred tank relations given in Eq. 3.23–3.25. This is shown in Fig. 10.1 together with the operating conditions for the simulation cases. The tank height on those relations are taken as the midway between first two impellers ($H = 1.85$ m). Single-phase results confirmed that impellers were not interacting much, giving the parallel independent double-loop structures at impeller regions with the same characteristics as single-impeller systems. This is expected as the impeller-impeller spacing is large enough compared to the impeller diameter, i.e. $C_1/D > 1.5$ (Nienow, 1998). As a consequence, the mean flow field at $H = 1.85$ m was closely resembling what it would be if there were a free-slip or symmetry boundary at this location similar to a real free-surface.

Moreover, interaction of the gas flow from the sparger with the impeller in a single-impeller system is expected to be similar to that with the bottom impeller of a multi-impeller system (Cui et al., 1996a). There is, of course, a local static pressure difference, which can be significant for tall tanks. Furthermore, under gassed conditions, the impeller regions in the fermenter also start interacting with each other rather than having independent compartmentalized flow structures. However, as discussed in Section 3.2.1 and 3.2.3, measurements of Smith et al. (1987) indicated that the bottom impeller behaved as a single impeller and that of Roušar and van den Akker (1994) showed that the bottom impeller was independent of the upper impellers and addition of upper impellers did not influence the liquid flow around the bottom impeller and the power drawn from it. Therefore, as an approaximation, the flow map constructed is expected to indicate the flow regime change for the bottom impeller.

10.1.4 Experimental data available

Overall gas holdup measurements and gassed/ungassed power uptake (for a water–air system) were reported for this fermenter (Noorman et al., 1993; Vrábel et al., 1999, 2000). There were no measurements on the local gas fractions and bubble sizes. This is probaby due to the scale of the system that obtaining such data is not trivial.

There have also been studies (experimental and CFD) of mixing and microbial kinetics of the same fermenter (Noorman et al., 1993; Noorman, 1993; Noorman et al., 1994; Larsson et al., 1996). The medium was a Newtonian glucose solution with minerals. We report on those partly here and partly in the coming chapters.

10.2 Numerical setup

The numerical modelling approach is based on the standard gassed-stirred tank case given Chapter 9. The Euler–Euler model was used together with population balances in order to simulate gas dispersion in the fermenter. The turbulence model employed is the standard $k-\varepsilon$ model unless mentioned otherwise.

10.2.1 Solution domain and computational mesh

The computational domain was constructed with the assumption of a flat-bottom tank. In view of rotational symmetry arguments, the computational domain was restricted to a 60 degree section of the tank, including one impeller blade and one baffle. Hence, the computational requirements were greatly reduced. Note that, this would correspond to a tank with 6 baffles in reality. However, as noted before, extra baffling is not expected to have a significant effect on the global flow field (Lane, 2005a).

The computational grid is the same as that used in single-phase simulations reported in Chapter 2 (see Fig. 2.3). It consists of 324k ($260 \times 52 \times 24$) structured elements (120 cells/blade).

Grid interface

The MRF model was used for the modelling of moving parts. For each impeller, a "moving zone" was defined as shown in Fig. 2.3(e). The grid interface between the moving and the stationary zone was set at a region extending axially from the impeller centreline in the range of $(-D/2, D/2)$ for the fermenter, and located radially at midway between the impeller tip and the baffle.

10.2.2 Boundary conditions

Boundary conditions employed follow from that of the standard tank given in Section 9.4.2.

Walls

No-slip boundary condition is assumed on all wall boundaries. The impeller and baffles are modelled as zero-thickness surfaces. The boundary layer at walls was modelled by applying standard wall functions (see Section 5.3). The impeller shaft was assumed to extend from the free surface down to the bottom wall in order to ensure high mesh quality.

Outlet

Degassing boundary condition was adopted at the free surface. It imposes a symmetry condition for the liquid phase, while the gas phase is free to leave the domain.

Inlet

Gas is introduced into the reactor through a ring sparger. We modelled the sparger by mass and momentum source terms in the governing equations being solved. Those source terms were calculated according to Eq. 9.28 and 9.29.

10.2.3 Population balance model

In this chapter, we used again the discrete method, in which scalar transport equations are solved for each pre-defined bubble class. The breakage and aggregation kernels follow from the Luo model (Fluent, 2009). Details of the PBM model are given in Chapter 8. All PBM simulations were run in the transient mode in order to ease convergence.

The bubble size bins used in the simulations are those given as Set 1 in Table 9.6. This set allows for a larger bubble size (maximum 12 mm) that might be expected in such a large scale reactor where coalescence effects can locally be significant.

Inlet source term for bin fraction

It was assumed that the initial size of sparged bubbles is 3 mm. Thus, at the sparger cells, a mass source term was defined for the appropriate bubble bin-fraction equation according to Eq. 9.28.

10.2.4 Discretisation schemes

Discretisation of the convective terms in the momentum and turbulence equations were done using the QUICK or second-order upwind scheme. For the scalar transport equations for the bubble classes, the first-order upwind scheme was used since convergence with higher-order schemes was not possible. For diffusive terms, the second-order accurate central-differenced scheme was used.

10.2.5 Pressure-velocity coupling

Pressure-velocity coupling was achieved by the PC-SIMPLE algorithm. In some simulations, the multiphase implicit coupled algorithm was used, in which the momentum equations and the shared pressure are solved simultaneously.

10.2.6 Convergence criteria

Simulations were considered converged when monitored relevant quantities (e.g. impeller torque, impeller discharge flow rate, integrated turbulent dissipation, volumetric gas outflow rate, bin fractions, Sauter diameter) had already reached a steady value or deviate within a narrow band around a steady value.

10.2.7 Solution initialisation

In order to ease and speed-up the convergence of two-phase simulations the following route was taken in most simulations. Two-phase simulations were started initially with zero gas flow rate. Once a converged solution had been reached, the actual gas flow was started. Furthermore, the gas fraction was initialized to 10^{-4} everywhere in the domain, and for population balance simulations, the bin fraction for 3 mm bubbles was set to 1.

10.3 Results and discussion

In this section, we report on main simulation results where we also make comparisons between the different modelling options used in this study. However, with level of detail less than that presented in Chapter 9, as some issues are already covered there (e.g. effect of different inlet/outlet conditions). To a certain degree, the modelling approach taken here also builds on the results of Chapter 9. Comparisons are also made with the experimental data of Vrábel et al. (1999, 2000). Here again, most of the simulation results such as gas fraction contours are given for the vertical plane located midway between the adjacent baffles (i.e. the mid-baffle plane).

We will first give some of the earlier simulation results where the bubble size was fixed to 3 mm. In later simualtions, the Sauter mean diameter was found to be significantly larger than this value, namely about 7 mm. Nevertheless, the results serve as an indicator for general trends and for the influence of varying operating conditions as well as numerical settings.

Standard model

We used what we call the "standard model", which provides a basis for comparing different modelling options. The set of conditions chosen for the standard model are given in Table 10.2.

10.3.1 Liquid flow patterns: Ungassed versus gassed mode

Interaction between impeller zones

LDA measurements of Roušar and van den Akker (1994) (see Section 3.2.1) showed that there is no interaction between the impeller zones in the absence of gas flow, i.e. mean axial velocities are zero at midway between the adjacent impellers. When there was gas flow, however, they observed a steady liquid stream connecting the adjacent impellers. The stream was starting from the lower impeller and ending up below the upper impeller. Their schematic representation of those flow patterns are given in Fig. 10.2 including the corresponding patterns for a single-impeller system. They reported that the steady liquid stream was observed, however, at the mid-baffle plane, and it did not apply to all angular positions. They suggested that an opposite stream should exist flowing from the upper zone downwards in the baffle plane, but they could not make measurements in this plane.

In Fig. 10.3, we make a similar comparison using the simulation results for $N = 115$ rpm. Velocity fields for both ungassed and gassed operation for Case 2 are given in the mid-baffle plane. In the absence of gas, all impeller zones are clearly separated. When gas is sparged, a steady liquid stream forms between all adjacent impellers. The direction of this stream is from lower to upper impellers, in line with the observations of Roušar and van den Akker.

In Fig. 10.4-10.9, the effect of aeration on the liquid flow field is given with respect to different angular locations and gassing rates. We find further accordance with the measurements of Roušar and van den Akker that the liquid stream connecting the adjacent impellers is not present in all planes. It also seems to be dependent on the degree of the gas flow rate. Compare for instance the $-20°$ plane views in Fig. 10.5(b) and (a). A clear liquid stream in the direction given above is present only at low gassing rate ($Fl = 0.040$). When we go to the $-10°$ plane closer to the baffles (Fig. 10.6), it has now disappeared also for $Fl = 0.040$ case. Finally, in the baffle plane (Fig. 10.7), we now see a steady stream in the opposite direction, i.e. starting from upper impellers towards lower impellers, as predicted by Roušar and van den Akker (1994). In this plane, the swirling component of the flow is redirected in the axial direction at the baffles, which contributes to the axial flow originated from the radial impeller discharge streams impinging at the wall. Consequently, axial currents near the baffle are much stronger (compare for instance the flow patterns near the free surface in the mid-baffle plane with that in the baffle plane).

Impeller discharge flow

It can be seen from Fig. 10.3 that the velocities are lower when gas is introduced, suggesting that power transmitted to the liquid is lower. A further observation supporting this is the following. The radial discharge flow from the Rushton turbine impinges at the wall and separates into two axial streams directed upwards and downwards. In the ungassed mode, those axial currents collide with their counterparts flowing in the opposite direction (coming from adjacent impellers) right at the midway between two impellers. Here the mean axial velocity becomes locally zero. Now, just above the bottom impeller, comparing the axial location of this zero mean velocity region (easier

to locate it at near tank wall region) for all angular planes, we see a shift towards the bottom impeller as the gas rate increases. This suggests that the power uptake and pumping capacity of the bottom impeller becomes lower with the increase of gas flow rate.

Another distinct difference compared with the ungassed mode is that the bottom impeller discharge stream is inclined slightly upwards due to gas flow from the sparger underneath. At higher gas flows, the inclination is also higher. This effect is present at all angular planes. Other impellers do not seem to show this behavior as the gas flow through those impellers is less.

Secondary circulation loops

At high gassing rates ($Fl > 0.04$), Roušar and van den Akker (1994) observed that, for both single- and 3-impeller geometries, the flow near the wall at the top of the tank changed its direction and a circulation cell was formed rotating in the opposite direction. This was attributed to the observation that the gas causes the impeller discharge stream to return to the central region rather than flowing upwards along the wall. As a consequence, the rising velocity of bubbles in the vicinity of the wall was lower. The circulation loop was reported to be at the mid-baffle plane and it was present also in the single-impeller tank. They could not measure near the baffles, where a fast rising stream of bubbles was observed at all experimental conditions.

Simulation results are also in line with those observations. In Fig. 10.3(c), the presence of the opposite circulation loop near the wall close to the free surface can be seen. It is restricted to a relatively small region in the tank. Near the baffles, where there is a strong upwards flow (as the swirling flow is redirected by baffles in the axial direction), the size of this loop is smaller (see Fig. 10.7(b) and (c)). Comparing the cases with gas flow number zero, 0.040 and 0.080, it is evident that the size and the strength of the loop increases with gassing rate. It is present to variable degrees in all planes except for the 10° plane (plane just downstream side of the baffle w.r.t. the prevailing swirling flow). In this plane, in contrast to the ungassed situation, the flow near the wall is downwards and it's strength increases with the gassing rate. The circulation loop seem to be related to the radial discharge flow from the top impeller which separates into two axial streams at the wall. The extent of those streams depends, as previously mentioned, on the power trasmitted to the liquid from the impeller and, in turn, on the cavity regime and gassing rate. Futhermore, it depends on the axial distance from the impeller level. Far from the impeller, the upward stream along the wall is weaker and it diverts away from the wall into the central part, inducing a circulation in the opposite direction in the near-wall region. Supporting this, we observed the same circulation loop in standard single-impeller tank simulations when there was no gas flow (see in Fig. 9.6 the mid-baffle plane). There, it emerged due to the large distance between the impeller and the free surface rather than the gas flow.

Another type of circulation loop has been observed near the wall, which seem to stem from the complex interaction between the action of baffles and the impeller discharge flow. In Fig. 10.10, where the flow patterns are plotted in the radial plane located midway between the baffle tip and tank wall, those loops can clearly be seen. For clarity, the fermenter is shown with a periodic repeat (120° sector). Above the top

impeller close to the free surface, a large circulation loop is present at the downstream side of the baffle. Similar loops are also present between the lower impellers, however with much smaller sizes. The strength of those loops increases with the increase of gassing rate. Between the lower impellers, yet another type of loop is present at the upstream side of the baffle, which rotates in the opposite direction. It's only present when there is gassing though its strength decreases with the increase of gassing rate.

10.3.2 Gas cavity and gas flow field at the bottom impeller

Prediction of gas cavities forming behind the impeller blades is important for two-phase flow regime in the reactor, as these are the regions where the bubbles are dispersed into the bulk region of the tank. Fig. 10.11(a) shows the clinging cavities present at the impeller for Case 2, that is when the aeration rate is increased at high stirring rate (115 rpm, 52.6 l/s). This is also evident from the location of Case 2 in the flow regime map in Fig. 10.1. When we decreased the impeller speed at this high aeration rate (i.e. 70 rpm, 26.3 l/s), the impeller was not able to disperse the gas into the reactor, resulting in behaviour similar to a bubble column, hence instabilities occurred in the steady-state simulations. This is in agreement with the experiments, where the fermenter was reported to be flooded at this operating condition (Vrábel et al., 1999). Furhermore, the flow regime map in Fig. 10.1 also shows that the bottom impeller is at the flooding state for Case 3.

The gas cavity structure forms as bubbles are captured in the low pressure zone behind the impeller blade. It is seperated into two parts (upper and lower pockets relative to the impeller centerline) due to the impeller disk. The gas circulation at those low pressure zones is shown in Fig. 10.11(b). Here, the gas relative velocity field (w.r.t. the rotational reference frame) is given in the axial plane located slightly above the bottom impeller centerline plane ($y = 1.17$ m). This plane coincides with the core of the upper gas pocket and shows the two circulation zones formed near the inner and outer blade edge.

10.3.3 Bubble size effect

Fig. 10.12 shows the effect of bubble size on the gas distribution and holdup. Simulations with monodispersed bubble size and the Schiller & Naumann drag law underpredicted the gas holdup, unless the bubble size was fixed to a value of about 1 mm. Smaller bubbles have smaller slip velocity, hence larger residence time in the reactor. Therefore, the holdup is higher. Furthermore, they're better flow followers, thus are more easily dispersed over the total volume, again leading to higher holdup.

There is no dispersion of 3 mm bubbles below the bottom impeller region. In the double-loop gross recirculation regions typical to disk turbines, gas entrapment is different than what we observe in the standard single-impeller tank simulations. In the standard tank, significant amount of gas is entrapped in both of the loops. In the multi-impeller fermenter, however, the prevailing gas accumulation is in the lower loop for all impellers except the bottom impeller. This is due to the impeller–impeller interactions mentioned in Section 10.3.1.

That is, there is a steady liquid stream starting from the lower impeller and ending up below the upper impeller which brings along bubbles with it. There is still some gas accumulation in the upper loops as part of this liquid stream still return back to the lower impeller, hence inducing downwards flow. This is most significant for the upper loop of the top impeller, where there is a large amount of gas entrapment especially for 1 and 2 mm bubbles.

10.3.4 Effect of discretisation schemes

The effect of different discretisation schemes on the gas distribution pattern is given in Fig. 10.13 and 10.15 for low and high aeration cases (Case 1 and 2), respectively. The numerical diffusion characteristic to the first-order upwind scheme results in smeared out gas patterns. Compare, for instance, the width of the gas jet coming from the sparger. The gas is also more uniformly dispersed due to this extra diffusion effect. Despite of this effect on gas distribution, the overall gas holdups for both first-order and higher-order schemes is about the same, and they are both lower than the experimental holdup. There is, however, a difference in gassed/ungassed power ratio predictions. Those results also show that there is no significant difference between the second-order upwind and the QUICK scheme, which is a weighted average of second-order upwind and second-order central scheme. Therefore, second-order upwind scheme was used in most of the simulations. Only when convergence was not possible due to numerical instabilities, we adopted the first-order scheme.

10.3.5 Outlet conditions: Degassing vs pressure outlet

In Fig. 10.16(a) and (b), we show simulation results with two alternative outlet conditions: (i) degassing condition, (ii) pressure outlet with only liquid backflow (see Section 9.4.2 for details). The integral quantities (holdup, power draw and mean axial velocity) are the same for both cases. This is in line with the standard tank simulation results given in Section 9.5.3. The gas distribution in the fermenter is also practically the same apart from the small region above the top impeller. Here, the gas distribution is more uniform near the outlet region when the degassing condition is used. This is due to the symmetry condition that applies for the liquid phase at the outlet, hence upwards currents here are forced to return back to the vessel, carrying along with them part of the gas bubbles. This is, however, a minor local effect, and the overall gas holdup do not change among those two simulations.

10.3.6 Drag formulations

Schiller & Naumann vs Ishii & Zuber

The simulations of the standard configured tank given in Chapter 9 showed that the drag force is the dominant force determining the global gas holdup in the reactor. The drag correlations used in those simulations have also been implemented here. In Fig. 10.16(b) and (c), we compare results with those correlations. The Schiller & Naumann drag law, which is valid for spherical bubbles, here again underestimates the

gas holdup in the fermenter for the simulations with monodispersed 3 mm bubbles. The Ishii & Zuber drag law, which accounts for spherical cap and ellipsoidal bubble regimes, resulted in a slightly lower slip velocity due to bubble deformation and, in turn, a higher holdup. The mean axial slip velocities are comparable to those obtained from the standard tank simulations given in Fig. 9.16. Despite the lower slip velocity, the holdup was 3.0% for Case 1, which is still lower than the experimental value of 4.7%. The underprediction is a consequence of the drag correlations used that have originally been derived for single bubble/particle moving in a stagnant fluid. It is reported in literature that, in a turbulent field, the slip velocity of bubbles can decrease as low as $40 - 50\%$ of that in a stagnant fluid (Lane et al., 2000), hence the holdup increases. Therefore, the drag coefficient needs to be corrected for turbulence effects.

Turbulent drag modification: Brucato model

Using the Brucato correlation for turbulence effects, we obtained a good agreement for the low stirring rate (70 rpm) case (see Section 10.3.9). However, simulations with 115 rpm resulted in overestimated holdups for both low and high aeration rates. In Fig. 10.16(c) and (d), the effect of drag modification due to turbulence can be seen. When Brucato turbulence correction was used, the mean axial slip velocity is reduced dramatically from 29.1 to 9.7 cm/s. The gas distribution at the outlet is very non-uniform. Most of the gas leaves through the region near the wall circumferentially upstream to the baffle (not visible at the mid-baffle plane). The overall gas holdup in the fermenter is largely overestimated. The reduced axial slip velocity values, however, are in line with those obtained from standard tank simulations (cf. Fig. 9.17).

Above results suggest the limited applicability of the Brucato model to different cases where the geometry and, in turn, the distribution of energy dissipation is different. As discussed in Section 6.7.8, we used the model correlation constant $K = 6.5 \times 10^{-6}$ as proposed by Lane et al. (2000), which is based on his bubbly flow simulations of the same standard stirred tank configuration. In standard tank simulations, the volume-averaged dissipation rate was about 0.6 $\mathrm{m}^2/\mathrm{s}^3$. However, for the large fermenter, we obtained values of about 1.0 $\mathrm{m}^2/\mathrm{s}^3$ at high stirring rates, which means a larger increase in the drag force due to turbulence. At low stirring rates, the value was about 0.3 $\mathrm{m}^2/\mathrm{s}^3$.

It is, however, not possible to make a conclusive judgement from above results, because the simulations we report here were performed for a fixed bubble size of 3 mm. Our later simulations with population balance modelling showed that the Sauter mean diameter can be as high as 6-7 mm in the fermenter. This difference in bubble size is significantly larger than that in the standard tank simulations. Note that the slip velocity (of single bubbles rising in still fluids) is rather insensitive to bubble size in the range 3–10 mm (see Fig. 6.1(b)). However, the extent to which the drag force on those bubbles will be influenced by the liquid turbulence field dependens on the ratio $d_\mathrm{p}/\eta_\mathrm{l}$ according to the Brucato model (see Section 6.7.8). Hence, this underestimatation of bubble diameters might also have an effect on the estimated holdups.

10.3.7 Virtual mass force

In Fig. 10.13–10.15, the influence of virtual mass (VM) force on the gas dispersion in the fermenter is shown. The inclusion of VM in the model did not make a change in the overall gas holdup. This is in line with the standard tank simulation results given in Section 9.5.9. The change in gas distribution in the fermenter on the other hand is more significant. Larger amount of gas accumulates in the recirculation regions arising from the impeller discharge flow. At those regions, relative acceleration between the phases is larger, hence larger the VM force acting on bubbles.

The power ratio is also significantly higher with VM force. This indicates that the gas distribution near the impeller should be different, which is not visible in the mid-baffle plane gas profiles. Therefore, we plotted in Fig. 10.14 the gas distribution in axial planes located at impeller centerlines. In the absence of VM force, the larger gas pockets behind the impeller blades are now clearly visible for the top, third and the second impeller. When the VM force is present, more gas is entrapped in the trailing stream behind the bottom impeller blade (cf. Fig. 10.14 bottom impeller). Thus, less gas is transported axially to the upper impeller region by the liquid stream connecting the adjacent impellers (cf. Fig. 10.13 (b) and (d)). This results in reduced levels of gas cavities at upper impellers. In Fig. 10.14, the torque acting on each impeller and the corresponding power draw and power number are given together with values from ungassed operation. The values correlate with the size of the gas cavity region behind the impeller blades. The lowest impeller has the lowest power draw as expected. The corresponding gassed/ungassed power ratio is 0.56 (drag only case). Above results are, again, in line with that of the standard tank simulations given in Section 9.5.9.

10.3.8 Lift force

Convergence was not possible when the lift force was included in the interfacial momentum exchange. The same convergence problem was also encountered in the standard tank simulations reported earlier. In simulations of a bubble column reactor (not reported here), we did not experience any convergence problem with the inclusion of the lift force. This seems to be due to highly rotational flow in stirred tanks, which brings a high level of coupling in the momentum equations and results in numerical instabilities.

10.3.9 Influence of stirring and aeration rate

High stirring, low aeration

Taking operating conditions of Case 1 (see Table 10.1) as the starting point, we now compare the gas distribution and integral parameters in the fermenter with respect to variations in stirring rate and gas flow rate. We take Case 1 as the "high stirring, low aeration ($Fl = 0.040$, $Fr = 0.262$)" condition. This is the default setting where we previously reported most of the results regarding variable discretisation schemes, outlet conditions, etc.

High stirring, high aeration

When we increase the aeration rate, we reach Case 2 corresponding to the "high stirring, high aeration ($Fl = 0.080$, $Fr = 0.262$)" condition. Experimental measurements show a two fold increase in holdup when going from Case 1 to Case 2, while the power ratio decreases from 0.65 to 0.54. Results given in Fig. 10.17 show the general trend for the holdup, although there is still high level of underprediction with the Schiller & Naumann drag and overprediction with the Ishii & Zuber drag with Brucato turbulence correction. In the flow regime map for the bottom impeller (Fig. 10.1), both Case 1 and 2 are near the complete dispersion condition.

Low stirring, low aeration

Starting again from Case 1, if we now decrease the stirring rate, we arrive at Case 3 corresponding to the "low stirring, low aeration ($Fl = 0.066$, $Fr = 0.097$)" setting. We start to experience difficulties here in reaching convergence with the steady-state simulations. For the Schiller & Naumann case, convergence was possible only with the first order discretisation. This is also reflected in the flow regime map, where Case 3 is rather close to the flooding condition. Fig. 10.18(a) and (b) are in line with this, where the bottom impeller is just able to disperse the sparged gas. The gas bubbles in the impeller discharge stream hardly reach the tank wall.

The experimental gas holdup is slightly less than that for Case 1. However, the predicton by the Ishii & Zuber drag with Brucato turbulence correction is much better than that for Case 1. It seems that the Brucato model works better for the lower mean energy dissipation cases (i.e. relatively lower stirring rates) due to its formulation which makes it equipment-dependent. Good agreement with the experimental holdup value also indicates that the predicted mean axial slip velocity (14.2 m/s) is more realistic for this particular case.

Low stirring, high aeration

Finally, increasing the aearation rate now, we reach Case 4 corresponding to the "low stirring, high aeration ($Fl = 0.131$, $Fr = 0.097$)" case. The gravitational forces dominate at this condition (low Froude number). Vrábel et al. (1999) reported that the fermenter was flooded at this operating condition. The flow regime map (Fig. 10.1) also predicts the flooding condition for the bottom impeller.

The two-phase flow is inherently transient at this regime, hence the convergence of the steady-state simulations was poor. Fig. 10.19(a) and (b) shows the flooding condition for all impellers. There is now even larger deviation in the prediction of gas holdups, but those values are not reliable anyway due to poor convergence of the simulations.

10.3.10 Dense bubbly flow regime

So far, the simulation cases investigated were operating in relatively dilute bubbly flow regime with a maximum holdup value of 8.9 % (Case 2). In our last simulation case,

Case 5, we increase the stirring rate further by about 15% while the aeration rate is now 3.5 times larger (relative to the "high stirring, high aeration" case, Case 2). Now, with 133 rpm and 182.0 l/s gas flow, the measured holdup value in the fermenter reaches 17%. At such levels of gas holdup, the so-called bubble swarm effect starts to become important (according to Laakkonen (2006), at holdups $> 20\%$).

Ishii & Zuber multiparticle drag law

We implemented the Ishii & Zuber multiparticle drag law via a user subroutine, which takes into account the bubble swarm effect. Details of the model are given in Section 6.7.7.

The simulations were run with the following settings:

- first-order upwind scheme (no convergence with higher-order schemes)
- multiphase coupled solver (no convergence with segregated solver)
- only drag force (no convergence with virtual mass force)
- no turbulence modification to drag (Brucato model underpredicts the slip velocity at high stirring rates thus overpredicts the holdup)

Furthermore, due to higher levels of gas flow in the fermenter, we've made a test simulation with the degassing outlet condition in addition to the pressure outlet condition which was used for dilute flows in previous simulations.

Population balance model

In earlier simulations, monodisperse bubble size distribution was assumed. This is even more questionable for a large scale fermenter when compared with a lab scale standard tank we reported in Chapter 9. Furhermore, the assumed bubble size of 3 mm is significantly lower than the Sauter mean diameter we obtained in later simulations with the population balance modelling. In the following results, we also take into account the polydispersity.

Gas distribution, impeller gas looding

In Fig. 10.20–10.26, we give a comparison between a monodispersed simulation with 8 mm bubble size, a simulation with the discrete model (DM) and a simulation with the degassing outlet condition again with DM. We used the bubble size of 8 mm based on the test simulations we did with DM, where the Sauter mean diameters were around this value, which is significantly larger than that obtained for our previous lab-scale standard tank.

One common observation we see in all angular planes in Fig. 10.20–10.25 and in the axial outlet plane in Fig. 10.26 is that the gas distribution at the top region between the impeller and the free surface is more uniform with the degassing condition at

the outlet. When the pressure outlet condition is used, the gas leaves the domain primarily near the tank wall. This is the expected behaviour, especially when the impeller is close to the free surface as in the current case, because, at the outlet, the flow quantities are extrapolated from the interior. By using pressure outlet condition, we simulate effectively not the actual free surface where the normal component of the liquid velocity should diminish, but somewhat a lower plane below the free surface. The degassing condition, however, imposes a symmetry condition for the liquid, hence there is a stronger flow reversal, entrapping more bubbles at this region. Note that, despite the significant difference in gas distribution here, in the rest of the fermenter the gas distribution is almost identical in DM simulations with and without the degassing condition. The overall impact on the total gas holdup in the fermenter is, however, not negligible at those relatively high gas loads. There is about 16% increase in holdup (from 13.3 to 15.5%) when the degasssing condition is employed.

Another observation is that the bottom impeller is loaded with large amount of gas (see the bottom impeller planes in Fig. 10.26). Therefore, the bottom impeller, although not flooded, is approaching the flooding–looding transition, not as effectively dispersing the gas from the sparger as do the other impellers. This is more evident for the monodispersed (8 mm) simulation case (see Fig. 10.20(a)). Due to hampered performance of the bottom impeller, the conventional gas transport mechanism (cf. Fig. 10.2(b)) between the bottom two impellers is interrupted. This can be seen in the gas fraction contours (see Fig. 10.20–10.25(a)), where the high gas containing recirculation loop structure below the second impeller is broken for the 8 mm case. Consequently, the power ratio is also lower. Noorman et al. (1994) reported that the bottom impeller was operating near flooding–looding transition but not flooded. Liquid velocity measurements of Larsson et al. (1996) also showed that the bottom impeller was not flooded. The flow regime map for the bottom impeller given in Fig. 10.1 further supports this.

Power characteristics: Ungassed vs gassed operation

Detailed power characteristics of individual impellers are given in Table 10.3–10.5 for both gassed and ungassed operation. Simulation values are compared with the measurements of Noorman et al. for the same fermenter. Liquid medium was either 22 m^3 water (Noorman et al., 1993) or 21 m^3 Newtonian glucose solution with minerals (Noorman et al., 1994). Impeller power input in water was evaluated by measuring the heat production (by monitoring the temperature increase by a Pt-100 resistance thermometer). Contribution of individual impellers was measured as follows. Fermenter was filled with water stepwise, covering from single impeller to all 4 impellers, and the corresponding heat production was measured at each step.

In ungassed operation, computed power number for each impeller is about the same, $N_P = 5.7 - 5.8$. This agrees very well with the experimental data of Noorman et al. (1993) for air–water system, which, at three different impeller speeds, showed that the ungassed power number was 5.8 for all impellers.

In gassed operation, the bottom impeller delivers the least amount of power for all simulation cases, the 8 mm case being the lowest among all. This is confirmed by the measurements as well (see Table 10.5), though the decrease in power under gassed conditions was somewhat higher. Specific impeller power input measured by Noorman

et al. (1994) was 0.76 kW/m^3, of which the bottom impeller contributes 20%, and the others each 27%. For the simulation case DM with degassing outlet, the bottom impeller delivers 23% of the total power input, whereas the middle two impellers each 26% and the top impeller 25% (see Table 10.3). Specific power for this case is 0.932 kW/m^3, higher than the measured value for glucose solution.

Bubble size distribution

From previous results given above, in the dense bubble regime, DM simulations with the degassing outlet condition seem to give the most realistic results. We shall now look in more detail at the relavant parameters for the bubble size distribution for this simulation case. Note that, bubble sizes were not measured for this system; for which the technical difficulties of doing such measurements at such large scales we could foresee. However, bubble sizes commonly observed in industrial fermenters were reported to be in the range $6-10$ mm (personal communication with the expert of the industrial partner of this project).

In Fig. 10.27 and 10.28, spatial distribution of bubble bin volume fraction, $\alpha_{2,\text{bin}-i}$ (see Eq. 9.35), is given at mid-baffle and impeller centerline planes for all bins. Overall, the largest volumetric contribution to the local gas content is due to relatively large bubbles, in particular the 12 mm bin, which prevails in most of the fermenter. Those large bubbles are most pronounced at the recirculation loops, behind the blades and above the sparger, where sparged bubbles (with intial diameter of 3 mm) rapidly coalesce. This is expected as those are the regions of high bubble density thus high probability of collision. Medium size bubbles (5-3 mm), exist primarily in the vicinity of the sparger and in the impeller discharge streams, and to a lesser extent behind the blades (especially 4.76 mm bin). Smaller bubbles of about 2 mm exist only at a very limited region near the impeller tips (not visible at the bottom impeller due to very low values). The smallest bubbles of about 1 mm (bin 5), located yet in a smaller region near the impeller tips, are not visible in the countour plot due to very low values (max 0.008). We also skipped those in Fig. 10.28. Note that, once again, as in the case of the standard tank, no breakup takes place in the sparged gas stream (no bubbles smaller than the initial 3 mm size).

In Fig. 10.29 and 10.30, spatial distribution of bubble bin fraction, $f_{\text{bin}-i}$ (see Eq. 9.36), is given at mid-baffle and impeller centerline planes for all bins. We can now see the regions where particular bubble size classes should prevail as a result of the local flow conditions. The largest bubble class, 12 mm, is by far the most significant, constituting most of the gas volume almost everywhere in the fermenter except the discharge streams of top three impellers. Bubbles of about 8 mm are also present at those locations (though to a lesser degree) as well as in the discharge streams. Mid-range (5-3 mm) bubbles are limited almost entirely to the impeller discharge streams especially of the upper three impellers. Again, smallest bubbles visible in the countour plots are of about 2 mm, which are limited to the immediate vicinity of the impeller blades (at the front, high pressure zones) and to some extent at the vortex streams detached from the impeller blades. The smallest bubbles of about 1 mm, located yet in a smaller region near the impeller tips, again are not visible in the countour plot due to very low values (max 0.044) and are not shown in Fig. 10.30.

In Fig. 10.31 the Sauter mean diameter distribution is given at several angular planes with respect to the baffle. Similar contour plots for the axial planes (impeller centerline planes, outlet plane and a plane just above the sparger) are given in Fig. 10.32. Overall, the mean diameters are between 9-12 mm at most places. We see that the maximum value of d_{32} is reached near the central shaft at the top quarter of the fermenter. At the outlet plane, d_{32} takes almost the constant value of about 11 mm. At the impeller regions, d_{32} is about 9-11 mm near the shaft and 5-7 mm near the blades except at the bottom impeller, where it is slightly higher due to lower power draw. Mean diameters decrease to about 4 mm when going further away from the blades where the gas cavities detach from the blades. In the impeller discharge streams, d_{32} is in the range 4-9 mm with diameters increasing when getting closer to the side wall. At the axial plane just above the sparger, a ring-shaped 3 mm region is clearly visible, as bubbles here have just been sparged with the same initial size. Smaller mean diameters of about 2-4 mm are seen at high shear regions: in the immediate vicinity of impeller blades (front side) and along the side wall where impeller discharge streams impinge and seperate. Note that, those high-shear impingement regions at the wall start circumferentially downstream to the baffle (w.r.t. the mean tangential flow direction) and extend to the mid-baffle symmetry boundary (compare the impingement regions between the $-30°$ (mid-baffle) and $0°$ (baffle) planes in Fig. 10.31). This is due to the MRF model assumption according to which the position of the impeller with respect to the baffle does not change. In reality, as impellers sweep the full $360°$, the discharge stream would impinge at the full circumferential extend of the side wall.

Radial liquid velocity profiles

Experimental mean and maximum radial velocity profiles in the impeller discharge stream were also reported for this fermenter, both under ungassed and gassed operation (Noorman et al., 1993; Noorman, 1993). Measurements were made with propeller anemometry. Both mean (over 3-12 min) and maximum (averaged over 2 s intervals) velocities were almost linearly proportional to the impeller speed (measured for 3 rotational speeds: 100, 115 and 133 rpm). The maximum velocity decreased linearly with the radial distance from the blade tip.

In the presence of aeration, both mean and maximum velocities were smaller than their ungassed counterparts, the effect being higher at higher gas flow rates. For the third impeller from below, the relative decrease with respect to the ungassed velocity was independent of radial position, whereas for the bottom impeller, the decrease was largest close to the impeller blade. The difference between both impellers was qualitatively in agreement with the power input measurements and suggested that the capacity of the bottom impeller to circulate the liquid was lower than that of the other impellers.

In Fig. 10.33, those experimental measurements are compared to the simulation data both for ungassed and gassed operation. In order to have a comparable velocity profile to that from the measurements, radial velocity profiles were circumferentially averaged over $60°$ sector at the impeller centerline plane. Note that, in simulations the impeller position is fixed with respect to the baffle as the MRF model was used. The experimental data, however, was obtained presumably by averaging over time when the propeller was fixed with respect to the baffles while the impeller was rotating. Therefore, close

to the impeller where the baffle effects are weak, we expect to have better correspondance between the circumferentially averaged simulation data and the time-averaged measurement data.

When there is no aeration, computed velocites of the bottom and third impeller are almost identical. Noorman et al. (1993) also obtained identical results with both impellers (though ungassed data for the third impeller was not reported). This is expected because the impeller–impeller clearance is sufficiently large thus impellers do not interact with each other and behave similar to an independent single impeller system (see also Section 2.4.3). However, computed ungassed velocities are significantly higher than measured ones despite the fact that computed power numbers correspond very well with the measurements for both impellers (see Table 10.3). Note also that, in Fig. 2.8(b), we showed that the computed velocities were also somewhat higher compared to the LDA data of Wu and Patterson (1989) for a standard tank, however to a much lower extent than that compared to the measurements of Noorman et al. (1993). Furthermore, the shape of the velocity profile was also in better accordance. A similar comparison between the data of Wu and Patterson (1989) and the standard tank predictions gave, however, a good agreement (Fig. 2.7(b)).

There is a significant decrease in the computed velocities when the fermenter goes to aerated operation similar to the experimental observations. However, gassed velocities are also higher than the measured ones. As gassed/ungassed power ratio was also predicted higher than the measured value, higher computed velocities are not surprising.

One possible source of dicrepancy for the poor prediction of radial velocities is the following. Simulation values reported here are circumferentially averaged radial velocity profiles at an axial plane through the impeller centerline. Values at this zero-thickness plane are interpolated from cell center values of adjacent grid cells. Experimental measurements were made with a propeller anemometry, which, having a finite dimension (15 mm diameter), would measure a representative mean velocity over an axial span of this dimension. As a result of this inherent difference between the measurement and simulation data, a difference is expected especialy at locations such as impeller discharge stream where values are expected to be sensitive to the axial location. Noorman et al. (1993) also noted that the flow at the bottom impeller was probably not radially oriented and the propeller was very sensitive for the direction of the flow.

In order to check the soundness of the above hyphothesis, we plotted circumferentially averaged radial velocity profiles at two additional axial planes which enclose the impeller blade coinciding with the upper and lower edges of the blade. A third profile was also plotted which is the arithmetic average of the profiles of upper and lower limiting planes and the centerline plane. Those are given in Fig. 10.34-10.36 for the bottom (both ungassed and gassed) and the third (gassed) impeller. They clearly show that the velocity profile is highly sensitive to the axial location within the axial span of the impeller blade. In the absence of aeration, the upper and lower plane profiles do not differ significantly although the centerline plane profile does which is significantly higher than the other two. The centerline plane profile is also the only one where the radial velocity increases continuously with decreasing radial distance to the blade, except in the vicinity of the blade tip. When aerated, there is a large difference between the upper and lower plane profiles of the bottom impeller (except at the blade tip and the tank wall where they converge to the same value). The experimental profile is rather

flat and both the centerline and the averaged velocity profile of the three axial planes are close to this flat profile (the former one, however, deviating when approaching the blade tip). For the third impeller, the upper and lower profiles do not differ significantly and both are lower than the centerline profile. Here, the radial velocity increases in the direction to the impeller, a trend which is predicted only by the centerline profile though values still being higher than the measured ones.

Above analysis shows that the radial velocity could vary significantly over a relatively small axial distance. For instance, in Fig. 10.36, the radial velocity increases 17.7 times when moving from the lower blade edge to the impeller centerline level (at radial position $2r/T = 0.35$, U_r/u_{tip} increases from 0.0286 to 0.535). This velocity increase takes place over an axial distance of 70 mm. If we assume that the same constant gradient is valid in the actual measurements, this would mean that, over the diameter of the propeller anemometer (15 mm), the change in velocity would be 3.8 times. Only a 1 mm shift in the axial positioning of the propeller would result in a 25% change in radial velocity measured.

Overall, some general trends of the measurements can be seen in the (centerline) velocity predictions in the impeller discharge stream although velocities are, in all cases, higher. Sensitivity of radial velocities (both ungassed and gassed) to the axial location in the impeller discharge stream suggests that the accuracy of measurements might have suffered from this, especially in such a large scale fermenter where gathering experimental data is in no way trivial.

10.3.11 Turbulent dispersion force

When bubbles move in a turbulent fluid, eddies on the order of the bubble size or larger would effectively contribute to the dispersion of bubbles. Therefore, in a lab-scale tank, turbulent dispersion effects are expected to be limited to regions of high turbulence level, such as the impeller discharge stream. In a large scale fermenter, however, turbulent dispersion effects could, in principle, be important in a larger part of the domain.

We tried to incorporate those effects in simulations of the large-scale fermenter by using the Simonin model which is one of the most comprehensive one. However, computational stability was severely effected, and despite many attempts to stabilise simulations, it was not possible to achieve a converged solution.

10.4 Conclusions

In this chapter, we presented two-phase flow modelling of the bubbly flow in a production scale 30 m^3 fermenter with 4 Rushton turbines. Modelling approach follows from the standard gassed-stirred tank case given Chapter 9. The main conclusions of this chapter are:

- The computational time is managable for monodisperse simulations, about 1 week CPU time on a single CPU. When PBM is employed, steady-state approach was

not possible in most cases (unless first-order schemes were employed), resulting in computational times of the order of several weeks.

- Achieving a converged solution proved to be more difficult than that for the standard stirred tank case. It was not possible to achieve convergence when the turbulent dispersion model and the lift force were included in simulations.

- Simulations showed that the drag force is the most important one among the other interfacial forces that were taken into account and accurate prediction of axial slip velocities is the key factor. Both Schiller & Naumann and Ishii & Zuber drag laws led to underpredicted holdups. Turbulence modification to drag coefficient using the Brucato model (with the correlation coefficient recommended by Lane) resulted in large underprediction of slip velocities and overprediction of holdups at high stirring rates. This shows that, it is not be applicable to multi-impeller large-scale systems.

- Simulations were able to predict the flow regime transition from loading to flooding, corresponding well with the experimental data.

- Population balance model employed showed that mean bubble sizes predicted are much larger than that for the lab-scale standard stirred tank studied earlier. Unfortunately, bubble sizes were not measured for the system simulated. However, it's in accordance with the bubble size range commonly observed in industrial fermenters, namely $6 - 10$ mm (personal communication with the expert of the industrial partner of this project).

- At high gas fractions, modification to the drag force is needed to account for the bubble swarm effect. The Ishii & Zuber multiparticle drag law for this regime resulted in good prediction of holdup without employing a turbulent drag modification model. At those relatively high gas loadings, use of degassing boundary condition at the outlet gave more realistic results especially if the top impeller is close to the free surface.

- Predicted radial velocity profiles at the impeller centerline level are higher than the experimental profiles both for ungassed and gassed operation. Sensitivity analysis of the radial velocities to the axial location suggests that the experimental measurements may also be susceptible to significant variations.

Tables

Table 10.1: Two-phase simulation cases

	Case 1	Case 2	Case 3	Case 4	Case 5
Impeller speed [rpm]	115	115	70	70	133
Tip speed [m/s]	4.2	4.2	2.6	2.6	4.9
Gas flow rate [l/s]	26.3	52.6	26.3	52.6	182.0
Gas flow rate [vvm]	0.07	0.14	0.07	0.14	0.50
Gas superficial vel. [cm/s]	0.77	1.53	0.77	1.53	5.3
Impeller Re	939,000	939,000	572,000	572,000	1,086,000
Gas flow number	0.040	0.080	0.066	0.131	0.239
Froude number	0.262	0.262	0.097	0.097	0.351
Ungassed power input [kW]	27.22	27.22	6.15	6.15	42.03
Spe. ungassed power [kW/m^3]	1.22	1.22	0.275	0.275	1.88

Table 10.2: Modelling conditions chosen for the standard model.

	Standard model
Interfacial forces	only drag force
Drag formulation	Schiller & Naumann law
Drag modification for turbulence	no
Drag modification for high gas fractions	no
Bubble size d_b	3 mm (monodisperse)
Outlet boundary condition	pressure outlet or degassing
Inlet boundary condition	mass and momentum source terms
Discretisation scheme	higher-order (QUICK or 2$^{\mathrm{nd}}$ order upw.)
Computational mesh	324k ($260 \times 52 \times 24$)
Rotational symmetry	60° sector (single blade & baffle)
Impeller model	MRF

Table 10.3: Dense bubble regime (Case 5) as simulated with the Ishii & Zuber multiparticle drag law. Impeller torque and power input are given for the simulation cases in Fig. 10.20, i.e. (a) 8 mm, (b) DM, (c) DM, degassing, as well as for the ungassed operation. Experimental data of Noorman et al. (1993) for an air–water system is also given, where the liquid volume was 22 m^3.

	Torque [Nm]				Power [kW]				Power Nr. [–]				
Imp.	(a)	(b)	(c)	Ung.	(a)	(b)	(c)	Ung.	(a)	(b)	(c)	Ung.	Exp.
4	67.6	72.9	62.0	125.2	5.7	6.1	5.2	10.5	3.1	3.3	2.8	5.7	5.8
3	56.7	65.5	65.0	126.0	4.7	5.5	5.4	10.5	2.6	3.0	3.0	5.8	5.8
2	49.8	66.0	65.5	126.1	4.2	5.5	5.5	10.5	2.3	3.0	3.0	5.8	5.8
1	48.7	57.0	57.1	125.7	4.1	4.8	4.8	10.5	2.2	2.6	2.6	5.7	5.8
Tot.	222.8	261.4	249.6	503.0	18.6	21.8	20.9	42.0	10.2	11.9	11.4	23.0	23.2

Table 10.4: Cont. Table 10.3. Specific power values. Experimental data of Noorman et al. (1994) was obtained for the same fermenter, where the liquid volume was 21 m^3 and the medium was a Newtonian glucose solution with minerals.

	8 mm	DM	DM + degas.	Ung.	Exp.(gassed)
Specific power [kW/m^3]	0.832	0.976	0.932	1.877	0.76

Table 10.5: Cont. Table 10.3. Gassed/ungassed power ratio values. Experimental data is from Noorman et al. (1993) for an air–water system.

Impeller	8 mm	DM	DM + degas.	Experimental
4	0.54	0.58	0.50	0.4
3	0.45	0.52	0.52	0.4
2	0.40	0.52	0.52	0.4
1	0.39	0.45	0.45	0.3
Total	0.44	0.52	0.50	0.4

Figures

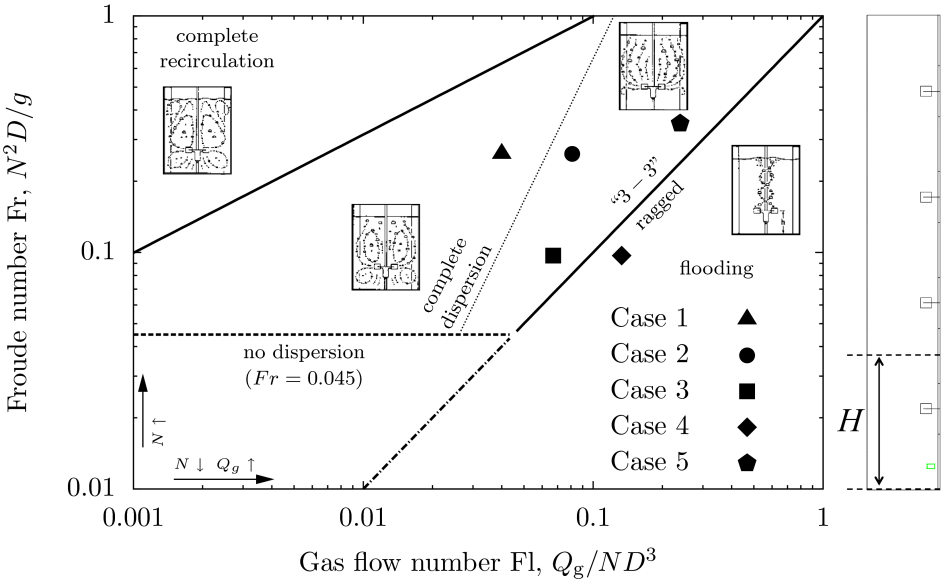

Figure 10.1: Flow regime map for the lower part of the fermenter consisting of the bottom impeller only. The fermenter height was assumed as $H = 1.85$ m, corresponding to the midway between two impellers, as shown at the r.h.s. Schematic representation of the bulk flow patterns are from Nienow et al. (1977).

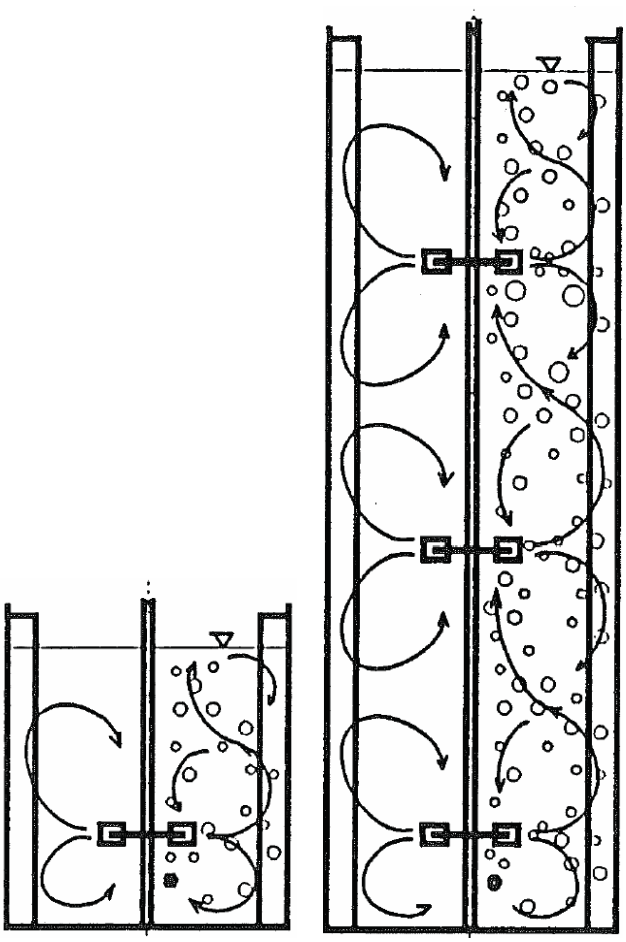

(a) Single-impeller (b) 3 impellers

Figure 10.2: Effect of gassing on the liquid flow field for single- and multi-impeller systems with Rushton turbines. Illustration is from Roušar and van den Akker (1994) and is based on their measurements in the mid-baffle plane.

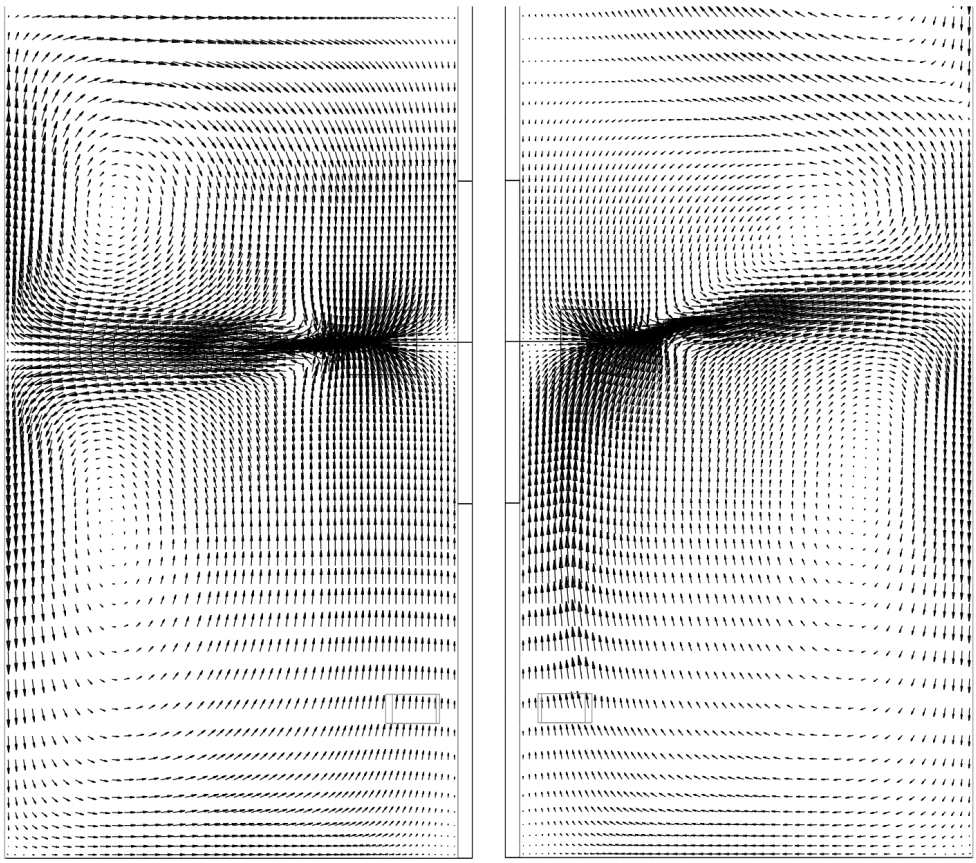

(a) Bottom impeller (no gas/gas)

Figure 10.3: Effect of gassing on the liquid flow field in the mid-baffle plane. Simulation of Case 2 ($d_\mathrm{b} = 3$ mm, 2nd upw. discretisation, Schiller & Naumann drag, VM force).

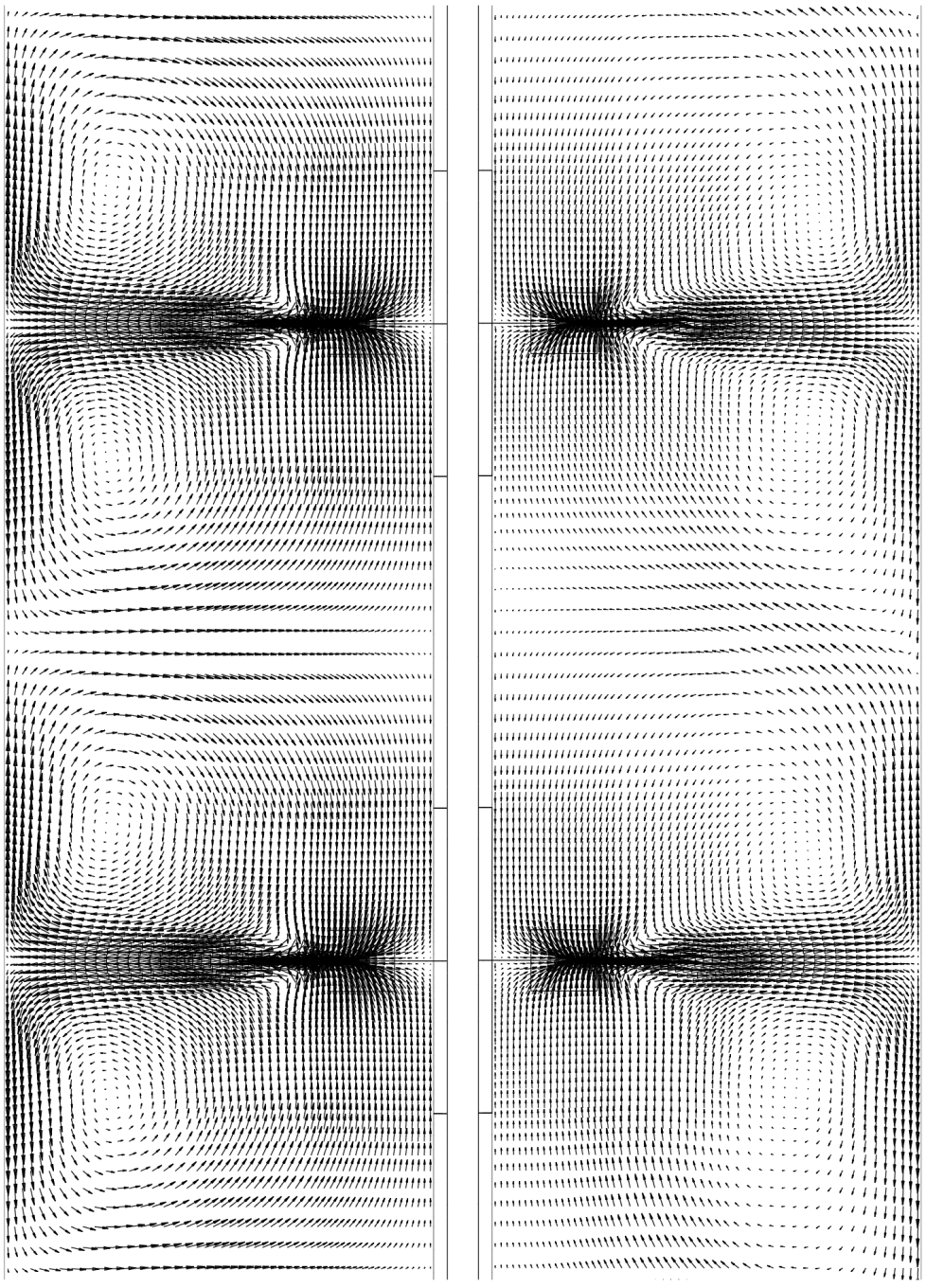

(b) Middle 2 impellers (no gas/gas)

Figure 10.3: (cont.)

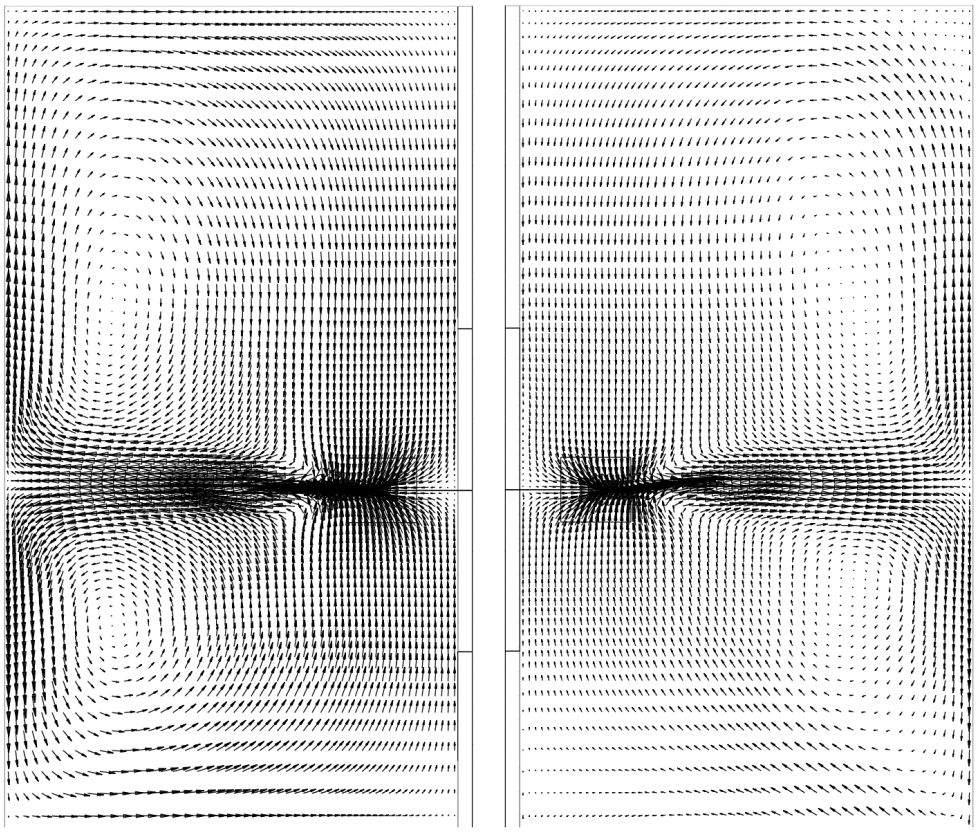

(c) Top impeller (no gas/gas)

Figure 10.3: (cont.)

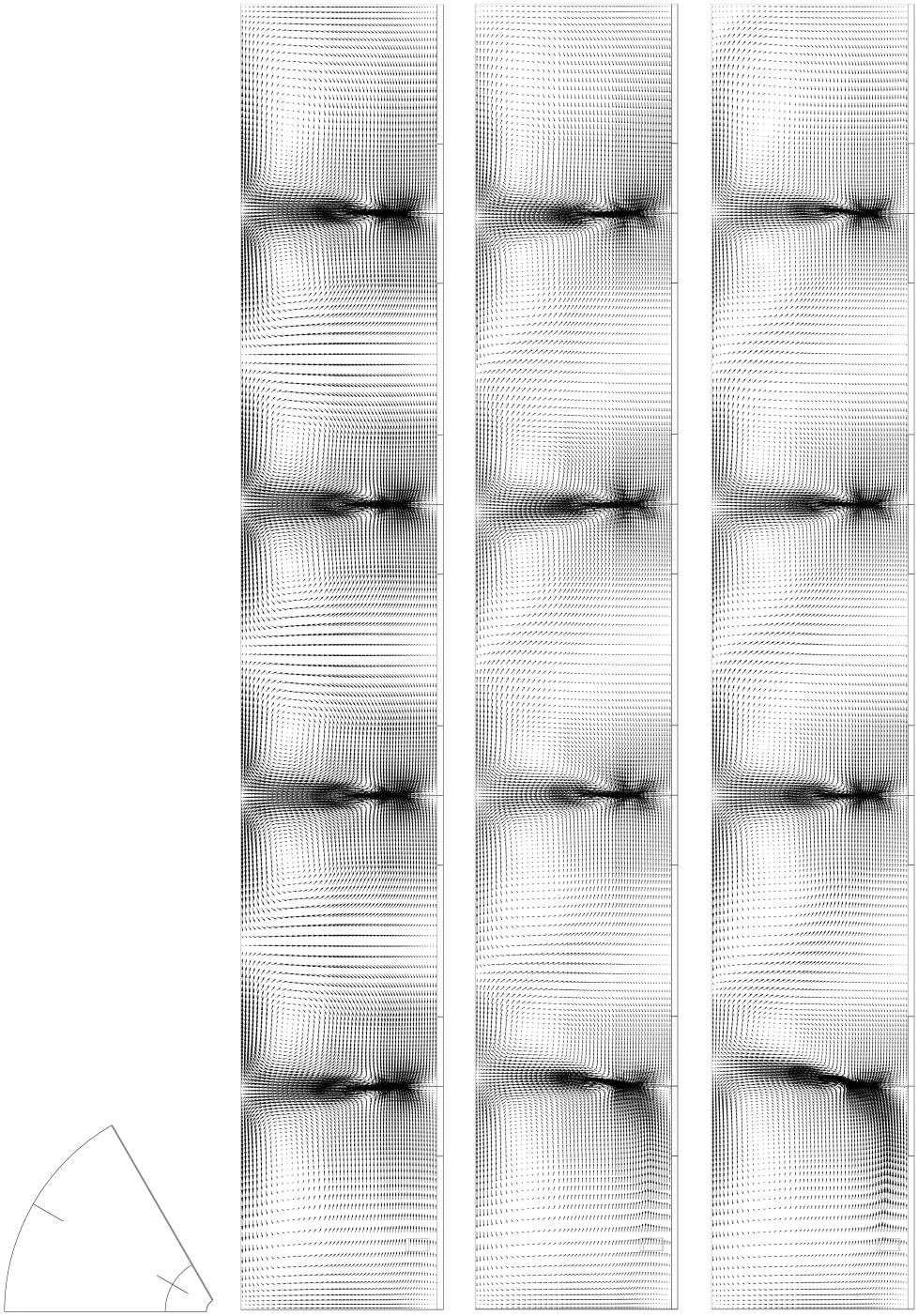

Figure 10.4: Effect of gassing on the liquid flow field at constant stirring rate (115 rpm). Planes are located at an angular position of -30° w.r.t. the baffle (i.e. mid-baffle plane). Impeller rotates counterclockwise w.r.t. the top view. (a) No gas, (b) $Fl = 0.040$, gassing rate 26.3 l/m^3 (Case 1), (c) $Fl = 0.080$, gassing rate 52.6 l/m^3 (Case 2).

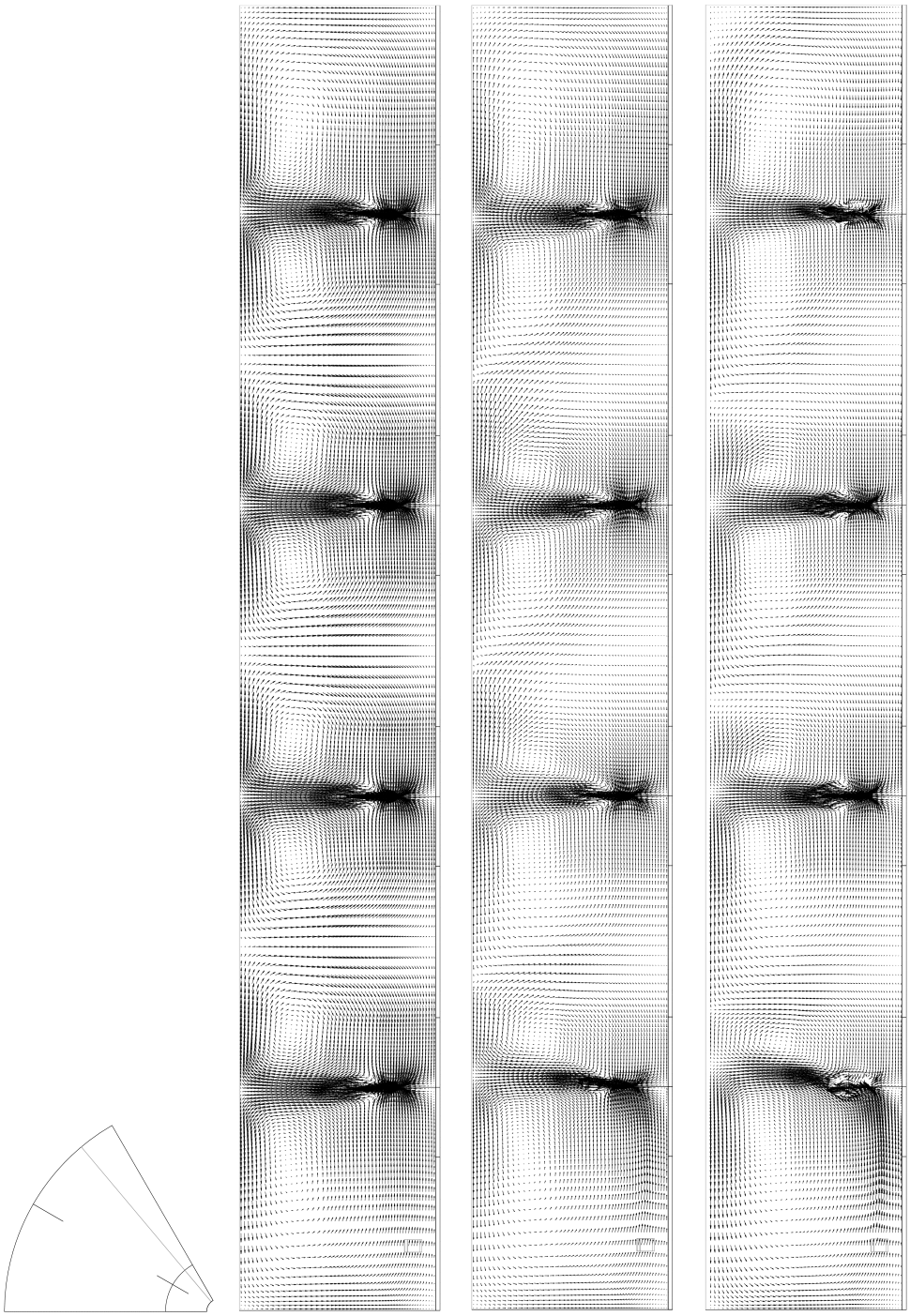

$-20°$ (a) No gas (b) $Fl = 0.040$ (c) $Fl = 0.080$

Figure 10.5: $-20°$ planes w.r.t. the baffle (cont. Fig. 10.4).

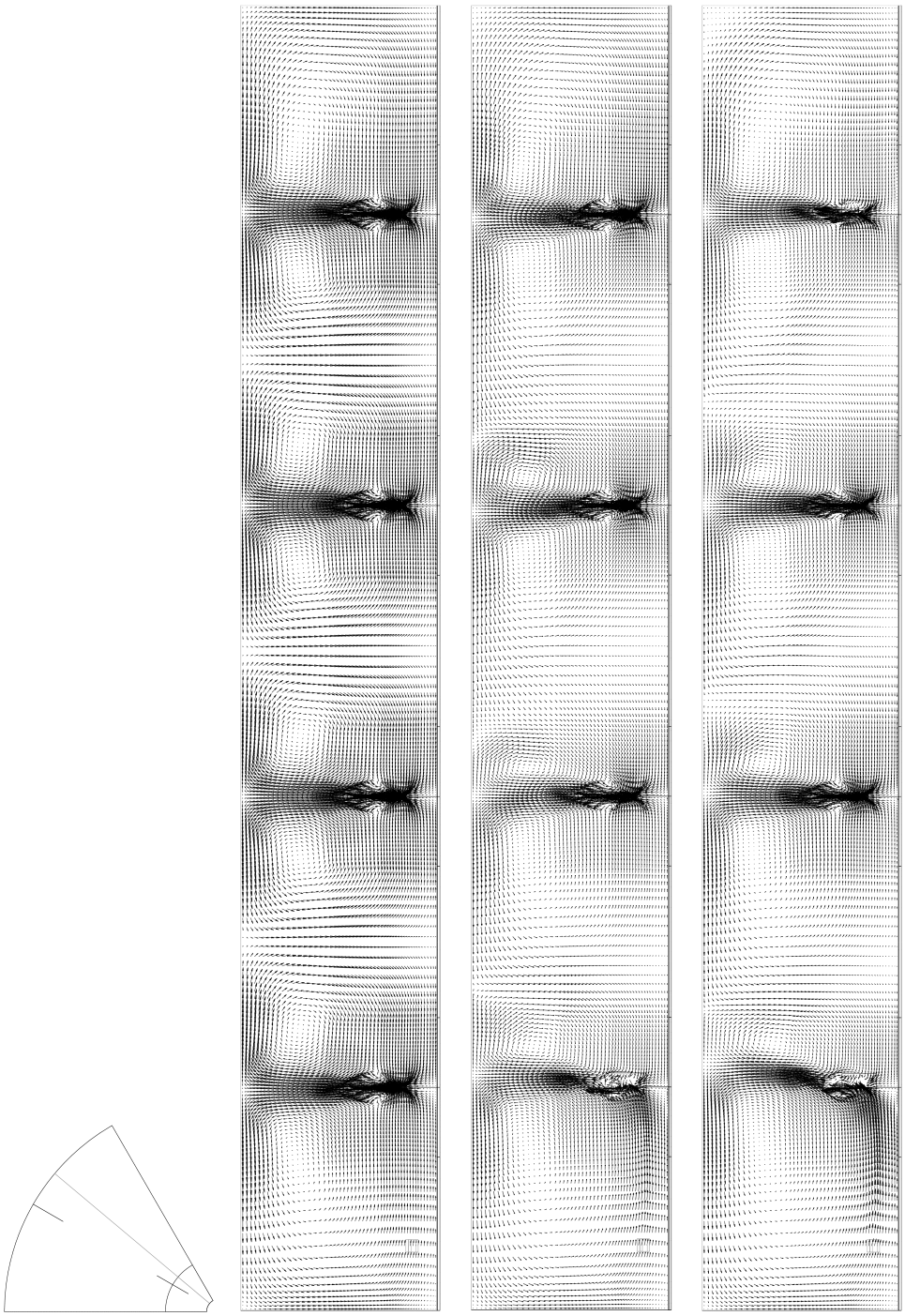

$-10°$ (a) No gas (b) $Fl = 0.040$ (c) $Fl = 0.080$

Figure 10.6: -10° planes w.r.t. the baffle (cont. Fig. 10.4).

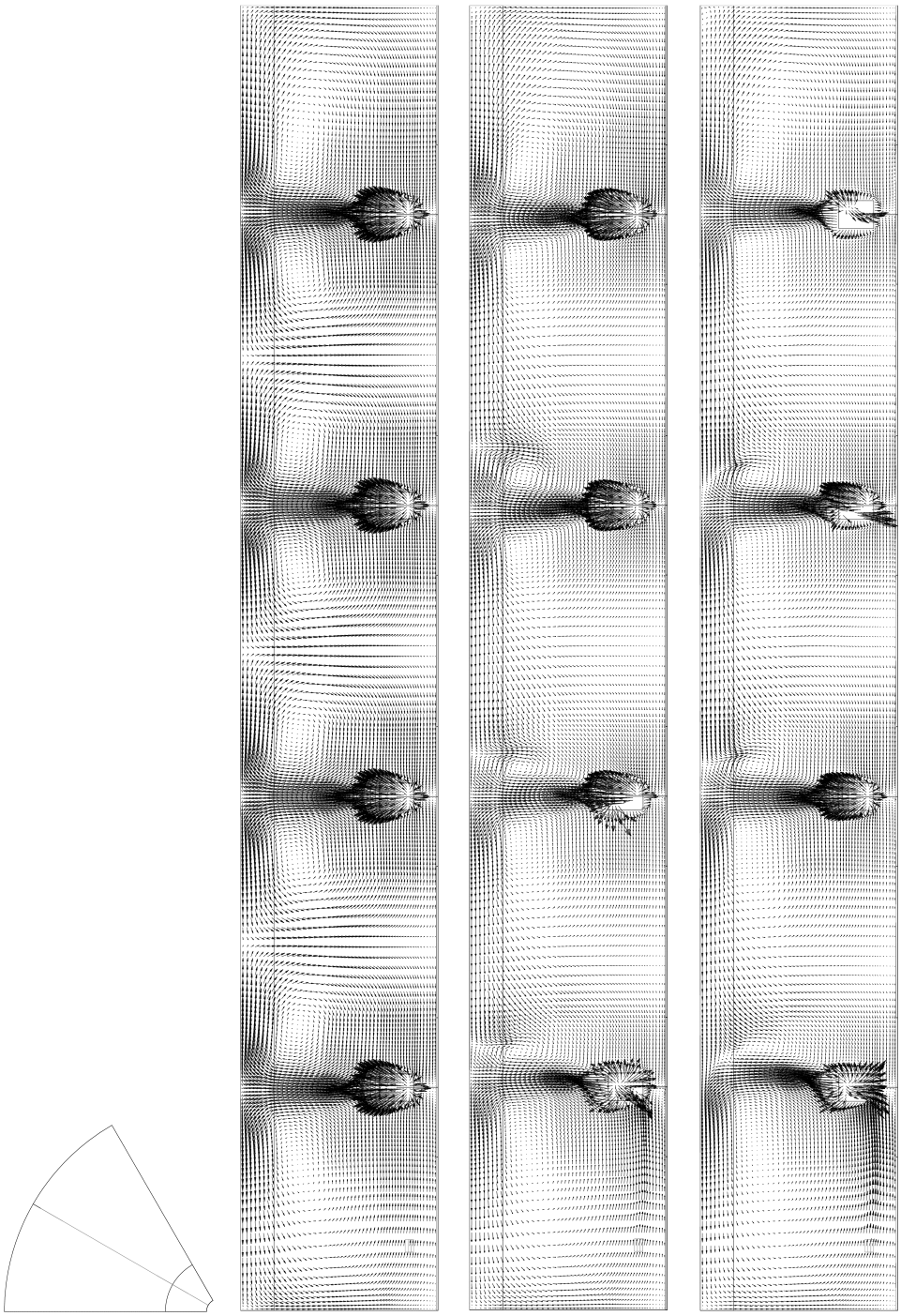

0° (baffle) (a) No gas (b) $Fl = 0.040$ (c) $Fl = 0.080$

Figure 10.7: 0° planes (i.e. baffle planes) (cont. Fig. 10.4).

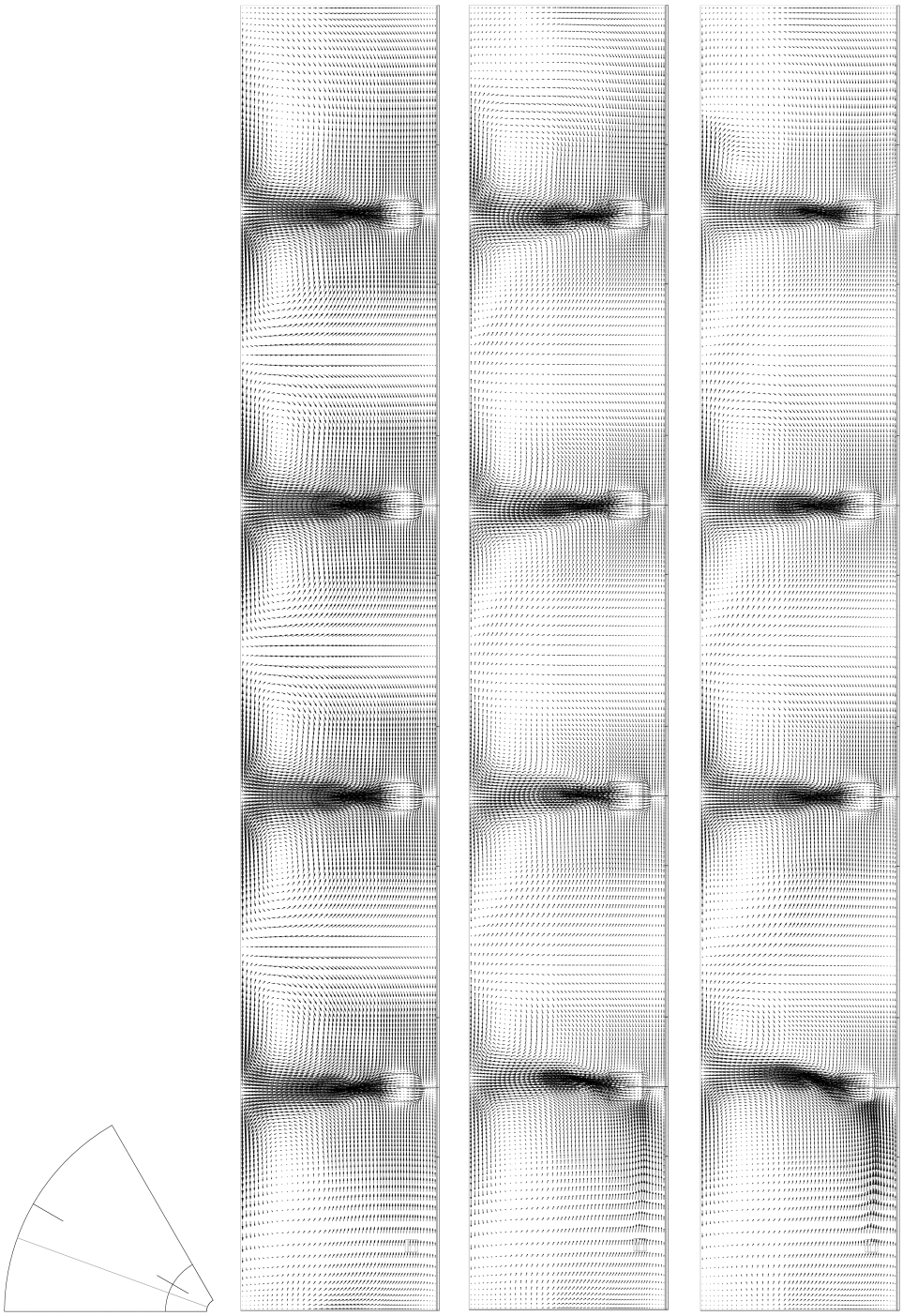

Figure 10.8: 10° planes w.r.t. the baffle (cont. Fig. 10.4).

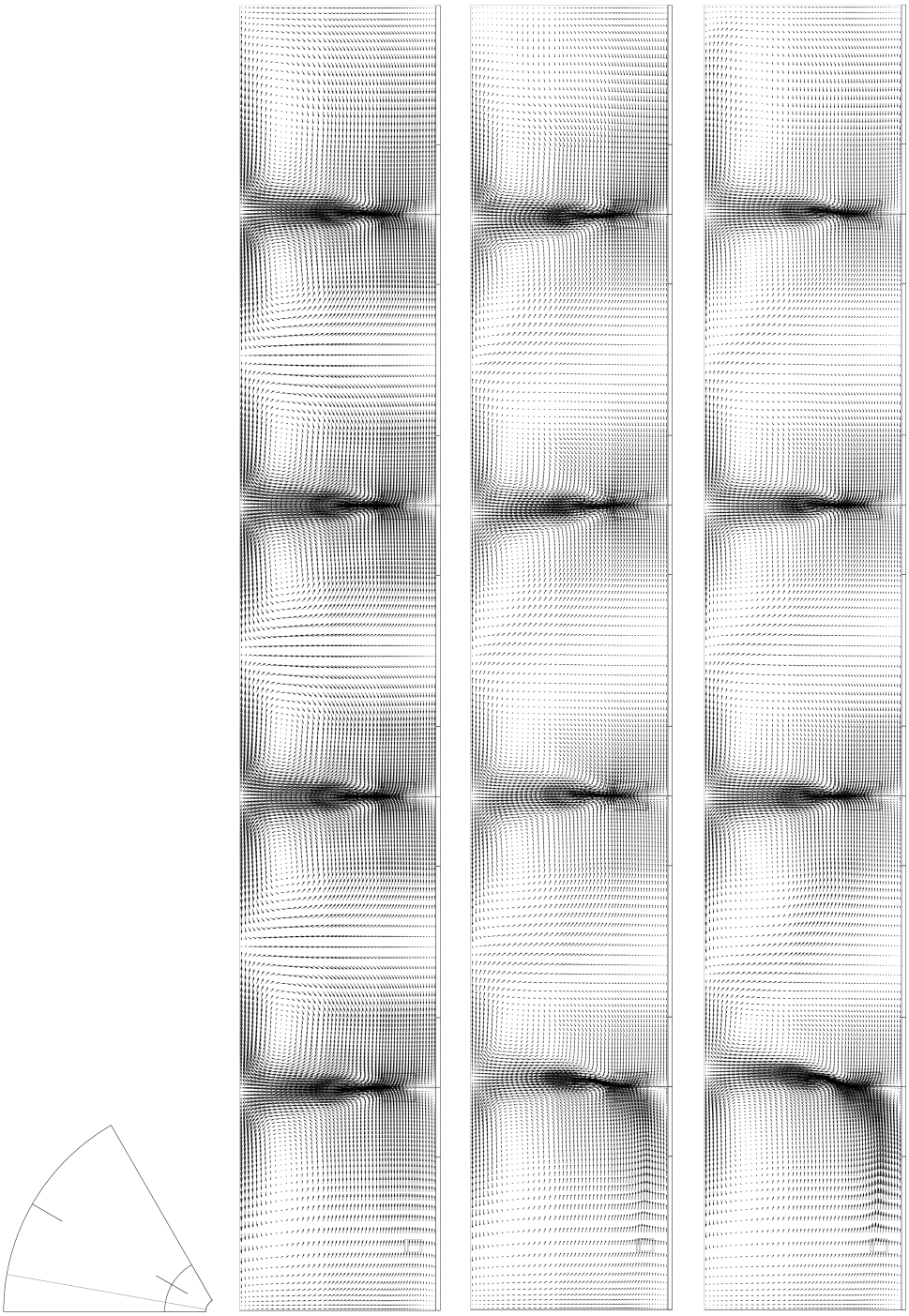

20° (a) No gas (b) $Fl = 0.040$ (c) $Fl = 0.080$

Figure 10.9: 20° planes w.r.t. the baffle (cont. Fig. 10.4).

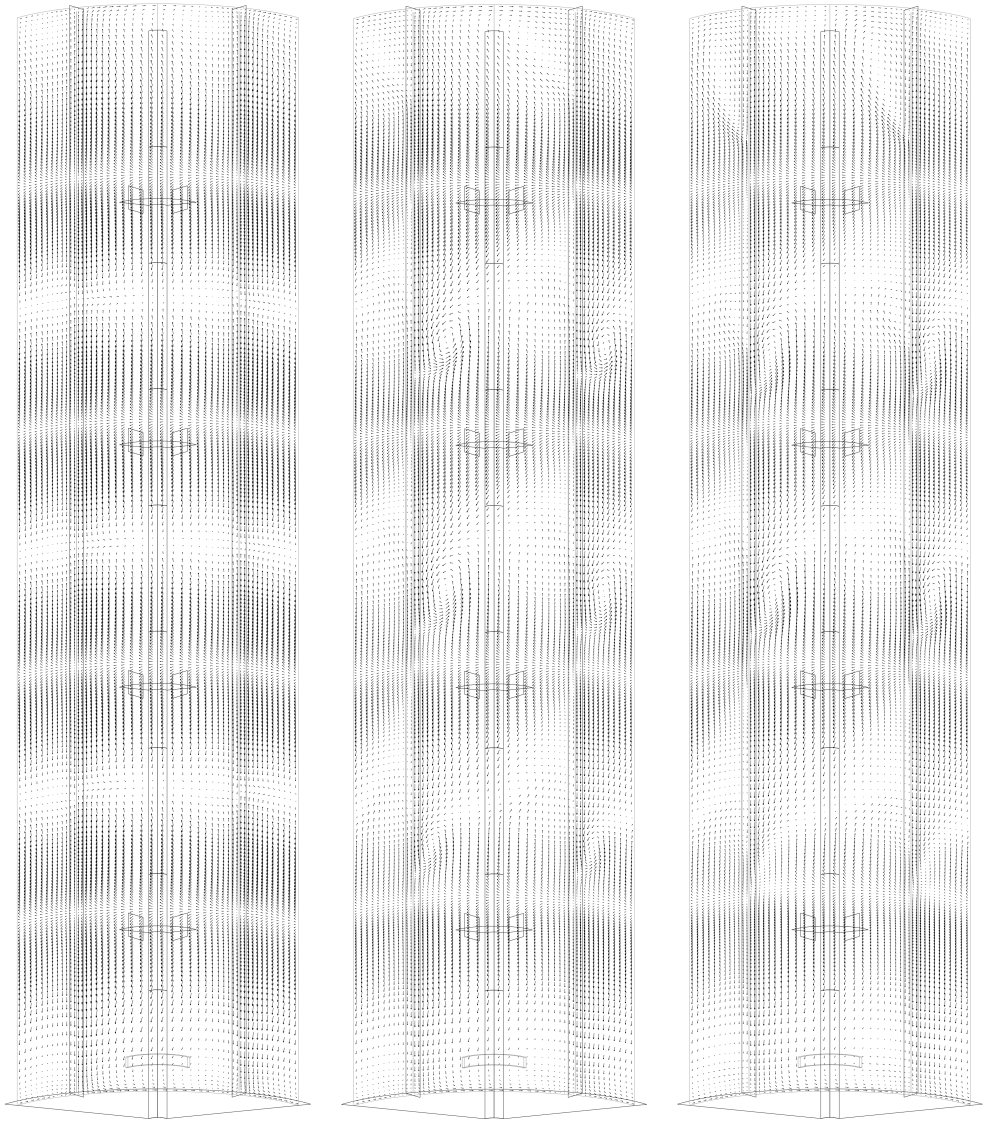

(a) No gas (b) $Fl = 0.040$ (c) $Fl = 0.080$

Figure 10.10: Radial plane midway between baffle tip and tank wall (cont. Fig. 10.4).

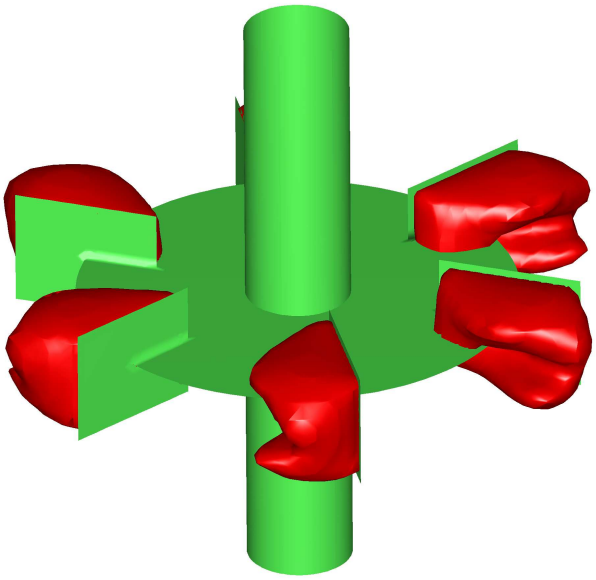

(a) Iso-surface of 75% gas fraction

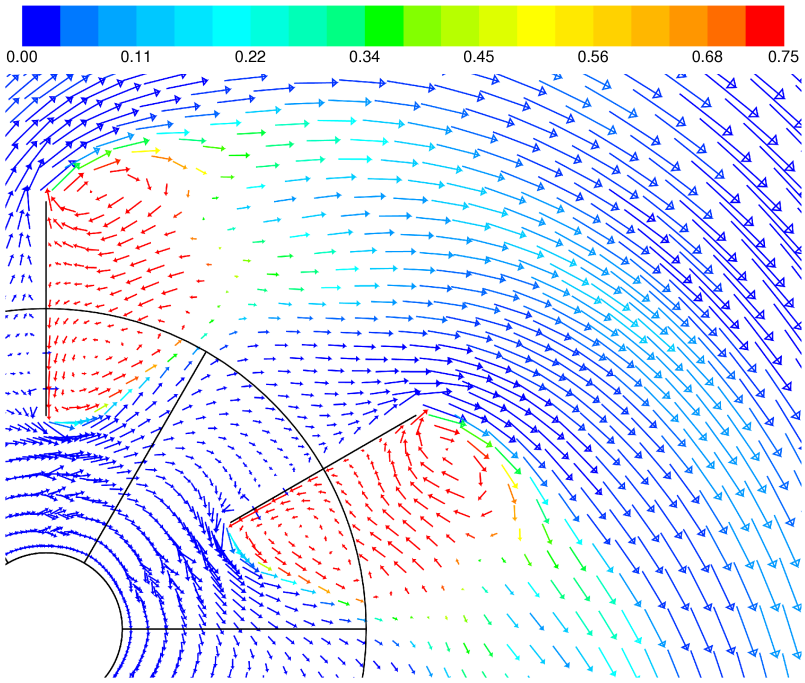

(b) Gas relative velocity field colored by gas fraction

Figure 10.11: Gas cavities and gas circulation zones formed at the bottom impeller blade. Operating condition is Case 2 (d_b = 3 mm, 2nd upw. discretisation, Schiller & Naumann drag, VM force). Gas relative velocity field (w.r.t. the rotational reference frame) is given in an axial plane located slightly above the bottom impeller centerline ($y = 1.17$ m).

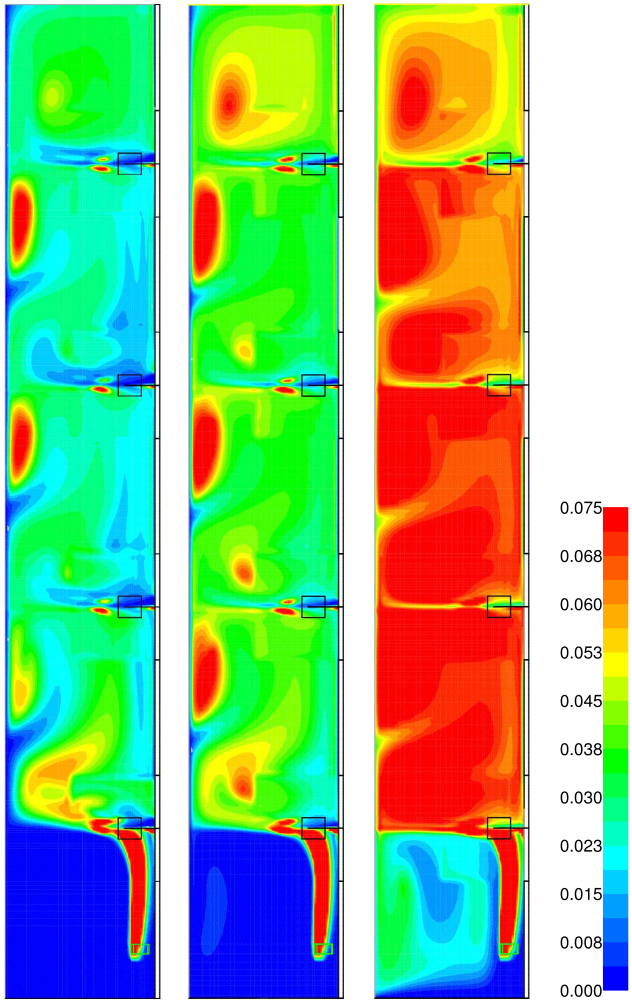

(a) 3 mm (b) 2 mm (c) 1 mm

Case 1: 115 rpm, $Q_g = 26.3 \times 10^{-3}$ m^3/s ($Fl = 0.040$, $Fr = 0.262$)
Model: Schiller & Naumann drag, 1st upw.

	Exp.	(a)	(b)	(c)
Holdup [%]	4.7[a]	2.6	3.7	6.8
$P_{g,\Gamma}/P_\Gamma$	0.65[b]	0.80	0.80	0.82

[a]Interpolated from experimental data of Vrábel et al. (1999)
[b]Experimental data from Vrábel et al. (2000)

Figure 10.12: Effect of bubble size on the gas distribution in the fermenter for Case 1. Gas volume fraction contours are given in the mid-baffle plane.

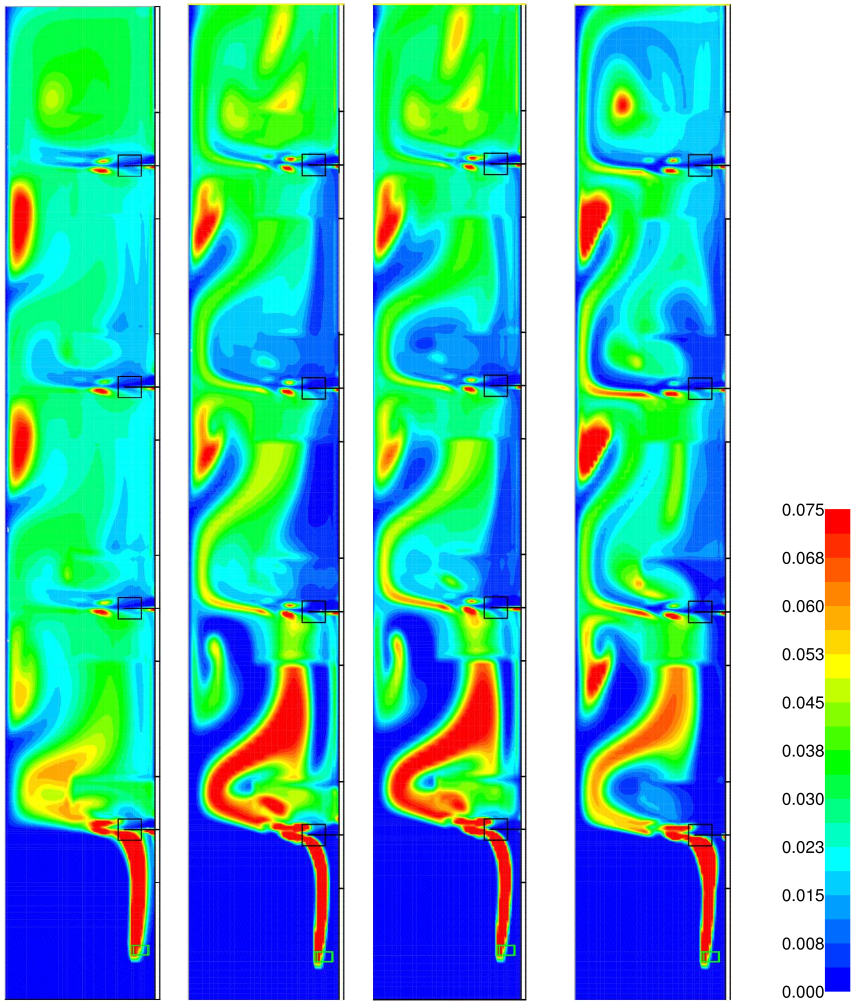

(a) 1st upw (b) 2nd upw (c) QUICK (d) 2nd upw, VM

Case 1: 115 rpm, $Q_g = 26.3 \times 10^{-3}$ m^3/s ($Fl = 0.040$, $Fr = 0.262$)
Model: $d_b = 3$ mm, Schiller & Naumann drag

	Exp.	(a)	(b)	(c)	(d)
Holdup [%]	4.7[a]	2.6	2.5	2.5	2.5
$P_{g,\Gamma}/P_\Gamma$	0.65[b]	0.80	0.63	0.63	0.81

[a]Interpolated from experimental data of Vrábel et al. (1999)
[b]Experimental data from Vrábel et al. (2000)

Figure 10.13: Effect of discretisation schemes and virtual mass force (VM) on the gas distribution in the fermenter for Case 1. Gas volume fraction contours are given in the mid-baffle plane.

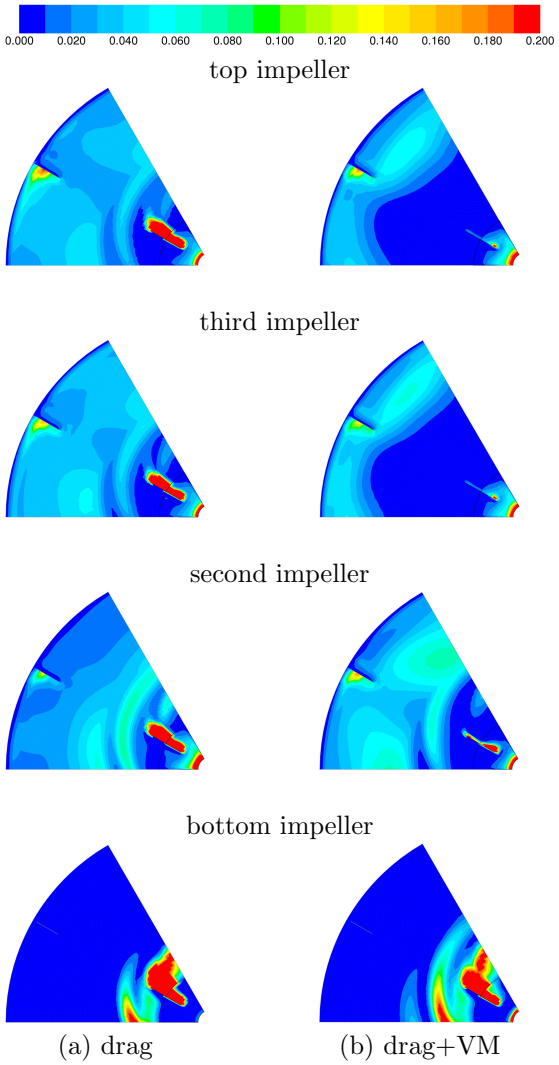

(a) drag (b) drag+VM

Case 1: 115 rpm, $Q_g = 26.3 \times 10^{-3}$ m^3/s ($Fl = 0.040$, $Fr = 0.262$)
Model: $d_b = 3$ mm, Schiller & Naumann drag, 2nd upw.

	Torque [Nm]			Power [kW]			Power Nr. [–]		
Impeller	(a)	(b)	no gas	(a)	(b)	no gas	(a)	(b)	no gas
4 (top)	60.2	85.8	93.2	4.4	6.2	6.7	3.7	5.2	5.7
3	62.7	83.0	93.8	4.5	6.0	6.8	3.8	5.1	5.7
2	60.6	82.5	93.8	4.4	6.0	6.8	3.7	5.0	5.7
1 (bot.)	53.0	57.9	93.9	3.8	4.2	6.8	3.2	3.5	5.7
Total	236.6	309.3	374.8	17.1	22.4	27.1	14.5	18.9	22.9

Figure 10.14: Gas distribution at impeller centerline planes corresponding to the simulation cases Fig. 10.13(b) and (d).

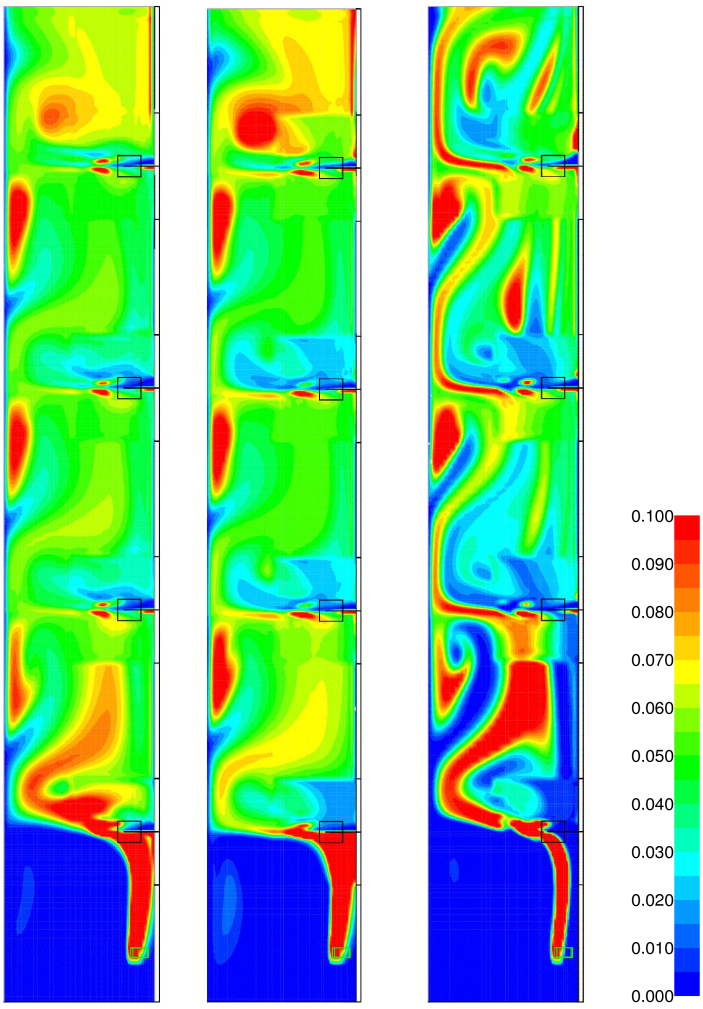

(a) 1st upw (b) 1st upw, VM (c) 2nd upw, VM

Case 2: 115 rpm, $Q_g = 52.6 \times 10^{-3}$ m^3/s ($Fl = 0.080$, $Fr = 0.262$)
Model: $d_b = 3$ mm, Schiller & Naumann drag

	Exp.	(a)	(b)	(c)
Holdup [%]	8.9[a]	4.6	4.6	4.2
$P_{g,\Gamma}/P_\Gamma$	0.54[b]	0.70	0.81	0.70

[a]Interpolated from experimental data of Vrábel et al. (1999)

[b]Experimental data from Vrábel et al. (2000)

Figure 10.15: Effect of discretisation schemes and virtual mass force (VM) on the gas distribution in the fermenter for Case 2. Gas volume fraction contours are given in the mid-baffle plane.

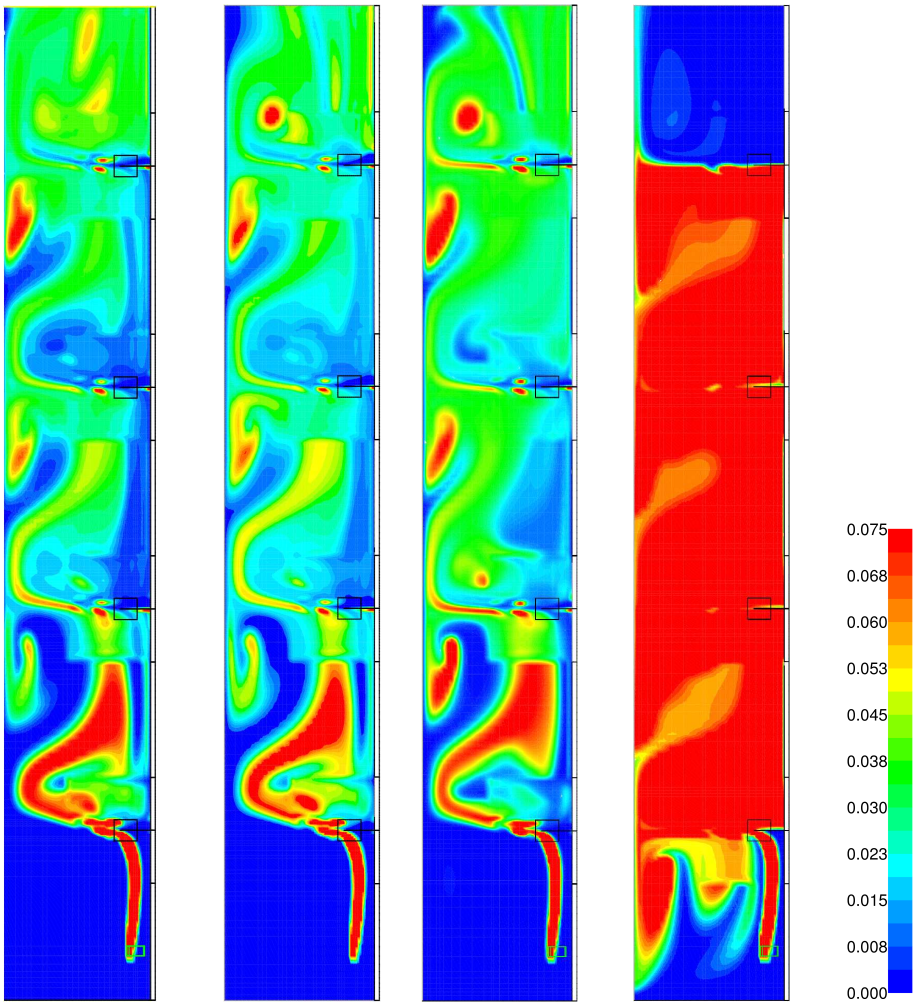

(a) Schiller, degas (b) Schiller, PO (c) Ishii, PO (d) Bru+Ishii, PO

Case 1: 115 rpm, $Q_g = 26.3 \times 10^{-3}$ m^3/s ($Fl = 0.040$, $Fr = 0.262$)
Model: $d_b = 3$ mm

	Exp.	(a)	(b)	(c)	(d)
Holdup [%]	4.7[a]	2.5	2.5	3.0	8.8
Mean axial slip velocity [cm/s]	–	29.1	29.1	23.5	9.7
$P_{g,\Gamma}/P_\Gamma$	0.65[b]	0.63	0.63	0.70	0.83

[a]Interpolated from experimental data of Vrábel et al. (1999)
[b]Experimental data from Vrábel et al. (2000)

Figure 10.16: Effect of different drag correlations and outlet boundary conditions on the gas distribution for Case 1. Outlet boundary conditions are degassing and pressure outlet (PO). Drag correlations are Schiller & Naumann, Ishii & Zuber and the Ishii & Zuber drag law in conjunction with the Brucato turbulence correction. Gas volume fraction contours are given in the mid-baffle plane.

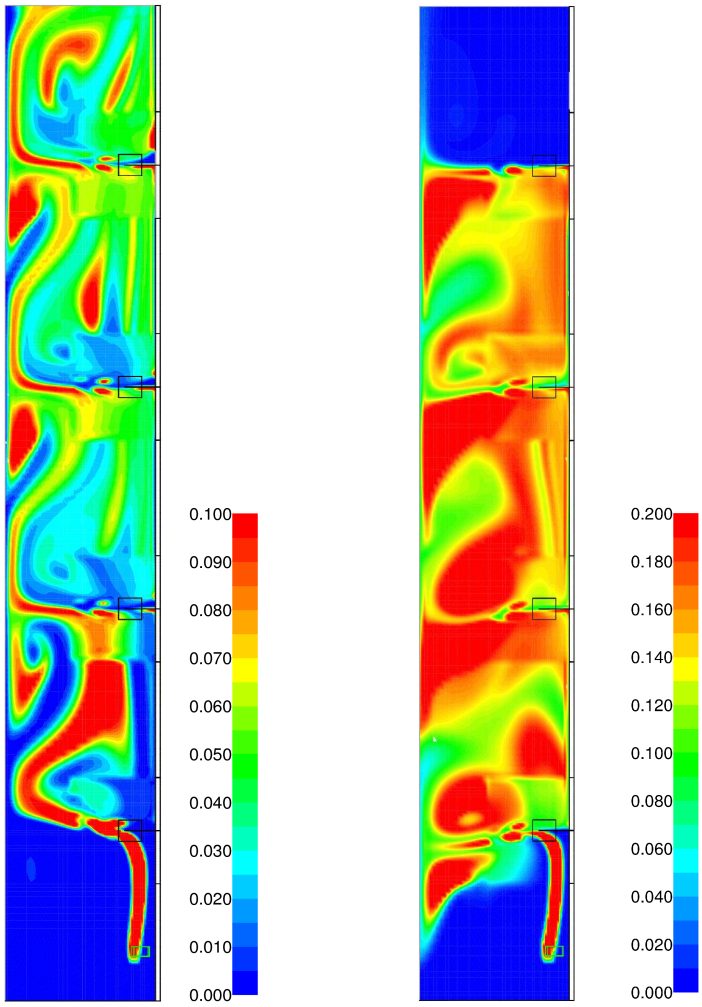

(a) Schiller (b) Bru+Ishii, PO

Case 2: 115 rpm, $Q_g = 52.6 \times 10^{-3}$ m^3/s ($Fl = 0.080$, $Fr = 0.262$)
Model: $d_b = 3$ mm, VM

	Exp.	(a)	(b)
Holdup [%]	8.9[a]	4.2	14.0
Mean axial slip velocity [cm/s]	–	29.0	9.9
$P_{g,\Gamma}/P_\Gamma$	0.54[b]	0.70	0.75

[a]Interpolated from experimental data of Vrábel et al. (1999)

[b]Experimental data from Vrábel et al. (2000)

Figure 10.17: Effect of different drag correlations on the gas distribution for Case 2. Gas volume fraction contours are given in the mid-baffle plane.

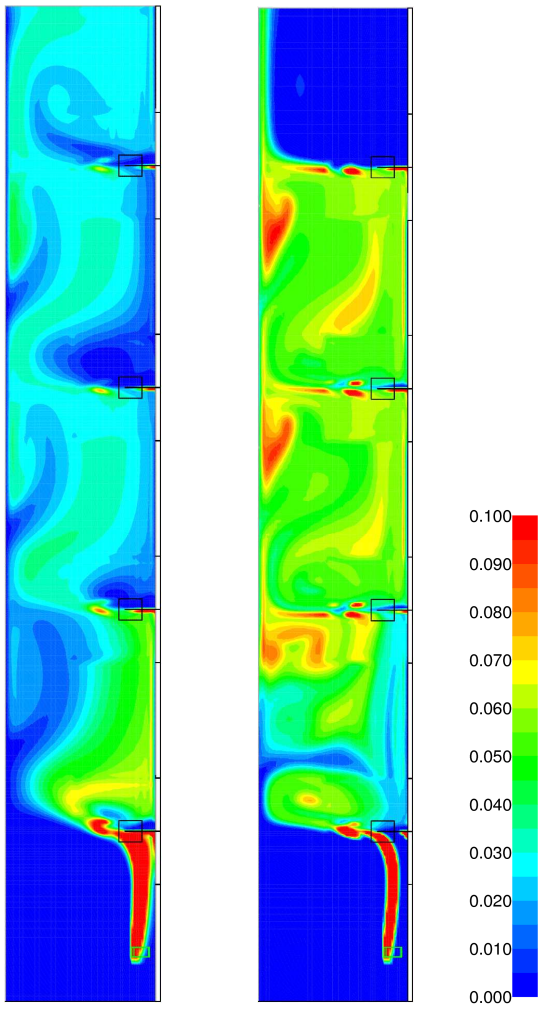

(a) Schiller, 1st Upw (b) Bru+Ishii, PO

Case 3: 70 rpm, $Q_g = 26.3 \times 10^{-3}$ m^3/s ($Fl = 0.066$, $Fr = 0.097$)
Model: $d_b = 3$ mm, VM

	Exp.	(a)	(b)
Holdup [%]	4.0[a]	2.2	4.1
Mean axial slip velocity [cm/s]	–	28.9	14.2
$P_{g,\Gamma}/P_\Gamma$	–	0.90	0.89

[a]Interpolated from experimental data of Vrábel et al. (1999)

Figure 10.18: Effect of different drag correlations on the gas distribution for Case 3. Gas volume fraction contours are given in the mid-baffle plane. Convergence was not possible with a higher-order (second-order upwind) scheme for (a).

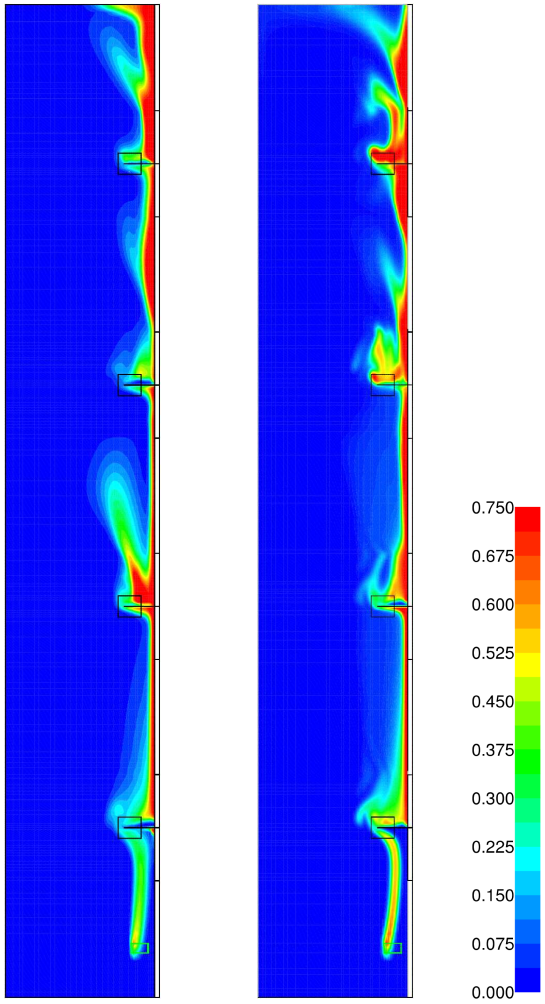

(a) Schiller, 1st Upw (b) Bru+Ishii, PO

Case 4: 70 rpm, $Q_g = 52.6 \times 10^{-3}$ m^3/s ($Fl = 0.131$, $Fr = 0.097$)
Model: $d_b = 3$ mm, VM

	Exp.[a]	(a)	(b)
Holdup [%]	7.3[b]	≈1.8	1.9
$P_{g,\Gamma}/P_\Gamma$	–	≈0.54	≈0.51

[a] Interpolated from experimental data of Vrábel et al. (1999)

[b] Flooding condition was observed (Vrábel et al., 1999)

Figure 10.19: Effect of different drag correlations on the gas distribution for Case 4. Gas volume fraction contours are given in the mid-baffle plane. Convergence of the steady-state simulations was poor at this condition for which the fermenter was reported to be under flooding condition.

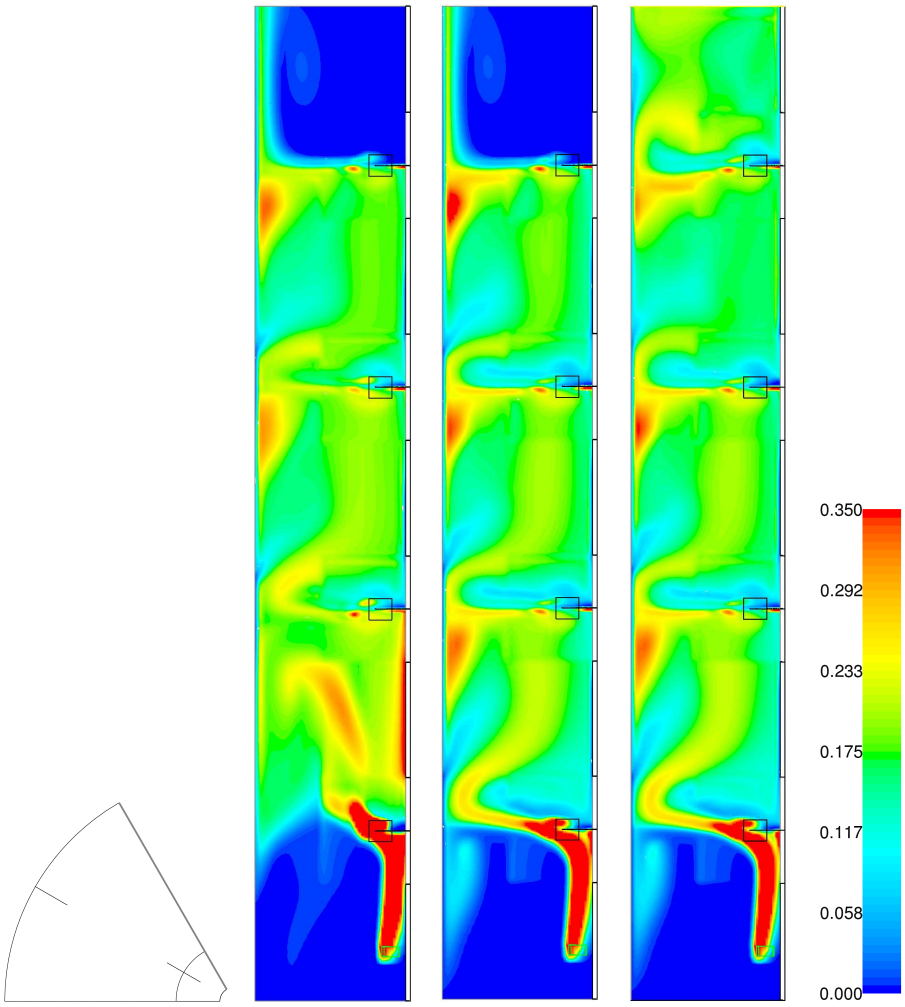

Case 5: 133 rpm, $Q_g = 182.0 \times 10^{-3}$ m^3/s ($Fl = 0.239$, $Fr = 0.351$)
Model: Ishii & Zuber multiparticle, 1st upw., multiphase coupled solver, steady

	Exp.	(a)	(b)	(c)
Holdup [%]	14[a]–17[b]	14.0	13.3	15.5
Mean axial slip [cm/s]	–	24.7	26.7	26.5
$P_{g,\Gamma}/P_\Gamma$	0.38[a]	0.44	0.52	0.50
Mean d_{32} [mm]	–	8.0	9.5	10.0

[a]Experimental data using fermentation broth (Noorman et al., 1994)
[b]Experimental data using air–water system (Vrábel et al., 1999)

Figure 10.20: Dense bubble regime (Case 5) as simulated with the Ishii & Zuber multiparticle drag law. Discrete model (DM) was used for population balances with the bubble size bins given as Set 1 in Table 9.6. Gas volume fraction contours at planes at an angular position of −30° w.r.t. the baffle (i.e. mid-baffle plane).

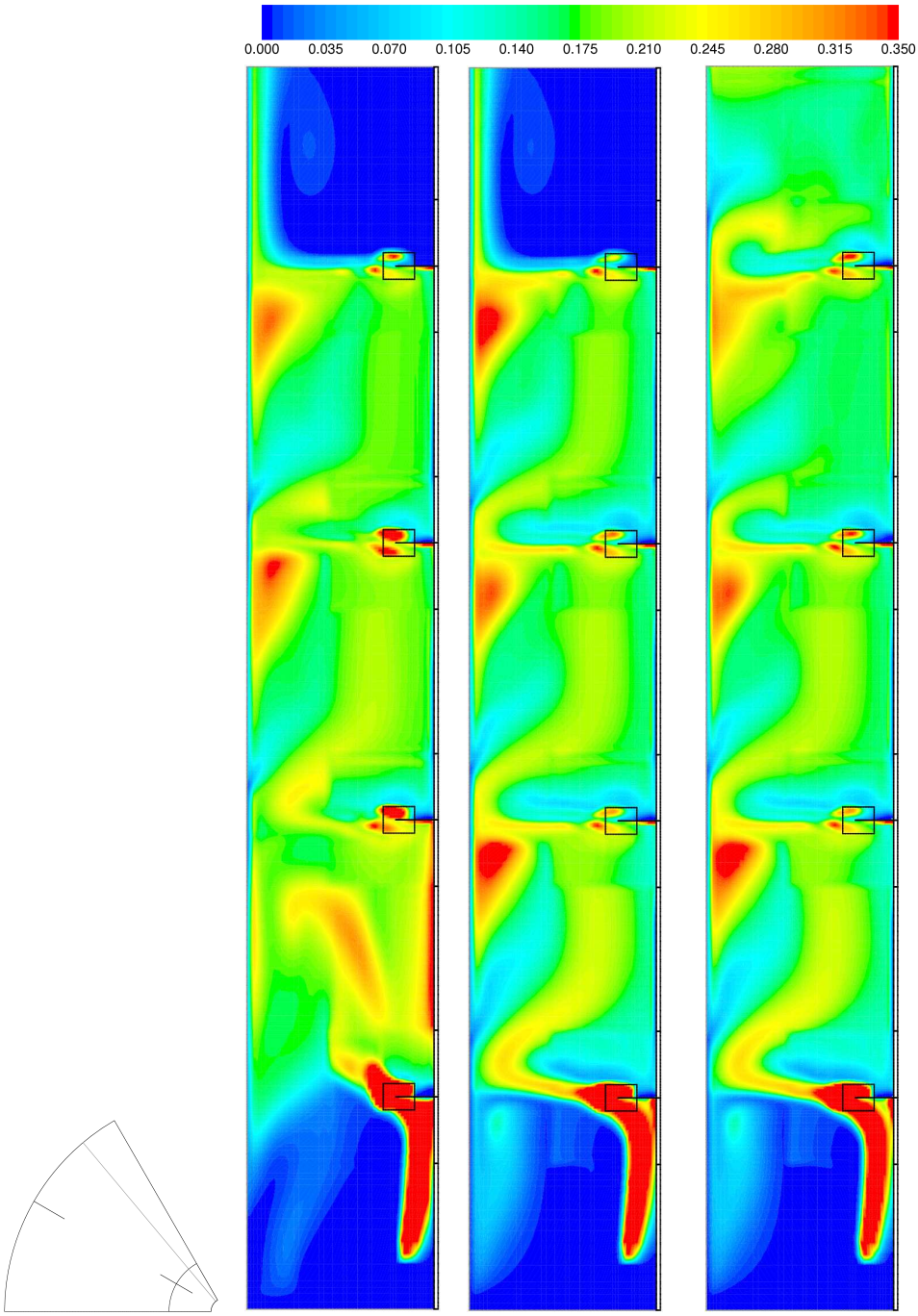

Figure 10.21: $-20°$ planes w.r.t. the baffle (cont. Fig. 10.20).

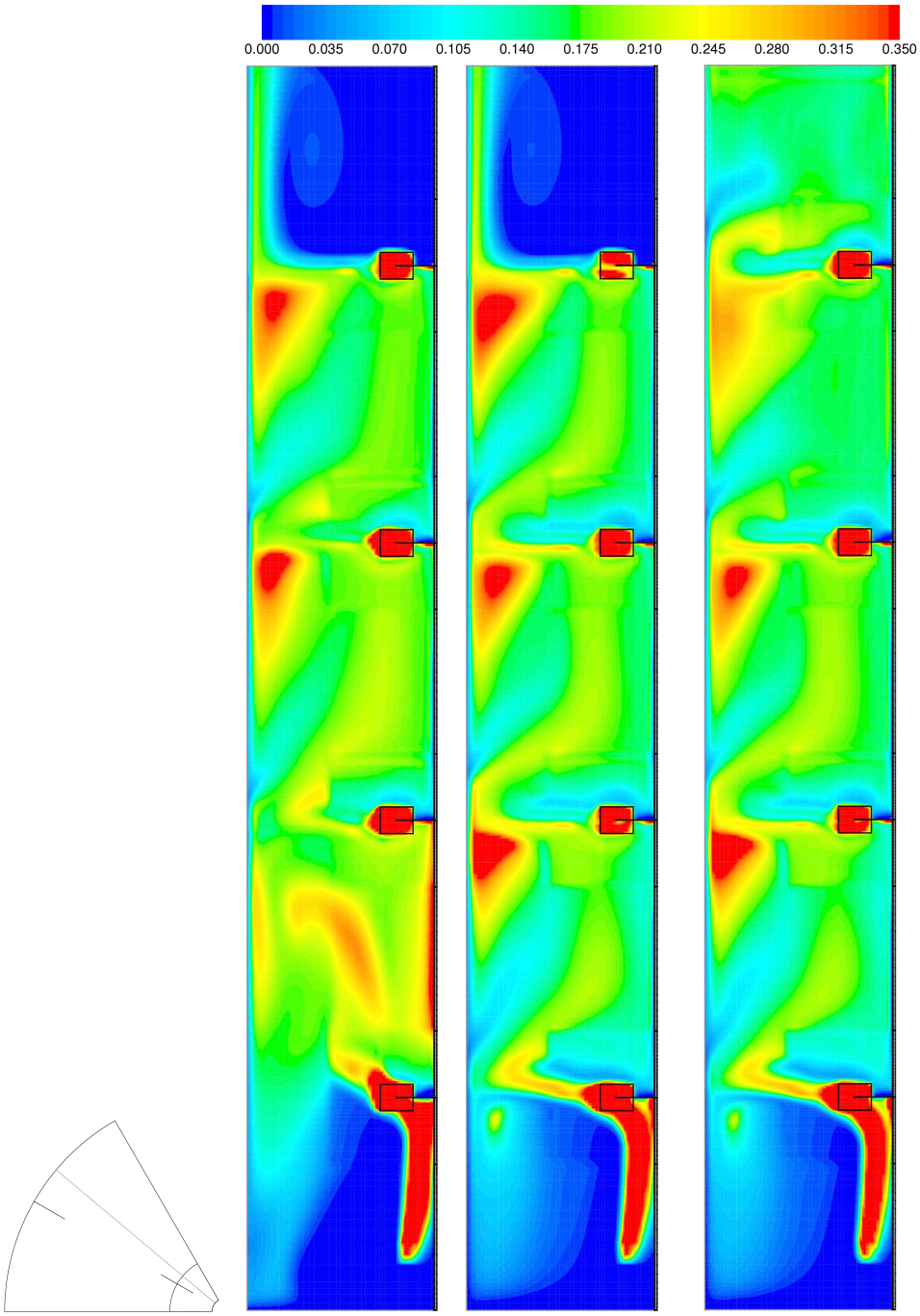

Figure 10.22: $-10°$ planes w.r.t. the baffle (cont. Fig. 10.20).

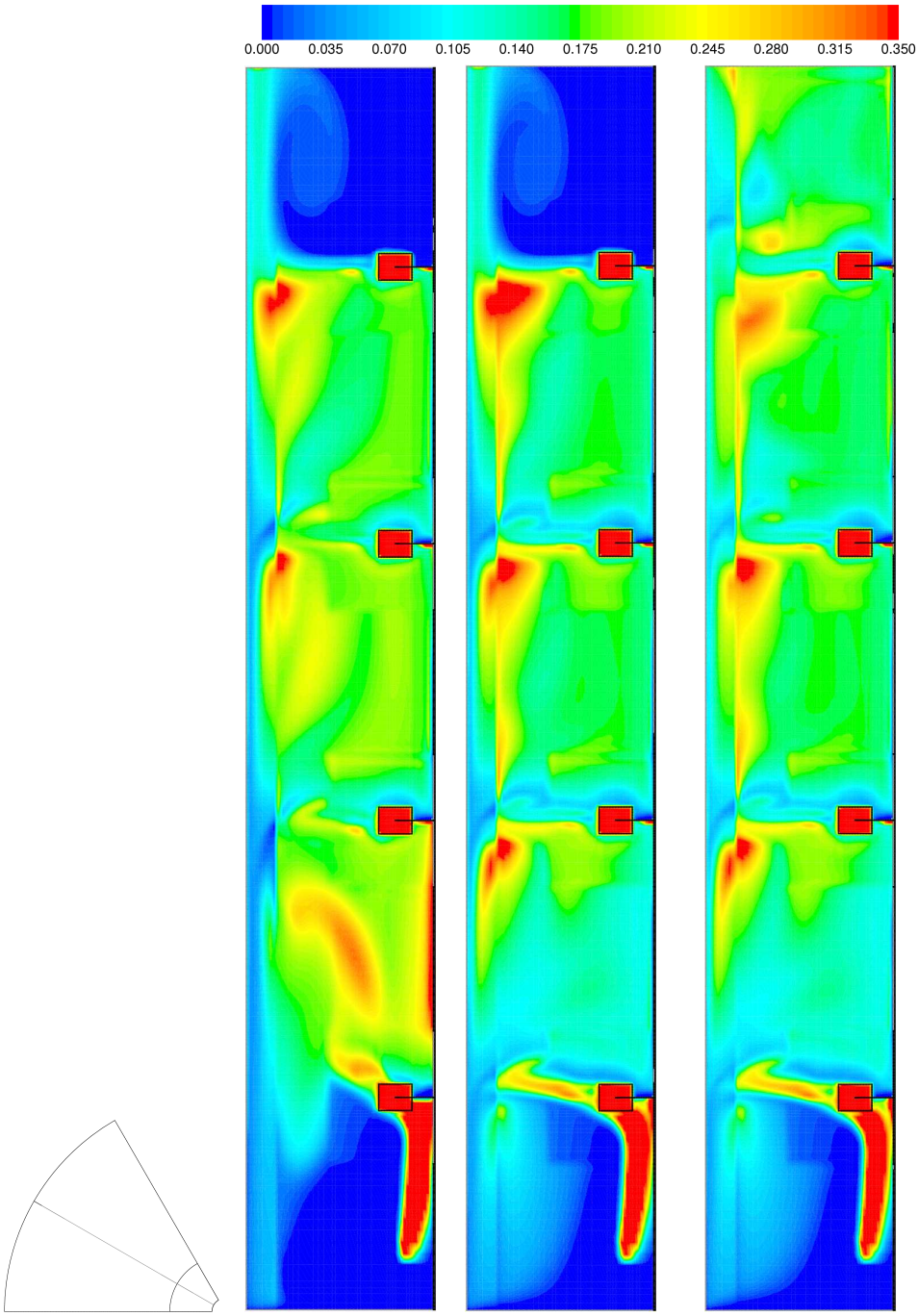

Figure 10.23: 0° planes (i.e. baffle planes) (cont. Fig. 10.20).

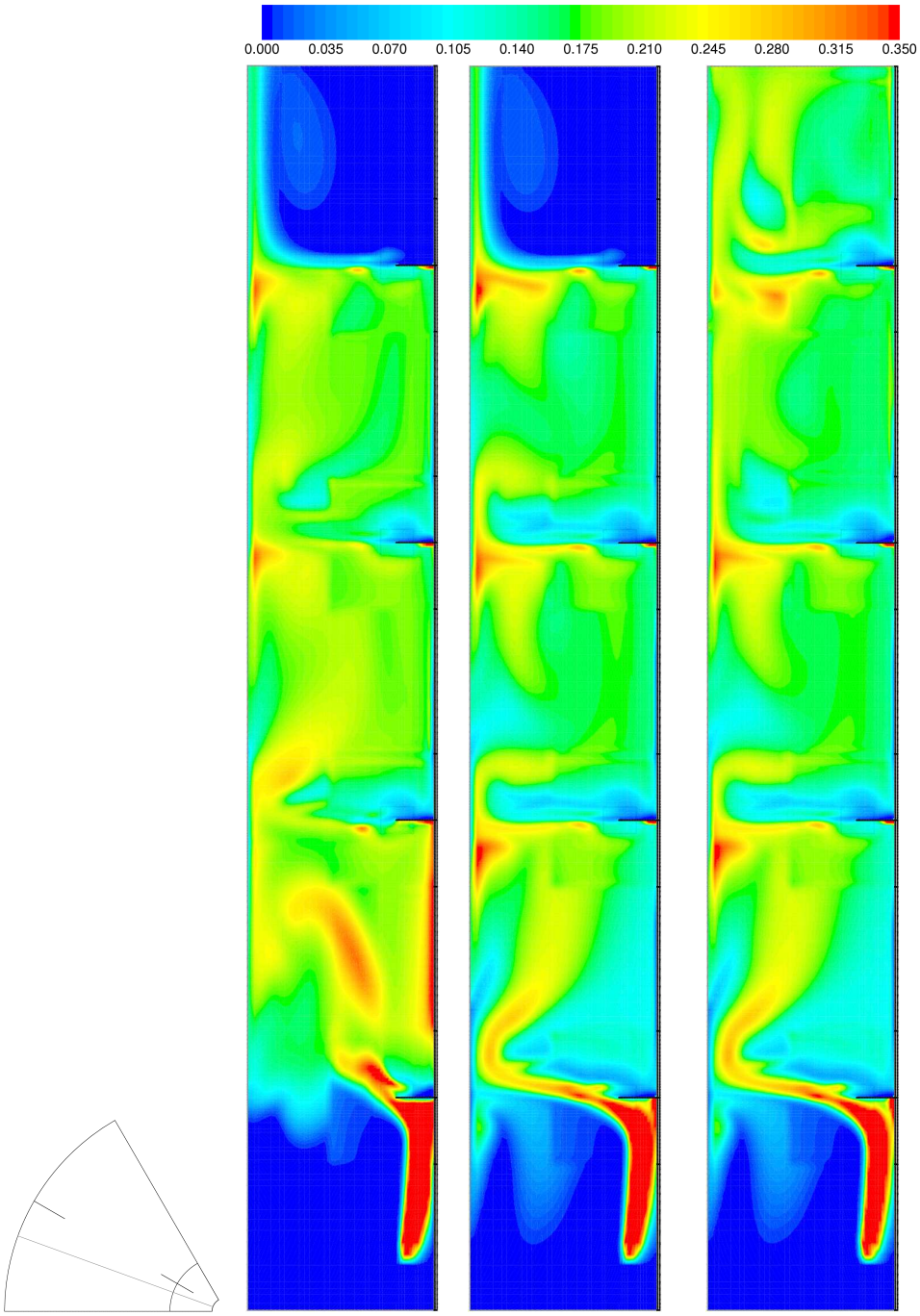

Figure 10.24: 10° planes w.r.t. the baffle (cont. Fig. 10.20).

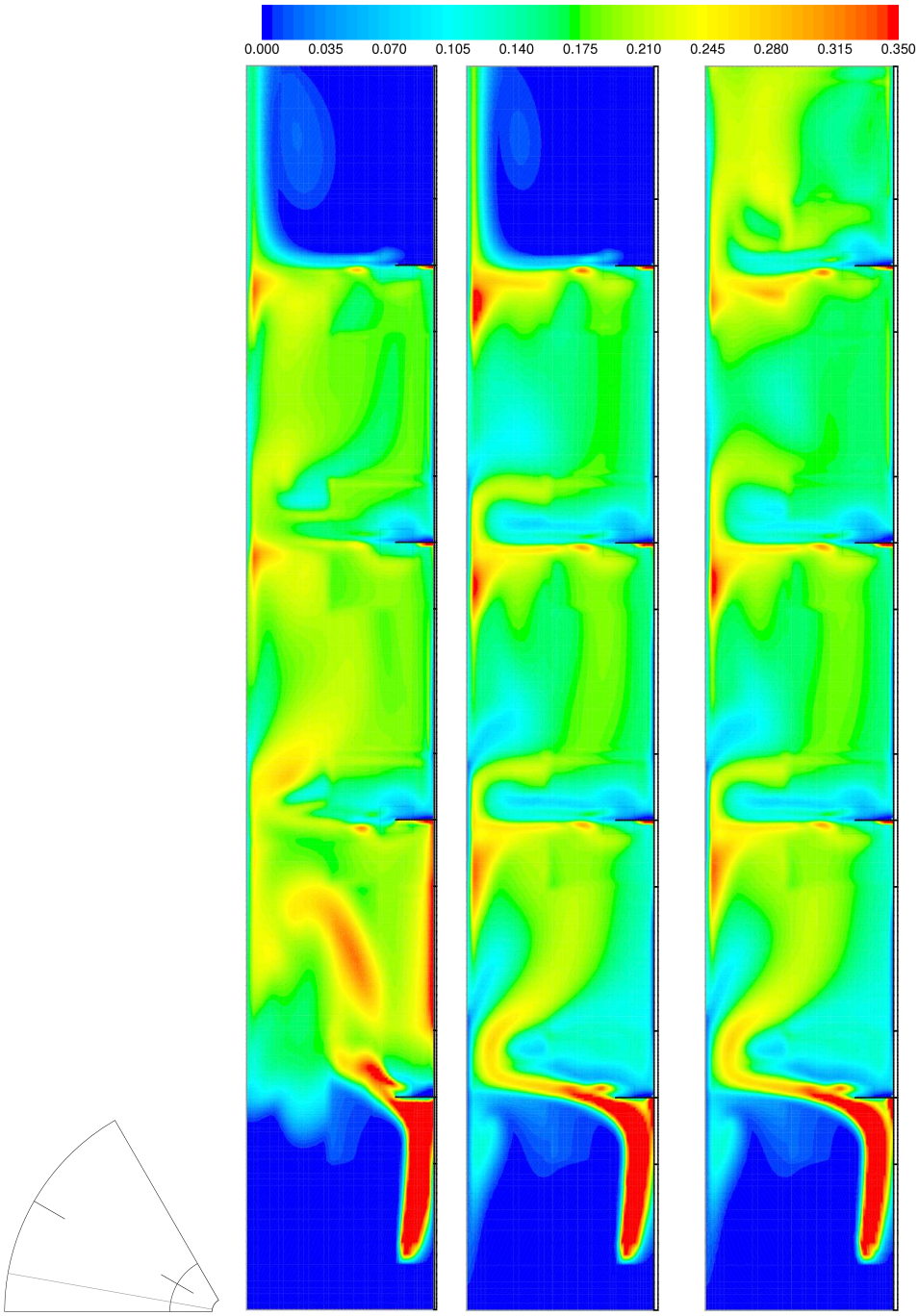

Figure 10.25: 20° planes w.r.t. the baffle (cont. Fig. 10.20).

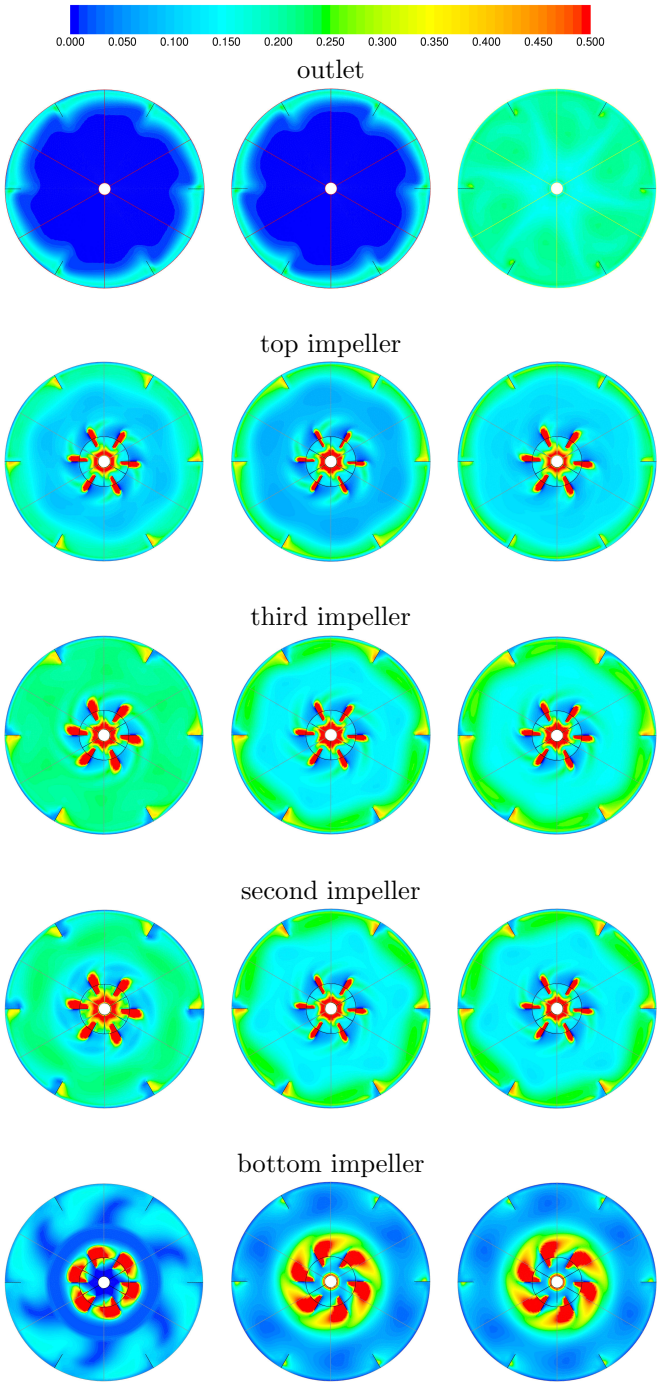

(a) 8 mm (b) DM (c) DM, degas

Figure 10.26: Axial planes (cont. Fig. 10.20).

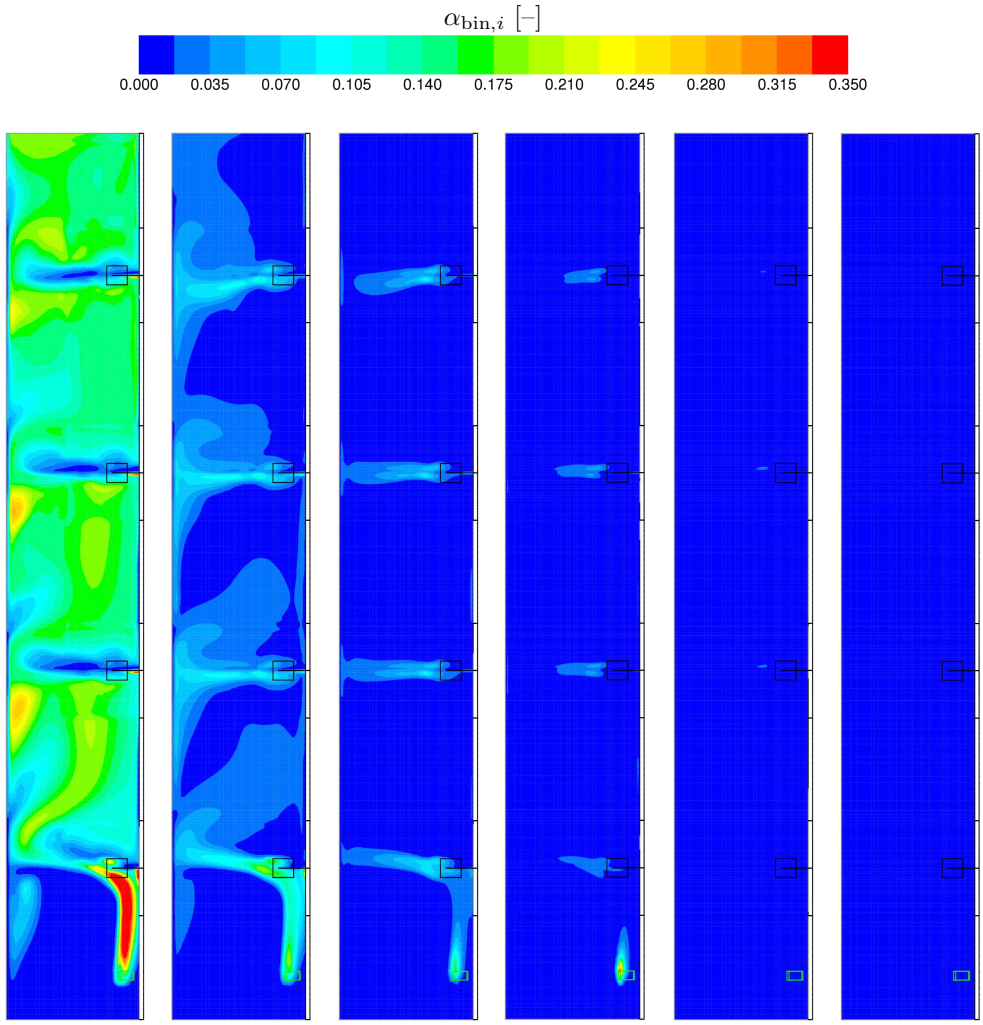

Case 5: 133 rpm, $Q_{\mathrm{g}} = 182.0 \times 10^{-3}$ m^3/s ($Fl = 0.239$, $Fr = 0.351$)
Model: Ishii & Zuber multiparticle, 1$^{\mathrm{st}}$ upw., mp-coupled, steady, DM, degas

Figure 10.27: Spatial distribution of bubble bin volume fraction, $\alpha_{\mathrm{bin},i}$, at mid-baffle plane for the simulation case given in Fig. 10.20(c). Initial bubbles size at the sparger is 3 mm (bin 3).

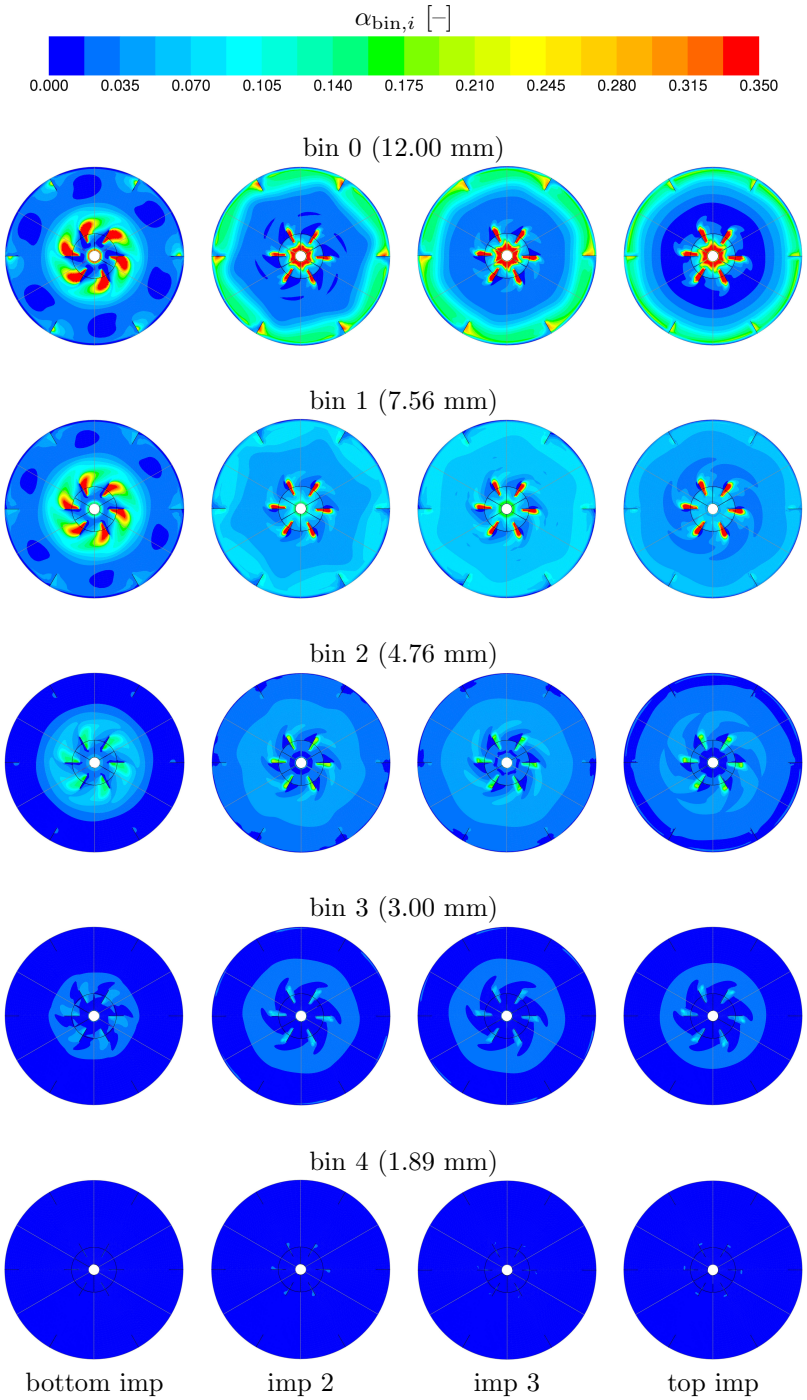

Figure 10.28: Spatial distribution of bubble bin volume fraction, $\alpha_{\mathrm{bin},i}$, at axial planes (cont. Fig. 10.27).

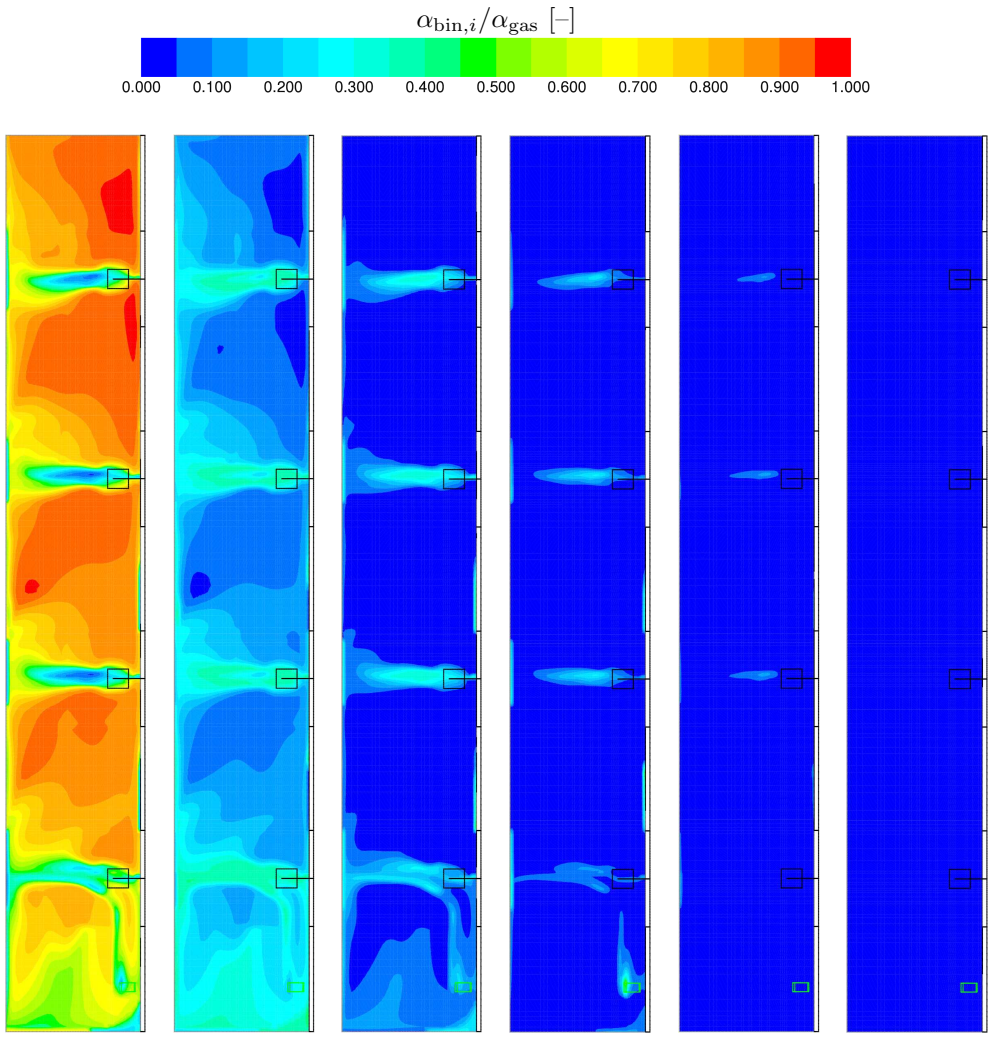

Case 5: 133 rpm, $Q_{\mathrm{g}} = 182.0 \times 10^{-3}$ m^3/s ($Fl = 0.239$, $Fr = 0.351$)
Model: Ishii & Zuber multiparticle, 1$^{\mathrm{st}}$ upw., mp-coupled, steady, DM, degas

Figure 10.29: Spatial distribution of bubble bin fraction, $f_{\mathrm{bin},i} = \alpha_{\mathrm{bin},i}/\alpha_{\mathrm{gas}}$, at mid-baffle plane for the simulation case given in Fig. 10.20(c). Initial bubbles size at the sparger is 3 mm (bin 3).

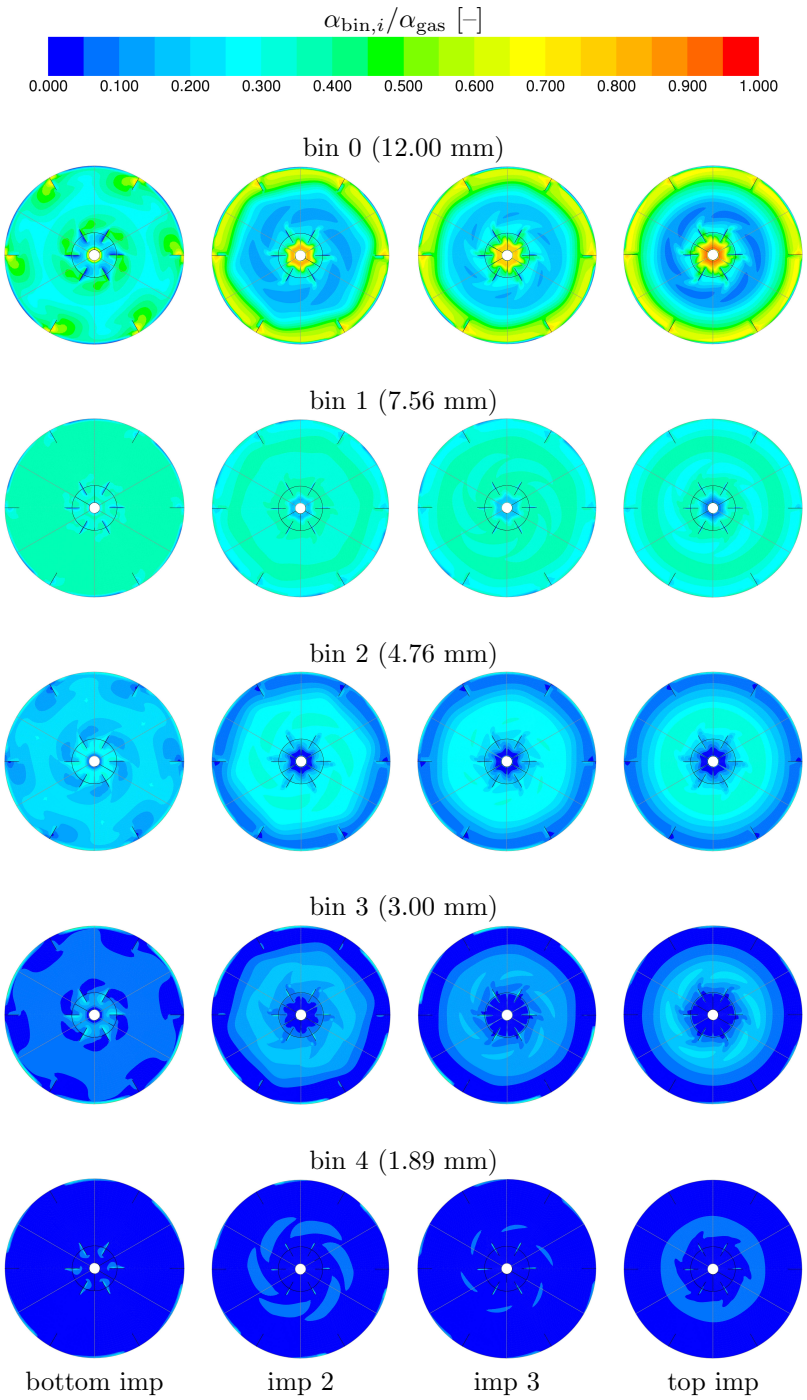

Figure 10.30: Spatial distribution of bubble bin fraction, $f_{\mathrm{bin},i} = \alpha_{\mathrm{bin},i}/\alpha_{\mathrm{gas}}$, at axial planes (cont. Fig. 10.29).

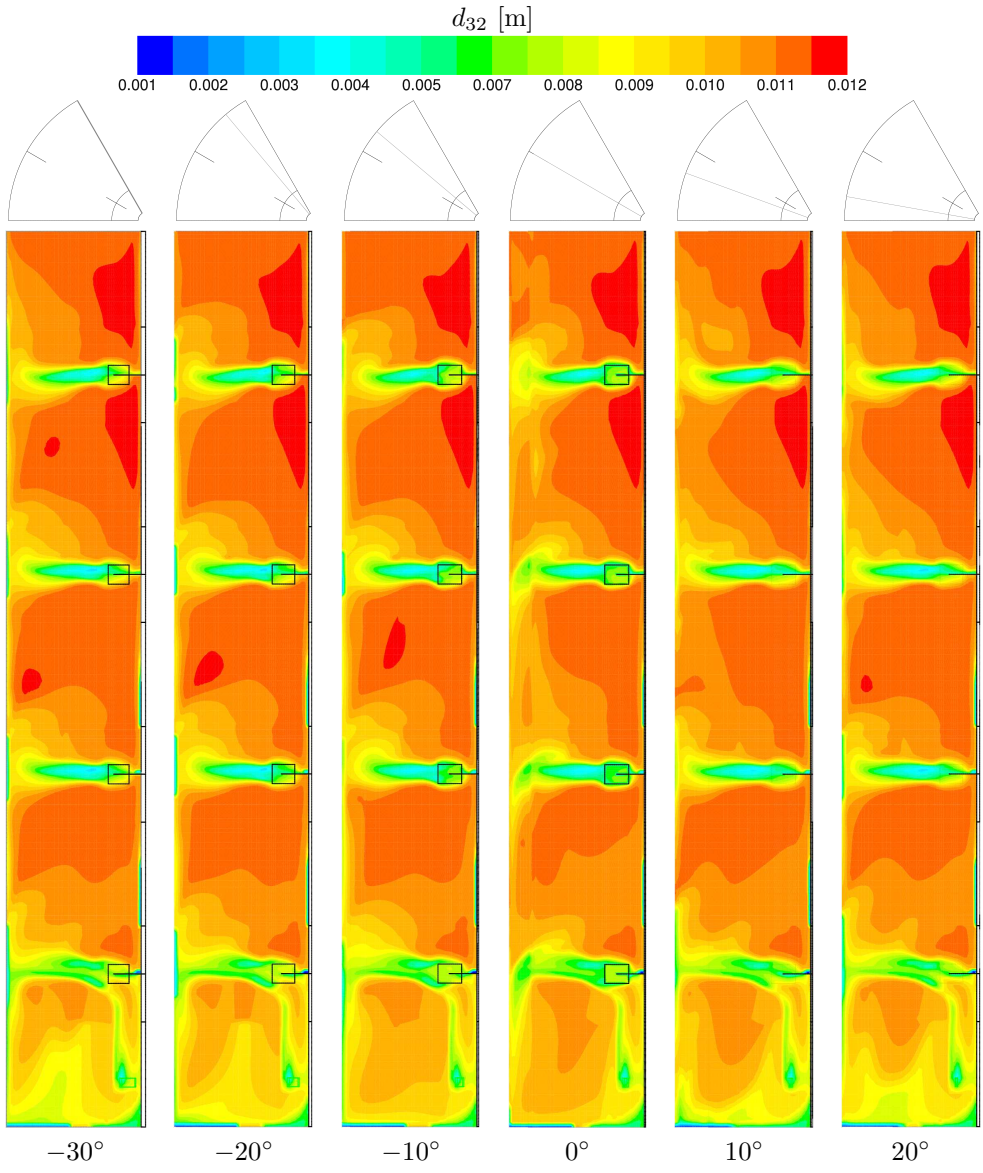

Case 5: 133 rpm, $Q_g = 182.0 \times 10^{-3}$ m^3/s ($Fl = 0.239$, $Fr = 0.351$)
Model: Ishii & Zuber multiparticle, 1st upw., mp-coupled, steady, DM, degas

Figure 10.31: Spatial distribution of Sauter mean diameters (cont. Fig. 10.27).

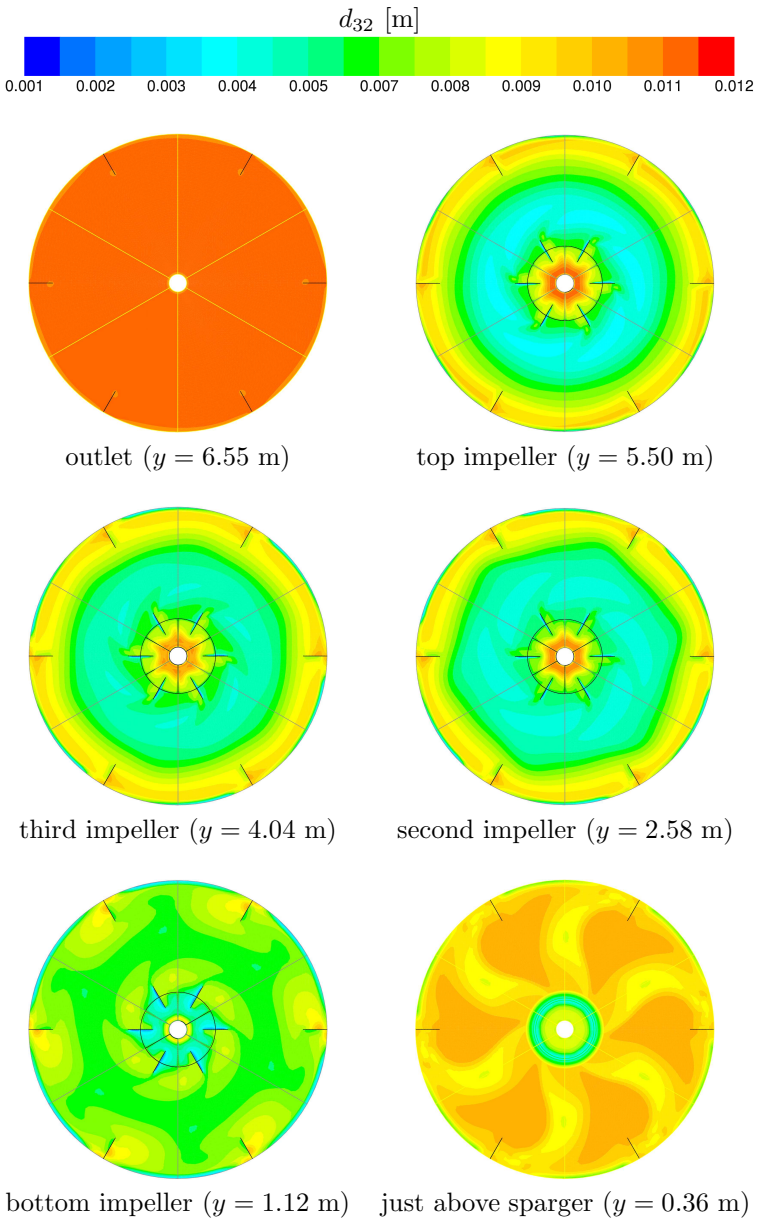

Figure 10.32: Axial planes (cont. Fig. 10.27).

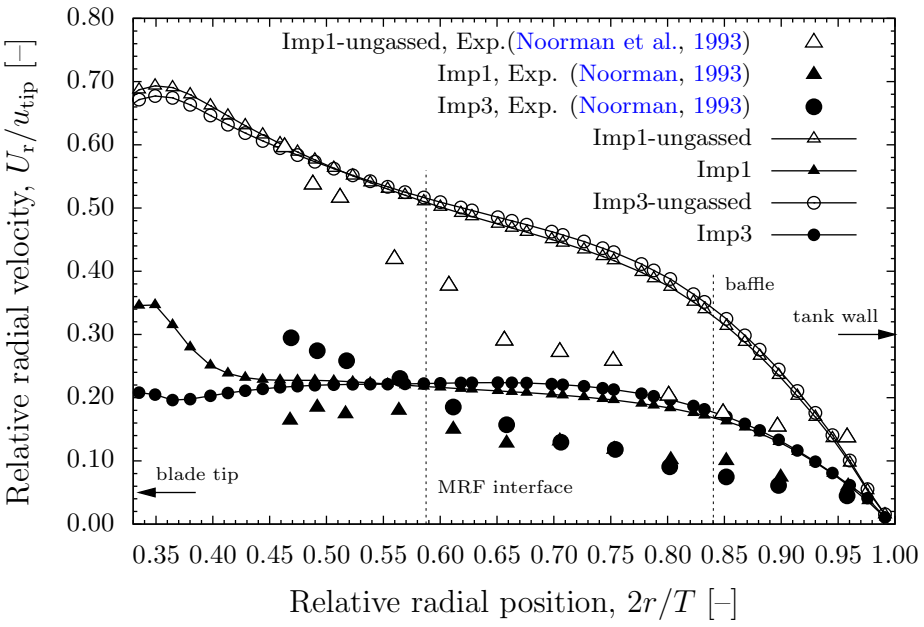

Figure 10.33: Circumferentially averaged mean radial velocity profiles (normalised by tip speed) at the impeller centerline plane for Case 5 (both ungassed and gassed operation). Experimental data at impeller 1 (bottom) and impeller 3 discharge streams (Noorman et al., 1993; Noorman, 1993) are compared to the simulation data (DM + degassing condition).

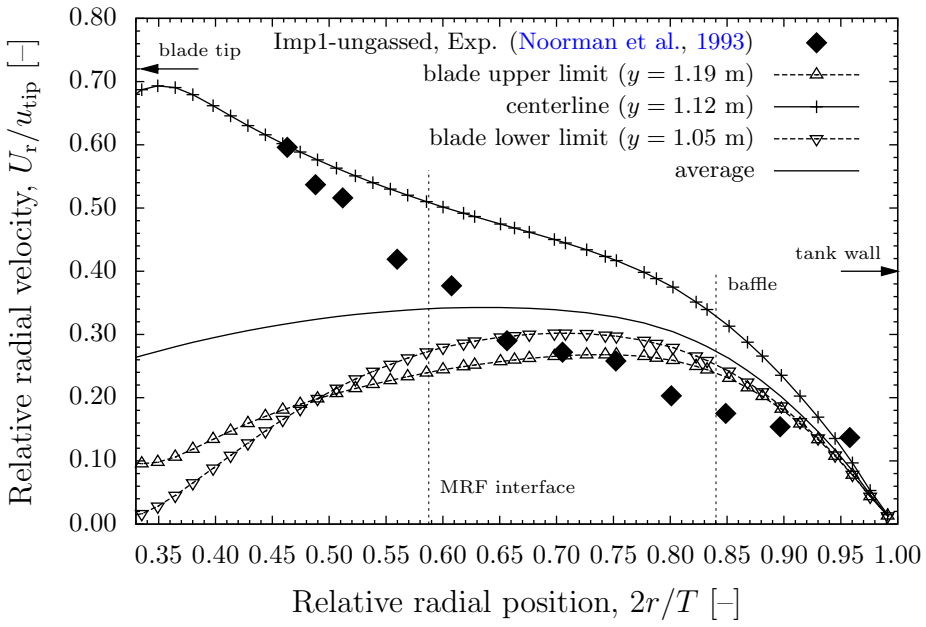

Figure 10.34: Circumferentially averaged mean radial velocity profiles (ungassed operation) for the bottom impeller are given at different axial planes: planes enclosing the impeller blade (upper and lower limits) and the impeller centerline plane. The average of those three profiles is also plotted (cont. Fig. 10.33).

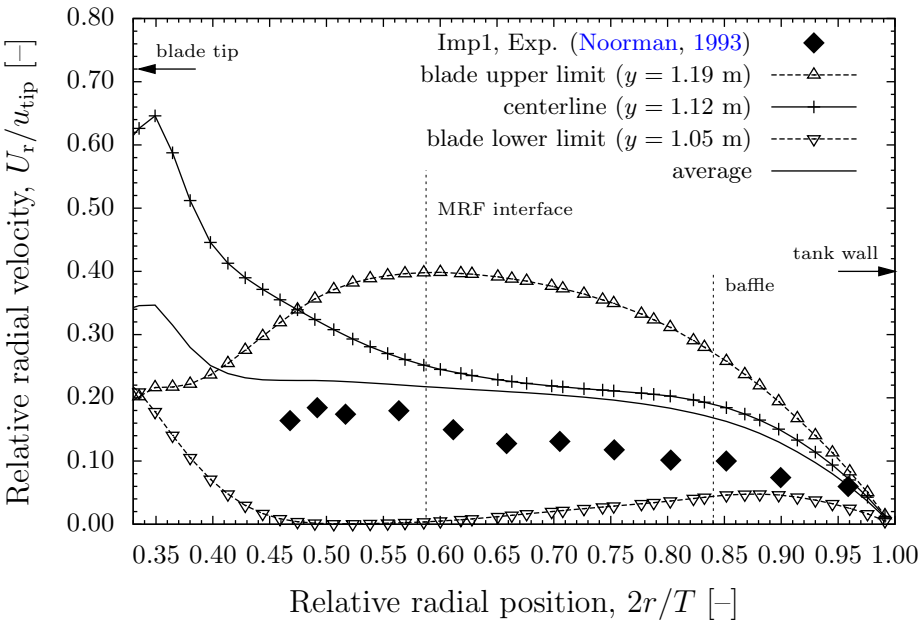

Figure 10.35: Circumferentially averaged mean radial velocity profiles (gassed operation) for the bottom impeller (cont. Fig. 10.34).

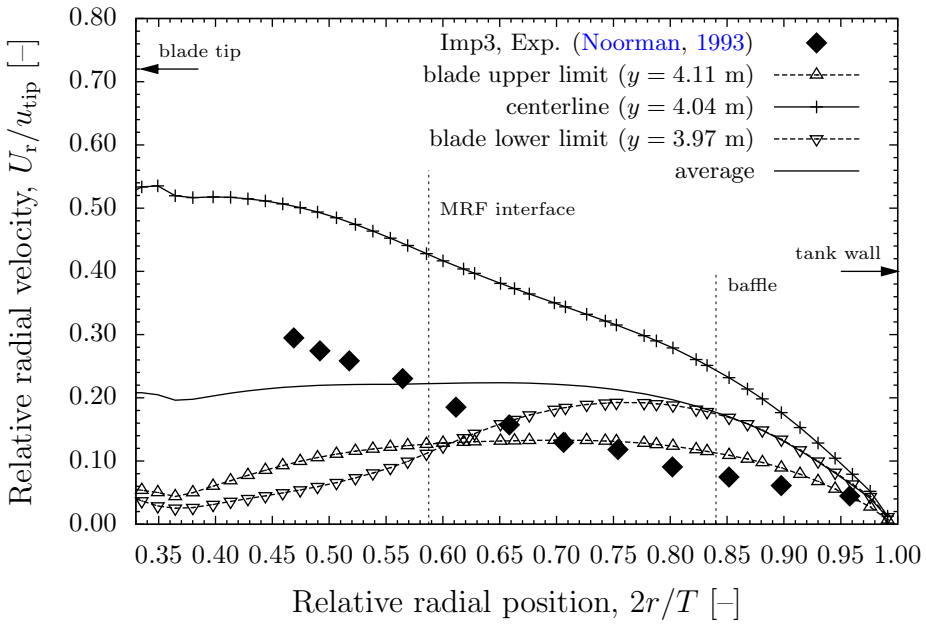

Figure 10.36: Circumferentially averaged mean radial velocity profiles (gassed operation) for the third impeller from below (cont. Fig. 10.34).

Chapter 11

Scalar mixing in the 30 m^3 fermenter

Characterisation of the mixing performance in the fermenter is crucial for the fermentation process, where one needs to ensure that the vital concentrations are kept within the desired limits. For instance, the substrate fed into the fermenter has to be distributed sufficiently fast and uniformly across the whole tank volume. In case of aerobic fermentations, transport rate of O_2 from sparged air bubbles to microorganisms and that of the removal of resultant CO_2 are vital process parameters, which are again determined by the mixing level in the fermenter.

In single-impeller systems, it usually requires several tank volumes to pass through the impeller region so that the relatively large quiescent fluid in the bulk regions is also drawn into the impeller region. As a result, mixing times are longer than the mean circulation times (Tatterson, 1991). In a fermenter with multiple radial impellers, the compartmantalisation of the flow causes larger mixing times, since the flow is divided into gross circulation loops with limited interaction time in a limited volume.

In this chapter, we report on the scalar mixing study conducted in the 30 m^3 fermenter based on the single-phase flow computations presented in Chapter 2. This provides a stepping stone to the kinetical study which is the topic of Chapter 12. Mixing times calculated are compared to the experimental data available for the same fermenter.

11.1 Mixing time and measure of mixedness

In the contex of mixing of two miscible liquids, the mixing time can be defined as the time needed for a liquid volume to be distributed over the total liquid volume to a desired degree of homogenisation on a defined scale. The mixing performance of a stirred tank is usually characterised by an empirical relation, the so-called mixing number, which is the product of the mixing time and the stirring rate, Nt_m, and is constant in fully turbulent single-phase flow. In Section 11.2.1 we reported on some commonly used relations for the prediction of mixing time in stirred reactors.

Roughly speaking, quantitative analysis of the mixing process can be done by appropriate passive tracer mixing experiments to give the homogenisation time, i.e. the mixing time. A passive tracer is introduced into the domain (usually at a convenient location such as from the free surface of a tank) and tracer concentrations at different locations are monitored. Mixing times to achieve a given degree of homogeneity (e.g. t_{95} for 95% homogeneity) can be calculated then from the time series data. There is, however, no unique definition on the way the degree of homogeneity is defined.

Some commonly used approaches are outlined below that describe the concentration variations in mixing equipment differently. We made an attempt to write them in a way such that an uniformity index, U, can be defined where $U = 1$ indicates perfect mixing in all cases:

- Relative concentration used as a measure of concentration variation:

$$U_{c/\overline{c}} = \left| \frac{c(t) - c_0}{\overline{c} - c_0} \right|, \tag{11.1}$$

  which, when starting from intial concentration $c_0 = 0$, reduces to $U_{c/\overline{c}} = c(t)/\overline{c}$. Here, $\overline{c}$ is the global mean concentration, which is equal to the final concentration in perfectly mixed state ($\overline{c} = c(t = \infty)$). Mixing time is then defined as the time it takes for the measured concentration $c(t)$ to stay within a given range of the final mean concentration $\overline{c}$. Hence, 95% homogeneity is reached at time t_{95} when $0.95 \leq c(t)/\overline{c} \leq 1.05$.

- Mean-square fluctuation in concentration (i.e. variance of concentration, σ_c^2) used in turbulent mixing as the statistical measure of the departure from mixture uniformity:

$$U_{\sigma_c^2} = 1 - \sigma_c^2 = 1 - \overline{(c')^2}. \tag{11.2}$$

  Since the instantaneous concentration is the sum of mean and fluctuating parts, $c'(\mathbf{x}, t) = c(\mathbf{x}, t) - C$.

- Coefficient of variation (CoV) used as a measure of concentration variation:

$$U_{CoV} = 1 - CoV = 1 - \frac{\sigma_c}{\overline{c}} = 1 - \sqrt{\frac{1}{N_\mathrm{m}} \sum_{i=1}^{N_\mathrm{m}} \left(\frac{c_i - \overline{c}}{\overline{c}} \right)^2}. \tag{11.3}$$

  Here, N_m is the total number of measurement locations and c_i is the molar concentration at the measurement location i. CoV can be normalised by the initial concentration variance in order to remove the effects of the initial state of the system. Then $U_{CoV} = 1 - CoV/CoV_0$ could be used as the uniformity measure.

- Largest deviation from mean, Δ_max, used as a measure of variation, which can be normalised by the global mean concentration:

$$U_{\Delta_\mathrm{max}} = 1 - \frac{\Delta_\mathrm{max}}{\overline{c}} = 1 - \frac{\max(c_\mathrm{max} - \overline{c}, \overline{c} - c_\mathrm{min})}{\overline{c}}, \tag{11.4}$$

  where c_max and c_min are the minimum and maximum concentrations measured.

- Largest deviation from mean at t scaled with that at $t = 0$:

$$U_{\Delta_{\max}/\Delta_{\max,0}} = 1 - \frac{\Delta_{\max}(t)}{\Delta_{\max}(t=0)} = 1 - \frac{\max(c_{\max} - \overline{c}, \overline{c} - c_{\min})}{\max(c_{\max}(t=0) - \overline{c}, \overline{c} - c_{\min}(t=0))}, \tag{11.5}$$

Note that above listed measures quantify how widely the concentration varies (i.e. the intensity of segragation), but do not contain any information about spatial arrangement and the length scale of blobs of different concentrations in the domain (i.e. the scale of segragation). Therefore, it is not alone sufficient to describe mixing.

A thorough analysis of wide range of industrial mixing problems (with objectives ranging from blending of miscible liquids to mixing in multiphase systems with possible particle size reduction, mass transfer and/or homogenous or heteregenous reactions), reveals three variables that are directly related to mixing objectives (Kukukova et al., 2009):

- a reduction in the segregation of concentration,
- a reduction in the scale of segregation,
- a mixing time scale to be accomplished or predicted.

Mixedness, i.e. the quality or state of being mixed, depends on the state of segregation of the system. Following from above variables, segregation is proposed to have three dimensions (Kukukova et al., 2009):

1. **Intensity of segregation:** The intensity of segregation is related to the instantaneous concentration variance. It's a measure of the molecular diffusion process, i.e. difference between purest concentration of A in the pocket A and that in the surrounding fluid B. The mechanism is purely molecular diffusion as even the smallest eddies are much larger than molecules. Intensity of segregation is quantified by the coefficient of variation, CoV (Eq. 11.3). It is evident from the equation of CoV that the intensity of segregation measures how widely the concentration varies, but no information is contained about the characteristic length scales or how fluid packets are arranged within the system. For this, we need the information about the scale of segregation of the system.

2. **Scale of segregation (striation thickness) or clustering:** The scale of segregation is related to the instantaneous length scales in the mixing domain. It's a measure of dispersion process due to convection and eddy motion (eddy diffusivity); i.e. size of the packets of A in the surrounding fluid B.

3. **Exposure or potential for reduction in segregation:** The last dimension, exposure, measures the instantaneous rate of reduction in segregation, i.e. the mixing time scale, or the driving force for change. It's a non-linear function of both intensity and scale of segregation and analogous to rate of mass transfer across an interface; larger interfacial area and concentration gradients give larger potential for mass transfer and exposure. In the course of turbulent mixing, the interfacial area rapidly increases while the concentration difference drops

continuously due to convective mass transfer. Those two counteracting local effects of scale and intesity make the exposure behave in complex ways. On top of this, further complexity originates from the fact that the scales of segregation are distributed over a range of values, and are themselves correlated to the interfacial area in a non-linear way.

Overall, in industrial mixing problems, all three variables explained above have a crucial role.

11.2 Turbulent mixing scales

Species mixing occurs across different length and time scales. Three distinct mixing scales are usually identified, namely the macro–, meso– and micromixing. Macromixing, also known as blending, occurs at the largest scales (that of the mixing equipment) due to convection. Micromixing refers to mixing at the smallest turbulent eddies and concentration striations. Mesomixing characterise the mixing at all intermediate scales. It occurs most typically near a feed pipe in a stirred tank reactor. When the feed rate is greater than the local mixing rate (i.e. the time constant for local mixing to molecular scale which depens on geometry, local shear rates and physical properties), this gives rise to a plume of higher concentration spreading from the feed location (Patterson et al., 2004). Alternatively, when the feed pipe is small such that the integral lenght scale of scalar is smaller than that of velocity (thus turbulence), mixing is faster than that in the bulk where those two length scales are similar. This process is described as mesomixing as it operates in scales smaller than macroscales but still larger than microscales (unless feed pipe and/or feed rate is very small) (Fox, 2003; Bałdyga and Bourne, 1999). Mixing is achieved ultimately by molecular diffusion, however hydrodynamic conditions in above given mixing scales are the time controlling factors in achieving a uniform mixture.

In chemical reaction engineering (CRE), it's common practice to model chemical reactors by a combination of two idealised flow models, namely plug-flow reactors (PFRs) and continuous-stirred-tank reactors (CSTRs). The PFR model is based on the turbulent pipe flow limit; all fluid elements entering the reactor leave the reactor at the same time with the same age. Mixing between fluid elements at different axial locations is neglected and that at the same axial location is assumed to be infinitely fast. Hence, concentration is uniform over the cross-section of the reactor and all fluid elements are said to be well micromixed (Fox, 2003). However, the PFR is not well macromixed since a fluid element's location in a PFR is a linear function of its age. In the CSTR model, on the other hand, it is assumed that no concentration gradients exist due to intense stirring. Consequently, the fluid is both well macromixed (a fluid element's location is independent of its age) and well micromixed (a fluid element's concentration is independent of its age due to interactions with other fluid elements).

From statistical point of view, well macromixed implies scalar means are independent of position, $C = C(t)$ only (statistical homogeneity in space), and well micromixed implies that scalar variances are null, $\sigma_c^2 = 0$ (Fox, 2003). We shall now further characterise those turbulent mixing scales.

11.2.1 Macromixing (bulk blending)

Macromixing determines bulk concentration gradients, which, in turn, define the environment concentrations in which meso– and micromixing take place. Therefore, the first criterion that a mixing equipment should meet is to ensure effective bulk mixing. Only after this can the finer scale mixing and molecular diffusion occur at a reasonable rate. Localised fine scale mixing of (initially segregated) streams which remain segregated on the large scale has no effect on the overall mixing (Patterson et al., 2004).

At the macroscales of the order of the process equipment size, transport of conserved quantities by bulk fluid motion (i.e. convection) is usually the dominant transport mechanism for momentum, heat and mass. Hence, the mean flow field is important. In the absence of effective bulk circulation (e.g. in pipe flow), the key criterion to achieve effective bulk mixing is that the largest scale of motion in the mixer must be larger than the largest scale of segregation in the feed (Kresta and Paul, 2004). This means, the integral turbulent scale should be larger than the integral scale of concentration fluctuations, $L > L_C$ (hence the turbulence spectrum is important).

Macromixing is characterised by the macromixing time scale, also reffered to as the blending time, in a batch sytem. It is usually expressed as the time that the concentration differences are reduced by 95% everywhere in the whole tank. It may depend on the position of addition of the feed, but not on the location of the concentration measurement. Usually, the slowest rate of mixing in the tank determines the bulk blending time.

Single-impeller, single-phase systems

In a stirred tank, typically certain number of tank turnovers (circulations), n, are required to reach a desired degree of macromixed state ($t_m = n \cdot t_c$). Therefore many earlier studies linked the macromixing time scale to either the mean circulation time ($t_m = n \cdot t_c = n\mathcal{V}_{tank}/Q = n\mathcal{V}_{tank}/N_Q N D^3$) or to the circulation time based on the longest circulation path in the reactor (e.g. Joshi et al. (1982)).

Later experimental studies showed that an empirical relation, which is also linked to the turbulence theory, can give very good predictions for a wide variety of tanks and impeller types. This relation, which is valid for a single-impeller stirred tank with $H = T$ operating in turbulent regime, is recommended for all impellers and all scales, and given by Grenville and Nienow (2004):

$$t_{95\%} = 5.2 \left(\frac{1}{N}\right) \left(\frac{1}{N_P}\right)^{1/3} \left(\frac{T}{D}\right)^2, \tag{11.6}$$

where t_{95} denotes the mixing time for 95% homogeneity. The striking result is that the mixing time is independent of the impeller type.

Macromixing time is usually expressed in a dimensionless form by multiplying it with the stirring rate to give the so-called mixing number, Nt_m. In fully turbulent flow, the mixing number is independent of Re and constant, though it was reported to increase with the scale (van't Riet and Tramper, 1991). This is also evident in Eq 11.6, that is, Nt_m = constant, since the power number is constant. At constant impeller speeds, $t_m \propto (T/D)^2$.

Rearranging Eq 11.6 and inserting the definition of the impeller power number, $N_P = P/\rho N^3 D^5 = \overline{\varepsilon}\mathcal{V}_{\text{tank}}/N^3 D^5$ ($\overline{\varepsilon}$ being energy dissipation rate per unit mass) gives, for $H = T$,

$$t_{95\%} \propto \left(\frac{1}{\overline{\varepsilon}}\right)^{1/3} \left(\frac{T}{D}\right)^{1/3} T^{2/3}. \tag{11.7}$$

This relation shows that, when scaling up with geometric similarity and equal power per unit mass, $t_{\text{m}} \propto T^{2/3}$. Furthermore, all impellers of the same diameter are equally energy efficient (same t_{m} achieved at the same $\overline{\varepsilon}$), and for the same $\overline{\varepsilon}$, mixing time is shorter with a larger impeller diameter. Eq. 11.6 and 11.7 were reported to give very good agreement with the experimental data, under both ungassed and gassed operation (provided that the impeller is not flooded), for different impeller types with very different D/T ratios, power numbers and flow patterns, and over a wide range of mean energy dissipation rates (Nienow, 1997).

The same functional relationship is found following the turbulence concepts from Corrsin (1964). In essence, it was suggested that the mixing time is inversely proportional to turbulent diffusion (Nienow, 1997):

$$t_{\text{m}} \propto (\varepsilon/L^2)^{-1/3}. \tag{11.8}$$

The critical assumption is that mixing time is determined by the lowest mixing regions, i.e. the flow away from the impeller at the regions with lowest energy dissipation rate ε (and not that in the vicinity of the impeller as one might intuitively guess). Hence, the relevant integral turbulent scale is that related to the tank diameter and not to the impeller diameter ($L \propto T$) and the relevant ε is that close to the tank wall (see also Section 11.2.2 for a discussion of the Corrsin mixing time).

Multi-impeller, single-phase systems

In a multi-impeller system with radial pumping impellers, the circulation flows are segregated between the impellers, leading to so-called axial flow barriers. Thus, although Eq. 11.6 suggests that the macromixing time is independent of impeller type in single-impeller systems, it is strongly affected by the impeller type in multi-impeller sytems.

Cui et al. (1996a) and Vrábel et al. (1999, 2000) studied the scalar mixing in the 30 m^3 fermenter. Variety of impeller combinations have been used. Measurements of Vrábel et al. (2000) using two different configurations, 4 Rushton turbines and Scaba type axial/radial turbine combination (bottom impeller being radial, remaining impellers being axial), showed that the mixing time was proportional to $\overline{\varepsilon}^{-1/3}$ as predicted from Eq. 11.7. The mixing time was reduced by a factor of about 2 when the axial/radial impeller combination was used instead of four radial impellers. This was attributed to the zoning (compartmentalisation) of the flow with the radial impellers (see Section 10.3.1) and the resulting axial flow barriers. Turbulent exchange would enhance the mixing across those axial flow barriers. Thus they also measured the axial velocity fluctuations in the bulk region away from the impellers (location was not specified) which were about $u'_y = 0.05 u_{\text{tip}}$ for both radial and radial/axial impeller configurations.

Similar observations were made also in earlier studies. The mixing time with axial flow impellers was found to be decreased by a factor of about 2 compared to that

with radial impellers at the same specific energy dissipation rate (Cooke et al., 1988; Nienow, 1998).

Mixing time correlations for multi-impeller systems are very limited compared to the single-impeller systems. No general purpose correlation for multiple impeller geometries exists to date (Cui et al., 1996a; Magelli et al., 2013). A commonly referred correlation for multiple Rushton turbines is that from Cooke et al. (Cooke et al., 1988; Nienow, 1998) which is similar to Eq. 11.6:

$$t_{95\%} = 3.3 \left(\frac{1}{N}\right) \left(\frac{1}{N_P}\right)^{1/3} \left(\frac{H}{D}\right)^{2.43}. \tag{11.9}$$

Based on the hyphothesis that the fundementals of mixing process are not system specific, Groen (1994) developed a universal mixing time correlation for both bubble columns and stirred tanks. The approach stems from a diffusion model where the diffusion coefficient is predicted from an application of Kolmogorov's theory for the inertial subrange to give:

$$\frac{t_{\mathrm{m}}\varepsilon^{1/3}}{T^{2/3}} = C(\gamma)^{-1/3} \left(\frac{H_{\mathrm{blade}}}{T}\right)^{-4/3} \left(\frac{L_{\mathrm{s}}}{H}\right)^{2} \left(\frac{H}{T}\right)^{2}, \tag{11.10}$$

where $C = 0.374$ for top injection and bottom detection which is the typical way the pulse-response studies are performed, and which gives the worst case approximation for the mixing time. The parameter γ is related to the material viscosity (or flow index for non-Newtonian fluids); for water and most fermentation broths (i.e. Newtonian fluids), $\gamma = 39.1$. For standard Rushton turbines, impeller blade height is given by $H_{\mathrm{blade}} = D/5$. The diffusion length is taken as the streamline length, which, for equally spaced n Rushton turbines, is given by $L_{\mathrm{s}} = H + nT$. Although this equation fitted the data quite well up to 150 m^3, it was criticised due to the fact that it depends on viscosity, which, if the Kolmogorov's theory was applied correctly, should not and the equation would then reduce to that of Cooke et al in Eq. 11.9 (Nienow, 1998).

Recently, Magelli et al. (2013) proposed two mixing time correlations for systems with either multiple axial and mixed impellers, or multiple radial impellers. Experimental data from a number of different vessel configurations, vessel sizes and impeller types have been used in the assesment of the correlations. Their analysis is based on the bulk flow model assuming that the homogenisation is achieved after a fixed number of circulations. It takes as a reference the model of Nienow (Nienow, 1997; Grenville and Nienow, 2004) for single-impeller systems and extends it to multiple impeller case. It has been assumed that the impeller spacing is wide enough ($2.4D$ or wider) for each impeller to behave independently from others, hence impeller discharge flow and power consumption of each impeller remains unchanged with respect to the single impeller configuration. Proposed equation for multiple non-interacting axial or mixed-flow impellers is

$$t_{95\%} = 2.4(E\varepsilon)^{-1/3} H^{2/3} n^{1/3}, \tag{11.11}$$

where the pumping efficiency E is derived from the ratio of gain in enthalphy of the fluid and the power input of the impeller:

$$E = \frac{N_Q^3}{N_P} \left(\frac{D}{T}\right)^4. \tag{11.12}$$

The mixing equation is similar to Eq. 11.7, but now with the additional dependencies on the number of impellers n, and on single impeller power and flow numbers, N_Q and N_P. Note that the dependency $t_{95\%} \propto (D/T)^{-1/3}$ in Eq. 11.7 is also preserved here, since the equation contains not only the term $(D/T)^{-4/3}$ but also a linear dependency on D/T, because N_Q itself depends linearly on T/D in the turbulent regime. The equation predicted the experimental data with the mean relative error of 21%.

The second correlation proposed by Magelli et al. (2013) describes systems with multiple radial impellers and is based on a modified bulk flow model to take into account the zoning. The flow model employed consists of a sequence of identical perfectly-mixed stages with turbulent material exchange in between, which provided the information on the global parameters related to the fluid dynamics behavior in the tank. The equation proposed is

$$t_{95\%} = 1.20(E\varepsilon)^{-1/3} H^{2/3} \left(\frac{n-1}{n^{2/3}} \right), \tag{11.13}$$

which predicted the experimental mixing times with the mean relative error of 18%.

Effect of aeration: Single-impeller systems

For single-impeller systems, Eq. 11.6 and 11.7 are suggested to apply also under aeration (as long as the impeller is not flooded), provided that the gassed version of the corresponding terms, i.e. N_{P_g} and $\overline{\varepsilon}_g$, are used (Nienow, 1997).

Effect of aeration: Multiple-impeller systems

An anticipated effect of the aeration on mixing is due to change of the mean flow structure. Particularly when radial impellers are used with sufficient spacing in between, aeration connects the otherwise separated flow loops around the impeller regions, hence breaks the axial flow barriers. In line with this, Vrábel et al. (1999) observed that the mixing time was reduced significantly in the limiting case of impeller flooding for the same 30 m^3 fermenter (4 Rushton turbines configuration) used in this study. Furthermore, at low stirring rate (75 rpm), the decrease in mixing time due to aeration was larger than that predicted from the turbulence theory (i.e. $t_m \propto \overline{\varepsilon}_T^{-1/3}$, where ε_T includes both mechanical and pneumatic contributions), which was attributed again to the change of global flow pattern (Vrábel et al., 2000).

In the non-flooding regime, however, Vrábel et al. (1999) found that there was no significant change in the mixing time under aeration. This indicates that there were no significant axial flow barriers. Some relatively small changes that have been observed are as follows. Mixing time first increases with the gas flow number N_{Q_G} at low aeration rates due to reduced mechanical power. At higher aeration rates a maximum is reached beyond which aeration dominates and mixing time decreases with aeration rate until flooding is reached. An exception to this was the observation that, at 70 rpm, the mixing time did not show the initial increase with aeration rate. This was attributed to the fact that, at low stirring rates, the pneumatic contribution dominates from the beginning (since $P_{g,\Gamma}$ scales with N^3) and mixing time decreases with aeration.

Supporting the results given above, measurements of Vrábel et al. (2000) using the

same fermenter (both 4 Rushton turbines and the Scaba axial/radial combinations) showed that there was no significant effect of aeration if the mixing time was plotted with respect to the total specific power input. Note that the total specific power input includes both mechanical and pneumatic contributions (see Eq. 9.4 and 9.13, respectively):

$$\overline{\varepsilon}_{\mathrm{T}} = P_{\mathrm{g},\Gamma} + P_{\mathrm{b}}. \tag{11.14}$$

As a result, the total effect of aeration depends on to what extent the decrease in the mechanical power draw due to aeration could be compensated by the pneumatic power input.

Other degrees of homogeneity

It is possible to calculate the mixing time for any degree of homogeneity if the mixing time for another homogeneity level is already known, because blending is a first order process (i.e. concentration fluctuations decay exponentially in time). If, for instance, t_{95} is known from experiments, one can calculate say t_{99} as follows (Grenville and Nienow, 2004):

$$\frac{dc'}{dt} = -kc', \tag{11.15}$$

$$\int_{c'_0}^{c'} \frac{dc'}{c'} = -k \int_0^t dt,$$

$$\ln\left(\frac{c'}{c'_0}\right) = -kt, \tag{11.16}$$

where k is the first order rate constant with the units s^{-1}. For t_{95} and t_{99}, the relative magnitude of the concentration fluctuations are $c'_0/c' = 0.05$ and 0.01, respectively. The mixing time for 99% homogeneity can now be given in terms of t_{95}:

$$t_{99\%} = t_{95\%} \frac{\ln 0.01}{\ln 0.05},$$

$$= 1.537\, t_{95\%}. \tag{11.17}$$

11.2.2 Micromixing

On smallest scales of motion (the Kolmogorov scale) and final scales of molecular diffusivity (the so-called Batchelor scale), transport of conserved quantities occurs due to random molecular motion and due to smallest turbulent eddies. Mixing at those scales is usually called micromixing, characterised by the local mixing time constant, and is influenced by the molecular and viscous diffusion and the dissipation rate of the turbulent energy.

In mixing of immiscible systems, turbulent eddies break up the fluid elements thus reduce the scale of segregation. This process requires energy as new surface area is generated, therefore the limiting scale of segregation is related to the smallest energy-containing eddies. In case of mixing of miscible liquids, blobs of scalar fluid are deformed and smoothened out continuously by the act of turbulent eddies and molecular

diffusion. However, these eddies are several times larger than the Kolmogorov scale η, which itself is much larger than a single molecule. This implies that even the smallest eddies would contain unmixed regions which cannot be mixed by turbulence alone, hence molecular diffusion is important.

Molecular diffusion is a very slow process (for most liquids and gasses, the momentum diffusivity is larger than or equal to the molecular diffusivity ($Sc = \nu/D_\mathrm{m} \geq 1$), hence it's easier to spread motion than the molecules), so the main mechanism to speed up mixing is by generation of interfacial area over which diffusion can act. This relies critically on initial bulk mixing throughout the tank and further reduction of scale by efficient turbulent diffusion. Overall, micromixing greatly accelerates the rate of generation of interfacial area available for diffusion, and therefore, is the limiting step for fast chemical reactions (Kresta and Paul, 2004).

From integral to Kolmogorov scales of motion

When the energy distribution among the turbulent scales is in equilibrium, the turbulent energy entering at the integral scales in tems of low frequencies (by the action of the impeller) is dissipated at the same rate at the smallest Kolmogorov scales of motion by viscous dissipation. The equilibrium is characterised by the $-5/3$ slope in the equilibrium region in the energy spectrum on a log-log scale, which is realised only over a small range of frequencies close to the Rushton turbine blades (Kresta and Paul, 2004).

The length scale of the largest eddies, the so-called integral scale of turbulent motion, L, is of the order of the blade width or feed pipe diameter. It can be estimated by assuming that eddies have a characteristic velocity u_L of the order of the r.m.s. turbulence intensity, $u_L \propto u' \equiv \sqrt{2k/3}$, with a corresponding energy of the order of $(u')^2 = 2k/3$. Assuming further that this energy is dissipated in a time scale $\tau_L = L/u_L$, one can derive the integral length scale of turbulence:

$$\varepsilon \propto \frac{2k/3}{\tau_L} = \frac{(2k/3)^{3/2}}{L},$$
$$L \propto \frac{k^{3/2}}{\varepsilon}. \tag{11.18}$$

The Reynolds number associated with these large eddies, the so-called turbulence Reynolds number,

$$Re(L) \equiv \frac{k^{1/2}L}{\nu} = \frac{k^2}{\varepsilon\nu}, \tag{11.19}$$

is large, so there is no direct effect of viscosity.

At the smallest Kolmogorov scales, η, the local Reynolds number, $Re(\eta)$, is sufficiently small such that the molecular viscosity is effective in dissipating the kinetic energy:

$$Re(\eta) = \frac{\eta u_\eta}{\nu} = 1, \tag{11.20}$$

hence the characteristic velocity of the Kolmogorov eddies is

$$u_\eta = \frac{\nu}{\eta}. \tag{11.21}$$

These eddies have energy of the order u_η^2 (per unit mass) and are dissipated in a time scale $\tau_\eta = \eta/u_\eta$, so the rate of dissipation of energy can be supposed to scale as

$$\varepsilon \propto \frac{u_\eta^2}{\tau_\eta} = \frac{u_\eta^3}{\eta}, \tag{11.22}$$

hence

$$u_\eta \propto (\varepsilon\eta)^{1/3}. \tag{11.23}$$

From Eq. 11.21 and 11.23 we obtain the characteristic length scale of the Kolmogorov eddies:

$$\eta = \left(\frac{\nu^3}{\varepsilon}\right)^{1/4}, \tag{11.24}$$

where the viscous forces in the eddy are approximately equal to the inertial forces due to velocity fluctuations. Size of the smallest eddies can vary several order of magnitudes, for instance from $\sim$ 1 μm in intense jet mixing to $>$ 100 μm in stirred tanks with low-shear impellers (Patterson et al., 2004). From the above relations, one can finally write the Kolmogorov velocity and time scales:

$$u_\eta = \frac{\nu}{\eta} = (\varepsilon\nu)^{1/4}, \tag{11.25}$$

$$\tau_\eta = \frac{\eta}{u_\eta} = \left(\frac{\nu}{\varepsilon}\right)^{1/2}. \tag{11.26}$$

The characteristic Kolmogorov rate of strain can also be defined from the velocity and length scales:

$$\begin{aligned} s_\eta &= \frac{u_\eta}{\eta}, \\ &= \left(\frac{\varepsilon}{\eta}\right)^{1/2}. \end{aligned} \tag{11.27}$$

Note that Kolmogorov's analysis relies on the hypothesis of local isotropy, that is, at sufficiently high Re, the directional information at large scales is lost as energy passes down to the smallest scales. Furthermore, the information about the geometry is also lost (similarity hyphothesis), that is, the statistics of small scale turbulent motions are universal and independent of the mean flow field and the boundary conditions. They are uniquely determined by ε and ν. The equilibrium range is defined as the range of scales in which this universality holds.

By using the Kolmogorov scales and Eq. 11.18 and 11.19, one can further derive the following ratios between the largest and the smallest eddies:

$$L/\eta \propto Re(L)^{3/4}, \tag{11.28}$$

$$u_L/u_\eta \propto Re(L)^{1/4}, \tag{11.29}$$

$$\tau_L/\tau_\eta \propto Re(L)^{1/2}. \tag{11.30}$$

Note that, with the increasing Reynolds number, the ratio L/η increases, hence at high Reynolds numbers, there will be a range of intermediate length scales, l. Reynolds number of those intermediate scales is relatively large, so eddies at those scales will not

be effected by the viscosity. Based on this, Kolmogorov's second similarity hypothesis states that, at sufficiently high Re, the statistics of the turbulent motions of scale l in the range $L \ll l \ll \eta$ is universal and determined uniquely by ε independent of ν.

The relation in Eq. 11.28 provides also an estimate for the computational power required to resolve all the active scales in turbulent flows. One needs a three dimensional grid with mesh spacing η to resolve all scales from L down to η, hence the total number of grids will scale as

$$N \propto (L/\eta)^3 \propto Re(L)^{9/4}. \tag{11.31}$$

Batchelor scale of concentration

When the diffusion time scales are longer than the Kolmogorov time scale τ_η, turbulence will continue to act on a blob of concentration (or temperature), deforming and stretching it to develope smaller striations. Only when the lamellae could diffuse at the same rate as the visocus dissipation scale would the striations diminish. Based on this argument, Batchelor developed an expression for the smallest such striations of thickness λ_B which diffuses at a time scale τ_B equal to the Kolmogorov time scale (Patterson et al., 2004):

$$\begin{aligned} \tau_\mathrm{B} = \frac{\lambda_\mathrm{B}^2}{D_\mathrm{m}} &= \tau_\eta, \\ &= \left(\frac{\nu}{\varepsilon}\right)^{1/2}, \\ \lambda_\mathrm{B} = \left(\frac{\nu D_\mathrm{m}^2}{\varepsilon}\right)^{1/4} &= \frac{\eta}{\sqrt{\nu/D_\mathrm{m}}} = \frac{\eta}{\sqrt{Sc}}. \end{aligned} \tag{11.32}$$

In other words, it is the size of a pure scalar blob that will diffuse into pure surrounding fluid in the same time for a Kolmogorov eddy of size η to dissipate (i.e. τ_η). For low viscosity liquids, the molecular Schmidt number, Sc, is of the order of 1000 and the Batchelor length scale is much smaller than the Kolmogorov length scale (about 30 time smaller for $Sc = 1000$). For gasses, Sc is of the order of 1 and $\lambda_\mathrm{B} \approx \eta$.

The Batchelor microscale in a stirred tank could be given based on an estimate for the dissipation, $\varepsilon \propto N_P N^3 D^2$ (Kresta and Paul, 2004):

$$\lambda_\mathrm{B} = \left(\frac{\nu D_\mathrm{m}^2}{N_P N^3 D^2}\right)^{1/4}. \tag{11.33}$$

This relation is usefull when scaling up stirred chemical reactors. The reaction kinetics and molecular diffusivity are constant on scale up. Therefore, one must ensure that the Batchelor scale remains also constant. When scaling up with geometric similarity, this means $N^3 D^2$ has to be kept constant provided that the fully turbulent regime is retained.

Corrsin mixing time

Corrsin (1964) analysed the decay of concentration fluctuations in a homogenous turbulent field and provided relations for blending time (for the full range from macro- to

microscales of concentration) in terms of Sc and concentration length scales. The rms fluctuations in this case follow an exponential decay:

$$I_s = \frac{\overline{c(t)'^2}}{\overline{c(0)'^2}} = e^{-t/\tau}. \tag{11.34}$$

The local intensity of segregation, I_s, for unmixed state is given by $I_s = 1$, and for complete mixing $I_s = 0$, that is, zero fluctuations. The time scale, τ, required for the decay of the concentration fluctuations can be related to the fluid material properties, ν and Sc, and to the largest scales of concentration fluctuations (macroscale of mixing), L_C. By integrating the approximate spectra from L_C to beyond λ_B, following relations were obtained for τ (Kresta and Paul, 2004):

$$\tau = \begin{cases} \left(\frac{5}{\pi}\right)^{2/3} \frac{2}{3 - Sc^2} \left(\frac{L_C^2}{\varepsilon}\right)^{1/3} & \text{for} \quad Sc = 1 \\ \frac{1}{2}\left[3\left(\frac{5}{\pi}\right)^{2/3}\left(\frac{L_C^2}{\varepsilon}\right)^{1/3} + \left(\frac{\nu}{\varepsilon}\right)^{1/2} \ln Sc\right] & \text{for} \quad Sc \gg 1 \end{cases} \tag{11.35}$$

For liquids, Sc is large, hence $\lambda_B < \eta$ and diffusion is very slow. The first term describes the effect of inertial scales which contain the most of the turbulent energy. It can be related to macro– (cp. Eq. 11.8) and mesomixing (cp. Eq. 11.47). The second term describes the smallest scales of mixing, that is, time required to reduce the concentration blob from the Kolmogorov lenght scale to the Batchelor length scale for large Sc where molecular diffusion is much slower than momentum diffusion. The effect of this second term, however, is usually low particullarly for low viscosity fluids. Therefore, practically, mixing time scales with $(L_C^2/\varepsilon)^{1/3}$.

The macroscale of concentration is usually taken to be the feed pipe diameter. An estimation of L_C can be made from the turbulent macroscale, $L_C = 0.39L$, where $L \propto k^{3/2}/\varepsilon$ (Patterson et al., 2004).

Scaling arguments can be developed based on the relations given above. The concentration macroscale is some fraction of D. The turbulent kinetic energy scales with the squared fluctuating velocity, $k \propto (u')^2$. This energy is dissipated in a time scale, L/u', thus

$$\varepsilon \propto \frac{(u')^3}{L}, \tag{11.36}$$

$$\tau \propto \left(\frac{L_C^2}{\varepsilon}\right)^{1/3} \propto \left(\frac{D^3}{(u')^3}\right)^{1/3} = \frac{D}{u'}. \tag{11.37}$$

That is, the time constant (and hence the mixing time) increases with an increase in the size of the system and decrease with the turbulent rms fluctuations. This has an important consequence when scaling up with constant Re. The dimension increase, so the mean velocity decreases as $U \propto 1/D$. It can be assumed that $U/u' \approx$ constant (Kresta and Paul, 2004), so $u' \propto 1/D$. Then the mixing time scales as $\tau \propto D/u' \propto D^2$. In order to maintain the same mixing time on scale-up, turbulence level has to be increased.

For a stirred tank, the recommended way to calculate the dissipation scale is from the power per impeller swept volume (Kresta and Paul, 2004). One can then write the following scaling argument:

$$\tau \propto \left(\frac{L_C^2}{\varepsilon}\right)^{1/3} \propto \left(\frac{D^2}{N_P N^3 D^2}\right)^{1/3} \propto \frac{1}{N_P^{1/3} N}, \tag{11.38}$$

which is in the same form as Eq. 11.6 except from the $(T/D)^2$ term. Dependence on $(T/D)^2$ can be retrieved if one uses the minimum dissipation instead of the maximum and take the tank diameter T as the integral length scale (see Section 11.2.1). Important point here to remember is that, in order to maintain constant blend time on scaling up, L_C^2/ε must be held constant. Scaling up based on a constant ε will always result in increased blend time.

Engulfment model of Bałdyga and Bourne

In liquids, micromixing takes place by the following three mechanisms (Bałdyga and Pohorecki, 1995):

- molecular diffusion,
- laminar deformation of striations below the Kolmogorov scale,
- mutual engulfment of regions with varying compositions which results in increase of the micromixed volume.

Engulfment of one fluid by another is caused by vorticity, which via generation of vortices, forms laminar structures. Diffusion and reaction take place within deforming laminated structures temporarily trapped inside stretching vortices. Fluid then returns temporarily to isotropy until a new generation of vortices out of old vortex material and its surroundings. This vortex activity repeats in a periodic manner until the concentration is uniform at the molecular scale (Baldyga and Bourne, 1984).

The engulfment-deformation-diffusion (EDD) model of Baldyga and Bourne (1984) models these processes in terms of a set of coupled, non-linear, parabolic partial differential equations to express unsteady diffusion and reaction in deforming laminated structures formed by engulfment in a turbulent fluid. The engulfment was identified as the limiting of these three mechanisms when $Sc \ll 4000$. Therefore, under those conditions, the EDD formulation reduces to the engulfment (E) model, which consists of only a set of coupled ordinary differantial equations much cheaper to solve (Baldyga and Bourne, 1989).

A rate constant, E, has been defined for this process (Bałdyga and Bourne, 1992):

$$E = 0.058 \left(\frac{\varepsilon}{\nu}\right)^{1/2}, \tag{11.39}$$

where $(\varepsilon/\nu)^{1/2}$ is the characteristic Kolmogorov rate of strain in the viscous subrange (Eq. 11.27). Corresponding characteristic time scale for micromixing was given by

$$\tau_E = E^{-1} = 17.3 \left(\frac{\nu}{\varepsilon}\right)^{1/2}. \tag{11.40}$$

It is noted that, for constant ρ and ε, the mixing time constant scales as $\tau_E \propto \sqrt{\mu}$.

The time scale of micromixing by engulfment can be compared with the molecular diffusion time at the Kolmogorov scale, $\tau_{\mathrm{m},\eta}$:

$$\tau_{\mathrm{m},\eta} = \frac{\eta^2}{D_{\mathrm{m}}} = \left(\frac{\nu^3}{\varepsilon D_{\mathrm{m}}^2}\right)^{1/2} = Sc\left(\frac{\nu}{\varepsilon}\right)^{1/2}. \tag{11.41}$$

This simplified approach ignores the mixing taking place at larger scales, hence predicts usually longer micromixing times for liquids. Note, however, that both τ_E and $\tau_{\mathrm{m},\eta}$ have the dependency on the Kolmogorov rate of strain, $(\varepsilon/\nu)^{1/2}$, and so is the second term of the Corrsin mixing time constant (Eq. 11.35).

For high viscosity fluids, where $Sc > 4000$, the mixing mechanism is provided by viscous streching rather than turbulent engulfment. In those fluids, the smallest eddy dissipated by viscosity is much larger than the smallest concentration striations, which are dissipated by molecular diffusivity, i.e. $\eta \gg \lambda_{\mathrm{B}}$. At the same ε or power per unit mass, higher viscosity generally reduces the mixing rate (Patterson et al., 2004).

Chemical reactions, the Damköhler number

Chemical reaction is a molecular level process, hence its progress is ultimately determined by mixing at the molecular level. When the rate of chemical reaction is fast relative to the rate of mixing, the observed kinetics is not of the reaction but of the mixing process. When those rates are similar, there are strong interactions between the two processes. For both of those two cases, one has to carefully take into account the mixing process. The relative rates of the chemical reaction and the mixing process is given by the so-called Damköhler number, Da:

$$Da = \frac{\text{mixing time}}{\text{reaction time}} = \frac{\text{reaction rate}}{\text{scalar dissipation rate}} \tag{11.42}$$

There are various definitions of Da based on the reaction order and the choice of the mixing time relation (see e.g. Kresta and Paul (2004)). Usually, the range $Da = 30 - 150$ is taken as the upper limit above which fast reaction conditions apply. The limit for slow reactions is given by $Da = 0.009 - 0.02$. Here, mixing has no effect on the kinetics. In the intermediate range, the local concentration field depends on the velocity field. The progress of the reaction is determined by the fluctuating concentration field and the reaction kinetics. Modelling of the turbulence is required.

11.2.3 Mesomixing

Mesomixing takes place at the intermediate scales by coarse-scale turbulent exchange between the fresh feed and its surroundings. It is the reduction stage of the scale of segregation (e.g. turbulent dispersion of the feed stream), which, in turbulent mixing, occurs over the inertial convective scales of turbulence. The initial scale is set by inlet conditions, such as feed pipe diameter, rather than by the local turbulence. Two mesomixing mechanisms are identified (Bałdyga et al., 1997):

- **Turbulent dispersion process of feed:** A feed (scalar) stream introduced to the reactor spreads out perpendicular to its local streamline with a time constant τ_D. Mesomixing controls the coarse-scale (though still fine and localised with respect to the macroscopic scales) turbulent exchange between the fresh feed and its surroundings, thereby determining the spatial evolution of the feed plume. Characteristic time for turbulent dispersion of a point source feed with a volumetric flow rate of Q_F, that is the mesomixing time scale, is given by (Bałdyga and Bourne, 1992)

$$\tau_D = \frac{Q_F}{U D_t}, \tag{11.43}$$

where U is the local fluid velocity in the surroundings. The turbulent diffusivity D_t is related to the turbulent kinetic energy k and its dissipation rate ε according to Eq. 11.51 (usually taken as $D_t = 0.1k^2/\varepsilon$). The turbulent diffusion time over a characteristic length scale L_D can be written as:

$$\tau_D = \frac{L_D^2}{D_t}. \tag{11.44}$$

Therefore, the characteristic length scale for the initial turbulent dispersion of the scalar, that is the mesomixing length scale, is

$$L_D = \left(\frac{Q_F}{U}\right)^{0.5}. \tag{11.45}$$

Note that the dispersion is local when L_D is smaller than the scale of the system, say the tank diameter T, while the assumption of a point source requires L_D to be larger than the feed pipe diameter d_F:

$$d_F \ll L_D \ll T. \tag{11.46}$$

In the case of a finite source, that is when $d_F \ll L_D$ is not satisfied, a single time constant (Eq. 11.43) does not fully characterise the sytem. A second parameter is then needed, which could be the ratio of feed velocity to the local velocity surrounding the feed point (i.e. U_F/U), or a second time constant based on the feed pipe diameter (i.e. d_F^2/D_t). It has been noted that the dispersive mesomixing can be significantly effected by both inhomogeneity of the turbulent field and whether the flow field is locally converging or diverging (Bałdyga and Bourne, 1999).

- **Inertial convective disintegration of large eddies in the course of dispersion:** Here, the scale of the concentration fluctuations is reduced by inertial action from the integral scale of concentration fluctuations, L_C, towards the Kolmogorov scale. A blob of passive scalar in a turbulent flow is disturbed by velocity fluctuations of slightly smaller scale, which, in turn, generates concentration fluctuations of smaller scale (the cascade in the concentration spectrum). This process can be decribed by formation of smaller eddies within large eddies and proceeds without any direct effect of molecular mixing. However, it has itself an effect on the micromixing process. The time constant for this process is given by (Bałdyga and Pohorecki, 1995):

$$\tau_I = A\left[\frac{(L_C)^2}{\varepsilon}\right]^{1/3}. \tag{11.47}$$

Here, the constant A is in the range $1-2$ and for fully turbulent flow in liquids $A = 2$. Now notice that, for fully turbulent flow, this relation actually is equivalent to the first term of the Corrsin mixing time in Eq. 11.35 (where the prefactor of the first term is ≈ 2). A mesomixing model based on this eddy breakup concept is given by Bałdyga et al. (1997).

By comparing the two time scales given above, τ_D and τ_I, one can determine the controlling mesomixing mechanism in the process.

11.3 Mixing in stirred bioreactors

Effective mixing is one of the main duties of stirred tanks in process industries as the rate of the transport processes and possible accompanying (bio)reaction kinetics rely on it. This is why the impellers are installed in the first place (among other duties like gas dispersion) rather than having simply a static bubble column arrangement. One of the process improvements made to promote good mixing in industrial reactors, for instance, is to position baffles a small distance away from the wall. This allows the fluid to circulate behind the baffles and enhance mixing in this region where otherwise a stagnation zone prevails (Barigou and Greaves, 1992).

In the specific case of fermentation where the rate of bioreactions could be slow (hence large scale fermenters are employed), efficient mixing could still be the critial part of the process. This is because the concentration gradients of vital components (e.g. sugar, oxygen, carbon dioxide) can induce stresses on the microorganisms and thereby change the metabolic raction pathways. Ensuring sufficient mixing, however, could be a delicate task. Increasing simply the power input could be detrimental for the process, as all power introduced ultimately dissipates into heat (let alone the shear damage to cells). Therefore, identifying the characteristic time scales of the relevant subprocesses is crucial either when optimising the operation of the fermentation process in a given equipment, or when scaling-up or scaling-down the process.

Scale-up and scale-down approach

When a new product is to be produced by new microorganisms in a totally new process, the only viable way is to scale-up by small volume steps (Groen, 1994).

A more common situation in industry is that one has to produce a new product (or use a new microorganism) in an available equipment, characteristics of which are already known. In that case, a scale-down approach could be taken, where the rate limiting step is found by comparison of the characteristic times of the relevant subprocesses at the production scale (Groen, 1994). Then the rate limiting steps are scaled down to lab-scale (hence the same production limiting step is ensured), and the product and/or process is optimised in this lab-scale. At the end, the optimised process is scaled up to the production scale.

In this process, if the characteristic time for the hydrodynamic processes is slower than the relevant biokinetic mechanisms, the microorganism can experience concentration variation and react on this situation. This leads to loss of the productivity of the

process. For instance, in Saccharomyces cerevisiae (bakers yeast) production, if oxygen gradients are present due to slow oxygen transport (from the gas phase to liquid and then to the organisms) compared with the oxygen consumption, this leads to anaerobic fermentation (Pasteur effect). If substrate gradients develop due to bad dispersion of the substrate from the feed zone, the excess of substrate leads to aerobic fermentation (Crabtree effect) and the production of ethanol (Groen, 1994).

Micromixing

Groen (1994) estimated that the micromixing time of a water-like fermentation broth is of the order of 0.02 s. He, therefore, concluded that its contribution to the total mixing process, which takes tens of seconds, is negligible. He also calculated the critical diameter of a fermenter at which micromixing (scale independent) dominates macromixing, which was about 1.4 mm.

Micromixing is the rate-limiting step in systems with fast chemical reactions, hence most relavant to chemically reacting systems. Micoorganisms directly experience the conditions (concentrations, temperatures, shear) in their local (micro)environment, which is on the order of micrometers (e.g. Saccharomyces cerevisiae is $5 - 10$ μm in diameter), hence much larger than molecular scales, but still much smaller than macroscales of mixing. Therefore, it is advisable to perform time scale analysis of the subprocesses as mentioned previously.

Scope of this study

In this thesis, we aimed at characterising the single- and two-phase hydrodynamics of the stirred fermenter being investigated. The detailed analysis and modelling of the microscale phenomena (biokinetics, metabolics) was not in scope. Therefore, we did not incorporate any subgrid scale micromixing model in this study. The mixing study reported in this chapter consists of a scalar injection and following the evolution of this scalar concentration field throughout the domain. As a result, the method employed enables the macro- and mesoscopic description of the passive scalar mixing process. Effect of different injection and detection methods was also investigated and reported.

11.4 Numerical computation of mixing time

In the CFD framework discussed in this thesis, there are two routes one can follow to compute the mixing time in the fermenter:

- One can introduce naturally buoyant particles into the domain and solve the equation of motion for those particles (i.e. Langrangian tracking). Mixing time can then be calculated from the particle statistics.
- Another route is to introduce a tracer species (same properties as the bulk fluid) and solve a transport equation for this passive scalar. This can be either done real-time by solving it simultaneously with the fluid flow equations or based on a

converged flow field (i.e. frozen field approach). A full concentration field is obtained as a result which provides more data for the mixing time calculation compared to experimental measurements with limited number of monitoring ports and limited flexibility on the location of these ports. From the time evolution of this concentration field, the mixing time can be calculated.

We have chosen the latter approach, that is, a convection-diffusion equation was solved for a passive tracer based on the converged single-phase flow field. Single-phase simulations predicted the relevant flow quantities reasonably well (turbulence quantities, power and flow numbers, velocites) thus provides a level of confidence on the flow field on which the scalar transport is based.

Flow macroinstabilities

One clear limitation of the adopted frozen field approach with the flow field computed by steady RANS simulations is the following. Presence of macroinstabilities (low-frequency mean flow variations) in stirred tanks (both single– and multiple impeller systems) is well-known (Jaworski et al., 2000; Hartmann et al., 2004). Those macroinstabilities manifest themselves in a variety of forms such as whirlpool type of precessing vortex moving around the tank centerline, which can contribute significantly to the kinetic energy contained in the velocity fluctuations. The numerical approach taken here cannot resolve those transient structures precessing in the full 360° domain. Furthermore, even if a transient simulation is performed without any domain reduction due to rotational symmetry, in a transient RANS simulation, it is not a priori clear which part of the velocity fluctuations are temporally resolved and which part is handled by the turbulence model. This applies particularly to flows with no clear spectral separation between the low-frequency coherent fluctuations and the turbulent fluctuations (Hartmann et al., 2004).

11.4.1 Transport equation for a passive scalar

The general transport equation solved for the mass fraction of species i has the following form:

$$\frac{\partial}{\partial t}\left(\rho Y_i\right) + \nabla \cdot \left(\rho \mathbf{U} Y_i\right) = -\nabla \cdot \mathbf{J}_i, \tag{11.48}$$

where Y_i is the species mass fraction and $\mathbf{J}_i$ is the species mass diffusion flux due to concentration gradients. For turbulent flows, $\mathbf{J}_i$ can be written as

$$\mathbf{J}_i = -\rho\left(D_{i,\mathrm{m}} + D_{i,\mathrm{t}}\right)\nabla Y_i, \tag{11.49}$$

where $D_{i,\mathrm{m}}$ and $D_{i,\mathrm{t}}$ are the laminar (molecular) and turbulent diffusion coefficient for species i in the mixture respectively. In the laminar case where the second term vanishes, this relation reduces to Fick's law. It is valid when the mixture composition is constant, or when $D_{i,\mathrm{m}}$ is independent of composition, hence applicable to dilute flows where $Y_i \ll 1$, for all i except the carrier fluid. Since the tracer species has properties of the bulk fluid, this is not a concern in the current case. In fully turbulent flow, D_{t} is several orders of magnitude larger than the molecular diffusion coefficient, hence precise specification of $D_{i,\mathrm{m}}$ is generally not necessary.

In Eq. 11.49, the gradient diffusion hypothesis was employed and the species transport by turbulent fluctuations is represented by the turbulent diffusivity D_t:

$$-\overline{u'y'_i} = D_{i,t}\nabla Y_i, \tag{11.50}$$

where y'_i is the fluctuation in the mass fraction of species i. In order to close the problem, the turbulent diffusivity has to be specified, which is a flow property, hence is solution dependant:

$$D_t = \frac{\nu_t}{Sc_t} = \left(\frac{C_\mu}{Sc_t}\right)\frac{k^2}{\varepsilon}, \tag{11.51}$$

where the turbulent momentum diffusivity (eddy viscosity) is given by

$$\nu^t = C_\mu\left(\frac{k^2}{\varepsilon}\right), \tag{11.52}$$

and $C_\mu = 0.09$ is a model constant. The turbulent Schmidt number is the ratio of turbulent diffusion of momentum to that of mass:

$$Sc_t = \frac{\nu_t}{D_t}, \tag{11.53}$$

which can also be thought of as a model constant. In Fluent, $Sc_t = 0.7$ is the default value.

11.4.2 Turbulent Schmidt number

The value of the turbulent Schmidt number depends on the local flow characteristics. Values in the wide range $0.1 \leq Sc_t \leq 1.3$ have been used in literature depending on the particular application (Montante and Magelli, 2004; Tominaga and Stathopoulos, 2007). For simple shear flows (e.g. axisymmetric jets, channel flow), a good agreement with experimental data was obtained for $Sc_t = 0.7$. Other values were suggested for different flows, e.g. $Sc_t = 0.9$ for near-wall flows, $Sc_t = 0.5$ for jets and mixing layers, $Sc_t = 0.2$ for jet in crossflow. In literature studies using the RANS approach, computed t_{95} values about two to three times longer than the measured values are reported (Jaworski et al., 2000).

RANS limitations

Yeoh et al. (2005) used $Sc_t = 0.8$ in their large eddy simulations (LES) of a standard stirred tank and found a reasonable agreement with the literature data with an average deviation of 18%. Note that, specification of Sc_t is only needed for sub-grid scales in LES, because in grid-resolved scales, the turbulent scalar flux is directly calculated. In another LES study, Hartmann et al. (2006) used $Sc_t = 0.7$ (Fluent default value for RANS). Their argument for taking $Sc_t < 1$ is as follows: In liquid systems with molecular Schmidt numbers ($Sc = \nu/D_m$) of the order of 10^3, the scalar spectrum contains higher frequencies than the dynamic spectrum. As a result, sub-grid scale scalar eddy diffusion is stronger than momentum diffusion due to sub-grid scale eddies. They did not expect results to be sensitive to Sc_t, because the sub-grid scale motion

was at least one order of magnitude smaller than resolved fluid motion, thus the latter would dominate the scalar transport.

Above argument is sensible for LES, but for RANS, where none of the turbulent scales are resolved, it is not likely to be valid. Indeed, in CFD studies with the RANS approach, strong dependence of mixing times on the value of Sc_t have been reported and smaller values of Sc_t were usually adopted. The influence of the turbulent Schmidt number value was attributed both to the eddy diffusivity (Eq. 11.50) and eddy viscosity (Eq. 11.51) approaches which are significant approximations (Montante and Magelli, 2004). This is not surprising, because the dispersive effects of all turbulent scales, from largest to the smallest, are collectively represented by a single value of Sc_t. Furthermore, in reality, turbulent transport of the scalar would be different in each spatial direction at any point due to anisotropy (especially in the impeller region).

Another issue with the RANS approach is that the $k-\varepsilon$ model was reported to underpredict the turbulent kinetic energy (i.e. the velocity fluctuation levels) in the impeller discharge stream by about 50% (Hartmann et al., 2006). This means, as $D_t = \text{const} \cdot k^2/\varepsilon$, the proportionality constant being C_μ/Sc_t (Eq.11.51), the calculated turbulent diffusion could be up to a factor of 4 smaller in the impeller discharge stream (assuming that ε is predicted correctly). It should be noted that, turbulent dissipation also suffer from those inaccuracies. Substantial underpredictions of ε (integrated over the reactor) up to 50% are reported in literature (Lane, 2005a).

Our $k-\varepsilon$ simulations reported in Chapter 2 showed that those large deviations could significantly be reduced if the grid employed is sufficiently fine. We obtained relatively good estimates of k and ε, except near the impeller blade where there was a large overprediction in both quantities (see Fig. 2.4 (c)). Recently, Coroneo et al. (2011) also investigated the sensitivity of RANS predictions (standard $k-\varepsilon$, MRF) on the discretisation scheme and the grid resolution. Results reconfirm our findings. They found that both local and integrated turbulence parameters were highly sensitive to grid resolution and the order of the discretisation scheme. Despite the substantial underpredictions (up to 50%) of ε, N_{P_ε} and k reported in many previous studies in literature that employ $k-\varepsilon$ model, good predictions of these quantities were obtained with sufficiently fine grid and high-order discretisation ($\approx 1.9 \times 10^6$ hexahedral cells ($126 \times 72 \times 192$) for full 2π domain, second-order upwind discretisation). The relative difference between N_{P_ε} and N_{P_Γ} normalised by N_{P_Γ} was reduced down to 7% (we obtained 5% in our simulations). Velocity predictions (including the prediction of flow number N_Q) were less sensitive to the grid resolution and the order of the discretisation scheme, again in line with our findings (see Table 2.3).

Coroneo et al. (2011) did also investigate the effect of grid size on tracer homogenisation. They pointed out that adjusting Sc_t to a value lower than the conventional value of 0.7 to fit experimental data is an arbitrary way to compansate for the underestimation of turbulence diffusivity resulting from the underestimation of the turbulent viscosity. They proposed that, when grid-independent turbulent quantities are assured, lowering the value of Sc_t is not necessary. In order to support their statement, they compared the measured and computed time evolution of CoV, where a reasonable agreement was achieved with the fine grid. Comparison with respect to time evolution of concentration as measured and computed at a detection point was not provided.

Delafosse et al. (2014), on the other hand, did obtain a grid-independent k and ε using

standard $k-\varepsilon$ and SM models, nevertheless still significantly overestimated the mixing time using the value of $Sc_t = 0.7$ and the best predictions were obtained with $Sc_t = 0.2$. A major difference is that they have a multi-impeller system with two Rushton turbines, unlike the reactor of Coroneo et al. (2011), which is stirred by a single Rushton turbine. Hence, the system possess the so-called axial flow barrier, at the axial plane midway between the impellers, across which the turbulent exchange relies on the local turbulent diffusivity. We had the same observation in our simulations, where grid-independence has been checked with respect to the integrated dissipation (see Section 2.2.3). The maximum deviation (with respect to the torque based calculation of dissipation) was 7.6%. The best agreement with the experimental data has been obtained with the value of $Sc_t = 0.2$.

Multi-impeller systems

The discussion above suggest that, apart from possible inaccuracies of turbulence predictions related to the impeller discharge stream, even more critical perhaps, is the prediction of turbulent quantities at regions with much less activity, hence are rate limiting. This also relates to the analysis of Nienow (1997) in Section 11.2.1 that mixing time is determined by the lowest mixing regions, i.e. the flow away from the impeller at the regions with the lowest energy dissipation rate ε. In multi-impeller systems, such relatively inactive regions are those located axially midway between impellers (Roušar and van den Akker, 1994; Vrábel et al., 1999, 2000; Jaworski et al., 2000; Bujalski et al., 2002; Montante and Magelli, 2004). Due to flow compartmentalisation associated with the radial pumping turbines, they act as transport barriers leading to "staged mixing" as discussed earlier in this chapter. The ungassed mean velocity profiles given in Fig. 10.3 clearly show the location of those axial flow barriers. As a result, axial tracer mass exchange between the adjacent impeller regions is based solely on local turbulent diffusion, and in turn, on the value of assumed Sc_t and predicted turbulent viscosity μ_t (via the relation $D_t = \nu_t/\mathrm{Sc}_t$). In a real stirred tank, however, there are large vortex structures leading to macroinstabilities, which promote the tracer flux through those barriers (Jaworski et al., 2000; Hartmann et al., 2004).

The argument given above, that radial pumping impellers generate axial exchange barriers, implies that, for axial pumping impellers, or axial-radial impeller combinations, one would expect mixing time results to be less sensitive to Sc_t. Such a mixing study with axial impellers was reported by Montante et al. (2005) that comprises both Newtonian and non-Newtonian fluids. They studied two tanks of diameter 29 and 48 cm, which have 4 and 3 PBT impellers, respectively. Mixing time predictions by RANS simulations (standard $k-\varepsilon$ model for fully developed turbulence and RNG $k-\varepsilon$ model for transition regime; both SM and MRF for impeller modelling) resulted in longer t_{95} with respect to the measured values. The error was less than 5% with $Sc_t = 0.1$ in almost all cases, while using the standard value, $Sc_t = 0.7$, the error increased up to 50%. In another study, Montante and Magelli (2004) investigated mixing times in a tank of fixed height ($H = 52.6$ cm, $T = 13$ cm) with varying number of Rushton turbines ($N = 4$, 8, 10 or 12), hence varying impeller spacing and bottom impeller clearance. As a result, flow structure of impeller discharge streams could be parallel, merging or diverging. The parallel flow structure gave the above mentioned flow compartmantalisation and axial barriers. In their RANS simulations ($k-\varepsilon$, SM), the error

in the t_{95} predictions for four different tank configurations range from 2.9% to 9% with $Sc_t = 0.1$, while it increased to about 140% with $Sc_t = 0.7$. These results are in line with the argument given above, showing that Sc_t has a larger impact on mixing time predictions when radial impellers are employed.

Overall, inherent limitations of RANS in accurately estimating turbulent scalar transport is evident. With those limitations, Sc_t becomes merely a model parameter for RANS simulations. With the appropriate value of Sc_t, however, rather accurate predictions of the shape of transient local concentration profiles and the values of mixing time can be obtained.

11.5 Experimental measurements of mixing in the 30 m^3 fermenter

Several experimental mixing studies of the 30 m^3 fermenter were reported in literature, which are briefly explained here.

Measurements of Noorman et al.

Mixing times for 30 m^3 fermenter were reported in several studies by Noorman et al (Noorman et al., 1993; Noorman, 1993) for different stirring and aeration rates including those relevant to our simulations reported in this chapter (115 rpm, ungassed operation). Both acid-pulse pH response measurements and fluorescein tracer measurements have been performed in air–water and in Saccharomyces Cerevisiae fermentation medium. Injection was from the top just below the surface level near the shaft and detection was close to the bottom impeller. Average values were reported after four individual runs. Results showed some variation. For the 115 rpm case (water only), t_{95} value from acid tracer measurements was reported as 120 s (Noorman, 1993) and 138 s (Noorman et al., 1993) in two different studies. The measured t_{95} by the fluorescein tracer method was 170 s for water and 180 s for the fermentation medium (Noorman, 1993). The variation of t_{95} with the stirring rate was much larger in acid tracer measurements than that in fluorescein tracer measurements, rendering the acid tracer data rather inaccurate. We used therefore only the fluorescein tracer data for comparison with our simulations results.

Measurements of Cui et al. and Vrabel et al.

Some further mixing studies of the fermenter have been performed by Cui et al. (1996b) and Vrábel et al. (1999, 2000). All these studies adopted fluorescent tracers introduced at the top. Cui et al. (1996b) employed 2 detectors located at the outflows of the bottom impeller and third impeller from the bottom. Vrábel et al. (1999) used an additional detection port close to the free surface. The three tracer detection ports used in the experiments are shown in Fig. 11.1. The 30 m^3 fermenter was filled with tap water to a liquid volume of 22 m^3. Sodium fluorescein tracer was injected at a rate of 150 g/l at 3 bars via the top port for a duration $100 - 1000$ ms by a needle fixed in

horizontal poisition 30 cm from tank wall directed to the shaft (Vrábel et al., 1999). The most reproducible results were obtained with the detection port at the bottom impeller outflow, hence this was used as the single detection position in the later study of Vrábel et al. (2000). Again, four repeats were carried out and the maximum standard deviation was found to be 9 s (Vrábel et al., 2000). Pulse response curves were detected at typical operating regimes for fermentations (stirring rates $70-133$ rpm, aeration rates $0-11$ m^3/min). There was a certain degree of noise in measurements due to reuse of the same tank water in multiple experiments, which was kept under 20% (aerated) and 15%(un-aerated) of the signal response magnitude by controlling the amount of tracer in each pulse (Cui et al., 1996b; Vrábel et al., 1999).

11.6 Simulations of mixing in the 30 m^3 fermenter

11.6.1 Geometry

The configuration of the fermenter is given in Fig. 11.1 (same configuration as that shown in Fig. 2.2). It is filled upto a liquid level of $H = 6.55$ m and has a diameter of $T = 2.09$ m. The liquid volume of the tank is 22 m^3. The impeller diameter is $D = T/3 = 0.70$ m, bottom and mutual impeller clearances are $C = 0.54T$ and $C_I = 0.70T$ respectively, and the baffle width is $0.08T$. The remaining parts are scaled with T and D in the same manner as given for the standard stirred tank geometry in Fig. 2.1.

11.6.2 Working fluid and operating conditions

The working fluid was water with density $\rho = 1000$ kg/m^3 and viscosity $\mu = 0.001$ Ns/m^2.

Two different operating conditions were chosen for the numerical study, 115 and 70 rpm cases (Case 1 and Case 2 in Table 2.2, which represent high- and low-stirring conditions). The flow is fully turbulent in both cases.

11.6.3 Turbulence model

Initial mixing simulations were started from converged steady-state solutions based on both $k-\varepsilon$ and RSM turbulence model calculations reported in Chapter 2. There was no difference in the computed tracer-response (mixing) curves, hence in later simulations only the solution with the $k-\varepsilon$ model was used.

11.6.4 Setup of numerical tracer experiments

As pointed out previously, we took the frozen field approach. After the steady-state single-phase fluid flow simulation has been completed (numerical settings and results are given in Chapter 2), the converged flow field is used for a transient simulation of the transport of the (dissolved) tracer species. This is basically the numerical simulation of

a well-known experimental method to determine the mixing time: The tracer is added locally at time $t = 0$, and from then on the tracer concentration is monitored over time by appropriate probes at one or several locations in the tank. The time after which the measured concentrations for the last time enter a certain range around the equilibrium concentration is then defined as the mixing time.

Domain periodicity

A major difference between the setup of mixing time simulations and the actual mixing experiments is the following. In simulations, rotational periodicity is assumed, thus the computational domain where the tracer is introduced is limited to 60° sector. Therefore, this mimics an experiment where the tracer is introduced at 6 rotationally symmetric points. Whether this would effect the computed mixing times should be checked.

11.6.5 Tracer entry methods and locations

The tracer is introduced into the domain by marking the grid cells constituting a region of pre-defined topology and location at $t = 0$. Marked cells are then patched a pre-defined initial species mass fraction. This mimics the addition of a tracer pulse in experiments approaching the dirac delta function. We introduced the tracer in the following four ways (see Fig. 11.2):

1. **Single-point injection at free surface**. The tracer is added close to the free surface near the baffle (at the stationary zone). This mimics closely the way the tracer was introduced in experiments. However, as pointed out earlier, due to rotational periodicity, this corresponds to tracer injection at 6 rotationally symmetric points. A spherical region was marked (15 cells) with a diameter of 10 cm at an axial level of 6.48 m close to the free surface (7 cm below the surface) and centered at an angular location of 25° with respect to the baffle (upstream). Initial tracer mass fraction at this region was patched to 1.0. The global mean tracer mass fraction (and also volume fraction since tracer fluid is also water) in the fermenter is $\overline{Y} = 1.427 \cdot 10^{-4}$.

2. **Single-point injection at impeller 4**. Here, the tracer is intoduced close to the top impeller near the axis at the moving MRF zone. Similar to the first entry method, again a spherical region was marked. Initial tracer mass fraction at this region was patched to 1.0. The aim is to see any possible effect of introducing the tracer in the MRF zone where a moving reference frame is defined. The global mean tracer mass fraction in the fermenter is $\overline{Y} = 3.840 \cdot 10^{-4}$.

3. **Multiple-point injection at impeller outflow regions**. In this method, four spherical regions of diameter equal to the blade height (14 cm) near the impeller tips were marked. Initial tracer mass fraction at this region was patched to 1.0. The resultant total volume of the tracer fluid is 0.15 % of the total fermenter volume ($\overline{Y} = 1.526 \cdot 10^{-3}$). The aim is to see the effect of introducing the tracer at a high flow rate location and at multiple locations simultaneously.

4. **Full free surface injection.** Here, the whole free surface was marked to a fixed depth of 30 cm. Initial tracer mass fraction at this region was patched to 1.0. The resultant volume of the tracer fluid is 4.06 % of the total fermenter volume ($\overline{Y} = 4.059{\cdot}10^{-2}$). Here our objective is two fold. First, to see if the tracer volume has an effect on the mixing time, which, in this case, is significantly larger then the other three methods. Secondly, this method is expected to indicate any possible effect of the rotational periodicity assumption. Introducing the tracer in this way mimics a large number of simultaneous point injections over the whole free surface. If the mixing time thus computed differs little from that computed with a single-point injection near the free surface, then no significant effect of the periodicity assumption is expected. This, of ocurse, excludes the effect of any macroinstabilities present in a real fermenter (as discussed in Section 11.4), which are not resolved by the numerical approach adopted here.

11.6.6 Tracer monitoring locations

Tracer monitoring points used in simulations are shown in Fig. 11.4(b). Those include the detection ports used in experimental measurements given in Fig. 11.1.

11.6.7 Initial and boundary conditions

Simulations started with the tracer mass fraction intially patched according to the tracer entry methods described earlier. Zero tracer mass flux condition was imposed on wall boundaries.

11.6.8 Transient settings

Second-order implicit time discretisation scheme was employed for the transient terms of the scalar transport equation. Initially, the time step was chosen according to the Courant criterion. That is, the time step is sufficiently small, so that fluid crosses no more than one grid cell per time step everywhere in the domain. This resulted in a time step of 0.003 s. In later simulations, time step size was progressively increased in order to evaluate its effect on computed mixing times.

11.6.9 Convergence criteria

Simulations were considered converged when the sum of the tracer residuals was lower than 10^{-7} at each time step. At this level of convergence, the concentration profiles had already approached to a constant value.

11.7 Results and discussion

Before reporting CFD predictions, a comparison is made between measured mixing times and those estimated from literature correlations given earlier. Those are shown

in Table 11.1. All correlation predictions are very poor; either t_{95} is overestimated (by Eq.11.9 and Eq.11.10), or greatly underestimated (by Eq.11.13). With those rather unsatisfactory predictions, we now turn to a more detailed analysis of mixing by simulations.

11.7.1 Tracer-response curves

Simulation results are typically reported in terms of tracer-response curves, that is the time evolution of tracer mass fraction Y normalised by the global mean value $\overline{Y}$. Note that, $Y/\overline{Y}$ is equivalent to the relative tracer mass concentration as $C/\overline{C} = Y\rho/(\overline{Y}\rho) = Y/\overline{Y}$.

Typically 95% mixing times are reported in literature, but more information is present in those response curves, which can be used to retrieve information on the flow field. Noorman (2011) listed four such parameters that can be determined from response curves:

- The time interval between the injection and the first response detected, the so-called lag time, reveals the shortest mean path in the reactor and provides information on the fastest circulation loops.

- The response curve after the lag time can usually be fitted to a log-normal distribution, giving a mean and variance. Those provide information on the mean flow rates, the distribution of circulation and back-mixing. From turbulence theory, the variance would scale to the power 1.5 with time, while, in case of convective mixing, scaling would be to the power of 1.0. Experimental data (Noorman, 2011) showed indeed a scaling close to 1.5 for single-phase operation, and a value close to 1.0 in case of an air-water system. According to authors, this indicated that, in bubbly flow, the dominant mechanism of mixing was convection due to transport of liquid in the bubble wakes. One can argue that the convection dominated transport could also be due to onset of large scale circulation loop in the entire reactor with gassing.

- The fourth parameter is the standard deviation of the actual data with respect to the best log-normal fit, which provides information on the magnitude of flow instabilities. Fourier analysis revealed that the noise is randomly distributed when the bottom impeller is flooded and has an amplitude about 5 to 10 times higher than that under loading conditions.

Based on the experimental data available for the single-phase operation to which we restricted ourselves in this chapter, we compared simulation results mainly in terms of mixing and lag times and the overall shape of the response curves.

11.7.2 Effect of tracer entry methods and location

Simulations

Computed transient response curves for four different tracer entry methods outlined in Section 11.6.5 are given in Fig. 11.3. All curves collapsed on the same S-shaped profile with similar mixing times ($t_{95} = 270.3 - 274.0$ s) except that for the multiple-point injection method, which resulted in a far shorter mixing time ($t_{95} = 25.6$ s). This shows that homogenisation can be reached much faster if tracer is introduced already in a segregated state at each impeller region. In such an experiment, each impeller zone behaves similar to a separate compartment (or tank) rather isolated from the rest of the tank by the axial flow barriers described earlier. When the expected equilibrium concentration of such an " isolated" compartment does not differ significantly from the global equilibrium concentration (in case of 95% mixing time, not more than ±5%), then the tracer exchange between compartments would not influence the computed t_{95}, and t_{95} approximates to the mixing time of the compartment.

In order to see the variation between those "compartments", a detailed mixing profile is given in Fig. 11.4 with data from multiple monitoring points. Shortest mixing time was detected at the port located midway between bottom and second impeller near the shaft ($t_{95} = 7.3$ s) followed by the top impeller outflow port ($t_{95} = 8.7$ s). Longest mixing time was detected at the bottom corner port ($t_{95} = 33.2$ s) followed by the bottom impeller outflow port ($t_{95} = 25.6$ s). Note that the prediction of mixing time from Eq. 11.6 for an equivalent single-impeller sytem results in $t_{95} = 13.5$ s. Note also the differences between the boundaries of those compartments. At the top boundary we have the symmetry condition which is, in effect, similar to the condition at boundaries axially midway between impellers that act as axial flow barriers. In contrast, at the bottom, a no-slip condition is imposed, thus velocities diminish when approaching the wall. The bottom corner port is located near both the bottom wall and the side wall and probes the longest mixing time.

Again from Fig. 11.3, introducing the tracer in the moving or stationary MRF zone seems to make no significant difference, as long as it is introduced at a single point. Mixing profiles of single-point injection at top and at the MRF zone of top impeller are practically identical. This is as expected and suggests the consistency of the impeller modelling method. Furthermore, the rotational periodicity assumption seems not to have a significant effect on results. The full free surface injection method gave almost an identical mixing profile with the single-point injection at the free surface.

Experiments

Vrábel et al. (1999) employed two injection points at the top of the same 30 m^3 fermenter studied here: the top port as depicted in Fig. 11.1 and another location axially 40 cm above the top port (at height 6.88 m) which is above the free surface when there is no gassing. The pulse response was measured at the bottom port. The difference in t_{95} was within experimental error. However, based on the decolorisation experiments of Cronin et al. (1994) on a smaller reactor ($D = 0.72$ m) with two Rushton turbines and their compartment model of the same reactor, they also concluded that variation of the position of tracer injection along the reactor would result in a bell-shape pro-

file of overall mixing time (i.e. the time when the last color disappears at whatever point in the reactor or the largest t_{95} at whatever location in the reactor as predicted by the compartment model) with respect to the reactor height. The shortest mixing time would be achieved if the tracer is added at the axial center of the tank, while the longest mixing would be achieved in case of addition at the top or at the bottom. They concluded that injection at the top of the reactor, as it is typically done, gives the worst mixing while injection in the middle can significantly improve mixing.

Above mentioned decolorisation experiments of Cronin et al. (1994) yielded both overall mixing times and local mixing times. Local mixing times monitored near the impeller closest to the injection point were 2 to 3 times shorter than the overall mixing times. The shortest overall mixing time was obtained when injection was at the axial center and the overall mixing time was longest when injecting at or near the liquid surface. When the injection location was anywhere else, intermediate mixing times were obtained that approach approximately to a constant value. Based on their results, they suggested to inject into each impeller zone separately. This fully supports our simulation results where we obtained the shortest mixing time with the multi-point injection at impeller zones.

Other experimental and CFD studies (Jaworski et al., 2000; Bujalski et al., 2002), again in dual Rushton turbine systems, agreed well with the results of Cronin et al. (1994). Shortest mixing times were obtained at an injection location approximately axial midway between the impellers. Mixing times obtained with other injection locations were much longer and assumed approximately the same value.

Contrary to results obtained with radial turbines, mixing times in multi-impeller systems with axial impellers are not sensitive to the location of injection points according to the results of Montante et al. (2005). This is not surprising as those sytems do not possess axial flow barriers and large convective flows easily carry scalars throughout the whole tank volume.

Injection conditions

Coroneo et al. (2011) investigated numerically the effect of tracer injection conditions such as instantaneous versus time-dependent injection that mimics realistic tracer addition conditions in experiments. The effect of initial tracer shape was also studied in their CFD simulations of a Rushton stirred single-impeller system. No significant effect was found as judged by the time evolution of the computed CoV.

11.7.3 Effect of tracer detection location

Based on measurements in the same fermenter studied here, Vrábel et al. (1999) reported that, when tracer was injected at the top, pulse response curves measured axially in the middle of the tank leveled out significantly faster than if measured at the top or at the bottom. This was attributed to the path length of the homogenisation process. Note that this is in line with their previous observation that the shortest mixing time was achieved when the tracer was injected axially in the middle of the tank. This suggest a symmetry in the effect of tracer injection and detection locations such that

swapping the injection and detection locations yield the same result.

In Fig. 11.5, we show a detailed plot of tracer profiles monitored at various locations when the tracer was injected at the top. The influence of detection location is clear; both the shape of response curves and the computed mixing times differ. Those results are in full agreement with the observations of Vrábel et al. (1999), that is, shortest mixing time is detected at the axial center of the tank, located at midway between the impeller 3 and impeller 2 ($t_{95} = 27.8$ s).

Note also that all response curves detected above the axial center of the tank overshoot before reaching to a steady value, whereas those detected at or below the axial center do not. The level of overshoot (i.e. oversaturation) for curves above the axial center increases when going away from the center, where, in the limit, the highest port (top corner) response curve approaches to the curve of overall maximum tracer mass fraction. Similarly, the level of undersaturation for curves below the axial center decreases when going away from the center, and the response curve for the lowest port (bottom corner) approaches to that for the overall minimum tracer mass fraction. The lag time (time elapsed until the first change in tracer mass fraction detected) of the response curves also increase when going from the reactor top to the bottom, indicating the tracer transit time along the reactor height.

In Fig. 11.6 we replotted the mixing time data given in Fig. 11.5 with respect to the reactor height. Resulting bell-shaped profile of t_{95} computed at different detection locations is in line with the observations of Cronin et al. (1994) and Vrábel et al. (1999) when they varied the tracer injection location along the reactor. This suggests again a symmetry in the effect of injection and detection locations.

Similar trends, that shortest mixing times being measured at axial centerline locations, are also observed in other studies (Jaworski et al., 2000; Bujalski et al., 2002). Here again, the experimental and simuations results of Montante et al. (2005) in an axial turbine system showed an opposite behavior. Their results were not sensitive to the location of detection points, suggesting again that the compartmentalisation due to radial turbines is the cause of the observed variation.

11.7.4 Scalar mass conservation

Tracer mass conservation was checked during simulations, which revealed an intriguing observation. We found that the tracer mass was not conserved and the degree of tracer loss was variying in different simulations. For single-point injection from top, there was about 11 % tracer loss at the end of the simulation ($\overline{Y}_0 = 1.427 \cdot 10^{-4}, \overline{Y}_{140\text{s}} = 1.270 \cdot 10^{-4}$). This was not expected as we had used higher-order discretisation schemes and ensured that the convergence criteria for the scalar residuals were sufficiently low so that, at each time step, concentration profiles had already reached a steady value.

Numerous test simulations have been run with the hope to correlate the tracer loss with the numerical parameters. Tracer injection method was kept the same as in experiments, that is, injection at the top port and detection at the bottom port. We varied the stirring rate, value of Sc_t, time step and the single-phase simulation setup. Note that, in order to be able to use the converged single-phase simulation data as the initial condition for subsequent two-phase simulations, Fluent requires that the

multiphase modelling is turned on (in our case the Euler–Euler model), but the two-phase equations are turned off. Therefore, this was the default setup for single-phase simulations. However, to test the effect of this, we have also run simulations in which the Eulerian model was turned off.

Results of the test simulations are outlined in Fig. 11.7. We plotted the instantaneous mean tracer concentration in the domain normalised by $\overline{Y}_0$, the initial mean concentration at $t = 0$ ($\overline{Y}_0 = 1.427 \cdot 10^{-4}$). Results show that there is a small amount of scalar mass increase in the very beginning for few simulations (115 rpm, $\Delta t = 0.100$ s cases), followed by scalar loss in all cases with the exception of simulations with the Eulerian model turned off. Note that the tracer mass fraction values were monitored at every 10 time steps during simulations, independent of the time step size. Hence, for simulations with a large time step, smaller number of data points was recorded. From Fig. 11.7, we see that the scalar loss is higher at

- higher Sc_t values
- smaller time steps (i.e. larger number of time steps)
- lower stirring rates

The rate of scalar mass loss is approximately the same in the beginning of the simulations. With the advance of the simulation time, the scalar loss decreases, and the rate of this decrease is higher at higher stirring rates, larger time steps and lower Sc_t values. The scalar loss ultimately stops and $\overline{Y}/\overline{Y}_0$ reaches a plateau value. Note that increasing the time step two orders of magnitude had a negligible effect on the response curves, which is in line with the observations of Montante et al. (2005).

We also found that the tracer injection method has an influence on the tracer mass conservation. In Fig. 11.8, the mass conservation for different injection methods is shown. Simulation with the multiple-point injection method, which reached the 95% homogeneity level much earlier than other simulations, had a minimal mass imbalance. Tracer mass increased slightly in the very beginning of the simulation, which then decreased and flattened out around the full mass conservation level.

Bug in the Fluent code

Fig. 11.7 clearly shows that the scalar mass is perfectly conserved in simulations in which the Eulerian model was turned off. This finding pointed to an abnormal behaviour in the code, which could possibly be a bug. The issue has been reported to the Fluent technical support engineers. Their analysis confirmed a bug in the code and revealed that the violation of mass conservation was due to the multiphase setup in mixing simulations combined with the use of periodic boundary conditions. This is a worrying finding as it indicates a major limitation in the code when one is interested in tracer mixing simulations (or mass transfer calculations for instance) in two-phase flow with periodic boundaries.

Effect of scalar loss in mixing time predictions

Later simulations which we report in coming sections showed that the effect of scalar mass loss in simulations was not significant for the cases studied. Both in 155 and 70 rpm simulations, computed t_{95} differed only 5 seconds (t_{95} was shorter when there was no scalar loss).

11.7.5 Comparison with experimental data

Effect of turbulent Schmidt number

Simulations showed strong dependence of mixing times on the value of the turbulent Schmidt number, which is in line with other CFD studies using the RANS approach. In literature studies, computed t_{95} values about two to three times longer than the measured values are reported (see Section 11.4.2 for a detailed discussion).

In Fig. 11.9 and 11.10, response curves computed with different Schmidt number values are comapred with the experimental data for the 115 rpm case, and in Fig. 11.11 for the 70 rpm case. When the Fluent default value, $Sc_t = 0.7$ was used, mixing was too slow and the deviation from experimental values of t_{95} were 83% (115 rpm case) and 73% (70 rpm case). The optimal value for both 115 and 70 rpm cases was found to be $Sc_t = 0.2$, which resulted in a realtive error of 2.9 and 0.078%, respectively.

The characteristic shape of the response curve differed when the tracer was detected at the middle port (Fig. 11.10). In contrast to the response curves taken at the bottom port, there was a certain level of overshoot without any lag-phase in the beginning. Those results are in line with the experimental data (Cui et al., 1996a; Vrábel et al., 1999). Actually, when the detection location moves towards the top port, we see from Fig. 11.5 that this trend continues with an increasing level of overshoot. This is also in agreement with the experimental observations (Vrábel et al., 1999). It is not posible to compare the predicted t_{95} unfortunately, since it was not reported in the experimental work. However, the general trend of the response curve is clearly beter predicted with lower values of Schmidt number (0.1–0.2).

Effect of stirring rate

Dimensionless mixing numbers, Nt_{95}, for different values of Sc_t are also given in Fig. 11.9 and Fig. 11.11. Because Nt_{95} is constant in fully turbulent single-phase flow, the consistency of simulations was checked by predicting the mixing time for 70 rpm from the value for 115 rpm (i.e. $t_{95\%,70\ \mathrm{rpm}} = (115/70) \times t_{95\%,115\ \mathrm{rpm}}$). The predicted mixing time was 253.8 s compared with the computed value of 254.8 s from the simulation with $Sc_t = 0.2$. The same consistency check was done for the experimental data reported and resulted in a predicted value of 246 s compared with the measured value of 255 s. As the fermenter operates under fully turbulent conditions for both stirring rates, this slight mismatch (about 3.5%) might indicate possible inaccuracies in the experimental measurements.

Lag times

The so-called lag times, t_{lag}, computed at different values of Sc_{t} were also compared with the measured values. Note that it's not clear at which homogeneity level the experimental lag times were determined. Therefore, lag times when the detected concentration reaches both 1% and 5% homogeneity levels are given in Fig. 11.9 and Fig. 11.11. As the 95% homogeneity level is the standard criteria for reported mixing times, we could assume that the measured lag times were based on 5% homogeneity level, hence both indicating a deviation level of 5%. Based on this assumption, for 115 rpm, closest agreement with the experimental data was achieved with $Sc_{\text{t}} = 0.2$ and 0.1, with the respective relative errors of 8.7% and 12.0%. For 70 rpm, the relative error was 34.0% and 8.0% for $Sc_{\text{t}} = 0.2$ and 0.1, respectively.

The large error in the computed lag time for the 70 rpm case is rather strange. We could also predict the lag time for 70 rpm from the experimental value for 115 rpm assuming that Nt_{lag} is constant in fully turbulent flow, similar to Nt_{95} (i.e. $t_{\text{lag,70 rpm}} = (115/70) \times t_{\text{lag,115 rpm}}$). This would result in a value of 24.5 s and the relative error would then be 8.9% and 12.2% for $Sc_{\text{t}} = 0.2$ and 0.1, respectively, which is very close to values reported above for the 115 rpm case. This seem to indicate that the experimental lag time reported (20 s) was possibly not accurate.

To conclude, best predictions of mixing and lag times are obtained with an adapted Schmidt number, namely $Sc_{\text{t}} = 0.2$, in contrast to the Fluent default value, $Sc_{\text{t}} = 0.7$.

11.7.6 Effect of time step size

Montante et al. (2005) reported that the simulation time step has a negligible effect on the computed t_{95}. Selection of the time step size seemed to have an effect only on the tracer evolution, if not chosen sufficiently small. They also reported that the first and second order discretisation schemes gave identical tracer concentration profiles.

Our simulation results plotted in Fig. 11.9 also show that the time step size has no effect on the response curve within the range of values investigated. Simulations with the time step size of $\Delta t = 0.003$ s and $\Delta t = 1.000$ s (both with $Sc_{\text{t}} = 0.1$) gave identical profiles.

11.7.7 Time evolution of tracer distribution

In Figs. 11.12 – 11.14, time evolution of the tracer transport through the domain is shown when the tracer was introduced from the top (115 rpm, $Sc_{\text{t}} = 0.2$). Both tracer mean mass fraction contours and 3D iso-surfaces of a very low tracer mass fraction value (about 100 times lower than the final equilibrium value) are given. The latter shows the very front of the propogating tracer, hence enables to identify regions in the full 3D domain where the tracer reaches last (e.g. dead zones or low mixing regions). According to iso-surface plots, such locations are those at the bottom wall near the shaft and behind the baffle, and under the bottom impeller. After about 15 seconds, the tracer iso-surface disappears from the domain, which actually corresponds to the overall tracer lag time in the domain and is quite close to the measured and predicted

lag times at the bottom port. At regions midway between impellers, where axial flow barriers are located, tracer transit time is longer especially near the wall.

The general trend and shape of tracer contours seem qualitatively quite similar to that reported by Montante and Magelli (2004), as predicted by a SM simulation of a fermenter with 4 Rushton turbines (with the difference that the tracer was injected from the bottom). The initial high concentration zone at the top levels out over time and large persistent concentration gradients develop near impellers and at regions midway between impellers (especially near the wall), where axial flow barriers are located. Ultimately, concentration gradients diminish and homogenisation is reached after about 160 seconds.

Graphical interpretation of scalar time evolution in MRF method

Finally, we note that, although important information could be extracted from the transient behavior of tracer distribution, exact graphical intrepretation with respect to physical reality should be done with care. This concerns only the graphical display of scalar distribution, and is inherent to the MRF methodology employed, that the velocities computed in the rotating frame, when used to convect a scalar in a transient manner, would produce a misleading behavior (Marshall and Bakker, 2003).

11.8 Conclusions

In this chapter, we report on the scalar mixing study made on the single-phase flow in the 30 m^3 fermenter presented in Chapter 2 and 10. The main conclusions of this chapter are:

- The turbulent Schmidt number is the key parameter, to account for lack of convective exchange by the mean flow at locations axially midway between impellers, which limit the transport of tracer across the tank.
- Best predictions of mixing and lag times were obtained with an adapted Schmidt number, namely $Sc_t = 0.2$, in contrast to the Fluent default value, $Sc_t = 0.7$. For $Sc_t = 0.2$, the mixing time (t_{95}) computed as 154 s (at 115 rpm) and 255 s (at 70 rpm), corresponding well with the experimental values from Vrábel et al. (1999), reported as 150 s and 255 s, respectively.
- Tracer injection and detection locations influence the shape of response curves and the computed mixing time. Shortest mixing times were detected near the axial center of the fermenter, located at midway between the second and the third impeller, in agreement with the experiments (Vrábel et al., 1999). Injection method has also an influence; when the tracer was introduced individually at each impeller, the shortest mixing time was achieved. Other injection methods investigated, however, gave identical response curves.
- It was found that the scalar mass in simulations was not conserved, if the single-phase simulation was set up as a multiphase sytem in which the secondary phase

equations were not solved. Scalar mass was perfectly conserved in a purely single-phase setup. This behavior was found to be due to a bug in the Fluent code.

- Simulation time step size had no significant effect on the response curves within the range of values investigated.
- Results showed that a good prediction of scalar macro– and mesomixing, in terms of mixing times and tracer response curves, could be obtained by a rather simple and computationally cheap model (RANS approach with the steady MRF model for velocity field estimation in a six-fold reduced domain via rotational symmetry assumption) with an adapted Sc_t.

Tables

Table 11.1: Comparison of measured mixing times for 95% homogenisation with that calculated from correlations available.

	t_{95} [s]	
	115 rpm	70 rpm
Measurement (Vrábel et al., 1999)	150	255
Correlation (Cooke et al. (1988), Eq. 11.9)	220.1	361.4
Correlation (Groen (1994), Eq. 11.10)	315.7	518.4
Correlation (Magelli et al. (2013), Eq. 11.13)	48.8	80.1

Figures

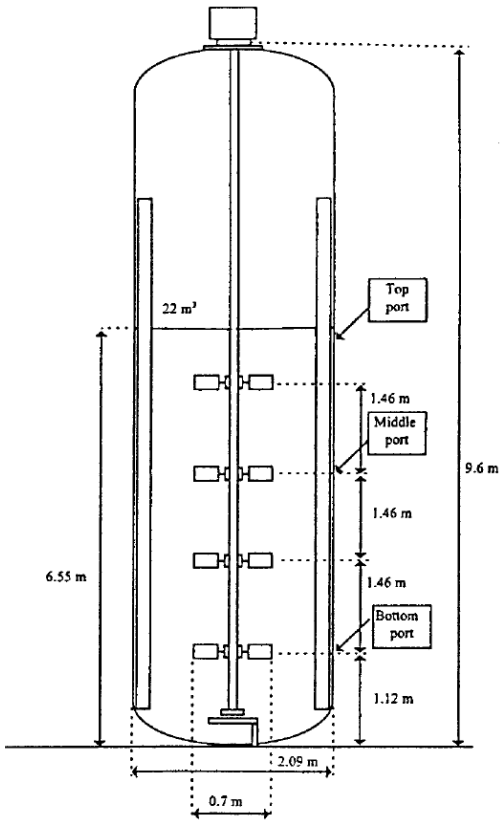

Figure 11.1: Schematic representation of the tracer injection and detection points in the 30 m^3 fermenter (from Vrábel et al. (1999)).

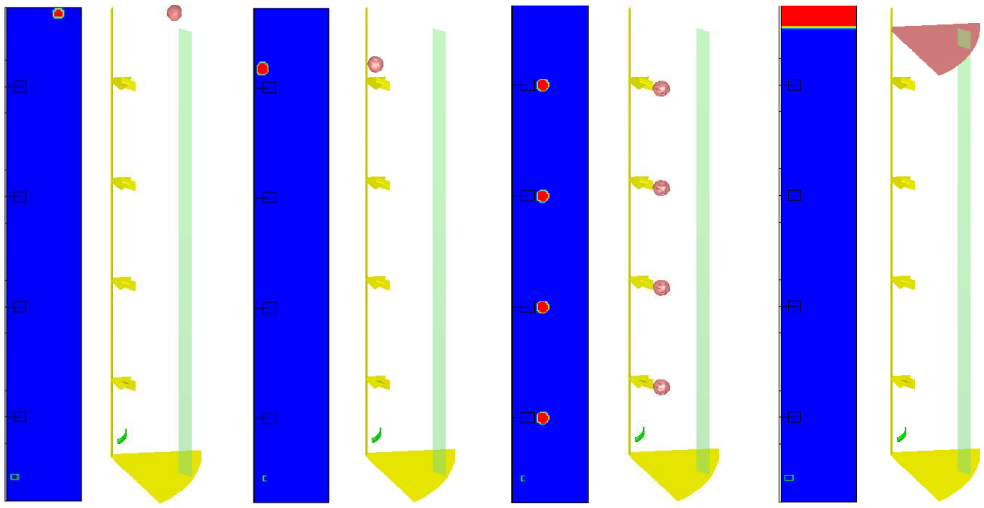

(a) Single, top (b) Single, imp4 (c) Multiple, outflow (d) Free surface

Figure 11.2: Different tracer entry methods used in test simulations. Both tracer mass fraction contour plots and iso-surfaces (tracer mass fraction of 0.5) are given.

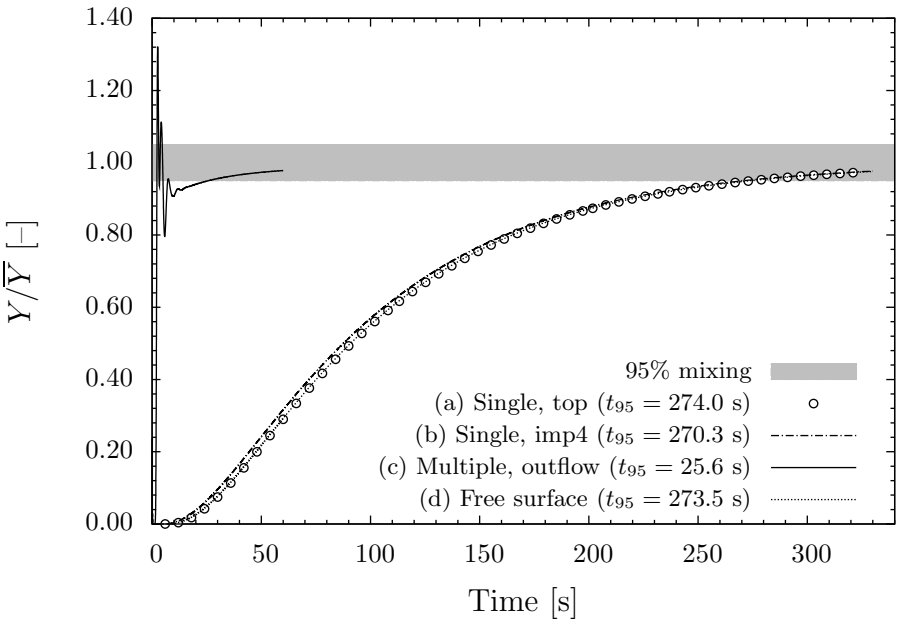

Figure 11.3: Tracer-response curves from simulations (115 rpm, $Sc_t = 0.7$, $\Delta t = 0.003$ s) where the tracer was introduced in four different ways as outlined in Section 11.6.5 and shown in Fig. 11.2. Tracer mass fraction was normalised with the mean mass fraction (integrated mass fraction over the whole domain). Detection point is similar to that in the experiments; located at the bottom impeller outflow region (axially at impeller centerline level, radially 4.6 cm away from the blade tip).

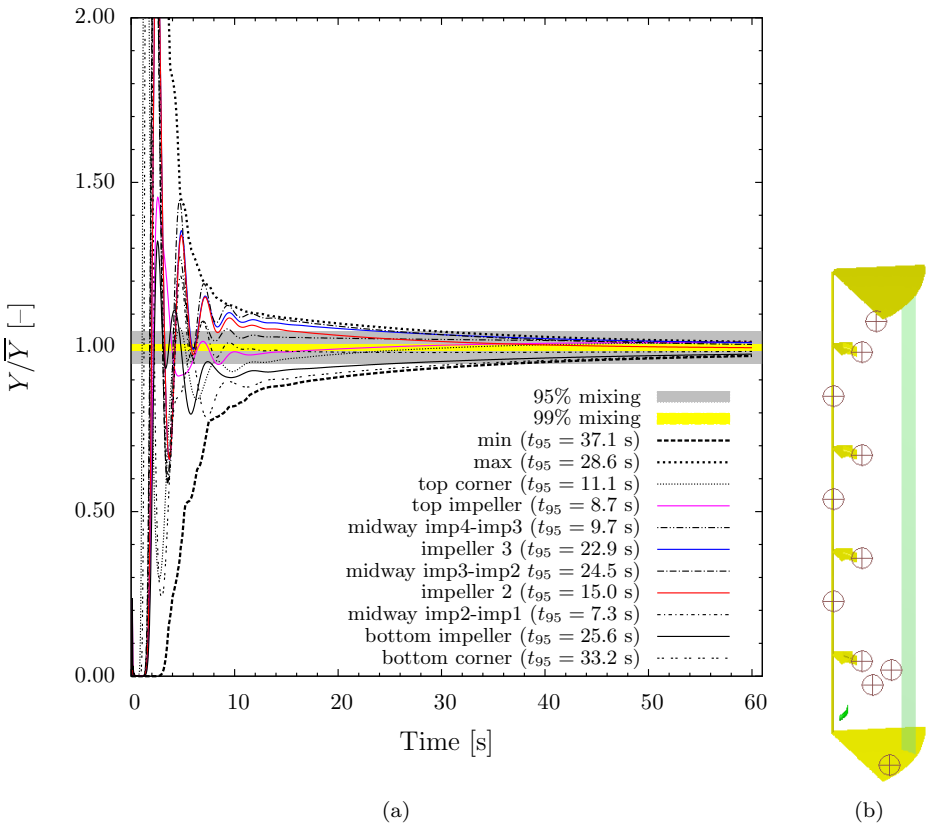

Figure 11.4: Detailed view of mixing for the multiple-point injection method (115 rpm, $Sc_t = 0.7$, $\Delta t = 0.003$ s). Normalised tracer mass fraction profiles at various detection points as well as global minimum and maximums are plotted. Both 95% and 99% mixing bands are indicated. Location of detection points are shown in (b).

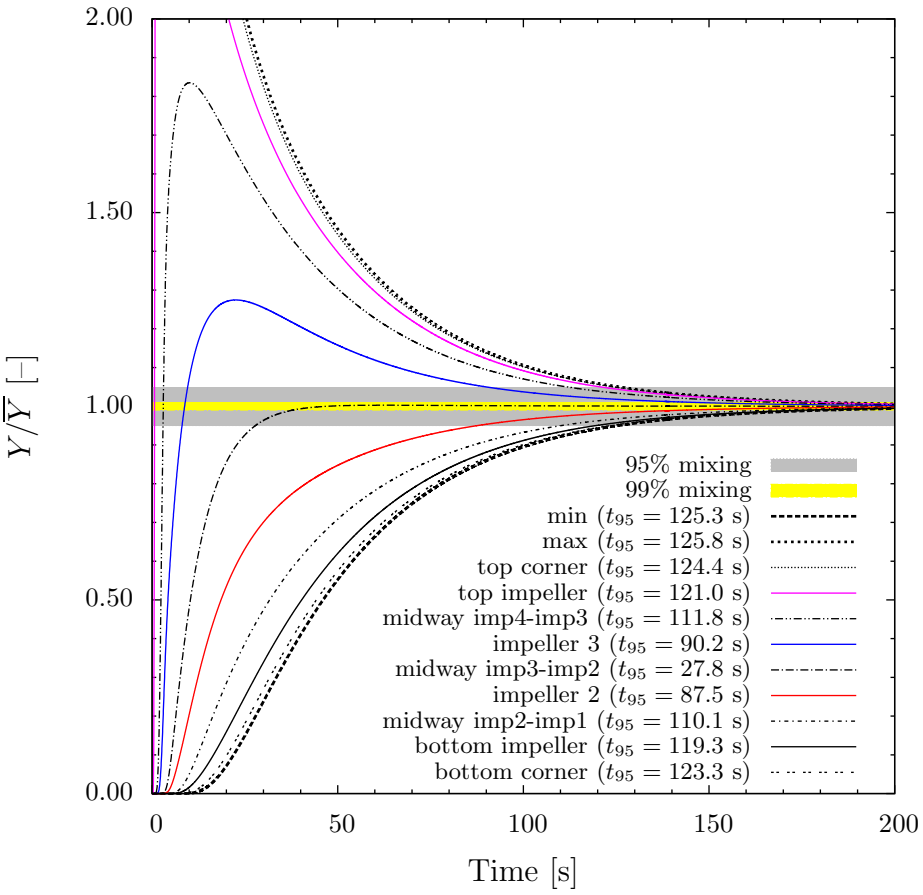

Figure 11.5: Tracer-response curves obtained at various detection points when the tracer was introduced from the top (115 rpm, $Sc_t = 0.1$, $\Delta t = 0.003$ s). Global minimum and maximum profiles are also plotted. Location of tracer detection points is shown in Fig. 11.4 (b).

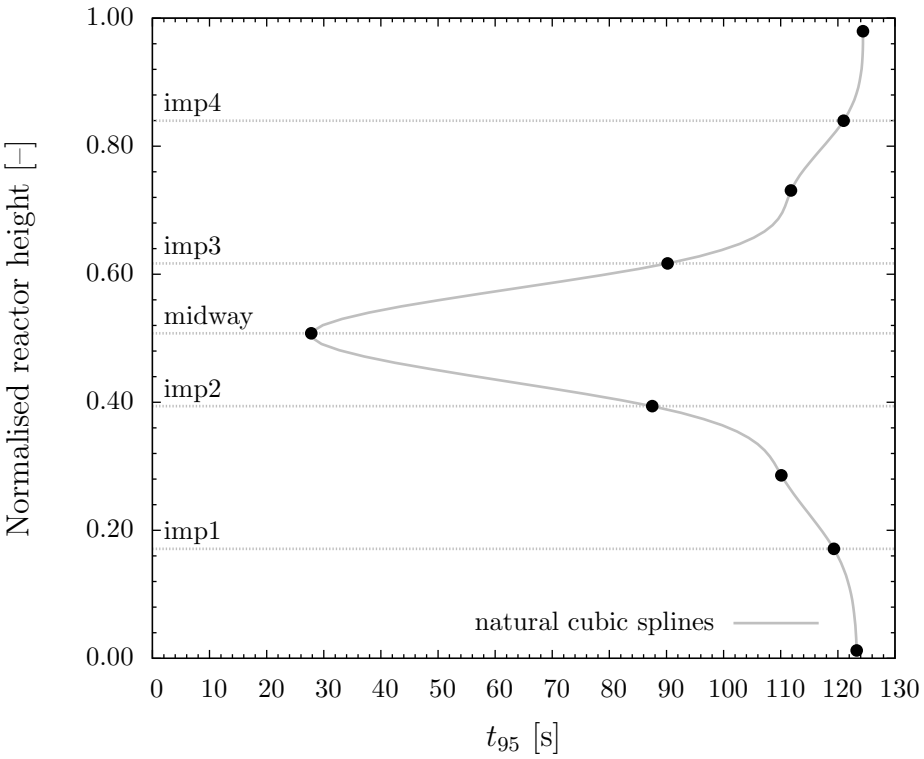

Figure 11.6: Plot of the mixing time data given in Fig. 11.5 with respect to the normalised reactor height. A trendline is drawn to guide the eye by smoothing the data by natural cubic splines. Impeller centerline locations and the midway location between impeller 2 and 3 (near the axial center of the tank) are also denoted.

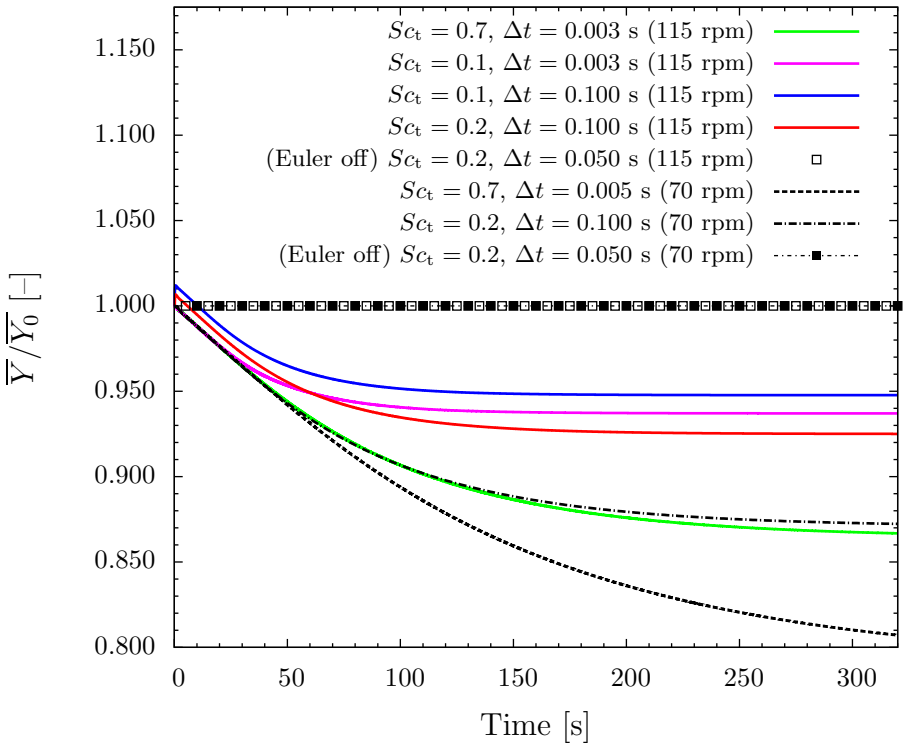

Figure 11.7: Tracer mass conservation depending on stirring rate, Sc_t, the time step and whether the single-phase simulation is based on Euler–Euler setup. Mean tracer concentration is normalised by that at $t = 0$, $\overline{Y}/\overline{Y_0}$. Tracer was injected at the top port and detected at the bottom port (bottom impeller outflow).

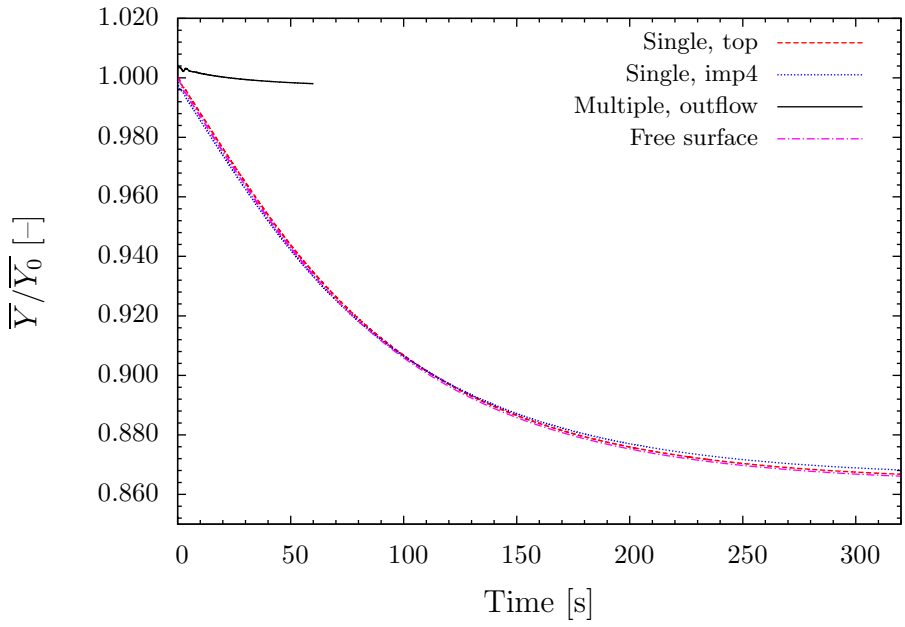

Figure 11.8: Tracer mass conservation (115 rpm, $Sc_t = 0.7$, $\Delta t = 0.003$ s) depending on different injection methods (as outlined in Section 11.6.5 and shown in Fig. 11.2). Mean tracer concentration is normalised by that at $t = 0$, $\overline{Y}/\overline{Y_0}$. Simulation with the multiple-point injection method ended earlier than others as it reached quickly the 95% homogeneity.

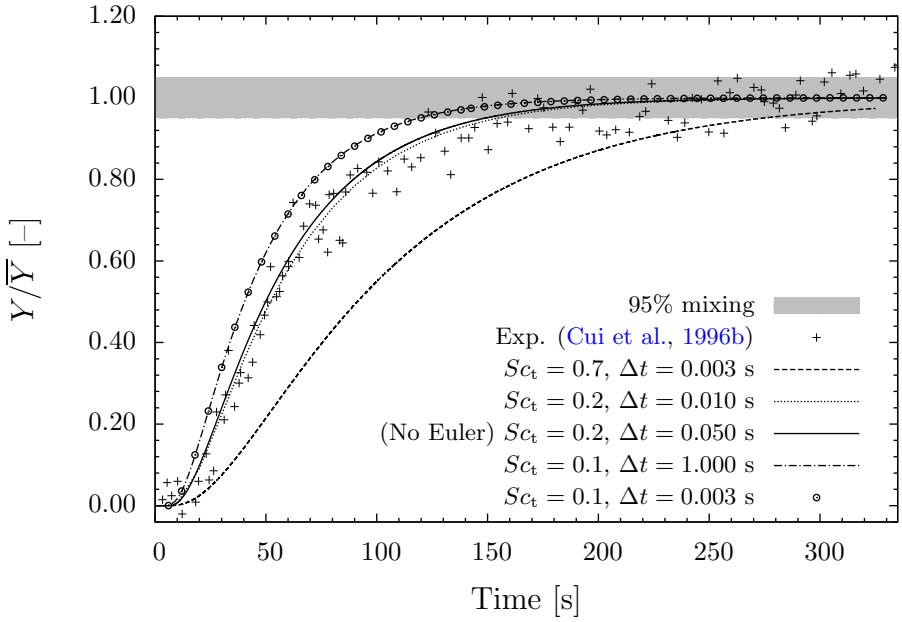

Case: 115 rpm, detection at bottom impeller outflow

	Exp.	$Sc_t = 0.7$	$Sc_t = 0.2$	$Sc_t = 0.1$
t_{95} [s]	150[a], 170[b]	274.0	154.5	118.7
Relative error in t_{95} [%][c]	–	82.7	2.9	−20.8
Nt_{95} [–]	288[a]	525.2	296.1	227.5
$t_{lag,1\%}$ [s]	15[d]	15.3	10.9	8.8
$t_{lag,5\%}$ [s]		26.6	16.3	13.2

[a]Measurements of Vrábel et al. (1999)

[b]Measurements of Noorman (1993)

[c]Relative deviation from the experimental value of Vrábel et al. (1999)

[d]Measurements of Noorman et al. (1993) and Cui et al. (1996b)

Figure 11.9: Predicted and measured relative tracer concentration for 115 rpm. Tracer was introduced at the top and detected at the bottom impeller outflow. Tracer injection and detection locations are similar to experiments (Cui et al., 1996b). The mixing time for 95% homogeneity and the lag time when the detected concentration reaches 1% and 5% homogeneity level are indicated in the table.

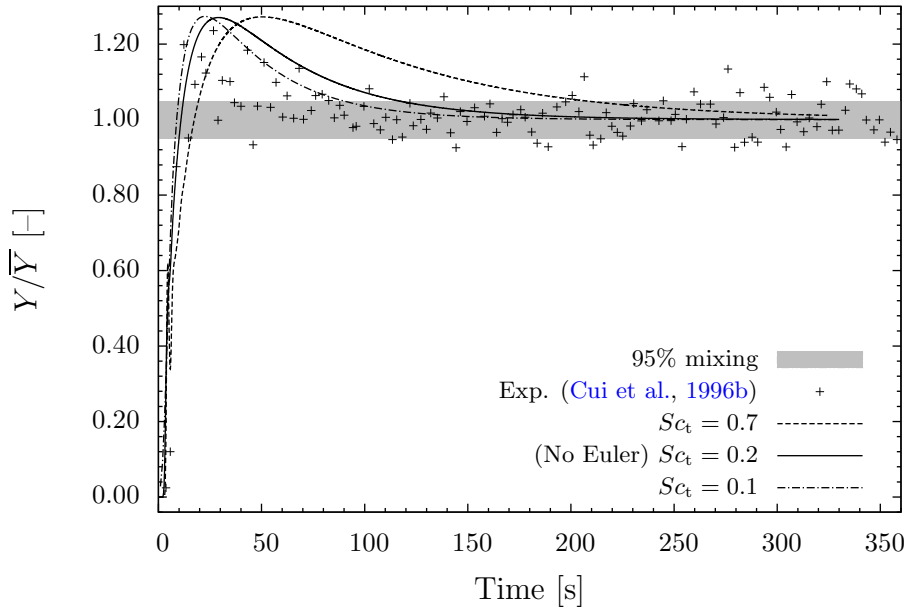

Case: 115 rpm, detection at third impeller outflow

	Exp.	$Sc_t = 0.7$	$Sc_t = 0.2$	$Sc_t = 0.1$
t_{95} [s]	–	206.5	116.1	89.3

Figure 11.10: Predicted and measured relative tracer concentration for 115 rpm. Tracer was introduced at the top and detected at the third impeller outflow. Tracer injection and detection locations similar to experiments (Cui et al., 1996b).

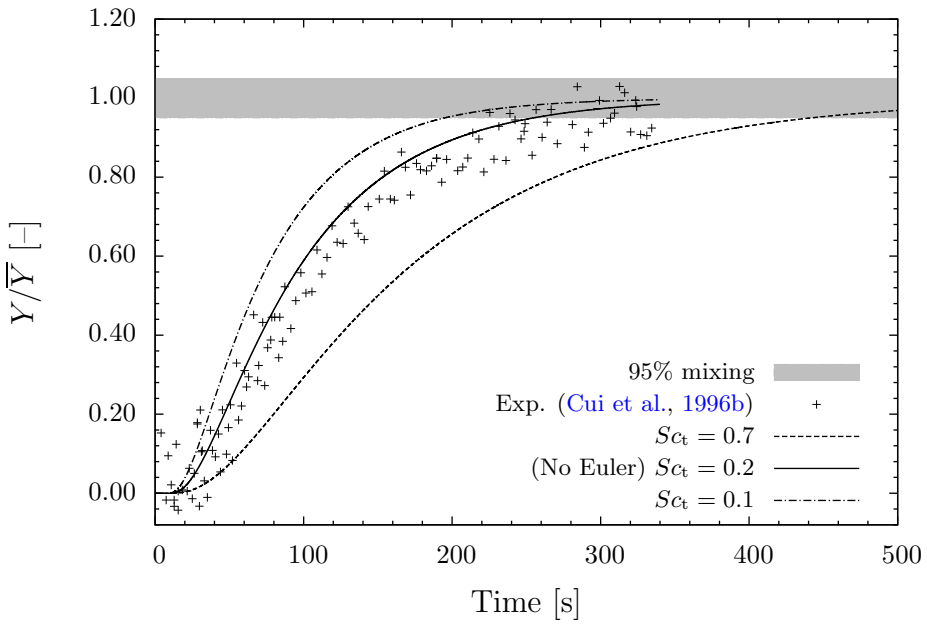

Case: 70 rpm, detection at bottom impeller outflow

	Exp.	$Sc_t = 0.7$	$Sc_t = 0.2$	$Sc_t = 0.1$
t_{95} [s]	255[a]	441.8	254.8	194.9
Relative error in t_{95} [%][b]	–	73.2	$-7.8 \cdot 10^{-2}$	−23.6
Nt_{95} [–]	298[a]	515.4	297.3	227.4
$(115/70) \times t_{95\%,115\ \mathrm{rpm}}$ [s]	246	450.1	253.8	195.0
$t_{\mathrm{lag},1\%}$ [s]	20[c]	26.1	17.9	14.9
$t_{\mathrm{lag},5\%}$ [s]		43.0	26.8	21.6

[a]Measurements of Vrábel et al. (1999)

[b]Relative deviation from the experimental value of Vrábel et al. (1999)

[c]Measurements of Cui et al. (1996b)

Figure 11.11: Predicted and measured relative tracer concentration for 70 rpm. Tracer was introduced at the top and detected at the bottom impeller outflow. Tracer injection and detection locations are similar to experiments (Cui et al., 1996b). The mixing time for 95% homogeneity and the lag time when the detected concentration reaches 1% and 5% homogeneity level are indicated in the table. As Nt_{95} is constant in fully turbulent single-phase flow, a predicton was made based on the mixing time for 115 rpm ($t_{95\%,70\ \mathrm{rpm}} = (115/70) \times t_{95\%,115\ \mathrm{rpm}}$).

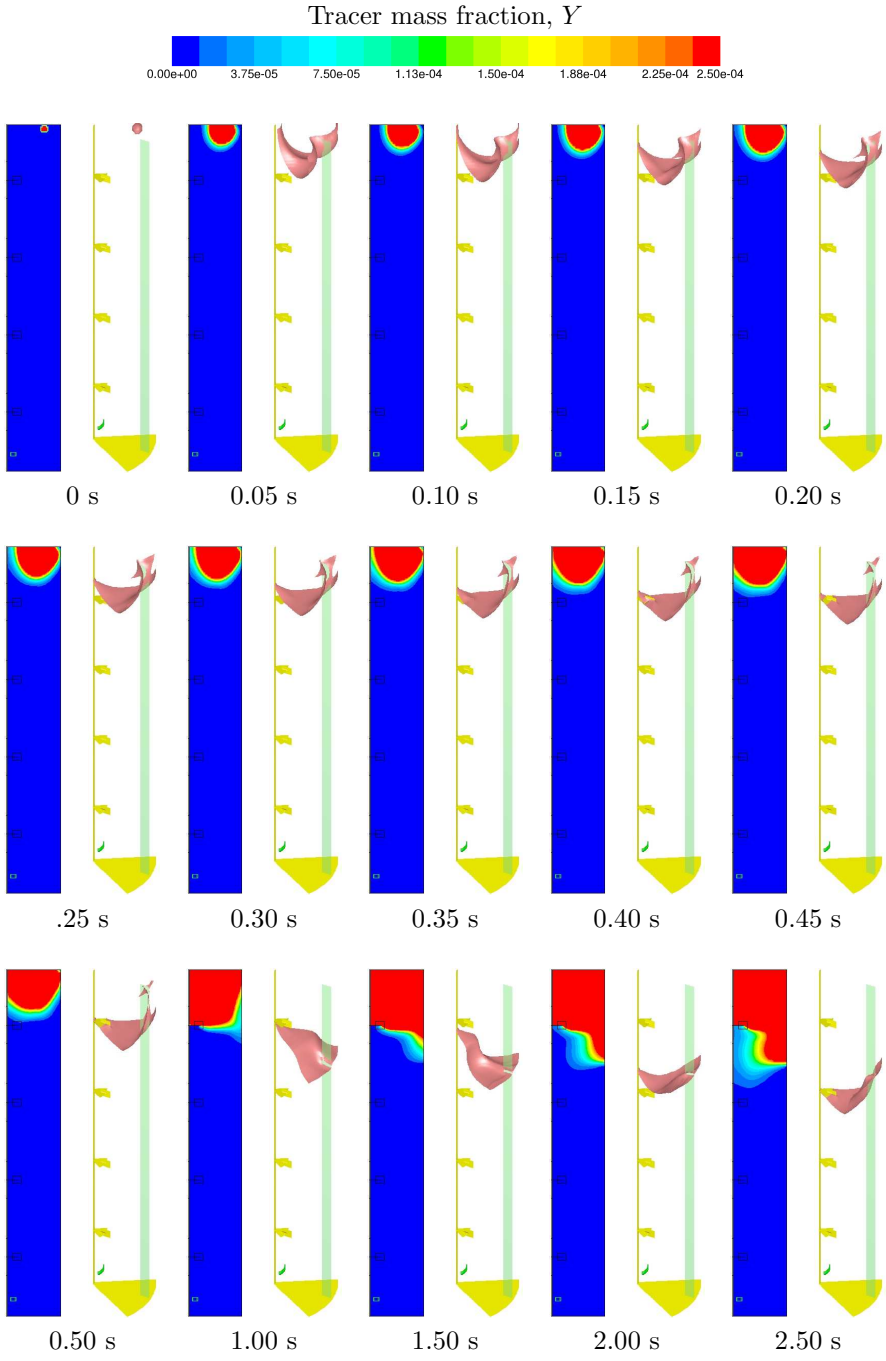

Figure 11.12: Time evolution of tracer transport when tracer was introduced from top (115 rpm, $Sc_t = 0.2$). Tracer mean mass fraction contours at an angular plane coinciding with the tracer injection location (25° with respect to the baffle) are given on the left. On the right, iso-surface of tracer mean mass fraction of 10^{-6} (i.e. about 100 times lower than the final equilibrium value, $\overline{Y} = 1.43 \cdot 10^{-4}$) are given.

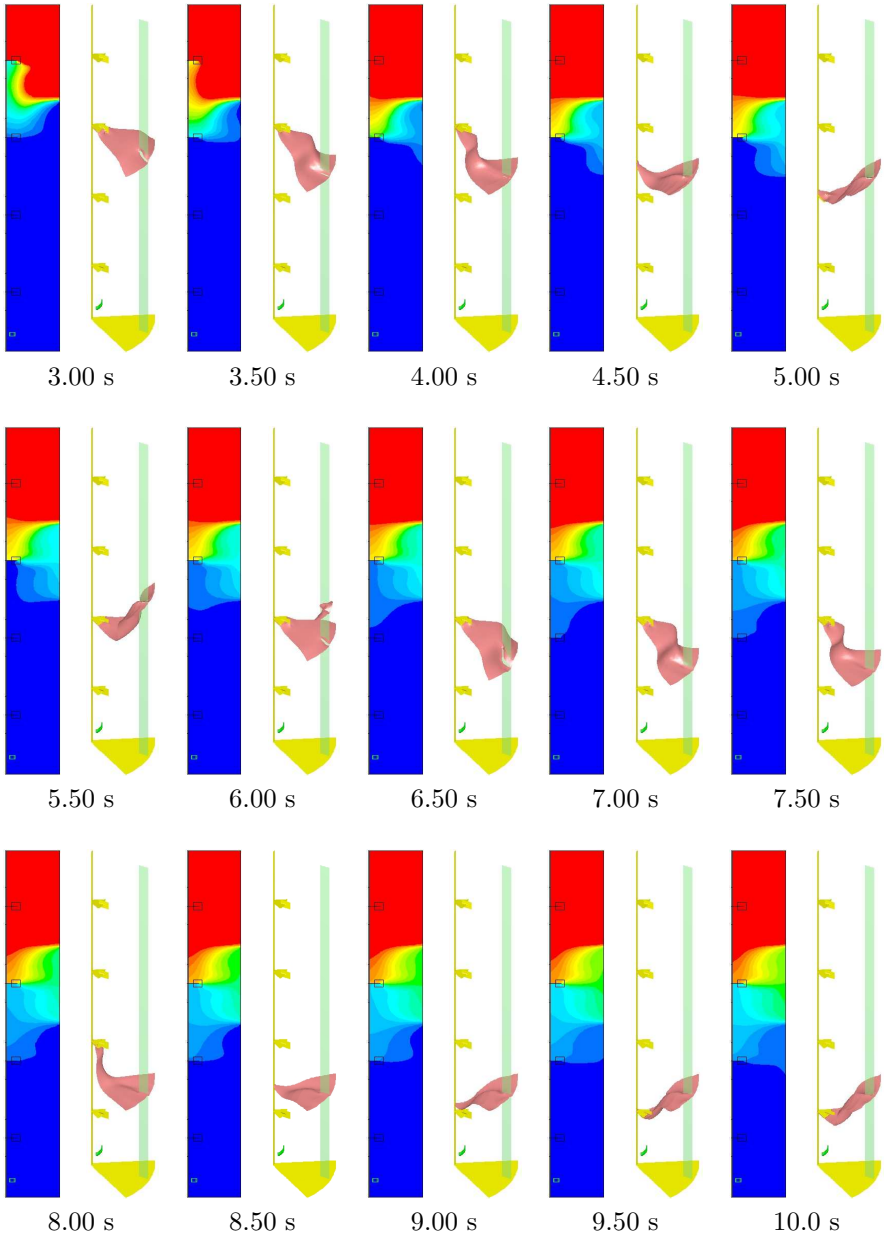

Figure 11.13: (cont. Fig. 11.12).

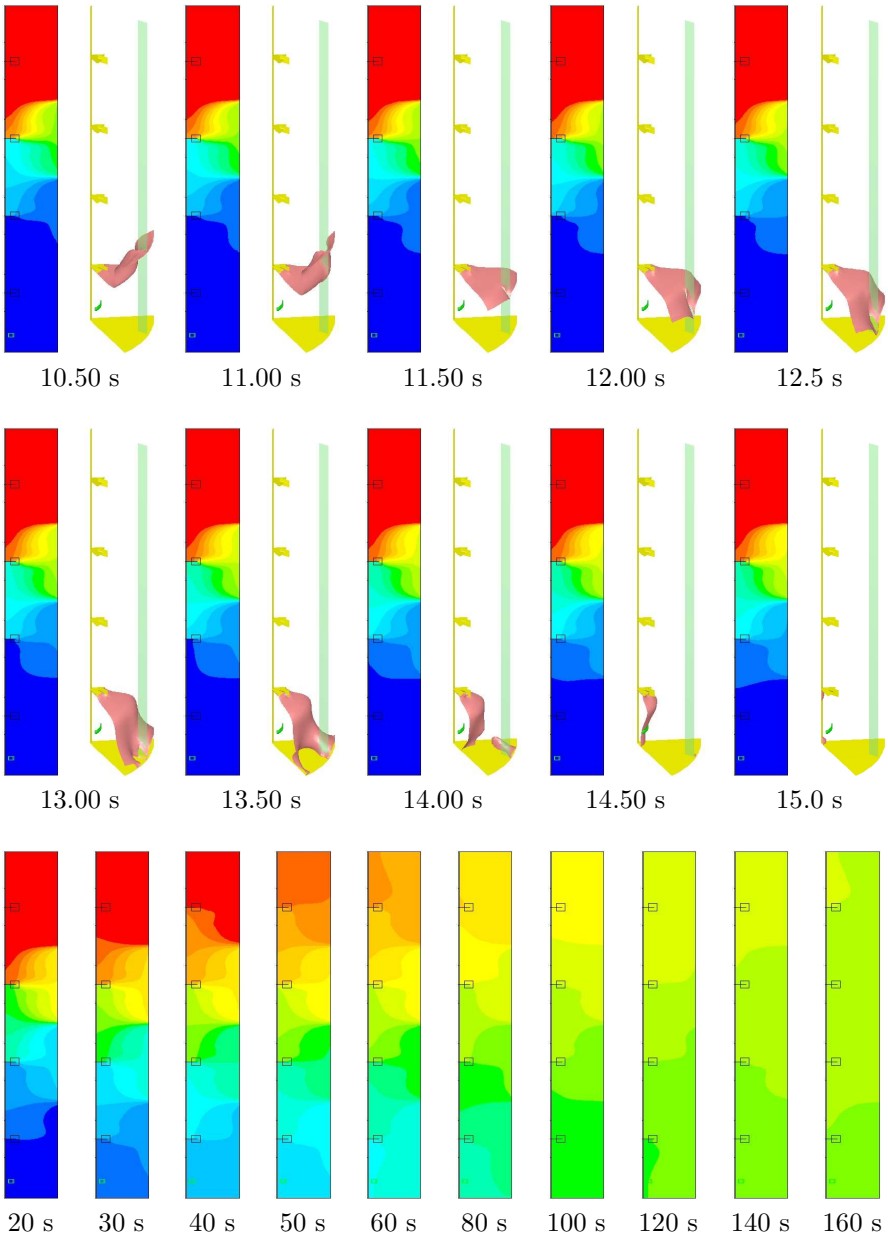

Figure 11.14: (cont. Fig. 11.12).

Chapter 12

Substrate uptake kinetics in the 30 m^3 fermenter

In this final chapter of results, we report on the sugar (glucose) uptake kinetics in the 30 m^3 fermenter. It builds on the gas dispersion and mixing studies reported in Chapter 10 and 11, respectively, and aims at applying the simulation methodology developed earlier on to a real industrial fermentation case with the addition of kinetics modelling.

In this study, we limited ourselves to the modelling of the fed-batch Saccharomyces cerevisiae (baker's yeast) cultivation studies that have been made on the same reactor. Simulations were performed under a number of simplifications of the underlying fermentation process. Results of those are compared with the experimental data reported.

12.1 Effect of transport processes on bioreactor performance

When the time constants of physical and biological transport processes taking place in the reactor exceed those of the bioreaction kinetics, scalar gradients are likely to form in the reactor. This would happen, for instance, when the degree of mixing is not sufficiently fast and when there are mass transport limitations. Among the examples of this situation is gradients of pH and any component fed in growth limiting concentrations and/or amounts to the reactor (Larsson et al., 1996). Alternatively, when the reaction rate is high (e.g. low substrate saturation constant), again gradients would form in the reactor. Due to the above mentioned rate limitations, cellular products and cell concentrations are not expected to form gradients, while CO_2 is an exception to this, forming gradients by a similar mechanism as O_2 (Larsson et al., 1996).

Generally, in large scale industrial bioreactors, the rate limiting process is transport phenomena rather than biokinetics (contrary to lab scale), because the reaction kinetics does not depend on scale. Fermentation process relies critically on sufficiently fast and

uniform supply of substrate to microorganisms in the fermenter and keeping vital concentrations within the desired limits. In case of aerobic fermentations, transport rate of O_2 from sparged air bubbles to microorganisms and that of the removal of resultant CO_2 are also vital process parameters. Those would inherently be coupled with the (radial and axial) distribution of bubble size, pressure and turbulence in the reactor.

Transport limitations would promote formation of local substrate gradients, which typically occur near feed inlets, where a region of high substrate concentration (the so-called feed zone) exist due to insufficient mixing (see the discussion in Section 11.2.3 regarding mesomixing). Such large substrate concentrations may result in, for instance, ethanol formation of Saccharomyces cerevisiae by the so-called "overflow mechanism" when glucose concentration is above 40 mgl^{-1} (Larsson et al., 1996). Furthermore, cells circulating in the fermenter could experience and respond to large variations of substrate concentration along their trajectory; ranging from feed concentration (for glucose typically 600 gl^{-1}) down to zero (at locations of high reaction rates), which may give rise to situations ranging from feast to famine.

Ultimately, the microenvironment inside the reactor is the determinant of the bioreactor performance as microorganisms react directly upon this, which itself is created by the microbial activity and physical conditions (e.g. flow, temperature, concentration) throughout the process. As a result, it's crucial to predict the effect of variations in the microenvironment on the process relevant variables such as yield and product quality.

12.2 Study of Larsson et al.

A series of papers were published reporting on fed-batch Saccharomyces cerevisiae cultivation studies performed on the 30 m^3 fermenter (Noorman et al., 1993; Noorman, 1993; Noorman et al., 1994; Larsson et al., 1996). Those studies collectively were a result of a joint effort supported by the Nordic Programme on Bioprocess Engineering at the time. Some comparison was also made of the experimental data with predictions from the CFD models developed, in which microbial kinetics and fluid dynamics were integrated. Among those studies, that of Larsson et al. (1996) provides the most extensive data, hence constitutes the base reference for comparison for our model predictions reported in this chapter.

12.2.1 Fed-batch technique

The fed-batch technique (i.e. a substance is fed to the reactor at a limited rate) is widely used in industry to avoid previously mentioned situations due to transport limitations. Usually the energy source substance (e.g. glucose) is fed to the process as the limiting component. In cases where it is beneficial to the process, a special feeding scheme is employed to maximise the cell productivity ($gl^{-1}h^{-1}$) over the process time. The feed is first fed exponentially until the maximum productivity is reached, and thereafter a constant feed rate is ensured to allow cell concentration to rise in expense of the growth rate. The substrate concentration at the constant feed regime is kept often below the saturation constant value for the organisms and substrate (for Saccharomyces

cerevisiae, 150 mgl^{-1} for growth on glucose) and it will gradually decrease throughout the process, approaching ultimately to zero (Larsson et al., 1996).

In fed-batch processes, feed solutions are usually added in concentrated form to avoid large volume build up. In the experiments of Larsson et al., glucose feed concentration was 600 gl^{-1}, which was introduced to the reactor at a single point. The mixing of the feed solution into the bulk could be adversely affected due to a non-optimal feed location and significant difference in feed and bulk viscosities. The rate of addition of the concentrated feed stream into the reactor could be as slow as what could be described as "dripping".

12.2.2 Experimental settings and operating conditions

In the study of Larsson et al. (1996), the fed-batch concept was adopted with glucose as the limiting component (i.e. bacterial growth was limited by glucose) which was initially present and also fed into the system continuously from top or bottom feed positions. Top feed position was at a height of 6.5 m, close to the stirrer shaft, and the bottom feed position was at a height of 0.9 m, just below the disc of the lowest impeller. We only simulated the top feeding case in this study due to time constraints, however application to the bottom feeding case is straight forward.

The medium was a Newtonian glucose solution with minerals. Glucose levels were measured at three sampling levels, at bottom, middle and top, with axial locations of $y = 0.97, 3.90$ and 6.35 m, respectively. Radial and tangential locations of those monitoring points were not reported. With the glucose analysis method adopted, results were within a 95% confidence limits of the mean. The total liquid volume in the fermenter was between $19.8 - 22.3$ m^3 due to feed of glucose solution.

The fermenter was operating under the conditions that we denoted as Case 5 in our study, that is, the stirring and gassing rates were 133 rpm and 0.182 m^3/s, respectively (see Section 10.3.10 and Table 10.1). Under those conditions, the bottom impeller is slightly above the flooding condition according to the flow regime map we constructed given in Fig. 10.1. Note that Noorman et al. (1993) found that the looding–flooding transition took place between impeller speeds of 115–133 rpm at the same gassing rate, while Larsson et al. (1996) reported that the impeller was not flooding at 133 rpm.

The feed rate, Q_{F}, glucose feed concentration, C_{sf}, initial reactor volume, $\mathcal{V}_{\mathrm{l}}(0)$ and initial concentrations of biomass, C_{x}, glucose, C_{s}, and ethanol, C_{e}, are given in Table 12.1. The dissolved oxygen concentration was always above 30% air saturation throughout the cultivation.

12.2.3 Integrated CFD and biokinetic model

The CFD model adopted by Larsson et al. was coupled to a biokinetic model to describe substrate (glucose) uptake kinetics in the fermenter. Monod type kinetics was employed. It was assumed that the maximum specific substrate uptake rate was constant (1.7 $\mathrm{gg}^{-1}\mathrm{h}^{-1}$) throughout the process and that the saturation constant was 180 mgl^{-1}.

12.2.4 Main findings

Glucose concentration in the reactor showed a variance. Glucose levels were found to differ at all monitoring points at all times. Gradients in time and space are due to three mechanisms which are superimposed:

- While glucose was fed continuously, its mean concentration in the fermenter was declining throughout the whole process. This long declining phase of the fed-batch cultivation with constant feed occurs on a time scale on the order of tens of hours and depends only on the cultivation technique.
- Macromixing in the reactor as well as the mass transfer on a micro scale influences gradients. Depending on the circulation time distribution of the reactor, this gives rise to fluctuations on the order of seconds to minutes.
- Local rapid fluctuations on the order of seconds or fractions of seconds occur due to turbulence. Turbulence measurements by thermal anemometry showed the dominance of low frequency, high amplitude flow variations which have fairly uniform time scale both at impeller and bulk zones (and both for ungassed and gassed situation). This seems to indicate the existence of low frequency, high amplitude phenomena in the reactor. This, together with observed short-time oscillations in substrate concentration, suggests that the limiting substrate that is fed to the process was transported over long distances without substantial mixing both in the impeller, and especially, in the bulk zone of the reactor. The turbulence level at the feed location has also an influence. When the feed location was at a stagnant region (top port), fluctuations were more pronounced (a peak of an amplitude of 40 mgl^{-1} observed at one stage) than that when the feed was supplied at a well mixed impeller region (bottom port), where the deviation from the mean was negligible.

The resultant biological effect of the above mentioned substrate gradients is that the specific glucose consumption rate will oscillate if the cellular response time is instant. From spatial variations observed at one instant during the process, the energy metabolism was calculated to be more than seven times higher for a cell at the top of the reactor than for one at the bottom. Assuming again instant cellular response, such conditions would induce production of ethanol in the high glucose top region, which may be consumed again in the bottom. This will cause a reduction in the yield of cells. At the other extreme, for very low glucose concentrations or complete exhaust, rapid microbial stress responses give rise to important changes in the protein structure of cells.

CFD predictions made on the other hand showed quantitative discrepancy between the measured and predicted concentration profiles, though there was a qualitative agreement. The predicted substrate concentrations were declining axially when going away from the feed point, similar to measurements, however the decline was at a higher rate. The discrepancy was higher at higher cell concentrations. It was left as an open question whether this was due to shortcomings of the CFD model or the biokinetic model. Assuming that the biokinetic model (Monod) for glucose uptake is accurate, this seemed to indicate that the CFD model underestimates the axial mixing. Unfortunately, they did not report the value of the turbulent Schmidt number used in

simulations, which has a direct effect on axial dispersion, as shown by our results in Chapter 11. On the other hand, it was also noted that the predicted axial concentrations were strongly dependent on the values of the maximum substrate uptake rate and the saturation constant.

Two separate strategies were proposed to reduce the aforementioned gradients and, in turn, their resultant effects. In case the gradients are originated due to mixing limitations in the reactor, one can introduce the substrate via multiple inlets at well-mixed regions. Furthermore, use of diluted feed solutions, despite giving a higher volume build up, may reduce the mixing time since the viscosity and density differences are reduced. If the gradients have a microbial origin, then the microorganisms with a higher saturation constant for the substrate can be used.

12.3 Computation of substrate uptake kinetics

The modelling approach taken is an extension to the single-phase mixing model described in Chapter 11. Spatial and temporal variations of glucose in the reactor was computed by solving the multiphase species transport equation. We followed again the frozen field approach, that is, a convection-diffusion equation was solved for glucose based on the converged two-phase flow field.

Integrated biokinetic model follows from that of Larsson et al., based on the Monod kinetics, and was implemented as a source term in the species transport equation via a user subroutine. Model constants were the same as described in Larsson et al. (1996).

12.3.1 Multiphase species transport equation

The species transport equation given in Eq.11.48 can be extended to multiphase flows. For each phase k, the local mass fraction of each species $Y_{i,k}$ is predicted by solving a convection-diffusion equation for the i^{th} species:

$$\frac{\partial}{\partial t}(\alpha_q \rho_q Y_{i,q}) + \nabla \cdot (\alpha_q \rho_q \mathbf{U}_q Y_{i,q}) = -\nabla \cdot \alpha_q \mathbf{J}_{i,q} + \underbrace{\alpha_q S_{i,q}}_{\text{sources}} + \underbrace{\sum_{p=1}^{n} (\dot{m}_{p^i q^j} - \dot{m}_{q^j p^i})}_{\text{interface mass transport}} . \quad (12.1)$$

The species mass diffusion flux $\mathbf{J}_i$ is calculated from Eq. 11.49. The second term on the r.h.s. denotes the source terms, which we used to define the glucose feed and biokinetics via user subroutines. The last term describes the interphase species transport, where $\dot{m}_{p^i q^j}$ is the mass transfer rate per unit volume from the i^{th} species of phase p to the j^{th} species of phase q. We are not concerned in this study with interphase transport, hence this term is null.

12.3.2 Biokinetic model

The microbiological growth on glucose substrate can be simplified by the following scheme (see e.g. Xu et al. (1999); Vrábel et al. (2001) for detailed description of uptake

metabolism):

$$\text{Glucose(S)} + \text{Biomass(X)} + \text{O}_2 \longrightarrow \text{Biomass(X)} + \text{Ethanol} + \text{CO}_2 + ... \tag{12.2}$$

For glucose limited growth of Saccharomyces cerevisiae, the substrate consumption rate, r_s, can be described by Monod kinetics (Noorman et al., 1993, 1994; Larsson et al., 1996):

$$r_s = -\frac{dC_s}{dt} = q_{s,max}\left(\frac{C_x C_s}{C_s + K_s}\right), \tag{12.3}$$

where the maximum specific substrate consumption rate can be assumed to take a constant value, $q_{s,max} = 1.7$ gS $gX^{-1}h^{-1}$, and the saturation constant is $K_s = 180$ mgS l^{-1} (the substrate concentration at which the consumption rate is at its half-maximum value) according to Larsson et al. (1996).

At large substrate concentrations ($C_s \gg K_s$), the rate of substrate consumption is at a maximum, limited by other factors such as oxygen, nutrients or the characteristics of the organism, and it is first-order with respect to C_x and zero-order with respect to C_s:

$$r_s = q_{s,max}\, C_x, \quad \text{for} \quad C_s \gg K_s. \tag{12.4}$$

During the substrate limited growth operation where the substrate concentration is low ($C_s \ll K_s$), the rate of substrate consumption is first-order with respect to both C_x and C_s:

$$r_s = \left(\frac{q_{s,max}}{K_s}\right) C_x C_s, \quad \text{for} \quad C_s \ll K_s. \tag{12.5}$$

The kinetic relation in Eq. 12.3 was implemented in the CFD code as a user defined source term in the transport equation solved for the glucose species (Eq. 12.1). Two assumptions were made in order to decrease the computational effort:

- Biomass concentration in the reactor is constant, $C_{x,1} \neq f(t, x, y, z)$. That is, the reactor is well-mixed and stationary regarding the biomass concentration at least within simulation time scales. Therefore, a transport equation was solved only for the glucose species. Measurements of Larsson et al. (1996) support this assumption that the biomass concentration during fermentation changes in a longer time scale. That is, it increases from its initial value, $C_{x,1}(0) = 0.15$ kg m^{-3}, to 10 kg m^{-3} in about 11 hours, and from 10 to 20 kg/m^3 in about 7 hours. Following experimental conditions, we took $C_{x,1} = 10$ g/l, which refers to the moment of the process after about 11 hours have lapsed.

- All species have the same properties as water (viscosity, density, diffusion coefficient), hence local concentration values in the liquid phase were calculated from local mass fractions, e.g. $C_{s,1} = \rho_1 Y_{s,1}$. This allowed us to decouple fluid dynamics from species transport and biokinetics calculations (i.e. frozen field approach). Equations for momentum, gas volume fraction, turbulence and bubble size bins were turned off while solving for the species transport.

Local values of the source term computed according to Eq. 12.3 were stored in user defined memory locations. This was to check if the fed-batch process has reached the

condition that the overall substrate consumption rate was equal to the substrate feed rate :

$$\int_{\mathcal{V}_t} \alpha_1 q_{s,max} \left(\frac{C_{x,1} C_{s,1}}{C_{s,1} + K_s} \right) dV = C_{sf,1} Q_F, \tag{12.6}$$

where $\mathcal{V}_t$ is the total reactor volume.

12.3.3 Micromixing effects

In Section 11.3, we discussed mixing effects on bioreactors. For water-like fermentations in large scale reactors, Groen (1994) estimated that micromixing time scale is too short (of the order of 0.02 s) compared with the macromixing time scales of the order of tens of seconds, hence its contribution to the total mixing process is negligible. Moreover, detailed analysis and modelling of the microscale phenomena (biokinetics, metabolics) was not the scope of this thesis. Therefore, we did not attempt to incorporate any subgrid scale micromixing model in this study. Possible effects of insufficient mixing on Saccharomyces cerevisiae production was discussed in Section 11.3.

As a result of the modelling approach we adopted, for any point in the reactor, the reaction rate is determined by the local average concentrations at the scale of the grid. This implies that all components are perfectly mixed at the grid scale and subgrid scale concentration fluctuations are null. Validity of this assumption is discussed in Section 12.5.6. In case micromixing effects cannot be neglected, kinetic equations have to be incorporated into mixing models locally via micromixing models (Bałdyga and Pohorecki, 1995).

12.4 Numerical setup

We performed simulations that mimic the measurements of Larsson et al. (1996). The stirring and gassing rates were 133 rpm and 0.182 m^3/s, respectively. This corresponds to our Case 5 in the dense bubble regime results of which we reported in Section 10.3.10 (see also Table 10.1). The Ishii & Zuber multiparticle drag law was used in combination with the discrete model for population balances.

12.4.1 Problems with pressure outlet boundary

As pointed out previously, we took the frozen field approach. Initially we used the converged two-phase solution based on the pressure outlet (PO) boundary at the free surface as plotted in Fig. 10.20(b). PO allows water in- and outflux across the free surface. This caused instability in substrate transport and uptake kinetics simulations.

We then defined a degassing boundary and performed a new hydrodynamics simulation as reported in Fig. 10.20(c) and subsequent figures. This ensured zero water flux across the free surface while gas was allowed to leave the domain. Kinetics simulations based on this converged two-phase solution with the degassing condition were stable. Results reported here are therefore from those simulations.

Settings for the substrate transport and uptake kinetics part of the simulations are described below.

12.4.2 Main simplifications and differences

There are a number of differences in the simulations with respect to the actual experiments. Furthermore, some simplifications were made in order to decrease the computational cost. Those are:

- In experiments, the liquid volume in the fermenter has increased from 19.8 to 22.3 m^3 due to glucose feed. In simulations, the liquid volume was constant at 22 m^3. Furthermore, the liquid level in experiments was reported to be approximately $H = 3.5T = 7.3$ m. In simulations, the liquid level was 6.55 m, same as the other simulations of this fermenter reported in previous chapters.

- The bottom impeller clearance from the bottom wall was 1.045 m, whereas it was 1.12 m in simulations.

- The headspace pressure in the fermenter was 1.29 bar, whereas it was kept as 1 bar in simulations. The effect of hydrostatic pressure was not taken into account.

- We modelled only the constant feed phase of the overall fermentation process and did not take into account the initial exponential feed phase.

- We assumed that the concentration of the biomass, C_x, does not change on the time-scale of the process interval of interest (i.e. quasi-steady-state or pseudo-steady-state in terms of biomass concentration). This assumption was discussed in Section 12.3.2.

- The measured concentrations reported by Larsson et al. (1996) were instant values that were influenced by turbulent fluctuations. Mean concentrations were not reported.

- We assumed that all species have the same properties (viscosity, density, diffusion coefficient) as water (also discussed in Section 12.3.2). Especially near the feed zone, this assumption would be rather crude.

12.4.3 Initial and boundary conditions

Initial concentrations and feed conditions used follow from Larsson et al. (1996) where they also conducted a CFD study and are given in Table 12.2. Those conditions correspond to the constant feed rate phase of the actual fed-batch Saccharomyces cerevisiae cultivation studies performed by Larsson and refer to the moment of the process after about 11 hours have lapsed. At that instant, the mean glucose concentration in the fermenter was 43.5 mg/l, and we patched the initial glucose concentration, $C_s(0)$, to this value everywhere in the domain.

Glucose feed

The constant glucose feed was introduced into the domain via a source term defined in the species transport equation. As the volume increase due to feed was neglected and the frozen field approach was taken, flow equations were not solved, thus no feed mass or momentum source was needed.

The source term was added at a group of grid cells that represent the top feed position of Larsson at a height of 6.5 m, close to the stirrer shaft (see Fig. 12.1). The gas fraction at those grid cells was patched to the value of zero. Note that, although feed location mimics closely the way glucose was introduced in experiments, the rotational periodicity assumption gives rise to 6 rotationally symmetric feed locations (each with 1/6 of the actual feed rate of Larsson) in reality. However, feed points are not far from each other as they're located close to the central shaft. For the case of passive tracer mixing, no significant effect of this was found on the concentration profiles detected near the bottom impeller (reported in Section 11.7.2). Effect of feed location is expected to be significant in the presence of fast chemical reactions.

On wall boundaries, zero species (glucose) mass flux condition was imposed.

Biomass

The biomass concentration was fixed to the constant value $C_{\mathrm{x},1} = 10$ g/l everywhere in the domain as discussed in Section 12.3.2.

12.4.4 Monitoring locations, postprocessing plane

A number of monitoring locations were defined that follow from the sampling locations of Larsson et al. Those are located at axial locations $y = 0.97, 3.90$ and 6.35 m from the vessel bottom wall and denoted as bottom, middle and top sampling levels. Note that the radial and tangential coordinates of the measurement points were not reported by Larsson et al. Illustration of the geometry and port locations they provided, however, suggests that they were close to the tank wall.

We specified 3 different monitoring locations (denoted as port 1, 2 and 3) for each of those axial planes in order to see the extent of spatial variations (see Fig. 12.1). Monitoring locations were chosen such that port 1 and 2 had the same angular location (-25° w.r.t. baffle), while port 3 was located at the same angular position with the baffle. Furthermore, port 2 and 3 had the same radial distance from the tank wall (30 cm), while port 1 was located at 2.5 cm from the tank wall.

We also specified a postprocessing plane for the time evolution of glucose concentration contours, which is -10 degrees with respect to the baffle (20 degrees from the mid-baffle plane) and is also shown in Fig. 12.1.

12.4.5 Transient settings

Second order implicit time discretisation scheme was employed for the transient terms of the species transport equation. Discretisation of the convective terms in the modelling equations are based on higher order QUICK scheme. Two different time steps, 5 and 50 ms, were chosen to see the effect of this on results.

12.4.6 Convergence criteria

Simulations were considered converged when the sum of the species residuals was lower than 10^{-7} at each time step. At this level of convergence, the concentration profiles had already approached to a constant value.

12.5 Results and discussion

12.5.1 Comparison with experimental data

Comparison of the experimental data of Larsson et al. (1996) with the predictions made with different values of turbulent Schmidt number and time step size are given in Fig. 12.2–12.5 and in Table 12.3. Glucose concentrations were monitored at the port 1 location (see Fig. 12.1).

Effect of turbulent Schmidt number

Fig. 12.2 and 12.3 shows that the value of Sc_t has a significant effect on concentration predictions. We tested both the Fluent default value, $Sc_t = 0.7$, and based on the foundings reported in Section 11.7.5, also $Sc_t = 0.2$, which gave the best fit to the experimental data in single-phase tracer mixing simulations. When the turbulent diffusion was low (i.e. $Sc_t = 0.7$), all predictions were below the measured values. The top sampling level profile showed an overshoot while the middle and bottom profiles were monotonically decreasing.

With the enhanced turbulent diffusion (i.e. $Sc_t = 0.2$), all monitored concentrations increased, the effect being larger when getting closer to the feed point (i.e. largest at the top sampling level). Predictions were closer to the experimental values except that at the top sampling level, where there was about $28 - 32\%$ overprediction depending on the time step (see Table 12.3). At the middle and bottom sampling levels, concentrations were underpredicted in the range $7 - 16$ and $51 - 54\%$ (depending again on the time step), respectively. Note that simulations started with the initial concentration, $C_s(0) = 43.5$ mg/l. Concentration at the top sampling level initially decreased from this value indicating that glucose feed stream had not yet arrived to the port location. It then started to increase with the incoming feed stream and reached finally an equilibrium concentration showing that locally the net substrate transport rate was equal to the consumption rate by the organisms. Concentration profiles reached the steady-state faster when $Sc_t = 0.7$ and when monitoring location was closer to the feed point near the free surface. This Schmidt number effect on the time to reach steady-state

was, however, found to be less when the time step was smaller as we will see in the next section.

Effect of time step size

Fig. 12.4 and 12.5 shows that the value of the time step does not have a significant effect on steady-state concentration predictions. Final concentrations are about the same for both $\Delta t = 50$ and 5 ms, though small time step resulted in slightly better predictions in general (see Table 12.3). Note, however, that the time evolution of concentrations are different (especially at the top region), to which organisms would respond. Therefore, a small time step size is recommended if one is interested to model detailed metabolics. With a smaller time step, steady-state was also reached faster in terms of the physical time, though simulations took much longer due to the large number of time steps required (about 1 month computation time when $\Delta t = 5$ ms versus 1 week when $\Delta t = 50$ ms). Therefore, simulations with $\Delta t = 5$ ms were not run, in terms of physical time, as long as those with a large time step.

Overall, best predictions were achieved with small Schmidt number and time step, namely $Sc_\mathrm{t} = 0.2$ and $\Delta t = 5$ ms. We note here that, in interpretation of the results, it is important to bear in mind the differences between the setup of experiments and simulations, such as the glucose sampling/monitoring locations. This is investigated in the next section.

12.5.2 Sampling, feed and monitoring locations

Differences in sampling levels and feed location

As stated earlier, the bottom impeller clearance of Larsson et al. was 7.5 cm shorter (1.045 m instead of 1.120 m), which is about half the blade height. Therefore, in their experiments, top sampling level was 92.5 cm above the top impeller centerline, middle sampling level was 6.5 cm below the third impeller centerline and the bottom sampling level was 7.5 cm below the bottom impeller centerline. Corresponding values in our simulations were, 85 cm above, 14 cm below and 15 cm below, respectively. Overall, although the axial locations are the same in absolute terms, there is a shift about half the blade height relative to impellers.

There is also a shift in the feed location relative to the top impeller for the same reason. In addition to that, as mentioned earlier, the rotational periodicity assumption in simulations gives rise to 6 rotationally symmetric feed locations near the central shaft in close vicinity to each other. For the case of passive tracer mixing, no significant effect of this was found on the concentration profiles detected near the bottom impeller (see Section 11.7.2). Effect of feed location is expected to be significant in the presence of fast kinetics.

Furthermore, Larsson et al. (1996) reported that the liquid level in the fermenter was approximately $3.5T$, hence about 7.3 m, which is 75 cm higher than that in our case. The liquid volume was varying between $19.8 - 22.3$ m^3 due to the glucose feed. This, however, does not seem to agree with that reported in other publications on the same

fermenter (e.g. Vrábel et al. (1999)), where the liquid level was 6.55 m for 22 m^3 liquid volume. The liquid level of 7.3 m should give an extra volume of about 2.6 m^3. In our case, the liquid level was 6.55 m for 22.4 m^3 liquid volume due to the flat bottom of the fermenter. In any case, due to this uncertainty in the liquid level, the location of the top sampling level and the feeding point relative to the liquid surface is also expected to differ between the measurements and the simulations, hence should be kept in mind when interpreting the concentration profiles.

Effect of monitoring location

As noted earlier, although Larsson et al. (1996) reported the axial locations where they did the concentration measurements, exact position of sampling points at those axial planes were not specified. Illustration of the geometry and sampling locations they provided, however, suggests that they were positioned at the impeller centerline level (for middle and bottom sampling levels) close to the tank wall. The predicted concentration profiles we reported previously were therefore from the port 1 monitoring location close to the wall (see Fig. 12.1), while the axial locations reported by Larsson et al. remained unchanged.

In order to see the effect of the monitoring location, we plotted the concentration profiles from two additional ports for each of the top, middle and bottom sampling levels (Fig. 12.6–12.8). Values are normalised by the concentration measured by Larsson et al. at the respective level. At the middle and bottom levels, two more monitoring points were defined that are located at impeller 1 (bottom) and impeller 3 outflow regions close to the blades.

The monitoring port location has quite a significant effect. Maximum deviation relative to the port 1 value is about 14% (for $Sc_t = 0.2$), 32% (for $Sc_t = 0.7$) and 10% (for $Sc_t = 0.7$) for the top, middle and bottom levels, respectively. Those values are indicative as the exact sampling locations during the experiments are unknown, but serve as a scale for the variations to be expected when comparing our simulation results with the measurements of Larsson et al.

An interesting observation is that, concentration profiles at the impeller 3 outflow region (middle sampling level) for $Sc_t = 0.2$ and 0.7 follow each other rather closely. Since the impeller outflow is a high convection region, the decrease in sensitivity to the value of Sc_t seems to be reasonable. This is, however, not the case for the impeller outflow profiles at the bottom sampling level where there is larger sensitivity to the value of Sc_t.

12.5.3 Glucose mass conservation

So far, results reported previously and the discussion following them assumed that the glucose species mass is conserved in simulations. We, however, reported in Section 11.7.4 that, due to a bug in the Fluent code, the scalar mass was not conserved in simulations in which the Eulerian model was turned on. As this was the case for the simulations reported in this chapter, we checked the glucose mass conservation in the manner described below.

Estimation of the steady-state glucose concentration

As a first approximation, we made an estimate of the steady-state glucose concentration in the fermenter based on the perfect mixing assumption, hence substrate and biomass concentrations in the reactor were taken as constant: $C_{\mathrm{x}}, C_{\mathrm{s}} \neq f(t,x,y,z)$. Imposing the condition that overall glucose consumption rate is equal to the glucose feed rate:

$$\begin{aligned}\int_{\mathcal{V}_{\mathrm{t}}} \alpha_1 q_{\mathrm{s,max}} \left(\frac{C_{\mathrm{x},1} C_{\mathrm{s},1}}{C_{\mathrm{s},1}+K_{\mathrm{s}}}\right) dV &= C_{\mathrm{sf},1} Q_{\mathrm{F}}, \\ \alpha_1 q_{\mathrm{s,max}} \left(\frac{C_{\mathrm{x},1} C_{\mathrm{s},1}}{C_{\mathrm{s},1}+K_{\mathrm{s}}}\right) \mathcal{V}_{\mathrm{t}} &= C_{\mathrm{sf},1} Q_{\mathrm{F}} \quad \text{(perfect mixing)}, \\ C_{\mathrm{s},1} &= 36.6 \text{ mg/l}. \end{aligned} \tag{12.7}$$

In Fig. 12.9, predicted mean (volume-averaged) glucose concentration profiles in the fermenter for different time steps and Schmidt numbers are compared with the estimated steady-state glucose concentration according to the calculation above. Simulated concentrations reach steady values (in the range 14.1 to 17.3 mg/l, for $Sc_{\mathrm{t}} = 0.2$ and 0.7, respectively) which are significantly lower than the estimated value assuming no glucose gradients exist in the reactor (i.e. perfect mixing). The level of underprediction is in the range $53-63\%$, for $Sc_{\mathrm{t}} = 0.2$ and 0.7, respectively, and the time step size does not seem to have a significant effect (about 1% higher mass loss with a 10 times larger time step). The assumption of well mixedness is of course very crude and we know from previous results that significant glucose gradients exist across the reactor.

Estimation of the glucose mass loss rate

The rate of glucose loss in the domain can be computed in a similar way from a species mass balance as we know the glucose feed rate, the rate of glucose consumption by the microorganisms at every grid cell and the fact that glucose concentration profiles reached steady values in the course of simulations. Once the steady-state is reached, if the mass conservation is violated, the difference between the feed and consumption rates would be non-zero and equal to the rate of glucose mass loss:

$$\text{Glucose mass loss rate} = C_{\mathrm{sf},1} Q_{\mathrm{F}} - \int_{\mathcal{V}_{\mathrm{t}}} \alpha_l (-r_s) dV \tag{12.8}$$

The first term at the right hand side, the feed rate, is equal to 14.9 g/s. The second term is basically the integrated biokinetic source term in the glucose transport equation being solved. In simulations, it varies between $7.9-9.4$ g/s, for $Sc_{\mathrm{t}} = 0.2$ and 0.7, respectively. This results in glucose loss rates in the range $53-63\%$ of the glucose feed rate, for $Sc_{\mathrm{t}} = 0.2$ and 0.7, respectively. Not surprisingly, those agree with the error levels in the predicted steady glucose concentrations reported previously.

We note here that both calculation given above are rough estimates, because the kinetic sink term in Eq. 12.8 itself is a function of glucose concentration, hence is influenced by the glucose mass loss. It will react upon it in a stabilising manner: if there is glucose mass loss due to numerics, the rate of glucose loss due to bioconsumption would be less than what it would be otherwise (and the other way around in case of artificial glucose mass generation, still acting in a stabilising manner).

One can also employ a third method to estimate the glucose loss in the domain. Namely, simulations could be run with the kinetic source term switched off and the mass conservation could be tracked. Just as we did in the passive tracer mixing study reported in Chapter 11, glucose could be introduced into the domain by patching an initial glucose mass fraction at a pre-defined location and topology in the domain. The difference with the case at hand here is that we have a continuous glucose feed and consumption in the domain, and that the simulation is two-phase. Assuming those do not influence the mass loss significantly then one can expect similar levels of species loss as found in the passive tracer mixing study reported in Section 11.7.4. There we found that the tracer loss was higher at higher Sc_t values, smaller time steps and lower stirring rates. There was also a small amount of tracer mass increase in the very beginning of few simulations. For single-point injection from top, there was about 11% overall tracer loss.

Unfortunately, due to time constraints in the course of this study, we were not able to run test simulations described above with the kinetic term switched off.

12.5.4 Spatial distribution of glucose gradients

Concentration profiles given previously (Fig. 12.2–12.5) indicates that large axial substrate gradients exist across the fermenter. Near the bottom port, conditions are close to depletion and this would have consequences for the fermentation process.

A more detailed picture is provided by the time evolution of the gradients in Fig. 12.10 and the final steady state distribution in Fig. 12.11(b) and 12.13. The time series in Fig. 12.10 shows that the glucose concentration decreases significantly from the initial value of 43.5 mg/l to about 30 mg/l within about 10 seconds. Behind the impeller blades, concentrations fall rapidly to global minimum levels. Note that the contour planes are located at $-10°$ w.r.t. the baffle and the blade, coinciding with the large gas cavities. Concentration and gas fraction distributions at the impeller centerline planes in Fig. 12.13 and 12.14, respectively, show the location of those gas cavities and the regions of low concentrations more clearly. Overall, steady concentration levels are reached in about 125 seconds with sustained large axial gradients. At the lower part of the fermenter, concentration levels are below 5 mg/l and at the upper part above 50 mg/l (note that the colormap maximum value was set to 50 mg/l in order to make the gradients at lower parts visible.)

In Fig. 12.11, steady state glucose concentration at the mid-baffle plane (i.e. -30 degrees w.r.t. the baffle) is compared with both experimental measurements and simulation results of Larsson et al. (1996). Both simulations show similar trends for the glucose gradients across the reactor. Large concentrations near the feed zone rapidly diminish when moving towards lower parts of the fermenter. Predictions of Larsson et al. (1996) show, however, larger deviations from the measurements. The reader is also referred to Fig. 10.20(c)–10.25(c) and Fig. 12.12(b) for the gas distribution at various angular planes on the same simulation case.

Large concentration differences are also present at radial and circumferential directions. At axial planes, larger gradients are seen at upper planes close to the feed location (see Fig. 12.13(a) and (b)). Lowest concentrations at those planes are located downstream

to the baffle (w.r.t. the rotational fluid motion), while, at lower planes, they are located behind the impeller blades where there are large gas cavities as shown in Fig. 12.14. Highest concentrations are seen near the feed location for upper planes and upstream to the baffle for lower planes.

12.5.5 Glucose consumption rate

Contour plot of the glucose consumption rate (i.e. the sink term, $-r_s$) is also given in Fig. 12.12(a). Trends are very similar to that of the glucose concentration at the same plane given in Fig. 12.11(b). This is due to the fact that, in most of the fermenter volume, glucose concentrations are low, hence the condition $C_s \ll K_s$ (where $K_s = 180$ mg/l) is nearly satisfied and Eq. 12.5 holds. Since the biomass concentration is also constant in simulations ($C_x = 10$ g/l), Eq. 12.5 can be reduced to the form

$$r_s = k' C_s, \tag{12.9}$$

$$\text{where } k' = \left(\frac{q_{s,\max} C_x}{K_s} \right). \tag{12.10}$$

Therefore, the consumption rate is directly proportional to the C_s (proportionality constant being k', i.e. the pseudo-first order rate constant, see Section 12.5.6), thus the trends seen in Fig. 12.12(a).

12.5.6 Micromixing effects

In the modelling approach adopted in this chapter, micromixing was not incorporated. Here, we make a comparison of micromixing and reaction time scales, in order to justify the modelling approach that assumes micromixing effects are negligible due to slow kinetics.

An estimation of the micromixing time can be given by the second term of the Corrsin relation (Eq. 11.35):

$$\tau_C = \frac{1}{2} \ln Sc \left(\frac{\nu}{\varepsilon} \right)^{1/2}. \tag{12.11}$$

The averaged value of this term over the reactor volume was calculated to be 0.8 s. The Bałdyga and Bourne relation for micromixing time in the engulfment regime, $\tau_E = 17.3\,(\nu/\varepsilon)^{1/2}$ (Eq. 11.40), could also be used since $Sc < 4000$ thus turbulent engulfment is the mixing mechanism. This gives a higher prediction due to a larger coefficient (17.3 instead of $0.5 \ln Sc \approx 3.0$), indicating that viscosity may play a role at scales significantly larger than the Kolmogorov scale, and the effective micromixing rate for reactions must include these scales (Kresta and Paul, 2004). The averaged value of τ_E over the reactor volume was calculated to be 4.6 s. In Fig. 12.15, the spatial distribution of τ_E at the mid-baffle plane is given for the simulation case of $Sc_t = 0.2$ and $\Delta t = 0.005$ s, when the steady-state was reached (i.e. after 138 seconds elapsed in the process). Large micromixing time values of up to 16 seconds are encountered at regions away from the impeller discharge streams (especially at the bulk zone below the bottom impeller). At the impeller centerline planes, values are much lower, with

locally high values near the tank wall. At the feed and top sampling planes, high values are located near the shaft.

An estimate of the characteristic time of the substrate uptake kinetics could be given by the reaction half-life or time constant. For substrate limited growth, which is a first-order process with respect to C_s (see Eq. 12.5), the substrate half-life is given by

$$t_{1/2} = \frac{-\ln 0.5}{k'} \approx 26 \text{ s}, \tag{12.12}$$

where $k' = (q_{\mathrm{s,max}}/K_\mathrm{s})\, C_\mathrm{x}(0)$, is the pseudo-first order rate constant, assuming the biomass concentration remains approximately constant (which is also the case in simulations). A general time constant for n^{th} order reactions can be defined as $1/kC^{n-1}$, hence the characteristic reaction time for our case could be given by

$$\tau_\mathrm{r} = \frac{1}{k'} = \frac{1}{(q_{\mathrm{s,max}}/K_\mathrm{s})\, C_\mathrm{x}(0)} \approx 38 \text{ s}. \tag{12.13}$$

A mixing Damköhler number (see Eq. 11.42) can be calculated based on the time constants of mixing process and biokinetics. From the estimates given above, Da would be in the range

$$Da = \frac{\text{micromixing time}}{\text{reaction time}} = 0.121 - 0.177, \tag{12.14}$$

based on the mean τ_E (4.6 s), and for the worst case scenario (i.e. the largest micromixing time and the shortest reaction time), would be $Da = 16/26 = 0.615$. This is above the limit for slow reactions, i.e. $Da = 0.009 - 0.02$ (see Section 11.2.2), but still much lower than the limit for fast reactions, i.e. $Da = 30 - 150$. Therefore we conclude that the micromixing is not expected to have a very significant effect on substrate uptake kinetics.

12.6 Conclusions

In this chapter, we reported on the substrate uptake kinetics accompanying the two-phase flow in the 30 m^3 fermenter presented in Chapter 2 and 10. The main conclusions are:

- Initial instabilities encountered in simulations were resolved by employing a degassing boundary at the free surface instead of pressure outlet.
- The value of Sc_t has a significant effect on predicted concentrations at monitoring points, especially at the top region. Overall, substrate concentrations were higher at lower Sc_t values (i.e. at higher turbulent dispersion).
- Simulation time step did not have a significant effect on predicted steady-state concentrations within the range of values investigated. The simulation time of about 1 month with a time step of 5 ms can be decreased to about 1 week if a time step of 50 ms is employed. The time evolution of concentrations are, however, different thus a small time step is recommended if one is interested to model detailed metabolics.

- General trends of substrate gradients were well captured with the adopted simulation method. Predictions were significantly better than that predicted by the CFD model of Larsson et al. (1996).
- Best predictions were obtained with $Sc_t = 0.2$ and $\Delta t = 0.005$ s. Variations between predicted and measured concentrations up to about 50% were present. Direct comparison with experiments, however, is obscured by the uncertainty in the exact location of sampling points and the liquid level in experiments.
- Species mass conservation is not satisfied due to a limitation in the Fluent code when the Eulerian multiphase model with species transport is coupled with periodic boundary conditions. The extent of this mass conservation violation should be checked by carefully designed test simulations (e.g. two–phase passive tracer mixing experiments with various stirring rates, Sc_t values, feed locations and concentrations, etc.). Simulations of the full domain without any rotational symmetry assumption is recommended to avoid the mass violation altogether. This would increase the computation time 6-fold relative to the simulation method adopted in this study.

Tables

Table 12.1: Initial concentrations and feed conditions for fed-batch Saccharomyces cerevisiae cultivation studies performed on the 30 m^3 fermenter by Larsson et al. (1996). The feed rate, Q_F, glucose feed concentration, C_{sf}, initial reactor volume, $\mathcal{V}_l(0)$ and initial concentrations of biomass, C_x, glucose, C_s, and ethanol, C_e, are shown. The stirring and gassing rates were 133 rpm and 0.182 m^3/s, respectively.

Feed characteristics	Top feeding	Unit
C_{sf}	597	kg m^{-3}
$Q_F(0)$	1.26×10^{-2}	m^3 h^{-1}
Q_F	$Q_F(0) \times e^{0.2t}$	m^3 h^{-1}
$Q_{F,max}$	9.0×10^{-2}	m^3 h^{-1}
Initial volume and concentrations		
$\mathcal{V}_l(0)$	20.8	m^3
$C_x(0)$	0.15	kg m^{-3}
$C_s(0)$	2.43	kg m^{-3}
$C_e(0)$	0.78	kg m^{-3}

Table 12.2: Initial concentrations and feed conditions used in the CFD study of both Larsson et al. (1996) and that we present in this chapter. Those conditions correspond to the constant feed rate phase of the actual fed-batch Saccharomyces cerevisiae cultivation studies performed by Larsson and refers to the moment of the process after about 11 hours have lapsed.

Feed characteristics	Top feeding	Unit
C_{sf}	597	kg m^{-3}
$Q_F = Q_{F,max}$	9.0×10^{-2}	m^3 h^{-1}
$Q_{F,s} = C_{sf} \times Q_F$	53.7	kg h^{-1}
Initial concentrations		
$C_x(0) = C_x$ (const.)	10	kg m^{-3}
$C_s(0)$ (mean conc. in fermenter)	43.5×10^{-3}	kg m^{-3}

Table 12.3: Comparison of the experimental data of Larsson et al. (1996) with the glucose concentration predictions made with different values of turbulent Schmidt number and time step size (see Fig. 12.2–12.5 for concentration profiles). The average of the absolute error in top, middle and bottom port concentration predictions is also given.

	Conc. [mg/l]			Relative error [%]			Mean error [%]
	Top	Mid.	Bot.	Top	Mid.	Bot.	
Experiments	40.8	11.2	4.3	–	–	–	–
$Sc_t = 0.7, \Delta t = 50$ ms	34.3	6.8	1.0	-15.9	-39.3	-76.7	44.0
$Sc_t = 0.2, \Delta t = 50$ ms	52.4	9.4	2.0	28.4	-16.1	-53.5	32.7
$Sc_t = 0.7, \Delta t = 5$ ms	35.4	7.8	1.1	-13.2	-30.4	-74.4	39.3
$Sc_t = 0.2, \Delta t = 5$ ms	53.8	10.4	2.1	31.9	-7.1	-51.2	30.1

Figures

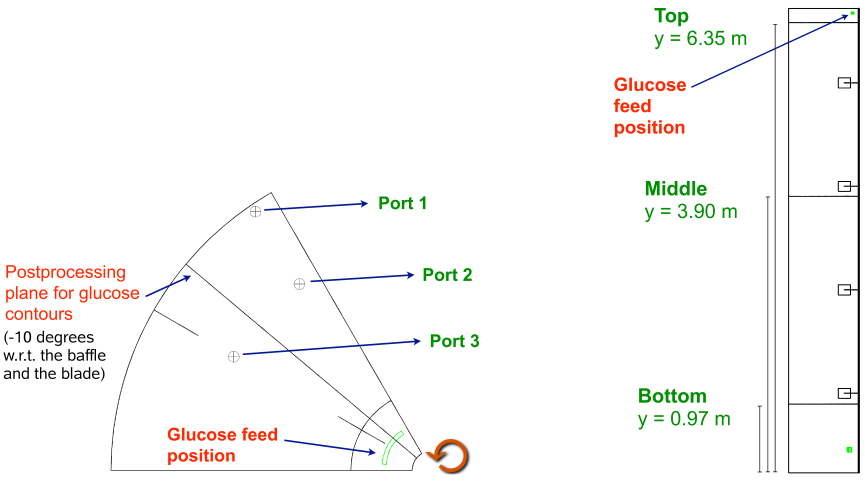

(a) Monitoring locations for each axial plane (b) Axial sampling locations

Figure 12.1: For each axial sampling level (top, middle and bottom) where Larsson et al. (1996) did the measurements, three monitoring locations (port 1, 2 and 3) are defined in simulations. Postprocessing plane for the time evolution of glucose concentration contours (Fig. 12.10) is also shown.

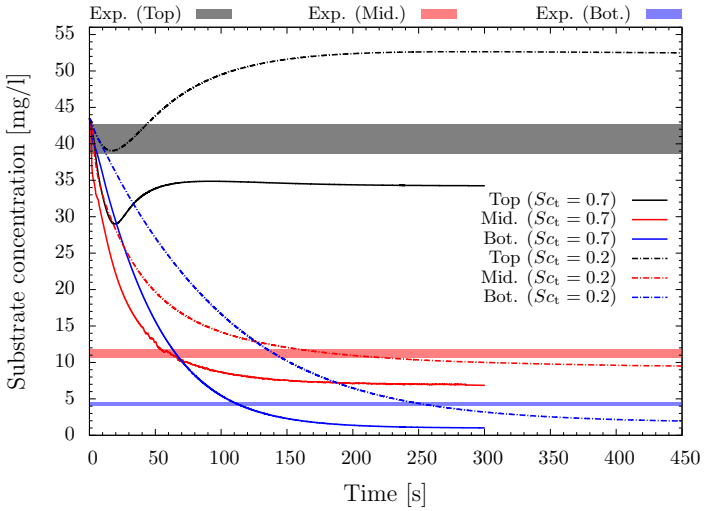

Simulation: $\Delta t = 50$ ms, port 1

Figure 12.2: Effect of the turbulent Schmidt number on predicted glucose concentrations with the time step $\Delta t = 0.050$ s. Detection location is port 1 (see Fig. 12.1(a)). Predictions are compared with the experimental data of Larsson et al. (1996), where measured values at top, middle and bottom sampling locations are 40.7, 11.2 and 4.3 mg/l, respectively and are plotted within a ±5% band.

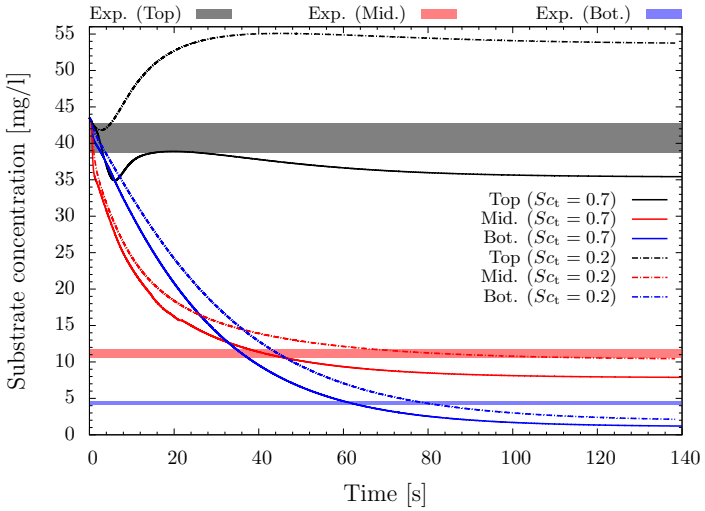

Simulation: $\Delta t = 5$ ms, port 1

Figure 12.3: Effect of the turbulent Schmidt number on predicted glucose concentrations with the time step $\Delta t = 0.005$ s. Detection location is port 1 (see Fig. 12.1(a)). Predictions are compared with the experimental data of Larsson et al. (1996), where measured values at top, middle and bottom sampling locations are 40.7, 11.2 and 4.3 mg/l, respectively and are plotted within a ±5% band.

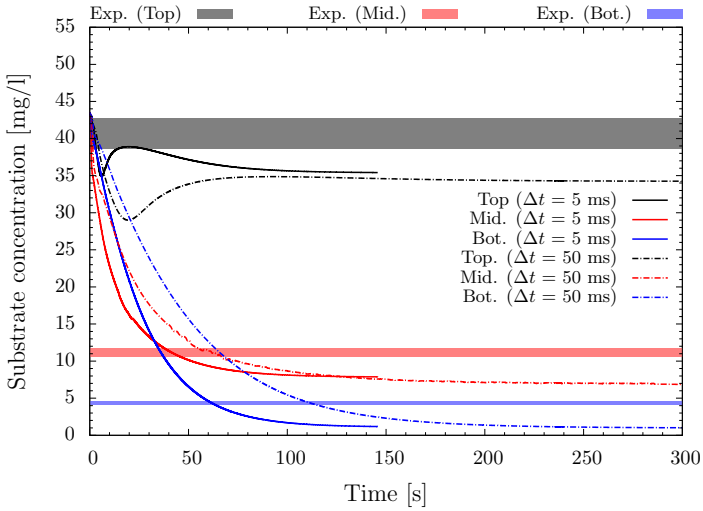

Simulation: $Sc_t = 0.7$, port 1

Figure 12.4: Effect of the simulation time step size on predicted glucose concentrations with $Sc_t = 0.7$. Detection location is port 1 (see Fig. 12.1(a)). Predictions are compared with the experimental data of Larsson et al. (1996), where measured values at top, middle and bottom sampling locations are 40.7, 11.2 and 4.3 mg/l, respectively and are plotted within a ±5% band.

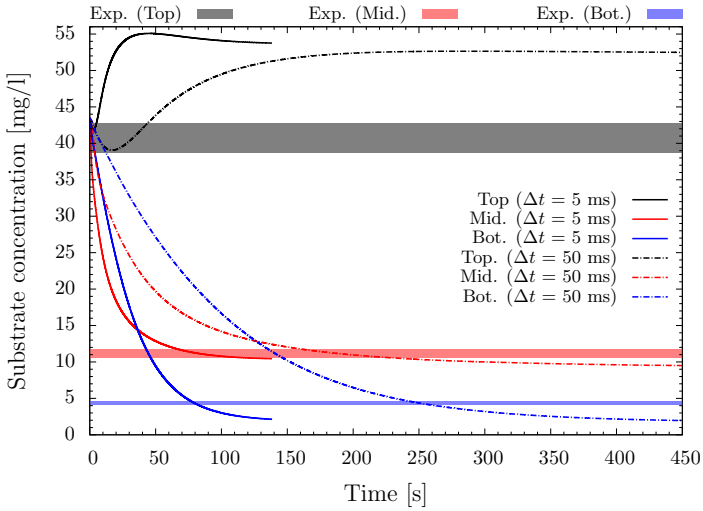

Simulation: $Sc_t = 0.2$, port 1

Figure 12.5: Effect of the simulation time step size on predicted glucose concentrations with $Sc_t = 0.2$. Detection location is port 1 (see Fig. 12.1(a)). Predictions are compared with the experimental data of Larsson et al. (1996), where measured values at top, middle and bottom sampling locations are 40.7, 11.2 and 4.3 mg/l, respectively and are plotted within a ±5% band.

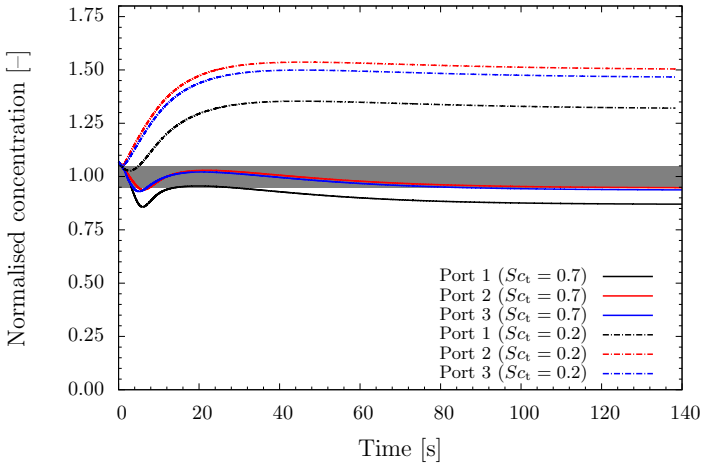

Simulation: Top sampling level, $\Delta t = 5$ ms

Figure 12.6: Effect of monitoring port location on predicted glucose concentrations at the top sampling level of Larsson et al. (see Fig. 12.1). Predictions are normalised by the experimental data of Larsson et al. (1996) measured at the top sampling location (40.7 mg/l). The ±5% band around the measurement value is also shown.

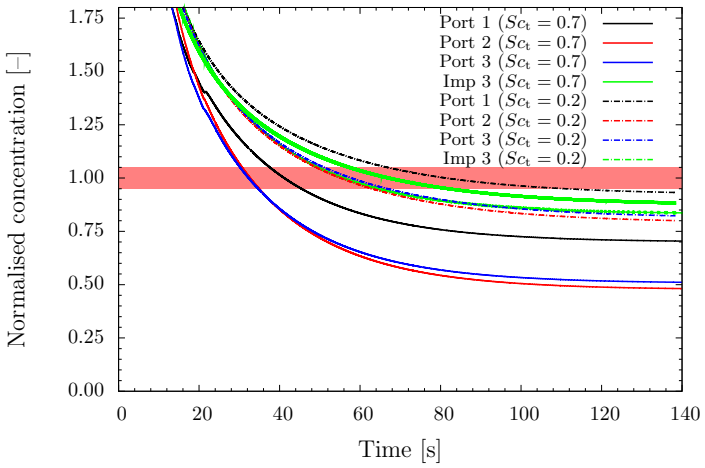

Simulation: Middle sampling level, $\Delta t = 5$ ms

Figure 12.7: Effect of monitoring port location on predicted glucose concentrations at the middle sampling level of Larsson et al. (see Fig. 12.1). Predictions are normalised by the experimental data of Larsson et al. (1996) measured at the middle sampling location (11.2 mg/l). The ±5% band around the measurement value is also shown.

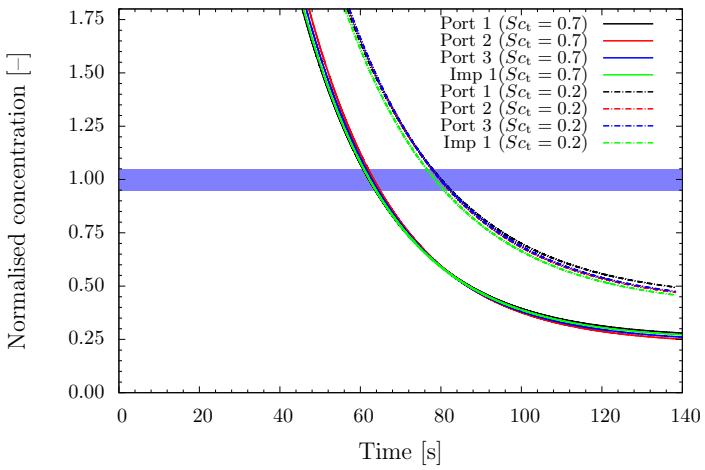

Simulation: Bottom sampling level, $\Delta t = 5$ ms

Figure 12.8: Effect of monitoring port location on predicted glucose concentrations at the bottom sampling level of Larsson et al. (see Fig. 12.1). Predictions are normalised by the experimental data of Larsson et al. (1996) measured at the bottom sampling location (4.3 mg/l). The ±5% band around the measurement value is also shown.

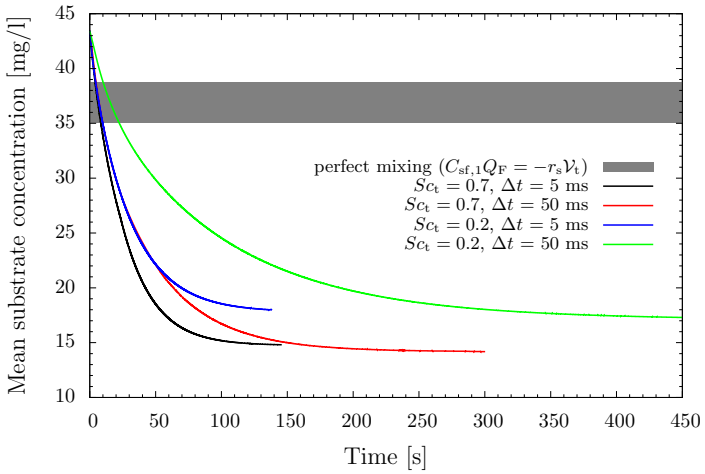

Figure 12.9: Volume-averaged mean glucose concentration profiles in the fermenter compared with the estimated steady-state glucose concentration (plotted within a ±5% band) assuming perfect mixing.

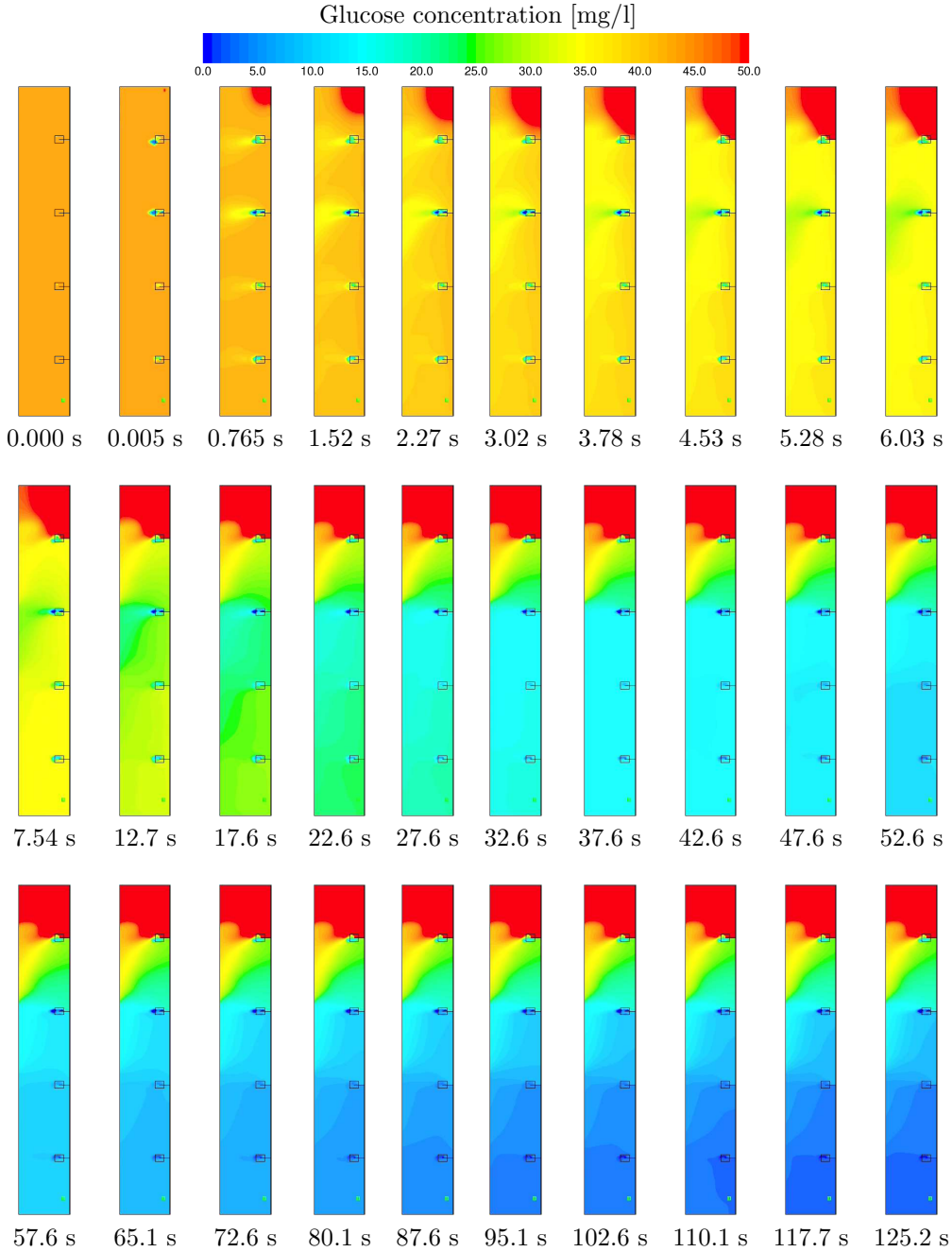

Figure 12.10: Evolution of glucose gradients for feed in the top when $Sc_t = 0.2$ and $\Delta t = 0.005$ s. Glucose concentration contours are given at an angular plane coinciding with the feed location which is -10° with respect to the baffle (see Fig. 12.1(a)). The colormap maximum value was set to 50 mg/l in order to make the gradients at lower parts visible (hence the dark red regions may represent a value in the range 50 mg/l $\leq C_s \leq$ 268.2 mg/l, since the actual maximum concentration in the domain was 268.2 mg/l).

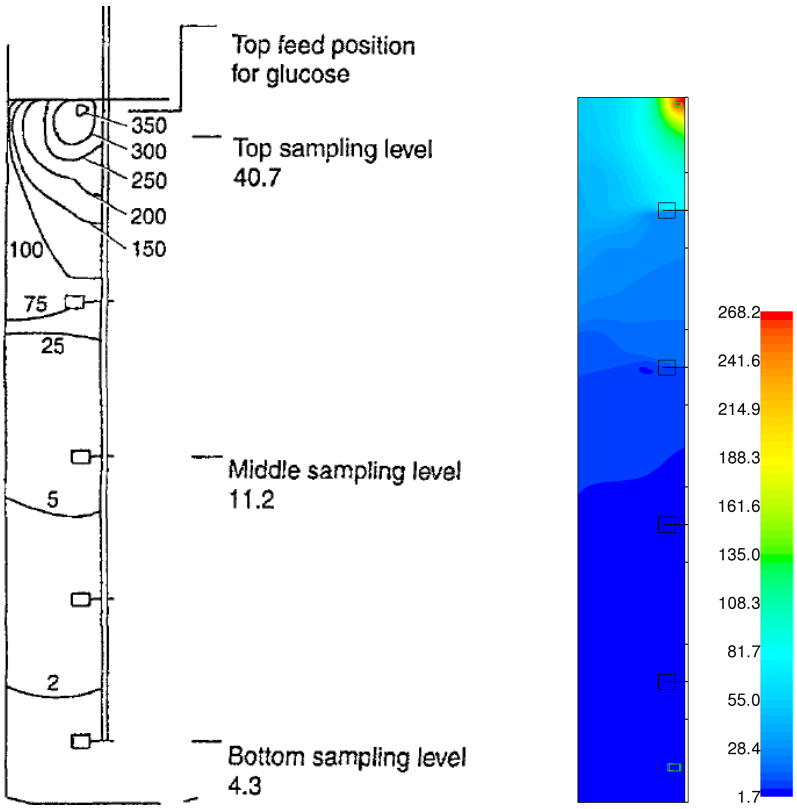

(a) Data of Larsson et al. (1996) (b) Simulation

Figure 12.11: Steady-state distributions of glucose concentration [mg/l]: (a) simulated (l.h.s.) and measured (r.h.s.) values reported by Larsson et al. (1996) for the cell concentration = 10 g/l and the mean substrate concentration = 43.5 mg/l, (b) our simulation (mid-baffle plane, $Sc_t = 0.2$, $\Delta t = 0.005$ s).

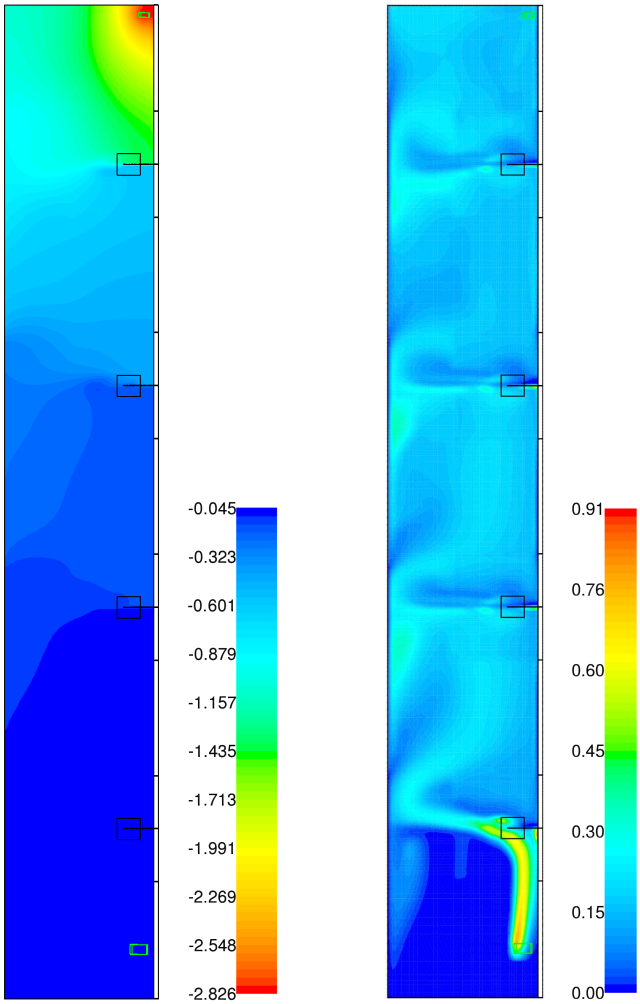

(a) $-r_s$ [mg/l-s] (b) Gas fraction [–]

Figure 12.12: Steady state distributions of (a) glucose consumption rate (i.e. the sink term, $-r_s$) and (b) gas volume fraction in the mid-baffle plane ($Sc_t = 0.2$, $\Delta t = 0.005$ s).

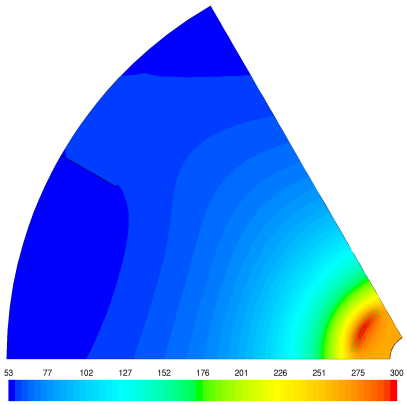

(a) feed plane ($y = 6.50$ m)

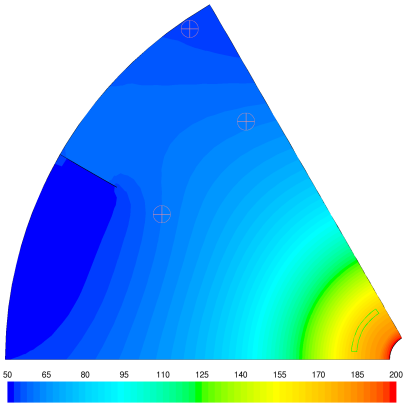

(b) top sampling level ($y = 6.35$ m)

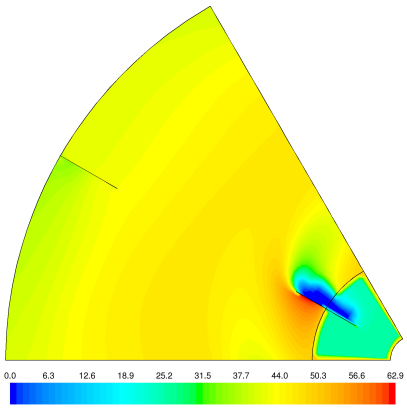

(c) top imp. centerline ($y = 5.50$ m)

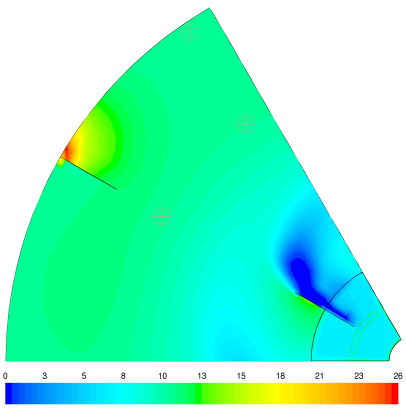

(d) third imp. centerline ($y = 4.04$ m)

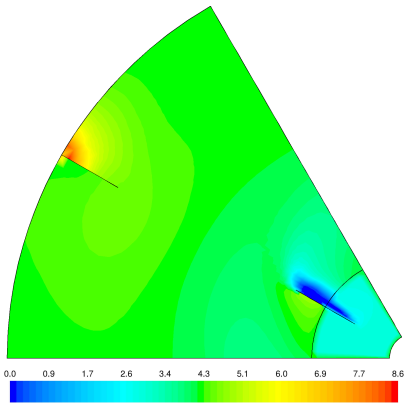

(e) second imp. centerline ($y = 2.58$ m)

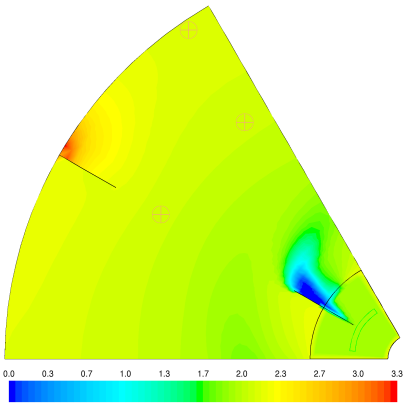

(f) bottom imp. centerline ($y = 1.12$ m)

Figure 12.13: Spatial distribution of glucose concentrations [mg/l] at various axial planes ($Sc_t = 0.2$, $\Delta t = 0.005$ s).

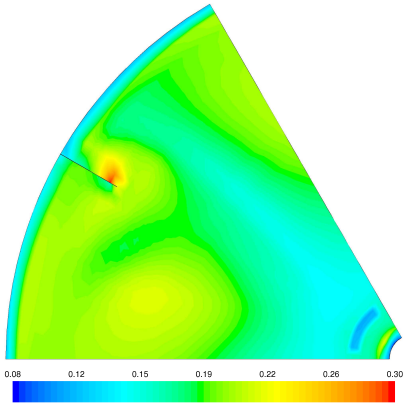

(a) feed plane ($y = 6.50$ m)

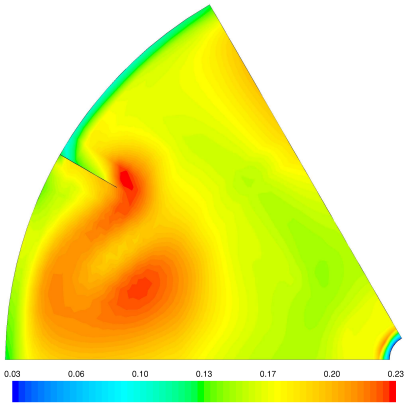

(b) top sampling plane ($y = 6.35$ m)

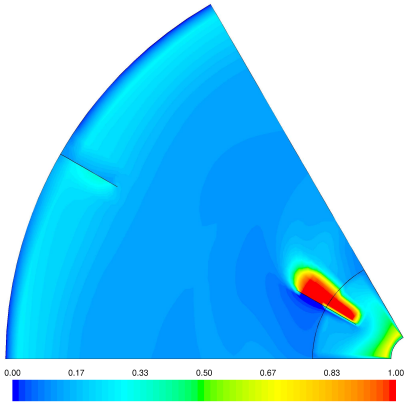

(c) top imp. centerline ($y = 5.50$ m)

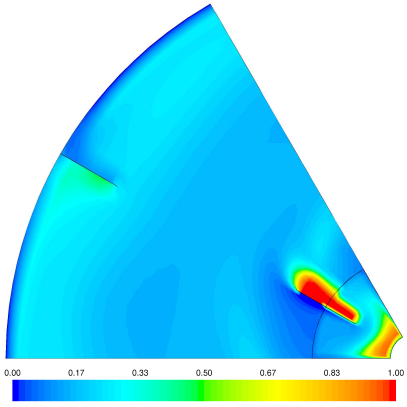

(d) third imp. centerline ($y = 4.04$ m)

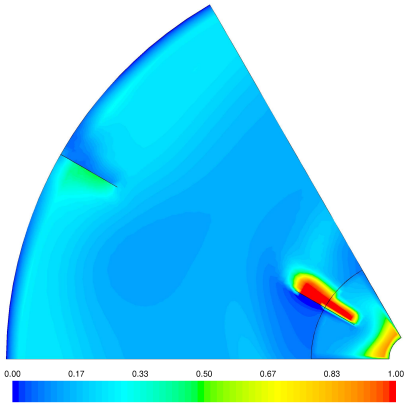

(e) second imp. centerline ($y = 2.58$ m)

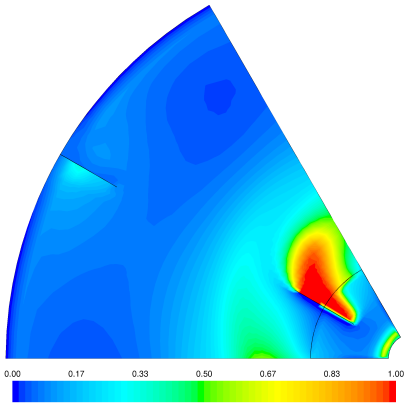

(f) bottom imp. centerline ($y = 1.12$ m)

Figure 12.14: Spatial distribution of gas fraction [–] at various axial planes ($Sc_t = 0.2$, $\Delta t = 0.005$ s). For gas distribution at angular planes for the same case, see Fig. 10.20(c) – 10.25(c).

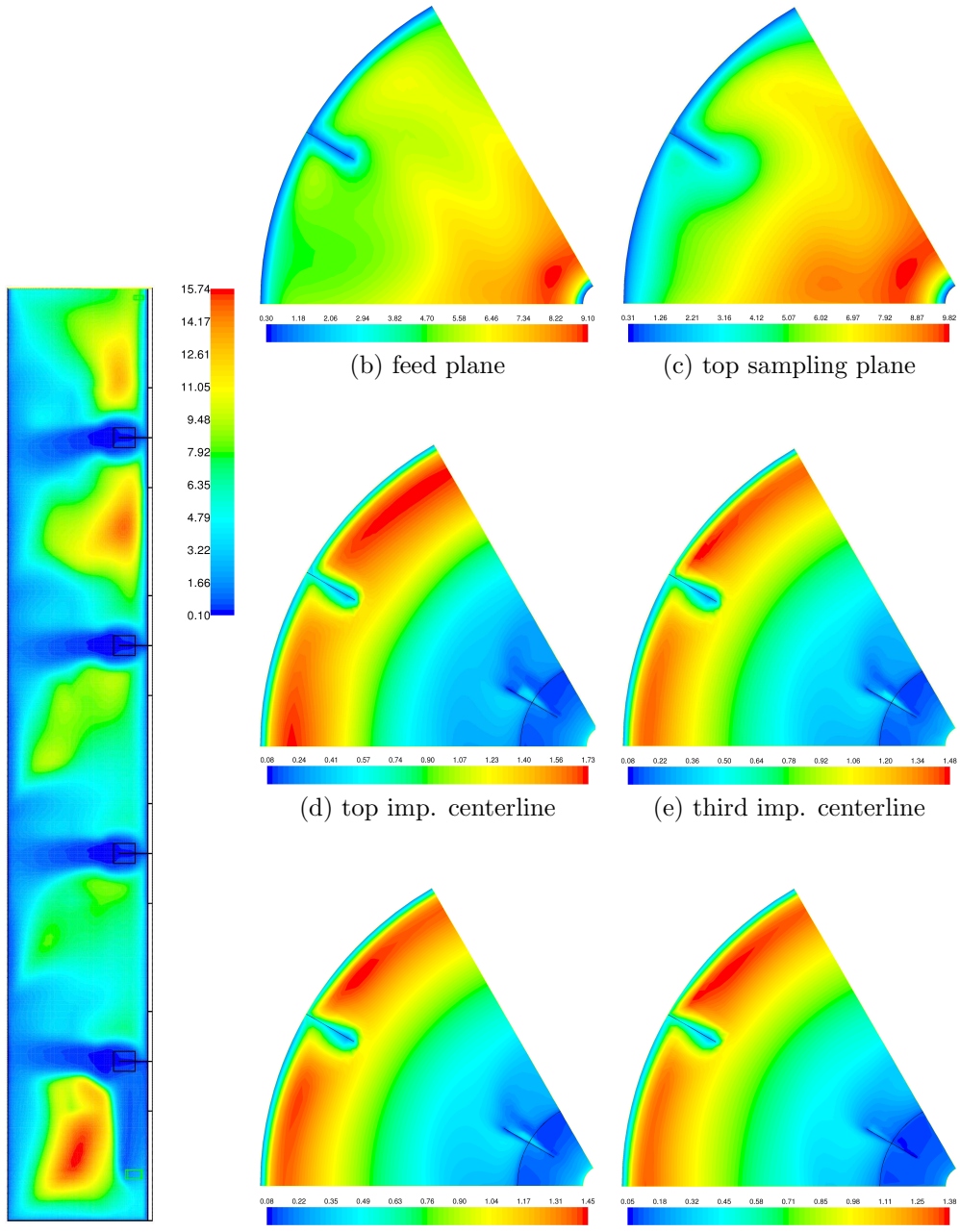

(a) mid-baffle plane (b) feed plane (c) top sampling plane

(d) top imp. centerline (e) third imp. centerline

(f) second imp. centerline (g) bottom imp. centerline

Figure 12.15: Spatial distribution of engulfment micromixing time constant [s], $\tau_E = 17.3\,(\nu/\varepsilon)^{1/2}$, according to Bałdyga and Bourne. Contours of τ_E are given at the mid-baffle and various axial planes ($Sc_t = 0.2$, $\Delta t = 0.005$ s), when the steady state was reached after 138 seconds elapsed in the process.

Chapter 13

Main conclusions and recommendations

13.1 General discussion

In this thesis, we presented a computationally cheap and efficient approach to predict the characteristics of gas dispersion into large-scale multi-impeller reactors. Such systems are commonly used in industrial fermentation processes. This relates also to the motivation and the scope of this work stated in Chapter 1. That is, to enable performance improvements of industrial fermenters by providing a better insight in the local transport phenomena via efficient computational methods. One emphasis was on attaining the above objective with a practical implementation in mind thus by a computationally affordable framework that could be transferred to the industrial partner. We therefore restricted ourselves accordingly in the modelling choices, and also chose a commercial CFD code, Fluent, in this respect as the implementation platform.

We first identified two model systems to test and establish the modelling framework. The first one was a standard configured laboratory-scale 0.783 m^3 stirred tank with a Rushton impeller ($H = T = 1.0$ m). The second one was a 30 m^3 fermenter stirred by 4 Rushton impellers ($H = 9.60$ m, $T = 2.09$ m) and represents an industrially relevant large-scale system (though at the lower end as fermenters could be much larger, e.g. 500 m^3). Detailed single- and two-phase measurement data was reported in literature for both systems.

We started by building a single-phase flow model and testing this against the experimental data available. The model verified and validified as such served also as the initial solution to start with for more demanding and less stable two-phase simulations. We actually made the initial tests on a model we had built of a smaller standard stirred tank geometry ($H = T = 0.294$ m), with a full-domain as well as 180 degree sector mesh, for which both experimental and simulation data was available (results not reported in this thesis). Large computational demands with this system made it soon clear that domain simplification was essential. We then built the models for the lab- and large-scale reactors described above according to six-fold rotational symmetry (a

60 degree sector). In this phase, building a sufficiently high quality structured mesh on the geometry with periodic conditions and mesh interfaces around the impeller proved to be less trivial than initially anticipated.

In the second phase, we implemented several multiphase modelling approaches and run numerous tests to establish a set of modelling parameters and boundary conditions. We started with testing the simplest multiphase modelling approach, i.e. the Algebraic slip mixture model (ASMM) with one-fluid formulation. We then adopted the more sophisticated Euler–Euler (two-fluid) approach which still is a workhorse for the simulation of bubbly flows in large-scale industrial equipment at not too low gas fractions. In this phase, computational time greatly increased and numerical stability became quickly the main challenge to overcome. A preference was made also at this stage regarding the two different impeller modelling approaches tested, namely the multiple reference frame (MRF) and the sliding mesh (SM) models. The MRF model was chosen as it was an oder of magnitude cheaper and gave comparable results to that with the SM model. We also tested again the effect of rotational symmetry assumption described above within the two-phase framework and opted for the six-fold domain reduction which led to a similar reduction in computational demands with results comparable to that with the full-domain. Furthermore, it became also clear that some of the stability issues experienced with the modelling of lift and turbulent dispersion forces were seemingly specific to stirred systems. Euler–Euler simulations run for a bubble column by Mijnarends (2007) as part of his Master's Thesis work, which we supervised in the course of this work, did not posses such stability problems with aforementioned forces.

We also note that during the course of this thesis work, several versions of Fluent became available and used, varying from release 6.2 to 12.0. More importantly, several bugs in the code in earlier versions were eliminated in later versions. Few of those bugs were found by us and reported to the Fluent technical support team. In this respect, the violation of scalar mass conservation in a Euler–Euler setup with periodic boundary conditions was particularly a worrying finding. It was a major limitation in the code for multiphase tracer mixing or mass transfer calculations with periodic boundaries.

Fluent Inc. was also acquired by ANSYS within this period (2006) and became officially ANSYS Fluent. We also note that many improvements were done (improved numerics as well as addition of new physical models) across the newer releases of Fluent. Many of those were not available to us unfortunately during the time of conducting the respective work (e.g. the implicit lift force implementation and the introduction of coupled multiphase solver and its improved variants that greatly increased the numerical stability). Furthermore, several new drag force models as well as the degassing boundary condition were introduced which were relevant for bubbly flows, while we had to implement them via user subroutines.

In the final phase of the thesis work, we moved towards the practical implementation of the model to an industrially relevant case, i.e. the microbial kinetics and substrate transport in the large scale fermenter for the baker's yeast cultivation process. We laid the foundations of this first in an earlier chapter on the scalar mixing in the fermenter. This helped also clearly identifying the rate limiting process in transport in such a fermenter, i.e. the exchange between the compartmentalised impeller zones. With those learnings, such as the modified turbulent Schmidt number to account for the underestimated axial turbulent transport, we moved to the final stage. The fi-

nal practical implementation and validation work has been completed during the two months extension time to the standard four years thesis period. We showed that with the relatively simple modelling approach adopted, realistic estimation of transient substrate concentrations was possible. This is a vital process parameter and have a direct effect in the fermenter performance. Note that, throughout this thesis we restricted ourselves to water-like systems which is sufficient for round cells like yeast. Other branching and filament type microorganisms would however introduce non-Newtonian effects (e.g. pseudoplastic), hence results reported in this thesis should be taken with care.

Finally, the reader would obviously recognise that a great deal of effort (and surely time!) was devoted to the theoretical and technical aspects relevant to the topic of this thesis. This not only for the sake of completeness. First of all, the subject at hand demands an understanding of a number of areas and their mutual interactions such as physics of turbulent bubbly flows and their numerical modelling, flow characteristics of gassed-stirred tanks and CFD methodologies for their modelling, population balances, turbulent mixing, etc. One can devote an entire career on either of those subjects. A study located on such a complex landscape should make it very clear on the details of the modelling framework and choices (which submodels with which interactions are adopted with which modelling parameters. This boils down to which exact equations are being solved ultimately). Because many aspects that have crucial effects on calculated results could easily go under the hood. One is then left with a blurred picture without real a understanding of the approach taken for getting the results. It's our observation that this is the case in many scientific articles and even in technical books on this subject, which may lead to confusion and inconsistencies. We found such blurred spots even in some relevant sections of the Fluent Theory Guide, that is, what was exactly implemented in the code was not fully clear. Besides this, there is also the situation that different schools of thought exist in several areas related to the turbulent bubbly flows and their modelling. We therefore aimed and tried our best to outline and work out the details of the theoretical framework in this thesis in a self-sufficient and consistent manner, so that frequent referring to outside references would not be needed. This came clearly with the cost of additional time requirements in writing of the thesis.

13.2 Main conclusions

The main findings and discussion of results were already given in the respective chapters of the thesis. Here we will give a brief outline of primary results.

13.2.1 Single–phase flow in a standard stirred tank and a multi–impeller fermenter

- Computational costs were greatly reduced by —first, reducing the domain to only a 60° sector (1/6) of the full tank by assuming flow periodicity, —second, employing a steady-state MRF model and —third, using the conventional $k-\varepsilon$ model. Results showed that above mentioned simplified approach did not result

in any significant change for the predicted quantities presented in this work.

- Despite the substantial underpredictions (up to 50%) of ε, N_{P_ε} and k reported in many previous studies in literature that employ $k-\varepsilon$ model, we found that good predictions of those quantities are possible, provided that the grid has a sufficient resolution.

- The findings presented in this study may provide a basis for efficient and affordable multiphase simulations of stirred systems.

13.2.2 Gas dispersion in a standard stirred tank

- The grid resolution of 46k (for the computational domain of 60 degree sector of the reactor) was generally sufficient for the estimation of integral quantities such as gas holdup, though the turbulent energy dissipation prediction improved with further grid refinement.

- Standard Schiller & Naumann drag correlation for spheres significantly underestimated the gas holdups. Ishii & Zuber correlation improved predictions by taking bubble deformation effects into account. However, turbulence modification of the drag force was required to bring holdup predictions close to the measured levels. The Brucato model (with the correlation constant of Lane) adopted for this purpose was found to have a limited applicability under varying operating conditions. Local gas fraction was overpredicted at several locations near the lower and upper recirculation loops.

- Bubble size predictions with the discrete model for population balances (with standard breakage and coalescence kernels) were generally good. Overall Sauter diameters predicted (global volume average) were reasonably close to experimental data (sample-average of 22 measurement positions). Local distribution of d_{32} at axial levels of the measurement grid were predicted also reasonably well, except at levels near the impeller where d_{32} was overpredicted at several locations.

- Direct experimental data on power consumption was available only for the Case 2, for which a very good agreement was achieved with the final model. Simulation values of gassed-to-ungassed power ratios were significantly higher than the correlation estimates. For an accurate prediction of gassed power, the precise form of the impeller gas cavities is crucial. Although the gross characteristics of the impeller cavity regimes were captured by the simulations, the inherent limitation of the Euler–Euler framework adopted is that gas–liquid interfaces are not resolved.

- The reduction in impeller liquid discharge flow (impeller pumping) due to gassing was generally similar to the reduction in impeller power draw due to gassing, which is supported also experimentally.

13.2.3 Gas dispersion in a large-scale fermenter with multiple impellers

- Simulations showed that the drag force is the most important one among the other interfacial forces that were taken into account and accurate prediction of axial slip velocities is the key factor. Both Schiller & Naumann and Ishii & Zuber drag laws led to underpredicted holdups. Turbulence modification to drag coefficient using the Brucato model (with the correlation coefficient recommended by Lane) resulted in large underprediction of slip velocities and overprediction of holdups at high stirring rates. This shows that, it is not generally applicable to multi-impeller large-scale systems.

- Simulations were able to predict the flow regime transition from loading to flooding, corresponding well with the experimental data.

- The population balance model employed showed that mean bubble sizes predicted are much larger than that for the lab-scale standard stirred tank studied earlier. Unfortunately, bubble sizes were not measured for the system simulated. However, it's in accordance with the bubble size range commonly observed in industrial fermenters, namely $6 - 10$ mm.

- At high gas fractions, modification to the drag force is needed to account for the bubble swarm effect. The Ishii & Zuber multiparticle drag law for this regime resulted in good prediction of holdup without employing a turbulent drag modification model. At those relatively high gas loadings, use of degassing boundary condition at the outlet gives more realistic results especially if the top impeller is close to the free surface.

- Predicted radial velocity profiles at the impeller centerline level are higher than the experimental profiles both for ungassed and gassed operation. Sensitivity analysis of the radial velocities to the axial location suggests that the experimental measurements may also be susceptible to significant variations.

13.2.4 Scalar mixing in the 30 m^3 fermenter

- The turbulent Schmidt number is the key parameter, to compensate for lack of convective exchange by the mean flow at locations axially midway between impellers, which limit the transport of tracer across the tank.

- Best predictions of mixing and lag times were obtained with an adapted Schmidt number, namely $Sc_t = 0.2$, in contrast to the Fluent default value, $Sc_t = 0.7$. For $Sc_t = 0.2$, the mixing time (t_{95}) computed as 154 s (at 115 rpm) and 255 s (at 70 rpm) corresponds well with the experimental values from Vrábel et al. (1999), reported as 150 s and 255 s, respectively.

- Tracer injection and detection locations influence the shape of response curves and the computed mixing time. Shortest mixing times were detected near the axial center of the fermenter, located at midway between the second and the third impeller, in agreement with the experiments (Vrábel et al., 1999). The injection

method has also an influence; when the tracer was introduced individually at each impeller, shortest mixing time was achieved.

- It was found that the scalar mass in simulations was not conserved, if the single-phase simulation was set up as a multiphase system in which the secondary phase equations were not solved. Scalar mass was perfectly conserved in a purely single-phase setup. This behavior was found to be due to a bug in the Fluent code.
- Simulation time step size had no significant effect on the response curves within the range of values investigated.
- Results showed that a good prediction of scalar macro– and mesomixing, in terms of mixing times and tracer response curves, could be obtained by a rather simple and computationally cheap model (RANS + steady MRF model in a six-fold reduced domain) with an adapted Sc_t.

13.2.5 Substrate uptake kinetics in the 30 m^3 fermenter

- Instabilities encountered in simulations were resolved by employing a degassing boundary at the free surface instead of pressure outlet.
- The value of Sc_t has a significant effect on predicted concentrations at monitoring points, especially at the top region. Overall, substrate concentrations were higher at lower Sc_t values (i.e. at higher turbulent dispersion).
- Simulation time step did not have a significant effect on predicted steady-state concentrations within the range of values investigated.
- General trends of substrate gradients were well captured with the adopted simulation method. Predictions were significantly better than that predicted by the CFD model of Larsson et al. (1996).
- Best predictions were obtained with $Sc_t = 0.2$ and $\Delta t = 0.005$ s. Variations between predicted and measured concentrations up to about 50% were present. Direct comparison with experiments, however, is obscured by the uncertainty in the exact location of sampling points and the liquid level in experiments.

13.3 Recommendations

In this final section, we conclude by general recommendations for future work to prospective researchers.

- Proper account of interphase forces is crucial in the numerical modelling of turbulent bubbly flow dynamics in stirred systems. This, however, is an active research area with potential open ends despite advancements. Significant time has been spend in the course of this thesis in search of a general formulation (e.g. for the drag force) valid for varying operating regimes, though without much success. The general approach in literature is to use fitted model constants with

limited applicability. Prospective researcher should be careful in this respect in the time spent and expectations thereon, keeping also in mind the assumptions made in the turbulent Euler–Euler modelling framework which may not allow such universality.

- Usually the drag is the dominant interphase force in the direction of the relative velocity. However, the lateral lift force may act critically to migrate bubbles towards or away from recirculation zones thereby affecting the gas dispersion in the system. Due to numerical instabilities, we were not able to account for lift effects. Present coupled multiphase solver and variants in Fluent have increased stability and it is recommended to take the lift force into account with those solvers.

- In population balance modelling, moments methods could be employed which do not require specification of bubble size bins prior to the simulation. Various models in this direction became available and improved in the newer releases of Fluent. As discussed in Chapter 8.2, QMOM would become computationally advantageous when large number of bins are needed (e.g. larger than 6) to describe the spatial variation of size distribution sufficiently. This might, in principle, be the case for the large fermenter, because, due to lacking experimental data, we could not check if the spatial mean bubble size (d_{32}) variations were relatively small like in the single-impeller tank case studied. In this respect, we also recommend the future researcher to check if the results are sufficiently independent of the resolution of the internal size coordinate (i.e. the number of bins) if the DM is used.

- Species mass conservation is not satisfied due to a limitation in the Fluent code when the Eulerian multiphase model with species transport is coupled with periodic boundary conditions. The extent of this mass conservation violation should be checked by carefully designed test simulations (e.g. two–phase passive tracer mixing experiments with various stirring rates, Sc_t values, feed locations and concentrations, etc.). Simulations of the full domain without any rotational symmetry assumption is recommended to avoid the mass violation altogether. This would increase the computation time about 6-fold relative to the simulation method adopted in this study.

- Throughout this thesis, we did not take the static pressure variation into account in bubble size modelling. This could be important in larger scale taller fermenters and when the interphase mass transport is of interest. Such a case would be for aerobic fermentations where dissolved oxygen and carbon dioxide concentrations are vital for microbial kinetics.

- For a more complete description of the fermentation process, thermal effects (heat generation by microbial kinetics, heat removal via cooling coils) and viscosity changes (e.g. due to addition of substrate and microbial activities) have to be taken into account in the modelling.

- Substrate uptake kinetics simulations showed that the simulation time step did not have a significant effect on predicted steady-state concentrations within the range of values investigated. The simulation time of about 1 month with a time step of 5 ms can be decreased to about 1 week if a time step of 50 ms is employed.

The time evolution of concentrations are, however, different thus a small time step is recommended if one is interested to model detailed metabolics.

- We highly recommend the prospective Fluent users to follow the so-called "Class 3" periodic error reports by ANSYS. Those bugs could potentially harm not only the solution itself, but in some cases also the postprocessing of correct solutions.
- We also highly recommend Fluent users to go through the relevant parts of the Fluent users and theory guides carefully and critically while implementing models. There are sometimes unclarities in the exact form of the user input required (e.g. form of the population balance source terms), as well as undocumented parts or even mistakes. In this respect, getting in contact with the Fluent technical support team is also recommended.
- Finally, anyone planning to devote a significant time in CFD modelling work is seriously advised to use ergonomic computer peripherals. Among those, using a RSI-preventive mouse is of tremendous importance for the writer of this thesis suffered from this as a result of countless hours being spend in geometry building and meshing.

Bibliography

Antal, S. P., Lahey Jr., R. T., Flaherty, J. E., 1991. Analysis of phase distribution in fully developed laminar bubbly two-phase flow. International Journal of Multiphase Flow 17 (5), 635–652.

Auton, T. R., 1987. Lift force on a spherical body in a rotational flow. Journal of Fluid Mechanics 183, 199–218.

Auton, T. R., Hunt, J. C. R., Prud'homme, M., 1988. Force exerted on a body in inviscid unsteady non-uniform rotational flow. Journal of Fluid Mechanics 197, 241–257.

Bakker, A., Smith, J. M., Myers, K. J., 1994. How to disperse gases in liquids. Chemical Engineering (New York) 101 (12), 98.

Bakker, A., Van den Akker, H. E. A., 1994. Computational model for the gas–liquid flow in stirred reactors. Chemical Engineering Research and Design 72 (A4), 594–606.

Baldyga, J., Bourne, J., 1984. Fluid mechanical approach to turbulent mixing and chemical reaction. part ii. micromixing in the light of turbulence theory. Chemical Engineering Communications 28 (4-6), 243–258.

Baldyga, J., Bourne, J., 1989. Simplification of micromixing calculations. i. derivation and application of new model. The Chemical Engineering Journal 42 (2), 83–92.

Bałdyga, J., Bourne, J. R., 1992. Interactions between mixing on various scales in stirred tank reactors. Chemical Engineering Science 47 (8), 1839–1848.

Bałdyga, J., Bourne, J. R., 1999. Turbulent Mixing and Chemical Reactions. John Wiley & Sons Ltd.

Bałdyga, J., Bourne, J. R., Hearn, S. J., 1997. Interaction between chemical reactions and mixing on various scales. Chemical Engineering Science 52 (4), 457–466.

Bałdyga, J., Pohorecki, R., 1995. Turbulent micromixing in chemical reactors - a review. The Chemical Engineering Journal and The Biochemical Engineering Journal 58 (2), 183–195.

Barigou, M., Greaves, M., 1992. Bubble-size distributions in a mechanically agitated gas-liquid contactor. Chemical Engineering Science 47 (8), 2009–2025.

Barigou, M., Greaves, M., 1996. Gas holdup and interfacial area distributions in a mechanically agitated gas-liquid contactor. Chemical Engineering Research and Design 74 (3), 397–405.

Bartels, C., Breuer, M., Wechsler, K., Durst, F., 2002. Computational fluid dynamics applications on parallel-vector computers: Computations of stirred vessel flows. Compt.and Fluids 31 (1), 69–97.

Batchelor, G. K., 1967. An Introduction to Fluid Dynamics. First Cambridge Mathematical Library Edition 2000. Cambridge University Press, New York, NY.

Behzadi, A., Issa, R. I., Rusche, H., 2004. Modelling of dispersed bubble and droplet flow at high phase fractions. Chemical Engineering Science 59 (4), 759 – 770.

Bel F'dhila, R., Simonin, O., 1992. Eulerian prediction of a turbulent bubbly flow downstream of a sudden pipe expansion. In: Proceedings of the Sixth Workshop on Two-Phase Flow Predictions. Erlangen, Germany.

Bird, R. B., Stewart, W. E., Lightfoot, E. N., 1960. Transport Phenomena. John Wiley & Sons, Inc.

Brucato, A., Ciofalo, M., Grisafi, F., Micale, G., 1998a. Numerical prediction of flow fields in baffled stirred vessels: A comparison of alternative modelling approaches. Chemical Engineering Science 53 (21), 3653–3684.

Brucato, A., Grisafi, F., Montante, G., 1998b. Particle drag coefficients in turbulent fluids. Chemical Engineering Science 53 (18), 3295–3314.

Bruijn, W., van't Riet, K., Smith, J. M., 1974. Power-consumption with aerated rushton turbines. Transactions of the Institution of Chemical Engineers 52 (1), 88–104.

Bujalski, W., Jaworski, Z., Nienow, A., 2002. Cfd study of homogenization with dual rushton turbinescomparison with experimental results: Part ii: The multiple reference frame. Chemical Engineering Research and Design 80 (1), 97 – 104, process and Product Development.

Bujalski, W., Nienow, A. W., Chatwin, S., Cooke, M., 1987. The dependency on scale of power numbers of Rushton disc turbines. Chem. Eng. Sci. 42 (2), 317–326.

Calderbank, P. H., 1958. Physical rate processes in industrial fermentation. part i: The interfacial area in gas-liquid contacting with mechanical agitation. Transactions of the Institution of Chemical Engineers 36, 443–463.

Campolo, M., Sbrizzai, F., Soldati, A., 2003. Time-dependent flow structures and lagrangian mixing in rushton-impeller baffled-tank reactor. Chemical Engineering Science 58 (8), 1615 – 1629.

Chahed, J., Roig, V., Masbernat, L., 2003. Eulerian–Eulerian two-fluid model for turbulent gas–liquid bubbly flows. International Journal of Multiphase Flow 29 (1), 23–49.

Clift, R., Grace, J. R., Weber, M. E., 1978. Bubbles, Drops and Particles. Academic Press.

Cooke, M., Middleton, J. C., Bush, J. R., 1988. Mixing and mass transfer in filamentous fermentations. In: Proceedings of Second International Conference on Bioreactor Fluid Dynamics. pp. 37 – 64.

Coroneo, M., Montante, G., Paglianti, A., Magelli, F., 2011. CFD prediction of fluid flow and mixing in stirred tanks: Numerical issues about the RANS simulations. Computers & Chemical Engineering 35 (10), 1959 – 1968.

Corrsin, S., 1964. The isotropic turbulent mixer: Part II. Arbitrary Schmidt number. AIChE Journal 10 (6), 870–877.

Costes, J., Couderc, J. P., 1988. Study by Laser Doppler Anemometry of the Turbulent Flow Induced by a Rushton Turbine in a Stirred Tank: Influence of the Size of the Units I. Mean Flow and Turbulence. Chem. Eng. Sci. 43 (10).

Cronin, D., Nienow, A., Moody, G., 1994. Experimental study of mixing in a proto-fermenter agitated by dual rushton turbines. Food and Bioproducts Processing: Transactions of the Institution of of Chemical Engineers, Part C 72 (1), 35–40, cited By 45.

Csanady, G. T., 1963. Turbulent diffusion of heavy particles in the atmosphere. Journal of the Atmospheric Sciences 20, 201–208.

Cui, Y. Q., van der Lans, R. G. J. M., Luyben, K. C. A. M., 1996a. Local power uptake in gas-liquid systems with single and multiple rushton turbines. Chemical Engineering Science 51 (11), 2631–2636.

Cui, Y. Q., Van Der Lans, R. G. J. M., Noorman, H. J., Luyben, K. C. A. M., 1996b. Compartment mixing model for stirred reactors with multiple impellers. Chemical Engineering Research and Design 74 (2), 261–271.

Darwin, C., 1953. Note on hydrodynamics. Mathematical Proceedings of the Cambridge Philosophical Society 49 (02), 342–354.

Davidson, P. A., 2004. Turbulence: An Introduction for Scientists and Engineers. Oxford University Press Inc., New York, USA.

Deen, N., 2001. An experimental and computational study of fluid dynamics in gas-liquid chemical reactors. Ph.D. thesis, Aalborg University, Denmark.

Deglon, D. A., Meyer, C. J., 2006. CFD modelling of stirred tanks: Numerical considerations. Minerals Eng. 19 (10), 1059–1068.

Delafosse, A., Collignon, M.-L., Calvo, S., Delvigne, F., Crine, M., Thonart, P., Toye, D., 2014. CFD-based compartment model for description of mixing in bioreactors. Chemical Engineering Science 106 (0), 76 – 85.

Delafosse, A., Line, A., Morchain, J., Guiraud, P., 2008. LES and URANS simulations of hydrodynamics in mixing tank: Comparison to PIV experiments. Chem. Eng. Res. Des. 86 (12), 1322–1330.

Derksen, J. J., van den Akker, H. E. A., 1999. Large eddy simulations on the flow driven by a rushton turbine. AIChE Journal 45 (2), 209–221.

Deutsch, E., Simonin, O., 1991. Large eddy simulation applied to the motion of particles in stationary homogeneous fluid turbulence. In: Turbulence Modification in Multiphase Flows, American Society of Mechanical Engineers (ASME), Fluids Engineering Division (FED). Vol. 110. pp. 35–42.

Drew, D. A., 1983. Mathematical modeling of two-phase flow. Annual Review of Fluid Mechanics 15, 261–291.

Drew, D. A., Passman, S. L., 1999. Theory of Multicomponent Fluids. Vol. 135 of Applied Mathematical Sciences. Springer-Verlag New York, Inc., New York, USA.

Elghobashi, S. E., Abou-Arab, T. W., 1983. A two-equation turbulence model for two-phase flows. Physics of Fluids 26, No. 4, 931.

Enwald, H., Peirano, E., Almstedt, A. ., 1996. Eulerian two-phase flow theory applied to fluidization. International Journal of Multiphase Flow 22 (Suppl. 1), 21–66.

Fluent, 2006. FLUENT 6.3 User's Guide. Fluent Inc.

Fluent, 2009. Ansys Fluent 12.0 Documentation. Ansys Inc.

Fox, R. O., 2003. Computational Models for Turbulent Reacting Flows. Cambridge Series in Chemical Engineering. Cambridge University Press.

Gentric, C., Mignon, D., Bousquet, J., Tanguy, P., 2005. Comparison of mixing in two industrial gas-liquid reactors using CFD simulations. Chemical Engineering Science 60 (8-9), 2253 – 2272, 5th International Symposium on Mixing in Industrial Processes (ISMIP5).

Geurst, J. A., 1985. Virtual mass in two-phase bubbly flow. Physica A: Statistical Mechanics and its Applications 129 (2), 233–261.

Ghobadian, A., Vásquez, S. A., 2007. A general purpose implicit coupled algorithm for the solution of eulerian multiphase transport equation. In: Proceedings of ICMF 2007, 6th International Conference on Multiphase Flow, Leipzig, Germany.

Grenville, R. K., Nienow, A. W., 2004. Handbook of Industrial Mixing: Science and Practice. John Wiley & Sons, Inc., Hoboken, NJ, Ch. 9.

Groen, D. J., 1994. Macromixing in bioreactors. Ph.D. thesis, Delft University of Technology, The Netherlands.

Günyol, Ö., Mudde, R. F., 2007a. Hydrodynamics of aerated stirred tanks. In: 6th International Conference on Multiphase Flow (ICMF 2007), Leipzig, Germany, July 9–13.

Günyol, Ö., Mudde, R. F., 2007b. Numerical investigation of an aerated stirred tank with a rushton impeller. In: 8th International Conference on Gas-Liquid and Gas-Liquid-Solid Reactor Engineering (GLS8), New Delhi, India, December 16–19.

Günyol, Ö., Mudde, R. F., 2009. Computational study of hydrodynamics of a standard stirred tank reactor and a large-scale multi-impeller fermenter. International Journal for Multiscale Computational Engineering 7 (6), 559–576.

Haberman, W. L., Morton, R. K., 1953. An experimental investigation of the drag an shape of air bubbles rising in various liquids. Technical Report 802, The David W. Taylor Model Basin, Washington, DC.

Hagesæther, L., 2002. Coalescence and break-up of drops and bubbles. Ph.D. thesis, Norwegian University of Science and Technology, Trondheim, Norway.

Hagesæther, L., Jakobsen, H. A., Svendsen, H. F., 2002. A model for turbulent binary breakup of dispersed fluid particles. Chemical Engineering Science 57 (16), 3251 – 3267.

Harmathy, T. Z., 1960. Velocity of large drops and bubbles in media of infinite or restricted extent. AIChE Journal 6 (2), 281–288.

Hartmann, H., Derksen, J. J., Van Den Akker, H. E. A., 2004. Macroinstability uncovered in a Rushton turbine stirred tank by means of LES. AIChE Journal 50 (10), 2383–2393, cited By 41.

Hartmann, H., Derksen, J. J., van den Akker, H. E. A., 2006. Mixing times in a turbulent stirred tank by means of LES. AIChE Journal 52 (11), 3696–3706.

Harvey, A. D., Rogers, S. E., 1996. Steady and Unsteady Computation of Impeller-Stirred Reactors. AIChE Journal 42 (10), 2701–2712.

Hayashi, K., Tomiyama, A., 2009. A drag correlation of fluid particles rising through stagnant liquids in vertical pipes at intermediate reynolds numbers. Chemical Engineering Science 64 (12), 3019–3028.

Heijnen, J. J., Hols, J., van der Lans, R. G. J. M., van Leeuwen, H. L. J. M., Mulder, A., Weltevrede, R., 1997. A simple hydrodynamic model for the liquid circulation velocity in a full-scale two- and three-phase internal airlift reactor operating in the gas recirculation regime. Chemical Engineering Science 52 (15), 2527 – 2540.

Hinze, J. O., 1975. Turbulence, 2nd Edition. McGraw-Hill, Inc.

Hounslow, M., Ryall, R., Marshall, V., 1988. A discretized population balance for nucleation, growth, and aggregation. AIChE Journal 34 (11), 1821–1832.

Hughmark, G. A., 1980. Power requirements and interfacial area in gas-liquid turbine agitated systems. Industrial & Engineering Chemistry Process Design and Development 19 (4), 638–641.

Ishii, M., Hibiki, T., 2006. Thermo-fluid dynamics of two-phase flow. Springer Science+Business Media, Inc., New York, USA.

Ishii, M., Zuber, N., 1979. Drag coefficient and relative velocity in bubbly, droplet or particulate flows. AIChE Journal 25 (5), 843–855.

Jaworski, Z., Bujalski, W., Otomo, N., Nienow, A., 2000. CFD study of homogenization with dual rushton turbines-comparison with experimental results. Part I: Initial studies. Chemical Engineering Research and Design 78 (3), 327–333, cited By 63.

Joshi, J. B., Pandit, A. B., Sharma, M. M., 1982. Mechanically agitated gas-liquid reactors. Chemical Engineering Science 37 (6), 813–844, cited By (since 1996): 86.

Khopkar, A. R., Ranade, V. V., 2006. CFD simulation of gas–liquid stirred vessel: VC, S33, and L33 flow regimes. AICHE Journal 52 (5), 1654–1672.

Kolev, N. I., 2007. Multiphase Flow Dynamics 2, Thermal and Mechanical Interactions, 3rd Edition. Springer-Verlag Berlin Heidelberg.

Kresta, S. M., Paul, E. L., 2004. Handbook of Industrial Mixing: Science and Practice. John Wiley & Sons, Inc., Hoboken, NJ, Ch. 2.

Kukukova, A., Aubin, J., Kresta, S. M., 2009. A new definition of mixing and segregation: Three dimensions of a key process variable. Chemical Engineering Research and Design 87 (4), 633–647.

Laakkonen, M., 2006. Development and validation of mass transfer models for the design of agitated gas-liquid reactors. Ph.D. thesis, Helsinki University of Technology, Finland.

Laakkonen, M., Moilanen, P., Alopaeus, V., Aittamaa, J., 2007. Modelling local bubble size distributions in agitated vessels. Chemical Engineering Science 62 (3), 721 – 740.

Lahey, R. T., Lopez de Bertodano, M., Jones, O. C., 1993. Phase distribution in complex geometry conduits. Nuclear Engineering and Design 141 (1-2), 177–201.

Lance, M., Bataille, J., 1991. Turbulence in the liquid phase of a uniform bubbly air–water flow. Journal of Fluid Mechanics 222, 95–118.

Lance, M., Marie, J. L., Bataille, J., 1991. Homogeneous turbulence in bubbly flows. Journal of Fluids Engineering, Transactions of the ASME 113 (2), 295–300.

Lane, G., 2005a. Computational modelling of gas-liquid flow in stirred tanks. Ph.D. thesis, The University of Newcastle, Australia.

Lane, G., Schwarz, M., Evans, G., 2005b. Numerical modelling of gas-liquid flow in stirred tanks. Chemical Engineering Science 60 (8-9), 2203 – 2214, 5th International Symposium on Mixing in Industrial Processes (ISMIP5).

Lane, G. L., Schwarz, M. P., Evans, G. M., 2000. Modelling of the interaction between gas and liquid in stirred vessels. In: Proceedings of the 10th European Conference on Mixing. Delft, The Netherlands, pp. 197–204.

Larsson, G., Törnkvist, M., Ståahl Wernersson, E., Trägåardh, C., Noorman, H., Enfors, S.-O., 1996. Substrate gradients in bioreactors: Origin and consequences. Bioprocess Engineering 14 (6), 281–289.

Lathouwers, D., 1999. Modelling and simulation of turbulent bubbly flow. Ph.D. thesis, Delft University of Technology, The Netherlands.

Launder, B. E., Spalding, D. B., 1974. The numerical computation of turbulent flows. Computer Methods in Applied Mechanics and Engineering 3 (2), 269–289.

Lister, J., Smit, D., Hounslow, M., 1995. Adjustable discretized population balance for growth and aggregation. AIChE Journal 41 (3), 591–603.

Luo, H., 1993. Coalescence, breakup and liquid circulation in bubble column reactors. Ph.D. thesis, Norwegian University of Science and Technology, Trondheim, Norway.

Luo, H., Svendsen, H. F., 1996. Theoretical model for drop and bubble breakup in turbulent dispersions. AIChE Journal 42 (5), 1225–1233.

Luo, J., Issa, R., Gosman, A., 1994. Prediction of impeller-induced flows in mixing vessels using multiple frames of reference. In: 8th European Conference on Mixing. No. 136 in Institution of Chemical Engineers Symposium Series. Cambridge, England, pp. 549–556.

Luo, J. Y., Gosman, A. D., Issa, R. I., Middleton, J. C., Fitzgerald, M. K., 1993. Full flow field computation of mixing in baffled stirred vessels. Chemical Engineering Research and Design 71 (A3), 342–344.

Magelli, F., Fajner, D., Nocentini, M., Pasquali, G., 1990. Solid distribution in vessels stirred with multiple impellers. Chemical Engineering Science 45 (3), 615–625.

Magelli, F., Montante, G., Pinelli, D., Paglianti, A., 2013. Mixing time in high aspect ratio vessels stirred with multiple impellers. Chemical Engineering Science 101, 712 – 720.

Magnaudet, J., Eames, I., 2000. The motion of high-Reynolds-number bubbles in inhomogeneous flows. Annual Review of Fluid Mechanics 32, 659–708.

Magnaudet, J., Legendre, D., 1997. Some aspects of the lift force on a spherical bubble. Applied Scientific Research 58, 441–461.

Manninen, M., Taivassalo, V., Kallio, S., 1996. On the mixture model for multiphase flow. VTT Publications 288, Technical Research Centre of Finland.

Marshall, E. M., Bakker, A., 2003. Computational Fluid Mixing. Fluent Inc., Lebanon, New Hampshire, USA.

Maxey, M. R., Riley, J. J., 1983. Equation of motion for a small rigid sphere in a nonuniform flow. Physics of Fluids 26 (4), 883–889.

Merle, A., Legendre, D., Magnaudet, J., 2005. Forces on a high-Reynolds-number spherical bubble in a turbulent flow. Journal of Fluid Mechanics 532, 53–62.

Middleton, J. C., 1992. Gas-liquid dispersion and mixing. In: N. Harnby, M. F. E., Nienow, A. W. (Eds.), Mixing in the Process Industries, 2nd Edition. Butterworth-Heinemann, Oxford.

Middleton, J. C., Smith, J. M., 2004. Handbook of Industrial Mixing: Science and Practice. John Wiley & Sons, Inc., Hoboken, NJ, Ch. 11.

Mijnarends, R., 2007. Euler-Euler modeling of air-water flow in a flat bubble column. Master's thesis, Delft University of Technology, The Netherlands.

Montante, G., Magelli, F., 2004. Liquid Homogenization Characteristics in Vessels Stirred with Multiple Rushton Turbines Mounted at Different Spacings: CFD Study and Comparison with Experimental Data. Chemical Engineering Research and Design 82 (9), 1179 – 1187, in Honour of Professor Alvin W. Nienow.

Montante, G., Motk, M., Jahoda, M., Magelli, F., 2005. CFD simulations and experimental validation of homogenisation curves and mixing time in stirred Newtonian and pseudoplastic liquids. Chemical Engineering Science 60 (89), 2427 – 2437, 5th International Symposium on Mixing in Industrial Processes (ISMIP5).

Moore, D. W., 1963. The boundary layer on a spherical gas bubble. Journal of Fluid Mechanics 16, 161–176.

Moore, D. W., 1965. The velocity of rise of distorted gas bubbles in a liquid of small viscosity. Journal of Fluid Mechanics 23 (04), 749–766.

Mudde, R. F., Simonin, O., 1999. Two- and three-dimensional simulations of a bubble plume using a two-fluid model. Chemical Engineering Science 54 (21), 5061–5069.

Murthy, B. N., Joshi, J. B., 2008. Assessment of standard $k - \varepsilon$, RSM and LES turbulence models in a baffled stirred vessel agitated by various impeller designs. Chem. Eng. Sci. 63 (22), 5468–5495.

Ng, K., Yianneskis, M., 2000. Observations on the distribution on energy dissipation in stirred vessels. Chem. Eng. Res. and Des. 78 (3), Part A, 334–3341.

Nienow, A. W., 1997. On impeller circulation and mixing effectiveness in the turbulent flow regime. Chemical Engineering Science 52 (15), 2557–2565.

Nienow, A. W., 1998. Hydrodynamics of stirred bioreactors. Applied Mechanics Reviews 51, 3–32.

Nienow, A. W., Warmoeskerken, M. C. G., Smith, J. M., Konno, M., 1985. On the flooding/loading transition and the complete dispersal condition in aerated vessels agitated by a rushton turbine. In: Proceedings of 5th European Conference on Mixing, Wurzburg, West-Germany. BHRA Fluid Engineering, Cranfield, England, pp. 143–154.

Nienow, A. W., Wisdom, D. J., Middleton, J. C., 1977. The effect of scale and geometry on flooding, recirculation, and power in gassed stirred vessels. In: Proceedings of 2nd European Conference on Mixing, Cambridge, England. BHRA Fluid Engineering, Cranfield, England, pp. F1.1–F1.16.

Noorman, H., 1993. Bioreactor Performance: The Large Scale. In U. Mortensen, K. Ch. A. M. Luyben and A. Moser, Nordic Programme on Bioprocess Engineering 1989–1993, Scientific Report, The Biotechnology Research Foundation, 73–81.

Noorman, H., 2011. An industrial perspective on bioreactor scale-down: What we can learn from combined large-scale bioprocess and model fluid studies. Biotechnology Journal 6 (8), 934–943.

Noorman, H., Enfors, S.-O., Hjertager, B., Larsson, G., Morud, D., Trägåardh, C., Törnkvist, M., 1994. Verification of integrated microbial and fluid dynamics: Saccharomyces cerevisiae production on 30 m^3 scale. In L. Alberghina, L. Frontali, P. Sensi, ECB6: Proceedings of the 6th European Congress on Biotechnology, 935–938.

Noorman, H., Hjertager, B. H., Morud, K., Trägåardh, C., Enfors, S.-O., Larsson, G., Törnkvist, M., 1993. Measurement and computational fluid dynamics simulation of Saccharomyces Cerevisiae production in a 30 m^3 stirred tank reactor. In U. Mortensen and H. Noorman, Proceedings of International Symposium on Bioreactor Performance, Helsingøor, Denmark, 15–17th March, 243–249.

Patterson, G. K., Paul, E. L., Kresta, S. M., Etchells III, A. W., 2004. Handbook of Industrial Mixing: Science and Practice. John Wiley & Sons, Inc., Hoboken, NJ, Ch. 13.

Poorte, R. E. G., Biesheuvel, A., 2002. Experiments on the motion of gas bubbles in turbulence generated by an active grid. Journal of Fluid Mechanics 461, 127–154.

Ramkrishna, D., 2000. Population Balances. Academic Press, San Diego.

Ranade, V. V., 1997. An efficient computational model for simulating flow in stirred vessels: A case of rushton turbine. Chemical Engineering Science 52 (24), 4473–4484.

Ranade, V. V., 2002. Computational Flow Modeling for Chemical Reactor Engineering. Academic Press, New York, NY.

Ranade, V. V., Tayalia, Y., Krishnan, H., 2002a. CFD predictions of flow near impeller blades in baffled stirred vessels: Assessment of computational snapshot approach. Chem. Eng. Com. 189(7), 895–922.

Ranade, V. V., Tayalia, Y., Krishnan, H., 2002b. CFD predictions of flow near impeller blades in baffled stirred vessels: Assessment of computational snapshot approach. Chemical Engineering Communications 189 (7), 895–922.

Revill, B. K., 1982. Pumping capacity of disc turbine agitators - a literature review. Proc. 4th Eur. Conf. on Mixing, Noordwijkerhout, The Netherlands, BHRA Fluid Eng., Cranfield, England, 11–24.

Richardson, J. F., Zaki, W. N., 1954. Sedimentation and fluidisation: Part I. Transactions of IChemE 32, 35–53.

Roušar, I., van den Akker, H. E. A., 1994. LDA measurements of liquid velocities in sparged agitated tanks with single and multiple Rushton turbines. In: Proceedings of the 8th European Conference on Mixing, IChemE. Rugby, UK, pp. 89–96.

Saffman, P. G., 1965. The lift on a small sphere in a slow shear flow. Journal of Fluid Mechanics 22 (02), 385–400.

Sanyal, J., Marchisio, D. L., Fox, R. O., Dhanasekharan, K., 2005. On the comparison between population balance models for CFD simulation of bubble columns. Industrial & Engineering Chemistry Research 44 (14), 5063–5072.

Schiller, V. L., Naumann, A., 1933. Über die grundlegenden Berechnungen bei der Schwerkraftaufbereitung. Zeitschrift des Vereines deutscher Ingenieure 77 (12), 318–320.

Simonin, O., 1990. Eulerian formulation for particle dispersion in turbulent two-phase flows. In: Proceedings of the Fifth Workshop on Two-Phase Flow Predictions. Erlangen, Germany, pp. 156–166.

Smith, J., Warmoeskerken, M., Zeef, E., 1987. Flow conditions in vessels dispersing gases in liquids with multiple impellers. In: Ho, C. S., Oldshue, J. Y. (Eds.), Biotechnology Processes. AIChE, New York, pp. 107–115.

Smith, J. M., Warmoeskerken, M. C. G., 1985. The dispersion of gases in liquids with turbines. In: Proceedings of 5th European Conference on Mixing, Wurzburg, West-Germany. BHRA Fluid Engineering, Cranfield, England, pp. 115–126.

Sokolichin, A., Eigenberger, G., Lapin, A., 2004. Simulation of buoyancy driven bubbly flow: Established simplifications and open questions. AIChE Journal 50 (1), 24–45.

Spelt, P. D. M., Biesheuvel, A., 1997. On the motion of gas bubbles in homogeneous isotropic turbulence. Journal of Fluid Mechanics 336, 221–244.

Spelt, P. D. M., Biesheuvel, A., 1998. Dispersion of gas bubbles in large-scale homogeneous isotropic turbulence. Applied Scientific Research (The Hague) 58 (1-4), 463–482.

Spelt, P. D. M., Sangani, A. S., 1998. Properties and averaged equations for flows of bubbly liquids. Flow, Turbulence and Combustion 58 (1-3), 337–386.

Speziale, C. G., Sarkar, S., Gatski., T. B., 1991. Modelling the Pressure-Strain Correlation of Turbulence: An Invariant Dynamical Systems Approach. J. Fluid Mech. (227), 245–272.

Stuhmiller, J. H., 1977. The influence of interfacial pressure forces on the character of two-phase flow model equations. International Journal of Multiphase Flow 3 (6), 551–560.

Tatterson, G. B., 1991. Fluid Mixing and Gas Dispersion in Agitated Tanks. McGraw-Hill Inc., New York.

Tchen, C. M., 1947. Mean value and correlation problems connected with the motion of small particles suspended in a turbulent fluid. Ph.D. thesis, Delft University of Technology, The Netherlands.

Thai Van, D., Minier, J. P., Simonin, O., Freydier, P., Olive, J., 1994. Multidimensional two-fluid model computation of turbulent dispersed two-phase flows. In: Numerical Methods in Multiphase Flows, American Society of Mechanical Engineers (ASME), Fluids Engineering Division (FED). Vol. 185. pp. 277–291.

Tominaga, Y., Stathopoulos, T., 2007. Turbulent Schmidt numbers for CFD analysis with various types of flowfield. Atmospheric Environment 41 (37), 8091 – 8099.

Tomiyama, A., 1998. Struggle with computational bubble dynamics. In: Proceedings of ICMF 1998, 3rd International Conference on Multiphase Flow. Lyon, France, pp. 1–18.

Tomiyama, A., Tamai, H., Zun, I., Hosokawa, S., 2002. Transverse migration of single bubbles in simple shear flows. Chemical Engineering Science 57 (11), 1849–1858.

van der Lans, R., 1985. Hydrodynamics of a bubble column loop reactor. Ph.D. thesis, Delft University of Technology, The Netherlands.

van't Riet, K., Smith, J. M., 1974. The hydrodynamics of rushton turbine agitator blades. In: Proceedings of 1st European Conference on Mixing and Centrifugal Separation, Cambridge, England. BHRA Fluid Engineering, Cranfield, England, pp. B2.17–B2.23.

van't Riet, K., Smith, J. M., 1975. The trailing vortex system produced by Rushton turbine agitators. Chem. Eng. Sci. 30 (9), 1093–1105.

van't Riet, K., Tramper, J., 1991. Basic Bioreactor Design. Marcel Dekker Inc. New York.

Vásquez, S. A., Ivanov, V. A., 2000. A phase coupled method for solving multi-phase problems on unstructured meshes. In: Proceedings of ASME FEDSM'00: ASME 2000 Fluids Engineering Division Summer Meeting, Boston, Massachusetts, USA. Vol. 251. pp. 743–748.

Venneker, B. C. H., 1999. Turbulent flow and gas dispersion in stirred vessels with pseudoplastic liquids. Ph.D. thesis, Delft University of Technology, The Netherlands.

Viollet, P. L., Simonin, O., 1994. Modelling dispersed two-phase flows: Closure, validation and software development. Applied Mechanics Reviews 47 (No. 6, Part 2), S80–S84.

Vrábel, P., Van der Lans, R., Van der Schot, F., Luyben, K., Xu, B., Enfors, S.-O., 2001. CMA: Integration of fluid dynamics and microbial kinetics in modelling of large-scale fermentations. Chemical Engineering Journal 84 (3), 463–474, cited By 23.

Vrábel, P., Van Der Lans, R. G. J. M., Cui, Y. Q., Luyben, K. C. A. M., 1999. Compartment model approach: Mixing in large scale aerated reactors with multiple impellers. Chemical Engineering Research and Design 77 (4), 291–302.

Vrábel, P., Van Der Lans, R. G. J. M., Luyben, K. C. A. M., Boon, L., Nienow, A. W., 2000. Mixing in large–scale vessels stirred with multiple radial or radial and axial up–pumping impellers: modelling and measurements. Chemical Engineering Science 55, 5881–5896.

Warmoeskerken, M. M. C. G., Smith, J. M., 1984. Flooding transition with gassed Rushton turbines. In: Fluid Mixing II. Institution of Chemical Engineers, Symposium Series No. 89, Bradford, England, pp. 59–67.

Warmoeskerken, M. M. C. G., Smith, J. M., 1985. Flooding of disc turbines in gas-liquid dispersions: A new description of the phenomenon. Chemical Engineering Science 40 (11), 2063–2071.

Wörner, M., 2003. A compact introduction to the numerical modeling of multiphase flows. Wissenschaftliche Berichte, FZKA 6932, Forschungszentrum Karlsruhe in der Helmholtz-Gemeinschaft.

Wu, H., Patterson, G., 1989. Laser-doppler measurements of turbulent-flow parameters in a stirred mixer. Chem. Eng. Sci. 44, 2207–2221.

Xu, B., Jahic, M., Enfors, S.-O., 1999. Modeling of overflow metabolism in batch and fed-batch cultures of escherichia coli. Biotechnology Progress 15 (1), 81–90, cited By 101.

Yeoh, S., Papadakis, G., Yianneskis, M., 2005. Determination of mixing time and degree of homogeneity in stirred vessels with large eddy simulation. Chemical Engineering Science 60 (89), 2293 – 2302, 5th International Symposium on Mixing in Industrial Processes (ISMIP5).

Yeoh, S. L., Papadakis, G., Yianneskis, M., 2004. Numerical simulation of turbulent flow characteristics in a stirred vessel using the LES and RANS approaches with the sliding/deforming mesh methodology. Chem. Eng. Res. and Des. 82, Part A, 834–848.

Zhang, Y., Yang, C., Mao, Z.-S., 2008. Large eddy simulation of the gas-liquid flow in a stirred tank. AIChE Journal 54 (8), 1963–1974.

Zhou, G., Kresta, S. M., 1996. Distribution of energy between convective and turbulent flow for three frequently used impellers. Chem. Eng. Res. and Des. 74 (3), 379–389.

Appendix A

Algebraic slip mixture model (ASMM)

The Mixture model or the so-called Algebraic Slip model is a simplification to the standard Euler–Euler model. A single set of continuity and momentum equations are solved for the mixture, and the volume fraction equation is solved for the gas phase. The relative velocities between the phases are given by algebraic expressions. The continuity equation for the mixture is obtained by summing up the continuity equations of both phases as given in Eq. 4.20:

$$\frac{\partial}{\partial t}(\rho_{\mathrm{m}}) + \nabla \cdot (\rho_{\mathrm{m}} \mathbf{U}_{\mathrm{m}}) = 0 \tag{A.1}$$

The mixture density ρ_{m} and the mass–averaged velocity $\mathbf{U}_{\mathrm{m}}$ appearing in the equations are defined as:

$$\rho_{\mathrm{m}} = \alpha_1 \rho_1 + \alpha_2 \rho_2 \tag{A.2}$$

$$\mathbf{U}_{\mathrm{m}} = \sum_{k=1}^{2} \frac{\alpha_k \rho_k}{\rho_{\mathrm{m}}} \mathbf{U}_k = \sum_{k=1}^{2} c_k \mathbf{U}_k, \tag{A.3}$$

where the mass fraction of phase k is:

$$c_k = \frac{\alpha_k \rho_k}{\rho_{\mathrm{m}}}. \tag{A.4}$$

When the momentum equation for all phases, as given in Eq. 4.34, are summed up, the interfacial force terms drop out and the momentum equation for the mixture is obtained:

$$\frac{\partial}{\partial t}(\rho_{\mathrm{m}} \mathbf{U}_{\mathrm{m}}) + \nabla \cdot (\rho_{\mathrm{m}} \mathbf{U}_{\mathrm{m}} \mathbf{U}_{\mathrm{m}}) = -\nabla P + \nabla \cdot (\underline{\underline{\mathbf{T}}}_{\mathrm{m}} + \underline{\underline{\mathbf{T}}}^{\mathrm{t}}_{\mathrm{m}}) + \nabla \cdot \underline{\underline{\mathbf{T}}}_{\mathrm{m,d}} + \rho_{\mathrm{m}} \mathbf{g} + \mathbf{F} \tag{A.5}$$

F is the body force term. It is usually assumed that the phase pressures are equal, so the mixture pressure reduces to $P_{\mathrm{m}} = \alpha_1 P_1 + \alpha_2 P_2 = P$. The mixture viscous, turbulent and diffusion stress tensors are defined respectively as:

$$\underline{\underline{\mathbf{T}}}_{\mathrm{m}} = \mu_{\mathrm{m}}(\nabla \mathbf{U}_{\mathrm{m}} + \nabla \mathbf{U}_{\mathrm{m}}^{T}) - \frac{2}{3}\mu_{\mathrm{m}} \nabla \cdot \mathbf{U}_{\mathrm{m}} \underline{\underline{\mathbf{I}}} \tag{A.6}$$

$$\underline{\underline{\mathbf{T}}}_{\mathrm{m}}^{\mathrm{t}} = \mu_{\mathrm{m}}^{\mathrm{t}} \left[(\nabla \mathbf{U}_{\mathrm{m}} + \nabla \mathbf{U}_{\mathrm{m}}^{T}) - \frac{2}{3} \nabla \cdot \mathbf{U}_{\mathrm{m}} \underline{\underline{\mathbf{I}}} \right] - \frac{2}{3} \rho_{\mathrm{m}} k_{\mathrm{m}} \underline{\underline{\mathbf{I}}} \tag{A.7}$$

$$\underline{\underline{\mathbf{T}}}_{\mathrm{m,d}} = -c_2 \rho_m \, \mathbf{U}_{d,2} \, \mathbf{U}_{d,2}, \tag{A.8}$$

where $\mu_{\mathrm{m}} = \alpha_1 \, \mu_1 \, + \alpha_2 \, \mu_2$ is the mixture viscosity, $\mu_{\mathrm{m}}^{\mathrm{t}}$ is the mixture turbulent viscosity, and k_{m} is the mixture turbulent kinetic energy density. The turbulent stress term in the mixture momentum equation is closed by solving a standard $k - \varepsilon$ model for the mixture phase (Fluent, 2006).

The drift velocity $\mathbf{U}_{d,2}$ is the velocity of the dispersed phase relative to the centre of the mixture mass. It is related to the relative (slip) velocity between the phases, $\mathbf{U}_{21} = \mathbf{U}_2 - \mathbf{U}_1$, as:

$$\mathbf{U}_{d,2} = (1 - c_2)\mathbf{U}_{21}. \tag{A.9}$$

Assuming that a local equilibrium between the phases is reached over a short length scale, the algebraic relation for the slip velocity is given by Manninen et al. (1996) as:

$$\mathbf{U}_{21} = \frac{\tau_2}{f_D} \frac{(\rho_2 - \rho_{\mathrm{m}})}{\rho_2} \, \mathbf{a} \tag{A.10}$$

For turbulent flows, the slip velocity contains a diffusion term due to the dispersion appearing in the dispersed phase momentum equation (Fluent, 2006):

$$\mathbf{U}_{21} = \frac{\tau_2}{f_D} \frac{(\rho_2 - \rho_{\mathrm{m}})}{\rho_2} \, \mathbf{a} - \frac{\nu_{\mathrm{m}}^{\mathrm{t}}}{\alpha_2 \sigma_D} \, \nabla \alpha_1 \tag{A.11}$$

The drag function, $f_D = C_{\mathrm{D}} Re/24$, is calculated from the drag model used, e.g. from Eq. 6.64. The particle relaxation time τ_2 is calculated from

$$\tau_2 = \frac{\rho_2 d_2^2}{18 \mu_1}, \tag{A.12}$$

where $\nu_{\mathrm{m}}^{\mathrm{t}}$ is the mixture turbulent kinematic viscosity, and the Prandtl dispersion coefficient takes the default value $\sigma_D = 0.75$. The acceleration of bubbles is calculated from:

$$\mathbf{a} = \mathbf{g} - (\mathbf{U}_{\mathrm{m}} \cdot \nabla)\mathbf{U}_{\mathrm{m}} - \frac{\partial \mathbf{U}_{\mathrm{m}}}{\partial t}. \tag{A.13}$$

Finally, the volume fraction equation for the secondary phase is obtained from the continuity equation for the secondary phase:

$$\frac{\partial}{\partial t}(\alpha_2 \rho_2) + \nabla \cdot (\alpha_2 \rho_2 \mathbf{U}_{\mathrm{m}}) = -\nabla \cdot (\alpha_2 \rho_2 \mathbf{U}_{d,2}). \tag{A.14}$$

Publications

Günyol, Ö. and Mudde, R.F., 2009. Computational study of hydrodynamics of a standard stirred tank reactor and a large-scale multi-impeller fermenter. International Journal for Multiscale Computational Engineering, 7(6), pp. 559-576.

Günyol, Ö., Noorman, H.J. and Mudde, R.F., 2009. CFD simulations of a large-scale fermenter with multiple impellers. In proceedings of 8th World Congress of Chemical Engineering, Topical conference 9th International Conference on Gas-Liquid and Gas-Liquid-Solid Reactor Engineering (GLS9), Montréal, Quebec, Canada, August 23–27.

Günyol, Ö., Noorman, H.J. and Mudde, R.F., 2008. CFD simulations of a large-scale aerated reactor with multiple impellers. In proceedings of Netherlands Process Technology Symposium 8, Veldhoven, The Netherlands, October 28.

Günyol, Ö., Noorman, H.J. and Mudde, R.F., 2008. CFD simulations of a large-scale aerated reactor with multiple impellers. In proceedings of Computational Fluid Dynamics in Chemical Reaction Engineering V, Whistler, British Columbia, Canada, June 15-20.

Günyol, Ö. and Mudde, R.F., 2007. Numerical Investigation of an Aerated Stirred Tank with a Rushton Impeller. In proceedings of 8th International Conference on Gas-Liquid and Gas-Liquid-Solid Reactor Engineering (GLS8), New Delhi, India, December 16–19, 2007.

Günyol, Ö. and Mudde, R.F., 2007. Hydrodynamics of aerated stirred tanks. In proceedings of 6th International Conference on Multiphase Flow (ICMF 2007), Leipzig, Germany, July 9–13, 2007.

Acknowledgements

The journey that brings me finally writing those very last few sentences of this thesis has started in a rather strange way. I was in Hamburg early 2005, where I'd completed my master's thesis and I had lost several months waiting for the outcome of my PhD application to a position at TU Delft. It had been told to me that I'd get the position almost for sure, assuring me not to make further applications, but it ended up being postponed as the fund was diverted to another project for some political reason. This left me naturally in deep disappointment. Later, after a friend's notice, I applied to another position at TU Delft, though rather reluctantly due to the bitter experience I had previously. I happened to be invited for an interview for this position, which was on modelling of slugs in pipe flow, but I was still reluctant. With the strong encouragement and even pushing of my parents, I did go to the interview. A few weeks later, I got an email from Prof. Rob Mudde, who was, strangely, not the hiring professor of the position I'd applied for, though he had also interviewed me (I remember him asking me what shape a falling rain drop would take and why). The email went on in the common way saying "... unfortunately we will not offer you this position, because ...", but it had an uncommon surprising twist at the end: "... but I, myself, have a position on CFD of fermenters, which I want to offer you". The thing was, this position escaped from my attention completely as I was turned off by the title which by then sounded too biological to me, so I didn't even read the details of the post. After reading the project description, I realised that I was completely wrong and it was a far better fit to me, so I replied to Rob "Yes!!". Later, I understood that I was swapped with another applicant, my later friend and colleague Usama Kadri, who had applied for the Rob's position, but who really suited better to the position I'd initially applied for. What a chain of circumstances! It should be clear by now that without the pushing of my parents and the trust of Rob, I wouldn't have started this journey in the Netherlands at all.

Secondly, this project wouldn't have existed without the financial support provided by DSM. Here, I'd like to acknowledge also Henk Noorman, who was the DSM lead of the project, for fruitful discussions and technical support in the course of this project.

I'm also grateful to my smart MSc student and a good friend later, Runo Mijnarends, who did a great work with writing, repairing and improving Fluent subroutines painstakingly (e.g. the degassing boundary UDF which I also used in this thesis work).

Jay Sanyal and Sergio Vasquez, the senior multiphase developers from Fluent, are acknowledged as well for deep discussions on the technical aspects of the multiphase solver and support in the search of a more accurate representation of the interface

momentum exchange.

PhD times are not always pleasantly memorable, but I was lucky enough to have great officemates who turned long days, sleepless nights and weekends into fun! Thanks to Annekatrien Daalmans, Maria Silakova, Anton Gryzlov (well, not really an officemate, but he was sneaking all the time into our fun office!), Jos van't Westende, Zaki Saldi, Adrian Toader, Marco Zoetewij, Mohammed Kamali, Laurens van Campen. So many good memories were collected during those hard working years... I also enjoyed the occasional intellectual discussions and scientific debates with Luis Portela, Roel Belt, Rob and Usama. And Annekatrien, you're the super hero who managed to help every colleague in every possible way during those years! We sort of shared a common path along our individual journeys and I really felt assured at difficult times knowing that you were there.

Many friends through those long years helped me feeling at home in Delft and keeping a proper work–life balance (though I was not very good at this..). I would refrain naming them all here, but I'm really gratefull to them all for making my life in Delft really an enjoyable one. I'm specially thankful to Elvin and Gönenç; we've been sharing most of the important things in our lives over the last 12 years!

My sister Özlem and Mustafa, along with my parents Şeniz and Metin, you deserve a special thank for supporting me at every moment during this long journey with ups and downs. Özlem and Mustafa are the great artists behind the cover design of this thesis!

Finally, Tessa... Besides having had to listen stories about rising bubbles every time I was drinking a beer, you had to go with me through the rough times in the last 5 years of this journey; sacrificing holidays and weekends during the making of this thesis. If I were strong during those difficult times, it was because I felt your unconditional support at every moment. I hope to thank you in terms of many, many moments of happiness to come and to be shared with you...

About the author

Özgür Günyol was born on February 6, 1979 in Ankara, Turkey. In 1997, he graduated from the Ayşeabla High School in Ankara. He then started his university studies at the Middle East Technical University (METU) in Ankara, where he earned a BSc degree (with distinction) in Chemical Engineering in June 2001. In October 2001, he started his master's degree studies in Hamburg University of Technology (TUHH) in Hamburg, Germany, with a full scholarship granted by the German Academic Exchange Service (DAAD) and the Turkish Educational Foundation (TEV). He completed his master's thesis on "Flow field investigation of a falling drop at elevated pressures by using CFD simulation" in the Department of Heat and Mass Transfer under the supervision of Prof.Dr.-Ing. Rudolf Eggers and Prof.Dr.Dr.h.c. Frerich J. Keil at TUHH. In May 2004, he obtained his MSc degree (with high distinction) in Process Engineering at TUHH. He continued to work as a researcher in the same department until the end of 2004. In June 2005, he started working on his PhD research in the Department of Multi-Scale Physics (formerly known as the Kramers Laboratory), Delft University of Technology (TU Delft) in Delft, the Netherlands, under the supervision of Prof.Dr. Robert F. Mudde. This research group became later part of the newly formed Transport Phenomena group in the Chemical Engineering Department of TU Delft. The dissertation presented here is the result of this research. Since October 2010, he has been working as a Research manager – Process scientist at Unilever R&D in Vlaardingen, the Netherlands.